Heinz Ulbrich
Lucas Ginzinger
Editors

Motion and Vibration Control

Selected Papers from MOVIC 2008

Springer

Motion and Vibration Control

Heinz Ulbrich • Lucas Ginzinger
Editors

Motion and Vibration Control

Selected Papers from MOVIC 2008

Springer

Heinz Ulbrich
Technische Universität München
Garching
Germany

Lucas Ginzinger
Technische Universität München
Garching
Germany

ISBN-13: 978-1-4020-9437-8 e-ISBN-13: 978-1-4020-9438-5

Library of Congress Control Number: 2008939844

Printed on acid-free paper

9 8 7 6 5 4 3 2 1

springer.com

Table of Contents

Preface

During the last decades, the growth of micro-electronics has reduced the cost of computing power to a level acceptable to industry and has made possible sophisticated control strategies suitable for many applications. These developments owe most to breakthroughs in the field of mechatronics. Mechatronics combines various topics from the fields of engineering and mechanics, mathematics and computer science into an integrated approach. This interdisciplinary view on technical issues enables the improved design of sophisticated systems necessary to meet the increasing demands in technical applications. All topics related to such applications are addressed by the prestigious international MOVIC conferences.

The International Conference on Motion and Vibration Control (MOVIC) is held every two years. The goal is to stimulate interaction between researchers active in the area of motion and vibration control and all other fields related to mechatronics.

Since the MOVIC conference was launched in Japan in 1992, conferences were held in Japan in 1994 and 1996, Switzerland in 1998, Australia in 2000, Japan in 2002, the USA in 2004 and Korea in 2006. The conference has developed into a very productive international event for the advancement of motion and vibration control technology.

The ninth conference, MOVIC 2008, took place at the Technische Universität München, Germany, from September 15–18, 2008, chaired by Professor Heinz Ulbrich. The primary purposes of MOVIC 2008 are to promote scientific and technological exchange between researchers from around the world and to enhance the understanding and the dissemination of all different aspects in this challenging and fast growing field of research.

Motion and vibration control is a fundamental technology for the development of advanced "intelligent" mechanical and structural systems related to many applications in industry such as vehicle systems, robots, spacecraft, and rotating machinery, only to name a few. Often the implementation of high performance, low power consumption design is only possible with the use of this technology. It is also vital to the mitigation of natural hazards for large structures such as high-rise buildings and

tall bridges, and to the application of flexible structures such as space stations and satellites.

Recent innovations in relevant hardware, sensors, actuators, and software have facilitated new research in this area.

The main topics of the Symposium were:

- Mechatronics
- Application of Control Theory and Techniques
- Control Devices, Sensors and Actuators
- Rotor Dynamics and Control
- Smart Sensors and Sensor Network
- Smart Structures Space Structures and Control
- Vehicle Dynamics and Control
- Application of Neural Networks, Fuzzy Logic and Genetic Algorithms
- Biologically Inspired Mechanisms
- Control of Civil Infrastructures
- Control of Fluid/Structure Interaction
- Control of Micro and Nano Structures
- Control Technology for Tele-Operation Systems
- Damage Detection and Structural Health Monitoring
- Dynamics and Control of Multibody Systems
- Humanoid Robot Dynamics and Control
- ITS and Intelligent Control System
- Noise Control and 3D Sound Rendering
- Nonlinear Dynamical Systems
- Shock Protective Systems
- Structural Acoustics
- Structural Control against Wind and Earthquake Loading
- System Identification and Modeling
- Virtual Reality and Simulation

About 300 papers were submitted to this conference. All of these papers had to pass a review process. For each of the papers three reviews were required. After this process 170 papers were selected for oral presentation, and an additional 20 papers were presented as posters. The 37 contributions published in the present publication were rated as the best in the reviewing process.

Since many of the contributions are related to more than one of the topics stated above, the papers in this book are arranged in alphabetical order of the family name of the first author. The papers cover a wide range of the fascinating field of mechatronics, and address both theoretical work and applications.

The editors wish to thank all the participants (about 300, from 30 different countries) especially for their valuable contributions to the fast growing field of mechatronics. Special thanks are given to the reviewers, the invited lecturers and the session chairmen for making the conference the great success it was.

A special vote of thanks goes to the staff of the Institute of Applied Mechanics of the TUM for their great help and excellent work to make the conference run smoothly. Last but not least I especially thank my Co-Chairman of MOVIC 2008, Dipl.-Ing. Lucas Ginzinger, for the excellent job he did in organizing MOVIC 2008.

Heinz Ulbrich
(Chairman MOVIC 2008)
Garching, September 2008

Active and Passive Switching Vibration Control with Lyapunov Function

Naoto Abe and Masayoshi Fujita

Abstract This paper presents experimental results for the switching vibration control method based on Lyapunov function of vibration system; switching between tuned mass damper and active mass damper without any thresholds. The vibration control device is a pendulum type mass damper which works as tuned and active mass damper. Experimental results show that the proposed switching vibration control has better performance than full time tuned and active mass damper.

1 Introduction

Active mass damper shows a good performance in the vibration control to winds and small earthquakes. However, it needs high power and an enough mobile range of the additive mass. Therefore, it cannot be useful against big earthquakes. On the contrary, tuned mass damper or dynamic vibration absorber, which is passive vibration control method, is effective against a specific frequency vibration by big earthquakes without any power. However precise parameters are required.

Active-Passive Composite Tuned Mass Damper (APTMD) has been proposed based on the above-mentioned two methods of the vibration control [2, 3] and has been implemented [1]. We proposed an effective switching methodology between the passive and active mass damper on the same structure of APTMD [4, 5]. APTMD has two additive cascaded masses; one is a passive mass damper and the other is an active mass damper attached on the passive mass damper. The vibration control structure has the following problems; the mass ratio of the passive to active

Naoto Abe
Meiji University, Higashimita, Tama-ku Kawasaki, 214-8571, Japan;
E-mail: abe@messe.meiji.ac.jp

Masayoshi Fujita
Meiji University, Higashimita, Tama-ku Kawasaki, 214-8571, Japan

H. Ulbrich and L. Ginzinger (eds.), Motion and Vibration Control, 1–10.

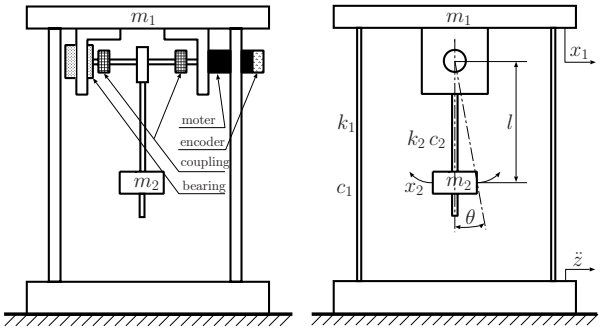

Fig. 1 Construction of the vibration system.

could not be solved, and the dynamic vibration absorber did not work as the optimal one since parameters were not equal to the design stage.

In this paper, a pendulum type mass damper is used, which is designed as the tuned mass damper, i.e. dynamic vibration absorber. And the pendulum has actuator, sensor and controller. Therefore the pendulum works as the dynamic vibration absorber without control input or as the active mass damper with actuator power by the proposed switching methodology. One mass is used by this structure as the tuned mass damper and the active mass damper.

In Section 2, we show our experimental model. Two switching control methodologies are introduced in Section 3. One is based of the energy of the vibration structure [4, 5], which had good property at the APTMD structure. The second one is using Lyapunov function, in other words, using derivative of a quadratic form along the dynamics. In Section 4, experimental results against two types of earthquakes are shown.

2 Structure of Experiment

The experimental structure is shown in Figure 1. The pendulum type dynamic vibration absorber is set under the simple vibration structure and the pendulum is controlled by an actuator. The structure has two-degree-of-freedom. At this structure, the dynamic vibration absorber is equal to the active mass damper and it is easy to set the stiffness coefficient by the pendulum length. The solution of the mass ratio of passive and active mass damper problem, which occurred in APTMD structure, is not necessary. The equations of the motion are derived by the structure model in Figure 1:

$$\begin{cases} m_1(\ddot{x}_1 + \ddot{z}) + k_1 x_1 + c_1 \dot{x}_1 + k_2(x_1 - x_2) + c_2(\dot{x}_1 - \dot{x}_2) = -u \\ m_2(\ddot{x}_2 + \ddot{z}) + k_2(x_2 - x_1) + c_2(\dot{x}_2 - \dot{x}_1) = u \end{cases} \tag{1}$$

where displacement x_2 is approximated by $x_2 = l\theta$ and the stiffness k_2 is derived by the pendulum length l, the mass m_2 and gravity acceleration g as $k_2 = m_2 g/l$. u is an input torque into the actuator and $\ddot{z}$ is earthquake acceleration.

The values of parameters are shown in Table 1. The mass ratio of the structure and additional mass is about 4.9%. The stiffness and damping coefficients have been identified by the sweep excitation and decay rate of the initial response, respectively. The design of the dynamic vibration absorber has tuned the length of the arm with obtained c_2 to match the height of two resonance points of the gain diagram.

The gain diagram of the identified parameters is shown in Figure 2 without limitation of the power and actuator's stroke range. In the active control case, the optimal regulator with state weighting matrix $Q = \mathrm{diag}[250\ \ 100\ \ 500\ \ 5]$ and input weighting $R = 1$ is used as the control law. It is known that $\mathcal{H}_\infty$ control has been effective in the active control case, however, our purpose is switching control between passive and active control. Therefore, the simple state feedback control is useful in a point of view of the initial condition problem of the compensator.

If there is no limitation of the actuator, the active control will have the best performance, however, against the big earthquake the actuator cannot work the same as the gain diagram in Figure 2.

Table 1 Parameter setting.

Name	Value
Mass [kg]	$m_1 = 5.1$ $m_2 = 0.25$
Stiffness [N/m]	$k_1 = 130.023$ $k_2 = 5.4561$
Damping coefficient [N·s/m]	$c_1 = 0.831$ $c_2 = 0.0924$
Height[mm]	832.5
Length of the pendulum [mm]	$l = 449.5$
Stroke area of x_2 [mm]	± 23
Limit of input [V]	± 0.4
Energy threshold δ_k and δ_m [J]	0.018

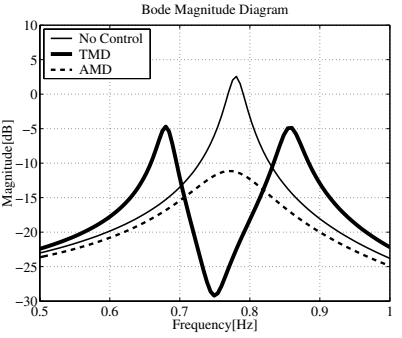

Fig. 2 Gain diagram of No control, TMD and AMD.

3 Switching Control

The dynamic vibration absorber and active control have respectively features. By using switching control between dynamic vibration absorber and active control, it is expected that it has good performance with each advantage of the tuned mass damper (TMD) and the active mass damper (AMD). When the vibration of the structure is small, AMD is effective and it has good performance. On the contrary, when the control input approaches to the limitation, or the device approaches to the stroke limitation by the big vibration, TMD without control input is effective.

In our experimental device, the pendulum type device moves as dynamic vibration absorber without control input. On the other side, the device moves as AMD by control input. The device can be easily changed between passive and active control by the existence of the control input.

We introduce two types of switching methodology; one is on the basis of the kinetic and mechanical energy of the structure as the same as APTMD [4, 5] and the other one is Lyapunov function method.

Switching control is not only methodology for the actuator restriction. When the feedback gain is chosen smaller one, the full time active control is available against the big earthquake, however, the performance against the small vibration decreases. The gain scheduled control, which is effective for the limitation of the stroke range of the moving mass, is also possible. In that case, it is hard to choose the scheduling parameter to switch between TMD and AMD.

3.1 Switching by Energy [4, 5]

The switching on the basis of the kinetic energy of the vibration structure had good performance in the APTMD case [4, 5]. When the kinetic or mechanical energy is smaller than some threshold then AMD works and when the energy is greater than the value then TMD works, because AMD gives up by the stroke restriction. This switching methodology is considered about the dynamics of the vibration structure.

$$\begin{aligned} \textbf{K.E.} \quad & \frac{1}{2}x^T \begin{pmatrix} 0 & 0 \\ 0 & M \end{pmatrix} x \; > \delta_k \Rightarrow \text{TMD} \\ & \qquad\qquad\quad \leq \delta_k \Rightarrow \text{AMD} \\ \textbf{M.E.} \quad & \frac{1}{2}x^T \begin{pmatrix} K & 0 \\ 0 & M \end{pmatrix} x \; > \delta_m \Rightarrow \text{TMD} \\ & \qquad\qquad\quad \leq \delta_m \Rightarrow \text{AMD} \end{aligned} \tag{2}$$

where δ_k and δ_m denote threshold of the kinetic energy and mechanical energy, respectively, that are decided by simulation. $x \in R^4$, $M \in R^{2\times 2}$ and $K \in R^{2\times 2}$ are defined as $x := [x_1 \; x_2 \; \dot{x_1} \; \dot{x_2}]^T$, $M := \text{diag}[m_1 \; m_2]$ and $K := \text{diag}[k_1 \; k_2]$, respectively.

3.2 Switching by Lyapunov function

We choose the quadratic form of the positive definite solution of the Riccati equation, which is used as the active control law. The derivative of the Lyapunov function $\dot{V}$ is an index for the switching. In both cases the systems are stable and the derivatives are calculated with state vector x and disturbance $\ddot{z}$. Comparing both values, the small one is selected as the control. In this case there is no threshold derived by trial and error like as δ_k in (2).

The Lyapunov function of AMD is defined as $V_{\mathrm{AMD}} = x^T P x$, where $P > 0$ is the positive definite solution of the Riccati equation ($A^T P + PA - PBR^{-1}B^T P + Q = 0$), which is used in the state feedback control. $P_L > 0$ is defined as the solution of Lyapunov equation with system matrix of TMD and weighting matrix Q, which is used to derive the state feedback control. Then the derivative of Lyapunov function of TMD and AMD are described as follows:

$$\dot{V}_{\mathrm{TMD}} = -x^T Q x + \ddot{z}^T W^T P_L x + x^T P_L W \ddot{z} \tag{3}$$

$$\dot{V}_{\mathrm{AMD}} = -x^T (Q + PBR^{-1}B^T P_L + P_L BR^{-1}B^T P)x + \ddot{z}^T W^T P_L x + x^T P_L W \ddot{z} \tag{4}$$

$$\dot{V}_{\mathrm{AMD}} - \dot{V}_{\mathrm{TMD}} = -x^T (PBR^{-1}B^T P_L + P_L BR^{-1}B^T P)x \tag{5}$$

where W denotes the matrix about disturbance in the state space description. Comparing with $\dot{V}_{\mathrm{TMD}}$ and $\dot{V}_{\mathrm{AMD}}$, the smaller one is considered as faster convergence.

$$\textbf{Lyapunov I} \qquad \begin{array}{l} \dot{V}_{\mathrm{AMD}} - \dot{V}_{\mathrm{TMD}} > 0 \Rightarrow \text{TMD} \\ \dot{V}_{\mathrm{AMD}} - \dot{V}_{\mathrm{TMD}} \leq 0 \Rightarrow \text{AMD} \end{array} \tag{6}$$

It is known that energy is a candidate of Lyapunov function in mechanical systems, therefore, another switching methods are derived by choosing kinetic energy $P_{L(K.E.)}$ and the mechanical energy $P_{L(M.E.)}$.

$$\textbf{Lyapunov II} \qquad P_{L(K.E.)} := \frac{1}{2} x^T \begin{pmatrix} 0 & 0 \\ 0 & M \end{pmatrix} x \tag{7}$$

$$\textbf{Lyapunov III} \qquad P_{L(M.E.)} := \frac{1}{2} x^T \begin{pmatrix} K & 0 \\ 0 & M \end{pmatrix} x \tag{8}$$

Note that the kinetic energy $P_{L(K.E.)}$ and mechanical energy $P_{L(M.E.)}$ are not common Lyapunov function of TMD (open-loop system) and AMD (closed-loop system). It is considered that more dissipated control method is chosen by comparing the derivative of energy.

In the switching control, it is necessary to consider stability. If the common Lyapunov function can be derived to TMD and AMD, stability of switching control can be proven. It is possible to derive the common Lyapunov function $x^T P_{\mathrm{common}} x > 0$ numerically by using linear matrix inequality (LMI).

$$\begin{cases} A^T P_{\mathrm{common}} + P_{\mathrm{common}} A > 0 \\ (A - BR^{-1}B^T P)^T P_{\mathrm{common}} + P_{\mathrm{common}} (A - BR^{-1}B^T P) > 0 \\ P_{\mathrm{common}} > 0 \end{cases}$$

where, A and $(A - BR^{-1}B^T P)$ are system matrices in the state space description of TMD (open-loop) and AMD (closed-loop), respectively. The existence of a common Lyapunov function P_{common} has been confirmed by using LMI though details are omitted.

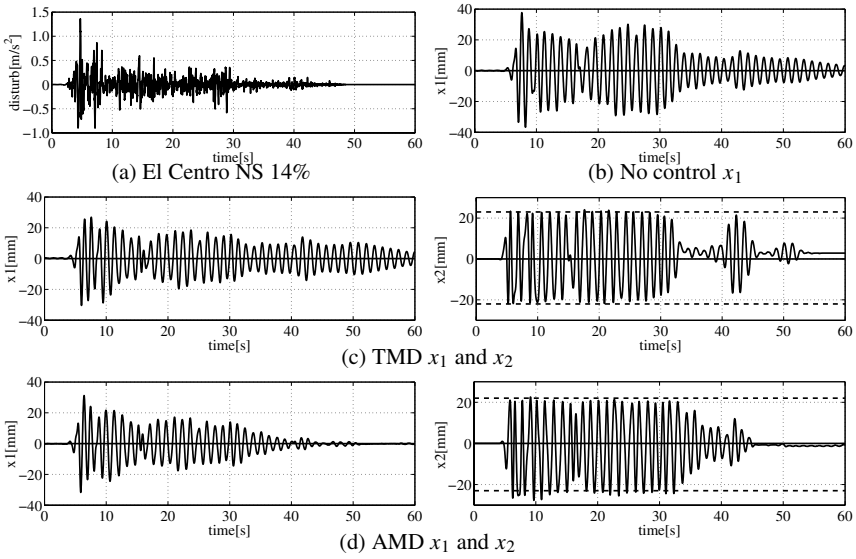

Fig. 3 (a) Earthquake (El Centro NS 15%) and displacements of (b) no control x_1, (c) TMD x_1 and x_2, (d) AMD x_1 and x_2 in El Centro.

4 Experiments

4.1 Experiment of El Centro Earthquake

We used acceleration of seismic wave (El Centro earthquake NS 15%) shown in Figure 3(a). As the features of this earthquake wave, it is extremely irregular and changes remarkably in a short time with the wide distribution of frequency elements. Time response of (b) displacement x_1 in no control case, (c) displacement x_1 and x_2 in full time TMD case and (d) displacement x_1 and x_2 in full time AMD case are shown in Figure 3, respectively.

When the response of (c) and (d) is compared, AMD does not function for 6–32 sec for the stroke limitation of the pendulum and TMD is more effective than AMD when the the maximum displacement is compared. The effect of AMD is higher than TMD after 32 sec. To make the best use of the advantage of both methods, that TMD is effective in a big vibration, and AMD is effective in a small vibration. This shows the meaning that introduces switching control.

Figure 4 shows the time responses of the switching vibration control by (a) the kinetic energy and (b) the mechanical energy with each status of the switching. The threshold of the switching by energy is the same in both cases, $\delta_k = \delta_m = 0.018$ J.

It is shown that the effect of the switching vibration control by energy is higher than that of the control with TMD (c) or AMD (d) in Figure 3. Comparing two waveforms with TMD and AMD, it is clear that each advantage is extracted. According

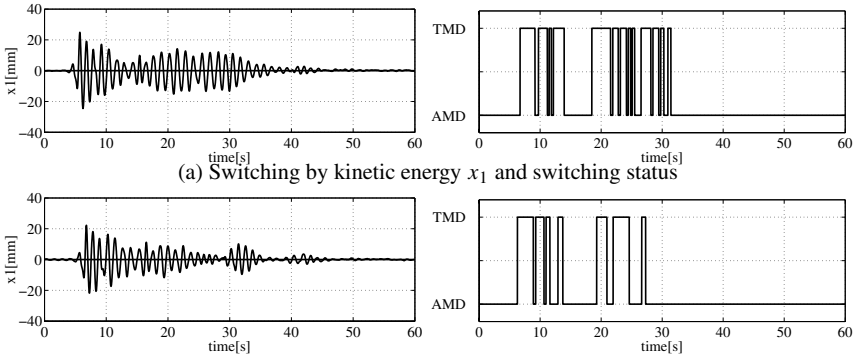

(a) Switching by kinetic energy x_1 and switching status

(b) Switching by mechanical energy x_1 and switching status

Fig. 4 Displacement x_1 and switching status of (a) switching by kinetic energy and (b) switching by mechanical energy in El Centro.

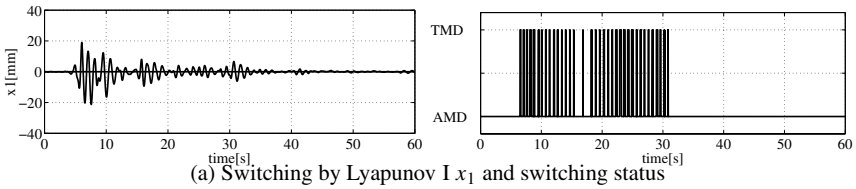

(a) Switching by Lyapunov I x_1 and switching status

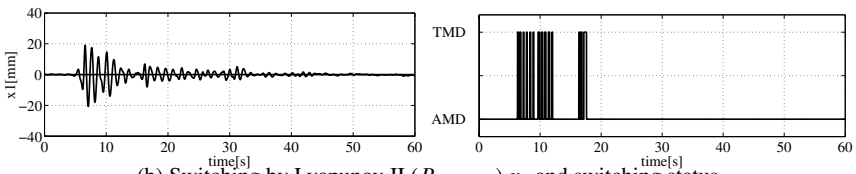

(b) Switching by Lyapunov II ($P_{L(K.E.)}$) x_1 and switching status

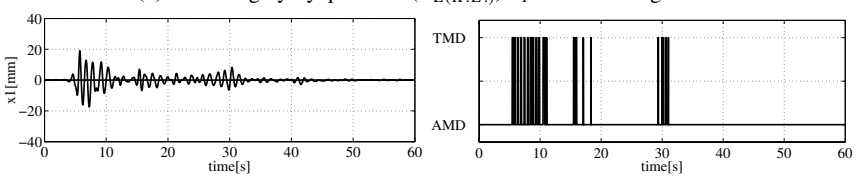

(c) Switching by Lyapunov III ($P_{L(M.E.)}$) x_1 and switching status

Fig. 5 Displacement x_1 and switching status of switching by (a) Lyapunov I, (b) Lyapunov II ($P_{L(K.E.)}$) and (c) Lyapunov III ($P_{L(M.E.)}$) in El Centro.

to the decrease rate of the the maximum displacement, the switching control by mechanical energy is effective and the switching status is also gradual (see Table 2).

Figure 5 shows displacement x_1 and status of switching by (a) Lyapunov I in Eq. (6), (b) kinetic energy $P_{L(K.E.)}$ in Eq. (7) and (c) mechanical energy $P_{L(M.E.)}$ in Eq. (8), respectively. When the switching methods of three kinds of by the Lyapunov function are compared, the suppression effect in the case by mechanical energy as a Lyapunov function is the highest from the decrease rate and the maximum accelera-

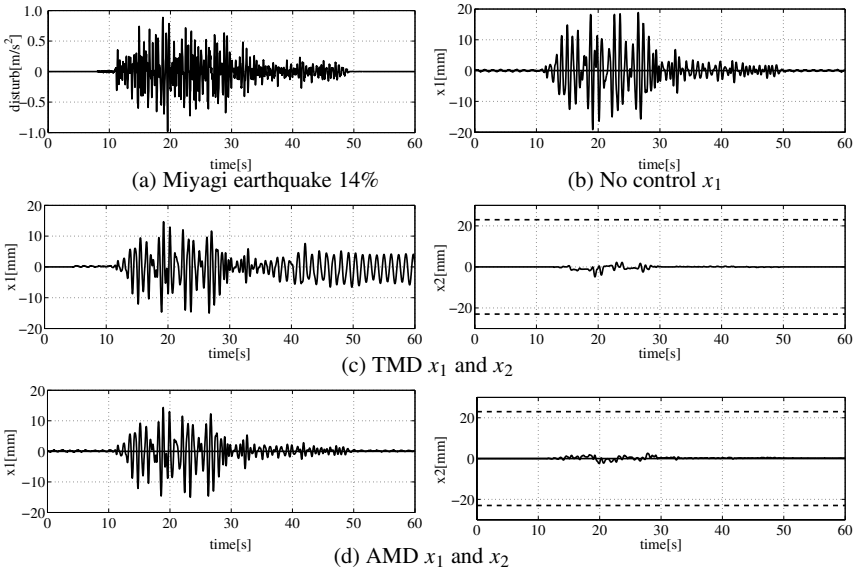

(a) Miyagi earthquake 14% (b) No control x_1

(c) TMD x_1 and x_2

(d) AMD x_1 and x_2

Fig. 6 (a) Earthquake (Miyagi 15%) and displacements of (b) no control x_1, (c) TMD x_1 and x_2, (d) AMD x_1 and x_2 in Miyagi.

tion (see Table 2). The switching control by the Lyapunov function suppresses even the acceleration than the switching control by energy though the switching is rapid.

4.2 Experiment of Miyagi Earthquake

The Miyagi Earthquake wave (15%) was used as the second earthquake shown in (a) of Figure 6. The condition is the same as the case of the El Centro seismic wave in Section 4.1.

AMD does not function for 14–27 sec and TMD is more effective than AMD in the maximum displacement point of view. This is because of the frequency element of the seismic wave. However, TMD is not good at the vibration suppression of a small vibration after 30 sec and the vibration continues. The effect of the vibration suppression of AMD is high in this time zone.

Figure 7 shows the time responses of the switching vibration control by (a) the kinetic energy and (b) the mechanical energy with the status of the switching. The threshold is the same in the case of El Centro earthquake. Because there is no time that the energy generated in vibration system to exceed the threshold, the switching is not done as for both kinetic energies and mechanical energy. The result is the same as AMD.

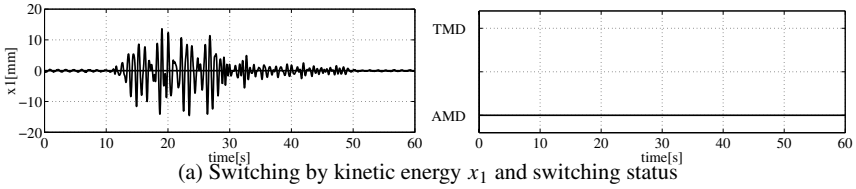

(a) Switching by kinetic energy x_1 and switching status

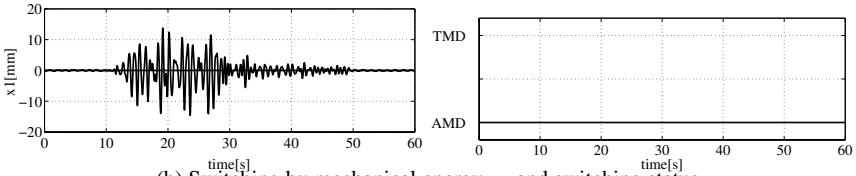

(b) Switching by mechanical energy x_1 and switching status

Fig. 7 Displacement x_1 and switching status of (a) switching by kinetic energy and (b) switching by mechanical energy in Miyagi.

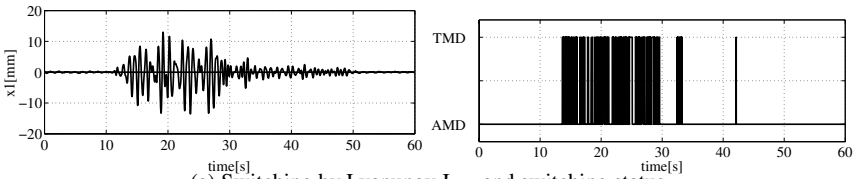

(a) Switching by Lyapunov I x_1 and switching status

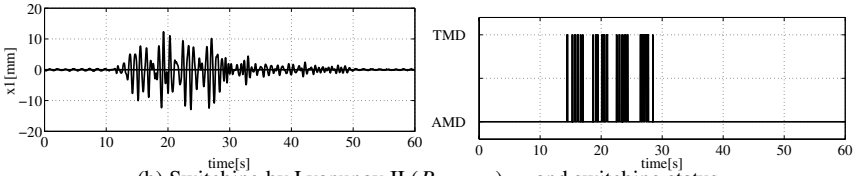

(b) Switching by Lyapunov II ($P_{L(K.E.)}$) x_1 and switching status

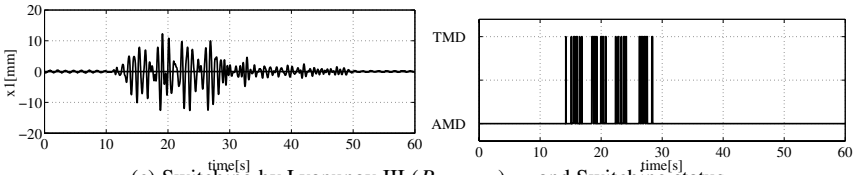

(c) Switching by Lyapunov III ($P_{L(M.E.)}$) x_1 and Switching status

Fig. 8 Displacements x_1 and switching status of switching by (a) Lyapunov I, (b) Lyapunov II ($P_{L(K.E.)}$) and (c) Lyapunov III ($P_{L(M.E.)}$) in Miyagi.

Figure 8 shows time responses of displacement x_1 switched by Lyapunov function. The results have been the same as the El Centro earthquake, switching control by the mechanical energy as Lyapunov function is the best performance.

Table 2 is the numerical data of the experiment that uses the El Centro seismic wave and Miyagi seismic wave as acceleration disturbance. The decrease rate is a

Table 2 Experimental data of El Centro NS 15% and Miyagi 15%.

Control law	El Centro NS 15%			Miyagi 15%		
	x_1 max [mm]	$\ddot{x}_1$ max [m/s^2]	decrease ratio[%]	x_1 max [mm]	$\ddot{x}_1$ max [m/s^2]	decrease ratio[%]
No Control	38.4	0.0268		19.2	0.0070	
TMD	30.4	0.0240	20.72	15.0	0.0075	21.78
AMD	32.4	0.0244	15.58	15.1	0.0073	21.12
K.E.	24.9	0.0194	35.13	15.1	0.0071	21.24
M.E.	22.2	0.0191	42.43	15.1	0.0070	21.26
Lyapunov I	21.3	0.0166	44.48	13.6	0.0065	29.32
Lyap II $P_{L(K.E.)}$	20.7	0.0165	46.16	12.9	0.0064	32.62
Lyap III $P_{L(M.E.)}$	19.9	0.0158	48.27	12.6	0.0063	34.14

ratio of the the maximum displacement and the the uncontrolled maximum displacement.

5 Conclusion

Switching control methods between the dynamic vibration absorber (TMD) and the active mass damper (AMD) have been considered. As the experimental results, the suppression by switching control has been more effective than TMD and AMD. The switching method by energy is intuitive and the status of switching was also gradual. The threshold for the switching was chosen by the trial and error of simulations. The dissipativeness of the switching method by Lyapunov function corresponding to the system dynamics was effective though the switching was rapid. When the mechanical energy is chosen to be a Lyapunov function, it is not necessary to look for the threshold by trial and error.

References

1. Kamada, T.: State of the Art in Vibration Control of Tall Buildings in Japan. In: *9th World Seminar on Seismic Isolation, Energy Dissipation and Active Vibration Control of Structures*, Kobe, Japan (2005).
2. Kondo, A. et al.: A Feasibility Study of a Second Order Selective Filter for Active-Passive Composite Tuned Mass Damper. In: *Proc. of the 4th Symposium of Motion and Vibration*, pp. 240–242 (1995) [in Japanese].
3. Fujita, T. et al.: Impact Multi-Tuned Mass Damper for High-Rise Buildings against Destructive Earthquake Input. *Transactions of the Japan Society of Mechanical Engineers, C* **61**(587), 158–163, (1995) [in Japanese].
4. Abe, N.: Active-Passive Switching Control on the basis of the AMD's Kinetic Energy. In: *Proc. 6th International Conference on Motion and Vibration Control, Movic2002*, Vol. 2, pp. 619–624 (2002).
5. Abe, N., Anzai, K. and Mizunoya, D.: Switching Vibration Control of Passive and Active Mass Damper. *Transactions of the Japan Society of Mechanical Engineers, C* **72**(713), 102–108 (2006) [in Japanese].

Performance Assessment of a Multi-Frequency Controller Applied to a Flexible Rotor Magnetic Bearing System – Contact Dynamics

Abdul-Hadi G. Abulrub, M. Necip Sahinkaya, Clifford R. Burrows and Patrick S. Keogh

Abstract Vibrations associated with external disturbances and rotor faults, such as cracks, usually exhibit themselves as harmonic components of the synchronous frequency. The essence of the multi-frequency form of the synchronous recursive open loop adaptive controller (ROLAC) is that it can minimise a number of vibration components simultaneously, for example, synchronous rotor vibration at frequency Ω, its harmonics and sub-harmonics within any defined range. This requires on-line identification of the speed dependent partial receptance matrix by using a multi-frequency test signal incorporating all of the pertinent harmonic components. The question arises: What is the degradation in performance if the rotor comes into contact with its retainer bearing? This may arise when a magnetically levitated rotor is installed on a movable base frame, for example on board a ship or an aircraft. A simulation study is described to examine this question. It comprises a flexible rotor supported by two active magnetic bearings. Eight displacement transducers are positioned along the rotor. A local PID controller is provided for each axis of the magnetic bearings to ensure stability and alignment of the rotor at a central position. An outer ROLAC loop is incorporated at each bearing to control the vibrations at discrete frequencies of 0.5Ω, Ω, 2Ω and 3Ω. In addition, a multi-frequency disturbance was applied to the rotor causing contact with its retainer bearing. The performance of the multi-frequency ROLAC is assessed in preventing contact, or recovering the rotor position if contact occurs.

1 Introduction

Magnetic bearings have many advantages as they provide contactless support, high speed operation, and the capability to operate in hostile environments such as very

A.G. Abulrub, M.N. Sahinkaya, C.R. Burrows and P.S. Keogh
Department of Mechanical Engineering, University of Bath, Bath BA2 7AY, UK;
E-mail: {A.Abulrub, M.N.Sahinkaya, C.R.Burrows, P.S.Keogh}@bath.ac.uk

H. Ulbrich and L. Ginzinger (eds.), Motion and Vibration Control, 11–20.

high/low temperatures [1]. However, magnetic bearing systems have to incorporate retainer or back-up bearings due to their limited force capacity. These bearings are used to protect the rotor and stator lamination and to avoid damage to pole faces if contact occurs. It is usual practice to run down a rotor if contact occurs, but in some applications shut down is not an option [2].

There have been many studies in the literature on the interaction of a rotor with a stator component. Johnson [3] studied synchronous rub dynamic behaviour. Subsynchronous response was examined by Childs [4], Muszynska [5] and Ehrich [6]. A detailed study was undertaken by Wu and Flowers [7] to illustrate different contact modes i.e. rub and bouncing. Various methods for vibration and contact force analysis are presented in the literature [8–11].

The conventional modelling of contact forces is to express them as a function of the rotor penetration depth into the bearing inner surface at the contact point [12]. The contact stiffness coefficient may also be related to the rotor penetration depth [13]. This approach suffers from the drawback of generating physically meaningless negative contact forces [14], which are not differentiable at zero penetration. The introduction of various nonlinearities into the contact force formulation is needed to overcome these deficiencies [8]. High contact stiffness characteristics impose numerical problems when integrating the equations of motion. An alternative technique based on a constrained Lagrangian formulation of the equation of motion overcomes these disadvantages [10, 15, 16]. Contacts are considered as constraints on the generalised coordinates, and are handled through Lagrange multipliers. This efficient modelling technique is used to design an effective controller.

The classical PID controller for active magnetic bearings (AMBs) has been reported in the literature [1]. Many industrial AMB systems operate with PID controllers, but modern controller designs must be introduced where system failure is not acceptable. There have been numerous control methods proposed for harmonic disturbance compensation and vibration attenuation such as H_∞ and H_2 control [17, 18], fuzzy logic control [19] and open loop adaptive control [20, 21]. ROLAC [22] is utilised in this study.

2 System Description and Modelling

The flexible rotor/magnetic bearing rig consists of steel rotor of total mass 100 kg, length 2 m and radius 0.025 m with four attached disks. Each disk is 10 kg and with 0.125 m radius. The rotor is levitated by two active magnetic bearings that provide a radial dynamic force of 1.75 kN. Eight eddy current displacement sensors are installed at four nodal planes at $\pm 45°$ to the vertical to provide on-line measurements of the rotor vibration. A schematic view of the rotor/bearing system is shown in Figure 1.

A finite element model of the rotor was used with 13 mass nodes. Each node (mass station) has four degrees of freedoms. The rotor dynamic behaviour satisfies the following equation of motion:

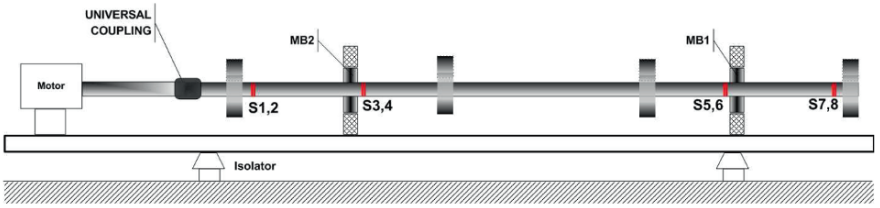

Fig. 1 A view of the experimental rotor/bearing system used in the simulations (S1,2 .. S7,8 shows the 8 sensor positions).

$$\mathbf{M}\ddot{\mathbf{q}} + (\mathbf{C} + \Omega\mathbf{G})\dot{\mathbf{q}} + \mathbf{K}\mathbf{q} = \mathbf{f} + \mathbf{B}\mathbf{u} \tag{1}$$

where

$$\mathbf{q} = [\mathbf{x}, \mathbf{y}, \boldsymbol{\theta}, \boldsymbol{\phi}]^T \tag{2}$$

M, **K** and **C** describe the flexible rotor mass, stiffness and damping characteristics and include local proportional and derivative PD controller parameters at the magnetic bearings locations. **G** is the gyroscopic matrix. **f** and **u** contain external disturbance forces (including the forces due to unbalance distribution) and the control forces, respectively. **B** is the distribution matrix for the control forces. The **x** and **y** vectors represent the two orthogonal linear displacements along X-Y axes for all nodal planes, and the angular deflection vectors $\boldsymbol{\theta}$ and $\boldsymbol{\phi}$ denote rotations around these axes.

3 Constrained Lagrangian Multiple Contact Model

The constrained Lagrangian modelling technique can be applied to any number of possible contacts depending on the system configuration. The experimental system shown in Figure 1 has two active magnetic bearings, each protected by a retainer bearings with a radial clearance of $c_r = 0.75$ mm. Four possible contact scenarios are possible for this system; no contact, contact at the first retainer bearing (at node k_1) only, contact at the second retainer bearing (at node k_2) only, and contact at both retainer bearings (at nodes k_1 and k_2) [10]. A single model to cover all of these cases can be established by assuming contacts at all possible nodes. Two holonomic constraint equations, h_1 and h_2, which constrain the radial displacement of the rotor at each bearing to the physical clearance c_r can be written as follows:

$$h_1 = c_r^2 - (x_{k1}^2 + y_{k1}^2) = 0; \quad h_2 = c_r^2 - (x_{k2}^2 + y_{k2}^2) = 0 \tag{3}$$

The holonomic constraint equations can be incorporated into the rotor bearing equations (1) through Lagrange multipliers λ_1 and λ_2 as follows:

$$\begin{bmatrix} \mathbf{M} & \mathbf{J}^T \\ \mathbf{J} & \mathbf{0} \end{bmatrix} \times \begin{bmatrix} \ddot{\mathbf{q}} \\ \boldsymbol{\lambda} \end{bmatrix} = \begin{bmatrix} \mathbf{f} - (\mathbf{C} + \Omega\mathbf{G})\dot{\mathbf{q}} - \mathbf{K}\mathbf{q} \\ \mathbf{D}(\mathbf{q}, \dot{\mathbf{q}}) \end{bmatrix} \tag{4}$$

where $\mathbf{J}$ is the Jacobian matrix of the constraint equations, i.e. it contains the partial derivatives of both constraint equations with respect to generalised coordinates $\mathbf{q}$, and $\boldsymbol{\lambda}$ is the Lagrange multiplier vector containing λ_1 and λ_2. This increases the number of unknowns, therefore two additional equations are introduced by double differentiating Eq. (3). The last 2 lines on the left hand side of Eq. (4) become:

$$\left[\begin{array}{ccccccccc|cc} 0 \cdots & -2x_{k1} & \cdots & 0 & \cdots & -2y_{k1} & \cdots & 0 & \cdots & 0 & 0 \\ 0 \cdots & 0 & \cdots & -2x_{k2} & \cdots & 0 & \cdots & -2y_{k2} & \cdots & 0 & 0 \end{array}\right] \tag{5}$$

and the right hand side:

$$\mathbf{D} = \begin{bmatrix} 2\,\dot{x}_{k1}^2 + 2\,\dot{y}_{k1}^2 \\ 2\,\dot{x}_{k2}^2 + 2\,\dot{y}_{k2}^2 \end{bmatrix} \tag{6}$$

In the case of noncontact at any of the retainer bearings, the corresponding value in the $\boldsymbol{\lambda}$ vector should be set to zero. This can be done by replacing the corresponding element in $\mathbf{D}$ to zero, and setting the corresponding row on the left hand side to unity (i.e. 1 at the diagonal element, 0 elsewhere). For example, in the case of contact at the first retainer bearing at node k_1 only, then the last two lines should be set to:

$$\left[\begin{array}{ccccccccc|cc} 0 \cdots & -2x_{k1} & \cdots & 0 & \cdots & -2y_{k1} & \cdots & 0 & \cdots & 0 & 0 \\ 0 \cdots & 0 & \cdots & 0 & \cdots & 0 & \cdots & 0 & \cdots & 0 & 1 \end{array}\right] \tag{7}$$

and

$$\mathbf{D} = \begin{bmatrix} 2\,\dot{x}_{k1}^2 + 2\,\dot{y}_{k1}^2 \\ 0 \end{bmatrix} \tag{8}$$

The contact forces, F_{c1} and F_{c2} can be calculated by using the Lagrangian multipliers as follows:

$$F_{c1} = 2c_r\lambda_1 \quad \text{and} \quad F_{c2} = 2c_r\lambda_2 \tag{9}$$

A change in the operational modes can be detected by using zero crossing of the constraint equations h_1 and h_2 in Eq. (3) during noncontact operation, and the Lagrangian multipliers during contact. When moving from noncontact to contact, the initial conditions of the velocities at the point of contact must be adjusted to satisfy the velocity constraints as discussed in [10]. To prevent potential drift of the constraints associated with the numerical integration process, virtual stiffness and damping coefficients are introduced in the $\mathbf{D}$ matrix in Eq. (6).

4 Multi-Frequency ROLAC

The open loop adaptive control (OLAC) strategy developed in [20] gives the optimum change of the control force in the frequency domain as follows:

$$\Delta \mathbf{U}(j\omega) = -(\mathbf{R}^T\ \mathbf{R})^{-1}\mathbf{R}^T\ \mathbf{Q_m}(j\omega) = \mathbf{H}(j\omega)\ \mathbf{Q_m}(j\omega) \tag{10}$$

where $\mathbf{U}(j\omega)$ and $\mathbf{Q_m}(j\omega)$ are the frequency response of the control force vector and rotor displacement measurements, respectively. $\mathbf{R}(j\omega)$ is the partial receptance matrix. The notation $()^T$ denotes the complex conjugate transpose. The recursive version is based on the following integral action (with integral gain α) on the recursive Fourier transform of the measurements [22]:

$$\mathbf{u}(j\omega, t) = -\alpha \int \mathbf{H}(j\omega) \cdot \mathbf{Q_m}(j\omega, t) \cdot dt \tag{11}$$

The recursive Fourier transform is calculated as follows:

$$\mathbf{Q_m}(j\omega, t) = \mathbf{I}(j\omega, t) - \mathbf{I}(j\omega, t - 2\pi/\omega_0) \tag{12}$$

where ω_0 is the fundamental frequency, and ω is any harmonic, i.e. $\omega = k\omega_0$. The Fourier integral $\mathbf{I}(j\omega, t)$ is defined as:

$$\mathbf{I}(j\omega, t) = \frac{\omega_0}{\pi} \int_0^t \mathbf{q_m}(\tau) e^{-j\omega\tau} d\tau \tag{13}$$

In the case of a multi-frequency vibration controller, the control force is constructed by the summation of forces at the frequencies of interest. For example, to include frequencies 0.5Ω, Ω, 2Ω and 3Ω, the fundamental frequency has to be set as $\omega_0 = 0.5\Omega$, and optimum force calculations should be carried out for $\omega = k\omega_0$ for $k = 1, 2, 4, 6$ as given in Eq. (11), and then summed up to give the multi-frequency control force:

$$\mathbf{u}(t) = \mathrm{Re}\left\{ \sum_k \mathbf{U}(j\,k\omega_0, t) e^{j\,k\omega_0 t} \right\}, \quad \text{for} \quad k = 1, 2, 4, 6 \tag{14}$$

The partial receptance matrix $\mathbf{R}$ can either be determined from the finite element model of the system, or can be identified in situ as described in [21].

5 Results and Discussion

The system described in Section 2 may be simulated using the constrained Lagrangian technique. The initial steady state orbits are obtained by introducing a small unbalance of 10 gm at the non-driven end disk. All simulations were run at a rotational speed of $\Omega = 10$ Hz. Local PID controllers are incorporated at both magnetic bearings with a proportional gain to produce an effective bearing stiffness of 10^6 N/m. The derivative gain is set to provide an equivalent damping of 5000 Ns/m. The retainer bearings are rolling element type and the coefficient of friction is taken as $\mu = 0.15$ between the rotor and inner surface of the retainer bearing.

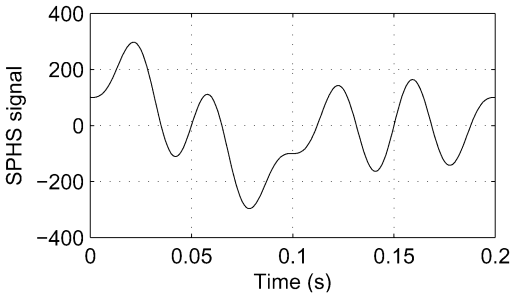

Fig. 2 A typical SPHS signal, s^*, with $\omega_0 = 5$ Hz, $N = 6$, and $A_i = 100$ for $i = 1, 2, 4, 6$ (zero otherwise).

After a predefined period of 10 synchronous cycles, a sudden external disturbance is introduced to initiate contact at the inner disk near MB1 along the X-direction. The external force is a Schroeder Phased Harmonic Signal (SPHS) defined as follows:

$$s(t) = \sum_{i=1}^{N} A_i \cos\left(i\,\omega_0\,t + \varphi_i\right) \tag{15}$$

where A_i and φ_i are the amplitude and phase, respectively, at the ith harmonic. The phase values are adjusted according to the following formulation in order to achieve a low peak factor signal for the given frequency amplitudes [23]:

$$\varphi_i = \varphi_{i-1} - 2\pi \sum_{m=1}^{i-1} p_m \quad \text{for} \quad i - 1 \cdots N \tag{16}$$

p_m is the ratio of the power at frequency $m\omega_0$ to the total power, i.e. $\sum_{m=1}^{N} p_m = 1$. A specific base SPHS signal, $s^*(t)$, was used in this study as shown in Figure 2 with $\omega_0 = 0.5\Omega = 5$ Hz, $N = 6$, and $A_i = 100$ for $i = 1, 2, 4, 6$, and zero for other values of i. This gives an amplitude of 300 in the time domain.

The first simulation was carried out to demonstrate the effectiveness of the synchronous ROLAC (S-ROLAC) and multi-frequency ROLAC (MF-ROLAC) under noncontact conditions. The integral constant for both S-ROLAC and MF-ROLAC was set to $\alpha = 7$. Both controllers retain the PID controller. The excitation force was a SPHS multi-frequency signal, $2\,s^*(t)$. Figure 3 shows the performance of the three controllers in terms of vibration suppression. The following normalised vibration cost function is used for each frequency component:

$$C_F(j\omega) = \sqrt{\frac{\mathbf{Q_m}^T(j\omega)\,\mathbf{Q_m}(j\omega)}{8c_r^2}} \tag{17}$$

As expected, the introduction of S-ROLAC reduces the cost function from 0.27 to 0.05 at the synchronous frequency, but does not influence the non-synchronous vibration components. When the MF-ROLAC is introduced, the cost function is reduced significantly at all excitation frequencies.

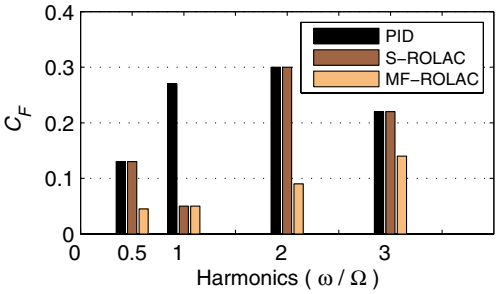

Fig. 3 Frequency components of rotor vibrations when subjected to a multi-frequency excitation under three different controllers.

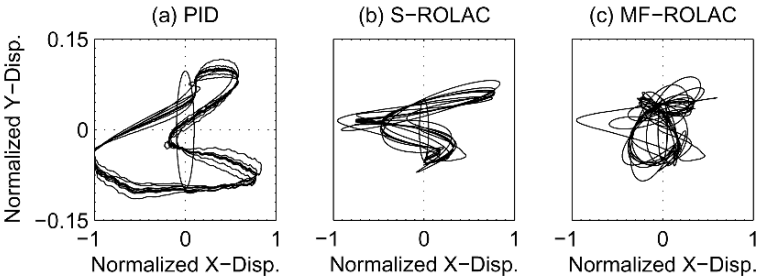

Fig. 4 Orbits at MB1 location as a result of a sudden multi-frequency excitation of $3.5\,s^*$.

A second set of simulations was carried out to demonstrate the ability of both ROLAC controllers to prevent contact. A sudden external multi-frequency disturbance, $3.5\,s^*(t)$, was introduced. Figure 4 shows the orbits at MB1 under three different controllers. Since the sudden excitation is along the x-direction only, the y-axis of the orbits are magnified to show a more detailed view. Displacements are normalised by the radial clearance of the retainer bearing c_r, i.e. unity indicates contact. Figure 4(a) shows that contact occurs at MB1 with the PID controller. The maximum contact force is predicted to be approximately 24 kN as shown in Figure 5. It is a bouncing motion and the rotor is trapped in this contact mode. However, S-ROLAC and MF-ROLAC react quickly and prevent contact with the retainer bearing as shown in Figures 4(b) and 4(c), respectively. The normalised vibration amplitudes settle to 0.8 and 0.37 for S-ROLAC and MF-ROLAC, respectively. Therefore, recovery was possible with both ROLAC controllers, but the vibration attenuation in of MF-ROLAC was superior.

In the third set of simulations, the amplitude of the external excitation was increased to $4.5\,s^*$. At this level of excitation, all three controllers were unable to prevent contact at the MB1 location as shown in Figure 6. The steady state contact force levels predicted by the constrained Lagrangian formulation were 31 kN with the PID controller as shown in Figure 6(a), and 12 kN with S-ROLAC as shown in Figure 6(b). However, with the MF-ROLAC controller, rotor position is recovered after a single contact with a significantly lower contact force of 1.8 kN as seen in Figure 6(c). It is clear from the corresponding time response in Figure 7 that the MF-

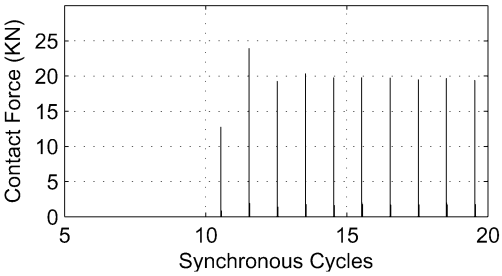

Fig. 5 Contact force at MB1 under PID controller as a result of a sudden multi-frequency excitation of 3.5 s^*.

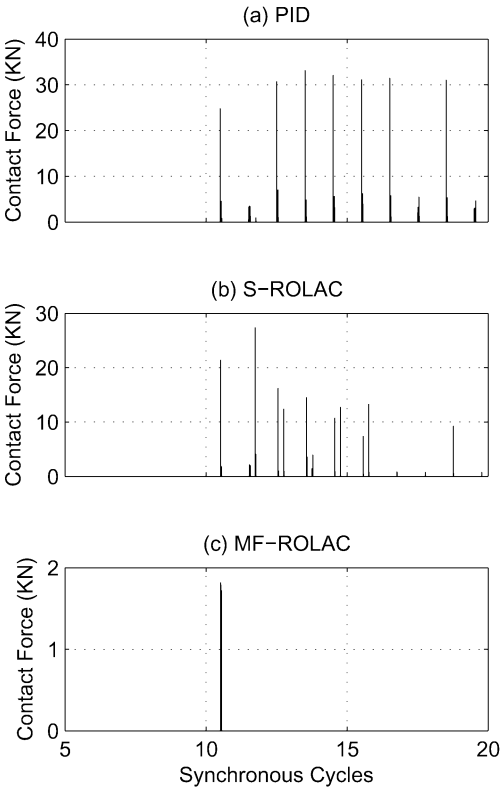

Fig. 6 Contact force at MB1 under three different controllers as a result of a sudden multi-frequency excitation of 4.5 s^*.

ROLAC not only recovered the rotor position, but also returned it to a low vibration level.

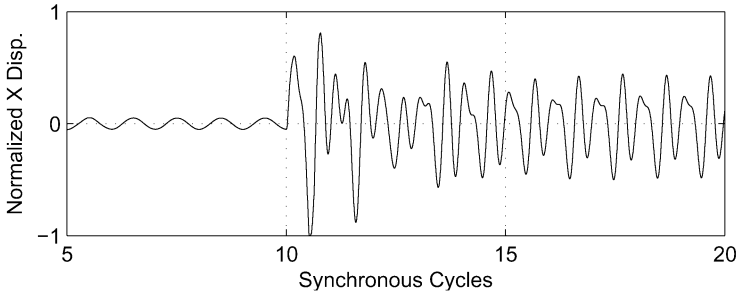

Fig. 7 x-displacements at MB1 location under MF-ROLAC as a result of a sudden multi-frequency excitation of 4.5 s^*.

6 Conclusions

This paper demonstrates the use of a constrained Lagrangian approach to simulate contact dynamics of a flexible rotor magnetic bearing system in order to assess the performance of a multi-frequency controller MF-ROLAC. A sudden multi-frequency external disturbance is introduced to initiate contact. Under a PID controller, the rotor is trapped in a bouncing contact mode, whereas under a MF-ROLAC, rotor contact with the auxiliary bearing is prevented. At higher external force levels, even if contact occurs, the MF-ROLAC reduces the contact force significantly and recovers the rotor position. Even the synchronous version of ROLAC exhibits performance benefits in terms of lowering contact forces significantly compared with a PID controller.

Acknowledgements The authors acknowledge with thanks the support of the Engineering and Physical Sciences Research Council of the UK under the Platform Grant GR/S64448/01.

References

1. Schweitzer, G.: Active magnetic bearings – Chances and limitations, in *Proceedings of the Sixth International IFTOMM Conference on Rotor Dynamics*, Sydney, Australia, pp. 1–14 (2002).
2. Schoeb, R. and Dasse K.: Magnetic suspension systems for biomedical applications, in *Proceedings of the Sixth International Symposium on Magnetic Suspension Technology*, Turin, Italy (2001).
3. Johnson, D.C.: Synchronous whirl of a vertical shaft having clearance in one bearing, *J. Mech. Eng. Sci.* **4**(1), 85–93 (1962).
4. Childs, D.W.: Rub induced parametric excitation in rotors, *ASME J. Mech. Des.* **10**, 640–644 (1979).
5. Muszynska, A.: Partial lateral rotor to stator rubs, Paper C281/84, in *Proceedings of 3rd International Conference Vibrations in Rotating Machinery*, University of York, UK, Mechanical Engineering Publications Limited, London, pp. 327–335 (1984).

6. Ehrich, F.F.: High order subharmonic response of high speed rotors in bearing clearance, *ASME J. Vib., Acoust., Stress, Reliab. Des.* **110**, 9–16 (1988).
7. Wu, F. and Flowers, G.T.: An experimental study of the influence of disk flexibility and rubbing on rotordynamics, in *Proceedings of ASME Conference on Vibrations in Rotating Systems*, DE-Vol. 60, ASME, New York, pp. 19–26 (1993).
8. Fumagalli, M. and Schweitzer, G.: Measurements on a rotor contacting its housing, in *Proceedings of 6th International Conference on Vibrations in Rotating Machinery*, University of Oxford, UK, Mechanical Engineering Publications, London, Paper No. C500/085/96, pp. 779–788 (1996).
9. Kirk, R.G.: Evaluation of AMB turbomachinery auxiliary bearings, *ASME J. Vibr. Acoust.* **121**, 156–161 (1999).
10. Sahinkaya, M.N., Abulrub, A.G., Keogh, P.S., and Burrows, C.R.: Multiple sliding and rolling contact dynamics for a flexible rotor/magnetic bearing system, *IEEE-ASME Trans. on Mechatronics* **12**(2) 179–189 (2006).
11. Keogh, P.S. and Cole, M.O.T.: Contact dynamic response with misalignment in a flexible rotor/magnetic bearing system, *Trans. ASME, J. Engrg. Gas Turbines and Power* **128** 362–369 (2006).
12. Xie, H., Flowers, G.T., Feng L., and Lawrence C.: Steady-state dynamic behaviour of a flexible rotor with auxiliary support from a clearance bearing, *ASME, J. Vibr. Acoust.* **121**(1), 78–83 (1999).
13. Kirk, R.G., Raju K.V.S., and Ramesh K.: Modeling of AMB turbo-machinery for transient analysis, in *Proceedings of MAG 97*, Alexandria, USA, pp. 139–153 (1997).
14. von Groll, G. and Ewins D.J.: A mechanism of low subharmonic response in rotor/stator contact – Measurements and simulations, *ASME, J. Vibr. Acoust.* **124**(3), 350–358 (2002).
15. Abulrub, A.G., Sahinkaya, M.N., Keogh, P.S., and Burrows, C.R.: Effective model reduction for magnetically levitated flexible rotors including contact dynamics, in *ASME DETC2005, 20th Biennial Conference on Mechanical Vibration and Noise*, Long Beach, USA (2005).
16. Abulrub, A.G., Sahinkaya, M.N., Keogh, P.S., and Burrows, C.R.: A constrained Lagrangian approach for modelling multiple contacts of flexible rotors, in *IFToMM 7th International Conference on Rotor Dynamics*, Vienna, Austria, September 25–28 (2006).
17. Cole, M.O.T., Keogh, P.S., Sahinkaya, M.N., and Burrows, C.R.: Towards fault-tolerant active control of rotor-magnetic bearing systems, *Control Engineering Practice* **12**, 491–501 (2004).
18. Shroder, P., Green, B., Grum, N., and Fleming, P.J.: On-line evolution of robust control systems: an industrial active magnetic application, *Control Engineering Practice* **9**, 37–49 (2001).
19. Sung-Kyung, and Reza Langari: Robust fuzzy control of a magnetic bearing system subject to harmonic disturbances, *IEEE Trans. Control Systems Technol.* **8**(2), 366–371 (2000).
20. Burrows, C.R. and Sahinkaya, M.N.: Vibration control of multimode rotor-bearing systems, *Proc. Royal Soc. London A – Math. Phys. Engrg. Sci.* **386**(1790), 77–94 (1983).
21. Burrows, C.R., Sahinkaya, M.N., and Clements, S.: Active vibration control of flexible rotors – An experimental and theoretical study, in *Proc. Royal Soc. London A – Math. Phys. Engrg. Sci.* **422**(1862), 123–146 (1989).
22. Abulrub, A.G., Sahinkaya, M.N., Keogh, P.S., and Burrows, C.R.: Experiments on ROLAC to recover rotor position following contact, in *The Tenth International Symposium on Magnetic Bearings (ISMB 10)*, Martigny, Switzerland, August 21–23 (2006).
23. Schroeder, M.R., Synthesis of low-peak-factor signals and binary sequences with low autocorrelation, *IEEE Trans. Information Theory* **IT16**(1), 85–89 (1970).

Passivity-Based Trajectory Control of an Overhead Crane by Interconnection and Damping Assignment

Harald Aschemann

Abstract This paper presents a passivity-based control scheme for the two main axes of a 5 t-overhead crane, which guarantees both tracking of desired trajectories for the crane load and an active damping of crane load oscillations. The passivity-based control is performed by interconnection and damping assignment according to the IDA-PBC approach for underactuated systems. The tracking capabilities concerning desired trajectories for the crane load can be significantly improved by introducing feedforward control based on an inverse system model. Furthermore, a reduced-order disturbance observer is utilised for the compensation of nonlinear friction forces. In this paper, feedforward and feedback control as well as observer based disturbance compensation are adapted to the varying system parameters rope length as well as load mass by gain-scheduling techniques. Thereby, desired trajectories for the crane load position in the 3-dimensional workspace can be tracked independently with high accuracy. Experimental results of an implementation on a 5 t-crane show both excellent tracking performance with maximum tracking errors of 2 cm and a high steady-state accuracy.

1 Introduction

In the last decade, numerous model-based trajectory control schemes for overhead travelling cranes have been proposed by different authors. Besides non-linear control approaches exploiting differential flatness [2], gain-scheduling techniques have proved efficient [1, 5]. Aiming at an increased handling frequency and a fully automated crane operation, the focus has to be on the motion of the crane load. Feedback control provides for tracking of desired trajectories for the crane in the 3-dimensional workspace with small tracking errors. In practical implementations,

Harald Aschemann
Chair of Mechatronics, University of Rostock, D-18059 Rostock, Germany;
E-mail: harald.aschemann@uni-rostock.de

H. Ulbrich and L. Ginzinger (eds.), Motion and Vibration Control, 21–30.

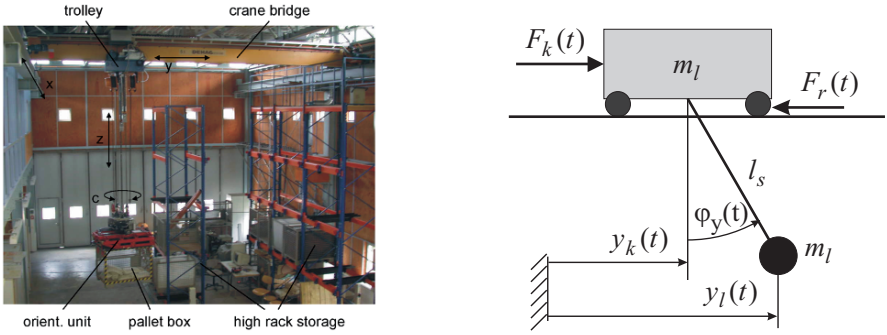

Fig. 1 Structure of the overhead travelling crane (left), Mechanical model of the y-axis (right).

however, tracking accuracy as well as steady-state accuracy strongly depend on the inclusion of appropriate control action to counteract disturbances, especially nonlinear friction acting on the drives as the dominant disturbance. Furthermore, a robust or adaptive control approach is necessary as regards varying system parameters like rope length or load mass during crane operation [5]. By this, the capabilities of an automated overhead crane can be extended in order to use it as a robot manipulator for the handling of heavy loads in a large cartesian workspace.

In this paper, the first principle modelling of the two main translational crane axes is addressed first. Aiming at a decentralised control structure, for each axis a separate design model is derived in symbolic form. Then, a state space model is established for the envisaged passivity-based control following the IDA-PBC approach for underactuated systems [3, 4, 6, 7]. The control design for the y-axis involves the control of the corresponding crane load position in y-direction, whereas the multi-variable control of the x-axis deals with both the crane load position in x-direction and the position difference of the two bridge drives, corresponding to a skew of the crane bridge. Feedforward control based on an inverse system model and friction compensation using disturbance observer have proved efficient to further reduce tracking errors. Thereby, desired trajectories for the crane load position in the xz-plane can be tracked independently with high accuracy. Experimental results of the closed-loop system show both excellent tracking performance and steady-state accuracy.

2 Modelling of the Crane y-Axis

As a decentralised control structure is envisaged, a separate design model of is used for each crane axis. Here, the modelling shall be presented only for the y-axis. The origin of the y-axis, $y_k = 0$, is located in the middle of the bridge. With a bridge length $l_{br} = 8.7$ m the available workspace in y-direction is characterised by $y_k \in [-4.35\,\text{m}, 4.35\,\text{m}]$. The crane axis is modelled as a multibody system with two

rigid bodies as shown in Figure 1. The trolley is modelled by a mass m_k, whereas the crane load is represented by a lumped mass m_l. The trolley is electrically driven by a motor force F_k. As the main disturbance nonlinear friction and damping are taken into account by the disturbance force F_r. This disturbance force is neglected at feedback control design but counteracted by both feedforward and observer-based disturbance compensation. The rope suspension is considered as massless connection, where rope deflections and small external damping are neglected. The two degrees of freedom for the mechanical model of the y-axis are chosen as the trolley position $q_1 = y_k$ and as the rope angle $q_2 = \varphi_y$. Then, the vector of generalized coordinates becomes $\underline{q} = [q_1, q_2]^T$. The rope length l_s is considered as a slowly varying system parameter and taken into account at control design by gain-scheduling techniques. By exploiting Langrange's equations, the equations of motion of the crane axis can be calculated and stated in the following matrix notation:

$$\underbrace{\begin{bmatrix} m_l + m_k & m_l\, l_s \cos(q_2) \\ m_l\, l_s \cos(q_2) & m_l\, {l_s}^2 \end{bmatrix}}_{\underline{M}} \ddot{\underline{q}} + \begin{bmatrix} -m_l\, l_s\, \dot{q}_2^2\, \sin(q_2) \\ m_l\, g\, l_s\, \sin(q_2) \end{bmatrix} = \underbrace{\begin{bmatrix} 1 \\ 0 \end{bmatrix} F_k}_{\underline{G}\, u} \tag{1}$$

3 Passivity-Based Control of Underactuated Systems

The open-loop underactuated system is governed by the Hamiltonian as the sum of kinetic and potential energy:

$$H(\underline{q}, \underline{p}) = \frac{1}{2} \underline{p}^T \underline{M}^{-1}(\underline{q})\, \underline{p} + V(\underline{q}) \tag{2}$$

At this, the generalised coordinates $\underline{q} \in \mathbb{R}^n$ and the generalised momentum $\underline{p} \in \mathbb{R}^n$ are used. With the symmetric, positive definite mass matrix $\underline{M}(\underline{q}) = \underline{M}^T(\underline{q}) > 0$ and the potential energy $V(\underline{q})$, the total energy of the underactuated system can be stated. As the friction as well as the damping forces are counteracted by an observer-based disturbance compensation, the passivity-based control design is based on the following state equations:

$$\begin{bmatrix} \dot{\underline{q}} \\ \dot{\underline{p}} \end{bmatrix} = \begin{bmatrix} \underline{0} & \underline{I} \\ -\underline{I} & \underline{0} \end{bmatrix} \begin{bmatrix} \nabla_{\underline{q}} H \\ \nabla_{\underline{p}} H \end{bmatrix} + \begin{bmatrix} \underline{0} \\ \underline{G}(\underline{q}) \end{bmatrix} \underline{u} \tag{3}$$

The matrix $\underline{G} \in \mathbb{R}^{n \times m}$ determines how the control input $\underline{u} \in \mathbb{R}^m$ acts on the system. For a fully actuated system $m = n$ holds, whereas for the crane as underactuated system $rank\,(\underline{G}) = m < n$ is given. The passivity-based control involves the design of a desired closed-loop Hamiltonian H_d

$$H_d(\underline{q}, \underline{p}) = \frac{1}{2} \underline{p}^T \underline{M}_d^{-1}(\underline{q}) \underline{p} + V_d(\underline{q}) \tag{4}$$

The matrix $\underline{M}_d = \underline{M}_d^T > 0$ denotes the mass matrix according to the desired kinetic energy and V_d the desired closed-loop potential energy. This energy function V_d to be determined must have a global minimum in the desired equilibrium $\underline{q}^*$. This leads to $\min V_d(\underline{q}) = V_d(\underline{q}^*)$. The control design (IDA – PC) can be divided into the following two steps:

1. Energy shifting by the control action $\underline{u}_{ev}(\underline{q}\,,\,\underline{p})$
2. Damping injection by the control action $\underline{u}_{di}(\underline{q}\,,\,\underline{p})$

The resulting control law is given by the sum of both control parts, i.e. $\underline{u} = \underline{u}_{ev} + \underline{u}_{di}$. For the calculation of the feedback control law, the following condition must hold for the closed-loop:

$$\begin{bmatrix} \dot{\underline{q}} \\ \dot{\underline{p}} \end{bmatrix} = \left(\underline{J}_d(\underline{q},\underline{p}) - \underline{R}_d(\underline{q},\underline{p})\right) \begin{bmatrix} \nabla_{\underline{q}} H_d \\ \nabla_{\underline{p}} H_d \end{bmatrix}$$

with the terms

$$\underline{J}_d = -\underline{J}_d^T = \begin{bmatrix} \underline{0} & \underline{M}^{-1}\,\underline{M}_d \\ -\underline{M}_d\;\underline{M}^{-1} & \underline{J}_z\,(\underline{q},\underline{p}) \end{bmatrix},\; \underline{R}_d = \underline{R}_d^T = \begin{bmatrix} \underline{0} & \underline{0} \\ \underline{0} & \underline{G}\,\underline{K}_d\;\underline{G}^T \end{bmatrix} > 0 \tag{5}$$

The matrix $\underline{J}_d$ describes the desired interconnection and $\underline{R}_d$ the damping matrix. The interconnection matrix $\underline{J}_d$ is extended by an additional interconnection part $\underline{J}_z$. The damping matrix $\underline{R}_d$ is introduced to provide sufficient damping in the closed-loop system. This is achieved be a negative feedback of the corresponding passive output, in the given case $\underline{G}^T\,\nabla_{\underline{p}} H_d$. As a result, the damping control action can be stated as

$$\underline{u}_{di} = -\underline{K}_d\,\underline{G}^T\,\nabla_{\underline{p}} H_d, \tag{6}$$

with the constant gain matrix $\underline{K}_d = \underline{K}_d^T$. The energy shifting control part $\underline{u}_{ev}$ is determined from

$$\begin{bmatrix} \underline{0} & \underline{I} \\ -\underline{I} & \underline{0} \end{bmatrix} \begin{bmatrix} \nabla_{\underline{q}} H \\ \nabla_{\underline{p}} H \end{bmatrix} + \begin{bmatrix} \underline{0} \\ \underline{G} \end{bmatrix} \underline{u}_{ev} = \begin{bmatrix} \underline{0} & \underline{M}^{-1}\underline{M}_d \\ -\underline{M}_d\,\underline{M}^{-1} & \underline{J}_z(\underline{q},\underline{p}) \end{bmatrix} \begin{bmatrix} \nabla_{\underline{q}} H_d \\ \nabla_{\underline{p}} H_d \end{bmatrix} \tag{7}$$

The first row is always true, whereas the second row leads to

$$\underline{G}\,\underline{u}_{ev} = \nabla_{\underline{q}} H - \underline{M}_d\,\underline{M}^{-1}\nabla_{\underline{q}} H_d + \underline{J}_z\,\underline{M}_d^{-1}\,\underline{p} \tag{8}$$

considering $\nabla_{\underline{p}} H_d = \underline{M}_d^{-1}\,\underline{p}$. The energy shifting control $\underline{u}_{ev}$ in case of an underactuated system can be stated using the left pseudo-inverse $\underline{G}^+ = (\underline{G}^T\,\underline{G})^{-1}\underline{G}^T$, which leads to

$$\underline{u}_{ev} = \underbrace{(\underline{G}^T\,\underline{G})^{-1}\underline{G}^T}_{=\underline{G}^+} \left(\nabla_{\underline{q}} H - \underline{M}_d\,\underline{M}^{-1}\nabla_{\underline{q}} H_d + \underline{J}_z\,\underline{M}_d^{-1}\,\underline{p}\right) \tag{9}$$

Introducing the orthogonal vektor $\underline{G}^{\perp}$ according to $\underline{G}^{\perp}\underline{G} = 0$, the control law $\underline{u}_{ev}$ must be subject to:

$$\underline{G}^{\perp}\left[\nabla_{\underline{q}} H - \underline{M}_d\, \underline{M}^{-1} \nabla_{\underline{q}} H_d + \underline{J}_z\, \underline{M}_d^{-1}\, \underline{p}\right] \stackrel{!}{=} 0 \tag{10}$$

This problem can be devided in two parts. A first equation that is independent on the momentum vector $\underline{p}$, and a second equation that depends on this momentum vector $\underline{p}$. This results in two partial differential equations that allow for calculating the closed-loop mass matrix $\underline{M}_d$ and the additional interconnection matrix $\underline{J}_z$.

$$\underline{G}^{\perp}\left[\nabla_{\underline{q}} V - \underline{M}_d\, \underline{M}^{-1} \nabla_{\underline{q}} V_d\right] = \underline{0} \tag{11}$$

$$\underline{G}^{\perp}\left[\nabla_{\underline{q}} (\underline{p}^T \underline{M}^{-1}\, \underline{p}) - \underline{M}_d\, \underline{M}^{-1} \nabla_{\underline{q}} (\underline{p}^T \underline{M}_d^{-1}\, \underline{p}) + 2\, \underline{J}_z\, \underline{M}_d^{-1}\, \underline{p}\right] = \underline{0} \tag{12}$$

The control design is straight-forward when the mass matrix $\underline{M}$ is constant and inpendent of $\underline{q}$ ist. In this case the closed-loop a constant mass matrix $\underline{M}_d$ is used and the additional interconnection matrix $\underline{J}_z = \underline{0}$ can be chosen as zero matrix. Then the control law is obtained by evaluating (11) directly.

4 Passivity-Based Control Design for the *y*-Axis

For the passivity-based control design for the y-axis, the equations of motion are employed with the vector of generalized coordinates $\underline{q} = [y_k,\ \varphi_y]^T$. For the input vector $\underline{G}$, an orthogonal vector $\underline{G}^{\perp}$ has to be determined such that $\underline{G}^{\perp}\underline{G} = 0$ holds. In the given case the required vector is $\underline{G}^{\perp} = [0,\ 1]$. At the control design, the desired energy function in terms of the sum of kinetic and potential energy has to be specified such that a global minimum is obtained in the desired equilibrium point $\underline{q}^* = [y_{k,d},\ 0]^T$. In order to simplify the controller design, the mass matrix $\underline{M}$ is linearized for small rope angles q_2: $\cos(q_2) \approx 1$. The resulting mass matrix becomes

$$\underline{M}_{lin} = \begin{bmatrix} m_l + m_k & m_l\, l_s \\ m_l\, l_s & m_l\, l_s^2 \end{bmatrix}, \tag{13}$$

which is independent of the generalized coordinates q_1 and q_2. Therefore, the symmetric mass matrix of the closed-loop $\underline{M}_d$ can be chosen as

$$\underline{M}_d = \begin{bmatrix} a_1 & a_2 \\ a_2 & a_3 \end{bmatrix} \tag{14}$$

The elements a_1,a_2 und a_3 of the mass matrix $\underline{M}_d$ are, according to the linearized mass matrix $\underline{M}_{lin}$, independent of the vector of generalised coordinates $\underline{q}$. To obtain an asymptotically stable closed-loop system, the new mass matrix $\underline{M}_d$ must be chosen positive definite. As a result, the following conditions for the elements of $\underline{M}_d$

can be stated: $a_1 > 0$ and $a_1\, a_3 > a_2^2$. Now, the potential energy of the closed-loop system V_d can be specified using (11) with $\underline{\underline{M}} = \underline{\underline{M}}_{lin}$.

$$\left(\frac{a_2}{m_k} - \frac{a_3}{l_s\, m_k}\right) \frac{\partial\, V_d}{\partial q_1} + \left(\frac{a_3\ (m_l + m_k)}{{l_s}^2\, m_l\, m_k} - \frac{a_2}{l_s\, m_k}\right) \frac{\partial\, V_d}{\partial q_2} = m_l\, g\, l_s\ \sin(q_2) \quad (15)$$

This partial differential equation for $V_d(q_1, q_2)$ equation can be solved using computer algebra packages like *Maple*. The following solution is obtained:

$$\begin{aligned} V_d &= \frac{{m_l}^2\, g\, {l_s}^3\, m_k\ \cos(q_2)}{a_2\, m_l\, l_s - a_3\ (m_l + m_k)} + \Gamma \\ \text{with} \quad \Gamma &= f\,(q_2 + q_1\, \gamma) \quad \text{and} \quad \gamma = \frac{a_3\ (m_k + m_l) - a_2\, m_l\, l_s}{l_s\, m_l\ (a_3 - a_2\, l_s)} \end{aligned} \quad (16)$$

Here, Γ represents a freely selectable energy function. This energy function Γ must chosen properly such that V_d has a global minimum in the desired equilibrium point $\underline{q}^*$. Therefore, the gradient vector as well as the Hessian of the potential energy function V_d are considered. The gradient becomes

$$\nabla_{\underline{q}}\, V_d\Big|_{\underline{q}=\underline{q}^*} = \left[\begin{array}{c} \dfrac{\partial \Gamma}{\partial q_1} \\ -\dfrac{{m_l}^2\, g\, {l_s}^3\, m_k\ \sin(q_2)}{a_2\, m_l\, l_s - a_3\ (m_l + m_k)} + \dfrac{\partial \Gamma}{\partial q_2} \end{array}\right]\Bigg|_{\underline{q}=\underline{q}^*} = \left[\begin{array}{c} \dfrac{\partial \Gamma}{\partial q_1}\Big|_{\underline{q}=\underline{q}^*} \\ \dfrac{\partial \Gamma}{\partial q_2}\Big|_{\underline{q}=\underline{q}^*} \end{array}\right] \stackrel{!}{=} \underline{0} \quad (17)$$

For the desired equilibrium point $\underline{q}^*$ the gradient of the freely selectable function $\nabla_q \Gamma$ at $\underline{q}^*$ must vanish. In addition, the Hessian is considered as sufficient condition for a minimum

$$\nabla_{\underline{q}}^2\, V_d\Big|_{\underline{q}=\underline{q}^*} = \left[\begin{array}{cc} \dfrac{\partial^2 \Gamma}{\partial q_1^2} & \dfrac{\partial^2 \Gamma}{\partial q_1\, \partial q_2} \\ \dfrac{\partial^2 \Gamma}{\partial q_1\, \partial q_2} & -\dfrac{{m_l}^2\, g\, {l_s}^3 m_k\ \cos(q_2)}{a_2\, m_l\, l_s - a_3\ (m_l + m_k)} + \dfrac{\partial^2 \Gamma}{\partial q_2^2} \end{array}\right]\Bigg|_{\underline{q}=\underline{q}^*} \stackrel{!}{>} 0 \quad (18)$$

For simplicity a quadratic function Γ of the form

$$\Gamma = \frac{K}{2}\,(\tilde{q}_2 + \tilde{q}_1\, \gamma)^2 \quad (19)$$

has been chosen, where K denotes a proportional gain. The variable $\tilde{q}_1 = y_k - y_{k,d}$ stands for the tracking error in terms of the difference between the trolley position y_k and the desired trolley position $y_{k,d}$. Accordingly, the tracking error $\tilde{q}_2 = \varphi_y - \varphi_{y,d}$ represents the deviation of the measured rope angle φ_y and the desired rope angle $\varphi_{y,d}$. By evaluating the gradient vector, the following conditions are obtained:

$$\nabla_{\underline{x}} V_d = \begin{bmatrix} K\ (\tilde{q}_2 + \tilde{q}_1\,\gamma)|_{\underline{q}=\underline{q}^*} \\ K\ (\tilde{q}_2 + \tilde{q}_1)|_{\underline{q}=\underline{q}^*} \end{bmatrix} = \begin{bmatrix} 0 \\ 0 \end{bmatrix} \tag{20}$$

Next, the Hessian is investigated. This leads to

$$\nabla^2_{\underline{x}} V_d = \begin{bmatrix} K\,\gamma^2 & K\,\gamma \\ K\,\gamma & K - \dfrac{m_l^2\, m_k\, g\, l_s^3 \cos(q_2)}{a_2\, m_l\, l_s - a_3\ (m_l + m_k)} \end{bmatrix}\Bigg|_{\underline{x}^*} \tag{21}$$

The first north-western subdeterminant is positiv for $K > 0$ and $\gamma > 0$. Considering $|q_2| < pi/2$, the determinant of the Hessian is positive definite only for:

$$-\frac{K\gamma^2 {m_l}^2\, g\, {l_s}^3 m_k}{a_2\, m_l\, l_s - a_3\,(m_l + m_k)} > 0$$

The nominator is always positive; hence, the denominator must be negative in order to meet the necessary condition. This leads to an additional condition for the choice of the free design parameters a_2 and a_3: $a_3\,(m_l + m_k) > a_2\, m_l\, l_s$. The following choice has been made: $a_3 = c\, l_{\max}$, $a_1 = c/l_{\max}$ and $a_2 = m$, with the two constants c and m. These constants are selected such that $c > m > 0$ holds. The maximum rope length is given by the value $l_{\max}$. Hence, all the conditions above are fulfilled. With the energy function V_d determined, the control law can be calculated. The nonlinear control action $u_{PBC} = u_{ev} + u_{di}$ consists of the sum of the energy shifting term u_{ev} and the damping injection term u_{di}. The energy shifting is achieved by the control part u_{ev} according to

$$\begin{aligned} u_{ev} = (\underline{G}^T\,\underline{G})^{-1}\,\underline{G}^T\left(\nabla_{\underline{q}}\, V - \underline{M}_d\,\underline{M}_{lin}^{-1}\,\nabla_{\underline{q}}\, V_d\right) &= K\gamma(\tilde{q}_2 + \gamma\,\tilde{q}_1)\left(\frac{a_2}{l_s\, m_k} - \frac{a_1}{m_k}\right) \\ + \left(\frac{a_1}{l_s\, m_k} - \frac{a_2\ (m_l + m_k)}{m_l\, {l_s}^2 m_k}\right)&\left(K\,(\tilde{q}_2 + \gamma\,\tilde{q}_1) - \frac{{m_l}^2 g {l_s}^3 m_k\ \sin(q_2)}{a_2\, m_l\, l_s - a_3\ (m_l + m_k)}\right) \end{aligned} \tag{22}$$

With the constant damping gain $K_d > 0$, the damping injection control can be calculated from (6)

$$u_{di} = -K_d\left(\frac{((m_l + m_k)\,\dot{q}_1 + m_l\, l_s\,\dot{q}_2)\, a_3}{a_1\, a_3 - {a_2}^2} - \frac{\left(m_l\, l_s\,\dot{q}_1 + m_l\, {l_s}^2 \dot{q}_2\right) a_2}{a_1\, a_3 - {a_2}^2}\right) \tag{23}$$

5 Implementation of the Crane Control

In addition to the passivity-based control u_{PBC}, some structural extension have turned out to be useful at implementation to improve trajectory tracking (Figure 2).

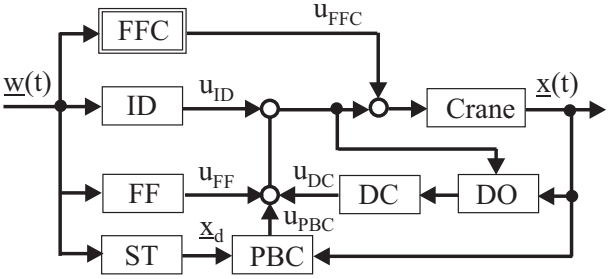

Fig. 2 Control implementation.

Hence, the stabilizing PBC is extended with feedforward control action based on an inverse system model. This feedforward control involves the following parts:

1. inverse dynamics control action u_{ID} based on the equation of motion without disturbance forces
2. feedforward compensation u_{FFC} of nonlinear friction and damping forces as main disturbances
3. a feedforward control action u_{FF} corresponding to the feedback control part u_{PBC}

The latter part u_{FF} is necessary to compensate for the feedback control in the ideal case if the design model matches the real system exactly. Then, the first two feedforward parts $u_{FFC}+u_{FF}$ would lead to a perfect trajectory tracking. In the given case of an imperfect system model with remaining uncertainties and disturbances, however, additional feedback control is mandatory. A trajectory planning module yields the desired values $\underline{w}$ for the crane load position $y_{l,d}$ as well as the corresponding first three time derivatives. For the feedforward control, however, the corresponding desired values for the trolley positions $y_{k,d}$ as well as the rope angle $\varphi_{y,d}$ and their time derivatives are required. As the system under consideration is differentially flat with the crane load position as flat control output, all the desired state variables and the control input can be calculated. In the implementation, the following linearized relationships have been used in the state transformation ST:

$$y_{k,d} = y_{l,d} + \frac{l_s}{g}\ddot{y}_{l,d}, \quad \dot{y}_{k,d} = \dot{y}_{l,d} + \frac{l_s}{g}\dddot{y}_{l,d}, \quad \varphi_{y,d} = -\frac{\ddot{x}_{l,d}}{g}, \quad \dot{\varphi}_{y,d} = -\frac{\dddot{x}_{l,d}}{g}. \tag{24}$$

With the control structure described above, sufficiently small control errors could be achieved. Nevertheless, the implemented model-based friction compensation can be significantly improved by an additional reduced order disturbance observer DO as well as an disturbance compensation DC as described in [1]. The complete control structure is adapted to the varying system parameters load mass m_l and rope length l_s by gain-scheduling.

6 Control of the x-Axis

The designed passivity-based control for the y-axis shall be used for the x-axis control as well. The crane bridge, however, is equipped with two electric drives, which have to be properly actuated to achieve both the desired motion in x-direction but also a vanishing position difference of both bridge sides. Due to an excentric trolley position on the bridge and different friction forces acting on the corresponding drives, an active synchronization of both bridge drives have to be provided instead of a simple division of the according passivity-based control action u_{PBC} in the form $u_{b,l} = u_{b,r} = 0.5 \cdot u_{PBC}$. The active synchronization is achieved by an underlying PD-control loop of high bandwidth, i.e. $m_\varphi = -K_{p,GLR}\,\varphi_{xb} - K_{d,GLR}\,\dot{\varphi}_{xb}$. The required force distribution can be derived from the following system of equations:

$$\begin{bmatrix} u_{PBC} \\ m_\varphi \end{bmatrix} = \begin{bmatrix} 1 & 1 \\ -\dfrac{l_{br}}{2} & \dfrac{l_{br}}{2} \end{bmatrix} \begin{bmatrix} u_{b,r} \\ u_{b,l} \end{bmatrix} \Leftrightarrow \quad \begin{bmatrix} u_{b,r} \\ u_{b,l} \end{bmatrix} = \begin{bmatrix} \dfrac{1}{2} & -\dfrac{1}{l_{br}} \\ \dfrac{1}{2} & \dfrac{1}{l_{br}} \end{bmatrix} \begin{bmatrix} u_{PBC} \\ m_\varphi \end{bmatrix} \tag{25}$$

Thereby, the control design for the y-axis can be used for the bridge position control as well. The x-position of the trolley depends on the y-position on the bridge and on the two position coordinates of the bridge, i.e. $x_{b,r}$ und $x_{b,l}$. This position can be calculated as follows:

$$x_k = x_{b,r} + \left(x_{b,l} - x_{b,r}\right)\left(\frac{1}{2} + \frac{y_k}{l_{br}}\right) \tag{26}$$

Consequently, by replacing the trolley mass m_k with the bridge mass m_b in (22) and (23), the resulting drive force $u_{PBC} = u_{ev} + u_{di}$ of the outer control loop in x-direction can be calculated.

7 Experimental Results

Tracking performance as well as steady-state accuracy w.r.t. the crane load position have been investigated by experiments with a 5 t-overhead travelling crane. The resulting tracking performance as regards desired trajectories in the xyz-workspace involving variations in rope length is shown in Figure 3.

8 Conclusions

This paper presents a gain-scheduled passivity-based control design for the translational axes of a 5 t-overhead travelling crane. The feedback control is extended by

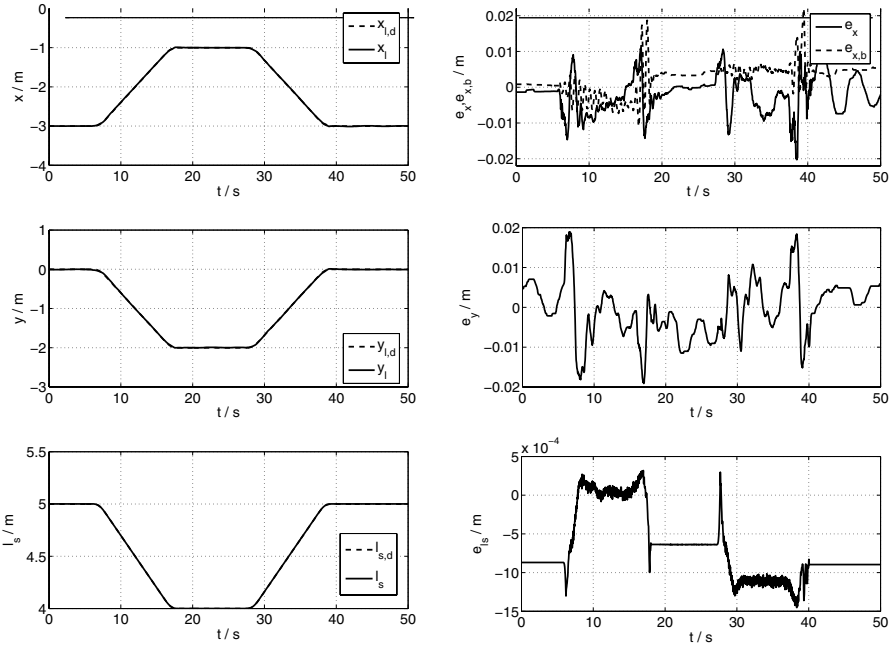

Fig. 3 Synchronised movement in the xyz-workspace with varying rope length.

feedforward control exploiting the differential flatness of the system. Furthermore, a reduced-order disturbance observer takes into account the remaining model uncertainties due to nonlinear friction acting on the trolley. The efficiency of the proposed control is shown by experimental results involving tracking of desired trajectories within the 3-dimensional workspace. Maximum tracking errors are approx. 2 cm.

References

1. Aschemann, H.: *Optimale Trajektorienplanung sowie modellgestütze Steuerung und Regelung für einen Brückenkran*. Fortschrittberichte VDI, Reihe 8, Nr. 929, VDI Verlag, Düsseldorf (2002).
2. Boustany, F., d'Andrea-Novel, B.: Adaptive Control of an Overhead Crane Using Dynamic Feedback Linearization and Estimation Design. In: *Proc. IEEE Int. Conf. on Robotics and Automation*, Nice, France, pp. 1963–1968 (1992).
3. Janzen, A.: Passivitätsbasierte Regelung mechatronischer Systeme. Diploma thesis, University of Ulm, Germany (2006).
4. Lozano, R., Brogliato, B., Egeland, O., and Maschke, B.: *Dissipative Systems Analysis and Control: Theory and Applications*. Springer (2000).
5. Nguyen, H.T.: State Variable Feedback Controller for an Overhead Crane. *J. Electr. Electr. Eng.* **14**(2), 75–84 (1994).
6. Rodriguez, H., Ortega, R., and Mareels, I.: A Novel Passivity-Based Controller for an Active Magnetic Bearing Benchmark Experiment. In: *Proc. of the ACC 2000*, Chicago, Illinois (2000).
7. van der Schaft, A.: *L_2-Gain and Passivity Techniques in Nonlinear Control*. Springer (2000).

Control of Vibration-Driven Systems Moving in Resistive Media

Nikolai N. Bolotnik, Felix L. Chernousko and Tatiana Yu. Figurina

Abstract The motion of a body controlled by movable internal masses in a resistive environment along a horizontal straight line is considered. Optimal periodic modes of motion are constructed for the internal masses to maximize the average speed of the velocity-periodic motion of the body. The maximum displacement allowed for the internal masses inside the body, as well as the relative velocities or accelerations of these masses are subjected to constraints. Three types of the resistance laws – piece-wise linear friction, quadratic friction, and Coulomb's dry friction – are considered.

1 Introduction

A rigid body with internal masses that perform periodic motions can move progressively in a resistive medium with nonzero average velocity. This phenomenon can be used as a basis for the design of mobile systems able to move without special propelling devices (wheels, legs, caterpillars or screws) due to direct interaction of the body with the environment. Such systems have a number of advantages over systems based on the conventional principles of motion. They are simple in design, do not require gear trains to transmit motion from the motor to the propellers, and their body can be made hermetic and smooth, without any protruding components. The

Nikolai N. Bolotnik
Institute for Problems in Mechanics of the Russian Academy of Sciences, 101 bld. 1, Vernadskii ave., Moscow 119526, Russia; E-mail: bolotnik@ipmnet.ru

Felix L. Chernousko
Institute for Problems in Mechanics of the Russian Academy of Sciences, 101 bld. 1, Vernadskii ave., Moscow 119526, Russia; E-mail: chern@ipmnet.ru

Tatiana Yu. Figurina
Institute for Problems in Mechanics of the Russian Academy of Sciences, 101 bld. 1, Vernadskii ave., Moscow 119526, Russia; E-mail: figur@ipmnet.ru

H. Ulbrich and L. Ginzinger (eds.), Motion and Vibration Control, 31–40.

said features make this principle of motion suitable for capsule-type microrobots [10] designed for motion in a strongly restricted space (e.g., inside narrow tubes) and in vulnerable media, for example, inside a human body for delivering a drug or a diagnostic sensor to an affected organ. Such systems can be driven to a prescribed position with high degree of accuracy, which enables them to be utilized in high-precision positioning systems in scanning electron and tunnel microscopes, as well as in micro- and nano-technological equipment [2, 12, 13].

Automatic transport systems moving due to periodic motion of internal masses are sometimes referred to as vibration-driven systems or vibration-driven robots. Some issues of the dynamics and parametric optimization of vibration-driven systems have been studied, e.g., in [1, 7, 11].

At the Institute for Problems in Mechanics of the Russian Academy of Sciences, vibration-driven minirobots for motion inside small-diameter tubes were designed [8].

Chernousko has initiated a systematic study in control and optimization of motion of systems with internal movable masses [3–5]. He solved a number of parametric optimization problems for two-body systems moving along a dry rough surface or in a viscous medium. Both velocity-controlled and acceleration-controlled motions of the internal mass were considered, the structure of the control law being prescribed. An optimal control problem for a two-mass system moving along a dry rough plane, with the structure of the control law unknown in advance, was solved in [6].

The present paper continues the studies in the optimization. Some simplifying restrictions that were imposed previously on the motion to be optimized are removed. In addition, an optimal control problem is solved for the motion of a rigid body with two internal masses along a dry rough plane. One of the masses moves horizontally along a straight line parallel to the line of motion of the body, while the other mass moves vertically. The vertically moving mass provides an additional possibility for the control of friction between the body and the supporting plane due to the change in the normal pressure force.

2 Two-Body System

In this section, we consider a two-body system consisting of the main body and the internal body that can move relative to the main body along a straight line. The motion of the system along a horizontal straight line in resistive media is studied for various laws of friction.

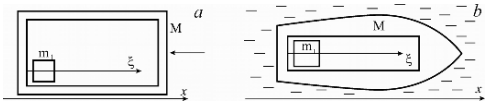

Fig. 1 Two-mass system in a resistive medium.

2.1 Statement of the Problem

Consider a system of two interacting rigid bodies, the main body of mass M and the movable internal body of mass m (Figure 1). In what follows, we will refer to the main body and the internal body as body M and mass m. Body M interacts with a resistive environment. We will study periodic motions of mass m relative to body M under which the entire system moves progressively in the environment.

Let x denote the coordinate measuring the displacement of body M relative to the environment; ξ the coordinate measuring the displacement of mass m relative to body M; $v = \dot{x}$ the absolute velocity of body M; $u = \dot{\xi}$ the relative velocity of mass m; and $w = \dot{u}$ the relative acceleration of mass m.

We will confine ourselves to simple periodic motions of mass m such that during each period T, this mass first moves with a velocity u_1 from the left-hand extreme position $\xi = 0$ to the right-hand extreme position $\xi = L$ and then returns to the initial position with a velocity u_2. Positive parameter L characterizes the limits within which mass m is allowed to move relative to body M. This law of motion can be written as

$$u(t) = \begin{cases} u_1, & 0 \le t < \tau, \\ -u_2, & \tau \le t \le T, \end{cases} \tag{1}$$

$$w(t) = u_1\delta(t) - (u_1 + u_2)\delta(t - \tau) + u_2\delta(t - T), \tag{2}$$

where

$$\tau = L/u_1, \quad T = L(u_1^{-1} + u_2^{-1}), \tag{3}$$

and $\delta(\cdot)$ is Dirac's delta function.

The motion of body M is governed by the equations

$$\begin{gathered} \dot{x} = v, \quad \dot{v} = -\mu w - r(v), \\ \mu = m/(M + m), \quad r(v) = -R(v)/(M + m), \quad vr(v) \ge 0, \end{gathered} \tag{4}$$

where $R(v)$ represents the resistance force applied to body M by the environment.

We will seek for the optimal parameters u_1 and u_2 such that the corresponding velocity-periodic motion of body M occurs with maximum average velocity. Thus we arrive at the optimization problem.

Problem 1. For the system of Eqs. (1)–(4), subject to the boundary conditions

$$x(0) = 0, \quad \dot{x}(0) = \dot{x}(T), \tag{5}$$

find the parameters u_1 and u_2 that satisfy the constraints

$$0 \le u_i \le U, \quad i = 1,\ 2 \tag{6}$$

and maximize the average velocity of mass M

$$V = x(T)/T. \tag{7}$$

To solve this problem use the following algorithm:

1. Substitute $w(t)$ of Eq. (2) into Eq. (4).
2. Solve the resulting equation subject to the initial conditions $x(0) = 0$, $\dot{x}(0) = v_0$ to obtain $x = x(t; u_1, u_2, v_0, L)$.
3. Find the initial velocity $v_0 = v_0^*$ using the periodicity condition

$$\dot{x}(0; u_1, u_2, v_0, L) = \dot{x}(T; u_1, u_2, v_0, L) \tag{8}$$

and the definition of Eq. (3) for T.
4. Substitute $x(T; u_1, u_2, v_0^*, L)$ into Eq. (7) to obtain

$$V = V(u_1, u_2, L). \tag{9}$$

5. Maximize the function $V = V(u_1, u_2, L)$ with respect to u_1 and u_2, subject to the constraints of Eq. (6).

In the subsequent subsections we will solve Problem 1 for three types of the resistance law $r(v)$. Piece-wise linear resistance, quadratic resistance, and Coulomb's friction will be considered.

2.2 Piece-Wise Linear Resistance

The piecewise-linear resistance (anisotropic linear friction) is characterized by the law

$$r(v) = \begin{cases} k_+ v, & v \ge 0, \\ k_- v, & v < 0, \end{cases} \tag{10}$$

where k_- and k_+ are positive coefficients. The particular case $k_+ = k_-$ corresponds to linear viscous friction.

For $k_+ = k_- = k$, velocity-periodic motion of body M with nonzero average velocity is impossible for any periodic motion of mass m. To prove this, integrate Eq. (4) for v with respect to t from 0 to T to obtain

$$v(T) - v(0) = -\mu[u(T) - u(0)] - k[x(T) - x(0)]. \tag{11}$$

This relation implies that $x(0) = x(T)$ if the functions $v(t)$ and $u(t)$ are T-periodic; hence, $V = 0$.

For arbitrary k_- and k_+, the function V of Eq. (9) is given by

$$V = \frac{\mu(1-e_1)(1-e_2)(k_- - k_+)u_1u_2}{(1-e_1e_2)Lk_-k_+},$$
$$e_1 = \exp(-k_-Lu_1^{-1}),\ e_2 = \exp(-k_+Lu_2^{-1}). \tag{12}$$

From this expression it follows that $V > 0$ ($V < 0$) for $k_- > k_+$ ($k_- < k_+$). This means that body M moves on the average in the direction of the lower resistance.

The maximum magnitude of the function V of Eq. (12) occurs for $u_1 = u_2 = U$. In this case, $\tau = L/U = T/2$, in accordance with Eq. (3). Therefore, in the optimal mode, the internal mass moves in both directions with the maximal speed U, each stroke taking a half-period.

2.3 Quadratic Resistance

The quadratic resistance is characterized by

$$r(v) = \kappa|v|v, \tag{13}$$

where κ is a positive coefficient.

For this case, Eq. (8) can be reduced to the quadratic equation

$$(u_2 - u_1 + \kappa LY)Z^2 + (\kappa LY^2 - 2u_1Y)Z - u_1Y^2 = 0;$$
$$Z = v_0 - \mu u_1, \quad Y = \mu(u_1 + u_2). \tag{14}$$

The initial velocity v_0^* is expressed by $v_0^* = Z^* + \mu u_1$, where Z^* is the solution of the quadratic equation. To simplify the calculations, we assume $v_0^* = 0$. For this assumption, the parameters u_1 and u_2 become related by

$$u_2 = (1 - \mu\kappa L)(1 + \mu\kappa L)^{-1}u_1. \tag{15}$$

We assume that $\mu\kappa L < 1$. If this condition is violated, the mode of motion with $v_0^* = 0$ does not occur.

The calculation of the average velocity of body M in accordance with Eq. (9) and maximization of this velocity lead to the expressions

$$u_1 = U, \quad u_2 = (1 - \mu\kappa L)(1 + \mu\kappa L)^{-1}U,$$
$$V_{\max} = -\frac{U(1-\mu\kappa L)}{2\kappa L}\ln\left(1 - \mu^2\kappa^2L^2\right). \tag{16}$$

The quantity $V_{\max}$ is positive and, hence, for the quadratic resistance law, the progressive velocity-periodic motion of the system is possible even in the isotropic case, in contrast to the linear resistance.

2.4 Coulomb's Friction

For Coulomb's dry friction, the function $r(v)$ of Eq. (4) is specified by

$$r(v) = \begin{cases} f_+ g, & \text{if } v > 0 \text{ or } v = 0,\ \mu w < -f_+ g, \\ -f_- g, & \text{if } v < 0 \text{ or } v = 0,\ \mu w > f_- g, \\ -\mu w, & \text{if } v = 0,\ -f_+ g \le \mu w \le f_- g, \end{cases} \tag{17}$$

where f_+ and f_- are the coefficients of friction that resists forward and backward motion of mass M, respectively; g is the acceleration due to gravity.

Introduce the dimensionless variables

$$\begin{gathered} x_i = u_i/u_0,\ i = 1, 2; \quad u_0 = \sqrt{L f_- g/\mu}, \\ x_0 = v_0/(\mu u_0), \quad F = V/(\mu u_0), \quad c = f_+/f_-, \quad X = U/u_0. \end{gathered} \tag{18}$$

In terms of these variables, the solution of Problem 1 is reduced to the determination of the optimal values of x_0, x_1, x_2, and F for given X and c. The final result is given by the following expressions:

If $c < 1$ and $X < (c/2)^{1/2}$, *then* $x_1 = x_2 = X,\ x_0 = -X,\ F = (1-c)X^3/c$.

If $c < 1$ and $X \ge (c/2)^{1/2}$, *then* $x_1 = x_2 = X,\ x_0 = -X,\ F = X - c(1+c)(4X)^{-1}$.

If $c = 1$ and $X \le (2)^{-1/2}$, *then* $|x_1| \le X,\ |x_2| \le X,\ x_0 = -x_2,\ F = 0$.

If $c > 1$ and $X \le (2)^{-1/2}c$, *then* $x_1 = 0,\ x_2 = 0,\ x_0 = 0,\ F = 0$.

If $c \ge 1$ and $X > (2)^{-1/2}c$, *then* $x_1 = X/c,\ x_2 = X,\ x_0 = (X^2 - c^2)(cX)^{-1}$, $F = (2X^2 - c^2)(2cX)^{-1}$.

From these expressions it follows that positive average velocity $V > 0$ of the two-body system can be achieved for any X if $c < 1$, i.e., if the coefficient of friction resisting the forward motion (in the positive direction of the x-axis) is less than the coefficient of friction resisting the backward motion. For $c \ge 1$, positive average velocity may occur only if $X > c/\sqrt{2}$, i.e., the maximum velocity allowed for the relative motion of mass m should be sufficiently large.

3 Three-Body System

In this section, an optimal control problem is solved for a three-body system consisting of the main body and two internal masses, one of which moves horizontally along the line parallel to the line of motion of the main body, while the other mass moves vertically. The main body moves along a dry rough plane. The motion of the

internal mass along the vertical is used to control the force of friction between the main body and the supporting plane due to the change in the normal pressure force.

3.1 Coulomb's Friction

Consider a mechanical system distinguished from the system studied in Section 2 by an additional internal mass m_2 that can move vertically. Let ξ_1 denote the displacement of mass m_1 along the horizontal and ξ_2 the displacement of mass m_2 along the vertical. Let body M move along a rough horizontal plane. Coulomb's friction is assumed to act between the body and the plane, the coefficient of friction being independent of the direction of the motion.

Proceed to the dimensionless variables, using $M + m_1 + m_2$, l, and $\sqrt{l/g}$ as the units of mass, length, and time, respectively. The unit of length l can be chosen arbitrarily, since the model of the system does not involve a characteristic length. In the normalized variables, the motion of body M is governed by the equation

$$\dot{x} = v, \quad \dot{v} = -\mu_1 w_1 - r(v),$$
$$r(v) = \begin{cases} fN\mathrm{sgn}(v), & \text{if } v \neq 0, \\ -\mu_1 w_1, & \text{if } v = 0,\ |\mu_1 w_1| \leq fN, \\ -fN\mathrm{sgn}(w_1), & \text{if } v = 0,\ |\mu_1 w_1| > fN, \end{cases} \qquad N = 1 + \mu_2 w_2, \tag{19}$$

where

$$\mu_i = m_i/(M + m_1 + m_2), \quad \ddot{\xi}_i = w_i, \quad i = 1,\ 2. \tag{20}$$

The quantity N in Eq. (19) represents the normal pressure force exerted on body M by the supporting plane.

We will construct T-periodic motions of masses m_1 and m_2 that satisfy the constraints

$$|w_1| \leq W_1, \quad -W_2^- \leq w_2 \leq W_2;$$
$$W_2^- = \min\left(1/\mu_2,\ W_2\right), \quad \mu_1 W_1 > f(1 - \mu_2 W_2^-) \tag{21}$$

and maximize the average speed of the corresponding velocity-periodic motion of body M. The period T is fixed.

In Eq. (21), positive quantities W_1 and W_2 constrain the magnitudes of the relative accelerations of the internal masses due to limited power of the actuators. The lower bound W_2^- for the relative acceleration of mass m_2 is due to the requirement that body M have permanent contact with the supporting plane. For $\mu_2 w_2 < -1$, the normal pressure force N would have been negative, which is impossible for the unilateral contact. The condition $\mu_1 W_1 > f(1 - \mu_2 W_2^-)$ is necessary for body M to be able to be moved from a state of rest.

Thus we arrive at the optimal control problem:

Problem 2. For the system of Eqs. (19) and (20) considered in the time interval $[0, T]$, find the control functions $w_1(t)$ and $w_2(t)$ that satisfy the constraints of Eq. (21), generate the motion subject to the boundary conditions

$$x(0)=0,\quad v(0)=0,\quad v(T)=0,\quad \xi_i(0)=\xi_i(T)=0,\quad \dot\xi_i(0)=\dot\xi_i(T) \quad (22)$$

and maximize the average velocity $V=x(T)/T$ of body M.

3.2 Solution of the Problem

It has been proven that the optimal control is provided by piece-wise constant functions

$$w_1(t)=\begin{cases} -W_1, & t\in[0,\tau_1),\\ W_1, & t\in[\tau_1,\delta_*),\\ \bar w_1, & t\in[\delta_*,T],\end{cases}\qquad w_2(t)=\begin{cases} -W_2^-, & t\in[0,\tau_2),\\ W_2, & t\in[\tau_2,\delta_*),\\ \bar w_2, & t\in[\delta_*,T],\end{cases} \quad (23)$$

and that body M moves forward ($v>0$) for $t\in(0,\delta_*)$ and remains in a state of rest for $t\in[\delta_*,T]$. In the optimal mode, body M never moves backward.

Using these observations, Eq. (19), and the boundary conditions $v(0)=v(\delta_*)=0$, we express the parameter τ_1 in terms of τ_2 and δ_*:

$$\tau_1=\frac{\delta_*[U_1+f(1+U_2)]-2f\widetilde U_2\tau_2}{2U_1};\qquad U_i=\mu_1W_i,\quad U_2^-=\mu_2W_2^-,\quad \widetilde U_2=(U_2^-+U_2)/2. \quad (24)$$

Using the definitions $\ddot\xi_i=w_i$ of Eq. (20), the conditions $\dot\xi_i(0)=\dot\xi_i(T)$ of Eq. (22), expressions (23) for the control functions, and relations (24), we calculate the constant quantities $\bar w_1$ and $\bar w_2$:

$$\bar w_1=\frac{f[\delta_*(1+U_2)-2\widetilde U_2\tau_2]}{\mu_1(T-\delta_*)},\quad \bar w_2=\frac{2\widetilde U_2\tau_2-U_2\delta_*}{\mu_2(T-\delta_*)}. \quad (25)$$

The average velocity of body M is expressed by

$$V(T)=\frac{U_1^2-k^2(1+U_2)^2}{4U_1T}{\delta_*}^2+f\widetilde U_2\frac{U_1+f(1+U_2)}{U_1T}\tau_2\delta_*-f\widetilde U_2\frac{U_1+f\widetilde U_2}{U_1T}\tau_2^2. \quad (26)$$

The optimal values of τ_2 and δ_* are determined by the maximization of the function V with respect to these parameters under the constraints

$$\delta_*[U_1+f(1+U_2)]\le U_1T+2f\widetilde U_2\tau_2,\quad 2\widetilde U_2\delta_*-U_2^-T\le 2\widetilde U_2\tau_2\le U_2T,$$
$$(1+U_2)\delta_*\le\frac{T}{2}+2\widetilde U_2\tau_2,\quad \max\left\{0,\ \frac{\delta_*[f(1+U_2)-U_1]}{2f\widetilde U_2}\right\}\le\tau_2\le\delta_*\le T. \quad (27)$$

These inequalities are derived from the conditions $0\le\tau_i\le\delta\le T$, expressions (24) and (25) , and the constraints

$$|\mu_1 \bar{w}_1| \le U_1, \quad U_2^- \le \mu_2 \bar{w}_2 \le U_2, \tag{28}$$

$$|\mu_1 \bar{w}_1| \le f(1 + \mu_2 \bar{w}_2), \tag{29}$$

The constraints of Eq. (28) express those of Eq. (21) for the controls of Eq. (23) in the time interval $[\delta_*, T]$. Inequality (29) follows from the condition that body M remains in a state of rest for $t \in [\delta_*, T]$ and Coulomb's friction law $r(v)$ of Eq. (19).

For the optimal controls $w_i(t)$ constructed in accordance with the algorithm described, the functions $\xi_i(t)$, characterizing the optimal motions of the internal masses, are defined by

$$\xi_i(t) = \frac{t}{T} \int_0^T \eta w_i(\eta) d\eta + \int_0^t (t - \eta) w_i(\eta) d\eta. \tag{30}$$

3.3 Limiting Cases

To assess the effect of introducing the internal mass moving vertically on the maximum average speed of the system, solve Problem 2 for two limiting cases, $W_2 = \infty$ and $W_2 = 0$. In the former case, the function $w_2(t)$, which controls mass m_2, is unbounded from above, while in the latter case, $w_2(t) \equiv 0$ and, hence, the motion of the internal mass along the vertical does not occur.

For $W_2 = \infty$, the optimal controls for $t \in [0, T]$ are given by

$$w_1(t) = W_1 \mathrm{sgn}(t - T/2), \quad w_2(t) = \mu_2^{-1}[T\delta(t - T) - 1], \tag{31}$$

where $\delta(\cdot)$ is Dirac's delta function. For this control, body M speeds up from $v = 0$ to $v = \mu_1 W_1 T/2$ with acceleration $\mu_1 W_1$ in the time interval $[0, T/2)$ and slows down to $v = 0$ with acceleration $-\mu_1 W_1$ in the interval $(T/2, T]$. The average velocity over the period T is $V = \mu_1 W_1 T/4$. Mass m_2 moves upward for $t \in (0, T/2)$ and downward for $t \in (T/2, T)$, with the velocity $\dot{\xi}_2$ uniformly decreasing at a rate of μ_2^{-1} from $\mu_2^{-1} T/2$ to $-\mu_2^{-1} T/2$ in the interval $(0, T)$. At the instant T, mass m_2 undergoes an elastic impact to restore the initial velocity. It is important that the motion of mass m_2 with acceleration $-\mu_2^{-1}$ provides zero normal pressure force and, hence, zero friction force between body M and the plane.

For $W_2 = 0$, the average velocity is determined by [6]

$$V = \frac{\mu_1 W_1 T}{16} \left(1 - \frac{f^2}{\mu_1^2 W_1^2}\right) \tag{32}$$

A comparison with the case $W_2 = \infty$ indicates that the activation of mass m_2 enables at least 4-fold increase in the maximum average velocity of body M.

4 Conclusion

Optimal velocity-periodic motions of mobile systems driven by periodic motions of the internal masses were calculated for various laws of resistance of the environment. It was shown that for any constraints on the displacements of the internal masses inside the main body, the maximum average speed of the body can be made arbitrarily high, provided that the velocities or accelerations allowed for the internal masses are large enough. For systems moving along a horizontal dry rough plane, the introduction of an internal mass moving vertically can lead to a significant increase in the average velocity due to the control of the normal pressure force.

Acknowledgements This research was partly financed by the Russian Foundation for Basic Research (07-01-12015 and 08-08-00438).

References

1. Bolotnik, N.N., Zeidis, I., Zimmermann, K. and Yatsun, S.F.: Dynamics of controlled motion of vibration-driven systems. *Journal of Computer and Systems Sciences International* **45**(5), 831–840 (2006).
2. Breguet, J.-M. and Clavel, R.: Stick and slip actuators: design, control, performances and applications. In: *Proc. Int. Symp. on Micromechatronics and Human Science (MHS)*, pp. 89–95. New York, IEEE (1998).
3. Chernousko, F.L.: The optimal rectilinear motion of a two-mass system. *Journal of Applied Mathematics and Mechanics* **66**(1), 1–7 (2002).
4. Chernousko, F.L.: On the motion of a body containing a movable internal mass. *Doklady Physics* **50**(11), 593–597 (2005).
5. Chernousko, F.L.: Analysis and optimization of the motion of a body controlled by a movable internal mass. *Journal of Applied Mathematics and Mechanics* **70**(6), 915–941 (2006).
6. Figurina, T.Yu.: Optimal control of the motion of a two-body system along a straight line. *Journal of Computer and Systems Sciences International*, **46**(2), 227–233 (2007).
7. Gerasimov, S.A.: Irreversible vibration-induced motion. *Mekhatronika, Avtomatizatsiya, Upravlenie [Mechatronics, Automation, Control]*, No. 9, 48–52 (2003) [in Russian].
8. Gradetsky, V., Solovtsov, V., Kniazkov, M., Rizzotto, G.G. and Amato P.: Modular design of electromagnetic microrobots. In: *Proc. 6th. Int. Conf. on Climbing and Walking Robots*. Catania, Italy, Sept. 17-19, pp. 651–658 (2003).
9. Li, H., Furuta, K. and Chernousko, F.L.: A pendulum-driven cart via internal force and static friction. In: *Proc. Int. Conf. "Physics and Control"*. St. Petersburg, Russia, Aug. 24–26, pp. 15–17 (2005).
10. Li, H., Furuta, K. and Chernousko, F.L.: Motion generation of the capsubot using internal force and static friction. In *Proc. 45th. IEEE Conf. on Decision and Control*, pp. 6575–6580. San Diego, CA, USA (2006).
11. Nagaev, R.F. and Tamm, E.A.: Vibration-induced displacement in a medium with quadratic resistance to motion. *Mashinovedenie [Machines Science]*, No. 4, 3–8 (1980) [in Russian].
12. Schmoeckel, F. and Worn, H.: Remotedly controllable mobile microrobots acting as nano positioners and intelligent tweezers in scanning electron microscopes (SEMs). In: *Proc. Int. Conf. on Robotics and Automation (MHS)*, pp. 3903–3913. New York, IEEE (2001).
13. Vartholomeos, P. and Papadopoulos, E.: Dynamics, design and simulation of a novel microrobotic platform employing vibration microactuators. *Trans. ASME. Journal of Dynamic Systems, Measurement and Control* **128**(1), 122–133 (2006).

Applying Iterative Learning Control for Accuracy Improvement of an Electromagnetically Actuated Punch

M. Dagen, H. Abdellatif and B. Heimann

Abstract This paper presents an application of Iterative Learning Control (ILC) for optimizing the cutting process of an electromagnetically actuated punch (EAP). In contrast to mechanical presses, with the EAP it is possible to change the ram's kinematics freely and to optimize it online. During the contact of the ram with the work piece, high transient forces are excited and deteriorate the positioning accuracy of the ram. By using a Sliding-Mode-Control it is not possible to compensate this. Thanks to the cyclic nature of the cutting process, we apply ILC in order to increase the accuracy of the ram. In this work we present a comparison study of two linear approaches. The first one consists in a filtered and phase lead compensated integral learning. In contrast, the second approach exploits explicit knowledge of the system's experimentally identified transfer function and performs a contraction mapping during the learning process. The experimental results show that both algorithms are capable to reduce the positioning error and to increase the accuracy of the system, even at high dynamics.

1 Introduction

Many industrial processes are characterized by a cyclic mode of operation. Thus, based on an identical initial condition the process performs the same task in a finite time span over lots of repetitions. The challenge is to follow a desired trajectory as good as possible. Conventional non-learning controls use the error in the time domain only and therefore cannot compensate tracking errors excited by deterministic disturbances or unconsidered dynamics of the system. Hence, a non-learning controller yields the same tracking error at each iteration.

M. Dagen, H. Abellatif and B. Heimann
Institute of Robotics, Hannover Centre of Mechatronics, Hannover, Germany;
E-mail: {dagen, abdellatif, heimann}@ifr.uni-hannover.de

H. Ulbrich and L. Ginzinger (eds.), Motion and Vibration Control, 41–51.

In contrast, Iterative Learning Control (ILC) uses information, i.e. the tracking error, of the previous pass. Hence, ILC is a powerful engineering method to improve the tracking error performance of iterative processes, e.g. batch processes, robot movements or cutting processes. A good overview concerning ILC can be found in [2, 3, 6]. An attractive aspect of the ILC is its simple implementation and practicability even for non-linear systems. In this paper we applied two linear ILC algorithms to an electromagnetically actuated punch (EAP).

The electromagnetically actuated punch presented in [4] uses a new drive-concept for cutting purposes. The reluctance forces of two electromagnets actuate an armature connected with the cutting tool's ram. In comparison to conventional presses, the advantage of the approach is the lack of any gearboxes in combination with marginal friction. Additionally, due to the direct drive-concept and small inertia, this concept leads to great dynamics behavior and a very compact architecture. Furthermore this approach provides the independency of the ram's velocity and its actual position. This allows the implementation of trajectories optimized for the actual cutting process. The EAP provides cutting forces up to 10 kN and strokes up to 4 mm. Hence, the EAP is qualified in the field of cutting micro-components, where high precision and high output levels are required.

2 Motivation and System Description

The challenge of our research is to develop and qualify a new drive-concept for presses to cut micro-components with high precision and high stroke rates. Therefore, a prototype was designed to experimentally verify control strategies during the cutting process. Figure 1 illustrates the prototype of the EAP and its 2D-scheme. The EAP consists of two high power electromagnets arranged in opposite direction. The armature is mounted with four linear bearings. The springs are used to linearize the characteristic force diagram of the electromagnets. To transmit the movement of the armature, the cutting tool positioned at the top of the EAP is connected by rods

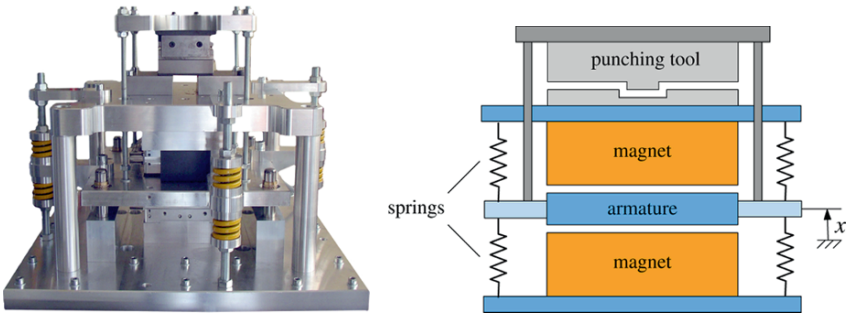

Fig. 1 Left: Prototype of the EAP, right: 2D-scheme.

with the armature. Currently, the EAP is controlled by a sliding-mode controller. The control input is the error of the armature's position between the desired and the actual position measured by a commercial eddy current sensor, the control output is the desired force of the electromagnets. At the absence of high disturbances, the controller is robust and provides good dynamics behavior. But at the presence of high disturbances caused by the cutting process, the controller is not able to follow the desired trajectory. Figure 2 illustrates this effect. In the first phase of the cutting process the die hit the sheet causing a decrease of the ram's velocity. The cutting force increases steadily and leads to an increasing tracking error. Then, after the die's break-trough, the cutting force drops abruptly. At this time, the control strategy is not able to subduct the system's energy fast enough. This results in an overshoot after the cutting process. Additionally, the abrupt relaxation of the system excites oscillations at the end. The deeper penetration of the die into the material leads to a shorter tool life. The high tracking error in the cutting phase and subsequent oscillations decrease the maximum stroke rate substantially. At present, increasing the dynamics of the controller and therefore reducing the described effects is not possible due to high measurement noise caused by the electromagnetic fields. Hence, we propose ILC to decrease the mentioned effects and therefore, to increase the quality of the produced elements and the tool life.

3 Principles of Iterative Learning Control

As mentioned in the Introduction, two ILC-Methods are compared experimentally. Approach 1 is based on a filtered and phase-lead compensated integral learning [1, 5, 9]. This algorithm can be called heuristic, since it is not based on an explicit plant model [8]. Its implementation is practical and its design is intuitive and exploits experimentally collected information. In contrast, approach 2 is designed based on explicit knowledge on the system and its transfer dynamics [2]. Hereby the contraction mapping is chosen. It is interesting to compare both algorithms, in order to find out, if an explicit model of the plant has benefits as suggested in [8]. Both

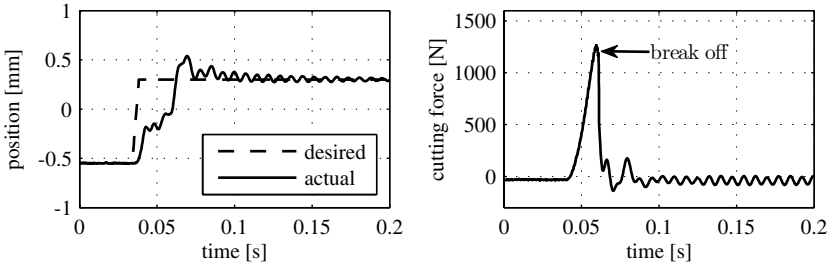

Fig. 2 Left: measured position of the ram at a desired cutting speed of 100 mm/s, right: disturbance force excited by the cutting process.

algorithms will be compared for learning trajectories with the presence of high disturbances due to the cutting process in terms of tracking performance, convergence, stability and also in terms of practicability issues.

A. Formulation of the Linear ILC Problem

A system that is supposed to achieve the same repetitive task over and over is considered. A general SISO or MIMO linear discrete-time system can be described by the state-space equations:

$$\begin{aligned} x(k+1) &= \boldsymbol{A}(k)\boldsymbol{x}(k) + \boldsymbol{B}(k)\boldsymbol{u}(k) + \boldsymbol{w}_1(k), \\ \boldsymbol{y}(k) &= \boldsymbol{C}(k)x(k) + \boldsymbol{w}_2(k), \end{aligned} \tag{1}$$

with $\boldsymbol{u}$ being the input and $\boldsymbol{y}$ being the output. It is assumed that $\boldsymbol{w}_1$ represents some deterministic disturbance that appears every repetition and that $\boldsymbol{w}_2$ is the measurement disturbance. The system is supposed to be under feedback control, such that 1 describes the closed-loop dynamics. The aim of ILC is to change the command input every trial j using the learning control law:

$$\boldsymbol{u}_{j+1}(k) = \boldsymbol{f}_{\mathrm{L}}(\boldsymbol{u}_j(k), \boldsymbol{y}_j(k), \boldsymbol{y}_d(k)) \tag{2}$$

such that the desired trajectory $\boldsymbol{y}_d$ is tracked:

$$\lim_{j \mapsto \infty} \parallel \boldsymbol{y}_j(k) - \boldsymbol{y}_d(k) \parallel = 0. \tag{3}$$

Iterativ Learning Control is called linear, when the learning law $\boldsymbol{f}_L$ makes an iterative change in the input that is a linear combination of the error $\boldsymbol{e}_j = \boldsymbol{y}_j - \boldsymbol{y}_d$ measured in the previous repetition and the last input sequence $\boldsymbol{u}_j$:

$$\boldsymbol{u}_{j+1} = \boldsymbol{T}\boldsymbol{u}_j + \boldsymbol{L}\boldsymbol{e}_j. \tag{4}$$

To achieve a zero-error-convergence, $\boldsymbol{T}$ has to be the identity matrix [7], such that the learning law becomes:

$$\boldsymbol{u}_{j+1} = \boldsymbol{u}_j + \boldsymbol{L}\boldsymbol{e}_j. \tag{5}$$

The matrix of learning gains $\boldsymbol{L}$ has to be designed in a further step to achieve desired convergence properties or stability. It is simple to derive the iterative error dynamics as

$$\boldsymbol{e}_{j+1} = (\boldsymbol{I} - \boldsymbol{P}\boldsymbol{L})\boldsymbol{e}_j, \tag{6}$$

where $\boldsymbol{I}$ is the identity matrix and

$$\boldsymbol{P} = \begin{pmatrix} \boldsymbol{CB} & 0 & \cdots & 0 \\ \boldsymbol{CAB} & \boldsymbol{CB} & \cdots & 0 \\ \vdots & \vdots & \ddots & \\ \boldsymbol{CA}^{N-1}\boldsymbol{B} & \boldsymbol{CA}^{N-2}\boldsymbol{B} & & \boldsymbol{CB} \end{pmatrix}, \tag{7}$$

with N being the length of the desired trajectory or input.

B. Brief Review on Stability and Convergence Issues

Most important design criteria of ILC are stability conditions and convergence behavior of the controller, presented by the entries of the matrix $\boldsymbol{L}$. Given the error dynamics in the iteration domain (6), it is obvious that asymptotic stability is achieved, when all magnitudes of the eigenvalues λ_i of $\boldsymbol{I} - \boldsymbol{PL}$ are less than 1. This can be expressed by means of the spectral radius as:

$$\rho(\boldsymbol{I} - \boldsymbol{PL}) = \max_i \parallel \lambda_i \parallel < 1. \tag{8}$$

More relevant from the point of view of application and practice is the monotonic decay of error e_j over the trials. Longman proposed a popular and practical criteria for monotonic convergence of tracking errors [5, 6]. It is based on a frequency domain analysis. By assuming that the matrix $\boldsymbol{L}$ is lower triangular, so that it is generated by a causal difference equation, (6) can be transformed to

$$\boldsymbol{E}_{j+1}(z) = [\boldsymbol{I} - z\phi(z)\boldsymbol{G}(z)]\boldsymbol{E}_j(z), \tag{9}$$

where $\boldsymbol{G}(z) = \boldsymbol{C}(z\boldsymbol{I} - \boldsymbol{A})^{-1}\boldsymbol{B}$ and $\phi(z)$ being the transfer function corresponding to $\boldsymbol{L}$ [6]. The substitution of $z = e^{i\omega T}$ yields the frequency transfer function. The condition

$$\|1 - e_j^{j\omega T}\Phi(e_j^{j\omega T})\boldsymbol{G}(e_j^{j\omega T})\| < 1 \; \forall \; \omega = 0 \ldots \omega_{Nyquist} \tag{10}$$

assures monotonous decay of the amplitude of all frequencies up to the Nyquist frequency [1, 5, 6, 9].

4 Design of the Implemented ILC-Algorithms

In the following, according to the EAP a SISO-System is assumed. The simplest design of ILC for SISO-Systems is achieved by selecting the learning matrix to a constant scalar: $L = \Phi_1$. It is well known and proven, that such approach is characterized by bad learning transients at high frequencies [2,5,6,8]. Even if mathematical convergence is guaranteed, the control error increases remarkably before decreasing

to zero [5]. To cope with this problem, a set of two approaches is presented for ILC in the following. The corresponding design and adjustment for the EAP is shown.

A. Approach 1: Zero-Phase Filtered ILC with Phase-Lead Compensation

The use of a low-pass zero-phase non-causal filter f to cutoff the high frequencies improves the performance of the ILC. An additional phase-lead compensation increases the learning bandwidth of the algorithm. The learning control law (5) becomes

$$u_{j+1}(k) = u_j(k) + \Phi_1 f(e_j(k+1+l)), \tag{11}$$

where l characterizes the linear phase-lead compensation. Obviously, zero-error convergence is not possible any more, even in the noise-free case due to the information filtering. This approach needs the adjustment of three parameters: the learning gain Φ_1, the cutoff frequency of the low-pass filter ω_c and the phase-lead l. This adjustment can be achieved experimentally [1, 5, 6] by the investigation of the closed-loop system dynamics in the frequency domain. It is necessary to mention, that this approach does not need any explicit knowledge or parametric modeling of the system's dynamics. Often, it is referred to as heuristic ILC [8]. In our case a 10th order butterworth filter is used. We adjust the learning gain, the learning bandwidth and the phaselead according to the experimentally investigated frequency response of the closed-loop feedback control system. In analogy to Section 3, the error evolution according to the control law (11) in the frequency domain can be derived:

$$E_{j+1}(z) = [1 - z_{1+l}\Phi_1 F(z)G(z)]E_j(z), \tag{12}$$

which modifies the condition of monotonic error decay (10) to

$$\|1 - \Phi_1 e^{j(1+l)\omega T} F(e^{j\omega T})G(e^{j\omega T})\| < 1, \tag{13}$$

where F is the filter-transfer function. For the optimization of the required parameters, we use the measured frequency response $\hat{G}(e^{j\omega T})$ being an estimate or measurement of the real frequency response G. The tuning of ω_c and Φ_1 is achieved by examining Nyquist-Plots of $G_\Phi = \Phi_1 e^{j(1+l)\omega T}\hat{G}$ with arbitrarily chosen amplification Φ_1 and $\hat{G}$. By assuming at first that $\hat{G} \approx G$, it is obvious that the monotonic error decay condition (13) is valid for all frequencies for which the plot remains within the unit-circle (centered at $+1$). The maximal cutoff frequency $\omega_{\max}$ can be chosen, such that (13) is fulfilled for all $\omega < \omega_{\max}$. In other words, the maximal possible cutoff frequency corresponds to the one, when the Nyquist plot leaves the first time the unit circle. The described approach based on conditions (10) and (13) is limited however by some restrictions and approximations of the closed-loop dynamics. Especially saturation effects of the power electronics and the electromagnets and other non-linearities could not be regarded in a linear system description. To account for the approximation the cutoff frequency is chosen smaller than the

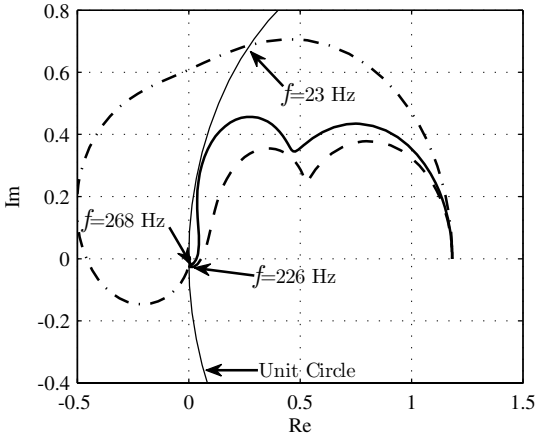

Fig. 3 Nyquist-plots of G_Φ with the learning gain $\Phi = 1.2$ and the linear phase-lead l =0 (dashed-dotted), $l = 17$ (solid) and $l = 20$ (dashed). The phase-lead of $l = 17$ increases the learning bandwidth to $f_c = 268$ Hz.

maximum one. In our case the cutoff frequency is determined to $\omega_c = 879\,\mathrm{rad/s}$ (140 Hz) instead of the maximum frequency $\omega_{\max} = 1696\,\mathrm{rad/s}$ (268 Hz). The linear phase lead helps to increase the learning bandwidth. As it is simple to deduce from (13), for the same gain Φ_1 and in the case of $l > 0$ the Nyquist plot leaves the unit circle at a higher frequency. One makes Nyquist plots of G_Φ for a range of integer phase leads and picks the value that keeps the plot less than 1 up to the highest frequency [6]. Figure 3 shows to Nyquist-plots with different phase-leads. A phase-lead of $l = 17$ increases the maximum bandwidth significantly. Using a phase-lead of $l = 0$ would simply allow a maximum frequency of 23 Hz for monotonic convergence. It is obvious, that for our range of application this bandwidth would be too small to get acceptable results.

B. Approach 2: Model-Based Contraction Mapping

The here chosen contraction mapping ILC defines the learning matrix $\boldsymbol{L} = \Phi_1 \hat{\boldsymbol{P}}^T$, where $\hat{\boldsymbol{P}}$ is an estimate of the Toeplitz matrix defined by (7). An estimate is necessary, because the exact model is always unknown. In case of a linear time invariant system (LTI), $\hat{\boldsymbol{P}}$ contains the values of the impulse response $g(k)$:

$$\hat{\boldsymbol{P}} = \begin{pmatrix} g(1) & & & \\ g(2) & g(1) & & \\ \vdots & \vdots & \ddots & \\ g(N) & g(N-1) & \cdots & g(1) \end{pmatrix}. \tag{14}$$

Experimental studies determined a linear transfer function 5th order using an ARX-structure. The model coefficients can be identified using standard procedures. Hence, the impulse response can be computed and inserted in (14). A filtering is not necessary for the contraction mapping ILC. Therefore, a zero-error convergence can be achieved theoretically. A further difference to approach 1 is that the condition on monotonic error decay can be derived in the iteration domain by claiming an exact Euclidean norm decay condition:

$$\| \boldsymbol{e}_{j+1} \|_2 < \| \boldsymbol{e}_j \|_2 \, . \tag{15}$$

It yields by regarding (5)

$$\| (\boldsymbol{I} - \hat{\boldsymbol{P}}\boldsymbol{L})\boldsymbol{e}_j \|_2 < \| \boldsymbol{e}_j \|_2, \tag{16}$$

or

$$\| (\boldsymbol{I} - \hat{\boldsymbol{P}}\boldsymbol{L}) \|_2 < 1. \tag{17}$$

Since $\boldsymbol{L} = \Phi_1 \hat{\boldsymbol{P}}^T$ and the spectral norm of the symmetric matrix $\hat{\boldsymbol{P}}\hat{\boldsymbol{P}}^T$ is equal to its maximal eigenvalue $\sigma_{\max}$, one obtains

$$\| (\boldsymbol{I} - \hat{\boldsymbol{P}}\boldsymbol{L}) \|_2 = \max_i |1 - \Phi_1 \sigma_i (\hat{\boldsymbol{P}}\hat{\boldsymbol{P}}^T)| < 1 \tag{18}$$

$$\Rightarrow -1 < 1 - \Phi_1 \sigma_{max} (\hat{\boldsymbol{P}}\hat{\boldsymbol{P}}^T) < 1, \tag{19}$$

and therefore a rule for the learning gain Φ_1 that allows monotonic error decay

$$0 < \Phi_1 < \frac{2}{\| \hat{\boldsymbol{P}} \|_2^2}. \tag{20}$$

In analogy to the first approach, we have to consider, that the chosen model is only an assumption. To account for the remaining model uncertainties, in this study the learning gain Φ_1 is defined significant smaller than the allowed upper bound given by (20).

5 Experimental Validation with Different Cutting Speeds

In the following, the proposed ILC algorithms are compared by experimental results. To compare the performance of the algorithms, we cut a 0.35 mm copper sheet with a trapezoid trajectory with three different maximum speeds: 10 mm/s, 100 mm/s and 200 mm/s. To compare the two proposed ILC-algorithms the Root-Mean-Square- or RMS-Criteria is used. Figure 4 shows the RMS-Error over the trails of both algorithms and the different cutting speeds. For the trajectories with a maximum speed of 100 mm/s and 200 mm/s the algorithms are able to reduce the tracking error to a

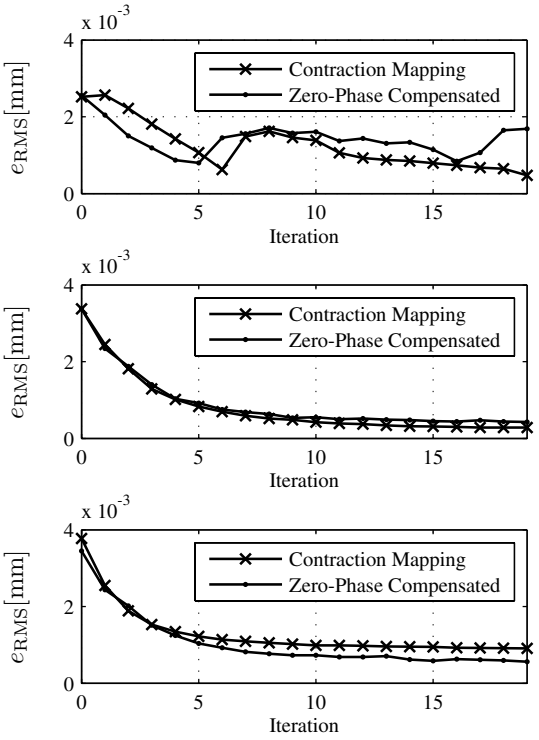

Fig. 4 RMS-error convergence for the EAP with a maximum cutting speed of 10 mm/s (top), 100 mm/s (middle) and 200 mm/s (bottom).

similar level and after nearly the same number of iterations. Figure 5 (top) apparently shows the enormous reduction of the tracking error at the 20th iteration with a cutting speed of 100 mm/s. An interesting point is, that the zero-phase filtered ILC with phase-lead compensation gives slightly better results at high velocities. With a look at the measured position at the 20th iteration illustrated in Figure 5 (middle) the reason becomes clear. Both algorithms reduce the tracking error during the cutting phase identically, but the ILC with phase-lead compensation is more efficient in reducing the oscillations after the cut than the contraction mapping. At lower cutting speeds, the contraction mapping gives slightly better results.

In contrast to the higher cutting speeds, the graph of the RMS-error with a cutting speed of 10 mm/s shows a strange behavior. Again, a look at the time-plot of the measured position clarifies the reason for this effect. Figure 5 (bottom) shows the measured position at the 19th and 20th iteration. At the 19th iteration the a good error tracking is achieved. But, at the following 20th iteration the tracking error increases significantly. At this iteration the cutting process differs slightly from the one before. The break-through of the material occurs a little later in comparison to the iteration before. But the feedforward-control of the ILC-algorithms already reduces the energy in the system to avoid the typical overshoot. Therefore, the ILC is

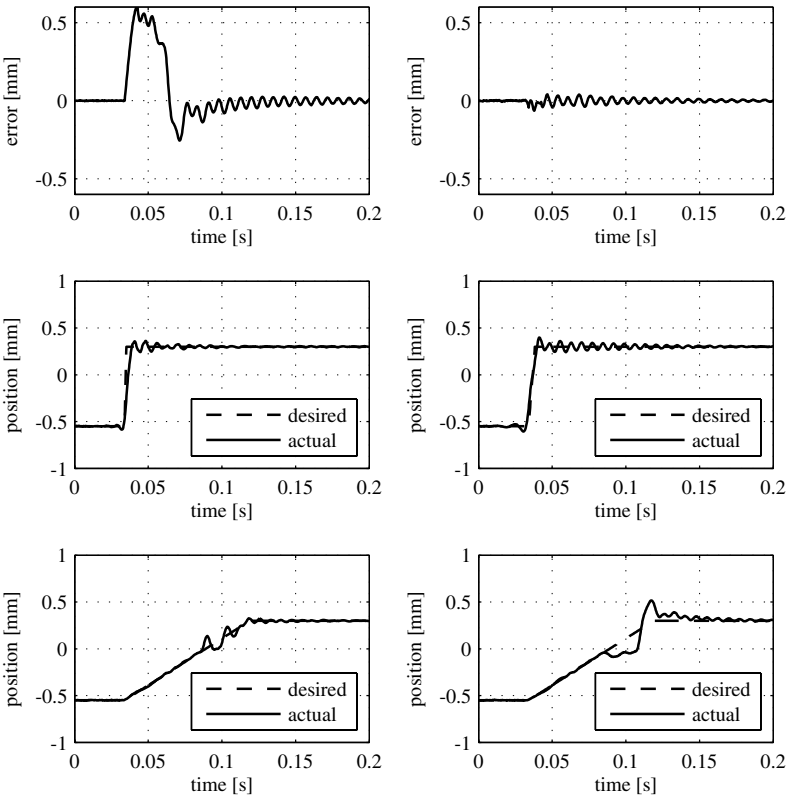

Fig. 5 Top: tracking error at the 1st (left) and 20th (right) iteration with a cutting speed of 100 mm/s and phase lead compensation, middle: measured position at the 20th iteration with a cutting speed of 200 mm/s, phase-lead compensated (left), contraction mapping (right), bottom: measured position at the 19th (left) and 20th (right) iteration with a cutting speed of 10 mm/s.

counterproductive for the cutting process, extends it and consequently the tracking error arises. At higher cutting speeds the kinetic energy of the ram is such high, that the die always cuts the sheet successfully. In this case the effect does not appear.

6 Conclusions and Outlook

In this study, two linear Iterative Learning Control algorithms were applied to an electromagnetically actuated punch to increase its accuracy during a cutting process. The presented experimental results are very promising. The tracking error is decreased by more than 90% in less than 20 iterations. Beside the expectable improvement of the produced elements and an increasing tool life, the time of the cutting process can be reduced by more than 60% allowing higher stroke rates. Fu-

ture works will deal with the optimization of the observed behavior of the ILC at slow cutting speeds.

References

1. Zhang, B., Wang, D., Ye, Y.: On learning transient and cutoff frequency tuning in ILC, in *Proc. of the 2004 IEEE Conference on Robotics, Automation and Mechatronics*, pp. 484–489 (2004).
2. Bien, Z., Xu, J.X.: *Iterative Learning Control – Analysis, Design, Integration and Application*. Kluwer Academic Publishers (1998).
3. Bristow, D.A., Tharayil, M., Alleyne, A.G.: A survey of iterative learning control. *IEEE Control Systems Magazine* **6**, 96–114 (2006).
4. Dagen, M., Heimann, B., Javadi, M., Behrens, B.A.: Design and control of an electromagnetically actuated punch. IFAC World Congress 2008. International Federation of Automatic Control, Seoul, Korea (2008).
5. Elci, H., Longman, R.W.: Simple learning control made practical by zero-phase filtering: applications to robotics. *IEEE Transactions on Circuits and Systems* **49**(6), 753–767 (2002).
6. Longman, R.W.: Iterative learning control and repettitive control for engineering practice. *International Journal of Control* **73**, 930–954 (2000).
7. Moore, K.L.: Iterative learning control: An expository overview. *Applied and Computational Control, Signals and Circuits* **1**, 151–214 (1999).
8. Norrlöf, M.: An adaptive iterative learning control algorithm with experiments on an industrial robot. *IEEE Transactions on Robotics and Automation* **18**(2), 245–251 (2002).
9. Ye, Y., Wang, D.: Better robot tracking accuracy with phase lead compensated ILC. In *Proc. of the 2003 IEEE Int. Conference on Robotics and Automation*, pp. 4380–4385 (2003).

Computer-Aided Integrated Design for Mechatronic Systems with Varying Dynamics

Maíra M. da Silva, Olivier Brüls, Bart Paijmans, Wim Desmet and Hendrik Van Brussel

Abstract Some mechatronic systems have different spatial configurations or operation positions, and, as a consequence, their dynamic behavior, described by their most significant eigenfrequencies and mode-shapes, may vary in the configuration space. This inevitably affects the performance and the stability of the control system. Regarding the design of mechatronic systems with variable configuration, two main issues are treated in this paper: (i) the derivation of a parametric model able to capture the varying dynamics and the control actions, (ii) the integrated design of the structure and the controller. To cope with these issues, a parametric model is derived using a flexible multibody system technique based on the finite element method. A global modal parameterization is applied for model-order reduction, yielding a concise description of the flexible multibody model. A linear parameter varying controller is derived via interpolation of local controllers for the reduced models. This methodology is applied to a pick-and-place assembly robot with a gripper carried by a flexible beam. Eventually, design tradeoffs are evaluated considering the performance of the active system for different structural configurations.

Maíra M. da Silva
Department of Mechanical Engineering, Katholieke Universiteit Leuven, Celestijnenlaan 300B, B-3001 Heverlee (Leuven), Belgium; E-mail: maira.dasilva@student.kuleuven.be

Olivier Brüls
Department of Aerospace and Mechanical Engineering, University of Liège, Chemin des Chevreuils 1, 4000 Liège, Belgium; E-mail: o.bruls@ulg.ac.be

Bart Paijmans
Flanders' Mechatronics Technology Centre, Celestijnenlaan 300B, B-3001 Heverlee (Leuven), Belgium; E-mail: bart_paijmans@hotmail.com

Wim Desmet
Department of Mechanical Engineering, Katholieke Universiteit Leuven, Celestijnenlaan 300B, B-3001 Heverlee (Leuven), Belgium; E-mail: wim.desmet@mech.kuleuven.be

Hendrik Van Brussel
Department of Mechanical Engineering, Katholieke Universiteit Leuven, Celestijnenlaan 300B, B-3001 Heverlee (Leuven), Belgium; E-mail: hendrik.vanbrussel@mech.kuleuven.be

H. Ulbrich and L. Ginzinger (eds.), Motion and Vibration Control, 53–62.

1 Introduction

This paper concerns the computer-aided integrated design for machines with varying dynamics. For instance, in machine tools, Cartesian mechanisms and pick-and-place machines, the relative motion between flexible components leads to time-varying boundary conditions, so that the eigenfrequencies and mode shapes are not constant but dependent on the spatial configuration. This nonlinear phenomenon inevitably affects the performance and the stability of the control system [5, 8]. Gain-scheduling control strategies, which take the variations of the dynamic properties into account, can be implemented to improve the system performance [5, 6].

Since the structural and the control dynamics may interact in non-intuitive ways, an optimal design of the mechatronic system can only be accomplished if the active system is evaluated in an early design phase [6–8]. The development of design tools for industrial mechatronic systems requires advanced simulation and modeling techniques able to predict the machine dynamics and the control actions.

The aim of this work is to propose a simulation platform and control design guidelines for systematic design and evaluation of mechatronic systems with varying dynamics. The general methodology for modeling and control design of such mechatronic systems is described in Section 2. This methodology is applied to an industrial 3-axis pick-and-place assembly robot with a gripper carried by a flexible beam (Figure 1a). Section 3 presents its mechanical model and its control design. In Section 4, design tradeoffs are evaluated considering the performance of the active system for different structural configurations. Finally, some conclusions are drawn in Section 5.

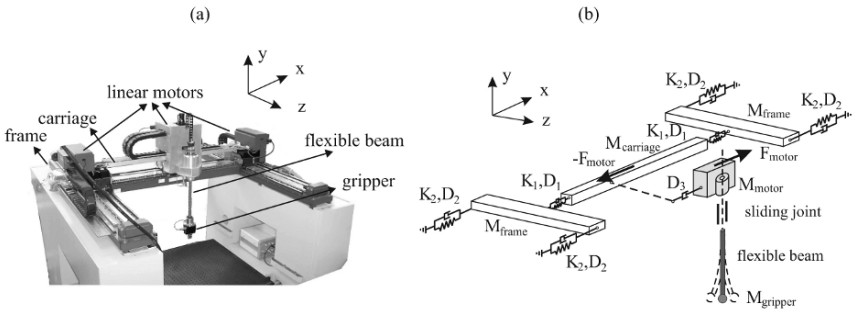

Fig. 1 (a) Pick-and-place machine and (b) Scheme of the flexible multibody model of the X-direction motion of pick-and-place machine.

2 Modeling and Control of Mechatronic Systems with Varying Dynamics

A mechatronic system is composed of rigid bodies, flexible bodies, joints, and control units. Thus, it can be modeled as a flexible multibody system coupled with a control system (see Section 2.1). The flexible multibody models can contain a large number of degrees of freedom (dofs) and, therefore, may be unsuitable for controller design purposes [8], since the order of the controller is related to the size of the model. In order to derive a concise description of the flexible multibody model, a model-order reduction, based on global modal parameterization (GMP) [1], is applied (see Section 2.2).

For time-variant systems, two kinds of control strategies can be employed: (1) non-adaptive controllers, such as robust controllers, that can take into account the variations as uncertainties or (2) adaptive controllers, such as gain-scheduling controllers that can adapt according to the parameter variations [5]. In this paper, a gain-scheduling controller, obtained from the interpolation of local H∞ controllers, is considered. The local H∞ controllers are derived via an extension of the four-block H∞-control problem [9] (see Section 2.3).

An appropriate way of describing a gain-scheduling controller is by the following state-space form:

$$\begin{aligned} \dot{\mathbf{x}} &= \mathbf{A}(\mathbf{l})\mathbf{x} + \mathbf{B}(\mathbf{l})\mathbf{u} \\ \mathbf{y} &= \mathbf{C}(\mathbf{l})\mathbf{x} + \mathbf{D}(\mathbf{l})\mathbf{u} \end{aligned} \tag{1}$$

where $\mathbf{x}$ is the state of the controller, $\mathbf{u}$ and $\mathbf{y}$ are, respectively, the input (error signal) and the output (actuation) and $\mathbf{l}$ is a vector of varying parameters. The interpolation technique to derive the gain-scheduling controller is based on affine functions of the poles and zeros of each local controller (see Section 2.4).

2.1 Flexible Multibody Model

Formalisms developed in the field of flexible multibody dynamics appear to be especially suitable for deriving models of mechatronic systems. In particular, the nonlinear finite element approach described in [4] is a general and systematic technique for the simulation of articulated systems with rigid and flexible components. The strongly coupled formulation, which is available in the Oofelie finite element software [3], has been chosen for the present developments.

According to [4], a flexible multibody system can be described using absolute nodal coordinates. Hence, each body is represented by a set of nodes and each node has its own translation and rotation coordinates. The various bodies of the system are interconnected by kinematical joints, which impose restrictions on their relative motion. If the nodal coordinates are gathered in a vector $\mathbf{q}$, the joints are thus represented by a set of m nonlinear kinematic constraints:

$$\mathbf{\Phi}(\mathbf{q}, t) = \mathbf{0} \tag{2}$$

According to the Lagrange multiplier technique, the formulation of the constrained equations of motion requires the introduction a $m \times 1$ vector of Lagrange multipliers $\boldsymbol{\lambda}$. In a mechatronic system, the dynamics of the controller are represented by a nonlinear state-space model with state variables $\mathbf{x}$ and output variables $\mathbf{y}$. Hence, the strongly coupled equations of the mechatronic system have the general structure [2]:

$$\mathbf{M}(\mathbf{q})\ddot{\mathbf{q}} = \mathbf{g}(\mathbf{q}, \dot{\mathbf{q}}, t) - \mathbf{B}^T\boldsymbol{\lambda} + \mathbf{L}\mathbf{y} \tag{3}$$

$$\mathbf{0} = \mathbf{\Phi}(\mathbf{q}, t) \tag{4}$$

$$\dot{\mathbf{x}} = \mathbf{f}(\mathbf{q}, \dot{\mathbf{q}}, \ddot{\mathbf{q}}, \mathbf{x}, \mathbf{y}, t) \tag{5}$$

$$\mathbf{y} = \mathbf{h}(\mathbf{q}, \dot{\mathbf{q}}, \ddot{\mathbf{q}}, \mathbf{x}, \mathbf{y}, t) \tag{6}$$

Eq. (3) represents the dynamic equilibrium of the mechanism, Eq. (4), the kinematic constraints, Eq. (5), the state equation and Eq. (6), the output equation. $\mathbf{M}$ is the mass matrix, which is not constant in general, $\mathbf{g}$ represents the internal, external and complementary inertia forces, $\mathbf{B} = \partial\mathbf{\Phi}/\partial\mathbf{q}$ is the matrix of constraint gradients, $\mathbf{L}$ is a Boolean localization matrix and $\mathbf{L}\mathbf{y}$ denotes the actuator forces. The control system is influenced by input measurements from the mechanical system, which can be positions $\mathbf{q}$, velocities $\dot{\mathbf{q}}$, accelerations $\ddot{\mathbf{q}}$ or internal forces $\boldsymbol{\lambda}$. Equations (3–6) are coupled equations of motion and can be solved numerically using an implicit time integration scheme [2].

2.2 Model Reduction

In linear structural dynamics, component-mode synthesis (CMS) provides an appropriate solution for the reduction of a finite element model. In CMS, the dynamic behavior of each substructure is formulated as a superposition of modal contributions. A more drastic reduction, based on the GMP and including all bodies and joints, has been proposed for flexible multibody systems [1].

The total motion, $\mathbf{q}$, in a flexible multibody system can be decomposed into rigid motion, $\mathbf{q}^r$, and elastic deformation, $\mathbf{q}^f$, in the following way:

$$\mathbf{q} = \mathbf{q}^r + \mathbf{q}^f \tag{7}$$

Considering the passive flexible multibody system (Eqs. 3–4) and the augmented coordinates $\mathbf{u} = [\mathbf{q} \quad \boldsymbol{\lambda}]^T$, the GMP is defined as the following mapping

$$(\boldsymbol{\theta}, \boldsymbol{\delta}) \longmapsto \begin{bmatrix} \mathbf{q} \\ \boldsymbol{\lambda} \end{bmatrix} = \begin{bmatrix} \rho(\boldsymbol{\theta}) \\ \mathbf{0} \end{bmatrix} + \begin{bmatrix} \mathbf{\Psi}^{\mathbf{q}\delta}(\boldsymbol{\theta}) \\ \mathbf{\Psi}^{\lambda\delta}(\boldsymbol{\theta}) \end{bmatrix} \boldsymbol{\delta} \tag{8}$$

where $\boldsymbol{\theta}$ are the independent parameters related to the actuation, ρ is the mapping between the rigid motion and the independent parameters, $\mathbf{q}^r = \rho(\boldsymbol{\theta})$, $\boldsymbol{\delta}$ are the

modal coordinates, and the $\boldsymbol{\Psi}^{\mathbf{q}\delta}$ and $\boldsymbol{\Psi}^{\boldsymbol{\lambda}\delta}$ are the flexible mode shape matrices which depend on the configuration.

The dofs can be rearranged in $\mathbf{u} = [\boldsymbol{\theta} \quad \mathbf{q}^g \quad \mathbf{u}^i]^T$, where $\boldsymbol{\theta}$ are the independent parameters (they should be kept since they represent the actuators), $\mathbf{q}^g$ are the constraint dofs (they should be kept in case additional external loads are required) and $\mathbf{u}^i$ are the remaining internal dofs including the Lagrange multipliers (they can be condensed during the reduction procedure). Accordingly, rigid modes $\boldsymbol{\Psi}^{\mathbf{u}\boldsymbol{\theta}}$, constraint modes $\boldsymbol{\Psi}^{\mathbf{u}\boldsymbol{\gamma}}$ and internal modes $[\boldsymbol{\Psi}^{\mathbf{u}\boldsymbol{\iota}} \quad \boldsymbol{\Psi}^{\mathbf{u}\boldsymbol{\varepsilon}}]$, divided into lower and higher-order modes, can be calculated (details in [1]). The model reduction relies on a truncation of the higher-order internal modes.

Performing the modal transformation, $\mathbf{q} = \boldsymbol{\Psi}\boldsymbol{\eta}$, where $\boldsymbol{\eta} = [\boldsymbol{\theta} \quad \boldsymbol{\delta}]^T$ and $\boldsymbol{\Psi} = [\boldsymbol{\Psi}^{\mathbf{u}\boldsymbol{\theta}} \quad \boldsymbol{\Psi}^{\mathbf{u}\boldsymbol{\gamma}} \quad \boldsymbol{\Psi}^{\mathbf{u}\boldsymbol{\iota}}]$, the equations of motion (Eqs. 3–4) yield the reduced model

$$\mathbf{M}^{\boldsymbol{\eta}\boldsymbol{\eta}}(\boldsymbol{\theta})\ddot{\boldsymbol{\eta}} + \mathbf{K}^{\boldsymbol{\eta}\boldsymbol{\eta}}(\boldsymbol{\theta})\boldsymbol{\eta} = \mathbf{g}^{\boldsymbol{\eta}} \tag{9}$$

where $\mathbf{g}^{\boldsymbol{\eta}} = \mathbf{L}^{\boldsymbol{\eta}}(\boldsymbol{\theta})\mathbf{y}$. For a given configuration θ, this equation defines a low-order linearized model which can be used for control design, as described in Section 2.3.

2.3 Control Design for Linear Time-Invariant Motion Systems

Weighting functions for high-dynamic mechatronic motion systems are explicitly derived using the four-block H∞-control problem [9]. An extension of this technique has been proposed by [5] in order to specify explicitly the maximum of the sensitivity, m_S, the maximum of the process sensitivity, m_{S_P}, the maximum of the complementary sensitivity, m_T and the bandwidth frequency, f_{BW} ,through the weighting functions. The augmented closed-loop system M becomes:

$$M = -\begin{bmatrix} \frac{W_1 S}{m_S} & \frac{W_1 S_P r_{S_P}}{|G_{fBW}|} \\ \frac{W_2 S_K}{m_T m_S r_{S_P}} & \frac{W_2 T}{|G_{fBW}| m_T} \end{bmatrix} \tag{10}$$

where S is the sensitivity, S_P the process sensitivity, S_K the control sensitivity, T the complementary sensitivity, $|G_{fBW}|$ is the gain of the system at the desired bandwidth, r_{S_P} can be interpreted as a reduction of the maximum gain of S_P, W_1 is chosen in order to guarantee that the controller have integral action up to $f_I = f_{BW}/4$ and W_2 is chosen in order to guarantee that the controller presents roll-off at the higher frequencies ($f_R = 4 f_{BW}$). The shaping filters typically have the following expressions, with $\alpha = 10$:

$$W_1(s) = \frac{s + 2\pi f_I}{s} \qquad W_2(s) = \alpha^2 |G_{fBW}| \frac{s^2 + 2.8\pi f_R s + (2\pi f_R)^2}{s^2 + 2.8\pi\alpha f_R s + (2\pi\alpha f_R)^2} \tag{11}$$

If $\gamma = \|M\|_\infty \leq 1$, the performance specifications are certainly met.

2.4 Gain-Scheduling Controller Derivation

From the procedure described in the previous section, a set of controllers can be derived for local configurations and then used to build a gain-scheduling controller represented in an LPV state-space form (Eq. 1). The technique used to create the LPV system relies on a linear interpolation of discrete poles, zeros and gains [5]. Equation (12) shows the technique applied for the vector of poles:

$$\begin{bmatrix} p_1(\mathbf{l}) \\ p_2(\mathbf{l}) \\ \vdots \\ p_n(\mathbf{l}) \end{bmatrix} = \begin{bmatrix} p_{0,1} \\ p_{0,2} \\ \vdots \\ p_{0,n} \end{bmatrix} + \begin{bmatrix} p_{1,1} \\ p_{1,2} \\ \vdots \\ p_{1,n} \end{bmatrix} f(\mathbf{l}) \tag{12}$$

where p_1 till p_n are the poles of the system, $p_{0,1}$ till $p_{0,n}$ and $p_{1,1}$ till $p_{1,n}$ are constants and $f(\mathbf{l})$ is an analytical function of the scheduling parameter $\mathbf{l}$. Similar affine functions have been made to describe the varying zeros and gains. Varying state-space matrices ($\mathbf{A}_s$, $\mathbf{B}_s$, $\mathbf{C}_s$, $\mathbf{D}_s$), representing subsystems, are created from a pair of poles and zeros:

$$\mathbf{A}_s(\mathbf{l}) = \mathbf{Re}\begin{bmatrix} p_i(\mathbf{l}) + p_{i+1}(\mathbf{l}) & -p_i(\mathbf{l})p_{i+1}(\mathbf{l}) \\ 1 & 0 \end{bmatrix} \qquad \mathbf{B}_s(\mathbf{l}) = \begin{bmatrix} 1 \\ 0 \end{bmatrix}$$
$$\mathbf{C}_s(\mathbf{l}) = \mathbf{Re}\begin{bmatrix} -z_i(\mathbf{l}) - z_{i+1}(\mathbf{l}) + p_i(\mathbf{l}) + p_{i+1}(\mathbf{l}) \\ z_i(\mathbf{l})z_{i+1}(\mathbf{l}) - p_i(\mathbf{l})p_{i+1}(\mathbf{l}) \end{bmatrix}^T \qquad \mathbf{D}_s(\mathbf{l}) = [1] \tag{13}$$

These subsystems are then concatenated, yielding an LPV state-space system that is quadratically dependent on the parameter $\mathbf{l}$ [5].

3 Pick-and-Place Machine: Modeling Details and Control System

The proposed design methodology is applied to an industrial 3-axis pick-and-place assembly robot with a gripper carried by a flexible beam (Figure 1a). The fast movements of this machine may excite the vibrations of the variable-length flexible beam (1st resonance frequency between 30 and 70 Hz). The Z-motion is gantry driven by two linear motors and the X-motion over the carriage is also driven by a linear motor. The vertical Y-motion is actuated by a rotary brushless DC-motor which drives the vertical flexible beam by a ball screw/nut combination. The position of the linear motors and the beam length are measured using optical encoders, and the acceleration at the gripper in the X-direction is measured using an accelerometer. The objective is to move the gripper as accurately and fast as possible along a prescribed trajectory in the working area.

3.1 Mechanical Model

A flexible multibody model has been built to simulate the pick-and-place robot motion in X and Y directions (see Figure 1b). All components are modeled as rigid bodies, excepted the flexible beam. The actuator force generated by the linear motor (X-direction), is applied to the linear motor mass (action) and to the carriage (reaction). The frames and the carriage masses are, respectively, 169.0 and 13.9 Kg. The linear motor weights 25.9 Kg and the gripper 1.25 Kg. These values can be found in the machine manual. The spring stiffness and the damping value between the carriage and the frame are, respectively, $K_1 = 9.15e6$ N/m and $D_1 = 1042$ Ns/m. The frame suspension is connected to the ground by four connecting points. The stiffness and the damping of these connections are, respectively, $K_2 = 5.3e7$ N/m and $D_2 = 5204$ Ns/m. The damping $D_3 = 100$ Ns/m represents the connection between the linear motor and the carriage. The stiffness and damping values are adjusted to match the experimental data. The flexible beam has a nominal diameter of 24 mm. The material properties are: density $\rho_s = 7800$ kg/m^3, Poisson's ratio $\nu = 0.3$, damping ratio 0.01 and elasticity modulus $E = 2.1 \cdot 10^{11}$ N/m^2.

Figure 2 shows the comparison between simulated and experimental FRFs for two beam lengths ($l = 0.41$ m with the first resonance frequency at 285 Hz and $l = 0.36$ m with the first resonance frequency at 350 Hz). The curves are in a good agreement up to 400 Hz, which confirms the validity of the model. Differences between the simulated and experimental FRFs are mainly due to the sensor position estimation error.

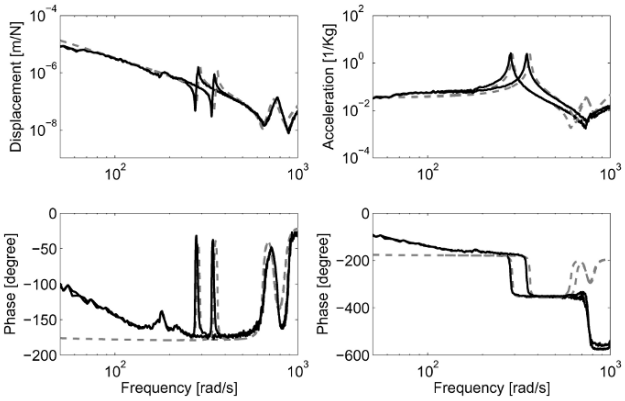

Fig. 2 Comparison between the simulated (- - -) and the experimental FRFs (—): (a) motor position/motor force; (b) gripper acceleration/motor force.

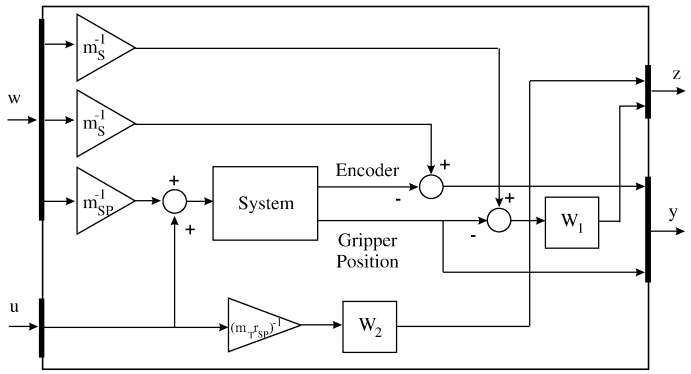

Fig. 3 General control configuration: w are the disturbances, z are the signal to be minimized, y are the controller inputs and u are the controller output.

3.2 Control System

A gain-scheduling controller is derived for the pick-and-place model considering the length of the flexible beam as the varying parameter, $\mathbf{l} = l$. The complete general control scheme is shown in Figure 3. The design of the weighting functions reflects the desired control specifications according to the guidelines presented in Section 2.3. The desired bandwidth frequency of the close-loop is $f_{BW} = 20$ Hz. In an attempt to reduce the settling time, the desired maximum of the sensitivity is $m_S = 2.64$ dB and the desired maximum of the complementary sensitivity is $m_T = 2.46$ dB. These values were estimated based on a second order system with $f_{BW} = 20$ Hz and a settling time of 0.15 s. Finally, it is desirable that the maximum of the process sensitivity should be $m_{S_P} = G_{f_{ST}}/r_{S_P}$, where the $G_{f_{ST}}$ is the gain of the plant at the first structural resonance and $r_{S_P} = 0.5$.

The H∞ control derivation is performed for four local configurations yielding four linear-time invariant (LTI) controllers. The resulting controllers (see Figure 4) are then interpolated via the methodology described in Section 2.4 yielding a gain-scheduling controller.

Figure 5 shows the active response of the flexible multibody model described in Section 3.1. The input in X-direction (see the pulse train in Figure 5), is applied while the length of the beam is continuously varying. The gain-scheduling controller adapts its gains according to the beam's length. It can be observed that the vibrations are quite well damped throughout the whole configuration space.

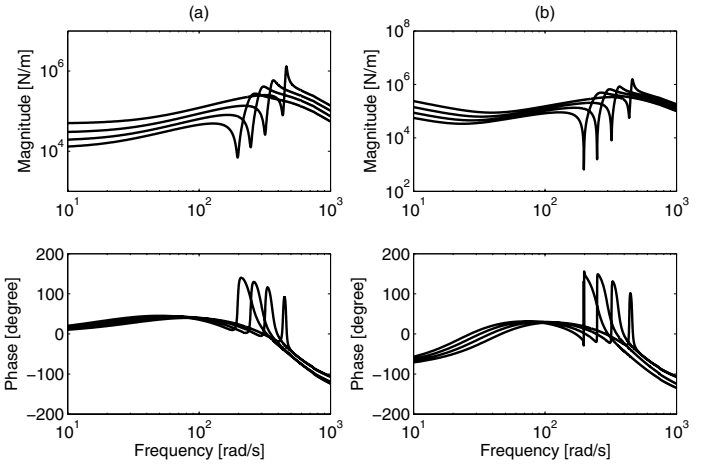

Fig. 4 Local LTI controllers for four equidistant values of $l \in [0.33, 0.53]$ m.

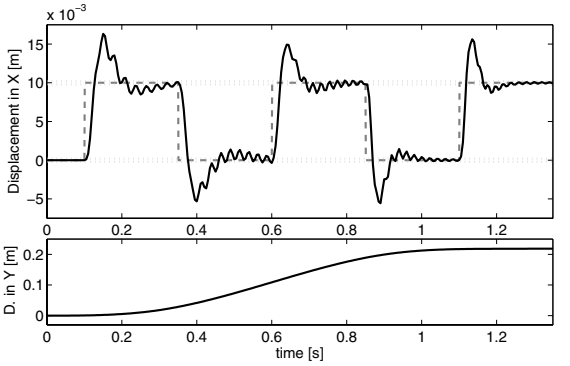

Fig. 5 Active system response to a pulse train in X-direction while the length of the beam is continuously varying.

4 Pick-and-Place Machine: Integrated Design

Some structural modifications can be evaluated in frequency and time domain, using the same control design specifications (f_{BW}, m_S, m_T and m_{S_P}) for the nominal machine. The diameter of the beam has a direct influence on the vibration of the effector and it is thus considered as a design variable. Table 1 shows the mean ($\mu(\gamma)$) and the standard deviation ($\sigma(\gamma)$) of the achieved H∞ controller norm considering the four local LTI controllers, and time-domain metrics: maximum overshoot and maximum settling time. It can be observed that thinner diameters present worse performance than thicker diameters but fulfill the design requirements.

Table 1 Frequency and time domain metrics for different structural designs.

diameter [m]	norm of the achieved H∞ controller $\mu(\gamma)$	$\sigma(\gamma)$	time domain overshoot [%]	settling time [s]
0.020	0.75	0.13	62	0.25
0.024	0.68	0.08	60	0.20
0.028	0.65	0.03	56	0.18
0.032	0.66	0.04	55	0.15

5 Conclusions

A simulation platform and control design guidelines for systematic design and evaluation of mechatronic systems with varying dynamics has been proposed and implemented for a pick-and-place robot. In this way, the designer is able to predict the machine dynamics and the control actions and to evaluate the performance of mechatronic system with varying dynamics in frequency and time domain.

Acknowledgements The research of Maíra M. da Silva is supported by CAPES, Brazilian Foundation Coordination for the Improvement of Higher Education Personnel, which is gratefully acknowledged. Olivier Brüls is supported by the Belgian National Fund for Scientific Research (FNRS) which is gratefully acknowledged. The authors would like to thank the reviewers for the constructive comments. Unfortunately, due to the 10-page limit, some suggestions were not implemented.

References

1. Brüls O., Duysinx P., Golinval J.-C.: The global modal parameterization for non-linear model-order reduction in flexible multibody dynamics. *Int. J. Numer. Meth. Engng.* **69** 948–977 (2007).
2. Brüls O., Golinval J.C.: The generalized-α method in mechatronic applications. *J. Appl. Math. Mech.* **86**(10), 748–758 (2006).
3. Cardona A., Klapka I., Géradin M.: Design of a new finite element programming environment. *Eng. Comput.* **11**, 365–381 (1994).
4. Géradin M., Cardona A.: *Flexible Multibody Dynamics: A Finite Element Approach*. John Wiley & Sons, England (2001).
5. Paijmans B.: Interpolating gain-scheduling control for mechatronic systems with parameter-dependent dynamics. PHD Thesis, Katholieke Universiteit Leuven, Belgium (2007).
6. Rieber J.M., Taylor D.G.: Integrated control system and mechanical design of a compliant two-axes mechanism. *Mechatronics* **14**(9), 1069–1087 (2004).
7. Van Amerongen J., Breedveld P.: Modelling of physical systems for the design and control of mechatronic systems. *Ann. Rev. Control* **27**, 87–117 (2003).
8. Van Brussel H., Sas P., Németh I., De Fonseca P., Van den Braembussche P.: Towards a mechatronic compiler. *IEEE/ASME Trans. Mechatronics* **6**(1), 90–105 (2001).
9. Van de Wal M., Van Baars G., Sperling F., Bosgra O.: Multivariable H∞/μ feedback control design for high precison waferstage motion. *Control Engng. Pract.* **10**(7), 739–755 (2002).

Development of a Repulsive Magnetic Bearing Device with an Adjustability Function of Radial Stiffness

Max Eirich, Yuji Ishino, Masaya Takasaki and Takeshi Mizuno

Abstract This paper studies the ability to adjust the stiffness in the radial direction on a non-contact levitated rotor by using an independent motion control of permanent magnets. The method of stabilization in the axial direction, by moving a magnet for support like an inverted pendulum, is applied. The repulsive forces in the radial direction depend not only on the size and physical characteristics of magnets but also on the relative positioning of magnets to each other in the axial direction. This work shows the principles and the one of necessary methods of motion control for successful adjustability of the radial stiffness.

1 Introduction

There are several methods to support a moving or rotating mass by using magnetic forces without any mechanical contact [1–4]. One of the principal methods is to use the repulsive forces of permanent magnets. In this type of magnetic bearing system the object is levitated by the repulsive forces between permanent magnets. Such a system does not need any energy to generate the levitation force and is stable in the direction of repulsive forces (F_R), but unstable in the normal direction to the F_R. In the previous works, experimental devices, using PD [5] and also state feedback control [6] were developed where the levitated object was a cylindrical rotor and permanent magnets were ring-shaped. While the permanent magnets for support where mechanically connected in this works, the independent motion control of permanent magnets has been proposed [7, 8]. The repulsive forces in radial direction can be changed by adjusting of the relative position of the magnets for support to each other. Since we use two pair of ring-shape permanent magnets, such adjustment

M. Eirich, Y. Ishino, M. Takasaki and T. Mizuno
Department Mechanical Engineering, Saitama University, Shimo Okubo 255, 338-8570 Saitama, Japan; E-mail: {meirich, yishino, masaya, mizar}@mech.saitama-u.ac.jp

H. Ulbrich and L. Ginzinger (eds.), Motion and Vibration Control, 63–70.

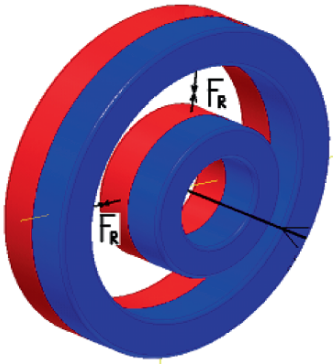

Fig. 1 Principle positioning of ring-shape permanent magnets.

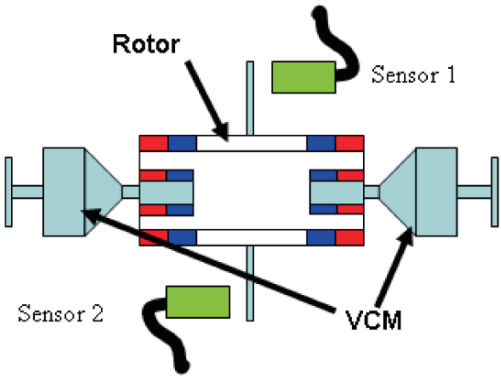

Fig. 2 Repulsive magnetic bearing apparatus. The inner and outer diameters of the outer magnet are 24 mm and 32 mm respectively. The magnet for support has a 7 mm inner and 12 mm outer diameter.

is achieved by controlling the motion of magnets for support independently. In this work, the feasibility of such stiffness adjustment is demonstrated experimentally.

2 Mechanical Construction, Modeling and Simplification

2.1 Mechanical Construction

Figure 1 shows the principal positioning of magnets. Figure 2 shows a schematic diagram of the developed magnetic bearing apparatus using the motion control of permanent magnets. It is an outer-rotor type and includes one ring-shape permanent magnet at the each end. Each voice coil motor drives an inner permanent magnet for support. The displacement of rotor is detected by sensors 1 and 2. Since all motions

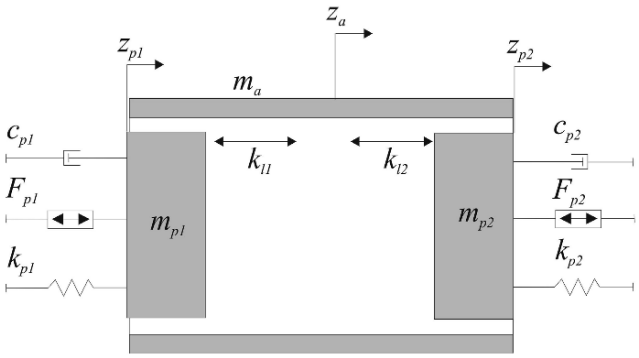

Fig. 3 Physical model of the magnetic bearing apparatus.

in the radial directions are passively supported by repulsive forces, we assume, for the simplicity, that the rotor moves only in the axial (horizontal) direction.

2.2 Modelling and Simplification

Figure 3 shows a physical model of the system illustrated by Figure 2 where $F_{p1}(t)$, $F_{p2}(t)$ is the force generated by VCM's, C_{p1}, C_{p2} is the damping due to the slide bearing and friction inside of VCM's, k_{p1}, k_{p2} is the stiffness of springs inside of VCMs, m_a is the mass of rotor, m_{p1}, m_{p2} is the left and right mass driving by the VCMs including permanent magnet, k_{l1}, k_{l2} is the lateral factor's between the magnets.

The total forces produced by voice coil motors are F_{p1} and F_{p2}. The gravitational force acting on the rotor and the radial forces between the permanent magnets are balanced in the equilibrium states.

Considering the symmetry, we assume that:

$$k_{l1} = k_{l2} \ (\equiv k_l), \tag{1}$$

$$m_{p1} = m_{p2} \ (\equiv m_p), \tag{2}$$

$$c_{p1} = c_{p2} \ (\equiv c_p), \tag{3}$$

$$k_{p1} = k_{p2} \ (\equiv k_a). \tag{4}$$

In addition it is assumed that the input signal to both amplifiers is the same. Then, we can simplify the physical model as shown in Figure 4.

The equations of motion for the simplified system are:

$$m_a \ddot{z}_a = k_l(z_a - z_p), \tag{5}$$

$$m_p \ddot{z}_p = k_l(z_p - z_a) - c_p \dot{z}_p - k_p z_p + k_i * i(t), \tag{6}$$

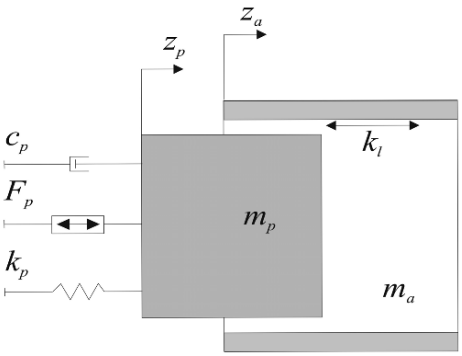

Fig. 4 Simplified physical model.

Table 1 Variables of the simplified system.

Variable	Value	Unit
m_a	0.050	kg
m_p	0.160	kg
k_p	8500	N/m
k_l	2500	N/m
k_i	10	N/A
L	19	mH
R	3	Ohm
c_p	90	Ns/m

$$L\frac{\mathrm{d}i}{\mathrm{d}t} = -k_i\dot{z}_p - Ri. \tag{7}$$

Equation (7) describes the electrical relations for the voice coil motor where i is the coil current, L the coil inductivity, R the coil resistance, and k_i the transducer constant of VCM.

Table 1 shows all variables from the simplified model together including the values and units.

3 Control Design

For optimization we choose the state-feedback control as one of control schemes for stabilization. From (5) to (7), the state space model describing the dynamics of the system is obtained as:

$$\dot{x}(t) = Ax(t) + Bu(t), \tag{8}$$

where

$$\mathbf{A}_s = \begin{bmatrix} 0 & 1 & 0 & 0 & 0 \\ \frac{k_1}{m_a} & 0 & -\frac{k_1}{m_a} & 0 & 0 \\ 0 & 0 & 0 & 1 & 0 \\ -\frac{k_1}{m_p} & 0 & \frac{k_1-k_p}{m_p} & -\frac{c_p}{m_p} & \frac{k_i}{m_p} \\ 0 & 0 & 0 & -\frac{k_i}{L} & -\frac{R}{L} \end{bmatrix}, \quad \mathbf{X}_s = \begin{bmatrix} z_a \\ \dot{z}_a \\ z_p \\ \dot{z}_p \\ i \end{bmatrix}, \quad \mathbf{B}_s = \begin{bmatrix} 0 \\ 0 \\ 0 \\ 0 \\ \frac{1}{L} \end{bmatrix}. \tag{9}$$

Since the system described by (8) and (9) is controllable, the closed-loop poles can be arbitrary assigned by state-variable feedback.

The control input is represented by

$$u(t) = Kx(t) = p_d\, z_a + p_v\, \dot{z}_a + q_d\, z_p + q_v\, \dot{z}_p + q_i i, \tag{10}$$

where

$$K = [p_d \;\; p_v \;\; q_d \;\; q_v \;\; qi]. \tag{11}$$

The poles of close loop system are selected due the simulation and later fine adjustment on the parameter of the matrix K while experimental operation. The poles are placed approximately at: -300, -250, -200, -150 and -100 [1/s]. The values of the matrix K for the closed-loop control become as follows:

$$p_d = 7547 \quad [\text{V/m}]$$
$$p_v = -60 \quad [\text{Vs/m}]$$
$$q_d = 45533 \quad [\text{V/m}]$$
$$q_v = 115 \quad [\text{Vs/m}]$$
$$q_i = 14 \quad [\text{V/A}]$$

4 Adjustability of Radial Stiffness

The amount of the repulsive forces is directly proportional to the lap of the magnet pair. When the overlap is full the repulsive forces are maximum (Figure 5). Since we can control the motion of magnets independently we can change the distance between two inner magnets and make the overlap area smaller. As a result, we achieve the decreasing of repulsive forces, shown in Figure 6.

5 Experiment

Figure 7 shows a photograph of the experimental device. The feasibility of stiffness in the radial direction was investigated. For decreasing the overlap area it is

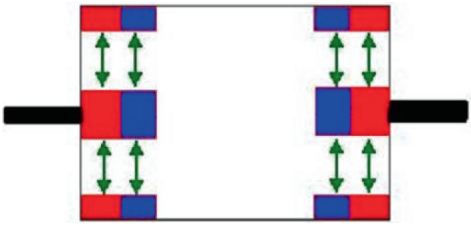

Fig. 5 Full overlapping of magnets delivers the maximal amount of repulsive forces.

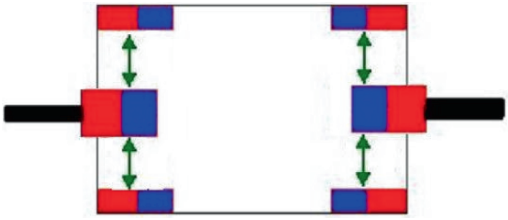

Fig. 6 Smaller repulsive forces as a result of smaller overlap.

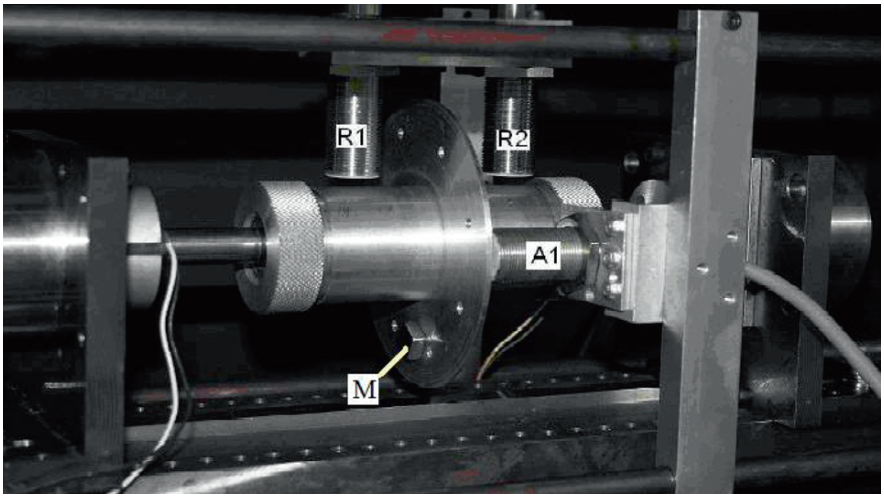

Fig. 7 Magnetic bearing apparatus. The sensors A1 and A2 (A2 is not depicted in the picture) detect the motion in the axial direction and sensors R1 and R2 in the radial direction.

necessary to increase the distance between the magnets for support. Therefore we added a constant offset signal with the same amount but with the opposite sign to each voice coil motor. After increasing the distance, the displacement in the radial direction, by adding of two different masses 16 g (0.156 N) and 64 g (0.647 N) on the point "M" in Figure 7, with changing of the offset value from 0 V to 1.5 V have been measured and compared. Figures 8 and 9 show the results in detail and Table 2 shows a summarized overview. The spring constant is denoted by K [N/mm].

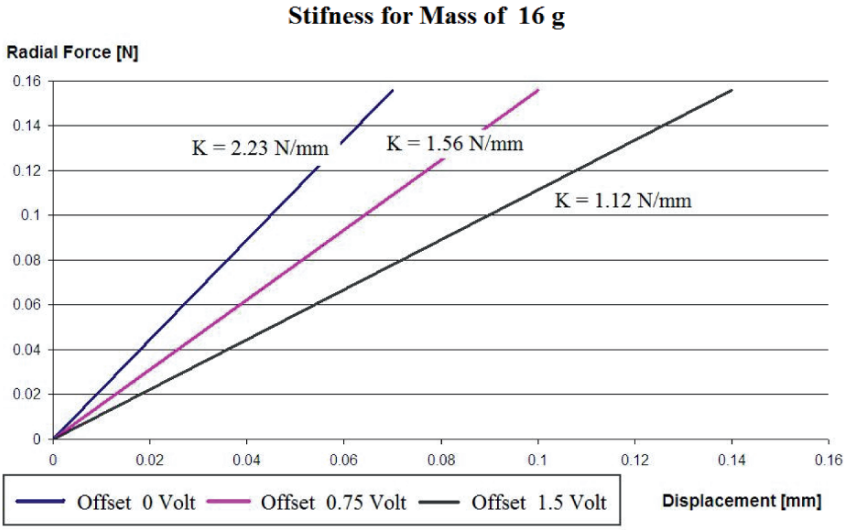

Fig. 8 Characteristic diagram of magnetic spring stiffness between of two ring-shape permanent magnets.

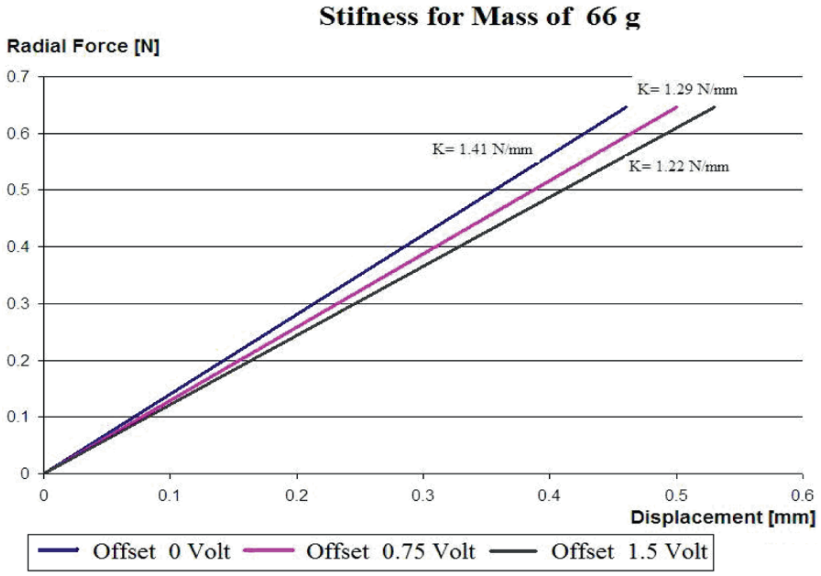

Fig. 9 Characteristic diagram of magnetic spring stiffness between of two ring-shape permanent magnets.

6 Conclusions

A repulsive magnetic bearing apparatus using independent motion control of permanent magnets, to achieve the adjustability on radial stiffness, was developed. The

Table 2 Overview on stiffness and offset relationship.

$\Delta m = 16$ g		$\Delta m = 66$ g	
V_{off}	K [N/mm]	V_{off}	K [N/mm]
0	2.23	0	1.41
0.75	156	0.75	1.29
1.5	*1.12*	1.5	1.22

experimental results show that the stiffness can be adjusted. In the current configuration the range of adjustment is 50%. However the adjustability can be improved by introducing more sophisticated control methods and by modifying the design of permanent magnets. Research in such improvement is under way.

References

1. Jayawant, B.V., *Electromagnetic Levitation and Suspension Techniques*, pp. 1–59, Edward Arnold Ltd., London, 1981.
2. Schweitzer, G., Bleuler, H. and Trixler, A., *Active Magnetic Bearings*, pp. 11–20, VDF Hochschulverlag AG an der ETH Zurich, 1994.
3. Mukhopadhyay, S.C., Ohji, T., Iwahara, M. and Yamada, S., Design, analysis and control of a new repulsive-type magnetic bearing system, *IEEE Proceedings Electric Power Applications* **146**, 33–40, 1999.
4. Kun-Xi Qian, Pei Zeng, Wei-Min Ru and Hai-Yu Yuan, Novel magnetic spring and magnetic bearing, *IEEE Transactions Magnetics* **39**(1), 559–561, 2003.
5. Mizuno, T., Ouchi, T., Ishino, Y. and Araki, K., Repulsive magnetic levitation systems using motion control of magnets, *Trans. Japanese Soc. Mech. Eng., Series C* **61**(589), 3587–3592, 1995.
6. Mizuno, T. and Hara, Y., Active stabilization of a repulsive magnetic bearing using the motion control of permanent magnets, *JSME International Journal, Series C* **43**(3), 2000.
7. Eirich, M., Ishino, Y., Takasaki, M. and Mizuno, T., Active stabilization of repulsive magnetic bearing using independent motion control of permanent magnets, in *Proceedings of the ASME International Design Engineering Technical Conferences*, DETC 2007–35134.
8. Eirich, M., Ishino, Y., Takasaki, M. and Mizuno, T., Active stabilization of repulsive magnetic bearing using independent motion control of permanent magnets, in *Proceedings of the 50th Japan Joint Automatic Control Conference* [No. 07–255], 2007.

Driver Assistance Technology to Enhance Traffic Safety

Raymond Freymann

Abstract It is shown in how far driver assistance systems can contribute to enhance the overall traffic safety. Thereby it must be considered as a goal to increase the performance of active safety systems in the scope of an integrated approach, allowing to realize a variety of interactions between the three elements involved in a traffic scenario, say the driver, the vehicle and the driving environment. Focus is pointed on the related technology, the inherent system complexity and aspects of customer acceptance.

1 Introduction

Safety is a basic need of mankind. This entails that aspects of safety are fundamental to the acceptance of any mobility system. In so far safety must be considered as a long term megatopic driving the automotive industry [1]. Safety in the context of automotive engineering [2] addresses two topic clusters: the *active safety* cluster focusing on the avoidance of traffic accidents and the *passive safety* cluster dealing with accident mitigation topics.

Active safety addresses as for example a full variety of chassis systems implemented to enhance the handling and driving characteristics of a vehicle, such as powerful braking and high precision steering systems as well as high stability axle configurations. Typical passive safety features relate as for instance to the crash optimization of the car body structure, collapsing steering columns and the multitude of integrated safety restraint systems, such as seat belts and airbags. The effectiveness of active and passive safety systems is impressively expressed by the statistical results from thoroughful (worldwide) traffic accident recordings and investigations (Figure 1).

Raymond Freymann
BMW Group Research and Technology, Hanauer Strasse 46, 80992 München, Germany

H. Ulbrich and L. Ginzinger (eds.), Motion and Vibration Control, 71–81.

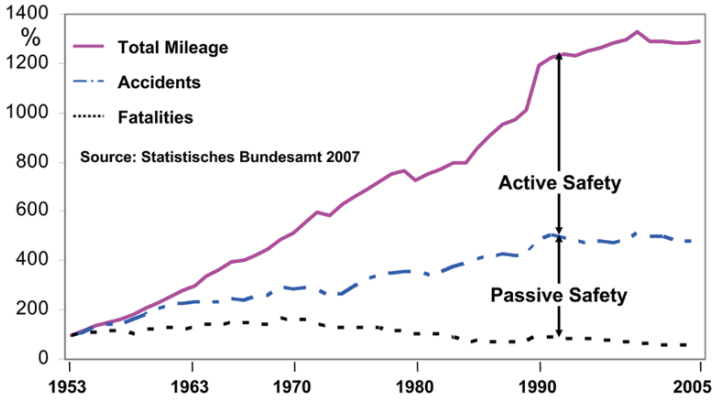

Fig. 1 Traffic accident situation in Germany.

But since we are still far off from a zero traffic accident scenario, the question in how to further reduce the still significant number of traffic accidents must be raised. There is consensus existing among experts that the most promising breakthrough technologies to cope with this topic will be located in the active safety area [3]. In this context great expectations have been attributed to safety relevant driver assistance systems. Indeed a deeper analysis of the situation clearly indicates the many possibilities offered by the driver assistance technology. Driver assistance addresses a full band of applications ranging from information based navigation topics through vehicle guidance and stabilization systems to autonomous driving scenarios.

In the following, focus will be pointed on the safety performance of driver assistance systems related to the different categories addressed. The complexity as well as the potential and risks inherent to the various systems will be discussed as well as their acceptance by "the customer".

2 The Diversity of Driver Assistance System

Focusing on traffic accidents indicates that there are always three elements involved in an accident scenario: the driver, the vehicle and the driving environment. In the past traffic safety initiatives were concentrating on the safety optimization of these three components independently from one another. By today, it is well understood that only an integrated optimization process, focusing on the optimization of the total system, say addressing simultaneously the optimization of the three elements involved, can lead to a significant further improvement in the traffic accident situation [4]. This indicates that the interaction (connectivity) between driver, vehicle and environment (Figure 2) must be a central part of a promising accident reduction

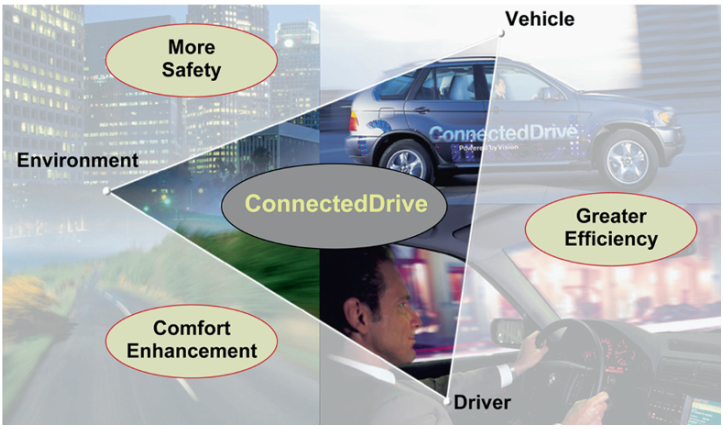

Fig. 2 ConnectedDrive: an integrated approach to active safety enhancement.

Anti-Lock Braking System	ABS	Parking Assistant	PA
Anti-Skid Control System	ASC	Lane Departure Warning	LDW
Dynamic Stability Control	DSC	Lane Change Assistant	LCA
Park Distance Control	PDC	Heading Control	HC
GPS-Navigation	NAVI	Extended Navigation	XNAVI
Active Cruise Control	ACC	Dynamic Performance Control	DPC
Adaptive Head Lights	AHL	Congestion Assistant	COA
Brake Force Display	BFD	Intersection Assistant	IAS
Active Front Steering	AFS	Preventive Pedestrian Protection	PPP
Night Vision	NIVI	Local Danger Warning	DWA
ACC Stop & Go	ACC S&G	Wrong Way Driver Information	WWI
X-Drive	XDR	Emergency Braking	EB
Intelligent Brake Assistant	IBA	Collision Avoidance	CA
Adaptive Drive	ADD	...	

Fig. 3 Driver assistance systems

approach. There is no need to say that this field of interest is directly related to the driver assistance technology.

It can be notified that driver assistance, as it has been introduced since the 70s (Figure 3), was primarily dedicated to the temporary support of the driver in form of the *stabilization of the vehicle* in critical driving situations. Control systems, such as ABS (Antilock-Braking), ASC (Active Stability Control) and DSC (Dynamic Stability Control), being nowadays part of an overall integrated chassis control management system, can be considered as typical technologies in this field. But along the time line a variety of systems were also introduced to assist the driver in the *guidance of the vehicle*. Representatives of that category are ACC (Active Cruise Control) and HC (Heading Control). Moreover it is of importance to consider, in the overall context of driver assistance, so-called information systems which support the driver in the *navigation of the vehicle*. Typical representatives within that category

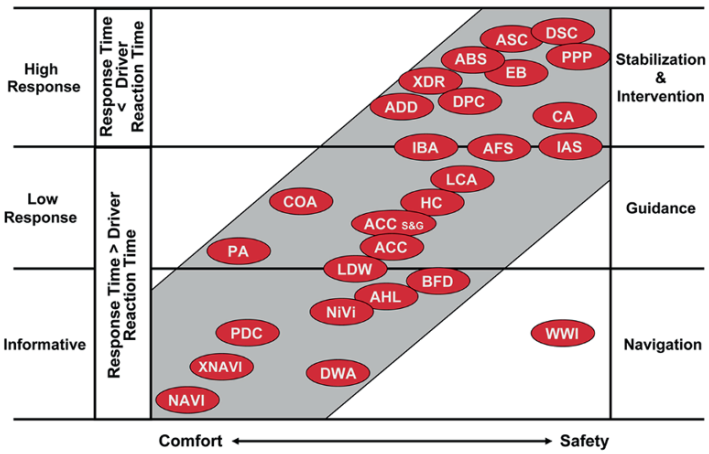

Fig. 4 Driver assistance systems classification.

are GPS navigation systems, actually already flanked by TMC (Traffic Message Channel) traffic jam information capabilities and in the future by additional ad-hoc traffic accident reporting systems making use of a direct wireless communication between vehicles and the traffic infrastructure (Car2X) [5].

The examples addressed indicate the wide range of application of driver assistance. In order to allow a more detailed discussion, it is helpful to cluster the various systems, as is indicated in Figure 4.

The categorization is realized by a distinction between "low response" and "high response" systems. In this context, "low response" means that the driver assistance (control) system action/reaction can be overrun at any time by the driver. Low response systems are related to vehicle navigation and guidance tasks. "High response" systems are characterized by the fact that their control system output, due to the short response time, cannot be overrun by the driver. These systems focus on the stabilization of the vehicle and the autonomous guidance intervention. According to Figure 4, "high response" driver assistance are directly addressing inherent safety critical (driving and traffic) situations.

It is true that the categorization levels of systems are not strictly defined in each case. As for example the distinction between an Active Cruise Control system (ACC) with enhanced braking capabilities and those of an Emergency Braking system (EB) could be rather difficult to define.

3 Active Safety Systems

It can be stated that the introduction of "high response" driver assistance control systems in production vehicles has up to now been restricted to applications allowing

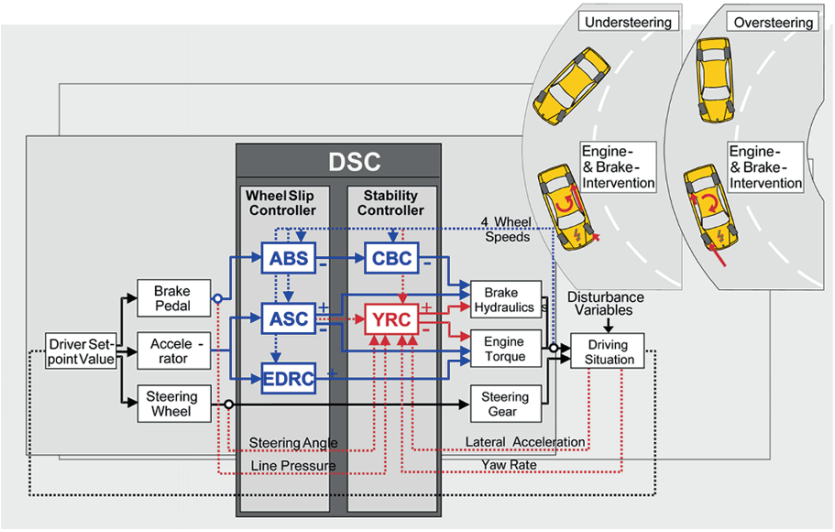

Fig. 5 Block diagram of DSC system.

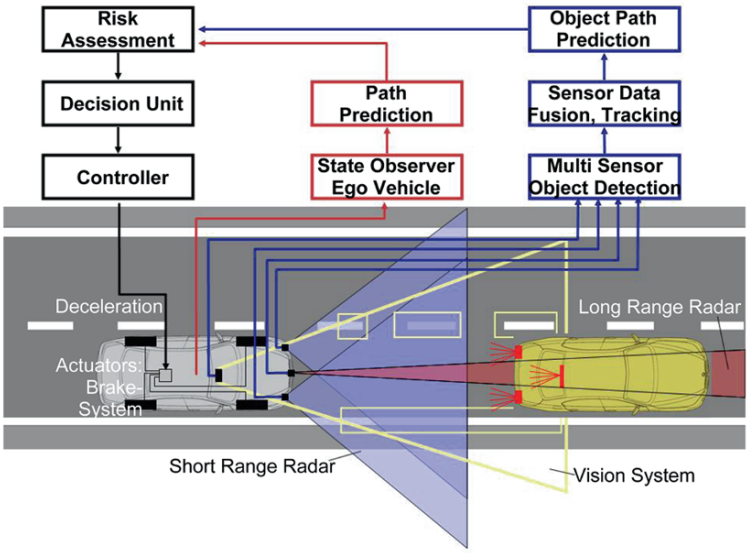

Fig. 6 Emergency brake system.

the required technology to be "completely part of the vehicle". All sensor information and control variables are vehicle fixed! This allows to realize even complex applications, such as dynamic stability control (DSC), as depicted in Figure 5, with an enormous reliability.

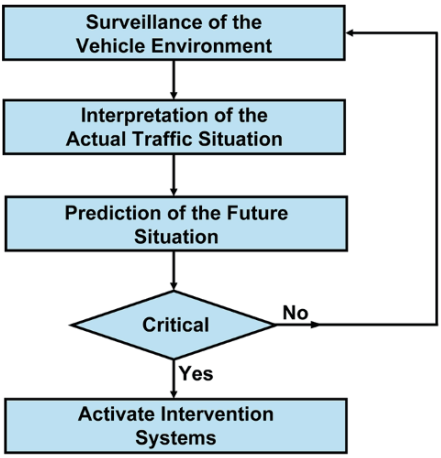

Fig. 7 Decision taking process for autonomous intervention.

This aspect of realibility becomes (by far) more questionable if systems, like autonomous collision avoidance (CA), shown in Figure 6, taking into account the driving environment as a sensorial control system input, are considered. This statement is based on the fact that systems relying on the driving environment information do require, apart from the basic detection via sensors, a clear interpretation of the actual traffic situation around the vehicle (Figure 7). This task might be difficult to solve in the case of real driving situations and it is not realistic to assume that it will be achieved correctly in most situations. Accordingly, there will always be a rest of risk remaining if environmentally sensing high response driver assistance systems were introduced. This remaining risk, which also from a legal point of view (liability) [6] opens a full range of questions, entails that "some more time" will elapse before we will see these systems operational in series production vehicles.

On the other hand there are plenty of realizable new advanced technologies under development which can significantly contribute to reduce the number of (severe) accidents. Analyzing accident cases (Figure 8) indicates that more than 50% of all severe accidents are at least affected by some lack of driver information!

Consequently it must be asked in how far this lack of information can be compensated by the driver assistance technology. In order to provide an additional meaningful information to the driver, the assistance system must acquire relevant data with regard to the traffic scenario "around" the vehicle. As will be shown in the following two examples of application, near and far field data will have to be considered.

Example 1: Lane Change Assistant. The near field perception capabilities of driver assistance research vehicles have been dramatically improved during the past years by the integration of radar, lidar and video systems (Figure 9). This entails that, in case of a lane change maneuver on a highway, the sensor system can easily

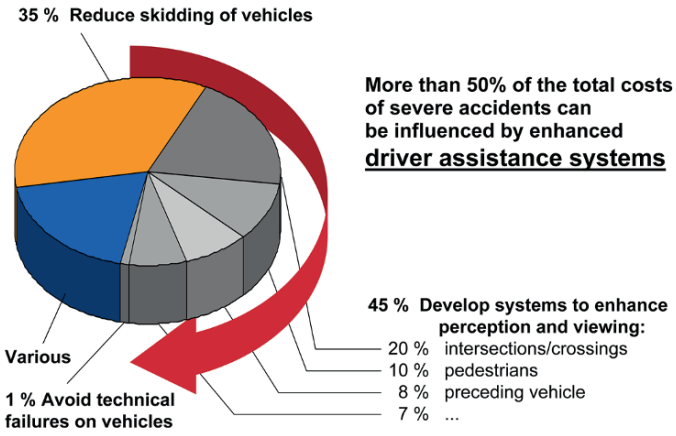

Fig. 8 What do we need to further reduce the total number of severe accidents?.

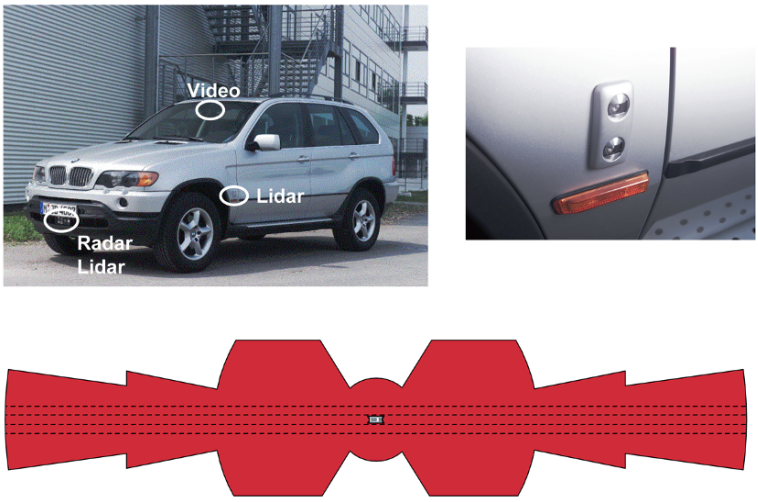

Fig. 9 Vehicle near field perception capabilities.

identify vehicles approaching on the pass lane [7]. The identification is achieved with regard to relative distance and speed data. These data allow us to evaluate if a lane change might be critical. In case the driver intends to perform a lane change, which is normally initiated by the activation of the blinker light and/or a steering wheel input, the assistance system is ready to give a (kinaesthetic, optical, acoustic, etc.) warning if required.

Example 2: Wireless ad-hoc communication. The perception of the far field cannot be realized via the on-board vehicle sensor network. It is however possible to

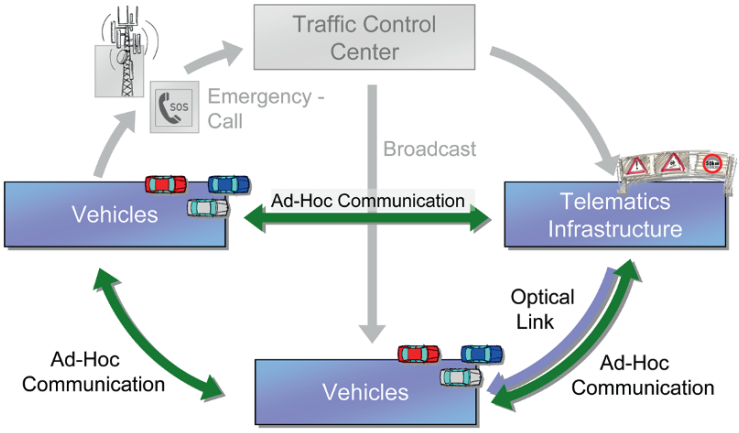

Fig. 10 Direct vehicle to vehicle communication.

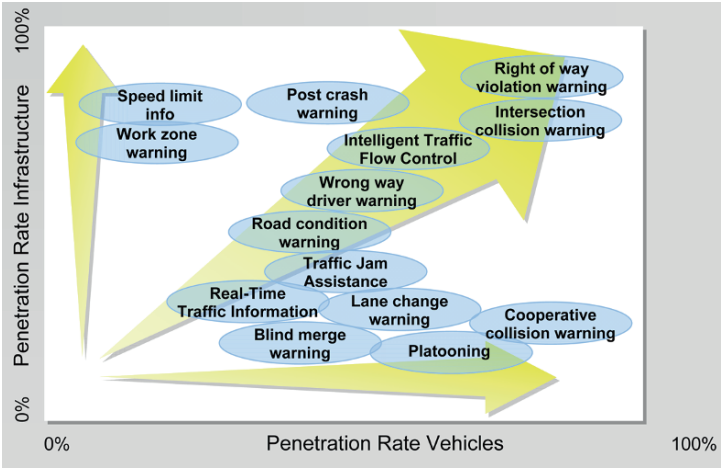

Fig. 11 Applications of ad-hoc connectivity.

provide relevant far field data to the vehicle by means of wireless communication technologies. Imagine that an accident has taken place on a (highway) road. This always entails a critical situation for all following vehicles.

Direct wireless communication (Figure 10) between the vehicles involved in the accident and the approaching vehicles could avoid that the drivers of these vehicles would get surprised when approaching/reaching the accident location.

It has to be mentioned that using (following) vehicles as “wireless hoppers” allows to pass the information along rather long distances.

All in all the wireless ad-hoc communication, with its many applications (Figure 11), must be considered as a highly promising technology in the scope of future accident reducing strategies [8].

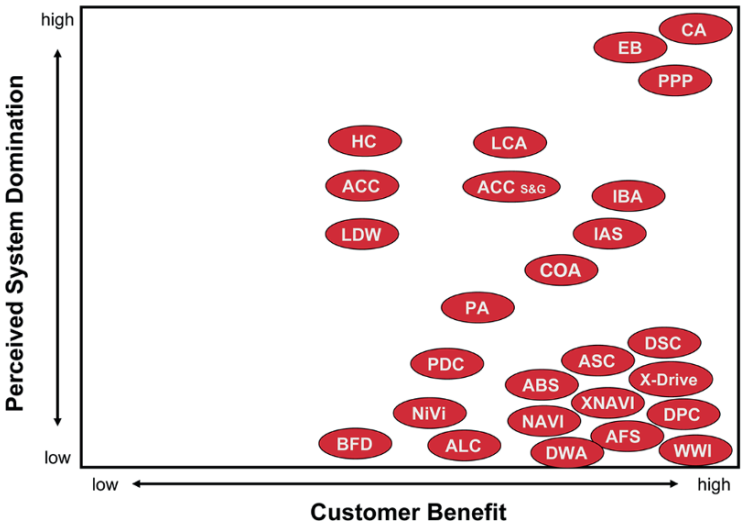

Fig. 12 Benefit/domination relationship of driver assistance systems.

From the topics addressed above it can be concluded that the field of driver assistance does apply to a broad variety of practical applications. With consideration of the actual level of technology available and the legal situation existing, it can be expected that next implementation steps of the technology will not be related to so-called "fast response" systems with an autonomous action. Apart from this futuristic vision, a far more realistic scenario foresees the introduction of a full variety of traffic safety enhancing driver assistance systems related to the levels of vehicle navigation and vehicle guidance [9].

4 Customer Acceptance

Having addressed a priori technical aspects in the previous chapters, focus will now be placed on customer relevant issues. This is of relevance since finally the customer decides about the integration of a driver assistance system (as a special option) into his vehicle. This directly entails that only systems which – from the *customers* view point – do provide a (significant) benefit can be a market success.

Customer research investigations clearly indicate that even if the customer is increasingly sensitive to safety aspects, he is not (yet) accepting safety relevant driver assistance systems which are directly interacting with the guidance of the vehicle. A system domination in this field of driver oriented activities is not accepted! Accordingly, it is of importance to thoroughfully investigate for any driver assistance system the relationship existing between the benefit to the driver and the domination percieved by the driver. In this context it can be foreseen that assistance systems,

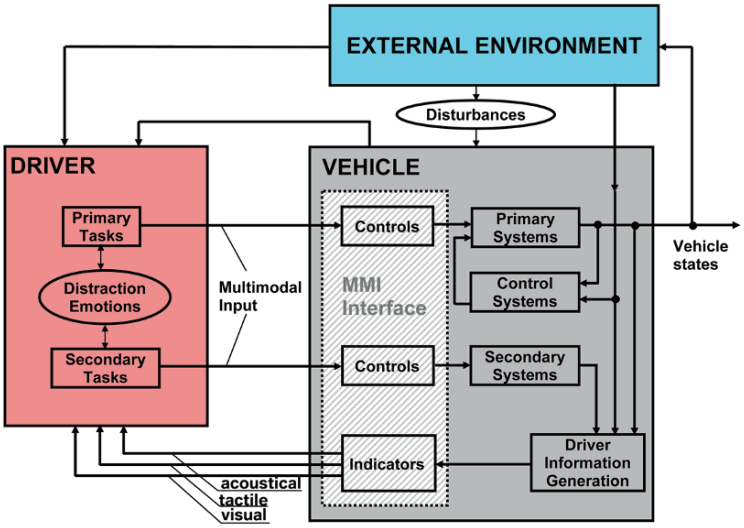

Fig. 13 Interaction between driver, vehicle and environment.

primarily located in the right lower corner of Figure 12, might find the acceptance of the customer and thus become a market success.

A further criterion of customer acceptance is related to the design of the HMI (Human Machine Interface) [10]. The driver expects that driver assistance systems do provide a support to the driving task but do not create an additional workload or distraction. This situation explains why driver assistance systems efficiently operating in the background, such as ABS and DSC, have found a high penetration rate. When driving, the driver must (and he also wants to) fully concentrate on the primary task of driving; occasionally required secondary tasks need to be easily achieved (Figure 13). This entails that it is of primary importance to focus on the easy handling and comprehensible operation of assistance systems. Intensive investigations with regard to these criteria are performed in the automotive industry in the scope of usability and (dynamic) simulator tests [11].

These reflections underline the high importance of HMI investigations in the development and integration process of driver assistance systems [12]. The realization of a real premium HMI functionality is of a vital importance to the system acceptance!

5 Conclusion

An overview of the high potential of driver assistance systems for enhancing driving and traffic safety was given. The key for the realization of efficient systems

is related to technologies in the sensor and the traffic/driving situation interpretation fields. A highly reliable technology is required if visionary "high response" autonomous actions in the vehicle guidance are considered. Since this technology is not yet available the next generation of systems will be primarily oriented to functionalities allowing to enhance the traffic safety by "low-response" information and guidance systems. Moreover it was clearly addressed that the overall layout of the HMI interface of driver assistance systems is of a primary importance with regard to the customer acceptance.

References

1. R. Freymann: *Auto und Fahrer im 21. Jahrhundert*. VDI-Berichte Nr. 1768, 2003.
2. H.H. Braess and U. Seiffert (Eds.), *Vieweg Handbuch Kraftfahrzeugtechnik*, 2nd edn. Vieweg & Sohn Verlagsgesellschaft mbH, Braunschweig/Wiesbaden, 2001.
3. J.N. Kanianthra: Highway Safety: Future Options That Will Make a Difference. Presentation given at the "84th Annual Meeting Transportation Research Board", Washington (DC), 13 January 2005.
4. T. Bachmann, K. Naab, G. Reichart, M. Schraut: Enhancing Traffic Safety with BMW's Driver Assistant Approach. ITS Paper No. 2124, 7th World Congress on Intelligent Transportation Systems, Turin, 2000.
5. R. Freymann: Potentiale von Car2X-Kommunikations-Technologien. In: *Proceedings VDA Technical Congress 2007*, Sindelfingen, 28–29 March 2007, pp. 257–274.
6. S. Becker et al.: RESPONSE – The Integrated Approach of User, System, and Legal Perspective: Final Report on Recommendations for Testing and Market Introduction of ADAS. Final Report of Telematics 2C Project TR4022, Commission of the European Communities, Directorate General XIII, Brussels, September 2001.
7. D. Ehmanns, P. Zahn, H. Spannheimer, R. Freymann: Integrated Longitudinal and Lateral Guidance Control – A New Concept in the Field of Driver Assistance Technology. *ATZ* **4**, 2003, 346–352.
8. R. Bogenberger, T. Kosch: Ad-hoc Peer-to-Peer Communication-Webs on the Street. ITS-Paper No. 2149, 9th World Congress on Intelligent Transportation Systems, Chicago, 14–18 October 2002.
9. R. Freymann: Aktive Sicherheit: eine wesentliche Technologie zur Erhöhung der allgemeinen Verkehrssicherheit. In: *VDI Jahrbuch 2006 – Fahrzeug und Verkehrstechnik*, VDI Verlag GmbH, 2006, pp. 286–308.
10. R. Freymann: HMI: A Fascinating and Challenging Task. In: *IEA Triennial Conference, Proceedings/Symposium: Vehicle Ergonomics*, Maastricht, 10–14 July 2006.
11. A. Huesmann, D. Wisselmann, R. Freymann: *Der neue dynamische Fahrsimulator der BMW Fahrzeugforschung*. VDI-Berichte Nr. 1745, 2003, pp. 59–67.
12. W. Reichelt, P. Frank: Fahrerassistenzsysteme im Entwicklungsprozess. In: *Kraftfahrzeugführung*, Th. Jürgensohn, K.-P. Timpe (Eds.). Springer, Berlin, 2001, pp. 71–78.

Improving Absorption of Sound Using Active Control

E. Friot, A. Gintz, P. Herzog and S. Schneider

Abstract Absorption of sound is a common problem especially at low frequencies. Absorbing materials available today perform well at medium and high frequencies but are much less performing at low frequencies at least when considering layers of realistic thickness. By contrast active control of sound is the most powerful at low frequencies where the sound field that is to be controlled is rather simple. Hence a combination of passive materials and active control seems to be a promising way to improve the efficiency of sound absorbing acoustic linings. The paper reflects upon two main directions. First, it studies the elimination by active control of sound of a sound field reflected by an absorbing layer. Such a procedure may be applied to improve the quality of acoustic testing facilities like anechoic chambers around or below its cut-off frequency. Secondly, the paper considers the design of hybrid absorbing materials consisting of a passive materials whose sound absorption is improved using either acoustic or mechanic actuators. Both studies are characterized by a strong link of numerical studies and experimental verification.

1 Introduction

Absorbing materials available today, perform well at medium and high frequencies but are much less performing at low frequencies at least when considering layers of realistic thickness. By contrast active control of sound is the most powerful at low frequencies where the sound field that is to be controlled is rather simple. Hence a

S. Schneider
Knorr Bremse SfS, Moosacher Straße 80, 80809 München, Germany;
E-mail: Stefan.Schneider@knorr-bremse.com

E. Friot, A. Gintz, P. Herzog
CNRS-LMA, 31 chemin Joseph-Aiguier, 13402 Marseille Cedex 20, France;
E-mail: {friot, gintz, herzog}@lma.cnrs-mrs.fr

H. Ulbrich and L. Ginzinger (eds.), Motion and Vibration Control, 83–91.

combination of passive materials and active control seems to be a promising way to improve the efficiency of sound absorbing acoustic linings.

The first part of this paper studies the estimation of the remaining reflexions in anechoic chambers below its cut-off frequency.A real-time active control procedure to suppress a scattered sound field has been presented in [2]. This study forms the basis of the considerations dealt with here. The second part focuses on the development of a hybrid panel used for sound isolation purposes in buildings. The performance of existing passive panels is limited by the properties of the absorbing material and its thickness. Using acoustic actuators, the low frequency properties of the absorbing materials is improved to yield higher absorption of sound, see [3, 4].

2 Estimation of a Reflected Sound Field

At low frequencies acoustic linings of anechoic chambers do not sufficiently absorb the incident sound field. The remaining reflections perturb measurements and define the cut-off frequency of such a chamber. Using todays absorbing materials anechoic chambers with a cut-off frequency below 80 Hz are difficult to design because of the significant thickness of the lining required to avoid reflexions at low frequencies. Here we consider a possibility of constructing an anechoic chamber with a cut-off frequency below 80 Hz using an active control of sound procedure. The objective of the study is to estimate and finally to cancel out the sound field reflected by the lining at a position within the chamber where measurement are to be carried out.

The sound field reflected at the boundary Γ_F of the fluid domain Ω_F, see Figure 1, can be evaluated using the boundary integral method. The sound field within the domain Ω_F at a position y can be expressed by the sound pressure p and the normal velocity v_ν at the boundary Γ_F using

$$p(y) + \int_{\Gamma_F} \frac{\partial \phi(x, y)}{\partial \nu} p(x)\, d\Gamma_F - a \int_{\Gamma_F} \phi(x, y) v_\nu\, d\Gamma_F = p^{\text{inc}}(y) \quad y \in \Omega_F \qquad (1)$$

with an incident sound field p^{inc} and the fundamental solution

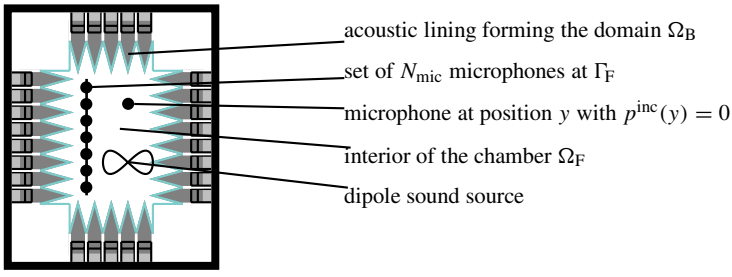

Fig. 1 Diagramm of the set-up used to estimate the sound field reflected at the boundary Γ_F.

$$\phi(x, y) = \frac{e^{\mathrm{j}k|x-y|}}{4\pi|x-y|} = \frac{e^{\mathrm{j}kr}}{4\pi r}, \quad r = |x-y|, \quad x \neq y\,. \tag{2}$$

of the Helmholtz equation in three dimensions, the wave number $k = \omega/c$ and $a = \mathrm{j}\omega\rho^{\mathrm{f}}$. Therein c denotes the speed of sound and ρ^{f} denotes the density of the fluid. If the point y in Eq. (1) is chosen such that $p^{\mathrm{inc}}(y) = 0$ holds true then this equation can be used to estimate the scattered sound field p^{scat} using

$$p^{\mathrm{scat}}(y) = -\int_{\Gamma_{\mathrm{F}}} \frac{\partial\phi(x, y)}{\partial v} p(x)\, d\Gamma_{\mathrm{F}} + a\int_{\Gamma_{\mathrm{F}}} \phi(x, y) v_v\, d\Gamma_{\mathrm{F}} \quad y \in \Omega_{\mathrm{F}} \tag{3}$$

from the measured sound pressure p and the fluid velocity v_v at a certain boundary Γ_{F}. Performing measurements for N_{mic} positions at that boundary of the source with $p^{\mathrm{inc}}(y) = 0$ enables the estimation of the diffraction filter H^{s} such that the sound pressure scattered at the boundary Γ_{F} can be obtained from the measured sound pressures and velocities as

$$p^{\mathrm{scat}} = H^{\mathrm{s}} \begin{bmatrix} p \\ v_v \end{bmatrix}.$$

Disadvantage of such an approach is that the sound pressure and the fluid velocity must be measured. But the sound pressure and the surface velocity on Γ_{F} are not independent. Their relation is determined by the properties of the domain Ω_{B}. Supposing that k is not an eigenvalue of the operator describing the sound propagation in Ω_{B}, a unique relation between the sound pressure and the fluid velocity can be found such that

$$Zv_v = p \quad \text{on } \Gamma_{\mathrm{F}} \tag{4}$$

holds true. The operator Z in Eq. (4) is often referred to as the acoustic impedance boundary operator [5]. Supposing further that this operator is not singular we have

$$v_v = Z^{-1}p = Yp \quad \text{on } \Gamma_{\mathrm{F}} \tag{5}$$

with the acoustic admittance Y of the boundary Γ_{F}. Using Eq. (3) with Eq. (5) yields

$$p^{\mathrm{scat}}(y) = -\int_{\Gamma_{\mathrm{F}}} \left(\frac{\partial\phi(x, y)}{\partial v} - a\phi(x, y)Y \right) p(x)\, d\Gamma_{\mathrm{F}} = H^{\mathrm{s}}p \quad y \in \Omega_{\mathrm{F}}\,. \tag{6}$$

Eq. (6) shows that the scattered sound field can be obtained from measuring the sound pressure p on Γ_{F} only. The estimation of these filters requires a dipole sound source that is placed such that the reference microphone does not receive any direct sound field from the source. The diffraction filters H^{s} can now be used to estimate the reflected sound field out of the measured sound field at the boundary Γ_{F} for any sound source.

The above proposed method has been used to estimate the reflections in a rectangular cavity measuring $2\times1.1\times1.2$ m^3 in the 20 to 400 Hz frequency range experimentally. The cavity was made of Siporex porous concrete and the walls were considered perfectly sound reflecting. The sound field close to the walls has been

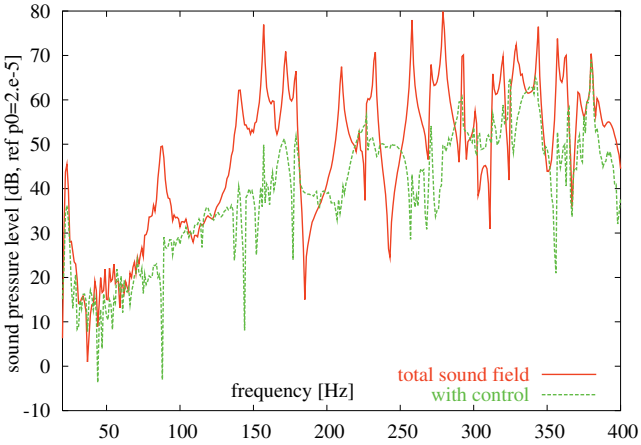

Fig. 2 Sound pressure measured in the cavity and sound pressure obtained after the estimated reflected sound field has been removed from the data.

measured at 32 positions that were equally distributed over the walls. A dipole sound source was rotated in the cavity and the sound pressure at the walls and the scattered field p^{scat} were recorded for each rotation. Using Eq. (6) the diffraction filter H^{s} was estimated out of the experimental data. Figure 2 shows the sound pressure measured in the cavity and the sound pressure obtained when the estimated reflected sound field has been removed from the data. At least up to 300 Hz the resonance peaks have been reduced by 20 dB. These promising results motivate the application of the proposed method to estimate the wall reflexions in the 40 to 160 Hz frequency range observed in the large anechoic chamber at the Laboratoire de Mécanique et d'Acoustique (LMA) in Marseille. Once the reflected sound field can be estimated, this information can be used to either feed active control procedures to cancel out this sound field in the chamber or to post-process experimental data.

3 Hybrid Absorbing Panels

The objective of the second part of this study was the numerical study of the feasibility of a hybrid absorbing panel to be used in buildings. Unless using absorbing materials of unrealistic thickness, passive acoustic wall treatments are not efficient in the low frequency range. In what follows we consider therefore to increase the sound absorption of these panels by the use of active control of sound. The basic concept of these hybrid panels consists of using an acoustic actuator (loudspeaker) behind the absorbing material to influence the acoustic properties of the absorbing material. A sample panel with dimensions $0.6\times0.6\times0.25$ m^3 containing four loudspeakers and an absorbing material of 7.5 cm thickness was build at the LMA. So far this panel was used to verify the validity of the numerical model later on used to

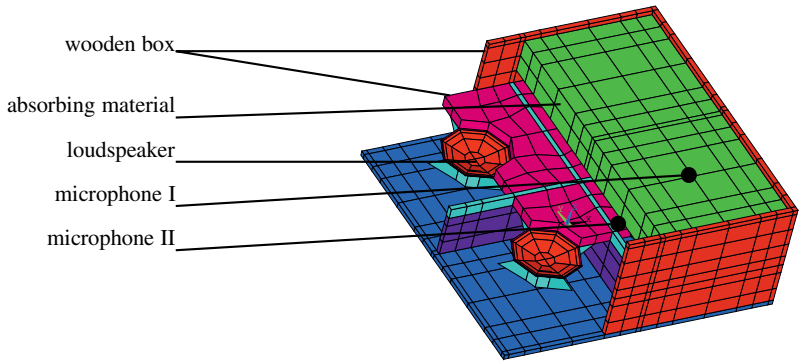

Fig. 3 Meshed geometry of the hybrid cell.

test several control strategies. Figure 3 shows the finite element model for this panel with the assembly of the different components. The absorbing material, a glass wool ISOVER PB 38, was modeled using the equivalent fluid model. The material parameters, $\sigma = 2.0\text{e}4$ Ns/m^4 and $\phi = 0.97$, have been identified using an impedance tube experiment. The passive absorption coefficient α of a layer of 7.5 cm thickness is below $\alpha = 0.3$ up to a frequency of 200 Hz. The electro-mechanical behavior of the loudspeakers has been modeled using the model proposed by Thiele and Small [6].

To influence the acoustic properties of the panel two strategies were considered in the present study:

1. A given sound pressure behind the absorbing layer
   The impedance of the layer at the surface facing the cavity is modified by prescribing an appropriate pressure behind the layer. From the definition of the flow resistivity σ of a porous material with a thickness e, see for example [1], $\sigma = (p_1 - p_2)/v_v/e$, with the sound pressure p_1 and p_2 on each side of the panel, it follows that for $p_2 = 0$, we have for the surface impedance Z of the panel $Z = \sigma e$. With an appropriate choice of the flow resistivity and the thickness of the material the surface impedance of the panel can be made equal to the impedance $Z = \rho^{\text{f}} c$ of a plane wave. Such a panel will be perfectly absorbent for plane waves in normal direction to the panel.
2. The control of the reflected sound field
   Under the assumption that the sound field p^{scat} reflected by the panel is known, this quantity can be used directly as input for the active control algorithm. If and how this sound pressure can be measured is still an open question. Note that possible microphone position used to estimate the scattered sound field are restricted to be within the panel. Microphones within the cavity are not allowed.

The performance of these two strategies was studied using a numerical model for a cavity measuring $1.2\times1.8\times2.4$ m^3. The walls are equipped with $2(2\times3+2\times4+3\times4) = 52$ panels covering the walls completely. In front of each membrane of the loudspeakers two points, one on each side of the absorbing ma-

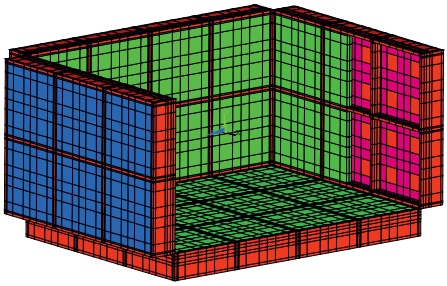

Fig. 4 Model of a acoustic cavity equipped with hybrid wall panels.

terial, see Figure 3, were chosen as possible microphone positions. Microphone I served to evaluate the reflected sound pressure and microphone II was used with control strategy one. A part of the meshed walls, including the hybrid panels, is shown in Figure 4. The matrix of the transfer functions of the microphones at positions I and II, H^{I} and H^{II} respectively, and the supply voltage U_q of the loudspeakers has been calculated in the 20 to 200 Hz frequency range using the computer code AKUSPOR developed at the LMA. A monopole sound source was used to generate an incident sound field p^{inc} in the cavity. The direct sound field at the microphones in front of the absorbing layer p^{I} and the total sound field behind the absorbing layer p^{II} were used to calculate the supply voltages U_q^{I} and U_q^{II} subsequently used to simulate the active control procedure. To asses the different control strategies two criteria were defined. The first

$$\eta_1 = \frac{\sum_{i\in\mathcal{I}} |p^i_{\mathrm{ctrl}}|}{\sum_{i\in\mathcal{I}} |p^i_0|} \tag{7}$$

compares the sound pressure p^i_{ctrl} at a set of points $\mathcal{I}$ obtained with control with the sound pressure p^i_0 obtained without control. Hence the reduction of the sound pressure is rated regardless of the incident sound field. The second criterion

$$\eta_2 = \frac{\sum_{i\in\mathcal{I}} |p^i_{\mathrm{inc}} - p_{\mathrm{ctrl}}|}{\sum_{i\in\mathcal{I}} |p^i_{\mathrm{inc}}|} \tag{8}$$

The sound pressure at various positions in the cavity with respect to the frequency are shown in Figure 6. We observe that both strategies reduce the significant impact of an acoustic mode of the cavity at 60 Hz. Hence the quite simple strategy of creating a zero sound pressure behind the absorbing material yields satisfactory results.

compares the sound pressure with control p^i_{ctrl} with the incident sound field and hence measures to what extent the sound field reflected by the walls has been removed by the active control procedure. Results for both criteria are shown in Figure 5. Both strategies yield a significant reduction of the total sound pressure in the cavity, see left sub-figure in Figure 5. The second control strategy became unstable

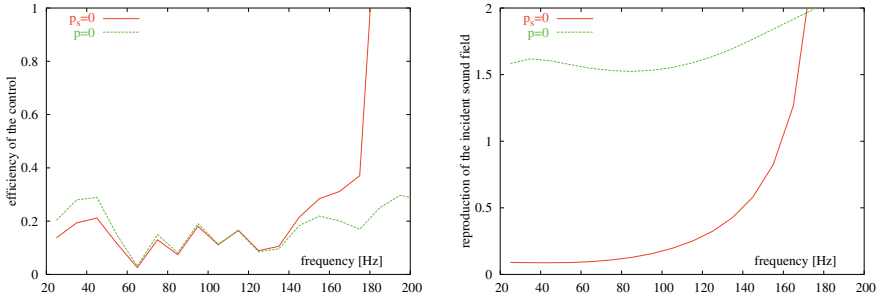

Fig. 5 Efficiency of the active control procedures. Criterion η_1 in the left sub-figure and η_2 in the right sub-figure.

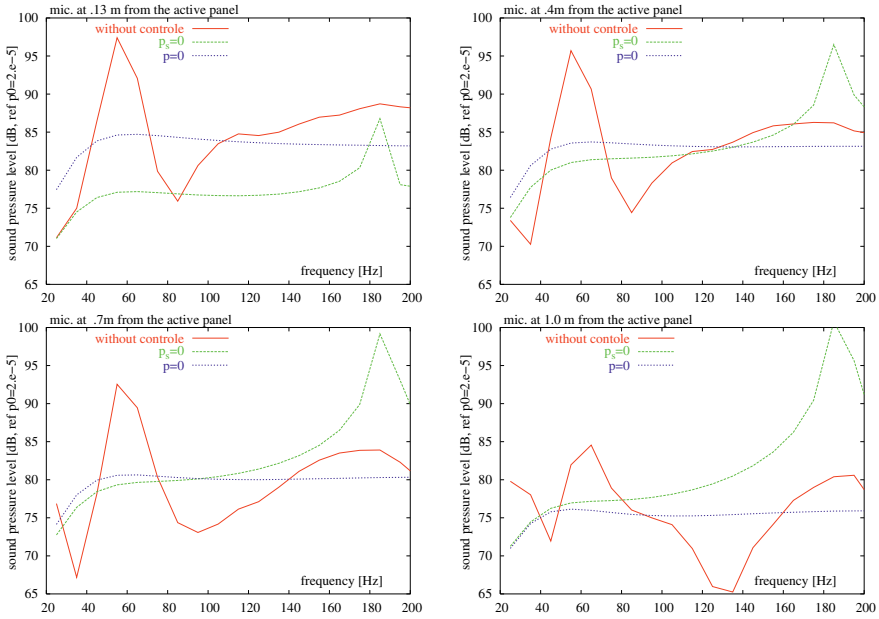

Fig. 6 Sound pressure in the cavity with and without active control.

for frequencies above 160 Hz, however. But only the control strategy two, which directly controls the reflected sound field, was able to reproduce the incident sound field, see right sub-figure in Figure 5. The sound pressure distribution at 45 Hz on the side of the absorbing material facing the cavity and in a part of the cavity are shown in Figures 7 and 8. Strategy two reproduces quite well the incident sound field everywhere on the surface of the absorbing material, but also within the cavity. Strategy one does not reproduce the sound field obtained under free-field conditions, as with this strategy the panels are perfectly absorbent only for plane waves, but the

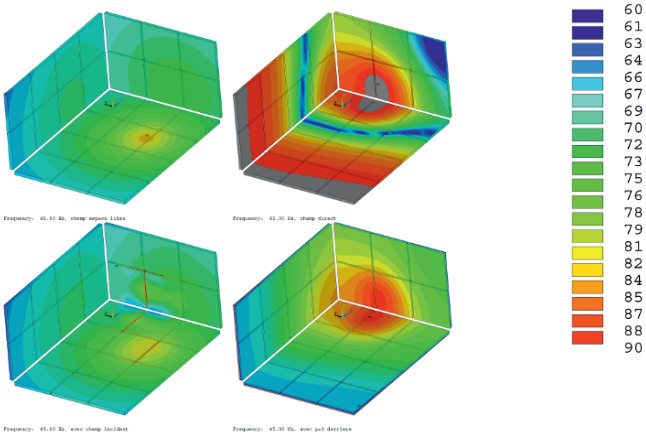

Fig. 7 Sound pressure level on the absorbing material. Incident sound field (upper left sub-figure), total sound field in the cavity without control (upper right sub-figure), sound field with control strategy two (lower left sub-figure) and with strategy one (lower right sub-figure). Frequency: 45 Hz. The gray scale gives the sound pressure level in dB [ref. 2e-5].

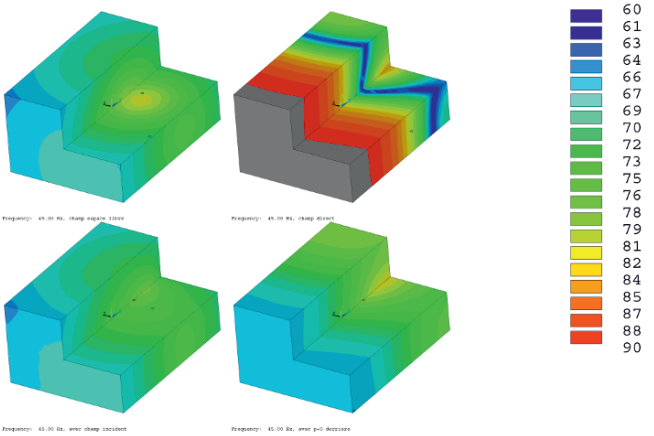

Fig. 8 Sound pressure level in the cavity (one quater of the cavity has been cut out). Incident sound field (upper left sub-figure), total sound field in the cavity without control (upper right sub-figure), sound field with control strategy two (lower left sub-figure) and with strategy one (lower right sub-figure). Frequency: 45 Hz. The gray scale gives the sound pressure level in dB [ref. 2e-5].

sound pressure level within the cavity is reduced to the level of the direct sound field.

4 Conclusion

Two situations have been considered where the sound field scattered by an acoustic wall treatment is to be determined and subsequently removed.

First, we have presented a method to estimate the reflexions of the acoustic lining of an anechoic chamber in the very low frequency range. Using estimated diffraction filters the sound field reflected by the lining can be evaluated using the results of sound pressure measurements close to the lining. The estimation of these filters requires a dipole sound source that is placed such that the reference microphone does not receive any direct sound field from the source. The estimated diffraction filters do not depend on the sound source and allow therefore the estimation of the reflexions at the walls occurring when measurements are performed in the anechoic room at low frequencies.

Secondly, we have studied hybrid wall panels with an improved low-frequency absorption. Two control strategies were considered: (a) zero sound pressure behind the absorbing material and (b) direct cancellation of the reflected sound field. Using numerical experiments we have shown that the quite simple strategy (a) yields a significant improvement of the sound absorption of the panels.

Acknowledgements The last author was financed by a grant from the French "Agence Nationale de la Recherche" under the project BLAN06-134753. Numerical simulations were run on a Linux Networx PC-Farm at the Center for Information Services and High Performance Computing at the Technische Universität Dresden, Germany.

References

1. Allard, J.F. (1993) *Propagation of Sound in Porous Media. Modelling Sound Absorbing Materials*. Elsvier, London/New York.
2. Friot, E., Bordier, C. (2004) Real-time active suppression of scattered acoustic radiation. *Journal of Sound and Vibration* **278**(3), 563–580.
3. Furstoss, M., Thenail, D., Galland, M.A. (1997) Surface impedance control for sound absorption: Direct and hybrid passive/active strategies. *Journal of Sound and Vibration* **203**(2), 219–236.
4. Mazeaud, B., Sellen, N., Galland, M.A. (2004) Design of an adaptive hybrid liner for flow duct applications. Presented at 10th AIAA/CEAS Aeroacoustics Conference, AIAA Paper 2004-2852.
5. Ohayon, R., Soize, C. (1998) *Structural Acoustics and Vibration*. Academic Press, New York.
6. Small, R. (1973) Vented-box loudspeaker systems – Part 1: Small-signal analysis. *Journal of the Audio Engineering Society* **21**(5), 363–372.

Modeling and Control of a Pneumatically Driven Stewart Platform

Hubert Gattringer, Ronald Naderer and Hartmut Bremer

Abstract Electrically driven Stewart platforms are used in the field of machine tooling and robotics, where very accurate positions have to be reached associated with heavy loads. In this paper we present a pneumatically driven Stewart platform powered by fluidic air muscles. Due to the elasticity of the muscles and air as driving medium, the robot is predestined for applications where compliance plays a major role. Compliant behavior is necessary for direct contact with humans. Fitness is an area, where this contact is given and a fast movement is needed for the body workout. Another field of application are simulators for computer games or 6D cinemas. To realize the six degrees of freedom $(x, y, z, \alpha, \beta, \gamma)$ for the Tool Center Point (TCP) there are six fluidic muscles. Due to the fact that the muscles are only able to pull on the platform, there is a spring in the middle that applies a compressive force to the moving part of the robot. The spring is a non modified spiral spring which is commonly used for the suspension of a passenger car. As a result of the kinematical model (inverse kinematics, forward kinematics) the workspace is optimized. To dimension and test the dynamical behavior, a Matlab/Simulink model is derived. This is done by applying the Projection Equation, a synthetical method for obtaining the equations of motions for multi body systems. Based on the dynamical model we develop a control concept in a cascaded structure (pressure control, linearization, position control). A laboratory setup is used to validate the simulation model. Both, simulations as well as experimental results demonstrate the success of the proposed concept.

Hubert Gattringer
Institute for Robotics, Johannes Kepler University Linz, Altenbergerstr. 69, 4040 Linz, Austria;
E-mail: hubert.gattringer@jku.at

Ronald Naderer
FerRobotics Compliant Robot Technology GmbH, Hochofenstr. 2, 4030 Linz, Austria,
E-mail: ronald.naderer@ferrobotics.at

Hartmut Bremer
Institute for Robotics, Johannes Kepler University Linz, Altenbergerstr. 69, 4040 Linz, Austria;
E-mail: hartmut.bremer@jku.at

H. Ulbrich and L. Ginzinger (eds.), Motion and Vibration Control, 93–102.

1 Introduction

In modern life, manufacturing companies without robotic systems are hard to imagine. Normally these are articulated robots for manipulation tasks and Hexapod systems in milling machines. In [12] and [13] a hexapod system is introduced using stiff electrical drives with a very high accuracy. Some basics for parallel kinematic robots can be found in [8, 9].

For applications where humans are directly involved, like fitness devices or simulators for virtual environments, compliance plays a major role. The compliance can be reached by using pneumatic muscles as driving units instead of stiff electric servo drives. In this paper we present a parallel kinematic built as a Stewart platform with a movable upper platform and a fixed lower platform connected by six fluidic muscles, see [14] for details. The muscles can only pull on the platform, so a pre-stressed spring in the middle of the hexapod delivers the compressive forces. Figure 1 shows the design of the system under consideration. To move the platform in the 3D space some kinematical calculations are done. The inverse kinematical problem is easily evaluated by vector chains, while the forward kinematics is solved numerically. The Projection Equation [2] is used to derive a dynamical model of the hexapod. By inserting the trajectories with their time derivatives, the inverse dynamical model can be used to improve the behavior in the sense of a feed forward control. The feedback control is realized as cascaded structure consisting of a pressure control, linearization of the muscle behavior and a linear position control, see [4]. Some basic concepts for controlling fluid muscles can be found in [10]. Singh et al. [16] show the design and control of a single pneumatic actuator that also acts against a pre-stressed spring. An enhancement of the valve-actuator behavior is shown in [15]. Aschemann et al. [1] give a contribution to a flatness-based trajectory control of a pneumatically driven carriage. In [7] instead of static characteristic lines a dynamical model of the muscle is described improving the dynamical behavior of the system.

2 Design

As already mentioned the hexapod consists of a moving platform and a fixed base platform coupled by six fluidic muscles. The muscles run with a maximum pressure of 6 bar delivering forces up to 6000 N/muscle by a weight of 0.2 kg, see Figure 5 for the characteristic lines of the used muscles. The platform in Figure 1 has a height of 0.5 m by a diameter of 0.4 m. The weight is about 20 kg. Due to the construction, friction effects only occur in the ball bearings at the ends of the muscles and are therefore negligible. The muscle itself does not have any friction. The spring applying all compressive forces is from a passenger car with a stiffness in longitudinal direction of about 10^5 N/m. The desired trajectories can either be planned offline, or directly taken from a force feedback joystick with six degrees of freedom, built again as a Stewart platform. A detailed description for this joystick is given in [11].

Fig. 1 Photo of the system. The left side of the photo shows the joystick, while the right side is the pneumatically driven hexapod.

The electrical buildup is shown in Figure 2. All the control schemes are designed by using Matlab/Simulink. With the Real Time Workshop the control code is built for a Real Time Application Interface (RTAI) patched linux kernel, running on an embedded computer board with a 1 GHz processor. Phytec eNET-CAN Boards on the PC104 bus of the embedded system perform the CAN communication (1MBaud) to special designed analog–digital and digital–analog converters. These are directly connected to the joystick and the hexapod. The measured values are the lengths of each actuator by linear potentiometers and the pressure in the muscles. The actuating values are the voltages for the pressure sensitive valves.

3 Kinematics

For the kinematical and the dynamical model of the robot (in Sect. 4) the vector $\mathbf{q} = (x,\ y,\ z,\ \alpha,\ \beta,\ \gamma)^T$ (TCP coordinates) is used comprising the minimal coordinates. x, y, z are the coordinates of the TCP, while α, β, γ is a representation of the orientation in Cardan angles, see Eq. (2) for a definition of the rotation sequence. Figure 3 shows a truncated model of the system. In contrast to serial robots, the inverse kinematics is easy to solve, see [9]. The length of the ith leg m_i is equal to

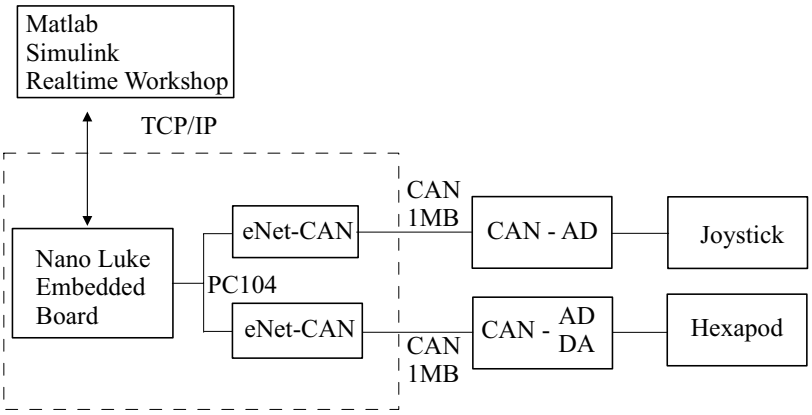

Fig. 2 Signals and electrical design.

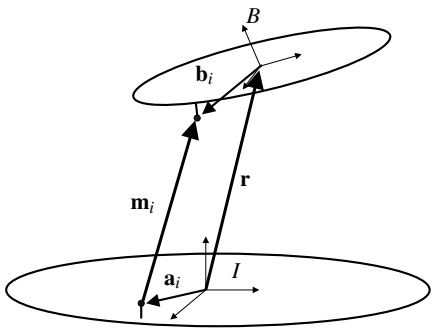

Fig. 3 Topology of a hexapod leg.

$$
\begin{aligned}
{}_I\mathbf{m}_i &= {}_I\mathbf{r} + \mathbf{A}_{IB}\,{}_B\mathbf{b} - {}_I\mathbf{a}_i, \\
m_i &= \sqrt{{}_I\mathbf{m}_i^T\ {}_I\mathbf{m}_i}
\end{aligned}
\tag{1}
$$

with the position $\mathbf{r}$ of the moving plate and the rotation matrix $\mathbf{A}_{IB}$ transforming coordinate system B to system I. By choosing Cardan angles as representation for the orientation for the moving plate, the rotation matrix is

$$
\mathbf{A}_{IB} = \mathbf{A}_{BI}^T = \left(\mathbf{A}_\gamma \mathbf{A}_\beta \mathbf{A}_\alpha\right)^T = \mathbf{A}_\alpha^T \mathbf{A}_\beta^T \mathbf{A}_\gamma^T \tag{2}
$$

where $\mathbf{A}_\alpha$ is an elementary rotation about the x axis, $\mathbf{A}_\beta$ about the y axis and $\mathbf{A}_\gamma$ about z, respectively.

In contrast to the inverse kinematics, the forward kinematics evaluates by given muscle lengths the position and orientation of the TCP. A satisfying analytical solution is not available. There are some approaches in [6] which are not usable in realtime computations. However, in this paper a numerical solution is chosen. A set of constraint equations $\boldsymbol{\phi}$ including the inverse kinematics,

$$
\phi = \left(\phi_1 \ \ldots \ \phi_6\right)^T, \quad \phi_i = m_i|_{\mathbf{q}^{(n)}} - m_{i,d} = 0, \quad i = 1, \ldots, 6,
$$

where $m_{i,d}$ is the desired length of muscle i leads to the Newton–Raphson iteration scheme [3]

$$\mathbf{q}^{(n+1)} = \mathbf{q}^{(n)} - \underbrace{\phi'\big|^{-1}_{\mathbf{q}^{(n)}}\ \phi|_{\mathbf{q}^{(n)}}}_{\delta^{(n)}} \tag{3}$$

with $\mathbf{q}^{(n)}$ the solution of the nth iteration, δ the Newton direction and $\boldsymbol{\phi}' = \partial\boldsymbol{\phi}/\partial\mathbf{q}$ is the appropriate Jacobian. Due to perfect starting points only two iterations per timestep are necessary for an adequate accuracy. To decrease the calculation time for Eq. (3) it is more efficient to evaluate $\boldsymbol{\delta}$ from

$$\phi'\big|_{\mathbf{q}^{(n)}}\,\delta^{(n)} = \phi|_{\mathbf{q}^{(n)}}$$

by solving this systems of equations iteratively, see [5] for details.

4 Dynamics

There are several methods for deriving the equations of motion. In this work, the projection equation – a synthetical method – is used. Linear momentum $\mathbf{p} = m\ \mathbf{v}_c$ and angular momentum $\mathbf{L} = \mathbf{J}\ \boldsymbol{\omega}_c$ are projected into the minimal space (minimal velocities $\dot{\mathbf{q}}$) via the appropriate Jacobians

$$\sum_{i=1}^{N}\left(\left(\frac{\partial_R\mathbf{v}_c}{\partial\dot{\mathbf{q}}}\right)^T\ \left(\frac{\partial_R\boldsymbol{\omega}_c}{\partial\dot{\mathbf{q}}}\right)^T\right)\begin{pmatrix}{}_R\dot{\mathbf{p}} + {}_R\tilde{\boldsymbol{\omega}}_{IR}\,{}_R\mathbf{p} - {}_R\mathbf{f}^e\\ {}_R\dot{\mathbf{L}} + {}_R\tilde{\boldsymbol{\omega}}_{IR}\,{}_R\mathbf{L} - {}_R\mathbf{M}^e\end{pmatrix}_i = \mathbf{Q}.$$

All the values like the translational velocity $\mathbf{v}_c$ or the rotational velocity of the center of gravity $\boldsymbol{\omega}_c$ can be inserted in arbitrary coordinate systems R. In contrast to $\boldsymbol{\omega}_c$, $\boldsymbol{\omega}_{IR}$ is the velocity of the used reference system. The matrix $\mathbf{J}$ is the inertial tensor, while $\tilde{\boldsymbol{\omega}}\,\mathbf{p}$ characterizes the vector product $\boldsymbol{\omega}\times\mathbf{p}$. $\mathbf{f^e}$ and $\mathbf{M^e}$ are imposed forces and moments acting on the ith body.

In the present case a body fixed reference system B is used for the description of the moving plate. The velocities in this system read

$${}_B\omega_c = {}_B\omega_{IB} = \left[\,\mathbf{A}_\gamma\mathbf{A}_\beta\mathbf{e}_1\ \mathbf{A}_\gamma\mathbf{e}_2\ \mathbf{e}_3\,\right]\begin{pmatrix}\dot{\alpha}\\ \dot{\beta}\\ \dot{\gamma}\end{pmatrix},$$

$${}_B\mathbf{v}_c = {}_B\dot{\mathbf{r}}_c + {}_B\tilde{\omega}_{IB}\,{}_B\mathbf{r}_c.$$

The weight of the muscles is about dimensions smaller than the moving plate and load, so it can be neglected. Special investigations have to be performed in the modeling of the muscles and the spring forces. The principle of virtual work reads

$$\delta W = \delta\mathbf{q}^T\mathbf{Q} = \sum\delta\,{}_I\mathbf{r}_i^T\,{}_I\mathbf{F}_i = \sum\delta\mathbf{q}^T\left(\frac{\partial_I\mathbf{r}_i}{\partial\mathbf{q}}\right)^T{}_I\mathbf{F}_i$$

with

$$ {}_I\mathbf{F}_i = F_i \frac{{}_I\mathbf{m}_i}{\| {}_I\mathbf{m}_i \|}. $$

F_i is the force of the ith muscle, while ${}_I\mathbf{m}_i / \| {}_I\mathbf{m}_i \|$ is the normalized direction, see Eq. (1). The spring for the compressive forces is included with the help of a potential $\mathbf{Q} = -(\partial V / \partial \mathbf{q})^T$, where the potential function V can be approximated by

$$ V = \frac{1}{2} c_{\text{trans},z} (z - l_0)^2 + \frac{1}{2} c_{\text{trans},xy} (x^2 + y^2 + \frac{1}{2} c_{\text{rot},\gamma} \gamma^2 + \frac{1}{2} c_{\text{rot},\alpha\beta} (\alpha^2 + \beta^2). $$

As can be seen in the potential function, there is a different stiffness in z ($c_{\text{trans},z}$) and x, y ($c_{\text{trans},xy}$) direction and in γ ($c_{\text{rot},\gamma}$) and α, β ($c_{\text{rot},\alpha\beta}$) direction. The values are evaluated by an identification process. l_0 is the length of the force free spring. The dynamical modeling process delivers the equations of motion in the form

$$ \mathbf{M}(\mathbf{q})\, \ddot{\mathbf{q}} + \mathbf{g}(\mathbf{q}, \dot{\mathbf{q}}) = \mathbf{B}(\mathbf{q})\mathbf{u}, \tag{4} $$

where $\mathbf{u} = (F_1 \ldots F_6)^T$ is the control input of the six muscle forces. $\mathbf{M}(\mathbf{q})$ is the mass matrix and $\mathbf{g}(\mathbf{q}, \dot{\mathbf{q}})$ contains all nonlinear effects like coriolis forces, gravitational forces and so on. To calculate the inverse dynamical model the equation of motion is solved for the forces $\mathbf{u}$ by premultiplying Eq. (4) with $\mathbf{B}^{-1}$. Due to the mechanical design, a singular position of the hexapod and therefore a singular matrix $\mathbf{B}$ is not possible.

5 Control

To test the performance of the robot on a test rig, an embedded system, running with a RTAI patched Linux kernel, is used to achieve the real time performance. A Nano Luke Board equipped with a 1 GHz processor fulfills the requirements to let all computations run in a sample time of 2 milliseconds. Matlab/Simulink is used to develop the overall software system whereas the computationally intensive functions are included as C code. Figure 4 shows the control concept in a schematic way for one leg.

The desired values in TCP coordinates can either be generated by a trajectory generator (offline) or by a joystick (online). The offline paths are needed for manipulation tasks, while the online ones are useful in the field of fitness where a trainer plans the motion. The TCP coordinates are via the inverse kinematics transformed to the desired lengths and a desired stroke h in % for each muscle is calculated,

$$ h_{d,i} = \frac{m_{d,i}}{m_0} 100\% $$

($m_0 \ldots$ total length of the muscles). A PID controller delivers in combination with the inverse dynamic model

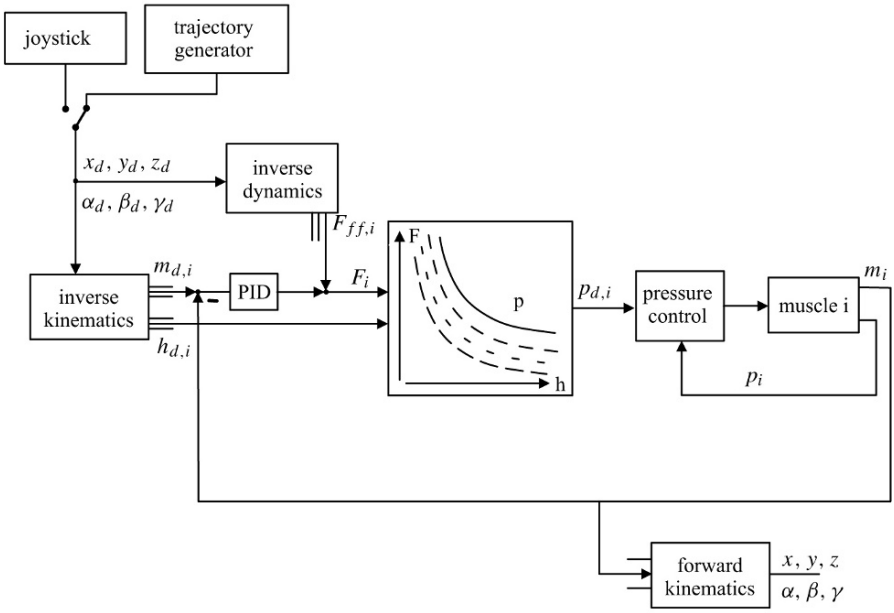

Fig. 4 Control concept.

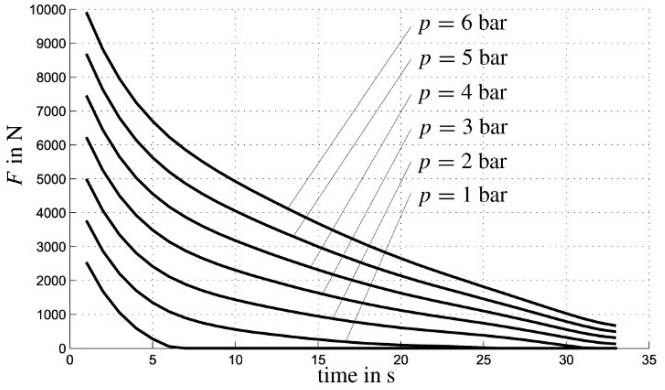

Fig. 5 Characteristic lines of a fluidic Festo muscle DMSP40.

$$\mathbf{F}_{ff} = \mathbf{B}(\mathbf{q}_d)^{-1}(\mathbf{M}(\mathbf{q}_d)\ddot{\mathbf{q}}_d + \mathbf{g}(\mathbf{q}_d, \dot{\mathbf{q}}_d))$$

the needed muscle force. The force–pressure–stroke relation of the muscles is represented by characteristic lines, see Figure 5, which can be approximated by a look up table to fulfill the requirement of low computational effort. The lines in Figure 5 are identified in a statical experimental process.

Assuming an input force F_i and the stroke $h_{d,i}$, the desired pressure $p_{d,i}$ is obtained as a direct result of this relation. A succeeding PID controller tracks the

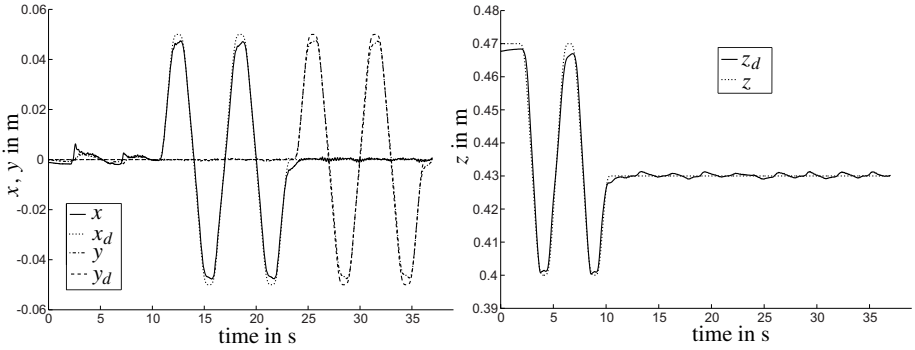

Fig. 6 Measured and desired TCP coordinates.

Fig. 7 Measured and desired length of muscle 1.

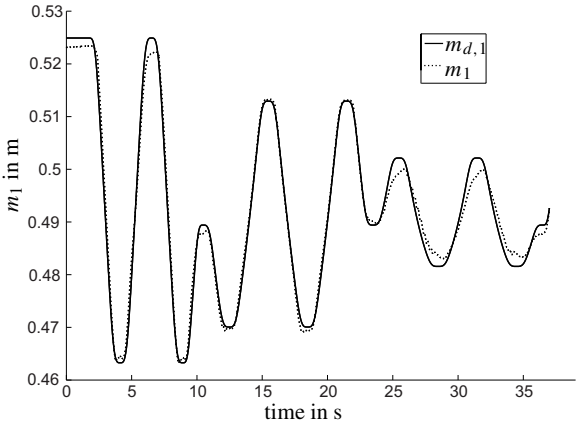

pressure of the ith muscle. The system is tested with desired trajectories shown in Figure 6. The maneuver is a fast movement in z-direction, followed by x and y movements for the TCP. There is a small control error due to limitations in the input variables of the pneumatic valves.

Figure 7 exemplarily shows the desired ($m_{d,1}$) and the measured (m_1) length of muscle 1. The behavior is satisfactory with respect to the required accuracy. The pressure control behavior for muscle 1 is shown in Figure 8.

6 Conclusions

In this paper we presented a new type of parallel mechanism using fluidic muscles as an innovative driving system. A main advantage is the simple design of the Stewart platform consisting of a moving plate, a fixed plate connected by six muscles and a pre-stressed spring. The six degrees of freedom ($x, y, z, \alpha, \beta, \gamma$) are interrelated to

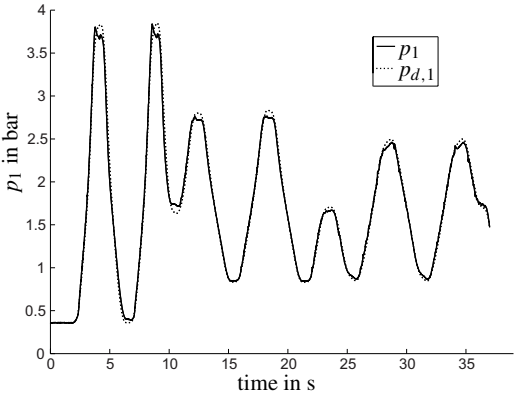

Fig. 8 Measured and desired pressure of muscle 1.

the lengths of the muscles $(m_1, \ldots, m_6)$ by kinematical computations. The inverse kinematical problem is easily solved by vector chains, while the forward kinematics is evaluated by a Newton iteration scheme. From a dynamical point of view, the system consists of nine bodies. A representation in minimal space, where constraint forces are faded out, is evaluated by the Projection Equation leading to a simulation model and an inverse dynamical model enhancing the control performance. Due to the high nonlinearities of the pneumatic muscles, a lot of work has to be done in the evaluation of the control concept. The shown cascaded scheme consisting of pressure control, linearization, model based feed forward control leads to a satisfying behavior. In the future investigations, observers to model the load (mass, center of gravity) have to be implemented.

Acknowledgements The authors gratefully acknowledge our industrial partner FerRobotics Compliant Robot Technology GmbH for their support during this project and the perfect co-operation.

References

1. Aschemann, H., Hofer, E.: Flatnessbased control of a carriage driven by pneumatic muscles. In *Proceedings of MMAR*, pp. 1219–1224 (2003).
2. Bremer, H.: *Dynamik und Regelung mechanischer Systeme*. Teubner Studienbücher, Stuttgart (1988).
3. Eich-Soellner, E., Führer, C.: *Numerical Methods in Multibody Dynamics*. Teubner, Stuttgart (1998).
4. Föllinger, O.: *Regelungstechnik – Einführung in die Methoden und ihre Anwendungen*. Hüthig Buch Verlag Heidelberg, Heidelberg (1996).
5. Hoffmann, A., Marx, B., Vogt, W.: *Mathematik für Ingenieure 1*. Pearson, München (2005).
6. Husty, M.: An algorithm for solving the direct kinematics of general stewart-gough platforms. *Mechanism and Maschine Theory* **31**(4), 365–379 (1996).
7. Kerscher, T., Albiez, J., Zöllner, J., Dillmann, R.: Evaluation of the dynamic model of fluidic muscles using quick-release. First IEEE/RAS-EMBS International Conference on Biomedical Robotics and Biomechatronics (2006).

8. Khalil, W., Dombre, E.: *Modeling, Identification and Control of Robots*. Kogan Page Science, London (2004).
9. Merlet, J.: *Parallel Robots*. Kluwer Academic Publishers, Dordrecht (2000).
10. Neumann, R., Bretz, C., Volzer, J.: Ein Positionierantrieb mit hoher Kraft: Positions- und Druckregelung eines künstlichen pneumatischen Muskels. 4. International Fluidtechnik Kolloquium (2004).
11. Ollmann, H.: *Modellierung, Konstruktion und Regelung einer 6-DOF Stewart Plattform*. JK University Linz, Linz (2006).
12. Riebe, S.: *Aktive Schwingungsisolierung und Bahnregelung von Hexapodsystemen*. VDI Verlag, Düsseldorf (2005).
13. Riebe, S., Ulbrich, H.: Stabilization and tracking control of a parallel kinematic with six degrees-of-freedom. 5th EUROMECH Solid Mechanics Conference (ESMC) (2003).
14. Schwandtner, J.: *Konstruktion, Modellierung und Regelung eines Hexapods mit Luftmuskel Aktuatorik*. JK University Linz, Linz (2007).
15. Singh, M.D., Liem, K., Kecskemethy, A., Neumann, R.: Design and control of a pneumatic hybrid actuator. In *PAMM Proceedings for Applied Mathematics and Mechanics*, pp. 497–498 (2005).
16. Singh, M.D., Liem, K., Neumann, R., Kecskemethy, A.: Modeling of a pneumatic hybrid actuator using an exponential approach for approximation of the valve-actuator behaviour. In *PAMM Proceedings for Applied Mathematics and Mechanics*, pp. 803–804 (2006).

Singularity-Consistent Torque Control of a Redundant Flexible-Base Manipulator

Naoyuki Hara, Yusuke Fukazu, Yoshikazu Kanamiya and Daisuke Sato

Abstract A path tracking control method for a kinematically redundant manipulator on a flexible base is proposed. The method is based on dynamic redundancy resolution through a vibration suppression constraint. It is shown that the end-effector path can pass via an algorithmic singularity without destabilizing the system. Simulation data from a planar system is presented, confirming that stable path tracking can be achieved within large portions of the manipulator workspace.

1 Introduction

Manipulators mounted on a flexible base have been studied widely in the past in view of two fields of applications mainly: nuclear waste cleanup [1, 2] and space robotics [3, 4]. In the former application, a manipulator is mounted on a long beam to ensure access to a remote site. In the latter application, the manipulator is mounted at the end of a large arm that allows for relocation of the manipulator base. Such systems are known as "macro-micro" manipulators. Examples include the Canadian SSRMS/Dextre and the Japanese JEMRMS/SFA manipulator systems on the International Space Station.

Flexible base mounted manipulators induce base vibrations via the reaction force. A few control methods have been proposed in the past that can ensure base vibration suppression control [5–8], design of control inputs that induce minimum vibrations [9], and end-point control in the presence of vibrations [10, 11].

Appropriate control methods depend very much on the structure of the manipulator, e.g. dual-arm or single-arm and the presence of kinematic and/or dynamic redundancy. In this work, we focus on a kinematically redundant flexible base manipulator. End-effector control in the presence of base vibrations becomes possible

Naoyuki Hara, Yusuke Fukazu, Yoshikazu Kanamiya and Daisuke Sato
Musashi Institute of Technology, Tokyo, Japan;
E-mail: c/o Yoshikazu Kanamiya (D.N. Nenchev): nenchev@ieee.org

H. Ulbrich and L. Ginzinger (eds.), Motion and Vibration Control, 103–112.

with such a manipulator. In addition, there is also a possibility for vibration suppression control via manipulator self-motion.

We should note, however, that redundancy resolution techniques usually suffer from the presence of algorithmic singularities [12]. In the case of a flexible base manipulator, algorithmic singularities are due to the imposed vibration suppression constraint, and are located inside the workspace. As noted in [13], it is physically impossible to realize vibration suppression at such manipulator configurations. The work of Hanson and Tolson demonstrates this fact [14]. Unfortunately, the importance of this problem has been usually underestimated in literature, even in recent studies [15].

We have addressed the problem of flexible base manipulator teleoperation control in the presence of both algorithmic and kinematic singularities in a recent work [16]. A velocity control framework has been designed, based on the Reaction Null-Space [17] and the Singularity-Consistent [18] methods, named Singularity-Consistent Vibration Suppression (SCVS) control. The aim was to achieve stable teleoperation control throughout the entire workspace.

The aim of the present work is twofold. First, we highlight a problem with the SCVS velocity controller related to the presence of algorithmic singularities due to the Reaction Null-Space constraint. Second, we develop a dynamic torque control framework and show how the algorithmic singularity problem can be tackled within such framework.

2 Background and Notation

The equation of motion of a manipulator mounted on a flexible base can be written in the following form [17]:

$$\begin{bmatrix} \boldsymbol{H}_b & \boldsymbol{H}_{bm} \\ \boldsymbol{H}_{bm}^T & \boldsymbol{H}_m \end{bmatrix} \begin{bmatrix} \dot{\boldsymbol{v}}_b \\ \ddot{\boldsymbol{q}} \end{bmatrix} + \begin{bmatrix} \boldsymbol{c}_b \\ \boldsymbol{c}_m \end{bmatrix} + \begin{bmatrix} \boldsymbol{D}_b \boldsymbol{v}_b \\ \boldsymbol{D}_m \dot{\boldsymbol{q}} \end{bmatrix} + \begin{bmatrix} \boldsymbol{K}_b \Delta\boldsymbol{\xi} \\ \boldsymbol{0} \end{bmatrix} = \begin{bmatrix} \boldsymbol{0} \\ \boldsymbol{\tau} \end{bmatrix} \tag{1}$$

where $\Delta\boldsymbol{\xi} \in \Re^k$ denotes the positional and orientational deflection of the base from its equilibrium, $\boldsymbol{v}_b$ is the twist (velocity/angular velocity) of the base, $\boldsymbol{q} \in \Re^n$ stands for the generalized coordinates of the arm, $\boldsymbol{H}_b(\boldsymbol{q}, \Delta\boldsymbol{\xi})$, $\boldsymbol{D}_b$, and $\boldsymbol{K}_b \in \Re^{k\times k}$ denote base inertia, damping and stiffness, respectively. $\boldsymbol{H}_m(\boldsymbol{q}) \in \Re^{n\times n}$ is the inertia matrix of the arm, $\boldsymbol{D}_m$ stands for joint damping and $\boldsymbol{H}_{bm}(\boldsymbol{q}, \Delta\boldsymbol{\xi}) \in \Re^{k\times n}$ denotes the so-called *inertia coupling matrix*. $\boldsymbol{c}_b(\boldsymbol{q}, \dot{\boldsymbol{q}}, \Delta\boldsymbol{\xi}, \boldsymbol{v}_b)$ and $\boldsymbol{c}_m(\boldsymbol{q}, \dot{\boldsymbol{q}}, \Delta\boldsymbol{\xi}, \boldsymbol{v}_b)$ are velocity-dependent nonlinear terms, and $\boldsymbol{\tau} \in \Re^n$ is the joint torque. No external forces are acting neither on the base nor on the manipulator.

Under the simplifying assumptions, described in [17], the equation of motion can be linearized around the equilibrium of the base, as follows:

$$\boldsymbol{H}_b \dot{\boldsymbol{v}}_b + \boldsymbol{D}_b \boldsymbol{v}_b + \boldsymbol{K}_b \Delta\boldsymbol{\xi} = -\boldsymbol{H}_{bm} \ddot{\boldsymbol{q}}. \tag{2}$$

Then, choose the control acceleration as

$$\ddot{\boldsymbol{q}}_c = \boldsymbol{H}_{bm}^{+}\boldsymbol{G}_b\boldsymbol{v}_b + (\boldsymbol{U} - \boldsymbol{H}_{bm}^{+}\boldsymbol{H}_{bm})\boldsymbol{\zeta}, \tag{3}$$

where $\boldsymbol{G}_b$ is a positive definite matrix, and $\boldsymbol{H}_{bm}^{+} \in \Re^{n\times k}$ denotes the Moore-Penrose generalized inverse of the inertia coupling matrix, $\boldsymbol{U}$ denotes the unit matrix of proper dimension, and $\boldsymbol{\zeta}$ is an arbitrary vector. Since $\boldsymbol{H}_{bm}\boldsymbol{H}_{bm}^{+} = \boldsymbol{U}$ and $\boldsymbol{H}_{bm}(\boldsymbol{U} - \boldsymbol{H}_{bm}^{+}\boldsymbol{H}_{bm}) = \boldsymbol{0}$, it becomes apparent that controlled damping can be achieved by a proper choice of matrix $\boldsymbol{G}_b$.

Note that the second term on the RHS of the above equation stands for the Reaction Null-Space. In [17], the term was used to ensure the desired end-effector motion constraint. In [16] it was shown that the desired end-effector motion can be realized without the Reaction Null-Space term.

We aim to control both end-tip motion and flexible base vibrations. Denote by $\boldsymbol{v}_e \in \Re^m$ the manipulator end-effector twist. Then we have:

$$\dot{\boldsymbol{v}}_e = \boldsymbol{J}\ddot{\boldsymbol{q}} + \dot{\boldsymbol{J}}\dot{\boldsymbol{q}} + \dot{\boldsymbol{v}}_b, \tag{4}$$

where $\boldsymbol{J}(\boldsymbol{q}) \in \Re^{m\times n}$ is the manipulator Jacobian.

3 Singularity-Consistent Redundancy Resolution with Vibration Suppression Capability

3.1 Redundancy Resolution via Additional Constraint

A well known method for resolving kinematic redundancy is to impose an additional constraint [12]. We derive such an additional constraint in terms of joint acceleration from the vibration suppression control acceleration (3):

$$\boldsymbol{H}_{bm}\ddot{\boldsymbol{q}} = \boldsymbol{G}_b\boldsymbol{v}_b. \tag{5}$$

Note that the Reaction Null-Space term has been thereby ignored.

Let us assume now that the dimension k of base deflection space equals the *degree of redundancy* of the manipulator, that is $k = n - m$. Combining the imposed end-effector acceleration constraint from (4) with the above additional constraint, we obtain:

$$\begin{bmatrix} \dot{\boldsymbol{v}}'_e \\ \boldsymbol{G}_b\boldsymbol{v}_b \end{bmatrix} = \boldsymbol{J}_{vs}\ddot{\boldsymbol{q}}, \tag{6}$$

where $\dot{\boldsymbol{v}}'_e = \dot{\boldsymbol{v}}_e - \dot{\boldsymbol{J}}\dot{\boldsymbol{q}} - \dot{\boldsymbol{v}}_b$, $\boldsymbol{J}_{vs} = \left[\boldsymbol{J}^T \ \boldsymbol{H}_{bm}^T\right]^T \in \Re^{n\times n}$. The joint acceleration can then be written as:

$$\ddot{\boldsymbol{q}} = \boldsymbol{J}_{vs}^{-1}\begin{bmatrix} \dot{\boldsymbol{v}}'_e \\ \boldsymbol{G}_b\boldsymbol{v}_b \end{bmatrix}. \tag{7}$$

Though the above solution was obtained in a straightforward manner, we must note that performance will inevitably degrade when matrix $\boldsymbol{J}_{vs}$ becomes singular. The condition $\det \boldsymbol{J}_{vs} = 0$ means that the linear system (6) becomes singular. When displayed in workspace, the singularities are mapped to both isolated points and continua. A well-known subclass of singularities are the kinematic singularities, defined by the condition $\det \boldsymbol{J}\boldsymbol{J}^T = 0$. For articulated manipulators, these appear mainly at the workspace boundaries. The rest of the singularities, referred to as "algorithmic singularities," are located within the workspace, though. Since the additional constraint used here is the vibration suppression constraint, we can expect that the capability to suppress vibrations will deteriorate around these algorithmic singularities [13]. In addition, the system may destabilize. This hinders the task planning problem significantly.

3.2 Singularity-Consistent Solution for the Acceleration

To cope with the singularity problem, we will rewrite the above joint acceleration (7) according to the Singularity-Consistent method [18]. First, we compose the column-augmented Jacobian and the respective homogeneous equation:

$$\bar{\boldsymbol{J}}_{vs}\ddot{\bar{\boldsymbol{q}}} = \boldsymbol{0}, \tag{8}$$

where

$$\bar{\boldsymbol{J}}_{vs} = \begin{bmatrix} \boldsymbol{J} & -\dot{\boldsymbol{v}}'_e & \boldsymbol{0} \\ \boldsymbol{H}_{bm} & \boldsymbol{0} & -\boldsymbol{G}_b\boldsymbol{v}_b \end{bmatrix} \in \Re^{n\times(n+2)} \tag{9}$$

and

$$\ddot{\bar{\boldsymbol{q}}} = \begin{bmatrix} \ddot{\boldsymbol{q}}^T & 1 & 1 \end{bmatrix}^T. \tag{10}$$

Next, we write the set of solutions to the above homogeneous equation as follows:

$$\ddot{\bar{\boldsymbol{q}}} = \bar{\boldsymbol{N}}_{vs}\boldsymbol{b}_{vs}, \tag{11}$$

where $\bar{\boldsymbol{N}}_{vs} = \begin{bmatrix} \bar{\boldsymbol{n}}_m & \bar{\boldsymbol{n}}_b \end{bmatrix} \in \Re^{(n+2)\times 2}$. The two column vectors of $\bar{\boldsymbol{N}}_{vs}$ are: $\bar{\boldsymbol{n}}_m = \begin{bmatrix} \boldsymbol{n}_m^T & \det \boldsymbol{J}_{vs} & 0 \end{bmatrix}^T$ and $\bar{\boldsymbol{n}}_b = \begin{bmatrix} \boldsymbol{n}_b^T & 0 & \det \boldsymbol{J}_{vs} \end{bmatrix}^T$, and $\boldsymbol{b}_{vs} = \begin{bmatrix} b_m & b_b \end{bmatrix}^T$ is a vector with arbitrary components. The last equation can be expanded as:

$$\ddot{\boldsymbol{q}} = b_m\boldsymbol{n}_m(\boldsymbol{q}, \dot{\boldsymbol{v}}'_e) + b_b\boldsymbol{n}_b(\boldsymbol{q}, \boldsymbol{v}_b) \tag{12}$$

$$-1 = b_m \det \boldsymbol{J}_{vs} \tag{13}$$

$$1 = b_b \det \boldsymbol{J}_{vs}. \tag{14}$$

$\boldsymbol{n}_m(\boldsymbol{q}, \dot{\boldsymbol{v}}'_e)$ denotes a vector field component that ensures *reactionless motion* along the desired end-effector trajectory. The $\boldsymbol{n}_b(\boldsymbol{q}, \boldsymbol{v}_b)$ vector field component, on the other hand, ensures vibration suppression.

It is easy to show that if the two arbitrary scalars b_m and b_b are determined from the last two equations, respectively, and substituted into (12), then the joint acceleration obtained will be the same as that in (7), and hence, the system may destabilize around singularities.

One possible way to deal with such problem is by proper choice of b_m and b_b. This is the essence of the Singularity-Consistent method. We sacrifice thereby performance in terms of end-effector acceleration along the desired path and in terms of vibration suppression capability, but gain overall stability.

We should note also an important property of the above solution: the $b_m \boldsymbol{n}_m$ component restricts the manipulator motion in a conservative way due to the Reaction Null-Space constraint $\boldsymbol{H}_{bm}\ddot{\boldsymbol{q}} = \boldsymbol{0}$.[1] The algorithmic singularities appear as a consequence of this constraint. The CoM should not be restricted to move in such conservative way, because inevitably an algorithmic singularity will be reached [16].

4 Pseudoinverse-Based Solution

To relax the constraint on the CoM motion, we will employ a Moore–Penrose generalized inverse (pseudoinverse)-based acceleration component for the end-effector motion. Recall that the general solution for the joint acceleration can be written as [12]:

$$\ddot{\boldsymbol{q}} = \boldsymbol{J}^{+}\left(\dot{\boldsymbol{v}} - \dot{\boldsymbol{J}}\dot{\boldsymbol{q}}\right) + (\boldsymbol{U} - \boldsymbol{J}^{+}\boldsymbol{J})\boldsymbol{\zeta}_a, \tag{15}$$

where $\boldsymbol{\zeta}_a$ is an arbitrary $n-$vector. We can then replace $b_m \boldsymbol{n}_m$ in (12), to obtain:

$$\ddot{\boldsymbol{q}} = \boldsymbol{J}^{+}\left(\dot{\boldsymbol{v}} - \dot{\boldsymbol{J}}\dot{\boldsymbol{q}} - \dot{\boldsymbol{v}}_b\right) + b_b \boldsymbol{n}_b(\boldsymbol{q}, \boldsymbol{v}_b). \tag{16}$$

When analyzing the above equation, recall that the set of joint accelerations $\ddot{\boldsymbol{q}}_n = b_b \boldsymbol{n}_b$ satisfies the two constraints: $\boldsymbol{J}\ddot{\boldsymbol{q}}_n = \boldsymbol{0}$ and $\boldsymbol{H}_{bm}\ddot{\boldsymbol{q}}_n = \boldsymbol{G}_b \boldsymbol{v}_b$. The former constraint means that vector $\boldsymbol{n}_b$ belongs to the null space of the Jacobian: $\boldsymbol{n}_b \in \mathcal{N}(\boldsymbol{J}_{vs})$. Hence, from a well known property of the pseudoinverse-based inverse kinematics solution for kinematically redundant manipulators, it can be concluded that the two components of the above joint acceleration are orthogonal [12]. Thus, their mutual interference will be minimized, and we can expect that the vibration suppression constraint will be enforced constantly during end-effector motion, without disturbing it.

[1] We should note that $\boldsymbol{n}_m$ is derived as the null-space vector of a matrix obtained from $\bar{\boldsymbol{J}}_{vs}$ by removing its last column.

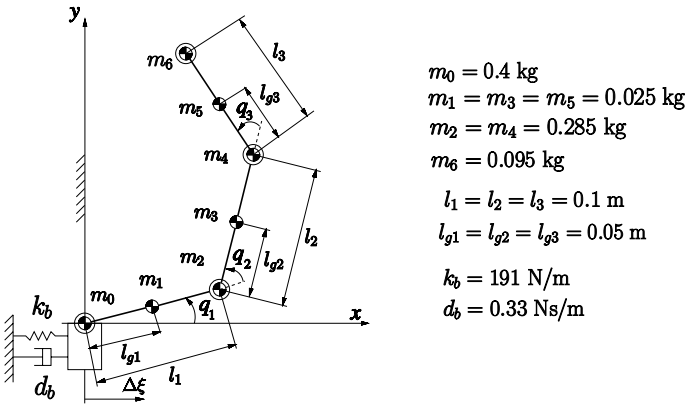

Fig. 1 A planar 3R manipulator on a flexible base.

5 Implementation of the Method

We will demonstrate the method with the help of the planar 3R manipulator shown in Figure 1. The base deflects along the x axis. Hence, the reaction moment and the reaction force component along the y axis can be neglected as a disturbance. We have: $n = 3,\ k = 1$. The parameters of the manipulator are shown in the figure.

End-tip path tracking control (meaning that $m = 2$) is envisioned according to the following control law:

$$\dot{\boldsymbol{v}}_{ref} = \ddot{\boldsymbol{p}}_d + \boldsymbol{K}_v(\dot{\boldsymbol{p}}_d - \dot{\boldsymbol{p}}) + \boldsymbol{K}_p(\boldsymbol{p}_d - \boldsymbol{p}). \tag{17}$$

$\boldsymbol{p}$ and $\boldsymbol{v} \equiv \dot{\boldsymbol{p}}$ denote end-tip position and velocity, respectively. The subscript $(\circ)_d$ denotes a desired quantity, $\boldsymbol{K}_v$ and $\boldsymbol{K}_p$ are positive definite feedback gain matrices.

Using (16), the reference joint acceleration is written as

$$\ddot{\boldsymbol{q}}_{ref} = \boldsymbol{J}^{+}\left(\dot{\boldsymbol{v}}_{ref} - \dot{\boldsymbol{J}}\dot{\boldsymbol{q}} - \dot{\boldsymbol{v}}_b\right) + b_b\tilde{\boldsymbol{n}}_b g_b v_{bx}, \tag{18}$$

where $\boldsymbol{v}_b = [v_{bx},\ 0]^T$ is the base velocity vector, g_b is the vibration suppression gain and $\boldsymbol{n}_b = \tilde{\boldsymbol{n}}_b g_b v_{bx}$.

Further on, the joint torque vector can be written as

$$\boldsymbol{\tau} = \boldsymbol{H}_m(\boldsymbol{q})\ddot{\boldsymbol{q}} + \boldsymbol{h}_{bm}^T(\boldsymbol{q})\dot{v}_{bx} + \boldsymbol{D}_m\dot{\boldsymbol{q}} + \boldsymbol{c}_m(\boldsymbol{q}, \dot{\boldsymbol{q}}), \tag{19}$$

according to the equation of motion. The joint damping term plays the important role of damping out the momentum, conserved during vibration suppression [17].

Next, insert the reference joint acceleration (18) into the last equation, to obtain the control torque as:

$$\boldsymbol{\tau}_c = \boldsymbol{H}_m \boldsymbol{J}^+ \left(\dot{\boldsymbol{v}}_{ref} - \dot{\boldsymbol{J}} \dot{\boldsymbol{q}} - \dot{\boldsymbol{v}}_b \right) + \boldsymbol{D}_m \dot{\boldsymbol{q}} + \boldsymbol{c}_m + \boldsymbol{h}_{bm}^T \dot{v}_{bx} + b_b \boldsymbol{H}_m \tilde{\boldsymbol{n}}_b g_b v_{bx} . \quad (20)$$

6 Simulation Results

Starting from initial configuration $q_1 = 0.0$, $q_2 = q_3 = 0.5$ rad (nonsingular), the manipulator end-tip is required to track a straight-line path parallel to the x axis. The desired current end-tip position, speed and acceleration along the straight-line are calculated from a fifth-order spline function. During this motion, the CoM accelerates/decelerates along the low-stiffness (x axis) direction. Hence, vibrations are induced, that are then to be suppressed by the vibration suppression component (the last term on the r.h.s. in (20)). We should also note that an algorithmic singularity will be encountered along the path.

In the first simulation, the final time for the spline function is set to 9 s. The vibration suppression gain is $g_b = 30$ kgs^{-1}, the feedback gain matrices are $K_p = \text{diag}\ [20000,\ 20000]\ \text{s}^{-2}$ and $K_v = \text{diag}\ [200,\ 200]\ \text{s}^{-1}$. Joint damping is set to $\boldsymbol{D}_m = \text{diag}\ [0.05,\ 0.05,\ 0.05]$ kgms^{-1}. The vibration suppression scalar b_b is determined from $b_b = 1/\det \boldsymbol{J}_{vs}$. In the neighborhood of the algorithmic singularity, vibration suppression is turned off (by setting $b_b = 0$) to avoid destabilization. The neighborhood is determined by a threshold, selected as $|b_b| = 1.0 \times 10^4$ m^{-2}s^{-2}.

The results from the simulation are shown in Figure 2. It becomes apparent that vibration is successfully suppressed during the motion. At around 5 s, the algorithmic singularity is crossed. From Figure 2(c) it can be observed that CoM acceleration increases around the singularity. Nevertheless, no significant base deflection is observed, and the end-tip error remains within acceptable limits.

In the next simulation, we shortened the execution time of the same path, from 9 s to 3 s, reading to higher overall velocities/accelerations (see Figure 3). The base deflects significantly around the algorithmic singularity. In addition, large peak velocities are observed and the system tends to destabilize. After passing the singularity, vibration suppression is invoked again, further vibrations are suppressed and the system stabilizes.

7 Conclusions

We have developed a path tracking control method for a kinematically redundant flexible base manipulator, capable of simultaneous vibration suppression, based on dynamic redundancy resolution. The effect achieved is similar to that of reactionless path motion control. In addition, we have shown that it is possible to cross an algorithmic singularity without destabilizing the system, despite using high PD-feedback gains.

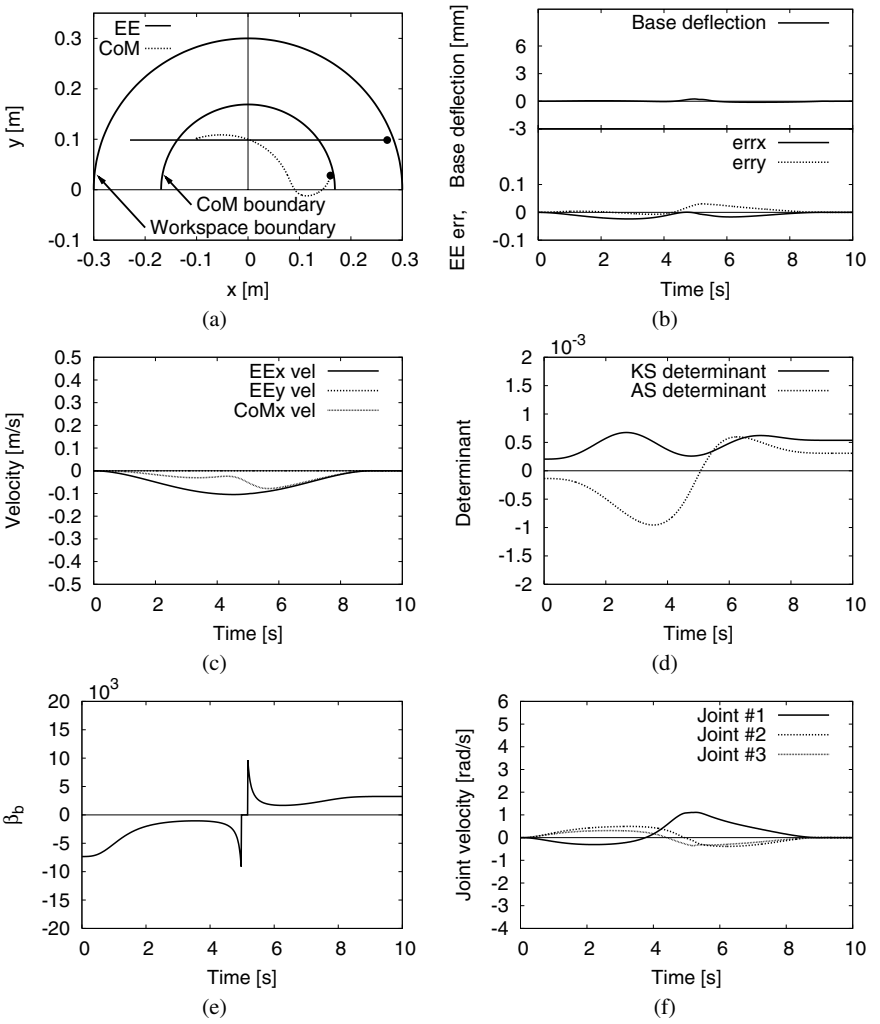

Fig. 2 Straight-line tracking and vibration suppression in case of a relatively slow movement.

Unfortunately, with faster movements, the base may deflect locally, around the singularity, since vibration suppression is switched off for a short time to avoid destabilization. We intend to tackle this problem in a future work by proper end-tip speed/acceleration replanting.

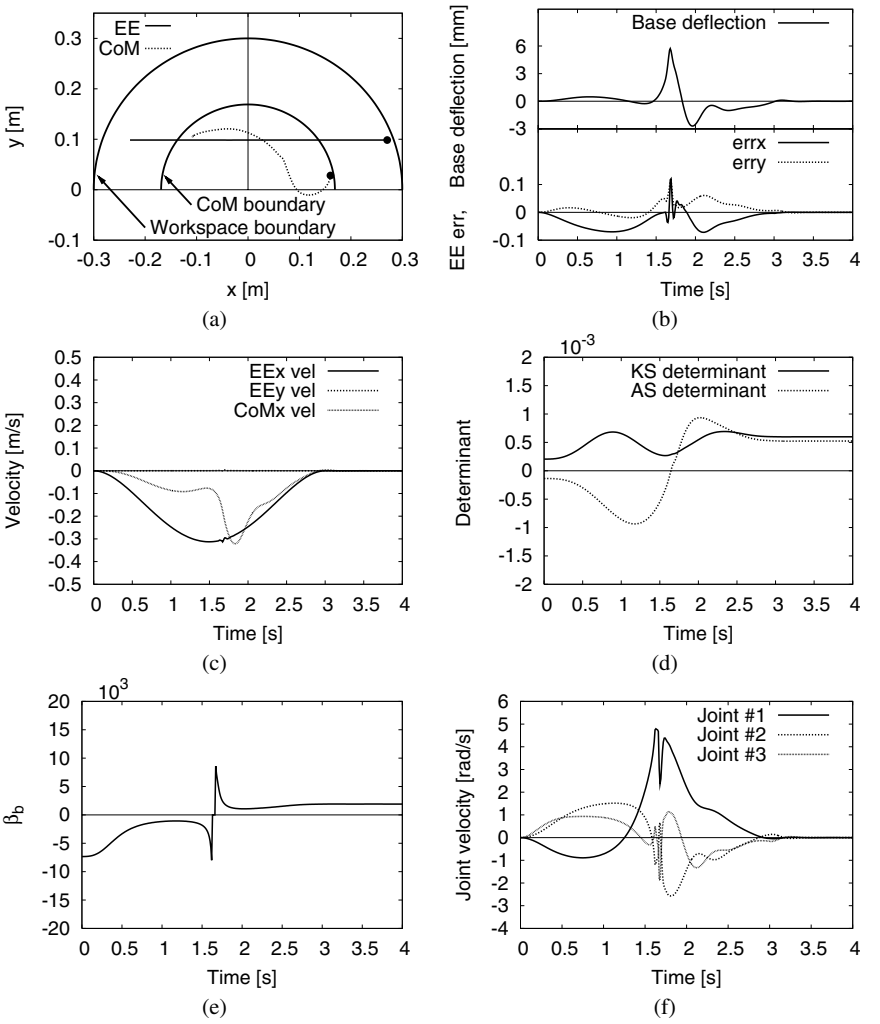

Fig. 3 Straight-line tracking and vibration suppression in case of a relatively fast movement.

References

1. Jansen, J. F., et al.: Long-reach manipulation for waste storage tank remediation. *ASME J.*, **31**, 67–73 (1991).
2. Kwon, D. S., et. al.: Input shaping filter methods for the control of structurally flexible, long-reach manipulators. In *Proc. IEEE Int. Conf. Robot. Automat.*, San Diego, CA, pp. 3259–3264 (1994).
3. Torres, M. A. and Dubowsky, S.: Path-planning in elastically constrained space manipulator systems. In *Proc. IEEE Int. Conf. Robot. Automat.*, Atlanta, GA, pp. 812–817 (1993).

4. Vallancourt, C. and Gosselin, C. M.: Compensating for the structural flexibility of the SSRMS with the SPDM. In *Proc. 2nd Workshop Robot. Space, Canadian Space Agency*, Montreal, PQ, Canada (1994).
5. Lee, S. H. and Book, W. J.: Robot vibration control using inertial damping forces. In *Proc. 8th CISM. IFToMM Symp. RoManSy 8*, Cracow, Poland, pp. 252–259 (1990).
6. Torres, M. A., Dubowsky, S. and Pisoni, A. C.: Vibration control of deployment structures' long-reach manipulators: The P-PED method. In *Proc. 1996 IEEE Int. Conf. Robot. Automat.*, Minneapolis, MN, pp. 2498–2504 (1996).
7. Lew, J. Y. and Trudnowski, D. J.: Vibration control of a micro/macro manipulator system. *IEEE Contr. Syst. Mag.*, **16**(1), 26–31 (1996).
8. Sharf, I.: Active damping of a large flexible manipulator with a shortreach robot. *Trans. ASME, J. Dyn. Syst., Meas. Contr.*, **118**, 704–713 (1996).
9. Cannon, D. W., et al.: Experimental study on micro/macro manipulator vibration control. In *Proc. IEEE Int. Conf. Robot. Automat.* , Minneapolis, MN, pp. 2549–2554 (1996).
10. Cannon, R. H., Schmitz, Jr. and E.: Initial experiments on the end-point control of a flexible one-link robot. *Int. J. Robotics Res.*, **3**(3), 62–75 (1984).
11. Mavroidis, C., Dubowsky, S. and Raju, V.: End-point control of long reach manipulator systems. In *Proc. 9th World Congr. IFToMM*, Milano, Italy, pp. 1740–1744 (1995).
12. Nenchev, D. N.: Redundancy resolution through local optimization: A review. *J. Robotic Systems*, **6**(6), 769–798 (1989).
13. George, L. E. and Book, W. J.: Inertial vibration damping control of a flexible base manipulator. *IEEE/ASME Trans. on Mechatronics*, **8**(2), 268–271 (2003).
14. Hanson, M. L. and Tolson, R. H,: Reducing flexible base vibrations through local redundancy resolution. *J. Robotic Systems*, **12**(11), 767–779 (1995).
15. Parsa, K., Angeles, J. and Misra, A. K.: Control of macro-micro manipulators revisited. *J. Dyn. Syst., Meas. Contr.*, **127**(4), 688–699 (2005).
16. Hishinuma, T. and Nenchev, D. N.: Singularity-consistent vibration suppression control with a redundant manipulator mounted on a flexible base. In *Proc. of the IEEE/RSJ Int. Conf. on Intelligent Robots and Systems*, Beijing, China, pp. 3237–3242 (2006).
17. Nenchev, D. N., et. al.: Reaction Null-Space control of flexible structure mounted manipulator systems. *IEEE Trans. on Robotics and Automation*, **15**(6), 1011–1023 (1999).
18. Nenchev, D. N., Tsumaki,Y. and Uchiyama, M.: Singularity-consistent parameterization of robot motion and control. *Int. J. Robotics Res.*, **19**(2), 159–182 (2000).

Semi-Active Control of a Targeted Mode of Smart Structures Submitted to Multimodal Excitation

S. Harari, C. Richard and L. Gaudiller

Abstract Active control of smart structures equipped with piezoelectric elements has shown its efficiency for two decades now. However, the electric power required by amplifiers for driving actuators appeared to be a severe limitation to the development of these techniques. In order to reduce this power requirement, semi-passive techniques developments such as Synchronized Switch Damping control were carried out. These ultra-low power techniques perform very well for monomodal excitation but their performances are limited in the case of multi-modal or complex vibrations. This paper deals with the implementation of an enhanced semi-active technique using methods developed for active control. A new multimodal control technique is proposed. It is based on SSD-Inductance semi-active technique. A Luenberger observer separates the modal variables from the voltage of the piezoelectric sensors. Then, the SSDI control can be targeted separately on each mode to control the vibration. This technique does not need operative power supply. An application of the proposed method on a clamped-free smart beam is proposed. Modal dampings of the controlled smart structure are first of all predicted by simulations. Then experimental results validate the proposed principle. Results obtained show the efficiency of the method and demonstrate its capabilities to control different modes on a broad frequency range.

S. Harari
LaMCoS, INSA-Lyon, CNRS UMR5259, F-69621 Lyon, France
LGEF, INSA-Lyon, F-69621 Lyon, France; E-mail: stephanie.harari@insa-lyon.fr

C. Richard
LGEF, INSA-Lyon, F-69621 Lyon, France; E-mail: claude.richard@insa-lyon.fr

L. Gaudiller
LaMCoS, INSA-Lyon, CNRS UMR5259, F-69621 Lyon, France;
E-mail: luc.gaudiller@insa-lyon.fr

H. Ulbrich and L. Ginzinger (eds.), Motion and Vibration Control, 113–122.

1 Introduction

The use of piezoelectricity is now well established for controlling structure. The high integrability of piezoelectric elements, their compactness, light-weight and their high bandwidth make them well suited to be used as actuators and sensors in smart structures.

Therefore smart structures are often used in active control. The two main limitations of this method are that it requires external power sources to allow energy exchanges between the actuators and the structure and that a large number of components are often necessary. However among active control technique, the modal method shows good performance for controlling some vibration modes with a minimum of components [3] and for concentrating energy on targeted modes. Gaudiller et al. showed that modal control is well adapted for reducing operative energy by using nonlinear modal control algorithms [4], for removing restored potential energy [9], while being adapted to complex smart structures via modal adaptive algorithm [2].

As an alternative to active control, passive control has been proposed. The method consists in connecting the piezoelectric element to a specific electrical passive network, which dissipates mechanical energy. This method is interesting because it does not require operating energy as in active control [6] but its efficiency must be reinforced.

In order to increase damping performance of passive techniques, semi-active control strategies have been developed. It consists of modify the electric boundary conditions of the piezoelectric elements synchronously with the structure motion. It is a reliable and stable way of controlling structures that is a great advantage compared with active control. Several methods have been investigated for semi-active vibration damping and energy reclamation using piezoelectric elements. This method based on nonlinear treatment demonstrated an intermediate performance between active and passive control; however, in the case of complex excitation, the damping obtained by semi-active techniques is less important. Several methods have been investigated to bypass this drawback. Corr and Clark [1] proposed a method by using numerical filtering techniques in order to target specific modes. The use of filters inevitably involves phase shifts, which leads to a loss of efficiency. A State-Switched Absorber (SSA) is used by Holdhusen and Cunefare [7] in case of multimodal disturbance. Synchronised Switch Damping (SSD) techniques [10] which are implemented in this paper consist of leaving the piezoelectric elements in open circuit except during a very brief period of time when the electric charge is either suppressed, in a short circuit or inverted with a resonant network. Richard et al. [11] showed that for a harmonic regime, optimal switching should occur on each extremum of the voltage of the piezoelectric element strain that is not true any more in the case of multimode excitation. Therefore statistical analysis to define optimization moments for the switching sequence was proposed in order to maximize the extracted energy and vibration damping [5, 12]. The main limitations are related in the case of complex or random excitation where the synchronization on the strain extremum is not trivial.

The proposed method is based on a modal approach using semi-active and active techniques. The method based on modal separation is presented on the first section. The second section describes the application on a free-clamped beam equipped with piezoelectric elements. The finite element model used for simulation is detailed and results are presented. The experimental set-up, the identification and then the results are described.

2 Principle

The aim of the method presented is to control a targeted mode of the structure under multimodal excitation.

2.1 Multimodal Smart Structure Modelling

When using classical hypothesis of structural modeling, and using finite element modeling, the dynamic behaviour of a smart structure can be described as:

$$m\ddot{\delta} + c\dot{\delta} + k^E\delta = -\alpha V \tag{1}$$

where δ is the displacement vector, m, c and k^E are respectively the mass, damping and stiffness matrices when the actuator is in short circuit, α is the electromechanical coupling vector and V is the actuator voltage.

The electric equation can be described by:

$$I = \alpha\dot{\delta} - C_0\dot{V} \tag{2}$$

where I is the current outgoing and C_0 the piezo element capacity.

The previous equations can be written in a modal basis ϕ after the following change of variables:

$$\delta = \phi q \tag{3}$$

where ϕ is the mode shape matrix and q the modal displacement vector.

In modal coordinates, Eqs. (1) and (2) become:

$$M\ddot{q} + C\dot{q} + K^E q = -\theta V \tag{4}$$

$$I = \theta^t\dot{q} - C_0\dot{V} \tag{5}$$

with M, C, K^E respectively the mass, damping and stiffness modal matrices and θ the modal electromechanical coupling vector defined by:

$$\theta = \phi^t\alpha \tag{6}$$

The norm of ϕ is chosen such that:

$$\phi^t M \phi = Id \tag{7}$$

Then:

$$K^E = diag((\omega^E)^2), \qquad C = 2diag(\xi)diag(\omega^D) \tag{8}$$

where ξ is the modal damping vector, ω^E and ω^D the frequency vectors when the actuator is in short circuit and in open circuit respectively.

The modal coupling coefficients k_{ij} of the structure are defined for the mode j and the piezoelectric element i as:

$$k_{ij} = \frac{(\omega_j^D)^2 - (\omega_{ij}^E)^2}{(\omega_j^D)^2} \tag{9}$$

2.2 Strategy for Complex Excitation

The proposed control is based on the SSDI technique (Synchronized Switch Damping on Inductor) which consists of adding a device in parallel with the piezoelectric element as shown in Figure 1a. The device is composed of a switch and an inductance L connected in series. The switch is almost always open, except when a voltage extremum occurs. At this moment, the switch is closed, until the voltage on the piezoelectric element has been reversed (Figure 1b). The inversion is possible thanks to the capacitance C_0 of the piezoelectric element and the inductance which constitutes an oscillator network. The inversion time corresponds to a half period of the oscillating circuit (Figure 1c). The voltage inversion is not perfect, because a part of the energy stored on the piezoelectric element capacitance is lost mainly in the inductance. This technique is fully described in [10].

When the structure is excited by a wide bandwidth excitation, many extrema appear on the voltage, which correspond to the modes of the structure excited. So the previous SSDI control strategy, which consists of inverting the voltage on each voltage extremum is not optimal. In order to obtain better performance, the idea of the method proposed here is to reverse the actuator voltage when the modal displacement of the targeted mode is extremum as depicted on Figure 1b for the q_1 modal variable. This inversion is then possible if the modal displacement is computed.

This modal displacement q_i can not be directly carried out by the sensors measurement. Several methods can be used to obtain the modal displacement. The technique used here is based on an observer [8]. The observer estimates the sensor voltage $\widehat{V_s}$ from the modal control signal, from the sensor measurements V_s and thanks to the model. The modal displacement q_i is then estimated and carried out by the internal closed loop observer due to the convergence between the voltage sensors measured V_s and the voltage sensors estimation $\widehat{V_s}$. The observer can be adjusted in order to eliminate quickly the estimation error.

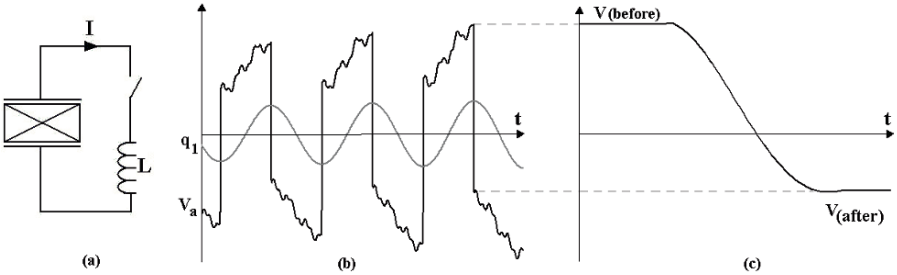

Fig. 1 (a) The SSDI circuit, (b) The voltage typical waveforms, where V_a is the piezoelectric actuator voltage and q_1 is the corresponding first modal displacement and (c) the voltage inversion.

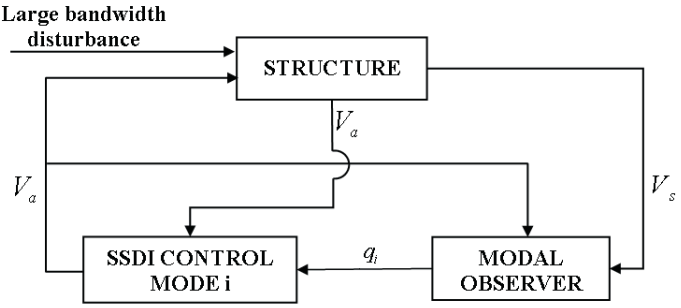

Fig. 2 Strategy of SSDI mulitmodal control.

The main limitation of this method is that it requires a modal model of the smart structure including both actuator and sensors. However, the parameters of the model can be identified accurately with an appropriate method. Moreover, the number of modes taken into account by the observer can be limited by the number of controlled modes.

3 Application

The method is applied on a clamped-free beam in spring steal (XC80) with three P188 piezoelectric inserts which are bonded on the beam with Araldite D epoxy resin. One is the actuator and two others are used as sensors. The method will be applied in order to control selectively the first mode, then the second mode of the structure. The placement of the sensors and the actuator are therefore optimized in order to obtain a large modal coupling coefficients k_1 and k_2 on the two first modes ($k_1, k_2 \cong 10\%$). The characteristics of the smart structure is given in Table 1.

Table 1 Smart beam characteristics.

Beam density	$\rho = 7800$ Kg.m^{-3}	Beam width	$b = 2.0 \times 10^{-2}$ m
Ceramic density	$\rho_c = 7700$ Kg.m^{-3}	Beam height	$h = 1.0 \times 10^{-3}$ m
Beam Young modulus	$E = 2.2 \times 10^{11}$ Pa	Beam length	$l = 3.0 \times 10^{-1}$ m
Permittivity component	$\epsilon_{11}^S = 12.75 \times 10^{-9}$ F/m	Actuator position	$x_A = 1.0 \times 10^{-3}$ m
	$\epsilon_{33}^S = 7.411 \times 10^{-9}$ F/m	Sensor 1 position	$x_{S1} = 1.3 \times 10^{-1}$ m
		Sensor 2 position	$x_{S2} = 1.7 \times 10^{-1}$ m
Elastic compliance	$S_{11}^E = 15.44 \times 10^{12}$ m^2/N	Actuator length	$l_A = 5 \times 10^{-2}$ m
constant	$S_{33}^E = 20.09 \times 10^{12}$ m^2/N	Sensors lengths	$l_s = 2.5 \times 10^{-2}$ m
Piezoelectricity contents	$d_{31} = -186$ pC.N^{-1}	Ceramic width	$b_C = b = 2.0 \times 10^{-2}$ m
	$d_{33} = 425$ pC.N^{-1}	Ceramic height	$h_C = 4.0 \times 10^{-4}$ m

3.1 Simulation

The simulated control (Figure 2) uses equations (4) and (5) and the modal characteristics are computed by a FE code. The vector of measurement V_s is introduced in the modal observer. The estimate modal displacement $\hat{q}_i$, obtained by the observer, allows to determine the optimal moment for the voltage inversion.

The characteristics of the equations of the smart structure are determined using a finite element model. The smart structure is modelled with the ANSYS FE code. The beam is modelled by using Solid45, eight node volume elements, with three degrees of freedom per node. The solid5 elements are used to model piezoelectric actuators and sensors. They are eight node elements with four degrees of freedom per node: three displacements and the electric potential. A mesh with 9,000 elements allows to obtain the modal model of the smart structure with a good accuracy.

The simulations are performed using the Matlab/Simulink^{TM} software environment. The observer uses the previous model of the smart structure until 1200 Hz. The structure is excited by a ten Volt pulse during 0.3 ms applied on the actuator. The observer gains are chosen in such a way that the system is stable and rapid compared to the dynamic of the controlled structure, without observer. The inductance is selected in order to minimize the losses in the SSDI device.

Two simulations are realized: successively, the first mode is controlled and then the second mode is controlled. The frequency responses are carried out via a FFT. Voltage on sensor 1 is used as a monitoring of the structure motion. Figures 3 and 4 compare this voltage in the controlled and non controlled cases. Simulations anticipate an attenuation of 18.73 dB on the first mode and 27.05 dB on the second mode. Frequency response comparison shows that no residual mode is excited. Vibration damping appears to be performant on the targeted mode.

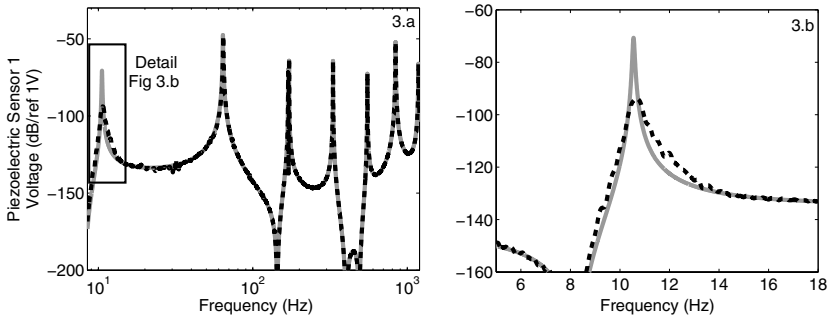

Fig. 3 Simulated frequency response on the first sensor when the smart stucture is uncontrolled (grey line) and when the first mode is controlled (black dotted line).

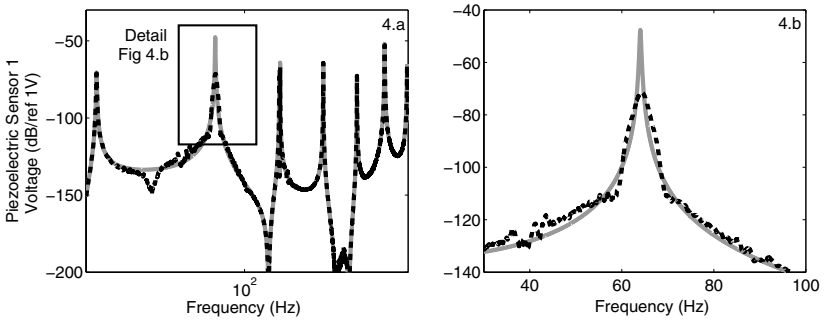

Fig. 4 Simulated frequency response on the first sensor when the smart stucture is uncontrolled (grey line) and when the second mode is controlled (black dotted line).

3.2 Experimentation

The proposed control strategy is implemented using a dSPACE DSP board DS-1104 and the programming and implementation are done using the Matlab/Simulink^{TM} software environment. The experimental set-up is presented in Figure 5.

Thanks to the two sensors voltages, the modal displacements of the eight first modes are numerically estimated by the observer and the extremum of the displacement targeted by the control are localized on the corresponding modal variable. The switch trigger is generated by the digital output of the control board, connected on a hard SSDI device. The excitation of the smart structure is carried out using an electromagnet driven by an audio amplifier. A pulse applied during 0.4 ms is applied on the electromagnet.

The modal model of the structure (Eqs.(4) and (5)) used by the observer has to be determined. The modal characteristics of the model are identified. The identification is realized using measured frequency responses using swept sine excitation. The results of experimental identification of the non-controlled structure and the corresponding computed results agree quite well.

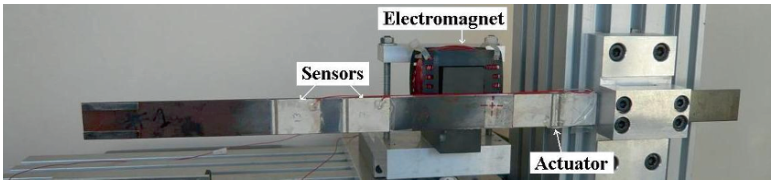

Fig. 5 Experimental setup.

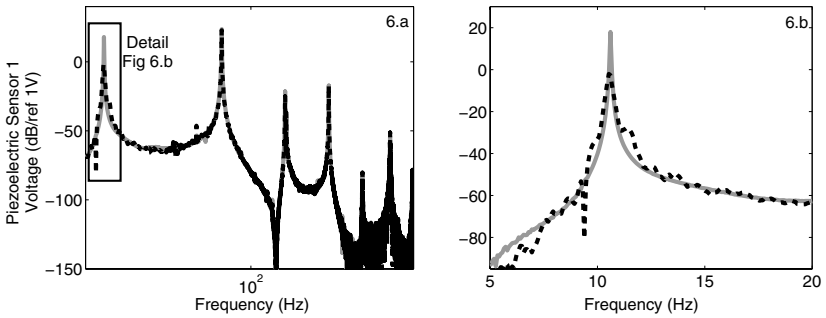

Fig. 6 Experimental frequency response on the first sensor when the smart stucture is uncontrolled (grey line) and when the first mode is controlled (black dotted line).

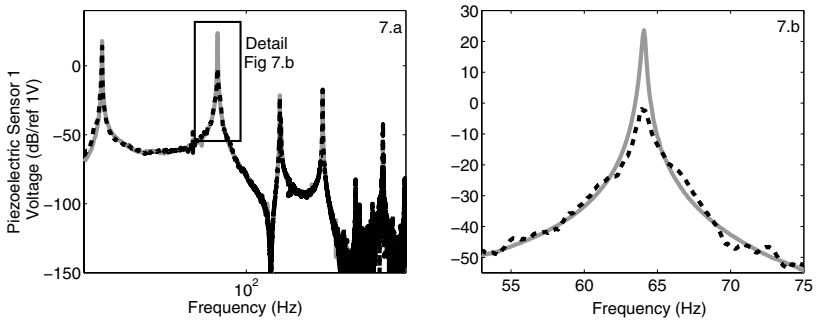

Fig. 7 Experimental frequency response on the first sensor when the smart stucture is uncontrolled (grey line) and when the second mode is controlled (black dotted line).

The impulsional response is presented Figure 6 when the first mode is controlled and Figure 7 when the second mode is controlled. The modal semi-active control induces a 19.88 dB attenuation on the first mode and 24.54 dB on the second mode. As simulated, on the considered bandwidth lying between 0 and 1200 Hz, spillover is not observed.

Experimental and simulated results of modal damping and modal damping ratio are summarized Table 2 and make it possible comparison. A good agreement is noted.

Table 2 Simulated and experimental modal damping ratio ξ and attenuation on first sensor.

	Simulation			Experimentation		
	Modal damping ratio		Attenuation	Modal damping ratio		Attenuation
	Uncontrolled	Controlled		Uncontrolled	Controlled	
Mode 1	$\xi = 0.0010$	$\xi = 0.0076$	-18.73 dB	$\xi = 0.0010$	$\xi = 0.0076$	-19.88 dB
Mode 2	$\xi = 0.0019$	$\xi = 0.0155$	-27.05 dB	$\xi = 0.0014$	$\xi = 0.0047$	-24.54 dB

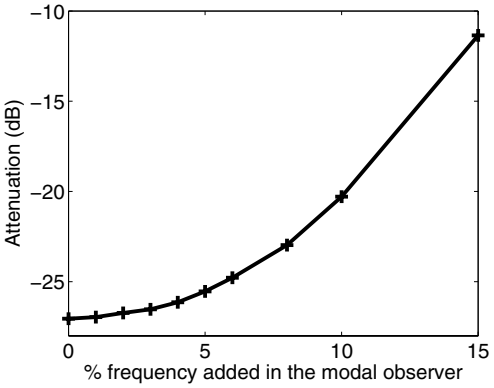

Fig. 8 Simulation robustess test on the control of the second mode.

3.3 Robustness

Robustness tests are carried out in simulation by modifying the frequencies used by the model of the observer. For a sufficiently fast observer such as the used observer, the simulations show that the control is stable and robust.

Unlike in usual modal active control, the stability and the performances are not too badly affected. Indeed, a bad identification causes a slight time shift in the moment of switch as this time definition is not very critical close to a maximum. This result is pointed out in Figure 8 which presents the increasing of the modal damping of the second mode in function of the frequency shift (in percent). For a variation of five percent of all the frequencies in the model used by the observer, the gain decreases from –27.05 dB to –25.54 dB. The robustness appears very good.

4 Conclusion

The control strategy presented in this paper allows a performant modal damping targeted on a specific mode of a structure thanks to a combination between SSDI semi-active and active control technique. The proposed method presents many advantages. This semi-active method can be used under wide bandwidth excitation with a good efficiency for the targeted mode. This method is as effective as the ori-

ginal SSDI which perform only when the excitation is monomodal. It requires low energy which is well adapted to on-board structures; moreover it induces large mass reduction. A simple battery must be useful to supply the observer and the power required by the switch could be easily self-powered. Mode targeting performance is a consequence of observer strategy which allows a very good mode filtering keeping a good accuracy in terms of frequency and phases. Moreover, the method presents a very good robustness. The results obtained by simulations are close to those obtained by experimentation. Simulations could be used as prediction of measurements. The current studies extended the method to control simultaneously several modes of the smart structure.

References

1. Corr, L.R, Clark, W.W.: A novel semi-active multi modal vibration control law for a piezoceramic actuator. *Journal of Vibration and Acoustics* **125**(2), 214–222 (2003).
2. Gaudiller, L., Bochard, S.: Adaptive active control of flexible structures subjected to rigid body displacements. *Journal of Sound and Vibration* **283**, 311–339 (2005).
3. Gaudiller, L., Der Hagopian, J.: Active control of flexible structures using a minimum of components. *Journal of Sound and Vibrations* **193**(3), 713–741 (1996).
4. Gaudiller, L., Matichard, F.: A nonlinear method for improving active control efficiency of smart structures subjected to rigid body motions. *IEEE/ASME Transaction of Mechatronics* **12**, 542–548 (2005).
5. Guyomar, D,. Badel, A.: Nonlinear semi-passive multimodal vibration damping: An efficient probabilistic approach. *Journal of Sound and Vibration* **294**(1–2), 249–268 (2006).
6. Hagood, N.W., Von Flotow, A.: Damping of structural vibrations with piezoelectric material and passive electrical networks. *Journal of Sound and Vibration* **146**(2), 243–268 (1991).
7. Holdhusen, M.H., Cunefare, K.A.: Optimization of a state-switched absorber applied to a continuous vibrating system. *The Journal of the Acoustical Society of America* **113**(4), 2227 (2003).
8. Luenberger, D.G.: An introduction to observers. *IEEE Transactions on Automatic Control* **16**, 596–602 (1971).
9. Matichard, F., Gaudiller, L.: Improvement of potential energetic exhange using non linear control. In *Proceedings IEEE/ASME, AIM – Advanced Intelligent Mechatronics*, pp. 807–812 (2005).
10. Richard, C., Guyomar, G., Bassaler, H., Audigier, D.: Enhanced semi passive damping using continuous switching of a piezoelectric device on an inductor. In *Proceedings of SPIE Smart Structures and Materials Conference: Damping and Isolation*, Vol. 3989, pp. 288–299 (2000).
11. Richard, C., Guyomar, G., Ching, C., Audigier, D.: Semi-passive damping using continuous switching of a piezoelectric device. In *Proceedings of SPIE Smart Structures and Materials Conference: Passive Damping and Isolation*, Vol. 3672, pp. 104–111 (1999).
12. Richard, C., Guyomar, D., Mohammadi, S.: Semi-passive random vibration control based on statistics. *Journal of Sound and Vibration* **307**, 818–833 (2007).

Model-Based Fault Detection on a Rotor in an Actively Supported Bearing Using Piezoelectric Actuators and the FXLMS-Algorithm

B. Hasch, O. Lindenborn and R. Nordmann

Abstract This paper examines the application of the Filtered-X Least Mean Square (FXLMS) algorithm in the domain of model-based fault detection and fault diagnosis to prevent errors in rotating machinery and increase the reliability. The advantage of this model-based approach is the combination of unbalance detection and vibration reduction. Using the FXLMS method, it is possible to detect harmonic disturbance and identify the fault unbalance in a stationary operating point. In reality, this fault may occur in aero engines e. g. due to burst of blade or loss of parts. The aim is to detect an unbalance at an early state before the rotor approaches the region of resonance, where this fault would lead to large radial displacements and forces. The experimental setup consists of an elastic shaft. One of its ball bearings is actively supported by two piezoelectric stack actuators. The rotor with its two disc elements has its first flexural mode at a frequency of 59 Hz and is able to operate up to a rotating frequency of 80 Hz. Eddy current sensors detect the radial displacement of the rotor. These displacement signals are provided to the adaptive filters, which realise external damping through the actuators and generate information about the fault even at low frequencies. When the filter parameters reach a constant value, quantitative information about the magnitude of the unbalance can be calculated using the plant model. This model-based approach guarantees detection of a fault occurring spontaneously, whereas signal-based methods have difficulty identifying this fault far away from resonance. The concept is explained in detail. Simulation results and experiments on the test rig show the suitability of the method.

Bernd Hasch
Chair of Mechatronics in Mechanical Engineering, Technische Universität Darmstadt, Petersenstrasse 30, 64287 Darmstadt, Germany; E-mail: hasch@mim.tu-darmstadt.de

Otto Lindenborn
Chair of Mechatronics in Mechanical Engineering, Technische Universität Darmstadt, Petersenstrasse 30, 64287 Darmstadt, Germany; E-mail: lindenborn@mim.tu-darmstadt.de

Rainer Nordmann
Chair of Mechatronics in Mechanical Engineering, Technische Universität Darmstadt, Petersenstrasse 30, 64287 Darmstadt, Germany; E-mail: nordmann@mim.tu-darmstadt.de

H. Ulbrich and L. Ginzinger (eds.), Motion and Vibration Control, 123–132.

1 Introduction

In rotating machinery, common recurring problems are significant vibrations generated by unbalances. Damping the vibrations is a usual approach to reduce critical displacements. A possible solution is the application of external damping with squeeze-film dampers (SFD) [6]. On top of that, active components and different control strategies are used to cope with this problem. Another advantage of active components is the possibility to optimise operational behaviour at different operating points and to carry out an action depending on the situation. Betschon and Schöb [1] use for example a rotor in magnetic bearings and adaptive feedforward control for vibration reduction. In [3] piezoelectric stack actuators are used to reduce vibrations of a shaft. Another interesting aspect is the vibration isolation to minimise forces caused by unbalance. This approach to isolate hard mounts as well as the reduction of vibrations through the FXLMS-algorithm is shown in [10].

It is also possible to use these active components for the improvement of reliability, safety and efficiency of systems. Therefore, faults have to be detected before they lead to a failure of the machine. Especially aircraft engines have to be fail-safe. Isermann [4] gives an overview and compares the different methods for model-based approaches for fault detection like parity equations, parameter estimation methods and state observers. Some faults that occur in rotating machinery are mass unbalance, cracked shafts and shafts with radial run-out. Platz [9] uses model-based methods to identify cracked and unbalanced shafts using residual vibrations and equivalent loads in the time and frequency domain. Harihara et al. [2] test signal-based and model-based methods for fault detection on an induction motor and shows, that model-based methods help to avoid the probability of false alarms. On the other side, they are more complex than signal-based methods. Patton and Chen [8] show the application of observer-based methods for a non-linear jet engine system, concentrating on the robustness of the observer.

The method presented in this paper first tries to reduce stationary vibrations caused by unbalance. In a second step, the parameters, which were estimated by the FXLMS-algorithm, are used to calculate the amplitude of the unbalance. Therefore, a model of the plant is used. When unbalance occurs spontaneously, the method produces a significant residual. In the subsequent section the test rig is presented and the control strategy is explained in more detail. This section is followed by the validation with results of the simulation and the experiment. Finally there are some concluding remarks.

2 Modelling of the System

This section begins with a description of the test rig, where the examinations take place. In the second part it is shown, how a reduction of the vibration and the following determination of the amplitude of the fault unbalance is realised with the developed strategy using the FXLMS-algorithm.

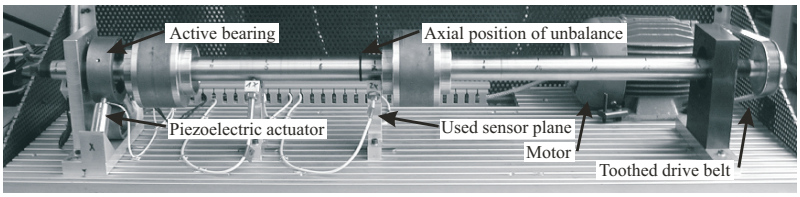

Fig. 1 Test rig with sensors and actuators.

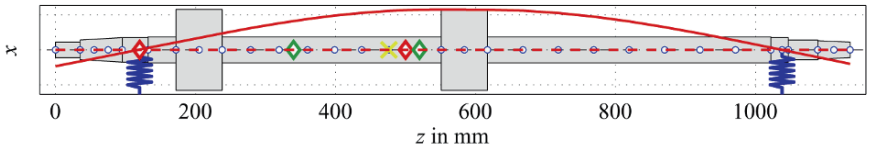

Fig. 2 First bending mode of the rotor showing sensor-outputs and force-inputs of the state space system.

2.1 Experimental Setup

The test rig consists of a flexible rotor with one actively supported roller bearing using two piezoelectric stack actuators visualised in Figure 1.

The rotational power is generated by a three-phase, asynchronous motor connected with the rotor by a toothed drive belt. To measure the orbits of the first mode, eddy current sensors are placed in the middle of the shaft where large amplitudes can best be detected. Furthermore, the current rotation speed is measured by an incremental sensor, which is located on left hand side directly behind the active bearing. One roller bearing of the shaft is actively supported by two piezoelectric stack actuators in radial direction at right angles towards each other as shown in Figure 1. It is possible to stimulate the rotor with a maximum frequency of 800 Hz. Force sensors, which work on the principle of strain gauge, are placed between the piezoelectric actuators and the bearing, to measure the force fed into the shaft. A circular spring element is used in order to keep the piezoelectric actuators pressurised in the whole working area and hold the collocated force sensors in place.

The supercritical shaft has an operating speed up to a rotating frequency of 80 Hz. The deformation of the rotor at first flexural mode of 59 Hz is visualised in Figure 2 for x-direction.

For controller synthesis, the flexible shaft is modelled with the Finite Element Method and reduced to a state space system. The piezoelectric actuators can be modelled as springs equivalent to the actuator stiffness and a base displacement, which represents the actuator deformation. The whole plant $\mathsf{G}(s)$, visualised in Figure 1, is a Multi-Input-Multi-Output (MIMO) state space system of the flexible shaft supported by an elastic mounting. The input of the plant consists of actuator input $\mathbf{u}(t)$ and disturbance input $\mathbf{d}(t)$ for x- and y-direction. The output vector $\mathbf{y}(t)$ includes the displacement in the middle of the rotor for x- and y-direction.

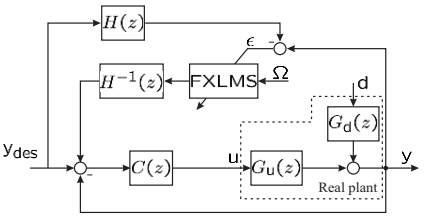

Fig. 3 Block diagram of the control strategy with feedback loop.

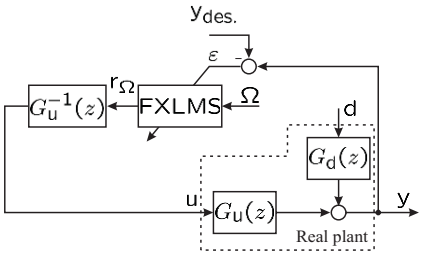

Fig. 4 Block diagram of the control strategy without feedback loop.

In the experiment a dSPACE real-time system is used to apply the control algorithm using a sample time of $T_0 = 0.0002\,\mathrm{s}$.

2.2 Control Strategy and Modelling of the Plant

The FXLMS-algorithm is a widely used method for rejection of periodic disturbance, for instance, in the field of active noise control. The basic structure of the FXLMS-algorithm is described in [7] for sensor disturbance on a discrete Single-Input-Single-Output (SISO) one degree of freedom system. Betschon and Schöb [1] propose a similar concept to suppress harmonic disturbances on rotors in magnetic bearings. The outcome of this is the block diagram in Figure 3, at which the transfer function of the plant $G(z)$ is split into the disturbance transfer function $G_\mathrm{d}(z)$ and the input transfer function $G_\mathrm{u}(z)$.Therein, $C(z)$ is the transfer function of the controller and

$$H(z) = \frac{C(z)G_\mathrm{u}(z)}{1 + C(z)G_\mathrm{u}(z)}$$

the transfer function of the closed loop. The concept is enhanced on MIMO systems.

No underlying feedback loop is used in this case. It is not essential, whereas a feedback controller is absolutely necessary in rotor test rigs with magnetic bearings. Provided that the desired value $\mathbf{y}_\mathrm{des}$ is constant and harmonic vibrations occur around this value, the block diagram of Figure 3 simplifies to the block diagram in Figure 4.

A first goal is to reduce vibrations caused by unbalance. Therefore, the rotating frequency Ω has to be available to the FXLMS-algorithm as reference signal. The algorithm calculates the signal $\mathbf{r}_\Omega(k)$, that is applied to the piezoelectric actuators

using the inverse transfer function matrix of the plant $\mathsf{G}_\mathrm{u}^{-1}(z)$. Equation (1) shows the cost function that has to be minimised with the help of the FXLMS-algorithm:

$$J_i = \epsilon_i^2 = (y_i - y_{\mathrm{des}i})^2 \tag{1}$$

Index i represents the coordinate for x- respectively y-direction, which are minimised independently. That means two adaptive filters are used. Equation (2) represents the result of the algorithm, with the amplitudes of the corresponding sine- and cosine function calculated in Eqs. (3) and (4).

$$\mathbf{r}_\Omega(k) = \mathbf{w}_0(k)\sin(\Omega k T_0) + \mathbf{w}_1(k)\cos(\Omega k T_0) \tag{2}$$

$$\mathbf{w}_0(k) = \mathbf{w}_0(k-1) + 2\eta\boldsymbol{\epsilon}\sin(\Omega k T_0 + \varphi_0) \tag{3}$$

$$\mathbf{w}_1(k) = \mathbf{w}_1(k-1) + 2\eta\boldsymbol{\epsilon}\cos(\Omega k T_0 + \varphi_0) \tag{4}$$

The convergence factor η is chosen according to Betschon and Schöb [1] and Na and Park [7]. φ_0 represents the phase shift between the reference signal and the rotor position. The inverse transfer function $\mathsf{G}_\mathrm{u}^{-1}(z)$ of the FEM model leads to $\mathbf{r}_\Omega$:

$$\mathbf{r}_\Omega = \mathsf{G}_\mathrm{u}(z)\mathbf{u} \tag{5}$$

The summation block in Figure 4 results in $\mathbf{y}$:

$$\mathbf{y} = \mathsf{G}_\mathrm{u}(z)\mathbf{u} + \mathsf{G}_\mathrm{d}(z)\mathbf{d} \tag{6}$$

Assuming that the algorithm minimises $\mathbf{y}$ to zero and solving Eq. (6) for $\mathbf{d}$, the result is Eq. (7):

$$\mathbf{d} = -\mathsf{G}_\mathrm{d}^{-1}(z)\mathsf{G}_\mathrm{u}(z)\mathbf{u} = -\mathsf{G}_\mathrm{d}(z)^{-1}\mathbf{r}_\Omega(k) \tag{7}$$

With Eq. (2) the result is Eq. (8):

$$\mathbf{d} = \mathsf{G}_\mathrm{d}^{-1}(z)(\mathbf{w}_0\sin(\Omega k T_0) + \mathbf{w}_1\cos(\Omega k T_0)) \tag{8}$$

If the inverse transfer function matrix $\mathsf{G}_\mathrm{d}^{-1}(z)$ is known, it is possible to suggest the force caused by unbalance.

$$\mathbf{d} = me\Omega^2 \begin{pmatrix} \sin(\Omega k T_0 + \varphi_\mathrm{u}) \\ \cos(\Omega k T_0 + \varphi_\mathrm{u}) \end{pmatrix}$$

The amplitude of the unbalance me and even its phase angle φ_u related to the radial position of the rotor can easily be calculated under ideal conditions. The influence of the circular preload spring coupling is neglected because the coordinates are weakly coupled. This simplifies the inversion of the transfer function matrices. Thus, it is possible to reliably generate a residual that indicates the occurrence of unbalance independently of the operation point. It is even possible to estimate the magnitude and phase if the axial position of the unbalance is known. If a rotor model is not available, a residual can still be generated, but there is no information about the magnitude of the disturbance.

3 Validation

In the simulation part the system behaviour of the presented control strategy is discussed under ideal conditions, where all assumptions are fulfilled. The experiments carried out demonstrate that the proposed results of the simulation can be qualitatively achieved on the described test rig.

In both, simulation and experiment, a test unbalance of $50{\cdot}10^{-6}$ kg m is fixed on the rotor as described. First, both adaptive filters are switched on at a stationary operation point of the rotor at 50 Hz, which leads to a reduction of vibrations caused by unbalance. At the same time, the calculation of the unbalance starts. When the adaptation of the filter parameters is finished, the estimation of the unbalance reaches its limit. The results of different stationary operation points are presented.

3.1 Simulation Results

The elucidated control strategy is implemented in MATLAB Simulink. The dynamics of the flexible shaft are represented by the Finite Element Method model described in Section 2.2. In the simulation $G_u^{-1}(z)$ is the exact inverse transfer function of $G_u(z)$, which represents the idealised case for this algorithm. A frequency of 50 Hz is chosen to show the behaviour exemplarily. Thus, vibrations in the middle of the shaft can be observed, but the operation point is a few Hz away from resonance frequency, where instability occurs caused by small damping [5].

Figure 5 shows the amplitudes of the vibrations in the middle of the rotor at a rotating frequency of 50 Hz. The signals are overlaid by an artificial noise to imitate the behaviour of the displacement sensors. The algorithm is activated at $t = 2$ s and

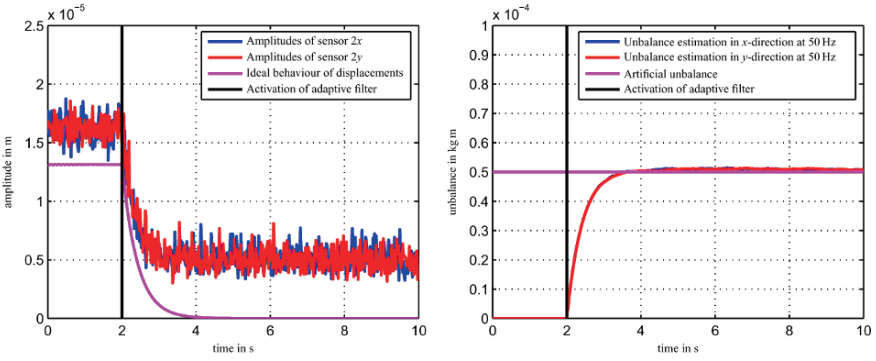

(a) Displacements in the middle of the rotor

(b) Estimation of unbalance for a given artificial unbalance of $50{\cdot}10^{-6}$ kg m

Fig. 5 Simulation results showing the behaviour of displacements in the middle of the rotor and unbalance estimation at a stationary operation point of 50 Hz.

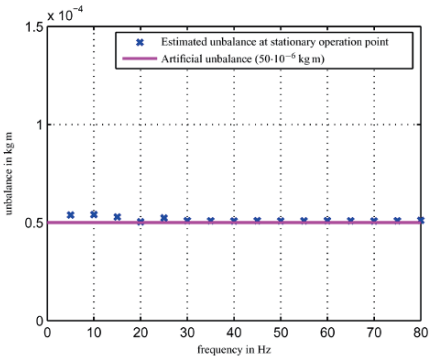

Fig. 6 Estimation of unbalance at stationary operation points with an unbalance of $50{\cdot}10^{-6}$ kg m.

a reduction of the vibrations to a minimum is visible. The ideal progression is illustrated, too. The diagram on the right hand side of Figure 5 shows the progression of the calculated unbalance. At first, there is no information about the magnitude of the unbalance available. By activating the algorithm the values increase and converge a limit. They are to be found near the set unbalance of $50{\cdot}10^{-6}$ kg m.

Figure 6 shows the amplitudes of the unbalance in the middle of the rotor for different rotating frequencies in ranges of 5 Hz, when the adaptation of the filter parameters has stopped. The mean value of the two estimations is presented. It is visible, that the calculation of the unbalance corresponds well to the set value during the whole operating range. It turns out that the estimation is worse in the area of low frequencies, where the signal to noise ratio is small.

3.2 Experimental Results

The algorithm runs on a dSPACE real time system that uses a sampling frequency of 5 kHz. The needed inverse transfer functions $G_{\mathrm{u}}^{-1}(z)$ and $G_{\mathrm{d}}^{-1}(z)$ are identical to the ones used in the simulation.

3.2.1 Behaviour of the System When the Algorithm Is Switched on

The experiment takes place at a rotating frequency of 50 Hz like in the simulation. Figure 7 shows the progress of the amplitudes of the vibration in the middle of the rotor. After the algorithm is switched on, the vibrations reduce to a minimum. The calculation of the amplitude of the unbalance starts at the same time. It becomes clear that the filter for x-direction shows a higher value than the filter in y-direction.

A cause for this might be the circular preload spring between the actuators, that leads to a larger coupling of the coordinates than assumed. Then the actuators influence each other. In the simulation, this interaction was neglected. Additionally,

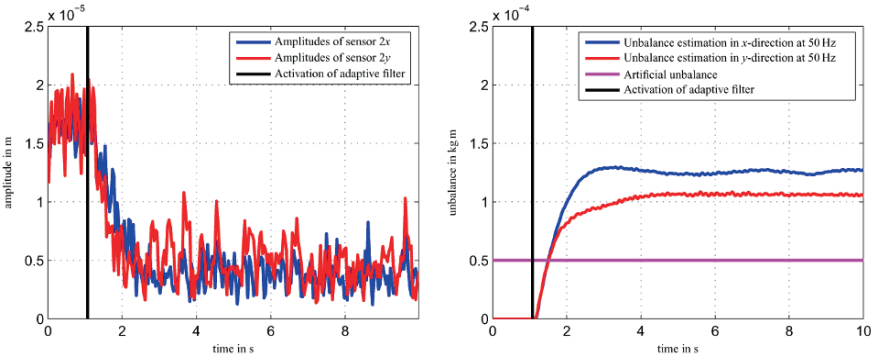

(a) Displacements in the middle of the rotor

(b) Estimation of unbalance for a given artificial unbalance of $50{\cdot}10^{-6}$ kg m

Fig. 7 Experimental results showing the behaviour of displacements in the middle of the rotor and unbalance estimation at a stationary operation point of 50 Hz.

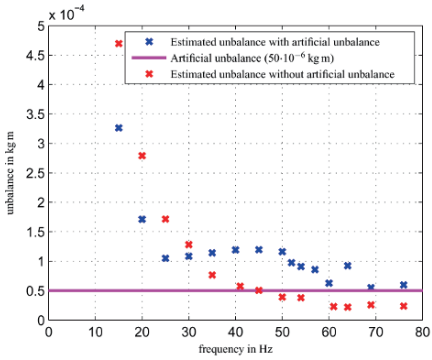

Fig. 8 Estimation of unbalance at stationary operation points with an artificial unbalance of $50{\cdot}10^{-6}$ kg m and estimation without artificial unbalance.

the estimation is twice as much as the set test mass for unbalance. The reason for that is, that the rotor is not fully balanced. Besides, the rotor has a slight radial run-out. The unbalance test mass is fixed on the side, where the deformation is greatest. Measurements without artificial test mass were made to verify this assumption (Figure 8). It shows, that the estimation of the unbalance increases extremely below rotating frequencies of 25 Hz. The influences, which were not taken into account in the simulation, are high at these low frequencies particularly. One of these is the stimulation of the rotor by the teeth of the toothed drive belt. Besides the sensor noise, the wanted harmonic signal is overlaid by higher harmonic vibrations. The estimation of the amplitudes above the first flexural mode decreases as a whole. This may come from the uncertainties of the model. Besides the measurements with the artificial test mass of $50{\cdot}10^{-6}$ kg m, measurements were made without test mass at different frequencies. These show, that the rotor is not fully balanced. An interesting aspect is, that the measurements become more reliable at higher frequencies,

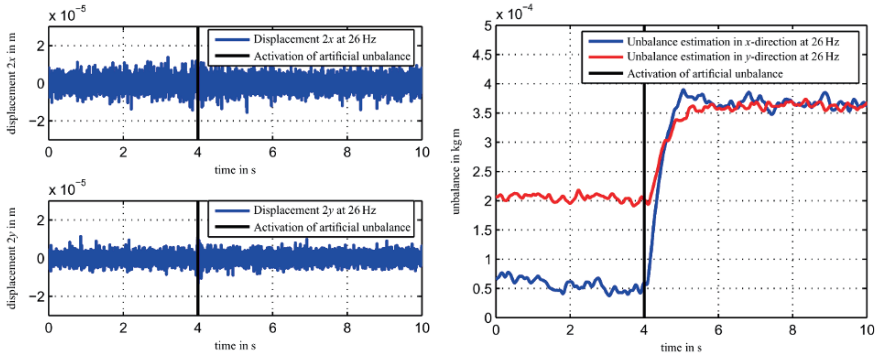

(a) Displacements in the middle of the rotor

(b) Estimation of unbalance for a spontaneous artificial unbalance

Fig. 9 Experimental results showing the behaviour of displacements in the middle of the rotor and unbalance estimation at a stationary operation point with an unbalance applied during operation.

because the desired harmonic signal caused by unbalance is smaller than with artificial test mass.

3.2.2 Behaviour of the System When Unbalance Spontaneously Occurs

Although it is not possible to give an accurate prediction of the magnitude of the unbalance in the whole operation area in the experiment, the concept is suitable to generate residuals that indicate the occurrence of the fault "unbalance". Therefore it is not essential to know what value the unbalance really has.

Figure 9 shows the behaviour of the system when the algorithm is activated and when unbalance occurs spontaneously. For this purpose an artificial test mass (magnet) was fixed in the middle of the rotor at $t = 4$ s and a constant rotating frequency of 26 Hz. In the left part of Figure 9, the signals of the displacement sensors are plotted against time. An attempt to detect the fault unbalance with limit value monitoring would hardly be possible because the displacements of the desired harmonic signal are pretty small far away from resonance. On the right hand side of Figure 9, a steep edge is visible shortly after the test mass is fixed at the rotating shaft. Before the artificial unbalance occurs, it is visible that the estimations for x- and y-direction differ. Even the amplitudes indicate only the magnitude of the unbalance, this signal can be used as a residual, that reliably indicates the fault unbalance. Even below the first bending mode, this method produces significant residuals for identification of spontaneously occurring unbalance such as blade loss or impact of foreign objects.

4 Conclusion

The remarkable result of this study is the multifunctional application of piezoelectric actuators in combination with the FXLMS-algorithm for vibration reduction and fault detection. For harmonic disturbance like unbalance the control strategy presented not only allows vibration reduction of the rotor initialised by the disturbance. Furthermore it is possible to identify the magnitude of the unbalance. The simulation results show the ideal case where the real plant is identical to the model used in the algorithm. Focus of future work is the experimental identification of the plant to improve the model and increase the performance of the fault detection. Another interesting aspect to be looked at is the reliable estimation of the phase.

References

1. Betschon, F., Schöb, R.: On-line-adapted vibration control. In *Proceedings of the Sixth International Symposium on Magnetic Bearings*, pp. 362–371 (1998).
2. Harihara, P.P., Kim, K., Parlos, A.G.: Signal-based versus model-based fault diagnosis – A trade-off in complexity and performance. In *Proceedings 4th IEEE SDEMPED*, pp. 277–282 (2003).
3. Horst, H.-G.: Aktive Schwingungsminderung an elastischen Rotoren mittels piezoelektrischer Aktoren. Diss., Shaker Verlag, Aachen (2005).
4. Isermann, R.: Model-based fault detection and diagnosis methods. In *Proceedings of the American Control Conference*, pp. 1605–1609, Vol. 3 (1995).
5. Kuo, S.M., Morgan, D.R.: Active noise control: A tutorial review. *Proceedings of the IEEE* **87**, 943–973 (1999).
6. Nordmann, R., Pfützner, H., Gasch, R.: *"Quetschöldämpfer" Rotordynamik*. Springer (2002).
7. Na, H.-S., Park, Y.: An adaptive feedforward Controller for rejection of periodic disturbances. *Journal of Sound and Vibration* **201**(4), 427–435 (1997).
8. Patton, R.J., Chen, J.: A robustness study of model-based fault detection for jet engine systems. In *Proceedings 1st IEEE Conference on Control Applications*, pp. 871–876, Vol. 2 (1992).
9. Platz, R.: *Untersuchungen zur modellgestützten Diagnose von Unwuchten und Wellenrissen in Rotorsystemen*. Fortschr.-Ber. VDI Reihe 11 Nr. 325, VDI Verlag, Düsseldorf (2004).
10. van der Poel, T., van Dijk J., Jonker, B., Soemers H.: Improving the vibration isolation performance of hard mounts for precision equipment. In *Proceedings IEEE/ASME International Conference on Advanced Intelligent Mechatronics* (2007).

Act-and-Wait Control Concept for a Force Control Process with Delayed Feedback

Tamás Insperger, László L. Kovács, Péter Galambos and Gábor Stépán

Abstract The act-and-wait control concept is applied to a force control problem with feedback delay. The point of the concept is that the feedback loop is switched off and on periodically during the control process so that the duration of the switch off period is larger than the feedback delay. The concept is compared to the traditional, continuous control concept, when the feedback loop is continuously active. Stability charts are constructed that plots the critical proportional gains, where the process looses stability, as function of the feedback delay. It is shown that the proportional gains can significantly be increased without loosing stability, if the act-and-wait concept is used. Consequently, the force error can significantly be decreased this way. The theoretical results are confirmed by experiments.

1 Introduction

Force control is a frequent mechanical controlling problem in engineering. The aim is to provide a desired force between the actuator and the environment (or workpiece). The main difficulty of this problem is that the force sensor and the environment touched by the actuator are elastic, moreover, the compliance of the environment is often unknown. In order to achieve high accuracy in maintaining the prescribed contact force against Coulomb friction, high control gains are to be used [1]. In these practical realizations of force control, however, the robot often loses stability, and starts to oscillate at a relatively low frequency. These oscillations are mainly caused by the digital effects and the time delay in the feedback loop [2]. In the

T. Insperger, L.L. Kovács and G. Stépán
Department of Applied Mechanics, Budapest University of Technology and Economics, Hungary; E-mail: {inspi, kovacs, stepan}@mm.bme.hu

P. Galambos
Department of Manufacturing Science and Technology, Budapest University of Technology and Economics, Hungary; E-mail: galambos@manuf.bme.hu

H. Ulbrich and L. Ginzinger (eds.), Motion and Vibration Control, 133–142.

current paper, we concentrate on the effect of the feedback delay on the stability properties of the process. Such time delays arise due to acquisition of response and excitation data, information transmission, on-line data processing, computation and application of control forces. In spite of the efforts to minimize time delays, they cannot be eliminated totally even with today's advanced technology due to physical limits. The information delay is often negligible, but for some cases, it still may be crucial, for example, in space applications [3], in controlling congestion in the Internet [4] or in robotic applications with time-consuming control force computation [5].

The problem with time-delayed systems is that the corresponding phase space is usually infinite dimensional, therefore, infinite number of poles are to be controlled using finite number of control parameters. Thus, complete pole placement is not possible for these systems using traditional constant feedback gains. The act-and-wait control concept is an effective tool to deal with pole placing for systems with feedback delay. The act-and-wait technique was introduced in [6] for discrete-time systems and in [7] and [8] for continuous-time systems. The point of the technique is that the controller is periodically switched on and off with switch off period being larger than the feedback delay. The resulted switched system can be described by a finite dimensional discrete map associated with finite number of poles. Thus, stabilization requires the control over finite number of poles instead of infinitely many ones.

In this paper, the act-and-wait concept is applied to a digital force control problem. The structure of the paper is as follows. First, in Section 2, the act-and-wait concept is summarized briefly for continuous-time systems based on [7]. Section 3 presents the mechanical model of the force control process under study using the traditional, continuous control concept. Section 4 deals with the application of the act-and-wait concept in the model. The two methods are compared in Section 5. Section 6 presents the experimental verification of the theoretical predictions. The paper is concluded in Section 7.

2 The Act-and-Wait Concept for Continuous-Time Systems

Consider the linear system

$$\dot{\mathbf{x}}(t) = \mathbf{A}\mathbf{x}(t) + \mathbf{B}\mathbf{u}(t), \tag{1}$$

where $\mathbf{x}(t) \in \mathbb{R}^n$ is the state vector, $\mathbf{u}(t) \in \mathbb{R}^m$ is the input, $\mathbf{A} \in \mathbb{R}^{n\times n}$ and $\mathbf{B} \in \mathbb{R}^{n\times m}$ are given constant matrices. Consider the autonomous delayed feedback controller

$$\mathbf{u}(t) = \mathbf{D}\mathbf{x}(t-\tau), \tag{2}$$

where $\mathbf{D} \in \mathbb{R}^{m\times n}$ is a constant matrix and τ is the delay of the feedback. We assume that the delay τ is a fixed parameter of the control system and cannot be eliminated or tuned during the control design.

System (1) with controller (2) imply the delay-differential equation (DDE)

$$\dot{\mathbf{x}}(t) = \mathbf{A}\mathbf{x}(t) + \mathbf{B}\mathbf{D}\mathbf{x}(t-\tau). \tag{3}$$

Due to the time delay, this system has infinitely many poles (called also characteristic roots or characteristic exponents) determined by the transcendental characteristic equation

$$\det\left(\lambda\mathbf{I} - \mathbf{A} - \mathbf{B}\mathbf{D}\,\mathrm{e}^{-\tau\lambda}\right) = 0. \tag{4}$$

The system is asymptotically stable if all the poles are located in the left half of the complex plane. Stabilization of system (1)–(2) rises the following pole placement problem: for given matrices $\mathbf{A}$ and $\mathbf{B}$ and for given feedback delay τ, we are looking for matrix $\mathbf{D}$ so that the real parts of all the infinitely many poles of the system are negative. The difficulty of this problem is that infinitely many poles should be controlled by finite number of control parameters, i.e., by the elements of matrix $\mathbf{D}$.

An effective way of managing pole placement problem for systems with feedback delay is the application of the so-called act-and-wait controller

$$\mathbf{u}(t) = g(t)\mathbf{D}\mathbf{y}(t-\tau), \tag{5}$$

where $g(t)$ is the T-periodic act-and-wait switching function defined as

$$g(t) = \begin{cases} 0 & \text{if} \quad 0 \le \mathrm{mod}(t,T) < t_{\mathrm{w}}, \\ 1 & \text{if} \quad t_{\mathrm{w}} \le \mathrm{mod}(t,T) < t_{\mathrm{w}} + t_{\mathrm{a}} = T. \end{cases} \tag{6}$$

Using controller (5) instead of (2), the delayed feedback term is switched off for period of length t_{w} (*wait*), and it is switched on for period of length t_{a} (*act*).

System (1) with controller (5) can be written in the time-periodic DDE form

$$\dot{\mathbf{x}}(t) = \mathbf{A}\mathbf{x}(t) + g(t)\mathbf{B}\mathbf{D}\mathbf{x}(t-\tau). \tag{7}$$

According to the Floquet theory of DDEs, stability is determined by the nonzero eigenvalues of the system's monodromy operator, called also characteristic multipliers. The system is asymptotically stable if all the characteristic multipliers are inside the unit circle of the complex plane.

In [7], it was shown that if the length t_{w} of the waiting period is larger than the feedback delay τ, then the system can be transformed into an $n \times n$ discrete map. This way, the number of characteristic multipliers can be reduced to n. For instance, if $t_{\mathrm{w}} \ge \tau$ and $0 < t_{\mathrm{a}} \le \tau$, then the solution over an act-and-wait period T can be given as

$$\mathbf{x}(T) = \underbrace{\left(\mathrm{e}^{\mathbf{A}T} + \int_{t_{\mathrm{w}}}^{T} \mathrm{e}^{\mathbf{A}(T-s)}\mathbf{B}\mathbf{D}\,\mathrm{e}^{\mathbf{A}(s-\tau)}\,\mathrm{d}s\right)}_{\mathbf{\Phi}} \mathbf{x}(0). \tag{8}$$

Stability properties of this discrete map are determined by the eigenvalues of the coefficient matrix $\mathbf{\Phi}$. Now, the stabilization problem can be composed in the fol-

lowing way: for given matrices $\mathbf{A}$ and $\mathbf{B}$ and for given feedback delay τ, we are looking for matrix $\mathbf{D}$ and parameters $t_w \geq \tau$ and t_a so that the eigenvalues of matrix $\mathbf{\Phi}$ are in modulus less than one. This way, the infinite dimensional pole placement problem is reduced to an n-dimensional one: n eigenvalues of $\mathbf{\Phi}$ should be placed using the control parameters in $\mathbf{D}$.

3 Model of Force Control Process with Feedback Delay

The 1 DoF mechanical model of the force control process is shown in Figure 1. Here, the modal mass m and the equivalent stiffness k represent the inertia and the stiffness of the robot and the environment, while equivalent damping b models the viscous damping originated from the servo motor characteristics and the environment. The force Q represents the controller's action and C is the magnitude of the effective Coulomb friction.

Considering a proportional force controller, the control force can be given as

$$Q(t) = F_\mathrm{d} - P(F_\mathrm{m}(t) - F_\mathrm{d}), \tag{9}$$

where P is the proportional gain, F_d is the desired force and F_m is the measured force. The equation of motion reads

$$m\,\ddot{q}(t) + b\dot{q}(t) + kq(t) = F_\mathrm{d} - P(F_\mathrm{m}(t) - F_\mathrm{d}) - C\mathrm{sgn}\dot{q}(t). \tag{10}$$

This type of control force computation was also considered in [1]. Assuming steady-state condition by setting all the time derivatives to zero, considering a constant Coulomb friction force and using that $F_\mathrm{m} = kq(t)$, the force error can be given as

$$F_\mathrm{e} = \frac{C}{1+P}. \tag{11}$$

Thus, the higher the gain P is, the less the force error is. Theoretically, there is no upper limit for the gain P, since the constant solution $q(t) \equiv q_\mathrm{d}$ of (9) is always

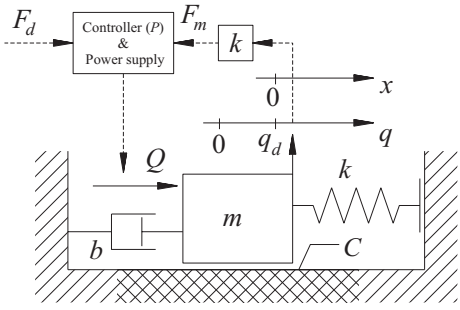

Fig. 1 Mechanical model of the force control process.

asymptotically stable when $C = 0$. Experiments show, however, that the real system with feedback delay is not stable for large gain P [9].

In practical realizations, the control force can be written in the form:

$$Q(t) = F_\mathrm{d} - P(F_\mathrm{m}(t-\tau) - F_\mathrm{d}) = kq_\mathrm{d} - P(kq_\mathrm{m}(t-\tau) - kq_\mathrm{d}), \qquad (12)$$

where τ is the time delay in the feedback loop. Thus, the equation of motion reads

$$m\,\ddot{q}(t) + b\dot{q}(t) + kq(t) = kq_\mathrm{d} - P(kq(t-\tau) - kq_\mathrm{d}) - C\mathrm{sgn}\dot{q}(t). \qquad (13)$$

Stability analysis of this system can be given by analyzing the variational system of Eq. (13) around the desired motion q_d. For this computation, we neglect the dry friction from the model. Considering that $q(t) = q_\mathrm{d} + x(t)$, the variational system reads

$$\ddot{x}(t) + 2\zeta\omega_\mathrm{n}\dot{x}(t) + \omega_\mathrm{n}^2 x(t) = -\omega_\mathrm{n}^2 P x(t-\tau), \qquad (14)$$

where $\omega_\mathrm{n} = \sqrt{k/m}$ is the natural angular frequency of the uncontrolled undamped system, and $\zeta = b/(2m\,\omega_\mathrm{n})$ is the damping ratio. This system is stable if all the roots of the characteristic equation

$$\lambda^2 + 2\zeta\omega_\mathrm{n}\lambda + \omega_\mathrm{n}^2 = -\omega_\mathrm{n}^2 P\,\mathrm{e}^{\lambda\tau}, \qquad (15)$$

have negative real parts. This transcendental equation has infinitely many characteristic roots in the plane of complex numbers. Still, stability boundaries can be determined by assuming pure imaginary characteristic roots in the form $\lambda = \mathrm{i}\omega$, where ω gives the angular frequency of the arising vibrations during loss of stability.

4 Application of the Act-and-Wait Control Concept

As it was mentioned in the introduction, the act-and-wait controller (5) can be used to reduce the number of poles of the system. If the length t_w of the waiting period is larger than the feedback delay τ, then the system can be transformed to a 2-dimensional discrete map. The variational system associated with the act-and-wait control concept reads

$$\ddot{x}(t) + 2\zeta\omega_\mathrm{n}\dot{x}(t) + \omega_\mathrm{n}^2 x(t) = -g(t)\omega_\mathrm{n}^2 P x(t-\tau), \quad t \in [t_j, t_{j+1}) \qquad (16)$$

that can be transformed into the state-space form (1) and (5) with

$$\mathbf{x}(t) = \begin{pmatrix} x(t) \\ \dot{x}(t) \end{pmatrix}, \quad \mathbf{u}(t) = \begin{pmatrix} x(t) \end{pmatrix}, \quad \mathbf{A} = \begin{pmatrix} 0 & 1 \\ -\omega_\mathrm{n}^2 & -2\zeta\omega_\mathrm{n} \end{pmatrix}, \quad \mathbf{B} = \begin{pmatrix} 0 \\ 1 \end{pmatrix}.$$

If $t_\mathrm{w} \geq \tau$ and $0 < t_\mathrm{a} \leq \tau$, then the monodromy matrix $\mathbf{\Phi}$ of the system can be determined according to Eq. (8). Let μ_1 denote the critical (maximum in modulus) eigenvalue. The system is stable if $|\mu_1| < 1$. The frequency of the arising vibrations

during loss of stability is related to the phase angle

$$\omega_1 = \frac{1}{T}\,\mathrm{Im}(\ln(\mu_1)) = \frac{1}{T}\arctan\left(\frac{\mathrm{Im}\mu_1}{\mathrm{Re}\mu_1}\right) \tag{17}$$

with $-\pi < \omega_1 \leq \pi$. The vibration frequencies are

$$f = \pm\frac{\omega_1}{2\pi} + \frac{k}{T} \quad [\mathrm{Hz}], \quad k = 0, \pm 1, \pm 2, \ldots . \tag{18}$$

The control force corresponding to the act-and-wait control concept can be given as

$$Q_{\mathrm{a\&w}}(t) = F_{\mathrm{d}} - g(t)P(F_{\mathrm{m}}(t-\tau) - F_{\mathrm{d}}), \tag{19}$$

where $g(t)$ is the T-periodic act-and-wait switching function defined in (6). Thus,

$$Q_{\mathrm{a\&w}} = \begin{cases} F_{\mathrm{d}} - P(F_{\mathrm{m}}(t-\tau) - F_{\mathrm{d}}) & \text{if} \quad 0 \leq \mathrm{mod}(t,T) < t_{\mathrm{w}}, \\ F_{\mathrm{d}} & \text{if} \quad t_{\mathrm{w}} \leq \mathrm{mod}(t,T) < t_{\mathrm{w}} + t_{\mathrm{a}} = T. \end{cases} \tag{20}$$

This means that the control force is just equal to the desired force for period of length t_{w}, and the feedback is switched on only for periods of length t_{a}.

5 Theoretical Stability Charts and Force Errors

In order to compare the act-and-wait control concept given by Eq. (20) to the traditional, continuous control concept given by Eq. (12), stability properties are analyzed as the function of control gain P and feedback delay τ. The mechanical parameters are $k = 16414$ N/m, $b = 1447$ Ns/m, $m = 29.57$ kg. The Coulomb friction is $C = 16.5$ N. The length of the waiting period was set to be equal to the feedback delay, i.e., $t_{\mathrm{w}} = \tau$, while the ratio of the acting period length and the delay was set to a fixed number $t_{\mathrm{a}}/\tau = 0.2$.

Panel (b) in Figure 2 presents the theoretical stability charts for both cases. Stability boundaries corresponding to the continuous control case were determined via the analysis of the characteristic equation (15). The boundaries corresponding to the act-and-wait concept were determined by numerical evaluation of the eigenvalues of matrix $\mathbf{\Phi}$ over a 200×200-sized grid of parameters τ and P. Both stability charts were checked using the first-order semi-discretization method developed to stability analysis of time-periodic DDEs [10].

Panel (a) shows the vibration frequencies corresponding to the upper stability boundaries. It can be seen that the continuous control case is associated with a single vibration frequency, while for the act-and-wait control case, a series of vibration frequencies arise according to Eq. (18). Panel (c) presents the maximum force error, which is determined by the maximum stable gain P and formula (11).

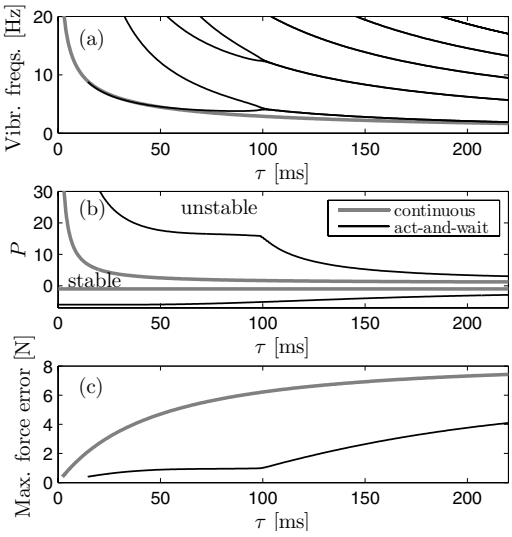

Fig. 2 Theoretically predicted stability charts (b), frequency diagram (a) and the maximum force error (c) for the continuous and for the act-and-wait control concept.

It can be seen that if the act-and-wait controller is used, then significantly higher proportional gains can be used without loosing stability that results in significantly smaller force error.

6 Experimental Validation

For the experimental validation of the theoretical results, a HIRATA (MB-H180-500) DC drive robot was used (see Figure 3). The axis of the robot was connected to the base of the robot (environment) by a helical spring of stiffness $k = 16414$ N/m. The contact force was measured by a Tedea-Huntleight Model 355 load cell mounted between the spring and the robot's flange. The driving system of the moving axis consisted of a HIRATA HRM-020-100-A DC servo motor connected directly to a ballscrew with a 20 mm pitch thread. The robot was controlled by a micro-controller

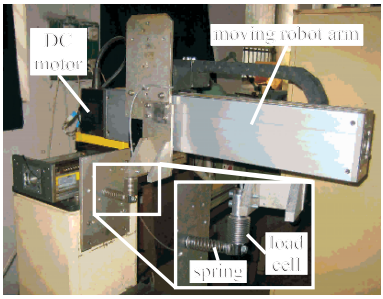

Fig. 3 Experimental setup.

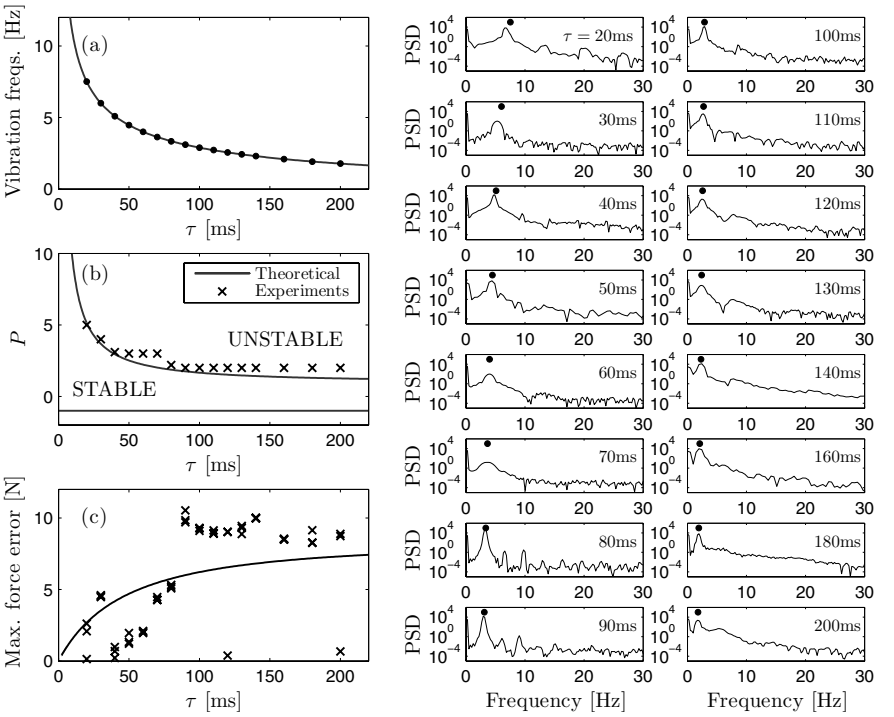

Fig. 4 Experimental and theoretical stability charts (b) and force errors (c), theoretical vibration frequencies (a), and experimental PSD diagrams (right panels) for the continuous control concept.

based control unit providing the maximum sampling frequency 1 kHz for the overall force control loop. This controller made it also possible to vary the time delay as integer multiples of 1 ms, and to set the control force by the pulse with modulation (PWM) of supply voltage of the DC motor. Time delay was varied between 20 and 200 ms, that are significantly larger than the sampling period 1 ms, therefore, the system can be considered as a continuous-time system. The modal mass and the damping ratio were experimentally determined: $m = 29.57$ kg and $b = 1447$ Ns/m. The Coulomb friction was measured to $C = 16.5$N. More details on the experimental identification of the system parameters can be found in [11]. The desired force was $F_\mathrm{d} = 50$ N.

During the measurements, the time delay was fixed and the proportional gains was increased slowly, until the process lost stability for perturbations larger than 50 N. The displacement of the force sensor was recorded during the loss of stability in order to analyze the frequency content of the motion. Then, the gain P was set to 90% of the critical value to obtain a stable process, the system was perturbed three times and the resulted force errors was documented (three for each fixed time delay).

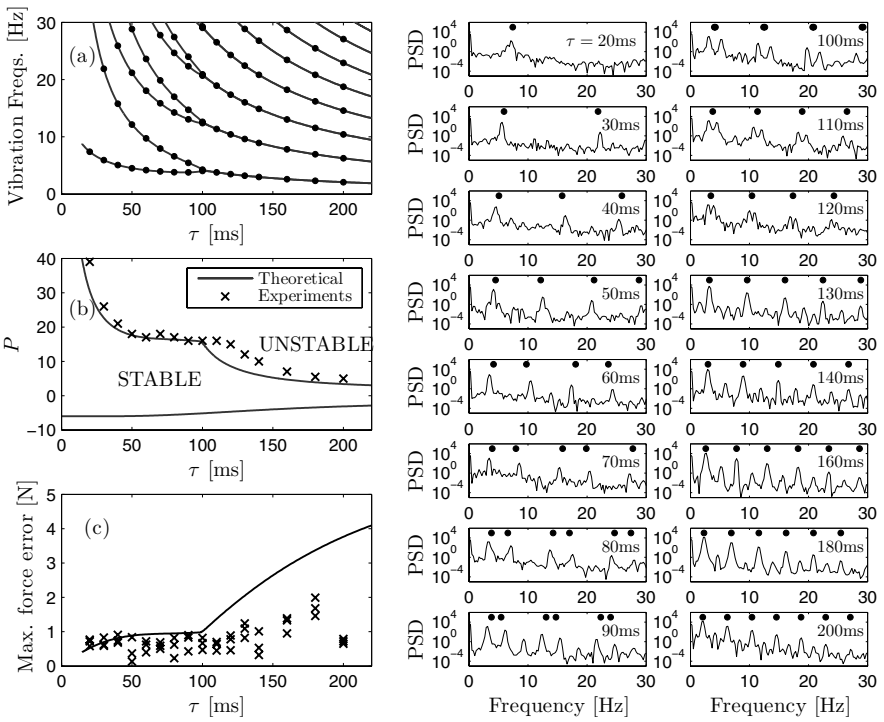

Fig. 5 Experimental and theoretical stability charts (b) and force errors (c), theoretical vibration frequencies (a), and experimental PSD diagrams (right panels) for the act-and-wait control concept.

Figure 4 presents the comparison of the theoretical and the experimental results for the continuous control case. In panels (b) and (c) crosses denote the experimental stability boundaries and the experimental force errors, respectively. Panel (a) presents the theoretically predicted vibration frequencies that are also shown in the experimental power spectra density (PSD) diagrams by black dots. It can clearly be seen that the experimental results shows good agreement with theoretical predictions. Especially the stability boundaries and the vibration frequencies coincide well. The experimental force errors were larger than the theoretical ones for certain cases.

Figure 5 presents similar comparison of the theoretical and the experimental results for the act-and-wait control case. The experimental results verify the theoretical predictions: for the act-and-wait control concept, the proportional gains can essentially be increased without loosing stability. Since the force error is inversely proportional to the gain P according to Eq. (11), it can significantly be decreased by using the act-and-wait concept. This is clearly confirmed by the experiments, the measured force errors were significantly smaller for the act-and-wait controller than for the continuous controller, as it is shown in panels (c) in Figures 4 and 5.

7 Conclusions

The act-and-wait control concept was applied to a force control problem with feedback delay and compared to the traditional, continuous control concept. Stability charts were constructed that plots the critical proportional gains, where the process looses stability, as function of the feedback delay. It was shown that the application of the act-and-wait concept allows the use of larger proportional gains without loosing stability. Since the force error decreases with the control gain applied, the accuracy of the force control process can significantly be increased if the act-and-wait concept is used. The theoretical results were confirmed by experiments for a range of feedback delays. Vibration frequencies at the stability boundaries were used to verify the model. The theoretically predicted frequencies agreed well with the experimentally determined PSD diagrams, and the decreasing tendency of the force error for increasing feedback delay were also confirmed by experiments.

Acknowledgements This work was supported in part by the János Bolyai Research Scholarship of the Hungarian Academy of Sciences (T.I.), by the Hungarian National Science Foundation under grants no. OTKA T068910 (G.S.) and K72911 (T.I.).

References

1. Craig, J. J.: *Introduction to Robotics Mechanics and Control*, Addison-Wesley, Reading, MA (1986).
2. Stépán, G.: Vibrations of machines subjected to digital force control, *International Journal of Solids and Structures* (2001) **38**(10–13), 2149–2159.
3. Kim, W.S., Bejczy, A.K.: Demonstration of a high-fidelity predictive preview display technique for telerobotic servicing in space, *IEEE Transactions on Robotics and Automation* (1993) **9**(5), 698–704.
4. Shakkottai, S., Srikant, R., Meyn, S.: Bounds on the throughput of congestion controllers in the presence of feedback delay, *IEEE/ACM Transactions on Networking* (2003) **12**(6), 972–981.
5. Kovács, L.L., Insperger, T., Stépán, G.: Teaching-in force control of industrial robots used in medical applications, in *Proc. 15th CISM-IFToMM Symposium on Robot Design, Dynamics and Control*, Rom-04-46 (2004).
6. Insperger, T., Stépán, G., Act-and-wait control concept for discrete-time systems with feedback delay, *IET – Control Theory & Applications* (2007) **1**(3), 553–557.
7. Insperger, T.: Act-and-wait concept for time-continuous control systems with feedback delay, *IEEE Transactions on Control Systems Technology* (2006) **14**(5), 974–977.
8. Stépán, G., Insperger, T.: Stability of time-periodic and delayed systems – A route to act-and-wait control, *Annual Reviews in Control* (2006) **30**(2), 159–168.
9. Stépán, G., Steven, A., Maunder, L.: Design principles of digitally controlled robots, *Mechanism and Machine Theory* (1990) **25**(5), 515–527.
10. Insperger, T., Stépán, G., Turi, J.: On the higher-order semi-discretizations for periodic delayed systems, *Journal of Sound and Vibration*, in press (2008).
11. Kovács, L,L., Galambos, P., Juhász, A., Stépán, G.: Experiments in the stability of digitally control of robots, in *Proc. 9th Conference on Dynamical Systems Theory and Applications* (2007).

Design of a Disturbance Observer and Model-Based Friction Feedforward to Compensate Quadrant Glitches

Z. Jamaludin, H. Van Brussel and J. Swevers

Abstract Accurate motion control requires measures to compensate the effects of friction that contribute to positioning and contour tracking errors. The complex nonlinear behaviour of friction at motion reversal causes a unique tracking error known as quadrant glitch. Friction can only be partly compensated using linear feedback control strategies such as PID, cascade P/PI or state-feedback control. Model and non-model based friction compensation strategies are necessary to acquire sufficiently high path and tracking accuracy. This paper analyses and validates experimentally three different friction compensation strategies for a linear motor-based xy feed drive of a high-speed milling machine: (i) friction model based feedforward, (ii) an inverse-model-based disturbance observer, and (iii) the combination of friction model feedforward and disturbance observer. Two different friction models are considered: a simple static friction model and the recently developed Generalized Maxwell-slip (GMS) friction model. The combination of feedforward based on the GMS friction model and the inverse model-based disturbance observer yields the smallest radial tracking error and glitches.

1 Introduction

Friction is a highly nonlinear phenomenon especially at velocity reversal. Quadrant glitches, characterized by spikes at quadrant locations during circular motion,

Z. Jamaludin
Department of Mechanical Engineering, Div. P.M.A., Katholieke Universiteit Leuven, Celestijnenlaan 300B, Heverlee, B-3001 Leuven, Belgium; E-mail: zamberi.jamaludin@student. kuleuven.be

H. Van Brussel
Department of Mechanical Engineering, Div. P.M.A., Katholieke Universiteit Leuven, Celestijnenlaan 300B, Heverlee, B-3001 Leuven, Belgium; E-mail: hendrik.vanbrussel@mech.kuleuven.be

J. Swevers
Department of Mechanical Engineering, Div. P.M.A., Katholieke Universiteit Leuven, Celestijnenlaan 300B, Heverlee, B-3001 Leuven, Belgium; E-mail: jan.swevers@mech.kuleuven.be

H. Ulbrich and L. Ginzinger (eds.), Motion and Vibration Control, 143–153.

are a direct result of this highly nonlinear behaviour. Friction can only be partly compensated using linear feedback control strategies such as PID, cascade P/PI or state-feedback control. More advanced technique must be incorporated to achieve sufficiently high path and tracking accuracy.

Several simple and advanced friction models are proposed in the literature. The most simple friction models consider the friction sliding regime only. These models are a static map between friction force and velocity, e.g. viscous, Coulomb and Stribeck friction models. A first attempt in describing the more complex friction behaviour in pre-sliding regime was accomplished in 1977 [4]. In 1995, the LuGre model is proposed. The model captures most of the observed frictional behaviours including Coulomb friction, Stribeck effect, and hysteresis [3]. The model is known for its simplicity and relatively good performance but it fails to describe the hysteresis non-local memory behaviour of friction force in pre-sliding regime.

The Leuven model is an improvement of the LuGre model that includes non-local memory hysteretic behaviour. Recently, a further improvement of the Leuven model, called the Generalized Maxwell-slip (GMS) friction model [1], is developed and exhibits superior results in simulation of friction behaviour in the pre-sliding and sliding regimes. The main disadvantage of the GMS model is its complexity and large number parameters, which complicates its application in control.

Various model and non-model based friction compensation schemes for different applications are discussed in literature. A survey on friction models and compensation methods for control of machines with friction is given in [2]. Several alternative approaches have been developed such as: a Maxwell-slip-model-based nonlinear gain scheduling controller yielding fast response and low steady-state error for friction compensation in electro-mechanical systems [7], a repetitive controller, a non-model based friction compensation approach yielding improve tracking performance and quadrant glitches [8], and the GMS friction model feedforward and a Kalman filter based disturbance observer, yielding the best tracking performance in friction compensation on a dedicated test setup (a tribometer) [6]. This paper focuses on the modelling, identification, and compensation of friction forces in machine tools for accurate drive control system. Both friction-model based feedforward, using a simple static friction model and the advanced GMS model, and an inverse-model disturbance observer [9] are considered.

This paper is organized as follows. Section 2 describes the experimental set-up. Section 3 discusses the different friction models and their identification methods. Section 4 discusses the experimental validation of the different friction compensation schemes and finally, Section 5 concludes the paper.

2 Experimental Set-up

The test setup that is considered in this paper is a linear-drive based xy feed table of a high-speed milling machine (see Figure 1). The upper stage y-axis is driven by a single ETEL iron-core linear motor. The bottom stage x-axis is driven by two ETEL

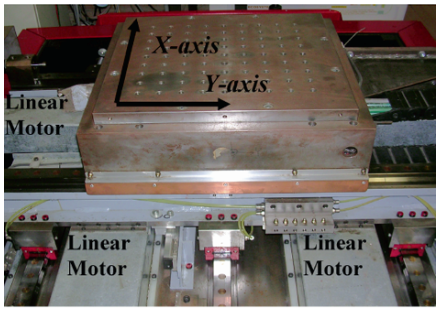

Fig. 1 A xy feed table with three linear drives for high speed milling application.

iron-core linear motors. The stages run on Schneeberger preloaded roller guideways. Both axes are equipped with a 0.25 µm resolution Heidenhain linear encoder. The velocity signal is calculated by means of numerical differentiation of the position in combination with a first-order low-pass filter. This filter is added to attenuate amplified measurement noise associated with the derivative action. The controller is implemented on a dSPACE 1103 DSP controller board linking the host computer to the ETEL drives. The dynamic coupling between both axes is negligible. The system dynamics can be described by two single-input single-output models.

The linear dynamic relation between input voltage and table position z [m], with $z = x$ and $z = y$ for the x and y axes respectively, is identified experimentally as a second order model with a time delay:

$$G(s) = \frac{Z(s)}{U(s)} = \frac{B}{s(s+A)} \cdot e^{-sT_d}, \tag{1}$$

with $A = 28.57$ volt/s, $B = 4.526$ m, $T_d = 0.00065$ s for the x-axis and $A = 20.00$ volt/s, $B = 8.916$ m, $T_d = 0.00065$ s for the y-axis.

3 Friction Models

Friction is categorized according to its presliding and sliding regimes. In pre-sliding regime, friction force is predominantly dependent on displacement. In sliding regime, the friction force is predominantly dependent on the sliding velocity.

3.1 Static Friction Model

Static friction models describe the steady-state friction behaviour in sliding regime and hence are dependent on the sliding velocity v. The considered static friction model incorporates Coulomb, viscous, and Stribeck friction,

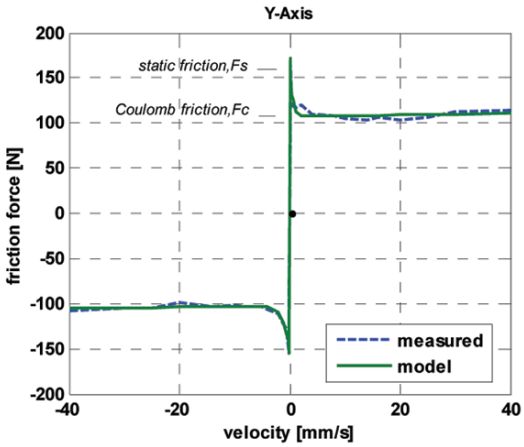

Fig. 2 Measured and modelled static friction-velocity map.

$$F(v) = \left\{ F_c + (F_s - F_c) \cdot \exp\left(- \left| \frac{v}{V_s} \right|^{\delta} \right) + \sigma \cdot |v| \right\} \cdot \text{sign}(v). \tag{2}$$

F_c, F_s, and σ represent the Coulomb, static and viscous friction coefficients respectively. The Stribeck friction model parameters are the Stribeck velocity V_s and the Stribeck shape factor δ.

3.1.1 Identification of Static Friction Model

At constant velocity, the motor force equals the friction force and is represented by the force control command signal. Constant velocity is enforced using a manually tuned PID controller and a constant velocity reference signal. This experiment is repeated for the following constant velocities of 0.010, 0.040, 0.080, 0.2, 0.4, 0.5, 1, 2, 4, 5, 8, 10, 14, 16, 20, 25, and 30 mm/s. Figure 2 shows the measured and the fitted static friction force model (2). The identified parameters are $F_c = 105$N, $F_s = 165$ N, $1/V_s = 0.001$ sμm^{-1}, $\sigma = 0.00004$ Nsμm^{-1}, and $\delta = 1$.

3.2 Generalized Maxwell-Slip Model (GMS) [1]

The GMS friction model incorporates: (i) the Stribeck curve for constant velocity, (ii) hysteresis function with non-local memory for the pre-sliding regime, and (iii) frictional memory for the sliding regime. It has similar structure to the Maxwell-slip structure, that consists of a parallel connection of N different elementary slip-blocks and springs (see Figure 3). Each block represents a generalized asperity of

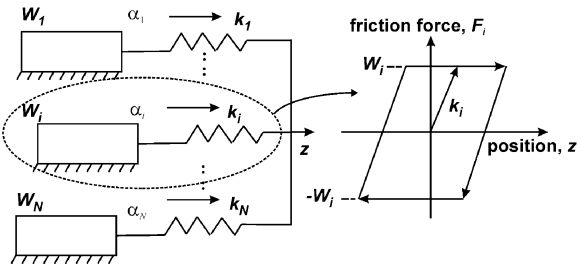

Fig. 3 Maxwell-slip friction with N-elementary slip blocks.

the contact surface that can either stick or slip and each element i has a common input, the position z, an elementary stiffness k_i, a state variable α_i that describes the element position, a maximum elementary Coulomb force W_i and a friction output F_i. A new state equation that characterizes sliding dynamics of each elementary slip-block replaces the original Coulomb law in the Maxwell-slip model structure.

Sticking occurs during motion reversal and as velocity approaches zero. During sticking, the dynamic behaviour of an elementary slip-block is then described by a spring model with stiffness k_i:

$$\frac{\mathrm{d}F_i}{\mathrm{d}t} = k_i v. \tag{3}$$

Slipping occurs if the elementary friction force F_i equals a maximum value $W_i = \alpha_i s(v)$. α_i is the normalized sustainable maximum friction force of each element during sticking and $s(v)$ is the Stribeck curve. The state equation describing the dynamic behaviour of an elementary slip-block is

$$\frac{\mathrm{d}F_i}{\mathrm{d}t} = \operatorname{sign}(v) \cdot C \cdot \left(\alpha_i - \frac{F_i}{s(v)}\right). \tag{4}$$

The constant parameter C indicates the rate at which the friction force follows the Stribeck effect in sliding. The total friction force is the summation of the output of all elementary state models and a viscous friction term σ (if present).

$$F(v) = \sum_{i=1}^{N} F_i(v) + \sigma \cdot v(t). \tag{5}$$

3.2.1 Identification of GMS Model Parameters

A GMS model with four elementary slip-blocks is selected, yielding a total of 13 model parameters: two parameters from each of the four elements and another five parameters from the state equations in sliding regime. Friction behaves as a hysteretic function of displacement with non-local memory behaviour in pre-sliding

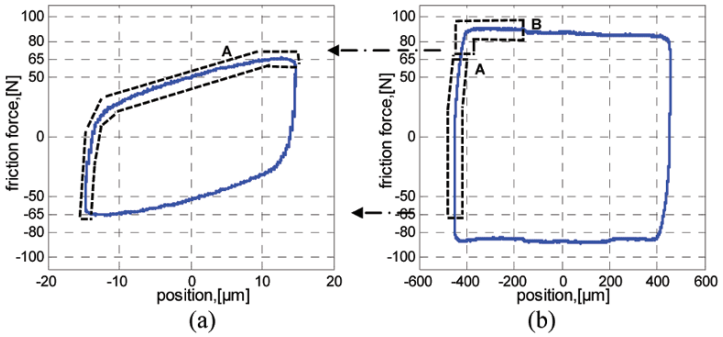

Fig. 4 Friction force and position for sinusoidal reference signal of 0.1 Hz and amplitudes of (a) 15 μm and (b) 450 μm.

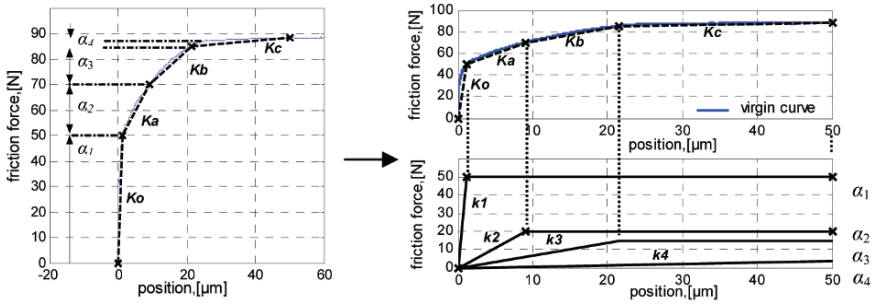

Fig. 5 Virgin curve with selected points for identification of GMS friction model parameters.

Table 1 Identified GMS friction model parameters.

$F_c = 105$ n	$F_s = 165$ N	$V_s = 1000$ μms^{-1}	$\sigma = 0.00004$ Nsμm^{-1}	$\delta = 1$
α_i [N]	$\alpha_1 = 0.566$	$\alpha_2 = 0.227$	$\alpha_3 = 0.170$	$\alpha_4 = 0.039$
k_i [N/μm]	$k_1 = 99.94$	$k_2 = 1.364$	$k_3 = 1.081$	$k_4 = 0.119$

regime. This behaviour is characterized by the so-called virgin curve. The virgin curve is derived from a sinusoidal excitation of the system. The frequency and amplitude of the sinusoidal are selected to minimize inertia effect and to remain in the pre-sliding regime. The measurement obtained with the small excitation amplitude (Figure 4a) provides detailed information about the friction-displacement behaviour in pre-sliding regime away from breakaway, while the measurement obtained with the larger excitation amplitude (Figure 4b) provides information close to breakaway. Figures 4a and b clearly indicate which part of the measurement is selected to compose the virgin curve (see Figure 5). The parts are combined, reduced by a factor of 2 (the combined parts constitute a double-stretched version of the virgin curve), and shifted to the origin (0 μm, 0 N) to generate the virgin curve.

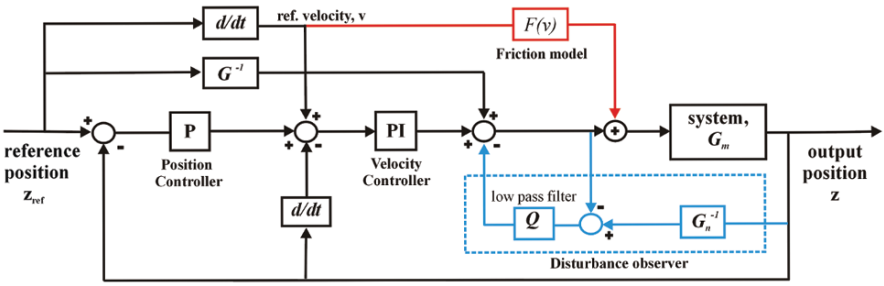

Fig. 6 Cascade P/PI controller with friction model-based feedforward and an inverse-model-based disturbance observer.

The four α_i's and k_i's slip-block parameters are estimated from the manually selected knots and slopes Ko, Ka, Kb, Kc of a piecewise linear function that approximates the virgin curve (see Figure 5). From the theory of superposition, K_i's, k_i's, and α_i's are related as in (6). The identified GMS model parameters and the static friction model parameters (F_c, F_s, V_s, σ, and δ) are summarized in Table 1.

$$\begin{aligned} \alpha_1 + \alpha_2 + \alpha_3 + \alpha_4 &= \Sigma W_i \\ k_1 + k_2 + k_3 + k_4 &= K_o \\ k_2 + k_3 + k_4 &= K_b \\ k_4 &= K_c \ . \end{aligned} \tag{6}$$

4 Friction Force Compensation Design and Experimental Validation

This section discusses the friction compensation design and the experimental validation for the considered system. Each axis is controlled independently using the same control structure shown in Figure 6. It consists of a position controller, static and GMS friction models feedforward, and an inverse-model-based disturbance observer.

4.1 Position Controller and Feedforward Friction Compensation

The position controller is a cascade PI velocity feedback and P position feedback controller. The parameters are selected based on gain margin and phase margin considerations of the open loop transfer function [5]. Velocity feedforward and an inverse-model position reference feedforward are added to eliminate tracking errors

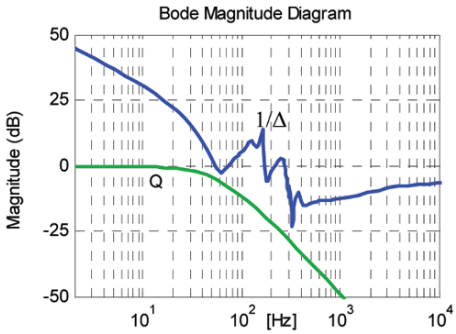

Fig. 7 Bandwidth limitations of the Q-filter.

caused by inertial effects and viscous friction. Feedforward friction compensation is based on either the static friction model (2), or the GMS model (3–5). The input to these models is the reference tracking velocity v.

4.2 Inverse Model-Based Disturbance Observer

The disturbance observer estimates the disturbance forces along with any modelling errors by subtracting the control command signal from the estimated input obtained by the inverse of the nominal plant model $G_n(s)$ which is identical to model (1) without delay. The delay is removed from the plant model in order to obtain a causal inverse. A low pass filter, known as the Q-filter [9], is added to provide system stability. The bandwidth of the filter Q is limited by the unmodelled dynamics, expressed as a multiplicative perturbation $\Delta(f)$,

$$\Delta(f) = \frac{G_m(f) - G_n(f)}{G_n(f)}. \tag{7}$$

$G_m(f)$ and $G_n(f)$ are the frequency response functions of the system and of $G_n(s)$ respectively. The robust stability of the disturbance observer inner loop is guaranteed if [9]

$$||T(j\omega) \cdot \Delta(\omega)||_\infty \leq 1\ . \tag{8}$$

$T(s)$ is the complimentary sensitivity transfer function of the disturbance observer loop. Figure 7 visualizes for the x-axis the Q-filter bandwidth limitation at 60 Hz. The magnitude of the Q-filter frequency characteristic must lie below the amplitude characteristic of the inverse multiplicative perturbation $\Delta(f)$ line and thus limits the observer overall compensation performance.

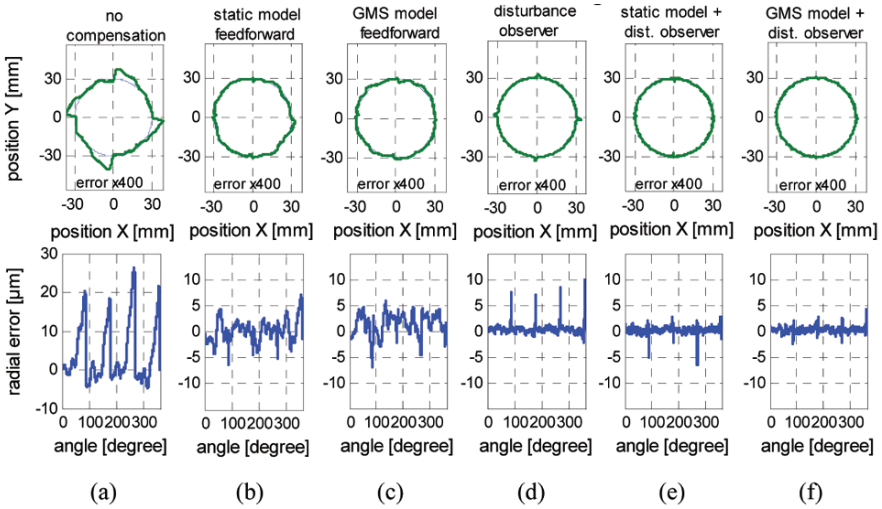

Fig. 8 Measured circular tests (30 mm radius) and radial tracking error for different friction compensation schemes at 100 mm/s tangential tracking velocity.

Table 2 Quadrant glitch magnitudes for different friction compensation strategies.

Friction Compensation Schemes	a	b	c	d	e	f
Quadrant Glitch Magnitude	22 µm	7 µm	6 µm	8 µm	5 µm	3 µm

4.3 Experimental Results

Friction compensation performance is validated based on the magnitude of the quadrant glitch that occurs near zero velocity or at motion reversal. It is typically demonstrated on a xy feed table during circular tracking test. The friction compensation performances is analysed and compared for the following different control configurations:

(a) no friction feedforward and no inverse model disturbance observer
(b) static friction model feedforward
(c) GMS friction model feedforward
(d) inverse model disturbance observer
(e) static friction model feedforward and inverse model disturbance observer
(f) GMS model feedforward and inverse model disturbance observer

Figure 8 shows the circular test results of the various friction compensation schemes. Feedforward friction compensation and inverse model-based disturbance observer reduce the quadrant glitches considerably.

A combined disturbance observer and feedforward of GMS friction model yields the best quadrant glitch reduction. A quadrant glitch magnitude of less than 3 micrometer was recorded. Table 2 summarizes the experimental results.

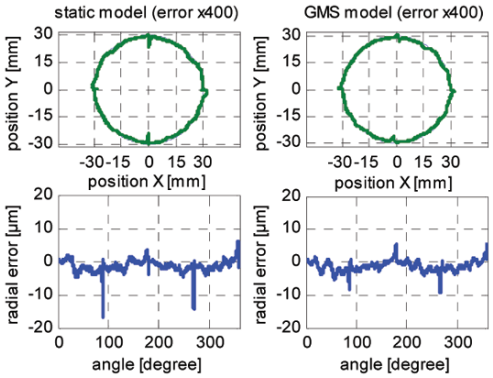

Fig. 9 Measured circular tests for tangential tracking velocity of 10 mm/s.

The improvement obtained by the GMS friction model over static friction model is small such that for this tangential tracking velocity (100 mm/s), the use of complex GMS friction model cannot be motivated. However, by reducing the tracking velocity to 10 mm/s, the presliding regime becomes more dominant and the benefit of using the GMS friction model that includes hysteresis with non local memory becomes more pronounced. This is illustrated in Figure 9.

5 Conclusions

Quadrant glitches, caused by the complex non-linear behaviour of friction at velocity reversal, can be compensated effectively using a combination of friction model feedforward and an inverse-model based disturbance observer. The benefits of using an advanced friction model like the Generalized Maxwell-slip (GMS) model are especially clear at slow motions where the pre-sliding friction is dominant. A simple approach based on separate pre-sliding and sliding measurements is presented to identify this complex GMS model.

Acknowledgements This work is supported by the Ministry of Higher Education, Malaysia and the Technical University Malaysia-Malacca. This work has been carried out within the framework of research project G.0446.06 of the Research Foundation – Flanders and also benefits from K.U.Leuven-BOF EF/05/006 Centre-of-Excellence Optimization in Engineering and from the Belgian Program on Interuniversity Poles of Attraction IAP VI/4 DYSCO (Dynamic Systems, Control and Optimization) initiated by the Belgian State, Prime Minister's Office for Science, Technology and Culture.

References

1. Al Bender, F., Lampaert, V., Swevers, J.: The Generalized Maxwell-Slip Friction Model: A Novel Model for Friction Simulation and Compensation. *IEEE Trans. on Automatic Control* **50**(11), 1883–1887 (2005).
2. Armstrong-Hélouvry, B.P., Dupont, Canudas de Wit, C.: A Survey of Models, Analysis Tools, and Compensation Methods for the Control of Machine with Frictions. *Automatica* **30**(7), 1083–1138 (1994).
3. Canudas de Wit, C. and Lishinsky, P.: Adaptive Friction Compensation with Partially Known Dynamic Friction Model. *Int. J. Adaptive Control and Signal Proc.* **11**, 65–80 (1997).
4. Dahl, P.R.: Measurement of Solid Friction Parameters of Ball Bearings. In *Proc. of 6th Annual Symp. on Incremental Motion, Control System and Devices* (1977).
5. Jamaludin, Z., Van Brussel, H., Swevers, J.: Classical Cascade and Sliding Mode Control Tracking Performances for a x-y Feed Table of a High-Speed Machine Tools. *Int. J. Precision Technology* **1**(1), 65–74 (2007).
6. Lampaert, V., Swevers, J., Al Bender, F., Ganseman, C., Prajogo, T.: Modification of the Leuven Integrated Friction Model Structure. *IEEE Trans. on Automatic Control* **47**(4), 683–687 (2002).
7. Tjahjowidodo, T., Al Bender, F., Van Brussel, H., Symens, W.: Friction Characterization and Compensation In Electro-Mechanical Systems. *J. of Sound and Vibration* **308**(3–5), 632–646 (2007).
8. Tung, E.D., Anwar, G., Tomizuka, M.: Low-Velocity Friction Compensation and Feedforward Solution Based on Repetitive Control. *J. Dynamics System Measurement and Control* **115**, 279–284 (1993).
9. Yi, L., Tomizuka, M.: Two-Degree-of-Freedom Control with Robust Feedback Control for Hard Disk Servo System. *IEEE/ASME Trans. on Mechatronics* **4**(1), 17–24 (1999).

Active Vibration Control of Multibody Rolling Contact System

Veli-Matti Järvenpää and Lihong Yuan

Abstract. The aim of this work is to use multibody analysis to study rolling contact vibrations and then test the active control methods to eliminate these vibrations. The system considered is the rolling contact of two metal rolls. The contact is softened by using a thin polymer coating on one roll. The polymer cover generates a regenerative vibration source to the contact because the polymer does not recover fully before re-entering to the contact. This phenomenon creates a limit cycle vibration condition to the contact. The modeling of the system is based on the multibody dynamics. The metal rolls are modeled as super elements by using multibody equations and the component mode synthesis approach. The polymer cover is modeled analytically by giving an expression for the contact line load. The nonlinear stiffness of the cover is included. The regenerative vibration source is introduced to the system as a time delay term in the line load equations. The time domain responses are solved by using numerical time integration. The active vibration control is carried out by introducing external force actuators into the multibody model. The strategy is to create a feedback force with same magnitude and an opposite phase as the regenerative vibration source. As results the time domain responses of several different cases are compared and discussed.

1 Introduction

The rolling contact of two paper machine calendering rolls is studied. The paper calendering process is used to produce a paper with constant thickness. So-called nip contact of two metal rolls is used to finish the paper surface. Calendering units are located at the end of the paper manufacturing line. In a unit the rolls are compressed together by hydraulic actuators to create optimal line load conditions for the

Veli-Matti Järvenpää and Lihong Yuan
Department of Mechanics and Design, Tampere University of Technology, FI-33101 Tampere, Finland; E-mail: {veli-matti.jarvenpaa, lihong.yuan}@tut.fi

H. Ulbrich and L. Ginzinger (eds.), Motion and Vibration Control, 155–164.

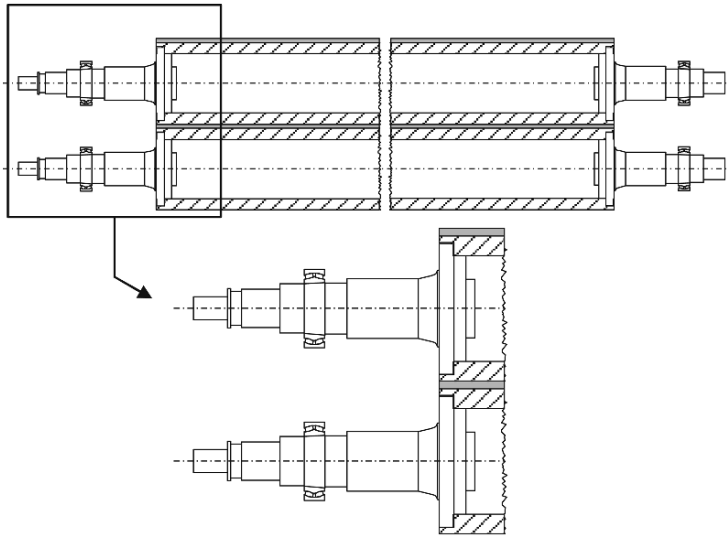

Fig. 1 The roll contact layout.

process. The paper web enters to the nip and undergoes deformations and surface polish to achieve equal thickness. The contact is softened by introducing a polymer cover on the surface of one roll due to the process requirements. The polymer cover layer increases the length of the contact in the running direction and therefore produces averagely more smooth paper surface finish. The polymer layer between the rolls, however, makes the dynamics of the rolling contact more complicated to understand. Because the polymer material is soft, hyperelastic and also viscoelastic the mechanical behavior of the rolling contact becomes nonlinear. It has been experienced that the polymer cover can create complex vibration phenomena. The dynamics is sensitive to the operational and design parameters and this can create undesired vibrations which are difficult to predict accurately. The aim in this paper is to use numerical simulation model of the roll contact to study the active control designs for the system. The model is based on the test roll unit in TUT's laboratory environment (Figure 1). This test unit is about half scale of the real size machine with 4.4 meter length cast iron rolls with one polymer coated roll. It includes build-in wireless strain and acceleration measurement and data transfer system. The paper web has not been included in the test unit, but this still is very beneficial environment to study the dynamics of the roll contact.

The numerical model is based on multibody dynamics [1, 2]. Each roll has its own 3D super element, which are based on the component mode synthesis approach by using modal coordinates with sets of lowest semi-definite eigenvectors [3, 4]. The basic geometry of the rolls is modeled by using finite element meshes. The main task is to introduce an appropriate contact formulation to the rolls. The contact of the rolls is 3-dimensional line contact, which includes the crowning of the roll surfaces and the non-linear polymer material characteristics. The contact model is an

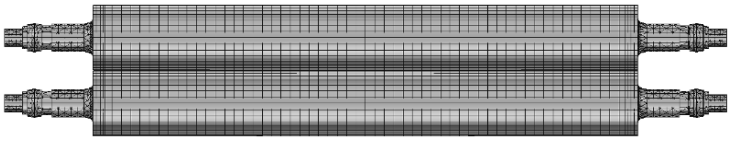

Fig. 2 The finite element meshes.

analytical formulation of the line load distribution. Because the rolls are making spin rotation, the line load needs to smoothly move on the surfaces within each element and across element boundaries. This has been modeled by describing equivalent element nodal forces to the surface elements as a function of the rotation angle. The contact formulation is described by an expression which relates the contact penetration and the contact width in the rolling direction. The penetration function is calculated from the nodal displacements and the line load is solved accordingly. The contact is described by contact force coupling in the right hand side of the system equations. The complete dynamical model consists of two super elements and the contact formulation. The time domain solution of the system requires a non-linear time integration procedure [5] and it is implemented in MATLAB environment.

The viscoelastic recovery of the polymer is included in the system equations as a time delay term. The method of steps is used in the numerical solution. The deformation history of the cover is recorded as a penetration function and this is introduced to the system equations as a delayed feedback or a regenerative vibration source. The time delay is non-constant depending on the roll rotation time. To obtain the correct deformation history at the right times according to the stepping of the time integration solution procedure, a time domain interpolation of the penetration history is used.

2 Equations of Motion

The modeling is based on following assumptions. Firstly, one spin rotation for each roll is considered. The other rotations are assumed small, because the roll bearings at roll ends limit roll movements. This simplifies the coordinate transformation significantly. The roll translations are included and they are compensated by forces due to the bearing stiffness. The rolls are illustrated in Figure 2. Secondly, the lumped mass formulation is used. Linear continuum element meshes are used for determining the modal vectors of the rolls. Finally, the deformations are described by a set of modal vectors. The semi-definite (free-free) modal vectors are used (Figure 3). The equations of motion of a roll are [3, 4]

$$\begin{bmatrix} (\mathbf{x}_G + \boldsymbol{\Omega}_{\boldsymbol{\eta}})^T \, \mathbf{M}_{xy} (\mathbf{x}_G + \boldsymbol{\Omega}_{\boldsymbol{\eta}}) & (\mathbf{x}_G + \boldsymbol{\Omega}_{\boldsymbol{\eta}})^T \, \mathbf{M}_S^T \, \boldsymbol{\Omega} \\ \boldsymbol{\Omega}^T \, \mathbf{M}_S (\mathbf{x}_G + \boldsymbol{\Omega}_{\boldsymbol{\eta}}) & \boldsymbol{\Omega}^T \, \mathbf{M} \boldsymbol{\Omega} \end{bmatrix} \begin{bmatrix} \ddot{\theta} \\ \ddot{\boldsymbol{\eta}} \end{bmatrix}$$

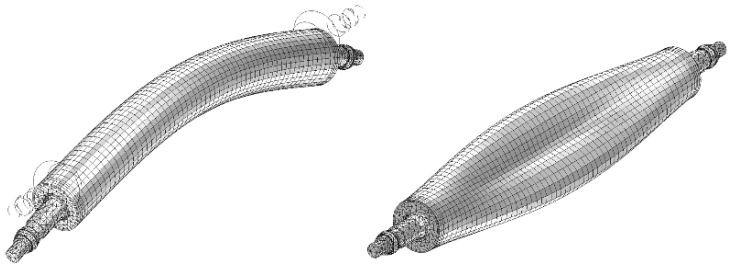

Fig. 3 The 1st free-free bending mode (left) and 1st shell mode (right) of a roll.

$$+\begin{bmatrix} 2(\mathbf{x}_G+\boldsymbol{\Omega}_{\boldsymbol{\eta}})^T\,\mathbf{M}_{xy}\,\boldsymbol{\Omega}\dot{\boldsymbol{\eta}} & \mathbf{0} \\ \mathbf{0} & 2\dot{\theta}\boldsymbol{\Omega}^T\,\mathbf{M}_S\,\boldsymbol{\Omega} \end{bmatrix}\begin{bmatrix} \dot{\theta} \\ \dot{\boldsymbol{\eta}} \end{bmatrix} \tag{1}$$

$$+\begin{bmatrix} 0 & \mathbf{0} \\ \mathbf{0} & \boldsymbol{\Omega}^T\,\mathbf{K}\boldsymbol{\Omega} \end{bmatrix}\begin{bmatrix} \theta \\ \boldsymbol{\eta} \end{bmatrix}-\begin{bmatrix} 0 \\ \dot{\theta}^2\,\boldsymbol{\Omega}^T\,\mathbf{M}_{xy}(\mathbf{x}_G+\boldsymbol{\Omega}\boldsymbol{\eta}) \end{bmatrix}=\begin{bmatrix} \mathbf{f}^T\,\frac{\partial \mathbf{R}^T}{\partial\theta}(\mathbf{x}_G+\boldsymbol{\Omega}\boldsymbol{\eta}) \\ \boldsymbol{\Omega}^T\,\mathbf{Rf} \end{bmatrix},$$

where θ is the rotation angle of a roll; $\boldsymbol{\eta}$ the vector of modal coordinates; $\boldsymbol{\Omega}$ the modal matrix; $\mathbf{x}_G$ the vector of initial x and y nodal coordinates; $\mathbf{M}$ the lumped mass matrix; $\mathbf{M}_{xy}$ the mass matrix with nodal mass in x and y directions only; $\mathbf{M}_s$ skew symmetric mass matrix; $\mathbf{K}$ the stiffness matrix; $\mathbf{f}$ the applied force vector and; $\mathbf{R}$ the rotation matrix in xy plane.

The roll xyz coordinate system is oriented that z axis is coaxial to the rotation axis and the xy plane is parallel to the cross-section of the roll.

3 Contact Modeling

The polymer cover is much softer than the metallic rolls. This makes the contact spring force modeling most suitable for this type of a contact. The principle is illustrated in Figure 4. The contact is described as a line contact by using a contact line load distribution between the rolls which represents the polymer cover of the upper roll [4]. This approach is similar as the elastic foundation model [7]. Typically the stiffness distribution is almost constant in the axial direction due to the proper design of the roll crowning. The crowning is introduced by the enforced displacement function $cr(z)$ which describes the total value of the crowning.

The contact line load is non-linear due to the viscoelastic material properties of the polymer cover [7]

$$p(z) = K_n\,\varepsilon(z,t)^{3/2}\,. \tag{2}$$

The K_n is the contact coefficient which takes into account the viscoelastic material behavior. Only the initial modulus and the initial recovery time are considered in [7].The contact penetration $\varepsilon(z,t)$ splits into three different components

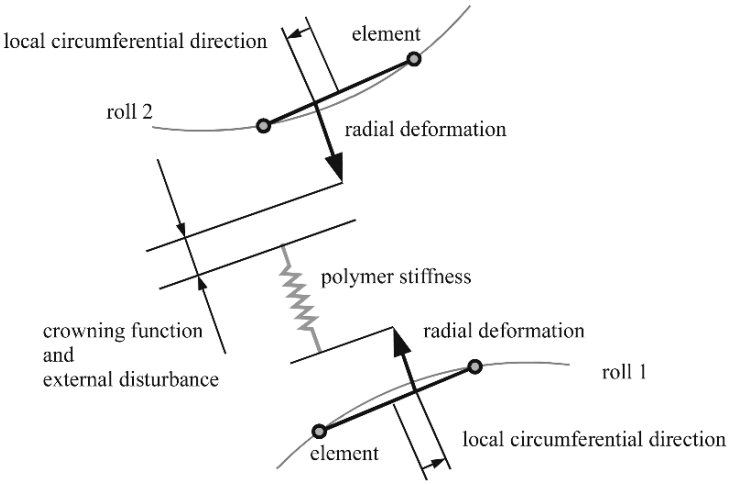

Fig. 4 The contact line load between opposing elements. The stiffness of the polymer coating and the crowning of the rolls are functions of z-axis of rolls.

$$\varepsilon(z,t) = x_1(z,t) - x_2(z,t) + cr(z) + z_{pw}(z,t), \tag{3}$$

where the first two parts represent the relative roll motion at the contact line, the third is the crowning function and the last $z_{pw}(z,t)$ is any external disturbance in the contact as for example the paper thickness variation, which is not considered here. The contact line load with the regenerative vibration source takes the form [8]

$$p(z) = K_n\{\varepsilon(z,t) - \gamma\varepsilon(z,t-T)\}^{3/2}, \tag{4}$$

where T is the delay time, which is the roll revolution time. An alternative way to represent the line load (4) is to use a cubic expression

$$\begin{aligned} p(z) = k_n([\varepsilon(z,t) - \gamma_e\,\varepsilon(z,t-T)] \\ + \alpha_2[\varepsilon(z,t) - \gamma_e\,\varepsilon(z,t-T)]^2 + \alpha_3[\varepsilon(z,t) - \gamma_e\,\varepsilon(z,t-T)]^3), \end{aligned} \tag{5}$$

where α_2 and α_3 are non-linear parameters and k_n is the contact coefficient. The decay factor is [9]

$$\gamma_e = e^{-T/\tau_{\text{relaxation}}}\,. \tag{6}$$

The material specific relaxation time is

$$\tau_{\text{relaxation}} = \tau_{\text{relaxation}}\,(c_{\text{polymer}}, E_{\text{polymer}}), \tag{7}$$

where c_{polymer} and E_{polymer} are the damping and the elastic modulus of the polymer, respectively. Depending on the relaxation time the contact is affected by the cover deformations not completely vanished.

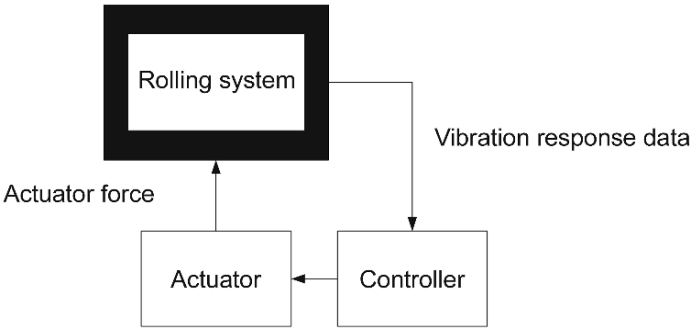

Fig. 5 The control design setup.

4 Control Design

The basis of the control scheme is to use the simulation model to represent a real-case rolling system as an input-output black box. This means that like in reality the detailed model of the rolling system is not available. The system can be observed by measurements only. Figure 5 illustrates this principle. The aim is use numerical data obtained from on-line simulation to close-loop control the actuator feedback force. Very simple linear control is used. The idea is to detect the rolling contact force amplitude, frequency and phase and adjust the actuator force accordingly to the opposite phase to kill the resonance limit cycle.

In numerical model this kind of approach is reasonably achievable. Real systems, however, include various uncertainties such as measurement inaccuracies and control loop delays, which are not considered here.

5 Numerical Results

Numerical simulation results are presented next. The aim is to study single running speed in which the delay effect causes limit cycle resonance in the contact vibrations. The reference result is the averaged contact line load response. In the method of steps procedure the initial history for the time delay determination must be created first. The rolls are accelerated to their desired speeds and the roll contact is closed. Relatively long initial simulation of 30 seconds is made to get rid of any transient effects and to obtain as smooth steady state running condition as possible. The desired line load is set to 14.9 kN/m and moderate Rayleigh damping is used for the rolls. No damping is introduced to the roll contact.

The characteristic of the roll contact vibration is the excitation of the roll beating vibration mode. This mode means that the upper and lower rolls have bending mode vibrations with opposite phases and the rolls are beating each other in the contact line. The natural frequency of this mode in this numerical study is about 92 Hz.

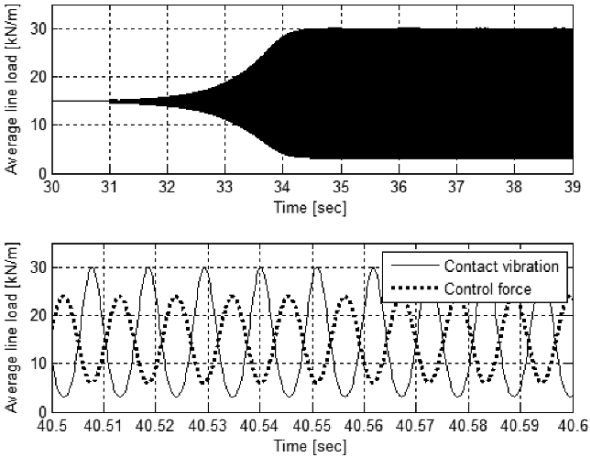

Fig. 6 The contact vibration resonance (upper) and the controlling principle (lower).

The running web speed of the rolls is 575 m/min. The time domain response of the contact line load is shown in Figure 6. The damping and the delay parameters are selected to produce large amplitude vibrations for illustrative purposes. The highest frequency component in the responses is the beating natural frequency and the limit cycle is clearly shown. Figure 6 illustrates the controlling principle of the actuator force as well.

Three cases of the actuator force location are considered. The actuator excitation is located at the bearings, at the roll shafts and most interestingly inside the roll cylinder at the contact line. In the design sense the bearing location is most natural because two other locations are on the surface of the rotating rolls.

5.1 Case 1: Actuator at Bearings

The actuator force is applied to the bearings by considering the stiffness of the bearings only (Figure 7). If the mounting structure of the roll installation is considered as well then the bearing location would be slightly more flexible. The controlled response is shown in the Figure 10 and it turns out that the actuator force at the bearing location has very small effect to the vibration levels.

5.2 Case 2: Actuator at Shafts

The actuator force is applied to the roll shafts (Figure 8). The actuator force at the bearing location has moderate effect to the vibration levels (Figure 10).

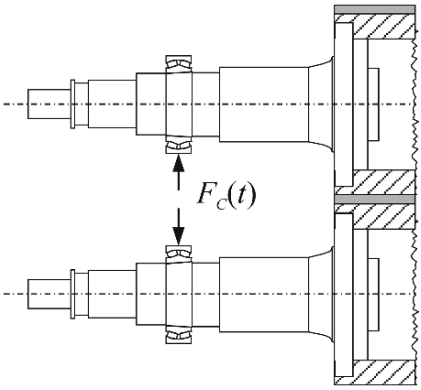

Fig. 7 The actuator setup Case 1.

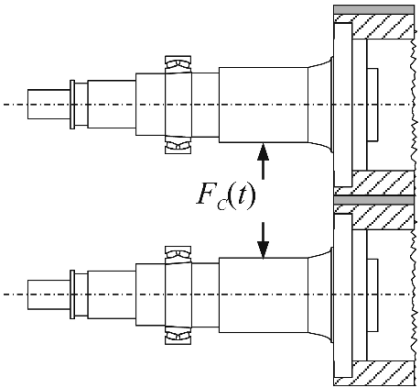

Fig. 8 The actuator setup Case 2.

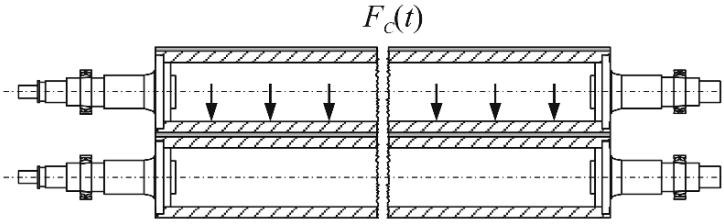

Fig. 9 The actuator setup Case 3.

5.3 Case 3: Actuator Inside Roll Cylinder

The actuator force is applied inside the upper roll cylinder at the contact line (Figure 9). This case is different because many force locations are used in the simulation. In this case the actuator forces have the best effect to the vibration levels (Figure 10).

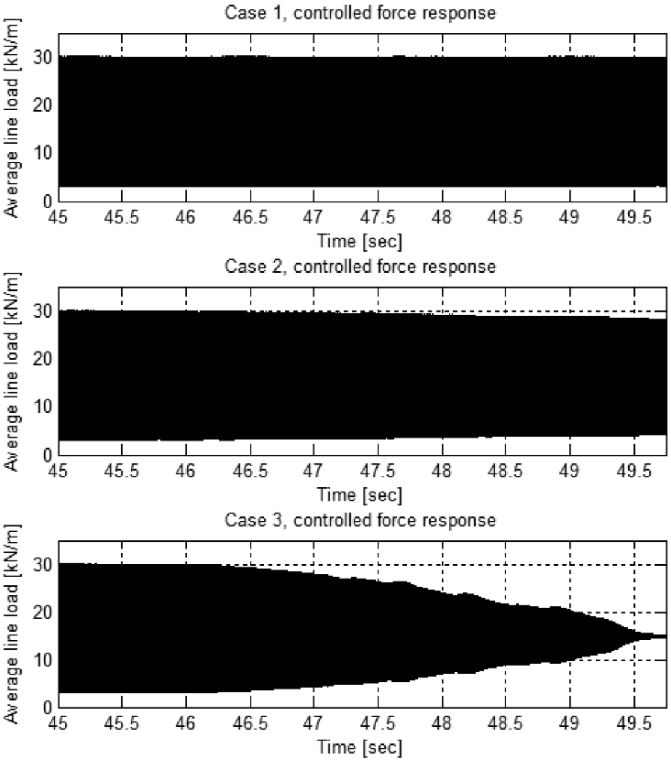

Fig. 10 The force responses in Cases 1 to 3.

6 Conclusions

The numerical modeling and active control study of a calandering roll contact with limit-cycle vibrations is presented. The modeling of the rolls, the non-linear line load contact and the time delay system is described. The resonance state of the roll system is detected in the numerical simulation results and the actuator force is applied in different locations in three cases to study how well this resonance can be controlled. According the results the best location is inside a roll cylinder which also is the most difficult location to implement in practice. The most practical location in the bearings shows the poorest performance in the results. However, the results illustrate mostly the relative performance of the three locations and the performance at the bearings can be somewhat improved by increasing the force amplitude. Also practical difficulties related to actual control of real systems are not considered. It can be concluded, however, that the results are promising. More research is needed to verify the applicability of the control to the real systems.

Acknowledgements The author would like to express gratitude to The Academy of Finland, which has provided funding for this project.

References

1. Cardona A., Géradin M., Modelling of superelements in mechanism analysis, *International Journal for Numerical Methods in Engineering* **32**(8), 1991, 245–266.
2. Shabana A., Substructure synthesis methods for dynamic analysis of multi-body systems, *Computers and Structures* **20**(4), 1985, 737–744.
3. Järvenpää V.M., Yuan L., Numerical modeling of paper machine roll contact with regenerative out-of-roundness excitation, in *Proceedings IUTAM Symposium on Multiscale Problems in Multibody System Contacts*, P. Eberhard (Ed.), Springer, Dordrecht, 2007, pp. 55–64.
4. Järvenpää V.M., *Numerical Modeling of a Roll Mechanism for Multi-Objective Dynamical Analyses*, Doctoral Thesis, Tampere University of Technology, Publication 569, Tampere, 2005.
5. Géradin M., Rixen D., *Mechanical Vibrations*, John Wiley & Sons, 1997.
6. Driver R., *Ordinary and Delay Differential Equations*, Springer-Verlag, New York, 1977.
7. Johnson K., *Contact Mechanics*, Cambridge University Press, 2003.
8. Yuan L., *Analysis of Delay Phenomena in Roll Dynamics*, Doctoral Thesis, Tampere University of Technology, 2002.
9. Sperling L., *Introduction to Physical Polymer Science*, Wiley-Interscience, New York, 1985.

Vibration Control of Hard Disk Drive with Smart Structure Technology for Improving Servo Performance

Itsuro Kajiwara, Toshio Uchiyama and Toshihiro Arisaka

Abstract In hard disk drives, vibration suppression is very important to boost the servo performance for achieving the enhanced density of the disk and following precision of the system. It has been expected that technology of smart structure will contribute to the development of small and light-weight mechatronics devices with the required performance. This study proposes a new vibration control mechanism with smart structures technology in order to achieve significant vibration suppression in hard disk drive systems. First, modeling of the system is conducted with finite element and modal analyses. Next, the control system design and closed-loop simulation are performed with the proposed vibration control mechanism composed of piezoelectric sensors and actuators. Finally, a multidisciplinary design optimization on actuator location and control system is examined to enhance the closed-loop performance of the system.

1 Introduction

In advanced mechanical systems such as magnetic and optical disk devices, structural vibration has to be suppressed to achieve the required control performance of the devices. It is required for developing the next generation hard disk drive (HDD) to suppress the actuator vibration under 40 kHz in order to achieve 2 Tb/in^2 of

Itsuro Kajiwara
Tokyo Institute of Technology, 2-12-1, O-okayama, Meguro-ku, Tokyo 152-8552, Japan;
E-mail: kajiwara@mech.titech.ac.jp

Toshio Uchiyama
Tokyo Institute of Technology, 2-12-1, O-okayama, Meguro-ku, Tokyo 152-8552, Japan;
E-mail: uchiyama.t.ac@m.titech.ac.jp

Toshihiro Arisaka
Hitachi Global Storage Technologies, Japan, Ltd. 1, Kirihara-cho, Fujisawa-shi, Kanagawa-ken 252-8588, Japan; E-mail: toshihiro.arisaka@hitachigst.com

H. Ulbrich and L. Ginzinger (eds.), Motion and Vibration Control, 165–176.

the areal density. It has been expected that technology of smart structures will contribute to the development of small and light-weight mechatronics devices with the required performance. So far, research on smart structures has been carried out using electro-rheological fluids, shape memory alloys and piezoelectric materials. The piezoelectric materials are generally installed on the structural surface as actuator and sensor to control the static and dynamic responses [1–3]. To date, distributed parameter systems such as cantilever type structures have been mainly taken as the controlled object [4–7]. In HDD applications of piezoelectric actuator and sensor, a track-seeking control using a piezoelectric actuator for dual-stage actuator was investigated [8] and a piezoelectric bimorph shunt damping was applied to reduce disk-spindle vibration [9]. Further enhancement of vibration control performance is necessary to achieve the required density of future HDD systems. The control performance of the smart structure highly depends on the location of the actuator corresponding to the control input position. Designing the actuator location with high controllability is expected to enhance the control performance of the structural vibration suppression.

In this study, the technology of the smart structure is introduced into the HDD to achieve the required vibration suppression. The smart structure is composed of the piezoelectric sensors and actuators in order to control the structural vibration [10, 11]. First, the finite element and modal analyses of the HDD are conducted to confirm the vibration modes and frequency response of the system. The vibration characteristics and problem of the system are made clear through the structural analysis. Second, two actuator mechanisms are considered as vibration control device: namely, one is the direct piezoelectric (PZT) actuation mechanism and another is the proof-mass actuation mechanism. The controller design and closed-loop simulation are conducted to evaluate the vibration control performance. Finally, a multidisciplinary design optimization on the actuator location and control system is studied to enhance the closed-loop performance of the system. The design problem to improve the $\mathbf{H}_2$ or $\mathbf{H}_\infty$ performance is defined, and the actuator location and control system are simultaneously designed by the presented 2-step procedure using genetic algorithm (GA), resulting in an enhanced performance for the vibration control. It has been verified by some simulations that an enhanced performance on the vibration suppression can be achieved by the proposed vibration control mechanisms and multidisciplinary design optimization approach.

2 Modeling of Controlled Object

The FEM model of the HDD as a controlled object is shown in Figure 1 which has 10,362 nodal points. The frequency response of the head displacement due to the voice coil input is shown in Figure 2. The resonance peaks existing in the frequency range 6–30 kHz may easily cause a vibration instability problem in the closed-loop system with respect to the head following control when enhancing the control performance. The smart structure technology is introduced into the HDD to control the

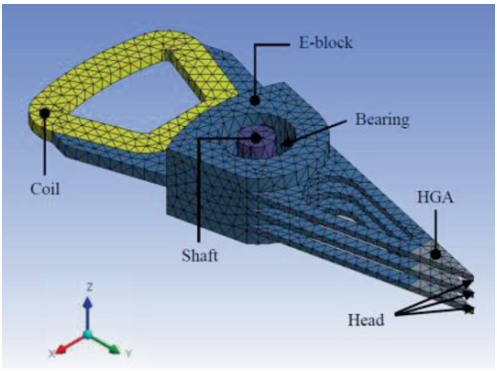

Fig. 1 FEM model of HDD.

actuator vibration for enhancing the following control performance. Piezoelectric elements are employed as actuator and sensor in the smart structure. A MEMS accelerometer is also supposed to be installed on the structural surface to detect the acceleration which is used for a feedback signal. In this study, modeling of smart structure is carried out with the finite element and modal analyses by which the modeling of arbitrary shape structures and the control system design can be effectively executed. Equation of motion of the n degrees-of-freedom system is described as

$$\mathbf{M}_s\ddot{\mathbf{x}} + \mathbf{C}_s\dot{\mathbf{x}} + \mathbf{K}_s\mathbf{x} = \mathbf{B}_{1s}\mathbf{w} + \mathbf{B}_{2s}\mathbf{u} \tag{1}$$

where $\mathbf{M}_s$ and $\mathbf{K}_s$ are the mass and stiffness matrices, respectively, and $\mathbf{C}_s$ is the assumed proportional viscous damping matrix. $\mathbf{x}$, $\mathbf{w}$ and $\mathbf{u}$ are the displacement, disturbance and control input vectors, respectively. The finite element analysis (FEA) is conducted by ANSYS. The degree-of-freedom of Eq. (1) becomes generally too large because of using FEA that the control system should not be designed directly to this spatial model. The coordinate transformation into the modal space is appropriate to conduct the model reduction for control system design. Adopting the lower natural modes $\mathbf{\Phi}$, Eq. (1) is transformed to the reduced-order state equation with the transformation $\mathbf{x} = \mathbf{\Phi}\boldsymbol{\xi}$:

$$\dot{\mathbf{q}} = \mathbf{A}\mathbf{q} + \mathbf{B}_1\mathbf{w} + \mathbf{B}_2\mathbf{u} \tag{2}$$

where

$$\mathbf{q} = \begin{Bmatrix} \boldsymbol{\xi} \\ \dot{\boldsymbol{\xi}} \end{Bmatrix}, \quad \mathbf{A} = \begin{bmatrix} \mathbf{0} & \mathbf{I}_r \\ -\mathbf{\Lambda} & -\mathbf{\Phi}^T\mathbf{C}_s\mathbf{\Phi} \end{bmatrix}$$

$$\mathbf{B}_1 = \begin{bmatrix} \mathbf{0} \\ \mathbf{\Phi}^T\mathbf{B}_{1s} \end{bmatrix}, \quad \mathbf{B}_2 = \begin{bmatrix} \mathbf{0} \\ \mathbf{\Phi}^T\mathbf{B}_{2s} \end{bmatrix}$$

$\mathbf{\Lambda}$ is the diagonal eigenvalue matrix and the modal matrix $\mathbf{\Phi}$ is normalized with the mass matrix. $\mathbf{B}_{2s}$ can be determined by the relation between the control input $\mathbf{u}$ and the force caused by the piezoelectric actuator [10, 11].

The output equation is generally described as

$$\mathbf{y}_2 = \mathbf{C}_2\mathbf{q} + \mathbf{D}_{21}\mathbf{w} + \mathbf{D}_{22}\mathbf{u} \tag{3}$$

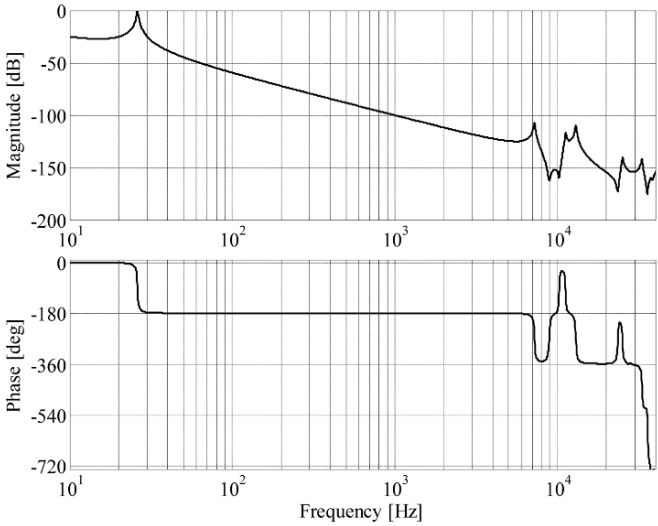

Fig. 2 Frequency response of the head displacement.

In this study, a rotational angle and acceleration are detected by the piezoelectric sensor and accelerometer as feedback signal, respectively. These sensors are suitable to be installed in the smart structures since the external reference is not required for them. In case of the piezoelectric sensor, the rotational angle $\mathbf{y}_s$ $(= \mathbf{a}_s \mathbf{V}_s)$ which is proportional to the output voltage $\mathbf{V}_s$ with a proportion constant $\mathbf{a}_s$ determined by the piezoelectric property is formulated by giving each coefficient matrix of Eq. (3) as

$$\mathbf{C}_2 = \mathbf{C}_0 \boldsymbol{\Psi}, \quad \mathbf{D}_{21} = \mathbf{0}, \quad \mathbf{D}_{22} = \mathbf{0}, \quad \boldsymbol{\Psi} = \begin{bmatrix} \boldsymbol{\Phi} & \mathbf{0} \\ \mathbf{0} & \boldsymbol{\Phi} \end{bmatrix} \tag{4}$$

where $\mathbf{y}_s = \mathbf{C}_0 \mathbf{x}_0$ and $\mathbf{x}_0 = (\mathbf{x}^T, \dot{\mathbf{x}}^T)^T$. In case of the acceleration output, substituting the modal transformation $\mathbf{x} = \boldsymbol{\Phi}\boldsymbol{\xi}$ into Eq. (1) yields the modal acceleration:

$$\ddot{\boldsymbol{\xi}} = -\boldsymbol{\Phi}^T \mathbf{C}_s \boldsymbol{\Phi} \dot{\boldsymbol{\xi}} - \boldsymbol{\Lambda} \boldsymbol{\xi} + \boldsymbol{\Phi}^T \mathbf{B}_{1s} \mathbf{w} + \boldsymbol{\Phi}^T \mathbf{B}_{2s} \mathbf{u} \tag{5}$$

From Eq. (5) and the detected acceleration $\mathbf{y}_a = \mathbf{C}_a \ddot{\mathbf{x}}$, each coefficient matrix in Eq. (3) for the output equation becomes

$$\mathbf{C}_2 = \mathbf{C}_a \boldsymbol{\Phi}[-\boldsymbol{\Lambda} \quad -\boldsymbol{\Phi}^T \mathbf{C}_s \boldsymbol{\Phi}], \quad \mathbf{D}_{21} = \mathbf{C}_a[\mathbf{0} \quad \boldsymbol{\Phi}]\mathbf{B}_1, \quad \mathbf{D}_{22} = \mathbf{C}_a[\mathbf{0} \quad \boldsymbol{\Phi}]\mathbf{B}_2 \tag{6}$$

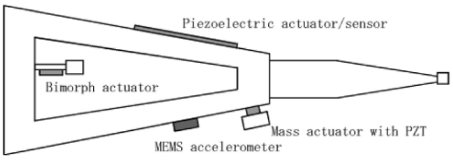

Fig. 3 Vibration control mechanism.

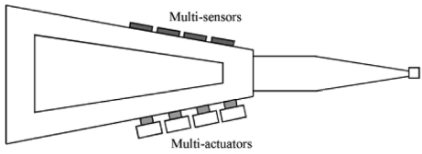

Fig. 4 Multi-input and multi-output system.

3 Vibration Control Mechanism and System

3.1 Vibration Control Mechanism

Figure 3 shows the candidates of the vibration control mechanism. Two actuator mechanisms are considered in this study: namely, one is the direct PZT actuation mechanism and another is the proof-mass actuation mechanism. In the direct PZT actuation mechanism, the tabular PZT actuators are directly attached on the structural surface and apply the control forces to the structure. In the proof-mass actuation mechanism, a minute mass connected to the top of the layered PZT whose back side is connected to the structural surface vibrates due to the vibration input to the PZT and causes the inertia force as control input. Figure 4 shows an image of multi-input and multi-output system using the multiple sensors and proof-mass actuation mechanisms.

3.2 Vibration Control System

The block diagram of the control system is shown in Figure 5. $\mathbf{H}_2$ and $\mathbf{H}_\infty$ control problems are considered in this study. The controller $\mathbf{K}(\mathbf{s})$ is obtained by conducting the control problem:

$$\min \|\mathbf{T}_{y_1 w}\|_2: \quad \mathbf{H}_2 \text{ control} \tag{7}$$

$$\min \|\mathbf{T}_{y_1 w}\|_\infty: \quad \mathbf{H}_\infty \text{ control} \tag{8}$$

where $\mathbf{T}_{y_1 w}$ is the transfer function matrix between the disturbance $\mathbf{w}$ and the controlled variable $\mathbf{y}_1$. The controlled variable is described as $\mathbf{y}_1 = (\mathbf{w}_z \mathbf{z}_1^T, \mathbf{w}_u \mathbf{u}^T)^T$, where $\mathbf{z}_1$ is the controlled response, $\mathbf{w}_z$ and $\mathbf{w}_u$ are the weight parameters for the controlled response and control input, respectively. In this study, acceleration and modal controls are considered by defining $\mathbf{y}_1$ as spatial acceleration and modal coordinates, respectively. The controller satisfying the control problem (7) or (8) is designed based on the LMI approach.

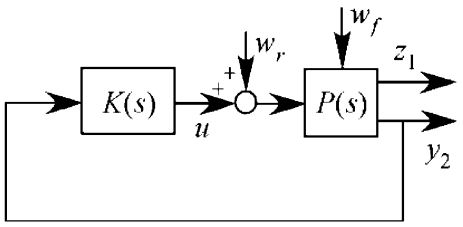

Fig. 5 Block diagram of the control system.

3.2.1 Acceleration Control

The controlled response $\mathbf{z}_1$ which is defined by the accelerations on spatial coordinates is described as

$$\mathbf{z}_1 = \mathbf{C}_{z_1}\mathbf{q} + \mathbf{D}_{z_{11}}\mathbf{w} + \mathbf{D}_{z_{12}}\mathbf{u} \tag{9}$$

Each coefficient matrix in Eq. (9) is obtained by the relation between the spatial and modal accelerations. This controlled response is appropriate to reduce high frequency response due to the acceleration evaluation.

3.2.2 Modal Control

In the modal control problem, $\mathbf{z}_1$ is composed of the modal coordinates and formulated as

$$\mathbf{z}_1 = \mathbf{W}_{10}\mathbf{q} \tag{10}$$

where $\mathbf{W}_{10}$ is the modal weight matrix defined by

$$\mathbf{W}_{10} = \mathrm{diag}[\mathbf{w}_1, \mathbf{w}_2, \ldots, \mathbf{w}_p] \tag{11}$$

Weighting each modal coordinate with each coefficient easily achieves the modal shaping which can mainly suppress the target modes vibration. Frequency weight functions are generally used for achieving the frequency shaping, however, the order of the controller in this case is increased according to the orders of the frequency weight functions. The modal control shown in Eqs. (10) and (11) does not increase the order of the controller and so is practically advantageous for developing the real systems.

The output feedback $\mathbf{u} = \mathbf{K}(s)\mathbf{y}$ is described as the state equation form:

$$\begin{aligned} \mathbf{q}_c &= \mathbf{A}_c\mathbf{q}_c + \mathbf{B}_c\mathbf{y} \\ \mathbf{u} &= \mathbf{C}_c\mathbf{q}_c + \mathbf{D}_c\mathbf{y} \end{aligned} \tag{12}$$

where the matrices $\mathbf{A}_c$, $\mathbf{B}_c$, $\mathbf{C}_c$ and $\mathbf{D}_c$ are designed by the LMI approach.

4 System Optimization with H_2 Control

Describing the piezoelectric actuator location and control design variables as η_s and η_c, respectively, a simultaneous optimization problem can be defined as

$$\begin{aligned} \min: \quad & \mathbf{J}(\eta_s, \eta_c) \\ \text{subj:} \quad & \mathbf{g}_c^{\min} \le \mathbf{g}_c(\eta_s, \eta_c) \le \mathbf{g}_c^{\max} \end{aligned} \tag{13}$$

where $\mathbf{J}(\eta_s, \eta_c)$ and $\mathbf{g}_c(\eta_s, \eta_c)$ are the objective and the constraint functions depending on both shape and control design variables such as the closed-loop norms described in the control problems (7) and (8). The optimization problem (13) is executed by GA [11].

The control design variable is the weight coefficient $\mathbf{q}_w$ multiplied to the controlled response in the performance index for controller design. The strategy for the optimization of the actuator location is that the both end nodal points at which the actuator is placed are employed as the design variables. In this case, the design variable takes a discrete value corresponding to a nodal point number as shown in Figure 6 and so GA is employed to search the optimal design variables. The design variables should be coded in GA to obtain an optimal solution. In this approach, the design variables are described by the binary code with $\mathbf{m}$ bits:

$$\underbrace{\boldsymbol{\eta}_1 \cdots \boldsymbol{\eta}_p}_{\text{node } i}, \quad \underbrace{\boldsymbol{\eta}_{p+1} \cdots \boldsymbol{\eta}_{2p}}_{\text{node } j}, \quad \underbrace{\boldsymbol{\eta}_{2p+1} \cdots \boldsymbol{\eta}_m}_{q_w}, \tag{14}$$

where η_k $(k = 1, \ldots, m)$ shows the genes, all of which can take the values of 0 or 1. The symbols $\eta_1 \ldots \eta_p$ and $\eta_{p+1} \ldots \eta_{2p}$ indicate the nodal point numbers of both ends of the piezoelectric actuator, and $\eta_{2p+1} \ldots \eta_m$ shows the variable of $\mathbf{q}_w$. The optimal values of the design variables maximizing the fitness function defined as $-\mathbf{J}$ are searched by GA composed of three basic operations: selection, crossover and mutation. The genetic operation in this approach is based on simple GA, and the appropriate condition of GA operation is set, namely: (1) the selection is based on the roulette selection strategy, (2) one-point crossover is adopted as the crossover strategy, (3) the mutation strategy is performed by inversion of a gene that is stochastically selected, and (4) the elitist preserving strategy is adopted to leave the large fitness individuals to the next generation.

5 Simulation Results

5.1 Control Effect of Proof-Mass Actuation Mechanism

The vibration control performance is evaluated with a proof-mass actuation mechanism. The purpose of this application is to reduce the vibration response between

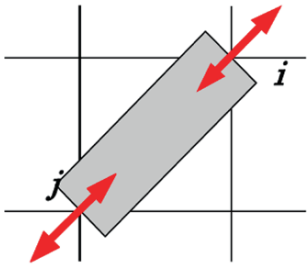

Fig. 6 Nodal points where piezoelectric actuator is placed.

the frequency range 6–20 kHz. Figure 7 shows the actuator/sensor location and disturbance input points in the smart carriage arm with the proof-mass actuation mechanism. The proof-mass actuation mechanism is placed at the same position with the spindle axis in y-direction so that the control force would not influence the movement of the arm in rotational direction. The mass and stiffness of the mass-actuation mechanism are set to $m = 1 \times 10^{-4}$ kg and $k = 3.55 \times 10^{6}$ N/m, respectively. The number of the adopted modes is 10 and $\mathbf{H}_\infty$ control is applied with the evaluation of the controlled acceleration of the head. The disturbance force is supposed to be applied at the voice coil motor (VCM). The conditions of the control system design are

$$\begin{cases} \text{Disturbance: } \mathbf{w} \text{ (VCM input)} \\ \text{Actuator location: At the spindle axis position in } y\text{-direction} \\ \text{Controlled variable: } \quad \mathbf{y}_1 = \begin{Bmatrix} \mathbf{w}_z \ddot{\mathbf{x}}_{\text{head}} \\ \mathbf{w}_u \mathbf{u} \end{Bmatrix} \\ \text{Observed output: } \quad \mathbf{y}_2 = \ddot{\mathbf{x}} \end{cases} \tag{15}$$

The acceleration at the proof-mass actuator location in x-direction is the sensor output and the head acceleration in x-direction is the controlled response. The controller is designed by giving $\mathbf{w}_z = 10^{-3}$ and $\mathbf{w}_u = 0.1$, and the closed-loop frequency response of the head displacement for the VCM disturbance is shown in Figure 8. Vibration in high frequency region is effectively reduced and the cut-off frequency may be extended from 1800 Hz to 5300 Hz by this control system. It has been verified by this simulation result that the enhanced vibration control performance can be achieved by the proposed vibration control mechanism.

5.2 Optimization of Direct PZT Actuation Mechanism

The multidisciplinary design optimization of actuator location and control system is conducted to enhance the vibration control performance. The direct PZT actuation mechanism is adopted in this case. The optimization problem is defined as

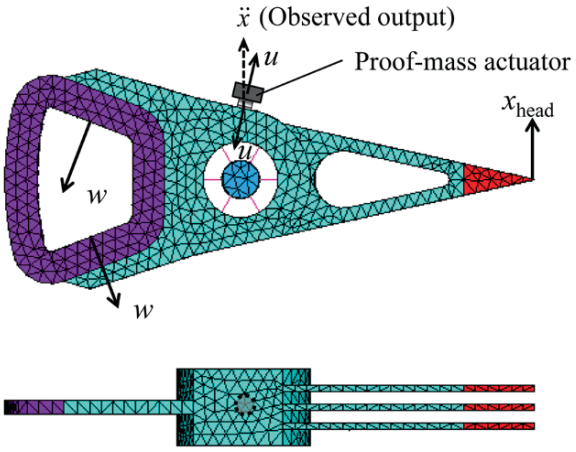

Fig. 7 Conditions of the proof-mass actuation mechanism.

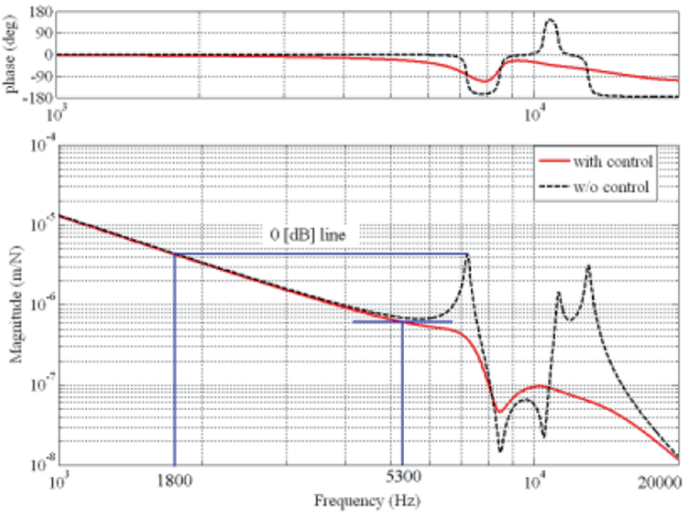

Fig. 8 Closed-loop FRF of $\mathbf{x}_{\text{head}}$ with $\mathbf{H}_\infty$ control.

$$\begin{aligned} \min: \quad & \mathbf{H}_z \\ \text{subj:} \quad & \mathbf{H}_u \leq \mathbf{H}_u^{\max} \end{aligned} \tag{16}$$

where $\mathbf{H}_z$ and $\mathbf{H}_u$ are the $\mathbf{H}_2$ norms with respect to the controlled response and control input, respectively. The control system is designed by the $\mathbf{H}_2$ modal control problem. First, each optimization of a single actuator location and control system corresponding to each mode of the three resonance peaks in the frequency range 6–20 kHz is conducted by GA. Next, the three inputs and one output system is

constructed by synthesizing three actuators optimally located and the control system is designed with this system.

The optimization problems for vibration suppression of each mode are defined as

$$\text{1st mode:} \quad \begin{cases} \min: \quad \mathbf{H}_z \\ \text{subj:} \quad \mathbf{H}_u \leq 8 \times 10^3 \\ \mathbf{W}_{10} = \text{diag}[1000, 1, 1], \mathbf{Q} = \mathbf{I}, \quad \mathbf{R} = 10^{-7}\mathbf{I} \end{cases} \tag{17}$$

$$\text{2nd mode:} \quad \begin{cases} \min: \quad \mathbf{H}_z \\ \text{subj:} \quad \mathbf{H}_u \leq y \times 10^2 \\ \mathbf{W}_{10} = \text{diag}[1, 1000, 1], \mathbf{Q} = \mathbf{I}, \quad \mathbf{R} = 10^{-7}\mathbf{I} \end{cases} \tag{18}$$

$$\text{3rd mode:} \quad \begin{cases} \min: \quad \mathbf{H}_z \\ \text{subj:} \quad \mathbf{H}_u \leq 7 \times 10^3 \\ \mathbf{W}_{10} = \text{diag}[1, 1, 1000], \mathbf{Q} = \mathbf{I}, \quad \mathbf{R} = 10^{-7}\mathbf{I} \end{cases} \tag{19}$$

The mode number is in order of the modes exist in the frequency range 6–20 kHz. In the control system design, the controlled variable is described as

$$y_1 = \begin{Bmatrix} \mathbf{Q}^{1/2}\mathbf{z}_1 \\ \mathbf{R}^{1/2}\mathbf{u} \end{Bmatrix} \tag{20}$$

where $\mathbf{z}_1$ is the controlled response, and $\mathbf{Q}$ and $\mathbf{R}$ are the weight matrices. The modal weight matrix $\mathbf{W}_{10}$ in Eq. (11) is given in the optimization problems (17), (18) and (19). The control design variable is the weight coefficient $\mathbf{q}_w$ multiplied to $\mathbf{Q}$ with respect to the controlled response. Node number of the FE model is used as the actuator location variable corresponding to the both end points of the actuator. In this case, the design variables take discrete values and so GA is employed to search the optimal design variables.

The optimal actuator location is shown in Figure 9. In Figure 9, the locations of the actuators 1, 2 and 3 are obtained by the optimization with (17), (18) and (19), respectively. The optimal control design variable q_w and the resulting performance indices with respect to controlled response and control input are

$$\text{Optimization problem (17):} \quad \begin{cases} \mathbf{q}_w = 1.00 \times 10^2 \\ \mathbf{H}_z = 1.29 \times 10^{-5}, \quad \mathbf{H}_u = 7.55 \times 10^3 \end{cases}$$

$$\text{Optimization problem (18):} \quad \begin{cases} \mathbf{q}_w = 3.02 \times 10^2 \\ \mathbf{H}_z = 8.66 \times 10^{-7}, \quad \mathbf{H}_u = 6.81 \times 10^2 \end{cases}$$

$$\text{Optimization problem (19):} \quad \begin{cases} \mathbf{q}_w = 1.58 \times 10^2 \\ \mathbf{H}_z = 2.18 \times 10^{-6}, \quad \mathbf{H}_u = 6.67 \times 10^3 \end{cases}$$

The three inputs and one output system is constructed by the three actuators optimally located. The sensor location is shown in Figure 9. The $\mathbf{H}_2$ modal con-

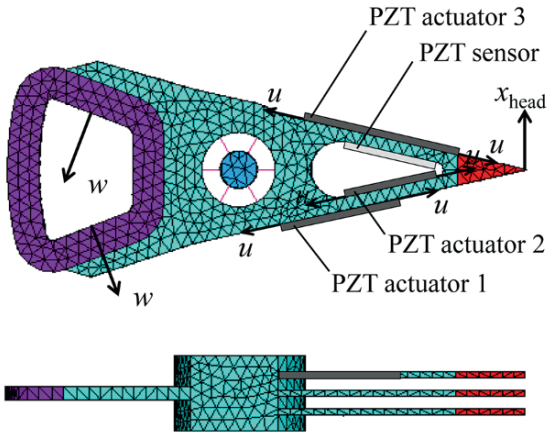

Fig. 9 Optimal actuator location.

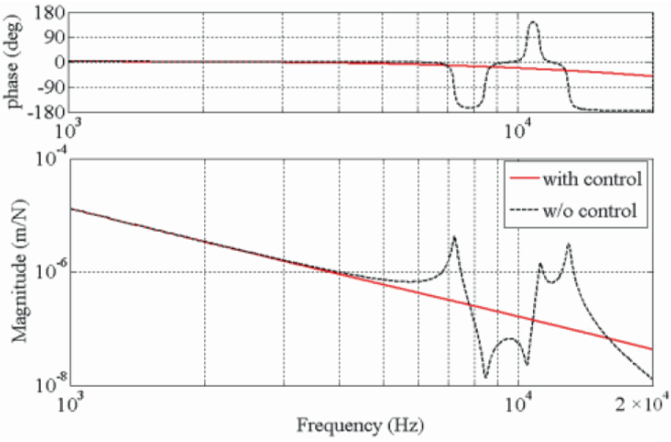

Fig. 10 Closed-loop FRF with three actuators.

troller is designed with this system by giving the weight parameters as $\mathbf{W}_{10} = \text{diag}[1000, 1000, 1000]$, $\mathbf{Q} = \mathbf{I}$ and $\mathbf{R} = 10^{-7}$. Figure 10 shows the closed-loop frequency response of the head displacement for the VCM disturbance. It is observed from Figure 10 that excellent vibration suppression has been achieved by this control system. It is also verified that the optimization of the multiple actuator locations and control system is significantly effective to realize an ideal vibration characteristics of the system.

6 Conclusions

The vibration control effects with the proposed vibration control mechanisms have been evaluated by simulation in this study. It can be expected that the proposed mechanisms practically realize a significant vibration suppression of the system. Furthermore, the enhanced vibration control performance has been achieved by the multidisciplinary design optimization of the actuator location and control system. It is also made clear that the system with multiple actuators effectively improves the closed-loop performance. In future, the micro-actuator for vibration control will be developed and implemented in the HDD system. The vibration control performance and robust stability against structural characteristic uncertainty will be evaluated by experiment and compared to the simulation results.

References

1. Crawly, E.F., Intelligent structures for aerospace: A technology overview and assessment, *AIAA Journal* **32**(8), 1994, 1689–1699.
2. Varadarajan, S., Chandrashekhara, K. and Agarwal, S., Adaptive shape control of laminated composite plates using piezoelectric materials, *AIAA Journal* **36**(9), 1998, 1694–1698.
3. Saggere, L. and Kota, S., Static shape control of smart structures using compliant mechanisms, *AIAA Journal* **37**(5), 1999, 572–578.
4. Ray, M.C., Optimal control of laminated plate with piezoelectric sensor and actuator layers, *AIAA Journal* **36**(12), 1998, 2204–2208.
5. Crawly, E.F. and de Luis, Use of piezoelectric actuators as elements of intelligent structures, *AIAA Journal* **25**(10), 1987, 1373–1385.
6. Tzou, H.S., Distributed modal identification and vibration control of continua: Theory and applications], *Trans. ASME, Journal of Dynamic Systems, Measurement, and Control* **113**, 1991, 494–499.
7. Sun, D., Wang, D., Xu, Z.L. and Wu, H., Distributed piezoelectric element method for vibration control of smart plates, *AIAA Journal* **37**(11), 1999, 1459–1463.
8. Kobayashi, M., Yamaguchi, T. and Horowitz, R., Track-seeking controller design for dual-stage actuator in magnetic disk drives, in *Proceeding of the American Control Conference*, 2000.
9. Lim, S.C. and Choi, S.B., Vibration control of an HDD disk-spindle system utilizing piezoelectric bimorph shunt damping: I. Dynamic analysis and modeling of the shunted drive, *Smart Materials and Structures* **16**, 2007, 891–900.
10. Kajiwara, I. and Uehara, M., Design of shape and control system for smart structures with piezoelectric films, in *Proceedings of AIAA, 42nd SDM Conference*, 2001, CD-ROM (No. 2001-1555).
11. Ohashi, F., Kajiwara, I., Iwadare, M. and Arisaka, T., Optimal design of smart carriage arm in magnetic disk drive for vibration suppression, *Microsystem Technologies* **11**(8–10), 2005, 711–717, DOI: 10.1007/s00542-005-0550-4.

An Industrial-Robots Suited Input Shaping Control Scheme

Amine Kamel, Friedrich Lange and Gerd Hirzinger

Abstract Compliance in robot mounted force/torque sensors is useful for soft mating of parts in many assembly tasks. Nevertheless, it generates nearly undamped oscillations when moving a heavy end-effector in free space. In this paper, input shaping control is investigated to damp such unwanted flexible modes. However, the conventional method presents a major drawback: To eliminate the oscillatory dynamics, the desired motion profiles have to be shaped and thus modified. This means that although the unwanted vibrations are damped, the robot motion does not meet the desired one. In this paper we first review the conventional input shaping technique. Second we show how the mentioned problem may be fixed in the design phase by discretizing the filter and by using a predictive approach that compensates the shaped signals time delay and minimizes the resulting control error. Simulation results are presented.

1 Introduction

Compliant force/torque sensors are frequently used in robot assisted assembly tasks. They do not only perform measurements, but also inhibit high frequency-motions that commonly occur in the contact phase. This advantage drops into a drawback if the end-effector is moved in free space. In fact, due to the sensor compliance, poorly damped oscillations emerge which lead to unprecise motion of the tool. Such oscillatory behavior is critical in many applications with high speed and precision requirements. In this paper we address the problem of wheel assembly to a continuously moved car (Figure 1).

Amine Kamel, Friedrich Lange and Gerd Hirzinger
German Aerospace Center, Institute of Robotics and Mechatronics, D-82234 Weßling, Germany;
E-mail: friedrich.lange@dlr.de

H. Ulbrich and L. Ginzinger (eds.), Motion and Vibration Control, 177–187.

Fig. 1 (a) Setup for wheel assembly. (b) Compliant end-effector with force/torque sensor in the center of the springs.

A camera is mounted at the tool to correct the motion profiles when needed and to detect the car hub. Undamped oscillations inhibit this process and have hence to be eliminated.

Input shaping also known as *command preshaping* is one of the easiest successfully applied feedforward control techniques that have been designed to suppress residual vibrations occurring within speedy maneuvers. Some pre-knowledge about the plant is used to generate commands which move the system without vibrations. The first form of input shaping, also called *posicast control*, was presented 1957 by Smith [1]. It consists in generating two transient oscillations that cancel each other and lead to a vibrationless response. The first paper of the conventional input shaping was presented by Singer and Seering [2]. Desired system inputs were convolved with an impulse train. The resulting commands move the system without residual vibration. Very good estimations of the plant parameters were essential to eliminate the oscillatory dynamics. Many researchers addressed this problem and developed robust input shapers by adding more impulses to the filter. Singhose [3] presented a design method to add any desired order of robustness to the filter.

To suite input shaping to industrial robots, three major matters have to be discussed:

1. Filtering the inputs induces some time delay which leads to system performance degradation. In the task presented above, positional ramps are commonly commanded to move the tool from a given Cartesian position to another. Hence the ramp response time delay has to be compensated.
2. The conventional theory of input shaping has been primarily developed in the continuous time domain. Hence the application to systems with long sampling period leads to implementation problems. This can be fixed by digitizing the shaper.
3. An input shaper modifies slightly the reference signals to damp the vibrations of the end-effector. This means, although the oscillations are eliminated, the tool will not move as desired since modified trajectories are commanded! Hence, an exact tracking of the desired path and a total vibrations damping seem to be two contradictory goals that cannot be simultaneously fully fulfilled. However

a tradeoff can be reached by minimizing the sum of the sensor deflection and the deviation between the desired and commanded signals. A formulation and a computationally efficient solution of such optimization problems are presented in this paper.

2 Review of the Conventional Input Shaping

The original method has been primarily developed for linear second order systems with the transfer function:

$$G(s) = \frac{y(s)}{u(s)} = K\frac{\omega_0^2}{s^2 + 2D\omega_0 s + \omega_0^2} \tag{1}$$

$$g(t) = \frac{K\omega_0}{\sqrt{1-D^2}}\, e^{-\omega_0 Dt} \sin(\omega_d t) \tag{2}$$

With a static gain K, a positive damping ratio D smaller than 1, a natural frequency ω_0 and a damped natural frequency $\omega_d = \omega_0\sqrt{1-D^2}$. $u(s)$ and $y(s)$ denote respectively the system input and output.

It is known that applying an impulse $A_0\delta(t-t_0)$ to such a plant will result in an oscillating response $g_0(t)$. However a well chosen second impulse $A_1\delta(t-t_1)$ can excite a second oscillation $g_1(t)$ that totally cancels the first one for $t \geq t_1$. This idea can be extended to an impulse sequence with n impulses

$$f_\delta(t) = \sum_{i=0}^{n-1} A_i\delta(t-t_i); \qquad t_i < t_{i+1}; \qquad i \in \{0, 1, \ldots, n-1\} \tag{3}$$

which compensates any oscillation immediately after applying the last impulse. By convolving this sequence with any desired command signal, new control inputs are generated which move the system without vibration. This command generation process is called input shaping. To eliminate the oscillations, the filter has to satisfy the following conditions (see [2])

$$\mathcal{C}(\omega_0, D) = \sum_{i=0}^{n-1} A_i e^{\omega_0 Dt_i}\cos(\omega_d t_i) = 0 \tag{4}$$

$$\mathcal{S}(\omega_0, D) = \sum_{i=0}^{n-1} A_i e^{\omega_0 Dt_i}\sin(\omega_d t_i) = 0 \tag{5}$$

The constraints (4) and (5) can be satisfied by setting all the amplitudes A_i to zero or by allowing them to have infinite values. Such trivial solutions are uninteresting for practical sakes and have to be eliminated. Therefore we require that:

$$\sum_{i=0}^{n-1} A_i = 1 \tag{6}$$

This condition makes sure that the filter has a unity static gain. Thus, the steady state values of the references and the commands will be the same. Since the range of the commands is dependent on the actuators, we can set constraints to the actuators' limitations and then solve for positive and negative amplitudes which satisfy them [7]. A general form of these constraints is:

$$A_{i_{\min}} \leq A_i \leq A_{i_{\max}} \quad \text{and} \quad \Delta A_{i_{\min}} \leq \Delta A_i \leq \Delta A_{i_{\max}} \tag{7}$$

Thereby $A_{i_{\min/\max}}$ and $\Delta A_{i_{\min/\max}}$ are the respective minimal/maximal allowed amplitude and increments values.

For a first order robustness, also the derivatives of (4) and (5) with respect to ω_0 are constrained to zero [2].

$$\sum_{i=0}^{n-1} A_i t_i e^{\omega_0 D t_i} \cos(\omega_d t_i) = 0 \tag{8}$$

$$\sum_{i=0}^{n-1} A_i t_i e^{\omega_0 D t_i} \sin(\omega_d t_i) = 0 \tag{9}$$

Equations (4), (5), (6), (8), (9) and the restrictions (7) define a constrained set of nonlinear equations (CSNE) that can be numerically solved for amplitudes A_i and time instants t_i to get a zero vibration robust input shaper.

3 Ramp Time Delay Compensation

Long sequences of impulses afford many design degrees of freedom and allow to accommodate the input shaper to complex and demanding constraints. However, the longer the sequence is, the bigger is the filtering time delay. In this section we focus on the ramp time delay compensation since positional ramps are common for the task presented above.

Let τ be the ramp response time delay when applying input shaping. Kamel et al. described in [9] the dependency of τ from the input shaper parameters and the plant parameters:

$$\tau = \frac{2D}{\omega_0} + \sum_{i=0}^{n-1} A_i t_i \tag{10}$$

$2D/\omega_0$ describes the delay caused by the plant (1) whereas $\sum_{i=0}^{n-1} A_i t_i$ is the shaping delay. By setting τ to zero, the dead time will be totally compensated:

$$\sum_{i=0}^{n-1} A_i t_i = -\frac{2D}{\omega_0} \tag{11}$$

Notice that the statement (11) compensates not only the input shaping time delay but the one of the plant too! This feature may now be included into the filter design by adding (11) to the CSNE as an additional constraint.

However requiring a total dead-time elimination leads often to huge amplitude values within short sequences of impulses. This can be avoided either by lengthening the sequence or by using predictive path scheduling within a known time delay (backward time shifting): When the desired trajectory is a priori known, then the control inputs may be time advanced [8]. In this case, (10) is used to enforce some known time delay τ_0 which can be compensated due to command shifting (see [9]).

4 Time-Discrete Input Shaping

The discretization of input shapers has been the emphasis of many publications [4–6]. Singer described in [4] a digital shaper by fixing the time between the impulses and only changing the magnitudes A_i. Based on the ideas in [4], Kamel et al. described in [9] a systematic design to generate a time discrete input shaper for low sampled robotic systems. This will be briefly reviewed in this section.

In order to fit the time instants of the impulses to the sampling period T we can explicitly constrain all t_i and τ_0 to be a multiple of T. An intuitive choice may be:

$$t_i = iT; \quad \tau_0 = mT \tag{12}$$

where $i \in \{0, 1, \ldots, n-1\}$ and $m \in \mathbb{N}$ are design parameters used to set the ramp time delay to a known value.

Adding (12) to the CSNE eliminates the time instants and replaces them by the known integers i. Note that the nonlinear statements are transformed to linear ones by fixing the time instants t_i. Thus the CSNE becomes a constrained set of linear equations (CSLE):

$$C\underline{A} = \underline{b} \tag{13}$$

with the $C \in \mathbb{R}^{6\times n}$, the amplitude set $\underline{A} \in \mathbb{R}^n$ and the right side $\underline{b} \in \mathbb{R}^6$ (see [9]). The problem can now be stated as follows: Find a vector of amplitudes $\underline{A}$ that satisfies the CSLE stated above. For $n > 6$, the statement (13) is under-determined. The problem has consequently for a given sequence length n an infinity of solutions from which we need to select one that satisfies (7) if it exists. This task can be solved by many numerical iterative tools. An iterative algorithm is presented in [9] to solve this problem and to keep the length of the impulse sequence to a minimum.

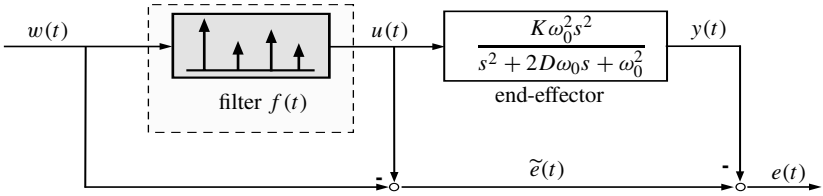

Fig. 2 Signal flow diagram of the total positional control error.

5 Minimization of the Quadratic Control Error

At this level, it is very important to realize that a good performance of the filter does not only depend on a good vibrations' damping, but also on other important criteria. In fact, the elimination of the oscillatory dynamics invokes implicitly a modification of the commands. This means concretely that the robot will effectuate vibrationless motions which unfortunately do not match exactly the desired motion. One way to deal with this problem is to minimize the positional control error due to the filtering and to the sensor deflections. To do so we first of all consider the signal flow diagram as stated in Figure 2.

$w(t)$ denotes the desired motion profile. For the following optimization task $w(t)$ is supposed to be a unity gain step $\sigma(t)$. Using these commanded references, the input shaper generates the system inputs $u(t)$:

$$u(t) = f(t) * w(t) = \sum_{i=0}^{n-1} A_i \sigma(t - t_i) \underbrace{=}_{(12)} \sum_{i=0}^{n-1} A_i \sigma(t - iT) \tag{14}$$

If the robot is supposed to be ideal (only rigid body interactions with no delay), then $u(t)$ corresponds to the measured position profile of the robot flange. In this case, the difference $\tilde{e}(t)$ between the references $w(t)$ and the input $u(t)$ is the position error caused by the input shaper. $y(t)$ denotes the deflections measured in the compliant sensor. One can easily verify that:

$$y(t) = \frac{d}{dt} g(t) * f(t) = \sum_{i=0}^{n-1} A_i \frac{d}{dt} g(t - iT) \tag{15}$$

where $g(t)$ is the impulse response of plant (1). The total position error reads:

$$e(t) = \tilde{e}(t) - y(t) = w(t) - u(t) - y(t) \tag{16}$$

5.1 Analytical Formulation of the Cost Function

Equations (14), (15) and (16) provide an analytical characterization of the control error occurring when applying a positional step. We define the following minimization problem:

$$\min_{\underline{A}\in\mathbb{R}} \quad \mathcal{I}_q \quad \text{subject to} \quad C\underline{A} = \underline{b} \quad \text{where} \quad \mathcal{I}_q(\underline{A}) = \underline{A}^T Q \underline{A} + \int_0^\infty e^2(t)\, dt \tag{17}$$

Q is a positive definite weighting matrix to penalize high amplitude values. One can already feed the problem at this level to a numerical iterative solver. However, the computational effort will be extremely high. Hence, it is recommendable to formulate and solve the problem analytically. Due to (6) and to the fact that the input shaper totally eliminates any oscillations immediately after applying the last impulse, the control error $e(t)$ exists only between $t = 0$ and $t = t_{n-1} = (n-1)T$. For the derivation below we suppose that a prediction over m sampling steps is performed. This means that $w(t)$ switches to 1 at $t = mT$.

$$\begin{aligned}\int_0^\infty e^2(t)\, dt &= \int_0^{(n-1)T} e^2(t)\, dt = \int_0^{(n-1)T} (w(t) - u(t) - y(t))^2\, dt \\ &= (n-m-1)T - 2\underbrace{\int_{mT}^{(n-1)T} u(t) + y(t)\, dt}_{l} + \underbrace{\int_0^{(n-1)T} (u(t) + y(t))^2\, dt}_{q}\end{aligned} \tag{18}$$

l and q denote the terms of the cost function that respectively lead to a linear and quadratic dependency on the magnitudes A_i. The linear term l can be easily computed:

$$\begin{aligned} l &= \sum_{i=0}^{n-1} A_i \int_{mT}^{(n-1)T} \sigma(t - iT) + \frac{d}{dt} g(t - iT)\, dt \\ &= \sum_{i=0}^{n-1} A_i \left(\int_{\max(m,i)T}^{(n-1)T} dt + \int_{\max(m-i,0)T}^{(n-i-1)T} \frac{d}{dt} g(t)\, dt \right) \\ &= \sum_{i=0}^{n-1} A_i \big[(n - \max(m,i) - 1)T + g((n-i-1)T) - g(\max(m-i,0)T) \big] \\ &= \sum_{i=0}^{n-1} A_i \theta_i \end{aligned} \tag{19}$$

To determine the quadratic term q we need first to compute some sub-integrals:

$$q_1 = \int_0^{(n-1)T} u^2(t)\,dt = \sum_{i,j=0}^{n-1} A_i A_j \int_{\max(i,j)T}^{(n-1)T} dt$$

$$= \sum_{i,j=0}^{n-1} A_i A_j\,(n - \max(i, j) - 1)\,T \tag{20}$$

$$q_2 = \int_0^{(n-1)T} u(t)y(t)\,dt = \sum_{i,j=0}^{n-1} A_i A_j \int_{\max(i-j,0)T}^{(n-j-1)T} \frac{d}{dt}g(t)\,dt$$

$$= \sum_{i,j=0}^{n-1} A_i A_j \left(g\left[(n-j-1)T\right] - g\left[\max(i-j,0)T\right]\right) \tag{21}$$

$$q_3 = \int_0^{(n-1)T} y^2(t)\,dt = \sum_{i,j=0}^{n-1} A_i A_j \int_0^{(n-1)T} \frac{d}{dt}g(t-iT)\frac{d}{dt}g(t-jT)\,dt$$

$$= h_{i,j}\,((n-1)T) - h_{i,j}(0) \tag{22}$$

where

$$h_{i,j}(t) = -\frac{K^2\omega_0^3\, e^{\omega_0 DT(i+j)}}{4(1-D^2)}\, e^{-2\omega_0 Dt}$$
$$\cdot\left[\frac{\cos\left(\omega_d T\,(j-i)\right)}{D} - \cos\left(2\omega_d t - \omega_d T\,(i+j) - \varphi\right)\right]$$

Therefore:

$$q = q_1 + 2q_2 + q_3$$
$$= \sum_{i,j=0}^{n-1} A_i A_j\big[(n - \max(i, j) - 1)T + h_{i,j}((n-1)T) - h_{i,j}(0)$$
$$+ 2(g[(n-j-1)T] - g[\max(i-j,0)T])\big]$$
$$= \sum_{i,j=0}^{n-1} A_i A_j \psi_{i,j} \tag{23}$$

The equations (18), (19) and (23) give an analytical formulation of the cost function:

$$\mathcal{I}_q(\underline{A}) = \underline{A}^T Q \underline{A} + \sum_{i,j=0}^{n-1} A_i A_j \psi_{i,j} - 2\sum_{i=0}^{n-1} A_i \theta_i + (n-m-1)T$$
$$= \underline{A}^T \underbrace{(\Psi + Q)}_{\widetilde{\Psi}} \underline{A} - 2\underline{A}^T \underline{\theta} + (n-m-1)T \tag{24}$$

Since analytical expressions for g and h are available, the computation of the matrix Ψ and the vector $\underline{\theta}$ does not need any numerical integration. Once computed, Ψ and $\underline{\theta}$ can be used to evaluate the costs for any given amplitude set $\underline{A}$. Hence the determination of the optimal solution $\underline{A}_{\text{opt}}$ does not need huge computational effort. At this level, an iterative solver can be used to compute the optimum. However an analytical solution can be derived to figure out the dependency of $\underline{A}_{\text{opt}}$ on Ψ, C and $\underline{\theta}$ and hence on the plant parameters.

5.2 Analytical Solution of the Minimization Problem

Using an appropriate Lagrangian function, the constraints (13) may be coupled to the cost function to compute a general solution for the problem formulated above:

$$\underline{A}_{\text{opt}} = P\left[2\underline{\theta} - C^T\left(\left(CPC^T\right)^{-1}\left(2CP\underline{\theta} - \underline{b}\right)\right)\right] \tag{25}$$

with $P = \left(\widetilde{\Psi} + \widetilde{\Psi}^T\right)^{-1}$. Note that this solution is only valid for regular matrixes P and C. Note also that the stated solution is a minimum if and only if P is positive definite. In fact, this restriction is not that dramatic, since we can always influence P by the choice of the elements of the matrix Q.

6 Results

The robot motion and the end-effector oscillation are fairly decoupled when using the approach of Lange and Hirzinger [8] to control the setup of Figure 1. Thus the desired motion of the end-effector almost coincides with the actual motion and thus deserves as input for the end-effector control. In particular, there is no interdependance with the robot joint states. Therefore input shaping can be directly applied to the desired positions/orientations of the Cartesian components of the robot motion.

The individual components can be modeled by independent second order transfer functions (1), considering only the dominant oscillation each. If several modes would be significant in each case, input shaping could be applied to each of them, thus yielding a sequence of input filters. In both cases, damping of the respective oscillations reduces as well the cross-couplings between the individual degrees of freedom.

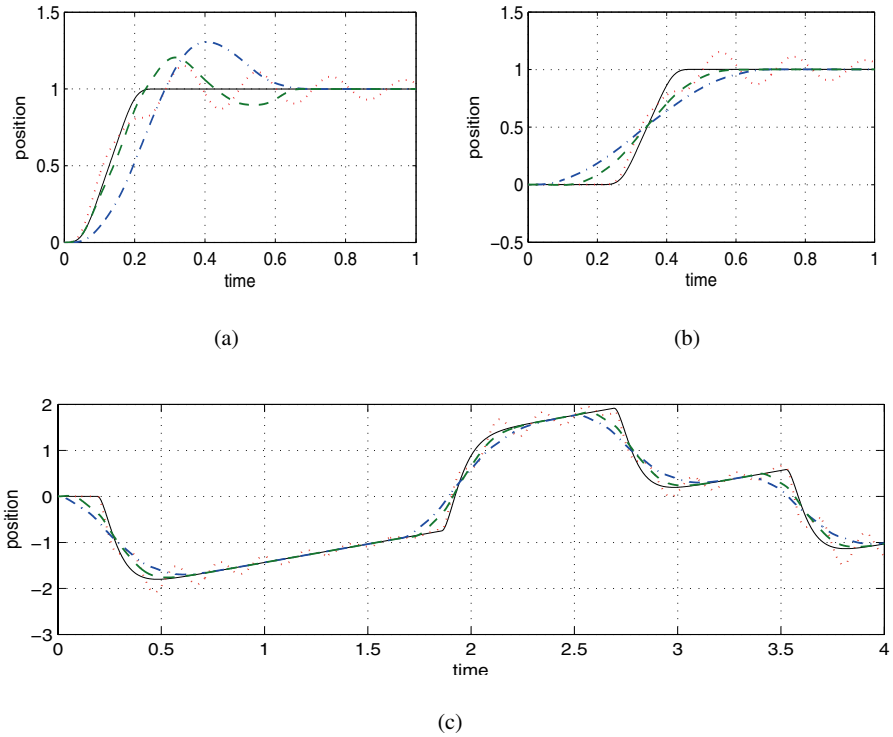

Fig. 3 Simulation results of the system response to finite rate step responses (a & b) and to a typical robot motion profile (c) with $w = 30$ rad/s, $D = 0.02$, $K = 8 \cdot 10^{-4}$ and $T = 12$ ms; (a) no prediction is applied i.e. $m = 0$, (b & c) predication over the first 18 sampling steps is applied i.e. $m = 17$. Dotted: step response without input shaping. Dashed-dotted: step response using an unoptimized input shaper ($n = 36$). Dashed: step response using an optimized input shaper ($n = 36$) with $Q = 0.1 \cdot I$ (I is the unity matrix).

Figure 3 shows samples of our simulation results. Both optimized and unoptimized filters could compensate the shaping time delay using a prediction over m sampling steps. One can clearly see, that an optimized input shaper does not only filter the oscillatory dynamics of the plant's output, but also tracks the references better than other shapers. For large impulse sequences, we could reduce the costs $\mathcal{I}_q$ up to 35%.

Notice that compared with the shapers presented in [9] which only minimize the sensor deflection, the current shaper minimizes also the deviation between the references and the commands. Thus the deflected end-effector pose is controlled to track the reference. Measurements of the sensor deflection are required only for the identification of the system. They are not more used for control.

7 Conclusion

The paper demonstrates that the well known method of input shaping can be modified to fit some principle features of today's industrial robots. A systematical and extendable computational framework is provided to generate such modified shapers. Since fixed robot paths can be commanded in advance, the resulting time delay is not unfavorable and could be compensated. Besides, control errors due to the shaping process and to the oscillation of a compliant tool are minimized. Future work will address the matter of the optimum sensitivity with respect to the plant parameters.

References

1. Smith, O.J.M.: Posicast Control of Damped Oscillatory Systems. In *Proc. of the IRE*, pp. 1249–1255, 1957.
2. Singer, N.C. and Seering, W.P.: Preshaping Command Inputs to Reduce System Vibration. *ASME, J. Dynamic Systems, Measurement and Control* **112**, 76–82, 1990.
3. Singhose, W.E., Seering, W.P. and Singer, N.C.: Input Shaping for Vibration Reduction with Specified Insensitivity to Modeling Errors. In: *Proc. Japan-USA Symp. on Flexible Automation*, Boston, MA, 1996.
4. Singer, N.C.: Residual Vibration Reduction in Computer Controlled Machines. Ph.D. Dissertation, AI-TR 1030, Artificial Intell. Lab., MIT, Cambridge, MA, January 1989.
5. Murphy, B.R. and Watanabe, I.: Digital Shaping Filters for Reducing Machine Vibration. *IEEE Trans. Robotics and Automation* **8**, 285–289, 1992.
6. Tuttle, T. and Seering, W.: A Zero-placement Technique for Designing Shaped Inputs to Suppress Multiple-mode Vibration. In *Proc. American Control Conference*, Baltimore, MD, pp. 2533–2537, 1994.
7. Singhose, W.E., Seering, W.P. and Singer N.C.: Time-Optimal Negative Input Shapers. *ASME, J. Dynamic Systems, Measurement, and Control* **119**, 198–205, 1997.
8. Lange F. and Hirzinger G.: Spatial Vision-Based Control of High-Speed Robot Arms. In: *Industrial Robotics: Theory, Modeling and Control*. Advanced Robotic Systems, Vienna, Austria, 2007.
9. Kamel, A., Lange, F. and Hirzinger G.: New Aspects of Input Shaping Control to Damp Oscillations of a Compliant Force Sensor. In: *Proc. IEEE Internat. Conf. on Robotics and Automation (ICRA)*, Pasadena, CA, May 2008.

Multi-Objective Road Adaptive Control of an Active Suspension System

Guido Koch, Klaus J. Diepold and Boris Lohmann

Abstract In the design of automobile suspension systems, the classical conflict between minimizing vertical chassis acceleration to increase passenger comfort and keeping the dynamic wheel load small in order to ensure safe driveability must be further eased due to increasing customer demands. In order to moderate the conflicting suspension objectives, a switching controller structure for an active suspension system is developed which schedules linear optimal regulators depending on the present dynamic wheel load and suspension deflection. The goal is to maximize ride comfort while the wheel load is below certain safety critical bounds and the suspension deflection remains within given construction-conditioned limits. Stability of the switching control system is analyzed using a multiple Lyapunov function approach. The performance of the road adaptive suspension control system is compared with a linear controller and the passive suspension system in simulations to point out the benefits of the developed control concept.

1 Introduction

An automotive suspension system is expected to provide an optimum of ride comfort for the passengers as well as safe driveability of the car, i.e. guaranteed tire-road contact. While the comfort aspect can be characterized by minimum vertical chassis acceleration, the safety aspect requires a stiff, well damped coupling between vehicle and road in order to keep dynamic wheel load deviations small. Another objective is that the suspension deflection should always remain below the constructionally given limits in order to prevent impulse-like accelerations of the suspended mass as well as excessive wear of the components. These three requirements are con-

Guido Koch, Klaus J. Diepold and Boris Lohmann
Institute of Automatic Control, Technische Universität München, 85748 Garching bei München, Germany; E-mail: guido.koch@tum.de, kj.diepold@mytum.de, lohmann@tum.de

H. Ulbrich and L. Ginzinger (eds.), Motion and Vibration Control, 189–200.

flicting, [2]. However, this conflict can be eased by controlled actuators in active suspension systems.

Some works on suspension controller design present the idea of adapting the control objectives and thus the controller dynamics to the current road excitation. In [1,4,5] switching controllers are presented that minimize either the vertical chassis acceleration or the suspension deflection. In [9], a control structure with adaptive properties has been presented using a wheel load adaptive skyhook-control concept for a *semi-active* suspension system.

The new approach in this paper is the design of a nonlinear controller structure that adapts to the current road disturbance in order to optimize the suspension regarding the three conflicting objectives comfort, safe driveability and suspension deflection limits. The main idea is that maximum comfort should be achieved while safety for every road excitation is preserved by keeping the dynamic wheel load and the suspension deflection below specified critical bounds. This is accomplished by a switching controller structure based on six linear quadratic optimal controllers and a switching logic. The required actuator force for control should be feasible.

The remainder of this paper is organized as follows: First, models for an active and passive vehicle suspension are presented in Section 2 and performance requirements are specified. In Section 3, the controller structure and the calculation of the scheduling variables initializing the switching are presented. Stability of the switched control system for the active suspension is analyzed in Section 4 using a multiple Lyapunov function approach. Finally, simulation results and a performance comparison are presented.

2 Modelling and System Requirements

The lift movement of the suspension system can be modelled using the well-known quarter car models illustrated in Figure 1 [7, 11]. In the high bandwidth active suspension considered here an ideal actuator is integrated.

The model of the passive suspension results from the active suspension model if $F(t) = 0$. The state-vector $\mathbf{x}$ and the output vector $\mathbf{y}$ are introduced as $\mathbf{x} =$

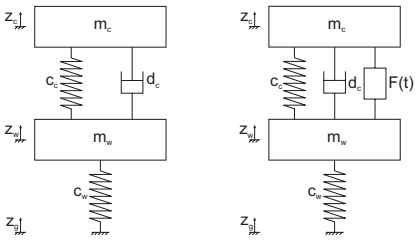

Fig. 1 Quarter car models of the passive (left) and active suspension (right).

Table 1 Notation and parameter values [7].

Model parameter	Symbol	Value	Unit
Quarter car chassis mass (sprung mass)	m_c	256	[kg]
Wheel assembly mass (unsprung mass)	m_w	31	[kg]
Suspension spring stiffness	c_c	20200	[N/m]
Tire stiffness	c_w	128000	[N/m]
Sprung mass damping coefficient	d_c	1140	[Ns/m]
Undamped uncoupled natural frequency of the sprung mass	$\omega_c = \sqrt{\frac{c_c}{m_c}}$	8.88	[rad/s]
Uncoupled natural frequency of the unsprung mass	$\omega_w = \sqrt{\frac{c_w}{m_w}}$	64.26	[rad/s]

$[\, z_c - z_w,\ \dot{z}_c,\ z_w - z_g,\ \dot{z}_w \,]^T$ and $\mathbf{y} = [\, \ddot{z}_c,\ F_{dyn},\ z_c - z_w \,]^T$ where F_{dyn} denotes the dynamic wheel load force. With the control input $u(t) = F(t)$ and disturbance input $u_d(t) = \dot{z}_g(t)$ the quarter-car model can be expressed as a state space model in the form

$$\dot{\mathbf{x}} = \mathbf{A}\mathbf{x} + \mathbf{b}u + \mathbf{e}u_d \ , \qquad \mathbf{y} = \mathbf{C}\mathbf{x} + \mathbf{d}u \ , \tag{1}$$

$$\mathbf{A} = \begin{bmatrix} 0 & 1 & 0 & -1 \\ -\frac{c_c}{m_c} & -\frac{d_c}{m_c} & 0 & \frac{d_c}{m_c} \\ 0 & 0 & 0 & 1 \\ \frac{c_c}{m_w} & \frac{d_c}{m_w} & -\frac{c_w}{m_w} & -\frac{d_c}{m_w} \end{bmatrix}, \ \mathbf{b} = \begin{bmatrix} 0 \\ \frac{1}{m_c} \\ 0 \\ -\frac{1}{m_w} \end{bmatrix}, \ \mathbf{e} = \begin{bmatrix} 0 \\ 0 \\ -1 \\ 0 \end{bmatrix}, \tag{2}$$

$$\mathbf{C} = \begin{bmatrix} -\frac{c_c}{m_c} & -\frac{d_c}{m_c} & 0 & \frac{d_c}{m_c} \\ 0 & 0 & c_w & 0 \\ 1 & 0 & 0 & 0 \end{bmatrix}, \ \mathbf{d} = \begin{bmatrix} \frac{1}{m_c} \\ 0 \\ 0 \end{bmatrix} . \tag{3}$$

The model parameters are given in Table 1.

2.1 Performance Requirements

In order to ensure maximum ride comfort, the rms-value of the vertical chassis acceleration $\|\ddot{z}_c\|_{rms}$ is to be minimized. The human sensitivity for vibration is frequency dependent and the most sensitive frequency range for mechanical excitation is 4–8 Hz [3]. Therefore, a fifth order shaping filter $G_c(j\omega)$ with an amplitude characteristic as depicted in Figure 2 and a state space representation

$$\dot{\mathbf{x}}_f = \mathbf{A}_f\mathbf{x}_f + \mathbf{b}_f\ddot{z}_c \ , \quad \ddot{z}_{c,f} = \mathbf{c}_f^T\mathbf{x}_f \tag{4}$$

is introduced, [3]. Its impulse response is $g_c(t)$ such that $\ddot{z}_{c,f} = g_c(t) * \ddot{z}_c$.

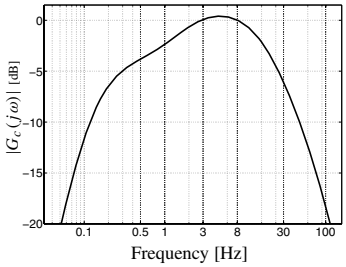

Fig. 2 Amplitude characteristic of the shaping filter $G_c(j\omega)$ [3].

An augmented plant model with state vector $\mathbf{x}_{reg} = [\,\mathbf{x}^T,\ \mathbf{x}_f^T\,]^T$ is used to incorporate the shaping filter in the controller design (Section 3) such that the controlled variables are $\mathbf{y}_{reg} = [\,\ddot{z}_{c,f},\ \ddot{z}_c,\ F_{dyn},\ z_c - z_w\,]^T$. With $\mathbf{h} = [\,0\ 1\ 0\ 0\,]$ the augmented plant model is

$$\dot{\mathbf{x}}_{reg} = \underbrace{\begin{bmatrix} \mathbf{A} & \mathbf{0} \\ \mathbf{b}_f\mathbf{h}\mathbf{A} & \mathbf{A}_f \end{bmatrix}}_{\mathbf{A}_{reg}} \mathbf{x}_{reg} + \underbrace{\begin{bmatrix} \mathbf{b} \\ \mathbf{b}_f\mathbf{h}\mathbf{b} \end{bmatrix}}_{\mathbf{b}_{reg}} u + \underbrace{\begin{bmatrix} \mathbf{e} \\ \mathbf{0} \end{bmatrix}}_{\mathbf{e}_{reg}} u_d \quad , \tag{5}$$

$$\mathbf{y}_{reg} = \underbrace{\begin{bmatrix} \mathbf{0} & \mathbf{c}_f^T \\ \mathbf{C} & \mathbf{0} \end{bmatrix}}_{\mathbf{C}_{reg}} \mathbf{x}_{reg} + \underbrace{\begin{bmatrix} \mathbf{0} \\ \mathbf{d} \end{bmatrix}}_{\mathbf{d}_{reg}} u \ . \tag{6}$$

Safety requirements

For stochastic road excitation the dynamic wheel load's rms-value should be bounded as follows[1]

$$\max\left(\|F_{dyn}\|_{rms}\right) \le \Gamma_{var} = \frac{F_{stat}}{3} \ , \tag{7}$$

where $F_{stat} = g\,(m_c + m_w)$ denotes the static wheel load. To ensure safety for singular excitation events like potholes, the primary control objective changes from comfort to safety, i.e. dynamic wheel load limitation, if

$$\frac{|F_{dyn}|}{F_{stat}} \ge \Gamma_{sing} = 0.75 \ . \tag{8}$$

[1] This is derived from the 3σ-rule and assures, assuming a normally distributed stochastic disturbance signal, that F_{dyn} remains within $\pm F_{stat}$ for 99.7% of the time [10].

Requirements on suspension deflection

A total of $|\Delta\hat{z}| = 0.1\,\text{m}$ maximum suspension deflection is used as a limit in the simulations of this study. Hitting the limit is modelled by an increase in c_c as follows

$$\tilde{c}_c = \begin{cases} c_c & \text{for} \quad -0.1 \le z_c - z_w \le 0.1 \\ 15 \cdot c_c & \text{for} \quad |z_c - z_w| > 0.1 \wedge \ \dot{z}_c - \dot{z}_w > 0\,. \end{cases} \tag{9}$$

3 Controller Design

For the road adaptive suspension control $n = 6$ linear quadratic optimal (LQR) controllers with different weighting matrices $\mathbf{Q}_y$ for separate primary control objectives are designed in order to analyze the potential of the concept. For the application of the classical LQR design formalism with output weighting in the cost functional

$$J_{LQR} = \int_0^\infty \left(\mathbf{y}_{reg}^T \mathbf{Q}_y \mathbf{y}_{reg} + u R u\right) dt \tag{10}$$

with $\mathbf{Q}_y = \mathbf{Q}_y^T \ge 0$ and $R > 0$ chosen according to Table 2, the cost functional needs to be slightly modified due to the direct feedthrough term $\mathbf{d}_{reg}$ present in the augmented suspension model. The resulting cost functional resulting from Eq. (10) is

$$J_{LQR} = \int_0^\infty \left(\mathbf{x}_{reg}^T \mathbf{Q} \mathbf{x}_{reg} + 2\mathbf{x}_{reg}^T \mathbf{s} u + u \tilde{R} u\right) dt \tag{11}$$

with $\mathbf{Q} = \mathbf{C}_{reg}^T \mathbf{Q}_y \mathbf{C}_{reg}$, $\mathbf{s} = \mathbf{C}_{reg}^T \mathbf{Q}_y \mathbf{d}_{reg}$ and $\tilde{R} = \mathbf{d}_{reg}^T \mathbf{Q}_y \mathbf{d}_{reg} + R$. We substitute the control input $\tilde{u} = u + \tilde{R}^{-1} \mathbf{s}^T \mathbf{x}$ in Eq. (11) in order to remove the mixed term $2\mathbf{x}_{reg}^T \mathbf{s} u$ such that the conventional LQR design formalism can be applied [6]. The optimal solution for each designed LQR-controller with weighting matrix $\mathbf{Q}_{y,i}$ is state feedback $u_i = -\mathbf{k}_i^T \mathbf{x}_{reg}$ with $\mathbf{k}_i^T = \tilde{R}^{-1}(\mathbf{b}_{reg}^T \mathbf{P}_{r,i} + \mathbf{s}_i^T)$ and $\mathbf{P}_{r,i}$ being the symmetric, positive definite solution of the algebraic Riccati-equation

$$\begin{aligned} &\mathbf{A}^T \mathbf{P}_{r,i} + \mathbf{P}_{r,i} \mathbf{A} - \left(\mathbf{P}_{r,i} \mathbf{b}_{reg} + \mathbf{s}_i\right) \tilde{R}^{-1} \left(\mathbf{b}_{reg}^T \mathbf{P}_{r,i} + \mathbf{s}_i^T\right) + \mathbf{Q}_i = \mathbf{0}\,, \\ &\mathbf{P}_{r,i} = \mathbf{P}_{r,i}^T > \mathbf{0}\,. \end{aligned} \tag{12}$$

Wheel load adaptation

Figure 3 shows the control structure in which the LQR-controllers are implemented. In the following the part of the switching logic is presented that schedules the controllers by the scheduling variable $q_{adp}(t)$ with $0 \le q_{adp}(t) \le 1$ depending on the dynamic wheel load. The basic concept is described in [9] but is modified here

Table 2 Controller weights $\mathbf{Q}_{y,i}$, $R = 1$ for all controllers.

$\mathbf{Q}_{y,i}$	Value	Controller Type
$\mathbf{Q}_{y,1}$	$diag\left(3.5 \cdot 10^5, 0,\ 0.1,\ 0\right)$	Most comfort oriented controller
$\mathbf{Q}_{y,2}$	$diag\left(8 \cdot 10^4,\ 0,\ 0.4,\ 0\right)$	Comfort oriented controller
$\mathbf{Q}_{y,3}$	$diag\left(4 \cdot 10^4,\ 0,\ 0.7,\ 0\right)$	Intermediate controller
$\mathbf{Q}_{y,4}$	$diag\left(10^4,\ 0,\ 0.9,\ 0\right)$	Safety oriented controller
$\mathbf{Q}_{y,5}$	$diag(10,\ 0,\ 1,\ 0)$	Most safety oriented controller
$\mathbf{Q}_{y,6}$	$diag\left(0,\ 5.2 \cdot 10^7,\ 10^{-3},\ 3 \cdot 10^{12}\right)$	Suspension deflection controller

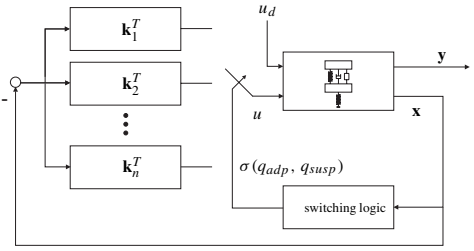

Fig. 3 Switching state feedback controller structure.

in details. In case of "hard" switching between the five comfort/safety oriented controllers $\mathbf{k}_i^T$, $i \in \{1, \ldots, 5\}$ (see Table 2) the piecewise continuous switching function is

$$\sigma\left(q_{adp}\left(t\right)\right) = \begin{cases} \lceil q_{adp}(t) \cdot 5 \rceil & \text{if} \quad 0 < q_{adp} \leq 1 \\ 1 & \text{if} \quad q_{adp} = 0 \end{cases} \tag{13}$$

where $\lceil \cdot \rceil$ denote Gaussian brackets also known as the ceiling function. The sixth controller is activated separately as described at the end of this section. The scheduling variable $q_{adp}(t)$ increases with increasing wheel load and correspondingly as $q_{adp}(t) \approx 1$, the most safety oriented controller $\mathbf{k}_5^T$ is chosen by the switching logic.

The current value of the scheduling variable is determined by two adaptation-rates as $q_{adp}(t) = \min(1, q_s(t) + q_f(t))$. The slow adaptation rate $q_s(t)$ (illustrated in the lower branch of block diagram in Figure 4) is used to adapt the suspension controller to different variances of the road excitation signal. The variance of the dynamic wheel load is

$$\sigma_{F_{dyn}}^2 = \lim_{T \to \infty} \frac{1}{T} \int_0^T F_{dyn}^2 dt.$$

After Laplace transformation we replace the integral term $\frac{1}{s}$ by a first order low pass filter thus approximating the dynamic wheel load's variance by

$$\sigma_{F_{dyn}}^2(s) \approx \frac{1}{\tau_s s + 1} F_{dyn}^2(s).$$

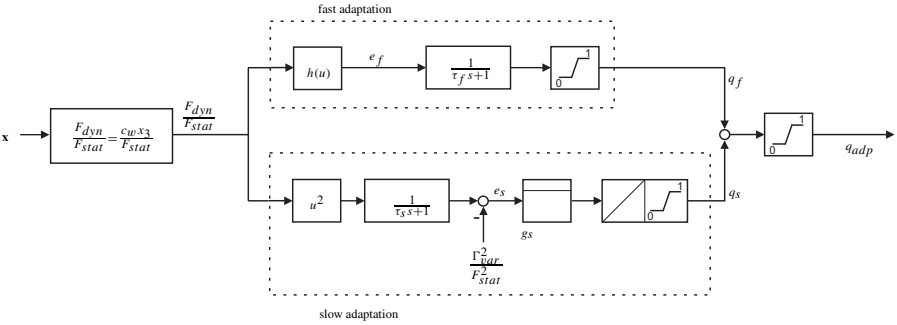

Fig. 4 Wheel load adaptation structure.

For τ_s the chassis mass eigenmodes' time constant is chosen resulting in $\tau_s = 2\pi\sqrt{m_c/c_c} \approx 0.71$ sec.

The dynamic wheel load filtered in this manner is compared to the upper bound Γ_{var} given by Eq. (7). The deviation

$$e_s(t) = \frac{\sigma^2_{F_{dyn}(t)}}{F^2_{stat}} - \frac{\Gamma^2_{var}}{F^2_{stat}}$$

is scaled by a constant $g_s = 1.5$ and is integrated by an output-limited integrator with an output signal range of [0, 1] resulting in q_s.

If the vehicle hits an occasional pothole on an otherwise smooth road, it is important that an instant switching to a safety oriented controller occurs. Therefore, it is necessary to introduce a fast adapting term $q_f(t)$ in the calculation of $q_{adp}(t)$ which is shown in the upper branch of the block diagram (Figure 4).

To ensure that this fast adaptation part remains inactive as long as the relative dynamic wheel load has not reached $\Gamma_{sing} = 0.75$ defined in Eq. (8), the wheel load is scaled by a nonlinear funtion h (based on a fourth order polynomial) shown in Figure 5 which output value e_f is only nonzero if $|F_{dyn}|/F_{stat} > 0.75$. Again a low pass filter for e_f with a time constant

$$\tau_f = \frac{5}{9} \cdot 2\pi\sqrt{\frac{m_w}{c_c + c_w}} \approx 0.05 \text{ sec}$$

is used. The output q_f is limited to a range of $q_f \in [0, 1]$ as well.

Suspension deflection adaptation

A second scheduling variable $q_{susp}(t)$ is calculated which determines when the sixth controller that suppresses excessive suspension deflection is activated by

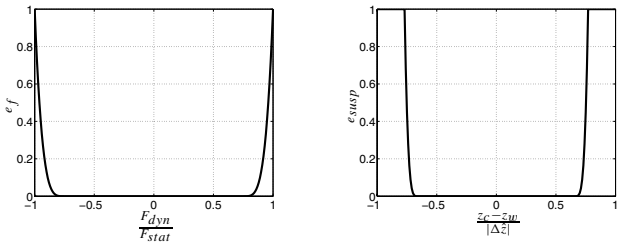

Fig. 5 Nonlinear scaling function $h(F_{dyn}/F_{stat})$ for fast wheel load adaptation (left) and $f(z_c - z_w/|\Delta\hat{z}|)$ for suspension deflection adaptation (right).

$\sigma(q_{adp}, q_{susp})$. This is described in detail in Section 4 because its switching behaviour determines the stability of the system. The scheduling variable $q_{susp}(t)$ is calculated similarly to $q_f(t)$ with $z_c - z_w/|\Delta\hat{z}|$ as input. Again a nonlinear function $f(z_c - z_w/|\Delta\hat{z}|)$ shown in Figure 5 is used being nonzero if $|z_c - z_w|/|\Delta\hat{z}| > 0.66$. The filter's time constant is $\tau_{susp} = 1/25\,\tau_f$ to ensure quick activation of the suspension deflection controller.

4 Stability Analysis

Stability analysis of switched systems is a very important issue because it is not guaranteed that switching between asymptotically stable subsystems (here: resulting from different controllers) results in an asymptotically stable switched system. A well known stability analysis approach uses quadratic Lyapunov functions of the form $V(\mathbf{x}) = \mathbf{x}^T\mathbf{P}\mathbf{x}$, $V(\mathbf{0}) = 0$, $V(\mathbf{x}) > 0$, $\dot{V}(\mathbf{x}) < 0$, $\mathbf{P} = \mathbf{P}^T > \mathbf{0}$. If a matrix $\mathbf{P}$ can be found such that these equations are fullfilled, the equilibrium $\mathbf{x} = \mathbf{0}$ of the switched system is uniformly asymptotically stable, [8]. For numerical stability analysis, the Lyapunov function and the condition for $\mathbf{P}$ has been formulated as a pair of linear matrix inequalities (LMI) for every closed loop system matrix $\mathbf{A}_{cl,reg,i} = \mathbf{A}_{reg} - \mathbf{b}_{reg}\mathbf{k}_i^T$ of the switched active suspension system

$$\left(\mathbf{A}_{cl,reg,i}^T\mathbf{P} + \mathbf{P}\mathbf{A}_{cl,reg,i}\right) < \mathbf{0} \qquad \text{for} \qquad i \in \{1, \ldots, n\} \tag{14}$$

$$\mathbf{P} = \mathbf{P}^T > \mathbf{0}\,. \tag{15}$$

These equations are solved numerically. Although no feasible solution for all six controllers exists, two feasible solutions $\mathbf{P}_1$ and $\mathbf{P}_2$ have been obtained for two subsets of LQR-controllers $\mathbf{k}_i^T$ with $i \in \{1, \ldots, 5\}$ and $\mathbf{k}_j^T$ with $j \in \{3, \ldots, 6\}$. Switching between controllers within each subset thus results in an asymptotically stable system for arbitrary switching signals $\sigma(\cdot)$ because the Lyapunov function is a common quadratic Lyapunov function (CQLF) of all systems within the subset [12].

Soft switching

Because the active suspension system is improper regarding the control input, a discontinuous control force resulting from a noncontinuous switching function $\sigma(q_{adp}(t),\ q_{susp}(t))$ would result in discontinuities of $\ddot{z}_c$ and thus decreasing passenger comfort. To avoid these discontinuities "soft" switching by interpolating between the controllers via $q_{adp}(t)$ and $q_{susp}(t)$ directly is preferable. Therefore, stability for linear interpolation between the state feedback controllers is analyzed.

Theorem 1. *If two closed loop system matrices* $\mathbf{A}_1$ *and* $\mathbf{A}_2$ *resulting from control loops with different state feedback controllers* $\mathbf{K}_1$ *and* $\mathbf{K}_2$ *for the same open loop system matrix* $\mathbf{A}_{ol}$ *have a CQLF characterized by* $\mathbf{P} : \mathbf{P} = \mathbf{P}^T > \mathbf{0}$*, the system matrix*

$$\mathbf{A}_{cl} = \mu\mathbf{A}_1 + (1-\mu)\mathbf{A}_2\ , \quad 0 \le \mu \le 1 \tag{16}$$

being a linear interpolation of $\mathbf{A}_1$ *and* $\mathbf{A}_2$ *has the same CQLF characterized by* $\mathbf{P}$.

Proof. A CQLF of the two closed loop systems is defined by

$$\exists \mathbf{P} : \mathbf{A}_i^T\mathbf{P} + \mathbf{P}\mathbf{A}_i < \mathbf{0}\ , \quad \mathbf{P} = \mathbf{P}^T > \mathbf{0} \quad \forall i \in \{1,2\}\ . \tag{17}$$

If we add the scaled Lyapunov functions for the closed loop system matrices we get

$$\mu \underbrace{(\mathbf{A}_1^T\mathbf{P} + \mathbf{P}\mathbf{A}_1)}_{<\mathbf{0}} + (1-\mu)\underbrace{(\mathbf{A}_2^T\mathbf{P} + \mathbf{P}\mathbf{A}_2)}_{<\mathbf{0}} < \mathbf{0}\ . \tag{18}$$

For state feedback $\mathbf{u} = -\mathbf{K}_i\mathbf{x},\ i \in \{1,2\}$ the closed loop system matrices have the form $\mathbf{A}_i = \mathbf{A}_{ol} - \mathbf{B}\mathbf{K}_i$. Considering this and the fact that linear interpolation between the controllers $\mathbf{K}_i$ would result in the state feedback gain matrix $\tilde{\mathbf{K}} = \mu\mathbf{K}_1 + (1-\mu)\,\mathbf{K}_2$, Eq. (18) can be transformed into

$$[\mathbf{A}_{ol} - \mathbf{B}\tilde{\mathbf{K}}]^T\mathbf{P} + \mathbf{P}[\mathbf{A}_{ol} - \mathbf{B}\tilde{\mathbf{K}}] < \mathbf{0}\ . \tag{19}$$

□

Multiple Lyapunov function approach for stable suspension deflection control

Because no CQLF could be obtained for the whole set of closed loop suspension system matrices $\mathbf{A}_{cl,reg,i}$, the stability for the switching control using all six controllers can be ensured using a multiple Lyapunov function approach, [12]. Asymptotic stability in the sense of Lyapunov while switching smoothly between the two numerically calculated Lyapunov functions $V_1(\mathbf{x})$ and $V_2(\mathbf{x})$ is ensured by two conditions:

1. Switching between the two Lyapunov functions is only allowed if the LQR-controller being activated by the switching is either $\mathbf{k}_3^T$, $\mathbf{k}_4^T$ or $\mathbf{k}_5^T$ because both Lyapunov functions are valid for these controllers.

2. It is only allowed to switch back to the Lyapunov function $V_l(\mathbf{x})$ with $l \in \{1, 2\}$ at time t_2 if the associated Lyapunov function has decreased since leaving it at time t_1 (with $t_1 < t_2$), i.e. $V_l(\mathbf{x}(t_2)) < V_l(\mathbf{x}(t_1))$ [12].

Due to the same quadratic structure of $V_1(\mathbf{x})$ and $V_2(\mathbf{x})$ for our control problem, it is sufficient if condition 2 is fulfilled for $l = 1$ to guarantee asymptotic stability.

Switching to $V_2(\mathbf{x})$ is only necessary if the suspension deflection controller $\mathbf{k}_6^T$ should be activated. Ensuring that condition 1 is satisfied, the wheel load adaptation parameter $q_{adp}(t)$ is smoothly increased automatically between $0.66 \leq q_{susp}(t) \leq 0.77$ (see Figure 5) such that $q_{adp}(t)$ is at the lower limit ($q_{adp}(t) = 0.5$) of the activation of controller $\mathbf{k}_3^T$ at least before the suspension controller $\mathbf{k}_6^T$ is enabled to be switched to. For $0.8 \leq q_{susp}(t) \leq 0.9$ the suspension controller $\mathbf{k}_6^T$ is definitely activated (with a similar function as $f(\frac{z_c - z_w}{|\Delta \hat{z}|})$ in Figure 5). Switching back to $V_1(\mathbf{x})$ is only possible if $q_{susp}(t) < 0.77$ and additionally condition 2 is fulfilled for $l = 1$.

5 Simulation Results

The performance of the designed controller is compared to that of a conventional, comfort focussed LQR-controller with $\mathbf{Q}_{y,LQR} = diag\left(2.5 \cdot 10^4,\ 0,\ 0.4,\ 0\right)$ and the passive suspension. As excitation signal $z_g(t)$ a superposition of two synthetic signals (bumps) and two subsequent real measured road track signals is used (Figure 6). The road excitation is zero for all points in time not depicted. Figure 7 shows that the power spectral density (PSD) of $\ddot{z}_c$ is significantly reduced in the range of the chassis' resonance frequency (approx. 1.41 Hz). In the frequency range from 4–8 Hz the adaptive controller performs best concerning comfort (approx. 17% better than the passive suspension and 8% better than the LQR-controller). The comfort gain vs. the LQR-controller would be more significant if a fully active suspension model without passive suspension would be considered. Only the adaptive controller keeps the suspension deflection limit at the first bump.

The proposed road adaptive controller achieves a comfort gain in an rms-sense of approx. 20% in comparison to the passive system and of 11% compared to the LQR-controller for the simulated road profile (Table 3). All control forces are in an acceptable range.

Table 3 Performance of the road adaptive controller.

Quantity	Unit	Passive	LQR	Road adaptive	Comment
$\|\ddot{z}_c\|_{rms}$	$\frac{\mathrm{m}}{\mathrm{s}^2}$	3.06	2.75	2.45	
$\|g_c * \ddot{z}_c\|_{rms}$	$\frac{\mathrm{m}}{\mathrm{s}^2}$	2.85	2.56	2.36	
$\|F_{dyn}\|_{rms}$	N	960.29	855.26	871.36	Limit: $\Gamma_{var} = 938.49$ N
$\|F(t)\|_{rms}$	N	-	156.19	262.66	
$\max(\|F(t)\|)$	N	-	2781	1771	

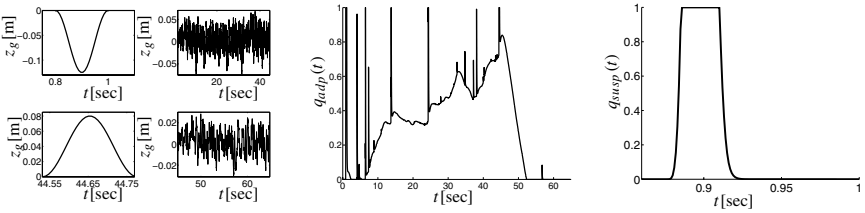

Fig. 6 Road signal $z_g(t)$ (left) and adaptation parameters $q_{adp}(t)$ (middle), $q_{susp}(t)$ (right).

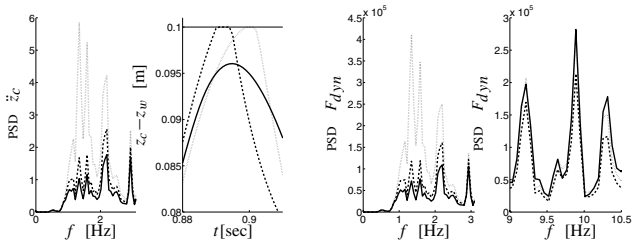

Fig. 7 Power spectral density (PSD) of the chassis acceleration $\ddot{z}_c$ (left), suspension deflection $z_c - z_w$ at the first bump (middle left), power spectral density of the wheel load $\ddot{z}_c$ for two frequency ranges (right); Adaptive controller (solid), LQR-controller (small dots), passive setting (large dots).

6 Conclusion

A road adaptive suspension controller has been designed that switches smoothly between different LQR-controllers depending on the current dynamic wheel load and suspension deflection. The primary control objective is to maximize passenger comfort while given limits for the dynamic wheel load and suspension deflection are not violated. Stability of the system is guaranteed by a multiple Lyapunov function approach implemented in the scheduling algorithm. The result is a performance gain of approx. 20% vs. the passive system and 11% vs. the LQR-controlled suspension. Only the road adaptive controller does not exceed the suspension limit.

References

1. I. J Fialho and G. J. Balas. Road adaptive active suspension design using linear parameter-varying gain-scheduling. *IEEE Transact. on Control Systems Technology*, 10(1):43–54, 2002.
2. D. Hrovat. Survey of advanced suspension developments and related optimal control aplications. *Automatica*, 33(10):1781–1817, 1997.
3. International Standard Organization. *ISO 2631-1:1997 – Mechanical Vibration and Shock – Evaluation of Human Exposure to Whole-Body Vibration*, 1997.
4. J. Lin and I. Kanellakopoulos. Nonlinear design of active suspensions. In *Proceedings of the 34th IEEE Conference on Decision and Control, New Orleans, LA*, pp. 3567–3569, 1995.

5. J. Lin and I. Kanellakopoulos. Road-adaptive nonlinear design of active suspensions. In *Proc. American Control Conference*, 1997.
6. G. Ludyk. *Theoretische Regelungstechnik 2*. Springer, Berlin, 1995.
7. M. Mitschke and H. Wallentowitz. *Dynamik der Kraftfahrzeuge*. Springer, Berlin, 2004.
8. J. J. E. Slotine and W. Li. *Applied Nonlinear Control*. Prentice Hall, Englewood Cliffs, NJ, 1991.
9. P. Venhovens. *Optimal Control of Vehicle Suspensions*. Delft University of Technology, Faculty of Mechanical Engineering, Delft, 1993.
10. T. L. Paez, P. H. Wirsching, and K. Ortiz. *Random Vibrations – Theory and Practice*. John Wiley and Sons, New York, 1995.
11. J. Y. Wong. *Theory of Ground Vehicles*. John Wiley & Sons, New York, 2001.
12. K. Wulff. *Quadratic and Non-Quadratic Stability Criteria for Switched Linear Systems*. PhD Thesis, National University of Ireland, Department of Computer Science, Maynooth, 2004.

Development & Control of Master-Slave Robot Hand Driven by Pneumatic Actuator

Hiroyuki Komatsubara, Nobutaka Tsujiuchi, Takayuki Koizumi, Hiroto Kan, Yoichiro Nakamura and Masanori Hirano

Abstract We present an artificial muscle-type pneumatic actuator as the driving source of a robot hand that is both safe and flexible. Some development of robot hands using pneumatic actuators has already taken place. However, in using a pneumatic actuator, a big compressor is needed. So the driving system also needs to be big, and enlargement of the driving system is a major problem.

Consequently, in this research, we develop a low-pressure, low-volume pneumatic actuator for driving a robot hand that works flexibly and safely on the assumption that it will be in contact with people. We examine the characteristics of this pneumatic actuator, and develop a five-fingered robot hand with pneumatic actuators. Furthermore, we construct a master-slave system to enable the robot hand to perform the same operations as a human hand. We make a joint model that has one degree of freedom using a pneumatic actuator, construct a control system for the joint model and verify its control performance. Consequently, in this research, we develop a low-pressure, low-volume pneumatic actuator for driving a robot hand that works flexibly and safely on the assumption that it will be in contact with people. We examine the characteristics of this pneumatic actuator, and develop a five-fingered robot hand with pneumatic actuators. Furthermore, we construct a master-slave system to enable the robot hand to perform the same operations as a human hand. We make a joint model that has one degree of freedom using a pneumatic actuator, construct a control system for the joint model and verify its control performance.

H. Komatsubara, N. Tsujiuchi, T. Koizumi and H. Kan
Department of Mechanical Engineering, Doshisha University, Kyotanabe Kyoto 610-0312 Japan; E-mail: {ntsujiuc, tkoizumi}@mail.doshisha.ac.jp, dth0345@mail4.doshisha.ac.jp

Y. Nakamura and M. Hirano
Department of Mechanical Engineering, SQUSE Inc., Shokushi-cho Nishinokyo Nakagyo-ku, Kyoto 604-8381, Japan; E-mail: {yoichiro_nakamura, masanori_hirano}@squse.co.jp

H. Ulbrich and L. Ginzinger (eds.), Motion and Vibration Control, 201–210.

1 Introduction

Recently, the range of places where robots are used has extended even to the office and home, and robots have come to support human activities. Since human activities are various and change depending on the lifestyle, a robot must be sufficiently flexible to adjust to supporting various tasks. Therefore, the development of an end effector that can perform a variety of operations is hoped for. It is also necessary for this kind of robot to functionally have a softness in the mechanism resembling the living human body, and for the actuator to have enough gentleness in driving that we can call it a "Safety actuator" [1]. For this purpose, an air pressure actuator that provides essential softness by using the compressibility of air can be beneficial. However, the past McKibben-type pneumatic actuator cannot be installed directly in the robot hand due to size limitation. Moreover, a complex structure is needed in installing the actuator by driving the fingers with wires. Therefore, a low-pressure pneumatic actuator was developed in this research. This actuator can enable a low-pressure drive by making the constituent material flexible and also contributes to the miniaturization of the compressor. Moreover, it is miniaturized from past pneumatic actuators so that it can be installed directly on the finger of the robot hand.

In our experiment, a robot hand that uses this pneumatic actuator was developed. When a work area such as a clean room is assumed, this robot hand should do work similar to a person's hand. What is more, we construct a master-slave system to enable the robot hand to perform the same operations as a human hand. It is necessary to construct a pneumatic actuator control system that makes complex movements enabled for that. Various studies have been performed on the control of the actuator [2, 3]. However, little research exists on controlling a robot hand with the actuator installed directly in the finger. So we installed the actuator to single joint and then, produced a joint model by which the winding and the progress operation is controlled. The purpose of this research is to construct a positional control by using the joint model, and to confirm its effectiveness.

2 The Structure of the Pneumatic Actuator

The most outstanding feature of a pneumatic actuator is its simplicity and convenience based on the compressibility of air, and the pneumatic actuator we developed during this research is a type in which expansion and contraction operations are performed by adjusting the pressure in a rubber balloon, which is assumed to be similar to a human muscle. Some actuators like this have already been developed [4]. A typical actuator of this kind is the McKibben-type artificial muscle [5]. Many research consortiums are developing robots using such a pneumatic actuator [6, 7].

However, a pneumatic actuator that uses an artificial muscle such as the McKibben-type artificial muscle needs a high level of air pressure to achieve the necessary driving power. This is because such a pneumatic actuator is required to generate a force equal to that of a hydraulic motor, hydraulic cylinder and electric

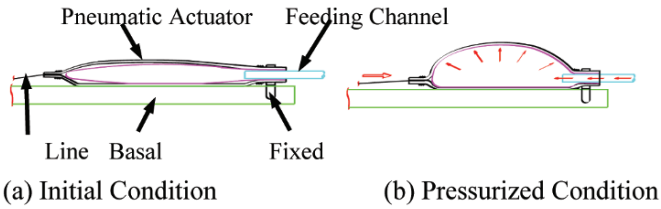

Fig. 1 Schematic of pneumatic actuator.

motor. Consequently, applications for prosthetic hands lack practicality because a big air compressor is needed when conventional actuators like those outlined above are used. We therefore adjusted the design of our robot hand and developed a pneumatic actuator that was able to generate enough power to drive the fingers and grasp objects using low air volume and low pressure.

Figure 1 shows the structure of the pneumatic actuator that we developed. It is composed of a rubber balloon, a net that covers the rubber balloon, and a feeding channel that sends compressed air to the balloon.

The actuator is inflated from the condition shown in Figure 1a to that in Figure 1b by sending compressed air to the balloon in the actuator through the feeding channel whereby the actuator generates the necessary force. Part of the actuator is fixed, as shown in Figure 1. The rubber balloon is about 0.21 mm thick and is covered by netting so that the actuator may efficiently shrink to the air volume sent.

The basic structure of the pneumatic actuator is the same as the McKibben-type artificial muscle described previously. However, our pneumatic actuator can be driven by lower pressure and lower air volume by making the components flexible. This means that the robot finger can be driven, and can generate enough force to grasp objects without the need for high pressure. What is more, this pneumatic actuator can be arranged directly in a robot hand because it can be miniaturized.

3 Control of Joint Model

3.1 Joint Model

Figure 2 shows the schematic of the joint model used in the experiment. The range of operation of the joint model is from −10 deg to 90 deg. A positional sensor is installed in the joint model, and the angle of the joint model is measured. In terms of the structure of the joint model, we arranged two actuators per joint, the lines of the pneumatic actuators are tied to an upper material, and the actuators are fixed to a lower material. When the pneumatic actuators shrink, this pulls the upper material. One actuator shrinks, another progresses, and the joint model performs the flexion operation and the extension operation. The amount of pressure change in both actuators is equated.

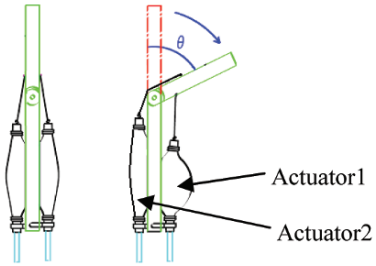

Fig. 2 Schematic of joint model.

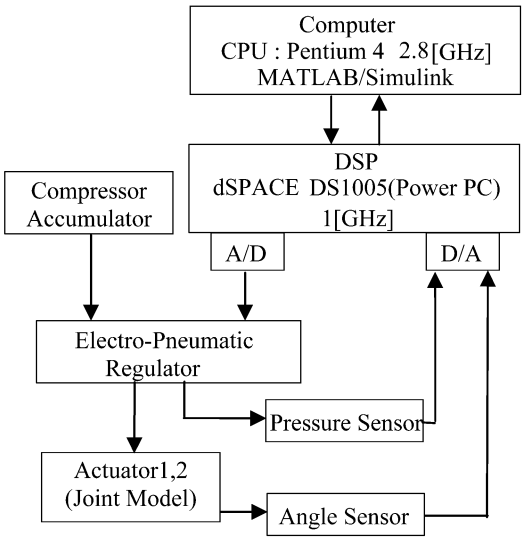

Fig. 3 Experiment apparatus.

3.2 Experimental Aparatus

The flow diagram for the experimental apparatus is shown in Figure 3. A PC/AT compatible machine (Pentium 4 2.8 GHz: Dell Corp.) acted as the host computer, and a control experiment was conducted by sampling for 0.001 s on a DSP board (DS1005: dSPACE Inc.) attached to an ISA Bus. An A/D-D/A converter and a counter were built onto the DSP board and were used to acquire output signals from a sensor. The control system was designed by MATLAB/SIMULINK. Compressed air to drive the joint model is collected using the compressor and the accumulator, and the inner pressure of the two actuators is controlled by the electro-pneumatic regulator. The pressure in each actuator is measured with the regulator's built-in pressure sensor. The angle of the joint model is measured with the linear encoder (Levex Corp. Wire in Pulse Coder).

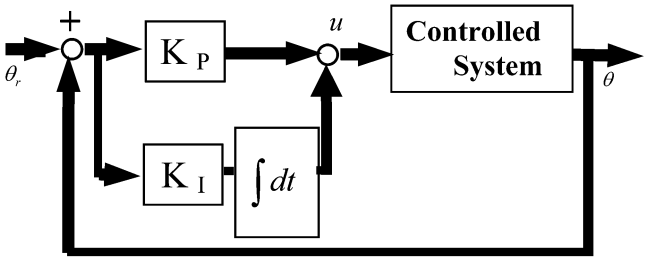

Fig. 4 Control system.

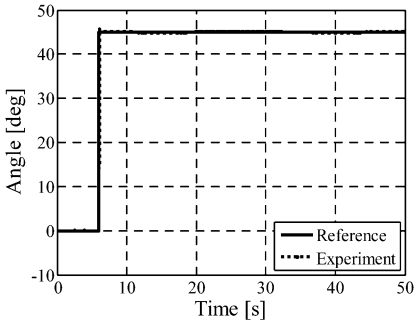

Fig. 5 Step signal response.

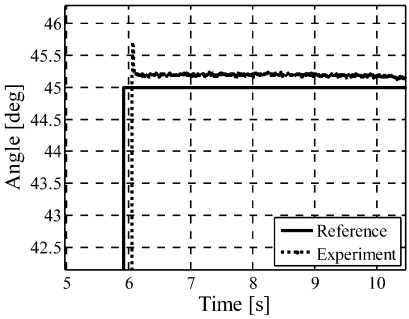

Fig. 6 Close-up in Figure 3.

3.3 Construction of Control System

A PI control system as shown in Figure 4 was constructed. θ_r is the reference value of the angle, θ is the measured angle. Moreover, because the vibration had happened by about ± 0.2 deg, the case beyond the limits of the instruction value ± 0.2 deg in this experiment the winding angle of two link arm was assumed to be PI control with the gap that assumed deflection to be 0 when the deflection between the instruction value and the winding angle was input to PI Controller. It was installed within the range of ± 0.2 deg and input 0 to the PI Controller.

The reference value of force is assumed to be a step signal, and a mixed sin-wave signal. The mixed sin-wave signal is a synthetic of 0.2 Hz and 0.075 Hz.

3.4 Experimental Results and Prospects

Figure 5 shows the experiment result and the reference value of the angle when the step input is assumed to be an instruction value. Moreover, a closeup is shown in Figure 6.

It has been understood to obtain the response to which the vibration in the neighborhood of the target value that has happened because of the PI control installs, and

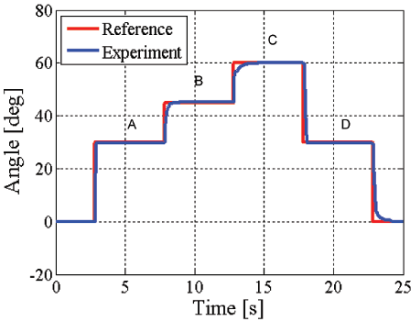

Fig. 7 Consecutive step response.

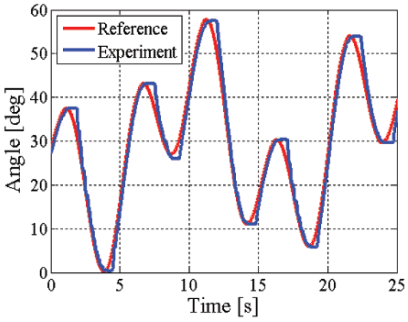

Fig. 8 Mixed sin-wave response.

is steady from Figure 6. As for the value of the steady state error 0.05 deg, it is understood that the accuracy is high.

Table 1 Steady state error and time constant of PI control system with GAP.

	A	B	C	D
Steady state error [deg]	0.38	0.22	0.05	0.19
Time constant [s]	0.0717	0.1402	0.0551	0.1829

Next, the angle reference value and the experiment result when giving and experimenting on the stairs reference value are shown in Figure 7. Moreover, is the angle of the reference value separate in to a section between section A , section B, section C, and section D. The steady state error and the time constant in each section are shown in Table 1. From Table 1, the experiment value displays high accuracy.

Next, the angle reference value and the experiment result when giving as an instruction value and experimenting on a mixed sinwave synthetic of 0.2 Hz and 0.075 Hz, are shown in Figure 8. In the delay at this time, both winding, and progressing were 0.2 s max and 0.7 s max in switching. Thus, it is understandable that the experiment value has high accuracy.

From this experiment, the position of the two link arm was controlled from the experiment on the above PI control with the gap. It was effective.

However, when the following progress operated in the experiment, overshoot was generated when the reference angle become large (Figure 9). It is thought that this is because of being not able to correspond to the bend and expand operation by a fixed gain. So, a control system that applied a switching gain respectively when the joint model bend and expand was constructed.

A rectangular wave of 50 deg is given as an angle reference value, and the result of the control is shown in Figure 9. Compared with the PI control experiment result of applying the fixed gain, it is improved, in state error 3.9 deg to 0.27 deg and time constants from 1.5 s to 0.8 s. It is thought that an appropriate PI control can be

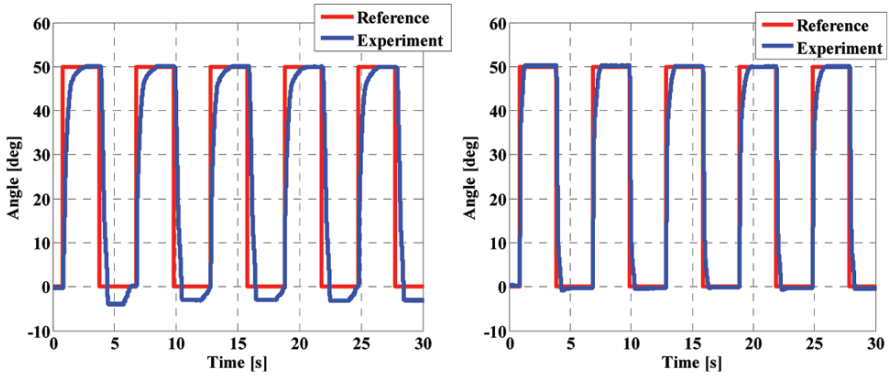

Fig. 9 Response of the rectangle input with fixed (left) and switching (right) PI control.

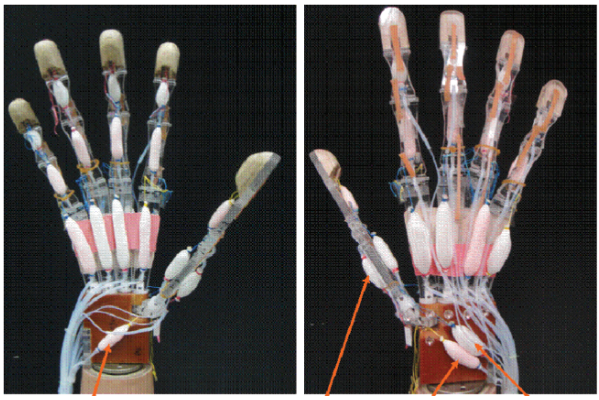

Fig. 10 Five-fingered robot hand.

achieved by using the PI control system that applied a different gain to each finger when it bends and expands.

4 Five-Fingered Robot Hand

By using the mechanism of the joint model, we produced a five-fingered robot hand that imitates a human's right hand (Figure 10). The pneumatic actuator was designed and arranged to make the fingers of this robot hand have the same movable range as that of a human's fingers.

This robot-hand's weight is 400 g, and the height is 500 mm (wrist included). The height without wrist is 200 mm.

The index finger, middle finger, ring finger, and little finger have DIP joints, PIP joints and MP joints. We arranged actuators for flexion operation in the DIP and PIP

Fig. 11 Five-fingered robot hand using pneumatic actuator

Fig. 12 Examples of the five-fingered robot hand holding an object.

Fig. 13 Data glove.

joints one by one. The extension operation is done by elastic gum. We arranged two actuators for flexion operation and extension operation in the MP joint. The thumb has an IP joint, an MP joint and a CM joint. In the thumb, we arranged actuators for flexion operation in the IP joint and in the MP joint one by one. In order to give the degree of rotation freedom and the degree of freedom of palmer adduction for the CM joint, we arranged four actuators. The pinching operation becomes possible by ensuring the thumb has a degree of rotation freedom.

Because the five-fingered robot hand has a movable range close to that of a human hand, it can assume positions for holding a variety of objects. Figure 12 shows an example of the five-fingered robot hand holding an object. This hand can hold objects weighing up to 500 g. Therefore, the robot hand using the pneumatic actuators can get enough power for daily activities such as holding a pen.

5 Master-Slave System

We constructed a master-slave system with the five-fingered robot hand above. The master-slave system is one that achieves robot hand operation similar to that of a human hand. A device such as a joystick is used in a conventional master-slave system to control a robot arm. However, when the five-fingered robot hand is operated,

Fig. 14 Master-slave system.

the operation is difficult when using such a device because the five-fingered robot hand has a large number of degrees of freedom. In this research, we constructed a master-slave system with a data glove (Roman-glove; LEVEX Corp.). The data glove is a wearable measuring device that can measure the angle of each joint of the fingers, as shown in Figure 13. Intuitively operating the robot hand without needing any training for the operation becomes possible by using the data glove.

Compressed air, which is the energy source, is collected with a compressor (DPP-AYAD compressor; KOGANEI Corp.) and an accumulator (DPT-T18-V air tank; KOGANEI Corp.). Compressed air is supplied to the actuator when the output value from the data-glove exceeds the threshold, and the air is expelled when the value falls below the threshold; thus, the robot hand is driven. We can achieve operation of the robot hand corresponding to that of a human hand in this way. The robot hand is driven by supplying compress air to the actuator according to the output value from the data glove. Figure 14 shows the robot hand to make the master slave system drive. The hand and the right of man to whom the left wore the data glove are the robot hands in Figure 14. It is understood that the robot hand does movement corresponding to the operation of man's hand from figure.

6 Conclusion

In this research, we developed a pneumatic actuator. To control of the robot hand freely, we conducted a control experiment for a joint model of the five-fingered robot hand. Moreover, we produced a five-fingered robot hand with these pneumatic actuators, and constructed a master-slave system. From this research, we obtained the following conclusions:

1. The robot hand has enough power for tasks in daily life
2. The PI control system with gaps is effective for the angle control of the joint model; and

3. The PI control system with a switching gain when it bends and expands is effective
4. We constructed a master-slave system that which achieves a level of robot hand operation similar to that of a human;

Acknowledgements This work was partially supported by Grant-in-Aid for Scientific Research (b)(19360122), Japan Society for the Promotion of Science.

References

1. M. Nobuto: Towards the Robots to Change Our Life Style, *Journal of the Robotics Society of Japan* **24**(3), 292–295 (2006).
2. F. Daerden and D. Lefeber: Pneumatic Artificial Muscles: Actuators for Robots and Automation, *European Journal of Mechanical and Environment Engineering* **47**(1), 11–21 (2002).
3. T. Noritsugu, M. Kubota, and S. Yoshimatsu: Development of Pneumatic Rotary Soft Actuator, *Transactions of the Japan Society of Mechanical Engineers, Series C* **66**(647), 2280–2285 (2000).
4. B. Verrelst, B. Vanderborght, J. Vermeulen, R. Van Ham, J. Naudet, and D. Lefeber: Control Architecture for the Pneumatically Actuated Dynamic Walking Biped "Lucy", *Mechatronics* **15**(6), 703–729 (2005).
5. Y. Sakaguchi: Pneumatic Servo of Rubber Artificial Muscle, *Hydraulics* **26**(8), 41–46 (1987).
6. S. Schulz, C. Pylatiuk, and G. Bretthauer: A "New Ultralight Anthropomorphic Hand", *Proceedings of IEEE International Conference on Robotics and Automation* **2001**(3), 2437–2441 (2001).
7. D. Sasaki, T. Noritsugu, and M. Takaiwa: Development of Pneumatic Soft Robot Hand for Human Friendly Robot, *Journal of Robotics and Mechatronics* **15**(2), 164–171 (2003).

Surface Acoustic Wave Linear Motor Using Glass Substrate

Hiroyuki Kotani, Masaya Takasaki and Takeshi Mizuno

Abstract A surface acoustic wave (SAW) linear motor is a kind of ultrasonic motor. The advantages of the SAW linear motor are its thin structure, high thrust force, high velocity and precise positioning. However, the stator transducer material (piezoelectric material) of the SAW linear motor has constraints of size and shape. To resolve this problem, a method is proposed to excite and propagate a SAW on a non-piezoelectric material surface. Excitation and propagation of the SAW on the non-piezoelectric material is realized by the combination of a $LiNbO_3$ plate and a glass substrate. The design and fabrication of the glass substrate transducer for the SAW linear motor are described. The design employs a novel transducer structure, which has been proposed previously. SAW excitation on the glass substrate stator transducer is applied for the SAW linear motor. The fabricated motor worked successfully. Driving characteristics of the glass substrate SAW linear motor are also reported.

1 Introduction

A surface acoustic wave (SAW) linear motor [1][2], which is a kind of ultrasonic motor, has many merits such as a large thrust force, high speed, quick response, and precise positioning. Since a silicon slider [3] has been employed for the motor, the motor can perform with a much larger output force of 10 N [4] and a fast no-load

Hiroyuki Kotani
Saitama University, Research Fellowship of the Japan Society for the Promotion of Science, Shimo-Okubo 255, Sakura-ku, Saitama 338-8570, Japan; E-mail: hktn121@mech.saitama-u.ac.jp

Masaya Takasaki
Saitama University, Shimo-Okubo 255, Sakura-ku, Saitama 338-8570, Japan;
E-mail: masaya@mech.saitama-u.ac.jp

Takeshi Mizuno
Saitama University, Shimo-Okubo 255, Sakura-ku, Saitama 338-8570, Japan

H. Ulbrich and L. Ginzinger (eds.), Motion and Vibration Control, 211–219.

speed of more than 1.5 m/s [5]. The motor has the possibility of a precise positioning resolution of several ten nanometers [6]. The driving frequency of the SAW device has been increased to 100 MHz for miniaturization [7]. Energy circulation driving methods have also been investigated for saving electric driving power [8].

The stator transducer of the SAW linear motor consists of a rectangular plate of 128° Y-cut X-prop lithium niobate ($LiNbO_3$) substrate, which is a piezoelectric single crystal, and surface electrodes (interdigital transducers, IDTs) on its surface. The $LiNbO_3$ wafer, however, has size and shape constraints (a maximum length of 100 mm). Therefore a SAW linear motor of large size or any desired shape cannot be realized.

To resolve this problem we proposed a method of SAW excitation and propagation on a non-piezoelectric material surface [9, 10] and its application for the stator transducer of the SAW linear motor. The method uses the combination of piezoelectric and non-piezoelectric materials. A glass substrate was taken as the non-piezoelectric substrate. Using this structure, the excited SAW can propagate on the glass substrate. The glass substrate transducer can be machined into a desired shape and the cost using this method is more reasonable than that of the conventional method. Previously, actuators using a glass substrate have been developed and reported [11, 12]. Moser [11] developed a glass motor using the electrostatic force. Hata [12] proposed an electrostatic microactuator constructed of a thin film metallic glass. These actuators using glass substrates are not ultrasonic actuators, for they apply electrostatic forces.

In this paper, we fabricate a glass transducer. SAW excitation on the glass substrate stator transducer is applied for the SAW linear motor and the fabricated motor works successfully. Driving characteristics of the glass substrate SAW linear motor are also discussed.

2 SAW Linear Motor

2.1 Principle

In a propagating Rayleigh wave, which is a kind of SAW, particles on the surface of an elastic material media move along an elliptical locus, as shown in Figure 1. The slider arranged on the elastic substrate surface is driven by a frictional force in the direction indicated by the arrow in the figure. The direction is the reverse of the Rayleigh wave propagation. The slider requires pre-loading for there to be sufficient frictional force for driving.

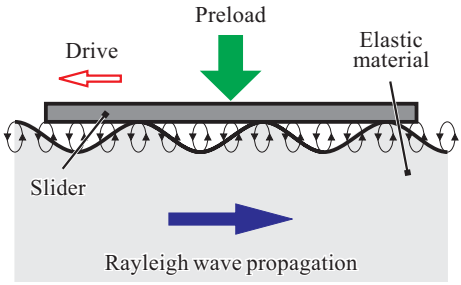

Fig. 1 Principle of the friction drive.

2.2 Basic Structure

Figure 2 outlines the basic structure of the conventional SAW linear motor. A $LiNbO_3$ 128° Y-cut X-prop substrate is used as a piezoelectric material for the SAW linear motor. When alternating current is applied to an IDT on the piezoelectric substrate, a Rayleigh wave is generated and propagates. To generate a unique propagating Rayleigh wave, the wave reflected at the end of the substrate should be blocked. Therefore, SAW absorbers are arranged behind each IDT. Absorbed vibrational energy is transformed into thermal energy. Additionally, thermal energy should be radiated, because $LiNbO_3$ is a brittle and frangible material with a sharp temperature gradient.

There are two IDTs on the stator transducer. The slider driving direction depends on which IDT the driving current is applied to and hence can easily be changed. At each end of the stator, IDTs as illustrated in Figure 3 are fabricated by means of deposition. The electrode materials are chromium and aluminum. In this research, the dimensions of the IDTs were 400 μm in pitch, 200 μm in electrode strip width, and 20 mm in width. An IDT is composed of 10 strip electrode pairs. The operating frequency of the transducer depends on the IDT's electrode dimensions and is approximately 4.8 MHz in the following experiments. At an operating frequency of

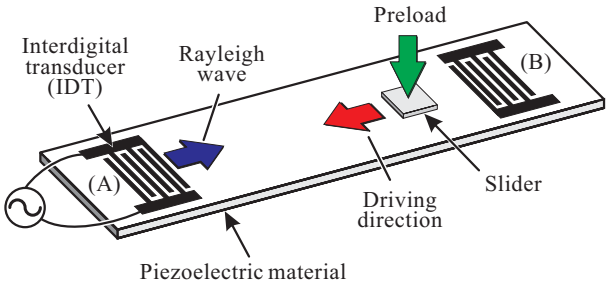

Fig. 2 Schematic view of the SAW linear motor.

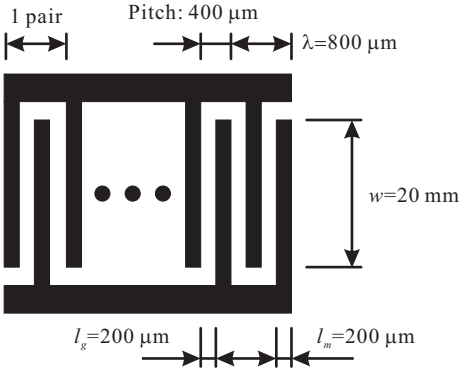

Fig. 3 Configuration of the IDT electrode.

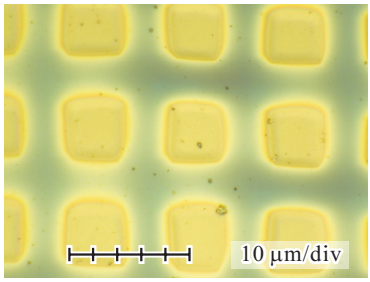

Fig. 4 Photograph of the slider with S-DLC films projections sample.

4.8 MHz, the vibration amplitude of the stator transducer surface is only a few ten nanometers.

To realize stable contact at the driving surface, a silicon slider has been employed [3]. The silicon slider has many projections on its surface, which are manufactured by dry-etching. The diameters of the projections are from 10 to 50 μm (several kinds of sliders were manufactured) and are much shorter than the wavelength of the excited Rayleigh wave. On the other hand, a SAW linear motor using a segment-structured diamond-like-carbon (S-DLC) film slider has been reported [13]. Figure 4 is a photograph of a S-DLC film projection sample. The silicon wafer with the films can substitute for the conventional silicon slider. DLC is a highly functional material and a surface coated with DLC film has properties such as hardness, wear-resistance and low friction. Previously, S-DLC films have been proposed to enhance the functions [14]. The S-DLC films appear as a distribution of square projections. Projections on the conventional silicon slider could be replaced with S-DLC films. In this research, a silicon wafer with S-DLC films was employed as the slider.

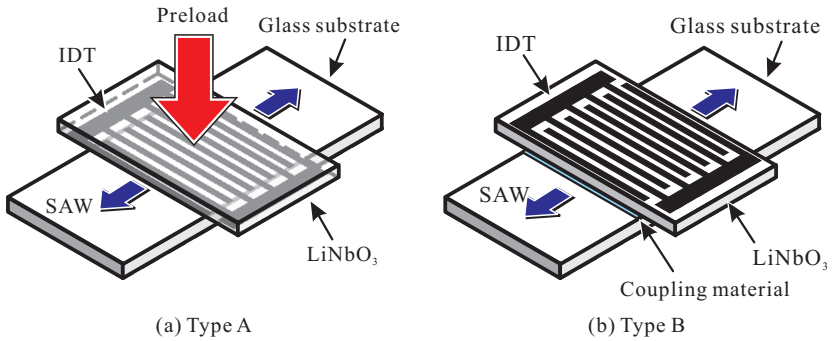

Fig. 5 Configurations for indirect excitation.

3 Indirect Excitation

We propose a method to excite and propagate a SAW on a non-piezoelectric material surface using a piezoelectric material. In this paper, the method is referred to as "indirect excitation". The conventional method (a SAW being generated by an IDT and propagating on the piezoelectric material directly) is referred to as "direct excitation". For indirect excitation, a combination of a piezoelectric substrate and a non-piezoelectric substrate was employed. A glass substrate was applied as the non-piezoelectric substrate and a $LiNbO_3$ substrate as the piezoelectric substrate. The excited SAW on the $LiNbO_3$ propagated on the glass substrate indirectly. The glass substrate can be machined into a desired shape and cut to a desired size. The cost of this method is less than that of the conventional method.

Configurations to realize indirect excitation are shown in Figure 5. There are two types of the indirect excitation. One is Type A, which is shown in Figure 5a. The IDT on the $LiNbO_3$ is connected to the glass substrate. The IDT is formed by a photolithographic process on the $LiNbO_3$ wafer. The $LiNbO_3$ wafer is cut to the same size as the IDT and the glass substrate is cut to a size corresponding to the electrode width of the IDT. The glass substrate is orientated such that the propagating direction is perpendicular to the IDT fingers. A preload is applied to the $LiNbO_3$ and enhances the acoustic connection between the glass and $LiNbO_3$ substrates. A Type A glass substrate SAW linear motor has previously been suggested and employed successfully [15]. The other indirect excitation type is Type B. The back side of the $LiNbO_3$ surface (with the IDT facing up) is connected to the glass substrate with a coupling material as shown in Figure 5b. A coupling material is used in contact testing applications; e.g., the general non-destructive testing using ultrasonic vibration to facilitate the transmission of vibration energy between the transducer and the target material. In this research, Type B indirect excitation was employed.

SAW excitation and propagation of Type B indirect excitation is illustrated in Figure 6. The $LiNbO_3$ excites a SAW, and the excited SAW propagates on the glass substrate surface through the coupling material. Silicone oil was applied as the coup-

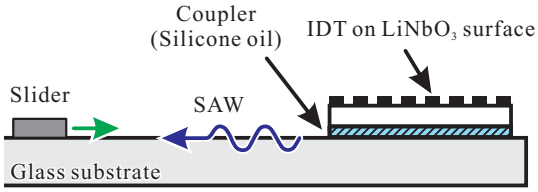

Fig. 6 Excitation and propagation of SAW using indirect excitation Type B.

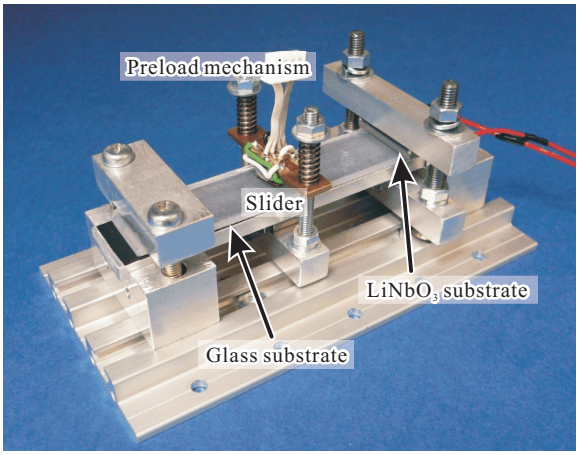

Fig. 7 Photograph of the SAW linear motor using a glass substrate.

ling material. In the configuration of Type B indirect excitation, a preload mechanism is unnecessary, because the excited wave is effectively transmitted on the glass substrate surface through the coupling material. Therefore the preload to enhance an acoustic connection between the $LiNbO_3$ and glass substrate is unnecessary.

4 SAW Linear Motor using a Glass Substrate

4.1 Experimental Apparatus

The indirect excitation method was applied for the SAW linear motor. Figure 7 shows the SAW linear motor with a glass substrate for the stator transducer fabricated on trial. The structure of the glass substrate SAW linear motor is shown in Figure 8. The transducer consists of piezoelectric and non-piezoelectric materials. A $LiNbO_3$ 128° Y-cut X-prop plate was used for the piezoelectric material as is

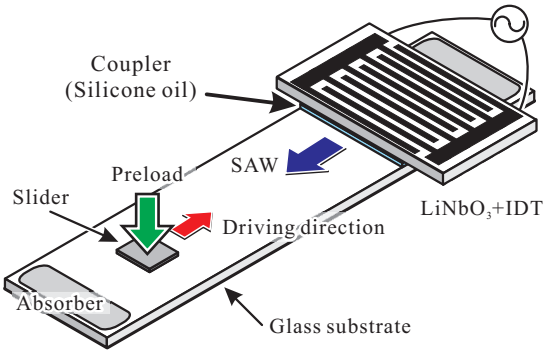

Fig. 8 Structure of the SAW linear motor using a glass substrate.

applied in conventional direct excitation. A silica-glass substrate was used for the non-piezoelectric material. The dimensions of the $LiNbO_3$ plate were 25 mm × 8 mm × 2 mm and the dimensions of the glass substrate were 100 mm × 20 mm × 2 mm. The $LiNbO_3$ plate with the IDT was aligned in the propagating direction and fixed. The driving stroke of the apparatus was about 68 mm. A silicon wafer with S-DLC films was used for the slider [13]. The size of the S-DLC films slider was 8 mm × 8 mm × 0.7 mm. The preload of the slider was provided by a combination of a beam and coil springs and measured as approximately 10 N with strain gauges.

4.2 Driving Characteristics

The glass substrate SAW linear motor worked successfully. Transient responses of the velocity to changes in the applied current for a preload of 10 N and a driving frequency of 4.768 MHz are plotted in Figure 9. It is seen that the slider velocity increased with increasing applied current. A maximum velocity of around 200 mm/s at 0.5 $A_{0\text{-}p}$ was observed. It was experimentally confirmed the glass substrate SAW linear motor obtained approximately the same slider velocity as did the conventional SAW linear motor.

5 Conclusion

Indirect excitation using a combination of glass substrate and $LiNbO_3$ plates was realized. A SAW linear motor employing the glass transducer was fabricated and worked successfully. The slider velocity increased with increasing applied current and a maximum slider velocity of 200 mm/s was observed.

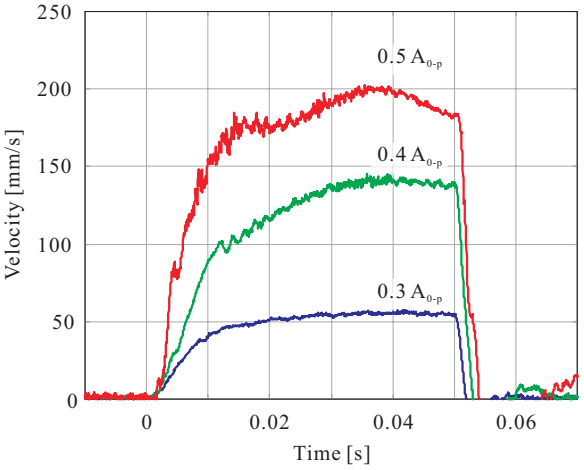

Fig. 9 Transient responses of the velocity to changes in the applied current.

Acknowledgements This study was partially supported by the Research Fellowship of the Japan Society for the Promotion of Science for Young Scientists.

References

1. Kurosawa M, Takahashi M, Higuchi T (1996) Friction drive surface acoustic wave motor. *Ultrasonics* **34**: 234–246.
2. Kurosawa M, Takahashi M, Higuchi T (1996) Ultrasonic linear motor using surface acoustic waves. *IEEE Transactions on Ultrasonics, Ferroelectrics and Frequency Control* **43**(5): 901–906.
3. Osakabe N, Kurosawa M, Higuchi T et al (1998) Surface acoustic wave linear motor using silicon slider. In *Proceeding of IEEE Workshop on Micro Electro Mechanical Systems*, pp. 390–395.
4. Kurosawa M K, Itoh H, Asai K (2003) Elastic friction drive of surface acoustic wave motor. *Ultrasonics* **41**: 271–275.
5. Nakamura Y, Kurosawa M K, Shigematsu T (2003) Effects of ceramic thin film coating on friction surfaces for surface acoustic wave linear motor. In *Proceedings 2003 IEEE Ultrasonics Symposium*, pp. 1766–1769.
6. Shigematsu T, Kurosawa M K, Asai K (2003) Nanometer stepping drives of surface acoustic wave motor. *IEEE Transactions on Ultrasonics, Ferroelectrics, and Frequency Control* **50**(4): 376–385.
7. Shigematsu T, Kurosawa M K (2006) Miniaturized SAW motor with 100 MHz drive frequency. *IEEJ Transactions on Sensors and Micromachines* **126**(4): 166–167.
8. Asai K, Kurosawa M K (2001) Surface acoustic wave motor using an energy circulation driving method. In *Proceedings of IEEE Ultrasonic Symposium*, pp. 525–529.
9. Takasaki M, Kotani H, Nara T et al (2005) SAW Excitation on glass plates for a tactile display application. In *Proceedings 2005 IEEE International Ultrasonics Symposium*, pp. 819–822.

10. Kotani H, Takasaki M, Nara T et al (2006) Glass substrate surface acoustic wave tactile display with visual information. In *Proceedings IEEE International Conference on Mechatronics and Automation*, pp. 1–6.
11. Moser R, Higuchi T (2002) Precise positioning using electrostatic glass motor. *Journal of the International Societies for Precision Engineering and Nanotechnology* **26**, 162–167.
12. Hata S, Kato T, Fukushige T et al (2003) Integrated conical spring linear actuator. *Microelectronic Engineering* **67–68**: 574–581.
13. Fujii Y, Kotani H, Aoki Y et al (2005) Surface acoustic wave linear motor using segment-structured diamond-like carbon films on contact surface. In *Proceedings 2005 IEEE International Ultrasonics Symposium*, pp. 2543–2546.
14. Aoki Y, Ohtake N (2004) Tribological properties of segment-structured diamond-like carbon films. *Tribology International* **37**: 941–947.
15. Kotani H, Takasaki M, Mizuno T (2007) Glass substrate surface acoustic wave linear motor. In *Proceedings 2007 IEEE Ultrasonics Symposium*, pp. 2547–2550.

Humanoid Robot *LOLA* – Research Platform for High-Speed Walking

Sebastian Lohmeier, Thomas Buschmann, Heinz Ulbrich and Friedrich Pfeiffer

Abstract This paper describes the design concept of the performance enhanced humanoid robot *LOLA*. Our goal is to realize a fast, human-like walking motion. The robot has 22 degrees of freedom, including 7-DoF legs with actively driven toe joints. It is characterized by its lightweight construction, a modular, multi-sensory joint design with brushless motors and an electronics architecture using decentralized joint controllers. Special emphasis was paid on an improved mass distribution of the leg apparatus to achieve good dynamic performance. The sensor system comprises absolute angular sensors in all links, two custom-made force/torque sensors in the feet and a high-precision inertial sensor on the upper body. The trajectory generation and control system currently being developed aim at faster, more flexible, and more robust walking patterns.

1 Introduction

Recent developments in enabling technologies (biped walking control, mechatronics, computer technology) have lead to the design of sophisticated humanoid robots, like *ASIMO* [5], *HRP-2* [9] and *WABIAN-2* [15]. Even if all robots achieve reliable dynamic walking – compared with human beings – high walking speeds still remain challenging.

Obviously, the control problems inherent in fast walking are the most challenging field, since there are still many unsolved problems, e.g. fast walking and running [6, 8], sudden turning motions, walking on rough terrain and trajectory generation in complex environments. In our opinion, however, a careful design of the mechanical hardware and the sensor system is just as essential, and and cannot be separated from controller design. Rather, all components must be seen as tightly coupled parts of a highly integrated mechatronic system. For example, the structural

Sebastian Lohmeier, Thomas Buschmann, Heinz Ulbrich and Friedrich Pfeiffer
Institute of Applied Mechanics, Technische Universität München, 85748 Garching, Germany;
E-mail: {lohmeier, buschmann, ulbrich, pfeiffer}@amm.mw.tum.de

H. Ulbrich and L. Ginzinger (eds.), Motion and Vibration Control, 221–230.

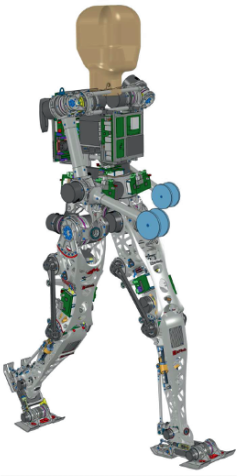

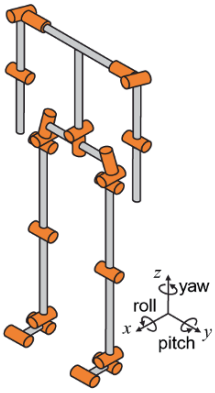

Joint	DoF
Head	2 (planned)
Shoulder	2
Elbow	1
Waist	2
Hip	3
Knee	1
Ankle	2
Toe	1
Total	**22+2**

Fig. 1 22-DoF humanoid robot *LOLA* (left) and kinematic configuration (right).

stiffness and mass distribution can positively influence the dynamics of the overall system. Moreover, the validity of model simplifications, e.g. the inverted pendulum model used in the stabilizing controller, can be aided if disturbances by the highly accelerated leg masses are minimized.

With the biped robot *JOHNNIE* which was developed at our institute from 1998 to 2003, a maximum walking speed of 2.4 km/h has been achieved [10]. Figure 1 (left) shows our new humanoid walking robot *LOLA*. The aim is to realize a fast, human-like walking motion, including a significant increase in walking speed (goal: 5 km/h) and more flexible gait patterns. Furthermore, we want to increase the robot's autonomous, vision-guided walking capabilities. *LOLA*'s physical dimensions are based on anthropometric data and correspond with a 180 cm tall adult. The weight of the robot is 55 kg without batteries.

LOLA's hardware approach tries to settle most of the technical problems discovered in experiments with *JOHNNIE* and a thorough hardware analysis. The distinguishing characteristics of *LOLA* are its redundant kinematic structure with 7-DoF legs, an extremely lightweight construction and a modular joint design using brushless motors. The sensor system was revised in order to improve signal quality and bandwidth. In our opinion, one of the keys to faster walking is greater robustness and stability. The new control architecture tries to achieve this by adding an on-line adaptation of gait parameters such as step length and width in real-time (cf. [1]).

2 Design Concept

Fast locomotion still poses a significant challenge for humanoid robots and requires an accurate design of the overall mechatronic system. Especially the legs and feet

require careful engineering in order to achieve a good dynamic behavior. Since the robot's mass and its distribution have a strong influence on global system dynamics, the lightweight construction is of great importance and must be balanced with the demand for high stiffness and powerful drives.

2.1 Kinematic Structure

One of the most important conceptual challenges is the definition of a kinematic structure, enabling a natural, stable and fast gait. From experiments and simulations we have seen that additional, redundant DoF can increase the robot's range of motion, flexibility and stability of gait patterns and walking speed. Considering results from biomechanical research on dynamics and kinematics of biped walking (e.g. [3, 14]) and experience with *JOHNNIE* [10] we chose a configuration with 22 actively driven DoF for *LOLA* (Figure 1 right): The legs have 7 DoF each, while the upper body has two and each arm has three DoF.

Nearly all humanoid robots are designed with 6-DoF legs – 3 DoF in the hip, one in the knee and two in the ankle. Each foot consists of one rigid body, therefore heel lift-off during terminal stance phase can hardly be realized. Even small disturbances lead to instabilities due to the line contact of the foot leading edge and the floor. In human walking heel lift-off in the stance leg occurs during terminal swing, i.e. shortly before the swing leg has floor contact [16]. Biped robots with one-piece foot segments, however, cannot perform forward roll across the forefoot. Especially for larger step lengths, this leads to an extended knee configuration at initial contact of the swing leg resulting in large joint accelerations.

Therefore an additional, actively driven link between forefoot and heel, equivalent to the human toes is proposed for *LOLA*. Heel lift-off in the stance leg allows the swing leg to be in a more extended configuration. Area contact of the toe segment stabilizes the robot and facilitates forward roll across the forefoot which is expected to reduce the joint loads in hip and knee compared to a 6-DoF leg configuration. There are only very few humanoid robots with actively driven toe joints, e.g. *H6* and *H7* [13]. Recently, Ogura et al. [15] presented the robot *WABIAN-2* walking with passive toe joints.

2.2 Further Requirements for High-Speed Walking

Besides a suitable kinematical structure, further design goals can be defined to improve the robot hardware for fast walking:

- Minimum overall mass,
- sufficient structural stiffness,
- high center of gravity,
- low moments of inertia of the leg links.

Obviously, the overall mass should be minimized, while a sufficient stiffness of the robot's structure must be maintained. This prerequisite is common to all mobile robots with high dynamic demands.

Unlike humans, the largest portion of a biped robot's weight resides in its legs, since motors and gears determine approximately a third of the overall weight. Therefore the center of gravity (CoG) height is lower than that of humans, i.e. typically at the height of the hip joint or even below. According to the *Linear Inverted Pendulum Model* (3D-LIPM) by Kajita et al. [7], the CoG trajectory of the robot is a piecewise hyperbolic curve, where the CoG lateral swing y_{CoG} increases with lower CoG positions:

$$y_{CoG} \sim \cosh\left(\sqrt{\frac{g}{z_{CoG}}}\, T_s\right)$$

The 3D-LIPM illustrates the influence of the CoG height z_{CoG} on the lateral swing of the upper body during walking: Especially at higher walking speeds, the stability of the robot increases when the lateral swing of the upper body is low. But mass distribution in the legs not only influences CoG height, but also the inertia of the leg segments. Therefore, during the final iteration of the mechanical hardware we chose three additional measures to further improve mass distribution: First, we designed the leg segments as investment cast parts using FE-based topology optimization methods to achieve high stiffness at a minimal weight (Section 3.4). Moreover, by choosing an appropriate kinematic actuation principle for the leg links, the mass distribution can strongly be influenced: For the knee joint, a roller screw-based linear actuator is used (Section 3.2). The ankle joint is actuated by a 2-DoF parallel mechanism with linear drives, where the motors are mounted on the thigh next to the hip joint (Section 3.3).

3 Mechanical Design

3.1 Modular Joint Concept

A detailed analysis by Gienger [4] has revealed that structural components make 43% of a humanoid robot's weight. With approximately 31% the drive chains make the second largest part, making the development of compact and lightweight joint units a crucial factor. From the manufacturing and maintenance point of view, a fully modular structure of the whole robot would be desirable, however, it collides with the demand for minimal weight. For *LOLA*, all joints have the identical structure with the sizes of gear and motor adapted to the requirements of each link. Many parts are standardized for all drives, but some housings are specialized because of weight and optimal load spread and distribution. This turned out to be the most reasonable way to realize the robot at minimal weight while taking into account ease of manufacturing [12].

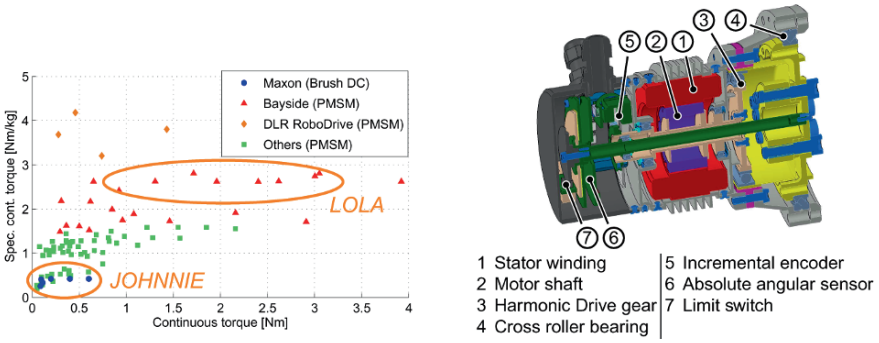

Fig. 2 Left: Comparison of the power density of commercially available DC motors and PMSM. Right: Mechanical design of Harmonic Drive based joints (e.g. hip joint yaw axis).

To realize highly integrated joint units with maximum power density it is necessary to use the latest technologies in the field of electrical drives, gears and sensors. We are using high performance permanent magnet synchronous motors (PMSM) from Parker Bayside because of their superior torque and speed capabilities (Figure 2 left). The motors come as kit motors, which facilitates a space- and weight-saving integration into the joint.

Except for the knee and ankle, all joints employ Harmonic Drive gears as speed reducers, which are the de-facto standard for humanoid robots. Their advantages are well known and include no-backlash and high reduction ratios at a low weight. The compact design of Harmonic Drive component sets allows a space-saving integration directly into the joint units. All gears are custom lightweight versions with a T-shaped Circular Spline which is, in our experience, the best tradeoff between weight and loading capacity. The Wave Generators, modified for low weight and inertia, are made from aluminum or steel. As an example, Figure 2 (right) shows the hip joint yaw axis.

3.2 Knee Joint

Even though the torques and velocities are comparable, using the hip joint pitch drive in the knee is problematic because its mass would unacceptably increase the thigh moment of inertia. In turn a large part of the enhanced hip joint output would be spent on accelerating a heavier thigh. By employing a roller screw-based linear drive (Figure 3 left), a better mass distribution in the hip-thigh area is achieved compared to a Harmonic Drive based solution with identical performance: The thigh inertia could be reduced by 65%, and the drive mass was reduced by more than 10%. Thus, the driving power of the knee could be enhanced without decreasing the hip joint's performance. The mechanism is nonlinear and the torque-speed characteristic corresponds to the human knee (Figure 3 right): The torque depends on the link

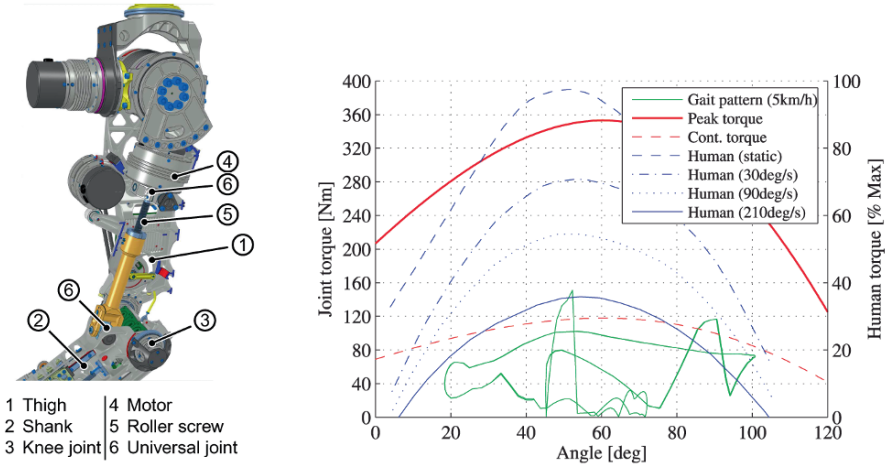

Fig. 3 Left: Knee joint with roller screw-based actuator. Right: Torque and speed requirements of knee joint (human torque capacity taken from [16]).

position and has its maximum at around 55°, which is advantageous for typical gait patterns of the robot. Conversely, maximum speeds increase at a stretched leg configuration, where they are needed.

Compared to ballscrews that were used in our first designs [11], roller screws have a significantly higher load rating which allowed us to further reduce the drive's weight. Moreover, due to their multi-point contact design, roller screws have the ability to survive shock loads which makes them particularly suitable for the robot's legs.

3.3 Ankle Joint

As shown in [11], both axes of the ankle joint show clearly different torque-speed characteristics. By employing parallel drives, the required peak motor torque can be reduced by approx. 35%. Different from our previous designs, where the drives acted as length variable steering rods, the ankle joint drives were modified in the final design which is shown in Figure 4: The ankle joint (3) is actuated by two linear drives (7) with the motors (4) mounted on the thigh (1) as close as possible to the hip joint. Each linear drive (7) is connected to the motor (4) via a timing belt (5) and a bevel gear (6) in the knee joint axis which is then connected to the roller screw (8). Each linear drive consists of a roller screw (8) which is fixed to the shank, and a linear bearing (9) which keeps the roller screw free from radial loads. A steering rod (10) connects the roller screw nut and the foot segment. The incremental encoders for motor control are mounted on the motor shaft, but the absolute angular sensors (11) are mounted on the joint axes.

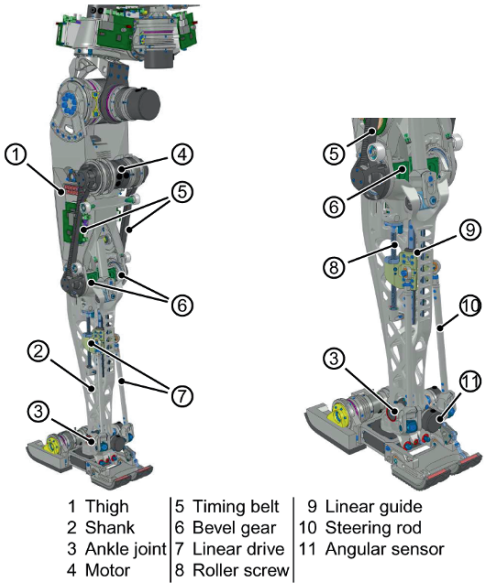

Fig. 4 2-DoF parallel mechanism in the ankle joint of *LOLA*.

3.4 Design of Structural Components

Both thigh and shank were designed as investment cast parts. By using Rapid Prototyping-based manufacturing, there are almost no limitations of a component's shape and it is possible to realize complex, thin-walled components. As an example, the design process of the shank is shown in Figure 5. It connects the 1-DoF knee joint and the 2-DoF ankle joint that are both actuated by roller screw drives. Therefore, loads are transmitted not only at the joint flanges, but also at the hinging points of the linear drives. Due to numerous points of force transmission of the linear drives, thigh and shank show quite complex multi-axial stress conditions and strict geometric constraints. Therefore we used the FEM-based topology optimization tool *OptiStruct* to find an optimal design proposal which meets weight and/or stiffness targets and other constraint criteria. Based on a mockup resembling the maximum allowable designed space, an optimization model is built. Realistic results can only be achieved if the force transmission by the roller screw drives is considered. Therefore the thigh and the linear drives of knee and ankle are modeled as elastic bending beams. The optimization result is the basis for the actual part design. After several iterations of structural analysis and design refinement, the final geometry of the component is developed. By using the original CAD data, the master pattern is made by laser-sintering of plastic, which is then cast from aluminum.

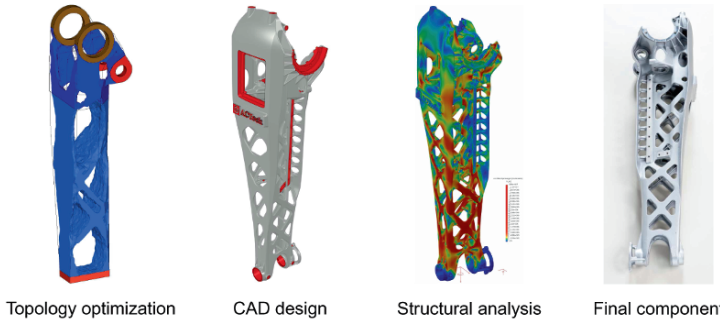

Fig. 5 Development process of structural components based on topology optimization, for example the shank.

4 Sensor System

4.1 Joint Sensors

Each joint contains an incremental rotary encoder, an absolute angular encoder used as link position sensor and a limit switch (cf. Figure 2 right). The incremental rotary encoder mounted on the motor shaft is mainly used for motor control. The absolute angular encoder (resolution 17 bit, accuracy 0.1°) compensates elasticities and nonlinearities in the drive chain and eliminates the need for a homing routine, making startup faster and easier. To improve operational security and to prevent the robot from self-destruction each joint incorporates a limit switch in the form of a light barrier.

4.2 Force/Torque Sensors

LOLA is equipped with two six-axes force/torque sensors that are tightly integrated into the foot structure. The required measurement range was determined using our detailed multibody simulation model [2] for a walking speed of 5 km/h. Based on these data and multiple iterations of FEM-analyses, an optimal design of the sensor body was developed (Figure 6). The sensor consists of a single aluminum part with four deformation beams in a classic "Maltese-cross" arrangement. Each beam holds two pairs of strain gauges that operate in a half bridge configuration in order to compensate for temperature dependency. Thin membranes mechanically decouple the individual beam deflections to a far extent and reduce cross talk. In order to protect the sensor from damage during experiments, we have integrated an overload protection. Mechanical end-stops engage into the flux of force at a vertical load corresponding three times the weight of the robot and thus unload the sensitive measurement beams. Special emphasis has been devoted to the strain gauge application.

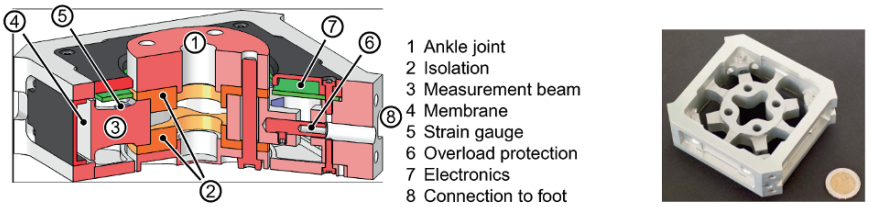

Fig. 6 Schematic display of the 6-axis force/torque sensor (left) and the monolithic sensor body before assembly (right).

The strain gauges are selected to match the elastic properties of the sensor material. An exact application in combination with an appropriate temperature treatment finally lead to a high zero point stability of the signal. The calibration was done using the least squares method. By applying more than 450 different load cases, a calibration error less than 0.5% could be achieved. At a total weight of 395 g the sensor includes all necessary electronics and a digital interface.

4.3 Inertial Measurement Unit

The inertial measurement unit (IMU) estimates the orientation and velocities of the upper body. Simulations and experimental results with the robot *JOHNNIE* have shown that the precision of this sensor significantly determines the performance of the stabilizing controller. Therefore, the IMU must show high accuracy and a high signal quality (i.e. low noise). Moreover, a low sensor bias results in a low long time drift and a reliable calibration. We are using the inertial measurement unit *iVRU-FC-C167* (from iMAR Navigation) in a custom made lightweight version. The sensor consists of three open-loop fiber-optic gyroscopes and three MEMS accelerometers. The sensor fusion comprises internal error models and is integrated into the sensor, which has a CAN interface.

5 Conclusions/Future Work

Despite recent advances, biped walking robots are still slow compared to humans and have limited autonomy. The intention of the research presented here is to diminish this gap. This paper focused on the design concept of our new, 22-DoF humanoid robot *LOLA* (180 cm, 55 kg). *LOLA*'s distinctive features are an extremely lightweight construction and a redundant kinematic configuration, which allows for more flexible and natural motions. All joints are equipped with absolute angular sensors and are driven by AC brushless motors through Harmonic Drive gears or linear mechanisms with roller screws. The electronics architecture is designed as

an "intelligent sensor-actuator network" with a central controller. The new decentral components increase the system's performance from a technological point of view. The trajectory generation and control system currently being developed aim at faster, more flexible, and more robust walking patterns. In the near future, we will integrate a camera head to enable autonomous locomotion. *LOLA* will serve as a research platform for fast walking and visual-guided, autonomous walking.

Acknowledgements This work is supported by the "Deutsche Forschungsgemeinschaft" (grant UL 105/29).

References

1. Buschmann, T., Lohmeier, S., Bachmayer, M., Ulbrich, H., Pfeiffer, F.: A collocation method for real-time walking pattern generation. In: Proc. Int. Conf. Humanoid Rob. (Humanoids) (2007)
2. Buschmann, T., Lohmeier, S., Ulbrich, H., Pfeiffer, F.: Dynamics simulation for a biped robot: Modeling and experimental verification. In: Proc. IEEE Int. Conf. Rob. Aut. (ICRA), pp. 2673–2678 (2006)
3. Carson, M., Harrington, M.E., Thompson, N., O'Connor, J., Theologis, T.N.: Kinematic analysis of a multi-segment foot model for research and clinical applications: a repeatability analysis. J. Biomech. **34**(10), 1299–1307 (2001)
4. Gienger, M.: Entwurf und Realisierung einer zweibeinigen Laufmaschine. No. 378 in Fortschrittberichte VDI, Reihe 1. VDI-Verlag, Düsseldorf (2005)
5. Hirai, K., Hirose, M., Takenaka, T.: The development of Honda humanoid robot. In: Proc. IEEE Int. Conf. Rob. Aut. (ICRA), pp. 1321–1326 (1998)
6. Honda Motor Co., Ltd.: New ASIMO – running at 6km/h (2005). URL `http://world.honda.com/HDTV/ASIMO/New-ASIMO-run-6kmh/`
7. Kajita, S., Kanehiro, F., Kaneko, K., Fujiwara, K., Yokoi, K., Hirukawa, H.: A realtime pattern generator for biped walking. In: Proc. IEEE Int. Conf. Rob. Aut. (ICRA), pp. 31–37 (2002)
8. Kajita, S., Nagasaki, T., Kaneko, K., Yokoi, K., Tanie, K.: A hop towards running humanoid biped. In: Proc. IEEE Int. Conf. Rob. Aut. (ICRA), pp. 629–635 (2004)
9. Kaneko, K., Kanehiro, F., Kajita, S., Hirukawa, H., Kawasaki, T., Hirata, M., Akachi, K., Isozumi, T.: Humanoid robot HRP-2. In: Proc. IEEE Int. Conf. Rob. Aut. (ICRA), pp. 1083–1090 (2004)
10. Löffler, K., Gienger, M., Pfeiffer, F., Ulbrich, H.: Sensors and control concept of a biped robot. IEEE Trans. Ind. Electron. **51**(5), 972–980 (2004)
11. Lohmeier, S., Buschmann, T., Schwienbacher, M., Ulbrich, H., Pfeiffer, F.: Leg design for a humanoid walking robot. In: Proc. Int. Conf. Humanoid Rob. (Humanoids) (2006)
12. Lohmeier, S., Buschmann, T., Ulbrich, H., Pfeiffer, F.: Modular joint design for performance enhanced humanoid robot LOLA. In: Proc. IEEE Int. Conf. Rob. Aut. (ICRA), pp. 88–93 (2006)
13. Nishiwaki, K., Kagami, S., Kuniyoshi, Y., Inaba, M., Inoue, H.: Toe joints that enhance bipedal and fullbody motion of humanoid robots. In: Proc. IEEE Int. Conf. Rob. Aut. (ICRA), pp. 3105–3110 (2002)
14. Novacheck, T.F.: The biomechanics of running. Gait & Posture **7**, 77–95 (1998)
15. Ogura, Y., Shimomura, K., Kondo, H., Morishima, A., Okubo, T., Momoki, S., Lim, H., Takanishi, A.: Human-like walking with knee stretched, heel-contact and toe-off motion by a humanoid robot. In: Proc. IEEE/RSJ Int. Conf. Rob. Sys. (IROS), pp. 3976–3981 (2006)
16. Perry, J.: Gait Analysis – Normal and Pathological Function, 3rd ed. edn. Slack (1992)

Active Control of Flexural Vibration: An Adaptive Anechoic Termination

B.R. Mace, E. Rustighi, N.S. Ferguson and D. Doherty

Abstract This paper describes an approach to the real-time, feedforward, adaptive broadband control of flexural vibrations of a beam. A wave interpretation is used: disturbance and control forces inject waves into the structure and the waves then propagate through it. The general aim is to implement an anechoic boundary to the structure which absorbs any energy incident upon it. Digital filters are implemented to estimate, in real-time, the amplitudes of the propagating waves incident on and reflected from the boundary by filtering the outputs of an array of sensors. The reflected wave is used as the cost function in a filtered-X LMS adaptive control. The feedforward reference signal used is either the primary disturbance or the incident wave – the former is rarely available outside the laboratory. Furthermore, for a finite, resonant structure, with potentially many modes in the frequency range of interest, the performance using the primary as a reference signal gives very poor performance due to the difficulty of approximating the resonant cancellation path. Control using the incident wave as a reference does not suffer from this problem. Experimental results are presented. Broadband attenuation of around 20 dB in the ratio of the reflected and incident powers is demonstrated experimentally. The effect on the input frequency response of the structure is that substantial damping is added to all the modes of vibration that lie within the broad frequency range of control: a reverberant structure becomes anechoic. The high frequency limit is caused by the delays in both the computational time and filtering phase lags. The adaptive system achieves significant attenuation for broadband incident disturbances.

B.R. Mace, E. Rustighi and N.S. Ferguson
Institute of Sound and Vibration Research, University of Southampton SO17 1BJ, UK;
E-mail: {brm, er, nsf}@isvr.soton.ac.uk

D. Doherty
Mott MacDonald, Stoneham Gate, Stoneham Lane, Southampton SO50 9NW, UK;
E-mail: daniel.doherty@mottmac.com

H. Ulbrich and L. Ginzinger (eds.), Motion and Vibration Control, 231–240.

1 Introduction

Active vibration control has received much attention in recent decades [1]. Modal approaches have appeal at low frequencies, but encounter difficulties at higher frequencies because of problems such as stability, robustness, spillover and the number of modes involved. Wave-based approaches are then appealing since they have the potential to provide control over a broad frequency band and require no prior knowledge of the modes of the structure.

With regard to flexural vibration of beams, approaches aimed at absorbing energy or minimising wave transmission have been presented in [2–4], for example. In this paper a somewhat different approach is suggested: application of wave-based active control using a control force, typically applied near a boundary, which absorbs the energy of waves incident upon the boundary. This has the effect of producing a non-reflecting, anechoic termination, so that the dynamics of the beam appear as if the beam extends to infinity. Since modes can be regarded as standing waves, this has the effect of removing modal behaviour or dereverberating the structure. Von Flotow [5] suggested a feedback approach using analogue control, but since the desired controller frequency response is not realisable the approach is only effective over a narrow frequency band.

In this paper a digital feedforward control solution is proposed. A filtered-X LMS algorithm [6] is used to provide adaptive control with the error signal being the amplitude of the propagating wave reflected from the boundary. The real-time error signal is provided by filtering the outputs of an array of sensors (here, a pair of accelerometers is used) by "wave filters", described in [7], and used for active control of flexural vibrations in [8] and, in [9], when nearfields are present. Two possible reference signals are considered: the first is the signal input to the primary, disturbing force – such a signal is rarely available except in the laboratory. The second potential reference signal is the wave incident upon the boundary, this being found in real-time using wave filters applied to the outputs of the same sensor array. Two cases are considered. In the first the end of the beam opposite that at which control is applied is anechoic. Good control can be achieved using either reference signal. In the second the beam is finite and reverberant – this is of course the situation encountered in practical situations of interest. Using the incident wave as a reference has very substantial benefits.

The next section describes the theoretical background. Then experimental results for broadband active control are presented.

2 Theory

2.1 Waves in Beams

Consider a thin, uniform Euler–Bernoulli beam lying along the x-axis and undergoing time harmonic motion at frequency ω. The displacement of the beam can be written as the sum of four wave components as

$$W(x,\omega) = \phi^+ \exp(-ikx) + \phi^- \exp(ikx) + \phi_N^+ \exp(-kx) + \phi_N^- \exp(kx), \quad (1)$$

where the time dependence $\exp(i\omega t)$ has been suppressed and where the wavenumber

$$k = \sqrt[4]{\rho A\omega^2/EI}. \quad (2)$$

Here ρ, A and EI are the density, area and bending stiffness of the beam. The presence of damping leads to a small negative imaginary part in k. In Equation (1) $\phi^{\pm}$ represent propagating waves while $\phi_N^{\pm}$ are evanescent or nearfield waves, which decay rapidly with distance. Note that the wave motion is dispersive, i.e. different frequencies propagate with different speeds. This complicates the situation compared to the non-dispersive case, sound propagation for example, where wave propagation merely involves a time delay.

A point force $F\exp(i\omega t)$ applied at $x = 0$ excites propagating waves $e^{\pm}$ and evanescent waves $e_N^{\pm}$ in the regions $x > 0$ and whose amplitudes are [10]

$$e^{\pm} = \frac{-i}{4EIk^3}F; \quad e_N^{\pm} = \frac{-1}{4EIk^3}F. \quad (3)$$

These waves subsequently propagate through the system according to Equation (1). If positive-going waves ϕ^+ and ϕ_N^+ are incident on a free end of the beam the reflected waves are determined by a matrix of reflection coefficients [10]

$$\begin{Bmatrix} \phi^- \\ \phi_N^- \end{Bmatrix} = \begin{bmatrix} -i & (1+i) \\ (1-i) & i \end{bmatrix} \begin{Bmatrix} \phi^+ \\ \phi_N^+ \end{Bmatrix}. \quad (4)$$

2.2 Active Anechoic Termination

The layout of the active anechoic termination is shown in Figure 1. A disturbance acts some distance from the boundary, generating waves which propagate towards the boundary. A second force, the control, is applied at the boundary, or at a small distance x_e from it, the aim being for it to absorb any waves incident upon it and hence to simulate the situation where the beam extends to infinity. This removes resonant behaviour, potentially over a broad frequency band.

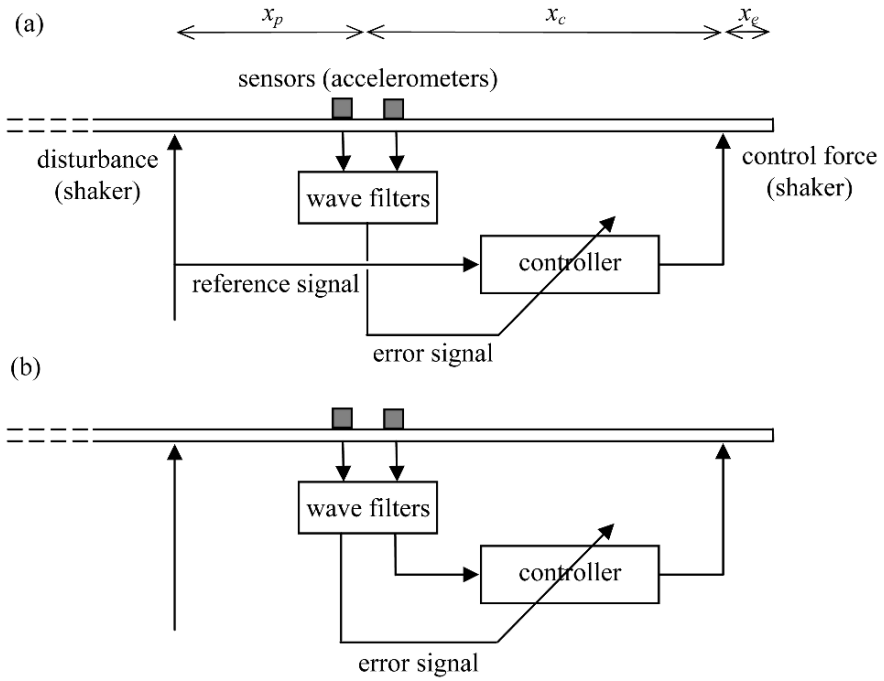

Fig. 1 Active anechoic beam: (a) primary disturbance as reference signal; (b) incident wave amplitude as reference signal.

A pair of sensors (accelerometers in the experimental work presented below) are attached to the beam at some distance from the end. The amplitudes of the waves in the beam can be estimated in real-time using wave filters [7–9]. The wave amplitudes mid-way between the sensors are estimated by the convolution of filters $\mathbf{g}(t)$ and the time domain sensor outputs $a_1(t)$ and $a_2(t)$, i.e.

$$\begin{Bmatrix} \phi_s^+(t) \\ \phi_s^-(t) \end{Bmatrix} = \mathbf{g}(t) * \begin{Bmatrix} a_1(t) \\ a_2(t) \end{Bmatrix}. \tag{5}$$

In practical implementations, such as that described below, digital control is typically used and digital FIR filters are designed to approximate these impulse responses. There are various issues to the design of these filters and details can be found in [7–9]. One is that the FIR filter length is finite, and hence the accuracy depends on the number of terms retained in the filters. More profoundly, the impulse responses are non-causal. In [7–9] a delay of a given number n_d of time steps is introduced into the filters so that, in effect, the filter output at a given time is the estimate of the wave amplitude n_d time steps earlier. This introduces time delays in the control loop and hence deteriorates the performance, especially at higher frequencies.

2.3 Feedforward Active Control and Reference Signals

Feedforward, adaptive control is used to provide the anechoic termination. The reference signal might be the primary disturbance (Figure 1a) if such a signal is available – this is the conventional approach to feedforward control. The alternative reference signal presented here is the amplitude of the positive going wave $\phi_s^+(t)$ as estimated by the wave filters (Figure 1b). In both cases the negative-going wave $\phi_s^-(t)$ is used as the error signal in a filtered-X LMS adaptive controller. (In a conventional system the response at a point or points might be used). The filtered-X LMS algorithm requires two FIR filters. The first, that of the control, adapts to copy the primary path from the reference signal to the error signal. The second, the secondary path, is an estimate of the path from controller output to error signal (i.e. from the input to the control shaker to the output of the wave sensors). This is required for proper adaptation. The performance of the system, i.e. the control achieved and the stability of adaptation, is better the more accurately both these paths are approximated by the FIR filters. The number of filter coefficients is of course limited by controller time delays and complexity. There are three cases of interest and the secondary path in particular depends on the approach used.

2.3.1 Incident wave as reference signal

Suppose that the disturbance excites an incident propagating wave whose amplitude at the centre of the pair of accelerometers is ϕ_s^+. The total negative-going propagating wave ϕ_s^- for a control force F_c is

$$\phi_s^- = (-i\exp(-i2k(x_c + x_e)))\phi_s^+ + G_w(\omega)F_c \tag{6}$$

and is the sum of the reflection of the incident propagating wave ϕ_s^+ generated by the disturbance and the net negative-going propagating wave injected by the control force. In Equation (6)

$$G_w(\omega) = -(i + \exp(-i2kx_e) + (1+i)\exp(-(1+i)kx_e))\exp(-ikx_c)/4EIk^3 \tag{7}$$

comprises three terms, representing the negative-going propagating wave injected by the control force, the reflection from the boundary of the positive-going propagating wave injected by the control force and the propagating wave reflected from the boundary due to the incidence of the nearfield wave injected by the control force. The secondary path $G_w(\omega)$ is such that

$$\phi_s^- = G_w(\omega)F_c \tag{8}$$

and is a smooth function of frequency so that it can in principle be accurately approximated by an FIR filter with relatively few terms.

An anechoic termination is one where the control force generates waves such that the net amplitude of the negative-going wave in Equation (6) is zero, i.e.

$$F_c = H_w(\omega)\phi_s^+; \quad H_w(\omega) = (i\exp(-ik(2x_e + x_c)))/G_w(\omega), \tag{9}$$

where $H_w(\omega)$ is the frequency dependent gain for incident wave amplitude control. Note that this is also a smooth function of frequency (unless the control force is applied far enough from the end so that the denominator becomes small in the frequency range of interest).

2.3.2 Primary disturbance as reference signal: other beam end anechoic

Now suppose that the input to the primary is used as a reference signal. This generates waves which propagate in both directions on the beam, hence contributing to the incident wave ϕ_s^+. If the far end of the beam (i.e. that opposite the control point) is anechoic so that no wave is reflected from it (i.e. the beam in effect extends uniformly to infinity) then the incident wave

$$\phi_s^+ = \exp(-ikx_p)\left(\frac{-i}{4EIk^3}\right)F_p \tag{10}$$

and the controller becomes such that

$$F_c = H_p(\omega)F_p; \quad H_p(\omega) = \frac{-\exp(-ik(x_p + 2x_e + x_c))}{(i + \exp(-i2kx_e) + (1+i)\exp(-(1+i)kx_e))}. \tag{11}$$

Again, both $H_p(\omega)$ and the secondary path (Equation (8)) are a smooth functions of frequency, readily approximated by FIR filters.

2.3.3 Beam with reflective end

Finally, consider the case of most practical significance, that where the beam is finite and where there are reflections from the end of the beam opposite that at which control is applied. The presence of reflections from the ends of the beam causes the beam to be resonant. The aim is then to provide active control over a broad band of frequencies which contains many resonances. Control using the incident wave amplitude as a reference signal merely involves the same situation as that described in Section 2.3.1 above: while the incident wave might be resonant, the primary and secondary paths are smooth functions of frequency.

This is not the case if the primary is taken as the reference signal. While the primary path is that of Equation (11) the secondary path (if the end is perfectly reflecting) is now

$$G_r(\omega) = G_w(\omega)/(1 + i\exp(-i(2kL + \theta))), \tag{12}$$

where L is the total length of the beam and θ is the phase of the reflection coefficient at the far end. What is important is the denominator: it involves the resonant

response of the structure, i.e. the contributions of subsequent reflections of the waves injected by the control from the far end of the beam to ϕ_s^-. There are typically many such resonances so that G_r is very difficult at best to approximate using a FIR filter with a moderate number of terms. An IIR filter might be used, but this leads to additional problems of stability and accurate approximation.

3 Experimental Results

In this section experimental results are presented. A thin steel beam of dimensions 6 m by 0.05 m by 0.00623 m was suspended by piano wire at four points along its length. The beam was excited by two electromagnetic shakers. The control shaker was attached at a distance $x_e = 0.019$ m from one end. The other end of the beam was either placed in a sandbox to simulate an anechoic boundary or was free, so that it reflected waves strongly. The primary shaker was fixed at a position close to the middle of the beam or close to the free end of the beam in these two cases respectively. The two accelerometers were attached to the beam between the two shakers. The other dimensions in Figure 1 are $x_p = 0.71$ m and $x_c = 2.57$ m. Nearfields arising from the primary disturbance can be neglected in the frequency range of interest. The beam wavenumber was measured as $k = 0.0827\sqrt{f}$ using a conventional 2-accelerometer technique.

Real-time control was implemented in Matlab using Simulink and the Real-Time Workshop. Other instrumentation used included anti-aliasing and reconstruction filters, power amplifiers and a host PC. The wave amplitudes of the incident and reflected waves were estimated in real-time from the accelerometer outputs using the wave filters described above. In the results shown $n_d = 5$ and the FIR control filter had 40 terms. The sampling frequency was 2048 Hz. Band-limited noise in the frequency range 102–922 Hz was fed to the primary shaker. Filtered-X LMS control was applied with an adaptation rate (i.e. the learning rate in the adaptive control) $\mu = 0.005$, the cancellation path from control shaker input to negative-going wave amplitude being estimated off-line. Results are presented in terms of the ratio of the reflected and incident powers after the adaptation is allowed to converge. These powers were measured off-line using a well-established frequency domain method so that they are independent of the wave amplitudes estimated from the real-time wave filters. Also shown are the input frequency responses (acceleration per unit force).

Figure 2 shows the ratios of the reflected and incident powers when the end of the beam was in the sandbox. The performances with primary (*PRef*) and incident wave (*WRef*) as reference signal are comparable, with attenuations of around 20 dB being attained over much of the frequency range: *WRef* control is perhaps better at lower frequencies but worse at higher frequencies when the effects of time delays in the wave filters and the primary path become substantial. Figure 3 shows the input accelerance for *WRef* control (that for *PRef* is similar). Figure 4 shows the ratios of the reflected and incident powers when the end of the beam is free and hence

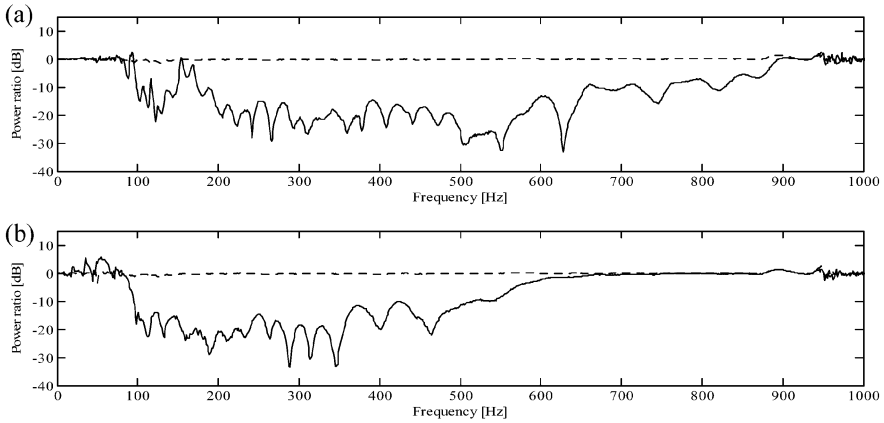

Fig. 2 Ratio of reflected and incident powers, beam end in sandbox: . . . no control; (a) primary disturbance as reference; (b) incident wave as reference.

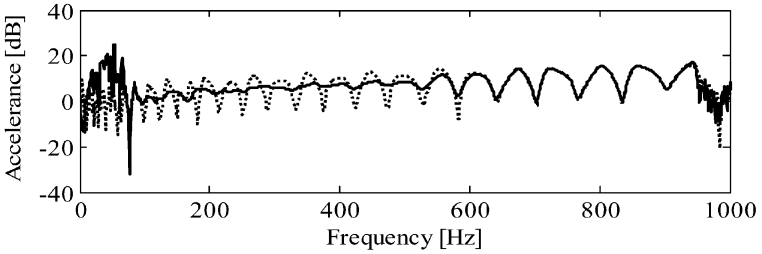

Fig. 3 Input accelerance, beam end in sandbox: . . . no control; incident wave as reference.

the beam is resonant. *PRef* control breaks down because of the resonant behavior, while *WRef* control still provides broadband control of 20 dB or so over most of the frequency range. The input accelerance (Figure 5) is clearly dereverberated in the frequency range of control.

4 Concluding Remarks

In summary, the active anechoic termination shown in Figure 1 is an adaptive, feed-forward control system with the following elements. A primary source of vibration lies some distance from the boundary near which a control force is applied. A pair of sensors is used to estimate the amplitudes of the incident and reflected propagating waves using real-time wave filters. The controller implements an adaptive, filtered-X LMS algorithm. The error signal is the amplitude of the net wave reflected from the end. The reference signal is either the signal input to the disturbance, if that is

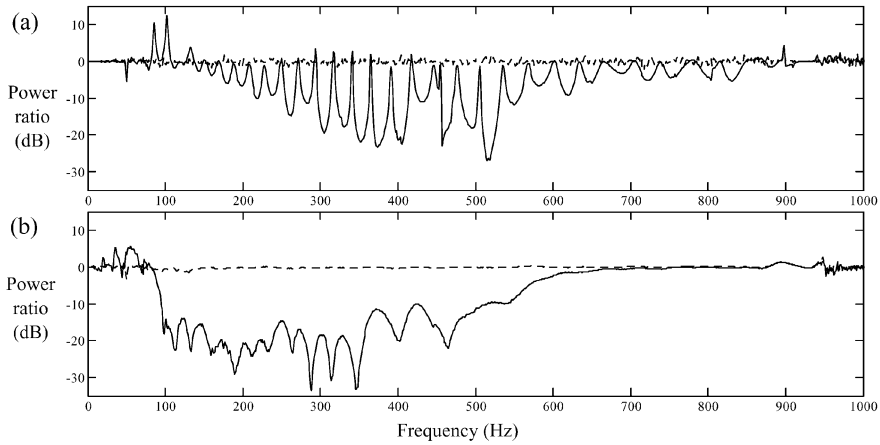

Fig. 4 Ratio of reflected and incident powers, beam end free: · · · no control; (a) — primary disturbance as reference; (b) — incident wave as reference.

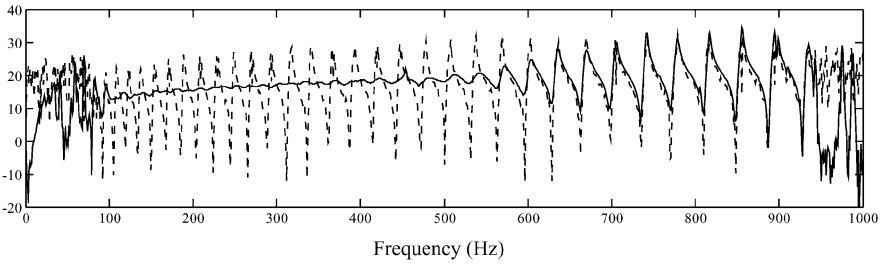

Fig. 5 Input accelerance, beam end free: · · · no control; — incident wave as reference.

available, or the amplitude of the positive going propagating wave. Experimental results showed broadband attenuation of 20 dB or so.

In practice it is unlikely that a reference signal from the primary would be available. In some cases the excitation might be spatially distributed – a turbulent boundary layer for example – so that a single primary reference signal does not even exist. Even if it were, major difficulties arise if the structure is finite, and hence resonant, as is normally the case, with perhaps many modes of vibration in the frequency range of interest. Using the primary as a reference leads to a cancellation path filter which shows strong resonant behaviour which is very difficult to approximate accurately enough except with an FIR filter of inordinate length. Convergence and performance of X-LMS control are thus severely compromised. Control based on the incident wave amplitude however does not suffer from these disadvantages: a reference signal is always available and the primary and secondary paths are both smooth functions of frequency.

In principle the system adapts to drive the amplitude of the reflected wave to zero. In practice the performance differs from the ideal because of various approx-

imations and compromises. The performance is limited by the sampling rate and various time delays in the system: hardware-related issues such as anti-alias and reconstruction filter delays and processor delays; wave filter design issues; control issues such as the length of the controller and cancellation path filters; physical time delays resulting from the time it takes for waves to propagate from one point of the system to another. Problems are exacerbated because bending wave motion is dispersive, so that different frequency components travel at different speeds, so that different time delays are associated with different frequency components. All these result in compromises that affect the overall performance of the system.

References

1. Fuller, C.R., Elliott, S.J., and Nelson, P.A., *Active Control of Vibration*. Academic Press, San Diego, 1997.
2. Mace, B.R., Active Control of Flexural Vibrations, *Journal of Sound and Vibration* **114**, 253–270, 1987.
3. Elliott, S.J. and Billet, L., Adaptive Control of Flexural Waves Propagating in a Beam, *Journal of Sound and Vibration* **163**, 295–310, 1993.
4. Schwenk, A.E., Sommerfeldt, S.D., and Hayek, S.I., Adaptive Control of Structural Intensity Associated with Bending Waves in a Beam. *Journal of the Acoustical Society of America* **96**, 2826–2835, 1994.
5. von Flotow, A.H. and Schafer, B, Wave-Absorbing Controllers for a flexible Beam, *Journal of Guidance, Control and Dynamics* **9**, 673–680, 1986.
6. Vipperman, J.S., Burdisso, R.A., and Fuller, C.R., Active Control of Broad-Band Structural Vibration Using the LMS Adaptive Algorithm. *Journal of Sound and Vibration* **166**, 283–299, 1993.
7. Mace, B.R. and Halkyard, C.R., Time Domain Estimation of Response and Intensity in Beams Using Wave Decomposition and Reconstruction. *Journal of Sound and Vibration* **230**, 561–589, 2000.
8. Halkyard, C.R. and Mace, B.R., Feedforward Adaptive Control of Flexural Vibration in a Beam Using Wave Amplitudes, *Journal of Sound and Vibration* **254**, 117–141, 2002.
9. Halkyard, C.R. and Mace, B.R., Adaptive Active Control of Flexural Waves in a Beam in the Presence of a Nearfield, *Journal of Sound and Vibration* **285**, 149–171, 2005.
10. Mace, B.R., Wave Reflection and Transmission in Beams, *Journal of Sound and Vibration* **97**, 237–246, 1984.

Enduring Rotary Motion Experiment of Devil Stick by General-Purpose Manipulator

Keisuke Nakamura, Shigeki Nakaura and Mitsuji Sampei

Abstract Devil stick is a type of juggling which uses two sticks, one held by juggler and one to be manipulated. Many varieties of tricks of devil stick have been performed. In this paper, one of the tricks called "propeller" is specifically examined. Previously, the motion of propeller was analysed theoretically, and a controller for stable propeller motion by output zeroing control was proposed, and the validity of the controller was confirmed by numerical simulations. In the analysis of propeller motion, several conditions were assumed for simplifying the control problem. The controller was implemented to a general-purpose manipulator, and several experiments were carried out. However, those experiments could not successfully verify the propeller motion because the assumptions used in theoretical analysis were unfeasible. To correct this problem, an additional compensator is proposed, and the validity of the compensator is confirmed by numerical simulations and experiments. Finally, the enduring rotary motion of 37 rotations was achieved by an experiment.

1 Introduction

Devil stick is a kind of juggling which uses two types of stick. One is called "center stick" which is manipulated and floats around in the air. The other one is called "hand stick" which the juggler holds on and is hitting and pushing the center stick. Many tricks with the devil stick have been performed practically, and some of those maneuver motions were studied as control problems [1].

In this paper, one of the tricks called "propeller" is examined. That is the motion to make the center stick rotate continuously by pushing with one hand stick (see Figure 1). Kawaida [2] analysed the motion of propeller theoretically and proposed a controller. Furthermore, he confirmed the validity of the controller by numerical

Keisuke Nakamura, Shigeki Nakaura and Mitsuji Sampei
Tokyo Institute of Technology, 2-12-1 O-okayama, Meguro-ku, Tokyo 152-8550, Japan;
E-mail: nakamura@sc.ctrl.titech.ac.jp, nakaura@ctrl.titech.ac.jp, sampei@ctrl.titech.ac.jp

H. Ulbrich and L. Ginzinger (eds.), Motion and Vibration Control, 241–251.

Fig. 1 Propeller motion
The center stick rotates counterclockwise. The numbers in this figure shows the order of the motion, which repeats the motion from number 1 to number 3 in order.

simulations. In the analysis of propeller motion, there were several assumptions for making the control problem simple.

The controller was implemented to a general-purpose manipulator, and several experiments were carried out [3, 4]. However, those experiments could not successfully achieve the propeller motion because the assumptions which were used in the analysis could not be realized by the manipulator. The purpose of this paper is to achieve the enduring rotary motion of devil stick by experiments. This is achieved by examining the experimental setup, and a new additional compensator is proposed.

This paper is organized as follows. In Section 2, modeling, assumptions of the model and state equations of the propeller motion are considered and explained. In Section 3, a controller for the propeller motion are designed. In Section 4, the experimental equipment, the results of previous experiments are explained. In Section 5, a new additional compensator is introduced, and the validity of the compensator is discussed. The results of experiments with an additional compensator is shown and compared with the experiments without it in Section 6. Finally, Section 7 concludes this paper.

2 Modeling and State Equations of the Devil Stick

The model of propeller motion and its parameters are shown in Figure 2 and Table 1 respectively. For the theoretical analysis, several conditions are assumed as follows:

Assumption 1 Friction force at the contact point is large enough, so the center stick does not slip on the hand stick but rotates around it.

Assumption 2 The center stick keeps contacting with the hand stick, so the contact point moves by rolling with rotation of the devil stick.

The schematic model of Assumption 1 and Assumption 2 is shown in Figure 3(a). From the assumptions, following equation represents the relationship between ϕ and d.

$$d(\phi) = -\rho\phi + d_0\,, \tag{1}$$

where d_0 is the initial position of the contact point d.

Continuous rotation makes d diverge, which means the hand stick is going farther from the center of the center stick. To achieve continuous rotation, it is essential to keep d close to the center, so two conditions are assumed as follows:

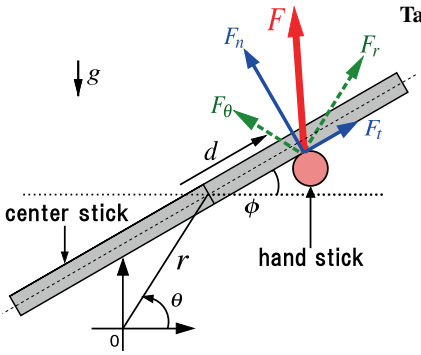

Fig. 2 Model of propeller motion in a vertical plane.

Table 1 Parameters of the model of propeller motion.

r, θ	:	Position of the center of gravity of the center stick in the polar coordinate
ϕ	:	Attitude angle of center stick
F	:	Force applied by the center stick
F_r, F_θ	:	(r, θ) direction's component of F
F_n	:	n direction's component of F
F_t	:	t direction's component of F
d	:	Position of the contact point from the center of gravity of the center stick
m	:	Mass of the center stick
J	:	Moment of inertia of the center stick
ρ	:	Radius of the hand stick
g	:	Acceleration of gravity

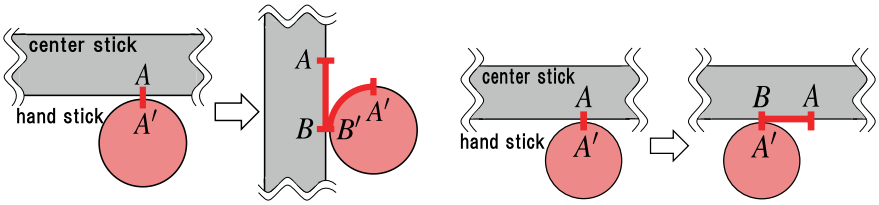

(a) Movement of the contact point by rotations

(b) Movement of the contact point by slipping

Fig. 3 Change of contact point.

Assumption 3 The contact point jumps to the initial position when the center stick is made one turn (ϕ increases 2π).

Assumption 4 The time for the jump is assumed to be zero.

The schematic model of Assumption 3 and Assumption 4 is shown in Figure 3(b). From the assumptions, equation(1) is rewritten as follows:

$$\begin{cases} d(\phi) = -\rho(\phi - \phi_{jump}) + d_{max} \quad (\phi_{jump} \le \phi < \phi_{jump} + 2\pi), \\ d(\phi + 2\pi) = d(\phi), \end{cases} \tag{2}$$

where ϕ_{jump} and d_{max} are ϕ and d at the moment of jump respectively.

From Figure 1, following equations of motion can be obtained.

$$\ddot{r} = r\dot{\theta}^2 - g\sin\theta + \frac{\cos(\theta - \phi)}{m}F_t + \frac{\sin(\theta - \phi)}{m}F_n \tag{3}$$

$$\ddot{\theta} = -\frac{2\dot{r}\dot{\theta}}{r} - \frac{g\cos\theta}{r} - \frac{\sin(\theta - \phi)}{rm}F_t + \frac{\cos(\theta - \phi)}{rm}F_n \tag{4}$$

$$\ddot{\phi} = \frac{d(\phi)F_n}{J} \tag{5}$$

Selecting state $\mathbf{x}$ and input $\mathbf{u}$ as

$$\begin{aligned} \mathbf{x} &= [r,\ \theta,\ \phi,\ \dot{r},\ \dot{\theta},\ \dot{\phi}]^T], \\ \mathbf{u} &= \mathbf{F} = [F_t, F_n]^T \end{aligned} \tag{6}$$

the state equation of the propeller motion is described as follows:

$$\frac{d\mathbf{x}}{dt} = f(\mathbf{x}) + G(\mathbf{x})\mathbf{u}\,, \tag{7}$$

$$f(\mathbf{x}) = \begin{bmatrix} \dot{r} \\ \dot{\theta} \\ \dot{\phi} \\ r\dot{\theta}^2 - g\sin\theta \\ -\frac{2\dot{r}\dot{\theta}}{r} - \frac{g\cos\theta}{r} \\ 0 \end{bmatrix}, \quad G(\mathbf{x}) = \begin{bmatrix} 0 & 0 \\ 0 & 0 \\ 0 & 0 \\ \frac{\cos(\theta-\phi)}{m} & \frac{\sin(\theta-\phi)}{m} \\ -\frac{\sin(\theta-\phi)}{rm} & \frac{\cos(\theta-\phi)}{rm} \\ 0 & \frac{d(\phi)}{J} \end{bmatrix}. \tag{8}$$

3 Control Objective and Design

When a juggler manipulates a center stick and the rotation is stable, the following behaviors of the center stick can be observed.

Behavior 1 The center of gravity(COG) of the center stick moves on a circle trajectory with a fixed center point.

Behavior 2 The period of the rotation of the COG corresponds to the period of rotation of the center stick.

Behavior 3 The center stick rotates at a uniform angular velocity.

To achieve Behavior 1, r has to be controlled to make it constant:

$$r = r_r\,, \tag{9}$$

where r_r is the desired radius of the circle trajectory.

Behavior 2 means $\theta - \phi$ has to be controlled to make it constant (see Figure 4). Moreover, since the trajectory of the COG is a circle, the hand stick should give the centripetal force to the center stick, which means

$$\theta - \phi = -\frac{\pi}{2}\,. \tag{10}$$

To achieve Behavior 1 and Behavior 2, input output linearization and output zeroing control are used. From equations (9) and (10), the output function is described as follows:

$$y = \begin{bmatrix} y_1 \\ y_2 \end{bmatrix} = \begin{bmatrix} r_r - r \\ -\frac{\pi}{2} - (\theta - \phi) \end{bmatrix}. \tag{11}$$

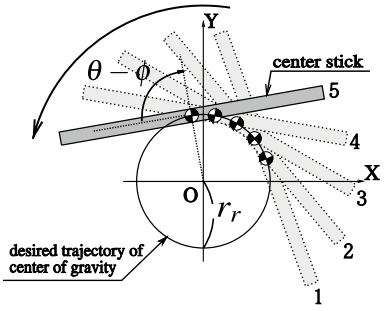

Fig. 4 Control objective
This figure shows the movement of the center stick. The numbers from 1 to 5 represent the order of the movement. The COG of the center stick follows a desired circle trajectory as the stick rotates.

As a result of input-output linearization, following linearized state equations are obtained.

$$\dot{\boldsymbol{\xi}} = A\boldsymbol{\xi} + B\mathbf{v}\,, \tag{12}$$

$$\dot{\boldsymbol{\eta}} = \zeta_1(\boldsymbol{\xi}, \boldsymbol{\eta}) + \zeta_2(\boldsymbol{\xi}, \boldsymbol{\eta})\mathbf{v}\,, \tag{13}$$

$$\mathbf{y} = C\boldsymbol{\xi}\,, \tag{14}$$

where

$$\boldsymbol{\xi} = \left[\, \xi_1,\, \xi_2,\, \xi_3,\, \xi_4 \,\right]^T = \left[\, r_r - r,\, -\tfrac{\pi}{2} - (\theta - \phi),\, -\dot{r},\, -(\dot{\theta} - \dot{\phi}) \,\right]^T, \tag{15}$$

$$\boldsymbol{\eta} = \left[\, \eta_1,\, \eta_2 \,\right]^T = \left[\, \phi,\, \dot{\phi} \,\right]^T, \tag{16}$$

$$\mathbf{v} = \ddot{\mathbf{y}}\,, \tag{17}$$

$$A = \begin{bmatrix} \mathbf{O}^{2\times2} & \mathbf{I}^{2\times2} \\ \mathbf{O}^{2\times2} & \mathbf{O}^{2\times2} \end{bmatrix}, \quad B = \left[\, \mathbf{O}^{2\times2}\ \mathbf{I}^{2\times2} \,\right]^T, \quad C = \left[\, \mathbf{I}^{2\times2}\ \mathbf{O}^{2\times2} \,\right],$$

$$\zeta_1(\boldsymbol{\xi}, \boldsymbol{\eta}) = \begin{bmatrix} \eta_2 \\ \frac{d(\eta_1)m(g\cos(\eta_1) - (-\xi_4+\eta_2)(2\xi_3\sin(\xi_2) + (-\xi_4+\eta_2)(r_r-\xi_1)\cos(\xi_2)))}{J - d(\eta_1)m(r_r-\xi_1)\sin(\xi_2)} \end{bmatrix}, \tag{18}$$

$$\zeta_2(\boldsymbol{\xi}, \boldsymbol{\eta}) = \begin{bmatrix} 0 & 0 \\ \frac{-d(\eta_1)m\cos(\xi_2)}{J - d(\eta_1)m(r_r-\xi_1)\sin(\xi_2)} & \frac{-d(\eta_1)m(r_r-\xi_1)\sin(\xi_2)}{J - d(\eta_1)m(r_r-\xi_1)\sin(\xi_2)} \end{bmatrix}. \tag{19}$$

The outputs of this system converge to zero by output zeroing control with state feedback, then Behavior 1 and Behavior 2 are achieved successfully.

Behavior 3 means $\dot{\phi}$ must not converge to zero and must not diverge when the center stick rotates stably. To achieve this behavior, the zero dynamics of $\dot{\phi}$ is analysed. The 2nd element of $\dot{\boldsymbol{\eta}}$ of equation (13) represents $\ddot{\phi}$. Therefore, $\dot{\phi}$ can be derived by solving the differential equation of $\dot{\boldsymbol{\eta}}$. From equations (13), (17), (18) and (19), the zero dynamics of $\ddot{\phi}$ can be obtained as follows by setting $\boldsymbol{\xi} = \mathbf{O}$:

$$\ddot{\phi} = \frac{d(\eta_1)m(g\cos\eta_1 + r_r\eta_2^2)}{J} = \frac{d(\phi)m(g\cos\phi + r_r\dot{\phi}^2)}{J}\,. \tag{20}$$

Since $d(\phi)$ is described as equation (2) which is a periodic function with the period of 2π, $\dot{\phi}$ at the moment of k-th jump is defined as p_k, and the relationship between p_k and p_{k+1} is derived as following recursion formula:

$$p_{k+1}^2 = \Lambda_1 p_k^2 + \Lambda_2 \,, \tag{21}$$

$$\Lambda_1 = e^{-4\pi m r_r(\rho\pi - d_{max})/J} \,, \tag{22}$$

$$\Lambda_2 = e^{-mr_r(\phi_{jump}+2\pi)(\rho(-\phi_{jump}+2\pi)-2d_{max})/J} \times \int_{\phi_{jump}}^{\phi_{jump}+2\pi} \frac{-2gm(\rho(\tau-\phi_{jump})-d_{max})\cos\tau/J}{e^{-mr_r\tau(\rho(\tau-2\phi_{jump})-2d_{max})/J}} d\tau \,, \tag{23}$$

The general term of this recursion formula is described as

$$p_k^2 = \begin{cases} \Lambda_1^k (p_0^2 - \frac{\Lambda_2}{1-\Lambda_1}) + \frac{\Lambda_2}{1-\Lambda_1} & (\Lambda_1 \neq 1) \,, \\ p_0^2 + k\Lambda_2 & (\Lambda_1 = 1) \,. \end{cases} \tag{24}$$

The value of p_∞ depends on Λ_1 and Λ_2. When

$$\begin{cases} 0 < \Lambda_1 < 1 \\ \Lambda_2 \geq 0 \end{cases} \tag{25}$$

are satisfied, $p_\infty = \sqrt{\Lambda_2/1-\Lambda_1}$ is obtained, which means stable rotation.

The condition to satisfy $0 < \Lambda_1 < 1$ is given from equation (22),

$$-4\pi m r_r(\rho\pi - d_{max})/J < 0 \Leftrightarrow d_{max} < \rho\pi \quad (\because r_r > 0, m > 0, J > 0) \,. \tag{26}$$

Since Λ_2 includes an integral term which is difficult to analyse, the condition $\Lambda_2 > 0$ is derived by numerical calculations.

4 Experiments

The schematic drawing of the experimental environment is shown in Figure 5(a). A commercial product of general-purpose manipulators is used in the experiments as a human arm. A linear encoder, a rotary encoder and a force sensor are attached to the end-effector of the manipulator to measure d, ϕ and $\mathbf{F}$ respectively. The manipulator has absolute angle sensors (resolvers) in each joint, and r and θ can be measured by those angles.

As discussed in Section 2, there are four assumptions to achieve the enduring rotary motion. Therefore, the following two phases are to be realized in the experiments.

Phase 1 From Assumption 1 and Assumption 2, the force $\mathbf{F}$ is applied to the center stick by the hand stick. In this phase, the center stick does not slip on the

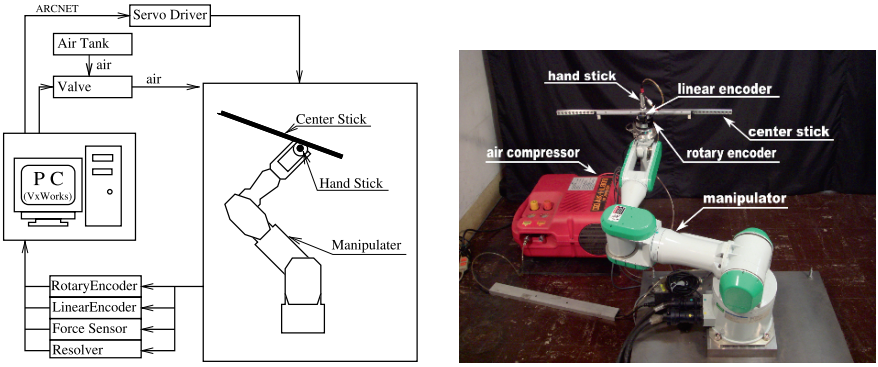

(a) Experimental environment (b) Experimental equipment

Fig. 5 Experimental environment.

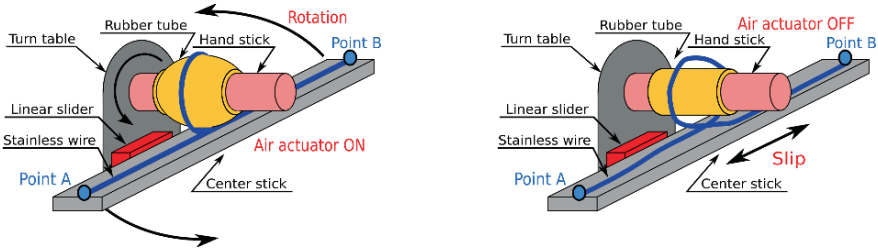

(a) Phase 1 (b) Phase 2

Fig. 6 Mechanism of switching phases.

hand stick but rotates around it. Furthermore, the contact point moves by rolling with rotation of the devil stick.

Phase 2 From Assumption 3 and Assumption 4, the hand stick slips along the center stick and comes back to the initial value of d (d_{max} in equation (2)), and the time for the slip is sufficiently short.

These two phases are switched in each rotation under the condition represented by equation (2).

A mechanism at the end-effector is designed to realize the switch between two phases. A linear slider and a turn table are attached between the center stick and the hand stick, which realise the motion of the direction of d and ϕ respectively. A rubber tube connected to an air valve is also attached between two sticks, and these two phases are switched by turning the valve on and off. A stainless wire is fixed at the edges of the center stick (Point A and Point B in Figure 6), and it is winded once onto the rubber tube. In phase 1, the rubber tube is pumped up, then the wire

Table 2 Parameters of experimental equipment.

m [kg]	J [kg m^2]	ρ [m]	g [m/s^2]	r_r [m]
0.385	0.015	0.01	2.54	0.05

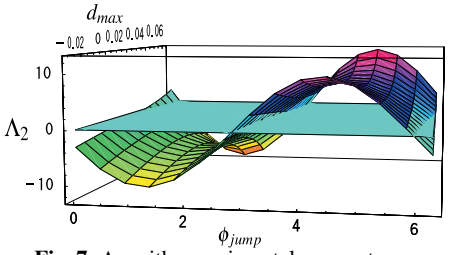

Fig. 7 Λ_2 with experimental parameters.

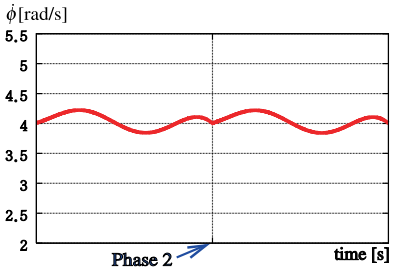

(a) $\dot{\phi}$ (numerical simulation)

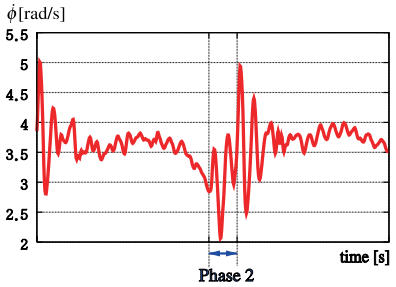

(b) $\dot{\phi}$ (experiment)

Fig. 8 Comparison of the simulation and the experiment (the influence of Phase 2 upon $\dot{\phi}$).

grips the tube, and the hand stick does not slip on the center stick but rotates around it (see Figure 6(a)). In phase 2, the rubber tube is deflated, then the wire releases the tube, and the hand stick can slip on the center stick freely (see Figure 6(b)).

Experimental parameters m, J, ρ, r_r have been chosen as shown in Table 2.

Several preliminary experiments were carried out in a vertical plane. However, realizing the continuous rotation of devil stick in a vertical plane needed more speed of the end-effector than that of the general-purpose manipulator. Therefore, the continuous rotation in those experiments was not successfully achieved.

To solve this problem, the plane at an angle of 15 degrees to the horizontal is used for the operation of propeller motion instead of the vertical plane used in the theoretical analysis. The acceleration of gravity is then reduced to $g = 2.54$ [m/s^2]. The experimental equipment is shown in Figure 5(b).

d_{max} and ϕ_{jump} are determined so as to satisfy the conditions (25) and (26). The result of calculation of Λ_2 with experimental parameters is shown in Figure 7. $\phi_{jump} = 3\pi/2$ [rad] and $d_{max} = 0.031$ [m] have been chosen, as a result.

As described above, Phase 2 has to be done in sufficiently short time. However, because of the limitation of the capacity of the general-purpose manipulator, Assumption 4 cannot be achieved by the manipulator.

Figure 8 shows the influences of Phase 2 upon $\dot{\phi}$ of both a simulation and an experiment. In numerical simulations, the jump of the state d can be achieved without

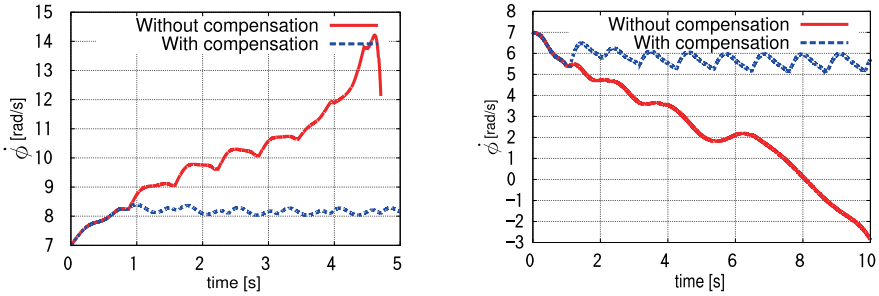

(a) Time behavior of $\dot{\phi}$ with acceleration disturbance

(b) Time behavior of $\dot{\phi}$ with deceleration disturbance

Fig. 9 Effect of the angular velocity compensation.

any effects. On the other hand, in the experiments, Phase 2 affects $\dot{\phi}$ severely. Since this disturbance is indigenous, a new controller to compensate it is to be designed.

5 Angular Velocity Compensation

As discussed in Section 4, it is essential to compensate the disturbance of $\dot{\phi}$ in order to realize the enduring rotary motion in experiments.

In numerical simulations, if the parameters d_{max} and ϕ_{jump} satisfy the conditions (25) and (26), $p_\infty = \sqrt{\Lambda_2/1-\Lambda_1}$, and the enduring rotary motion will be realized. That means d_{max} and ϕ_{jump} can be constant values.

Since $\dot{\phi}$ is affected by Phase 2 and is described as the recursion formula (23) which is the function of d_{max} and ϕ_{jump}, those parameters can be used for angular velocity compensation. Here, the angular velocity compensation using d_{max} is used because the change of d_{max} affects both Λ_1 and Λ_2, and Λ_1 determines the common ratio of the recursion (23) which severely affects the $\dot{\phi}$ of the next rotation.

In addition, since the recursion (23) includes an integral term and the value of p_{k+1} depends on p_k, a proportional controller is adopted to determine the value of d_{max} in order to simplify the problem. The controller is described as follows:

$$d_{max} - d_{desired} = K_p(\dot{\phi} - \dot{\phi}_{desired}), \tag{27}$$

where $d_{desired}$ and $\dot{\phi}_{desired}$ are the desired d and $\dot{\phi}$ when the center stick rotates stably (the values are from numerical simulations), and K_p is a proportional gain.

Algorithmically, $\dot{\phi}$ in each rotation is measured just before Phase 2, and d_{max} is determined in each rotation. The compensation using d_{max} is used as a subsidiary controller of the original controller discussed in Section 3.

The simulative comparison between the systems with and without angular velocity compensation is shown in Figure 9. As seen in the figure, the system without angular velocity compensator is enormously affected by both acceleration and deceleration disturbance and cannot success to keep rotation. Clearly, it can be said that the new angular velocity compensator is useful to realize the enduring rotary motion. This compensator is also useful in terms of easy implementation.

Moreover, practically, changing d_{max} means changing the hitting point of the center stick in each rotation. For jugglers, it is very difficult to know the contact force between the center stick and the hand stick. That means a juggler manipulates a center stick by watching it, only depends on the information of the position, which is strongly related to d_{max}. Therefore, it can be said that this angular velocity compensator is exactly what jugglers do, and the compensator provides us how the jugglers determine where to hit the center stick in each rotation, which is quite important to know.

6 Experiments with Angular Velocity Compensation

The angular velocity compensator discussed in Section 5 is applied to the experiments.

The experiment without angular velocity compensation can control the angular velocity at first, but once $\dot{\phi}$ is increased, the system cannot keep rotation (see Figure 10). On the other hand, the system with angular velocity compensation can manipulate the angular velocity by changing d_{max} (see Figure 11).

As a result, the enduring rotary motion of 37 rotations was achieved. The validity of the original controller by output zeroing control and the additional controller for compensation is confirmed by not only numerical simulations but also experiments.

However, as shown in Figure 11, the rotation tends to stop when the angular velocity of the center stick becomes fast. In such case, the hand stick has to get back to d_{max} in shorter time than usual ideally because the angle of switching phases should be the same in each rotation. However, it is impossible because of the capacity of the manipulator. The next possible work is to use an appropriate manipulator for the experiments.

7 Conclusion

In this paper, the control problem of the enduring rotary motion of devil stick was investigated.

As a theoretical analysis, the state equations of the system were derived, and the controller was designed by input-output linearization and output zeroing control. The zero dynamics of $\dot{\phi}$ was analysed and the conditions to realize continuous rotation were obtained.

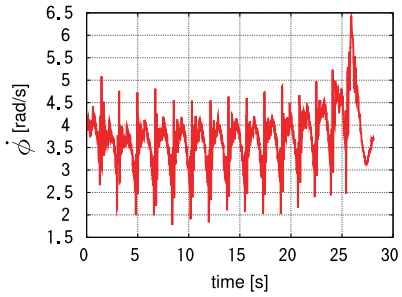

(a) Time behavior of $\dot{\phi}$

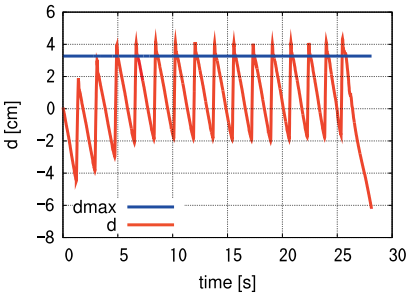

(b) Time behavior of d and d_{max}

Fig. 10 Experiment without angular velocity compensation.

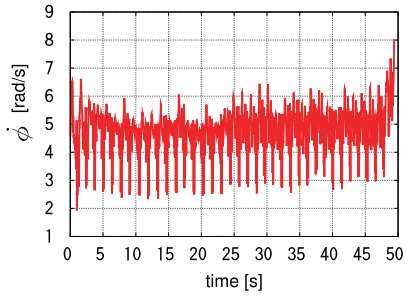

(a) Time behavior of $\dot{\phi}$

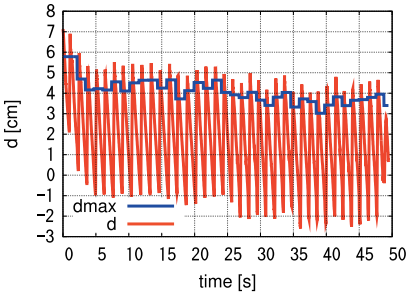

(b) Time behavior of d and d_{max}

Fig. 11 Experiment with angular velocity compensation.

This control system was implemented to experiments, but the continuous rotation was not realized because of an unfeasible assumption.

A new angular velocity compensator using d_{max} was designed, and the validity of the compensator was confirmed by numerical simulations and experiments.

References

1. Schaal, S., Atkeson, C.G., Open Loop Stable Control Strategies for Robot Juggling, in *Proc. IEEE Int. Conf. on Robotics and Automation*, Vol. 3, pp. 913–918, Atlanta, USA (1993).
2. Kawaida, Y., Nakaura, S., Ohata, R. and Sampei, M., Feedback Control of Enduring Rotary Motion of Devil Stick, in *Proc. of 42nd IEEE Conf. on Decision and Control*, Vol. 4, pp. 3396–3401, Maui Hawaii, USA (2003).
3. Nakaura, S., Kawaida, Y., Matsumoto, T. and Sampei, M., Enduring Rotatory Motion Control of Devil Stick, in *Proc. of 6th IFAC NOLCOS Symp.*, pp. 1073–1078, Stuttgart, Germany (2004).
4. Nakaura, S., Fujimoto, D. and Sampei, M., Enduring Rotary Motion Control of Devil Stick by General-purpose Manipulator, in *Proc. SICE 5th Annual Conf. on Control Systems (Seigyo-Bumon-Taikai)*, pp. 381–384, Sendai, Japan (2005) [in Japanese].

Active Damping of Vibrations of a Lightweight Beam Structure – Experimental Results

T. Pumhössel and H. Springer

Abstract Lightweight beam structures are used in various fields of applications, e.g. in aerospace industry and civil engineering. The natural damping of such structures is often very small which may result in a reduced lifetime. One possibility to increase the damping is the use of active damping devices to apply state-dependent moments and/or forces to the mechanical structure. In this contribution, a single axial force is applied to a cantilever beam by using a string along with a piezoelectric actuator. To introduce artificial damping to the lateral vibrations of the beam, a nonlinear parametric feedback control law is used which is based on axial velocity feedback of the tip of the beam. A test rig was built where the lateral vibrations of the beam are measured with a laser-measurement device, and a piezoelectric sensor measures and indicates the actual force in the string. Both signals are feed into the realtime-controller, which calculates the corresponding control signal for the piezoelectric actuator. The experimental results show highly increased damping capabilities compared to the uncontrolled system.

1 Introduction

In various fields of applications, e.g. in aerospace industry and civil engineering, lightweight beam structures are widely used. These structures often possess a very low natural damping, which may lead to a reduction of lifetime. Several active methods exist to introduce artificial damping by using feedback controlled forces and/or moments applied to the structure. The method of application is of great interest for

T. Pumhössel
Technical University of Vienna, Institute of Mechanics and Mechatronics, Vienna, Austria;
E-mail: thomas.pumhoessel@tuwien.ac.at

H. Springer
Technical University of Vienna, Institute of Mechanics and Mechatronics, Vienna, Austria;
E-mail: helmut.springer@tuwien.ac.at

H. Ulbrich and L. Ginzinger (eds.), Motion and Vibration Control, 253–262.

a practical realization of the control concept. In [1], for example, a single axial force is applied to a cantilever beam by using a string inside the beam along with a piezoelectric actuator, whereas in [2] a string is located on the outside of a beam and is driven by a DC-motor. The application of a single axial force to a beam results in a time dependent stiffness matrix, as shown for example in [3]. To introduce artificial damping to the lateral vibration of the beam, the stiffness parameter, and therefore the axial force has to be controlled in a proper way. In many cases, axial velocity feedback of the beam with constant amplification is used, see [3,4], whereas in [5,6] the amplification depends on the actual axial velocity of the beam.

In this contribution, a test rig is presented consisting of a preloaded cantilever beam with a string inside, connected to the free tip of the beam on one end, and to a piezoelectric actuator on the other end, as proposed in [1]. The actual force in the string is measured by a piezoelectric force sensor. The lateral beam vibration is measured by a laser measurement device. Both signals are feed into a realtime controller which calculates the control signal for the piezoelectric actuator. The experimental results demonstrate the increased damping of the lateral beam vibrations compared to the uncontrolled system. It is shown that state-dependent amplification gives much better results than simple axial velocity feedback with constant gain.

2 Differential Equations of the Closed-Loop System

The derivation of the equations of motion and the feedback control-law is only briefly discussed in this paper, for details see [1, 7, 8]. Figure 1 shows a schematic diagram of the investigated mechanical system. The cantilever beam is slotted lengthwise to give space for the string (see section A-A). At the free end, the string runs through an axial borehole in the beam and is connected to its tip. The lower end of the string is guided through the baseplate and is connected to an actuator system (not shown in Figure 1) which provides a constant displacement u_0, resulting in preloading the beam with the force F_0, and a time-dependent displacement $\tilde{u}_A(t)$ which causes a time-dependent force $\tilde{F}(t)$ in the string. The dimensions and properties of the mechanical system can be seen in Table 1.

The nonlinear equations of motion where calculated using the Bernoulli–Euler beam theory up to terms of cubic order and d'Alemberts principle. Therefore, lateral and axial displacement fields of beam and string are inroduced (see Figure 1, right). Using a Rayleigh–Ritz approach, the beam-string system is reduced to a model with three degrees of freedom, $V_B(t)$ for the lateral motion of the beam, and $U_S(t)$ and $V_S(t)$, respectively, for axial and lateral motion of the string, represented by the generalized displacement vector

$$\mathbf{q}(t) = \left\{ V_B(t),\ U_S(t),\ V_S(t) \right\}^T. \tag{1}$$

Using d'Alemberts principle results in the nonlinear equations of motion

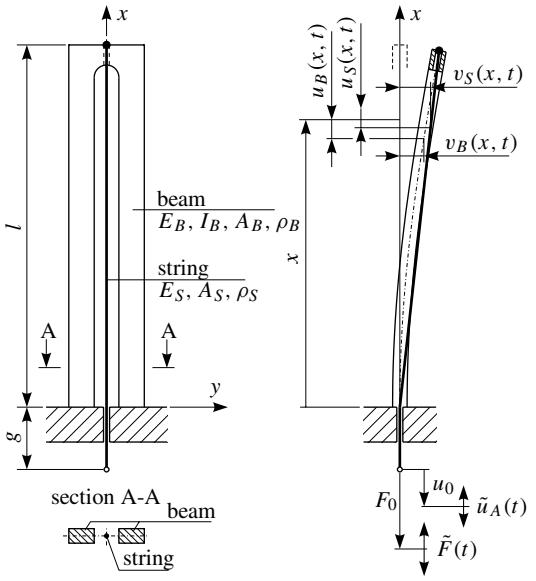

Fig. 1 Schematic diagram of the beam-string system and definition of displacement fields.

$$\mathbf{M}(\mathbf{q})\ddot{\mathbf{q}} + \mathbf{g}(\mathbf{q}, \dot{\mathbf{q}}) + \mathbf{K}(t)\mathbf{q} = \mathbf{f}(t). \tag{2}$$

More information about the symmetric mass-matrix $\mathbf{M}(\mathbf{q})$ and the vector of generalized forces $\mathbf{g}(\mathbf{q}, \dot{\mathbf{q}})$ can be seen in [1]. The elongation $\tilde{u}_A(t)$ of the actuator is part of the stiffness matrix

$$\mathbf{K}(t) = \begin{bmatrix} \bar{k}_{11,1} + \dfrac{\bar{k}_{11,2}}{k}\dfrac{F_0}{l} + \tilde{k}_{11}\dfrac{\tilde{u}_A(t)}{l} & 0 & 0 \\ 0 & \bar{k}_{22} & 0 \\ 0 & 0 & \dfrac{\bar{k}_{33}}{k}\dfrac{F_V}{l} \end{bmatrix}, \tag{3}$$

and of the external excitation vector $\mathbf{f}(t) = \{0, k\tilde{u}_A(t), 0\}^T$.

A material damping matrix $\mathbf{C} = \text{diag}\{c_{11}, c_{22}, c_{33}\}$ is introduced, where the related damping ratios can be found in Table 1. The damping ratio D_{11} was calculated based on the envelope curve of the measured lateral vibrations of the uncontrolled beam, assuming an exponential decay of the form ae^{-bt}, and determining a and b by using the method of minimization the quadratic error. The damping ratios D_{22} and D_{33} are of minor importance for the numerical results and therefore are set to the standard-values for steel. Finally, the equations of motion of the open-loop system can be written in the form

$$\mathbf{M}(\mathbf{q})\ddot{\mathbf{q}} + \mathbf{C}\dot{\mathbf{q}} + \mathbf{g}(\mathbf{q}, \dot{\mathbf{q}}) + \mathbf{K}(t)\mathbf{q} = \mathbf{f}(t). \tag{4}$$

Table 1 Dimensions and properties of experimental setup.

Property	Symbol	Value	Unit
material of beam	AlMgSi0.5 T66	–	–
length	l	0.3008	m
cross-section	A_B	8.25×10^{-5}	m^2
geometrical moment of inertia	I_B	7.487×10^{-11}	m^4
density	ρ_B	2700	kg/m^3
Young's modulus	E_B	0.7×10^{11}	N/m^2
material of string	steel	–	–
cross-section	A_S	0.1767×10^{-5}	m^2
density	ρ_S	7850	kg/m^3
Young's modulus	E_S	2.1×10^{11}	N/m^2
length	g	0.094	m
prestress force	F_0	−100	N
max. elongation of actuator	$\tilde{u}_{A,\max}$	90	µm
max. operating voltage of actuator	$U_{A,\max}$	100	V
material damping ratio	D_{11}	1.416597×10^{-3}	–
material damping ratio	D_{22}	0.01	–
material damping ratio	D_{33}	0.01	–
output gain of controller card	k_R	10	–
gain of piezo-amplifier	V_{PA}	10	–

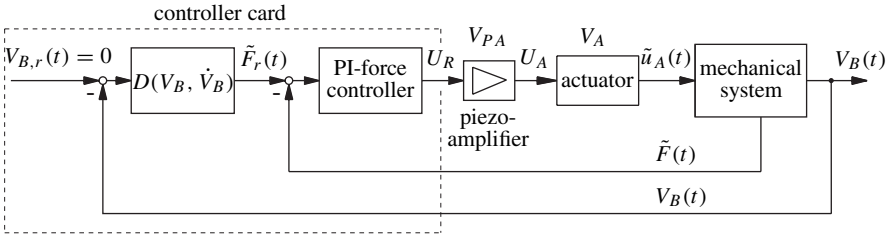

Fig. 2 Block-diagram of closed-loop system.

To introduce artificial damping to the lateral motion of the beam, the force $\tilde{F}(t)$ in the string has to be controlled in a proper way. Figure 2 shows the block diagram of the closed-loop system. An underlying PI-force controller is used to ensure that the actual force in the string approaches the reference force properly. The elongation $\tilde{u}_A(t)$ of the piezoelectric actuator can then be written in the form

$$\tilde{u}_A(t) = k_F k_R V_{PA} V_A \left(k_p(\tilde{F}_r - \tilde{F}) + k_i \int_0^t (\tilde{F}_r - \tilde{F}) d\tau \right), \tag{5}$$

where k_R represents the fixed output amplification factor of the controller card and V_{PA} the constant gain of the piezo-amplifier. The piezoelectric actuator is modelled as a combination of a spring, which is already included in the equations of motion, and a linear element that provides an elongation proportional to the applied voltage.

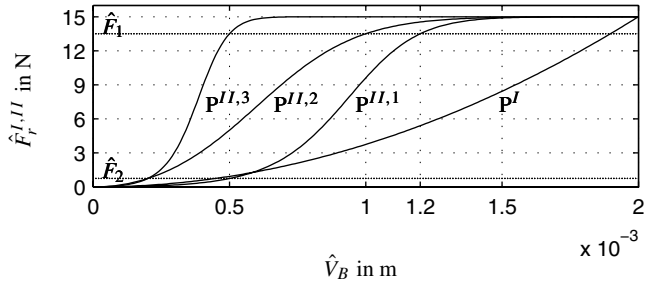

Fig. 3 Effect of the controller parameter-sets $P^{II,1}$, $P^{II,2}$ and $P^{II,3}$ on the behaviour of the reference force $\hat{F}_r^{II}$ in terms of the lateral vibration amplitude $\hat{V}_B$ of the beam, compared with the result of control law I.

The factor of proportionality is defined by $V_A = \tilde{u}_{A,\max}/U_{A,\max}$ with $\tilde{u}_{A,\max}$ being the maximum elongation at the maximum applied voltage $U_{A,\max}$ according to the datasheet of the manufacturer. For the sake of simplicity, k_F is chosen to $k_F = 1/(k_R V_{PA} V_A)$. Equation (5) can then be written in the form

$$\tilde{u}_A(t) = k_p(\tilde{F}_r - \tilde{F}) + k_i \int_0^t (\tilde{F}_r - \tilde{F}) d\tau. \tag{6}$$

The control concept used in this contribution is based on axial velocity feedback of the tip of the beam with constant amplification, see [3] for example, and with state-dependent amplification, see [7]. In the first case, the control law can be written in the form

$$\tilde{F}_r(t) \stackrel{\downarrow}{=} \tilde{F}_r^I(t) = -\mu^I \dot{u}_B(l,t) = \mu^I \frac{\pi^2}{8l} V_B \dot{V}_B. \tag{7}$$

In the second case, the reference force is defined by the equation

$$\tilde{F}_r(t) \stackrel{\downarrow}{=} \tilde{F}_r^{II}(t) = -\mu^{II}(V_B, \dot{V}_B)\dot{u}_B(l,t). \tag{8}$$

Using $\mu^{II}(V_B, \dot{V}_B)$ as proposed in [7] leads to

$$\tilde{F}_r^{II}(t) = \eta \frac{\pi^2}{8l} \frac{\omega_B V_B \dot{V}_B}{(\omega_B V_B)^2 + \dot{V}_B^2 + \gamma e^{-\beta(\omega_B^2 V_B^2 + \dot{V}_B^2)}}, \tag{9}$$

Inserting the approximations $V_B(t) \simeq \hat{V}_B \cos(\omega_B t)$ and $\dot{V}_B(t) \simeq -\omega_B \hat{V}_B \sin(\omega_B t)$ into equation (7), where ω_B represents the first natural frequency of the beam, shows that the amplitude $\hat{F}_r^I$ of the reference force decays very fast with the amplitude $\hat{V}_B$ of the lateral beam vibration, see Figure 3. State-dependent amplification results in a complete different behaviour. The force amplitude $\hat{F}_r^{II}$ remains constant for large deflections until it decays. Therefore, a larger damping effect can be expected compared to control law I. The slope of the decay is controlled by the coefficients β

Table 2 Controller parameters for both control laws.

Control Law I		
Symbol	P^I	Unit
μ^I	10454.7	Ns/m

Control Law II				
Symbol	$P^{II,1}$	$P^{II,2}$	$P^{II,3}$	Unit
$\hat{V}_{B,1}$	0.5e-3	0.2e-3	0.2e-3	m
s_1		0.05		–
$\hat{V}_{B,2}$	1.2e-3	1.0e-3	0.5e-3	m
s_2		0.90		–
η		7.315		Nm
β	93.134	65.467	515.054	$(s/m)^2$
γ	0.296	0.025	0.044	$(m/s)^2$

General Controller Parameters		
Symbol	P^I to $P^{II,3}$	Unit
$\hat{F}_{r,\max}$	15	N
$\hat{V}_{B,\max}$	2e-3	m
ω_B	174.912	s^{-1}
k_p	0.01×10^{-6}	–
k_i	0.007	–

and γ which are calculated in more details in [7]. Figure 3 shows the results for three different sets of parameters $P^{II,1}$, $P^{II,2}$ and $P^{II,3}$. Table 2 gives detailed information about the controller parameters for both control laws.

3 Test Rig and Experimental Results

Figure 4 shows the experimental setup. The test rig consists of the top- and the baseplate, connected by four pillars. The available space in between the two plates is used for the piezoelectric actuator, which is directly coupled to the piezoelectric force sensor, and the tensioning device which allows to apply a constant static preload F_0 to the beam. The string is directly connected to the force sensor and runs through the top plate and the beam clamping device. The detailed view on the left side of the figure shows the slotted beam including the string. On the free end of the beam, the string is feed through an axial borehole in the beam. A bushing clamped onto the string allows to apply a compression force to the beam. To apply a certain initial deflection to the tip of the beam, a simple mechanical lever mechanism is used, mounted directly on the top plate.

The right half of the figure shows the electronic equipment. The lateral vibration $V_B(t)$ of the beam tip is measured by a laser measuring head. The output signal of the Laser Control Unit, which allows to adjust the data sampling frequency of the laser, is directly feed into the realtime controller card in the host computer as well as the force input signals F_0 and $\tilde{F}(t)$. Therefore, two different charge amplifiers are used. To allow a quasistatic measuring of the prestress force during application with the tensioning device, a charge amplifier (CA 2) with a very large input impedance

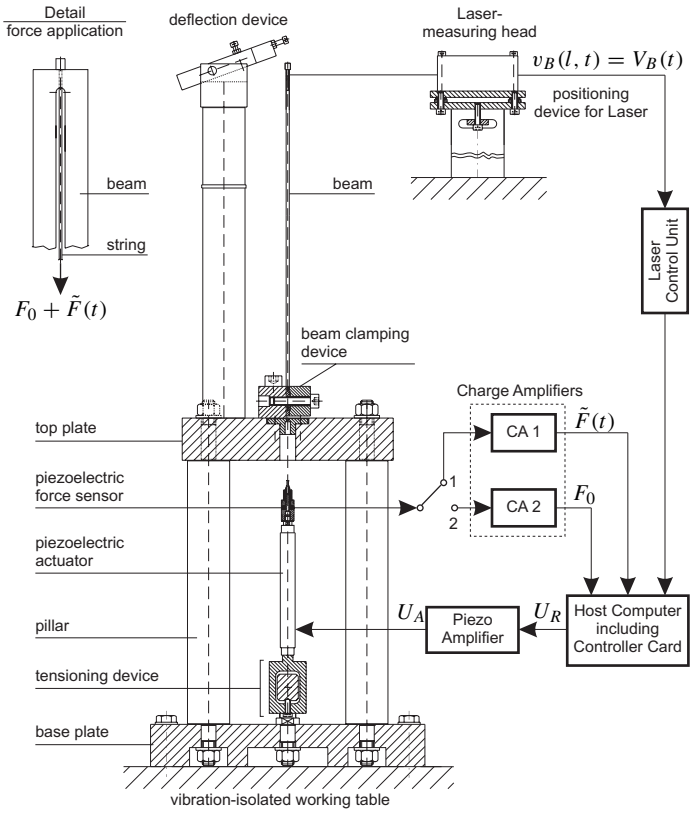

Fig. 4 Experimental setup consisting of mechanical test rig on the left hand side, measurement and control equipment of the feedback loop on the right hand side.

is used. If the closed-loop control is working, the time dependent force component $\tilde{F}(t)$ is measured with a conventional charge amplifier (CA 1). With this informations, the controller card calculates the output voltage U_R according to the specified control law. The piezoelectric actuator is driven by the piezo-amplifier with constant gain. This results in an elongation of the actuator, and therefore in a variation of the force in the string.

Figure 5 shows on the left side some measurement results for control law I, and on the right one results for control law II with parameters-set $\mathrm{P}^{II,3}$. As initial conditions a deflection $V_B(0) = 2$ mm and velocity $\dot{V}_B(0) = 0$ of the beam tip were used. Comparing the time series of the force $\tilde{F}(t)$ demonstrates the difference of the two control laws. With control law I (axial velocity feedback and constant amplification) the force amplitude decays very fast with time, whereas the use of state-dependent amplification results in a constant amplitude up to about 1 s until the decay starts. The top of Figure 5 shows the effect of the control laws on the lateral vibration $V_B(t)$ of the beam. To give a better impression of the amount of artificial damping

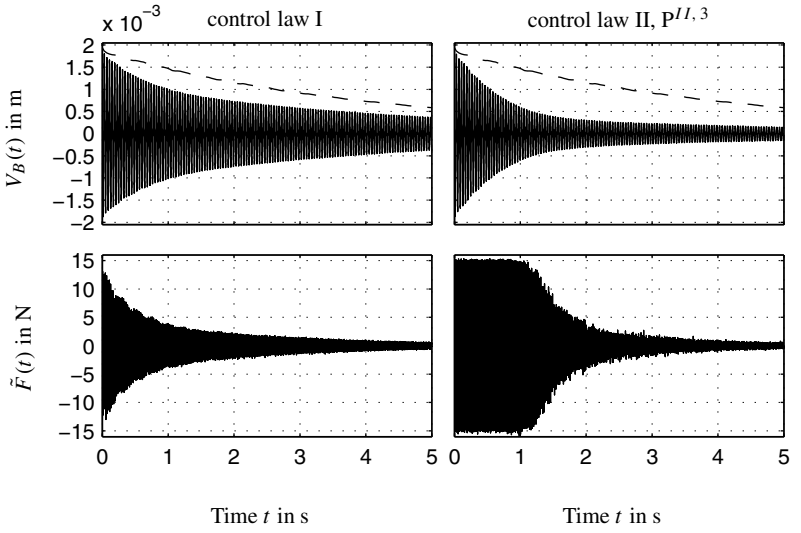

Fig. 5 Time series of the lateral beam vibration $V_B(t)$ and the force $\tilde{F}(t)$ in the string for control law I (left), and control law II (right). Initial condition – 2.0E-3 m lateral deflection of beam tip. Dashed line – envelope curve of uncontrolled system.

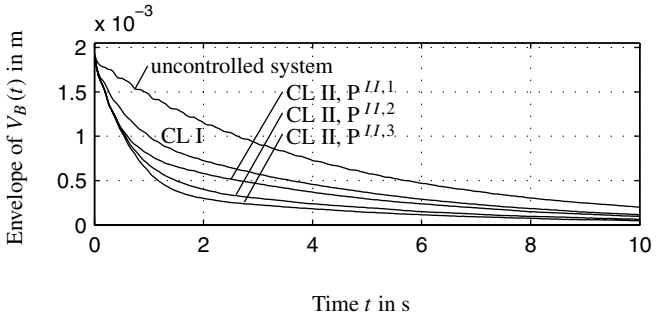

Fig. 6 Envelope curves of $V_B(t)$ of the uncontrolled system, for control law I and for control law II for different sets of parameters $P^{II,1}$, $P^{II,2}$ and $P^{II,3}$. Initial condition - 2.0E-3 m lateral deflection of the beam tip.

introduced by the controller, the envelope curve (dashed line) of the uncontrolled, free vibrating beam is shown for comparison. Using state-dependent amplification results in a faster decay of the vibration amplitudes of $V_B(t)$ especially at the beginning where the force amplitude is constant. The envelope curves of $V_B(t)$ for the three different sets of parameters $P^{II,1}$, $P^{II,2}$ and $P^{II,3}$ are summarized in Figure 6. The parameter-sets are chosen in a way that with increasing parameter-set number i of $P^{II,i}$, the amplitude of the force in the string remains constant for a larger range

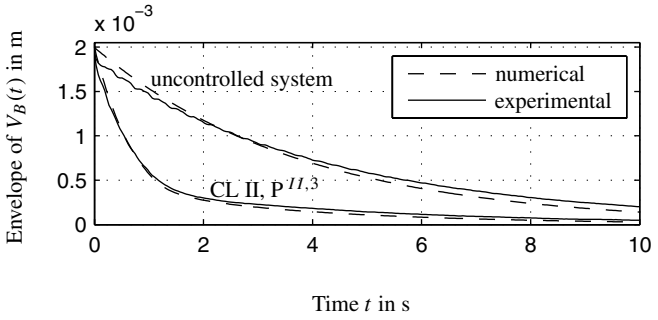

Fig. 7 Comparison of the envelope curves of $V_B(t)$ for the uncontrolled system and for the closed-loop control law II obtained from measurement data with numerical results.

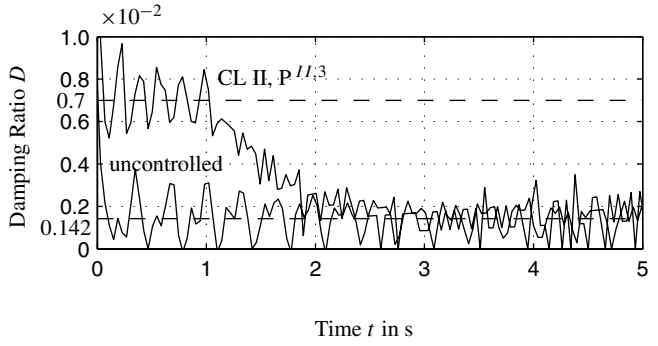

Fig. 8 Time series of the damping ratio D calculated from the amplitude decay of $V_B(t)$ (experimental result) by using the logarithmic decrement.

of lateral vibration amplitudes of the beam (remember Figure 3). The longer the amplitude of $\tilde{F}(t)$ remains constant, the faster decays the lateral beam vibration i.e., the larger is the artificial damping effect caused by the feedback control law.

In Figure 7, a comparison of numerical and experimental results for the uncontrolled system and for the closed-loop system using state-dependent amplification with parameters-set $\mathrm{P}^{II,3}$ can be found. The simulation results are obtained from a numerical solution of equations (4), (6) and (9) using a standard software package. Considering the results for the uncontrolled system shows that the assumption of a velocity-proportional material damping does not fit the reality properly. Nevertheless, the numerical solution for the closed loop system (control law II) is close to the experimental result. Especially for large amplitudes, the damping effect in this range is dominated by the artificial damping introduced by the control law.

Figure 8 shows the damping ratio D calculated from measurement data of one single period using the logarithmic decrement. Until about 1 s, where the amplitude

of the force $\tilde{F}(t)$ is constant, see Figure 5, the mean value of the damping ratio D is constant and approximately 0.7. This is about 4.9 times higher than the material damping ratio of $D = 0.142$ of the uncontrolled system.

4 Conclusions

In this contribution, a test rig was presented that consists of a cantilever beam and an actuator system to apply a single axial force to the tip of the beam was presented. A control law for the single force based on axial velocity feedback with constant and state-dependent amplification was implemented. The experimental results show that the damping of lateral vibrations of the beam is highly increased compared to the uncontrolled system, when a state-dependent amplification is applied.

References

1. Pumhössel, T., Springer, H.: Active Vibration Control of Nonlinear Cantilever Shaped Blades in Turbomachinery. In: *Proc. of 7th IFToMM Conf. on Rotor Dynamics*, Technical University of Vienna, Austria, Sept. 25–28 (2006).
2. Nudehi, S., Mukherjee, R., Shaw, S.: Active Vibration Control of a Flexible Beam Using a Buckling-Type End Force. *Journal of ynamic Systems, Measurement, and Control*, **128**, 278–286 (2006).
3. Springer, H., Kovyrshin, S.: Active parametric vibration control of a smart beam. In: *Proc. of 8th Int. Conf. on Vibrations in Rotating Machinery*, University of Wales, Swansea, Sept. 7–9 (2004).
4. Rahn, C.D., Mote, C.D.: Axial Force Stabilization of Transverse Vibration in Pinned and Clamped Beams. *Journal of Dynamic Systems, Measurement, and Control*, **118**, 379–380 (1996).
5. Habib, M., Radcliffe, C.: Active Parametric Damping of Distributed Parameter Beam Transverse Vibration. *Journal of ynamic Systems, Measurement, and Control*, **113**, 295–299 (1991).
6. Rahn, C.D., Mote, C.D.: Parametric Control of Flexible Systems. *Journal of Vibration and Acoustics*, **116**, 379–385 (1994).
7. Pumhössel, T.: Parametric Control of Blade Vibrations in Rotating Machinery. In: *Proc. of ISCORMA-4 Int. Symposium on Stability Control of Rotating Machinery*, Calgary, Canada, Aug. 27–31 (2007).
8. Nayfeh, A.H., Pai, P.F.: *Linear and Nonlinear Structural Mechanics*. Wiley, New York (2004).

Investigation of Excitation Methods in Active Control of Sound Transmission through a Thin Planar Structure

Akira Sanada and Nobuo Tanaka

Abstract This study deals with the active control of sound transmission through a thin planar structure. The effect of the active sound transmission control depends significantly on the methods used to excite the structure, such as the location of the actuators. However, the principle to determine the excitation method has not been revealed clearly thus far. In this study, the methods used to excite a panel with point actuators for active sound transmission control in the case of normal incidence are investigated by simulations. Further, various actuation methods using point actuators, e.g., center-point control, four-point control, sixteen-point control, etc., are compared. On the basis of the simulation results, we propose an effective excitation method in which the point actuators are located on the nodal lines at frequencies slightly less than the resonant frequencies of the panel at which the transmitted sound power significantly decreases. Then, it is shown that the proposed method can suppress both the transmitted sound and vibrations in a low-frequency range. Finally, experiments are carried out to confirm the simulation results and the validity of the proposed method.

1 Introduction

The sound insulation property of a planar structure is dominated by the mass law; hence, it is difficult to suppress the sound power transmitted through a lightweight barrier, particularly, in a low-frequency range. Recently, a number of investigations

Akira Sanada
Industrial Technology Center of Okayama Prefecture, 5301 Haga, Okayama-shi Okayama, Japan;
E-mail: akira_sanada@pref.okayama.lg.jp

Nobuo Tanaka
Tokyo Metropolitan University, 6-6 Asahigaoka, Hino-shi, Tokyo 191-0065, Japan;
E-mail: ntanaka@cc.tmit.ac.jp

H. Ulbrich and L. Ginzinger (eds.), Motion and Vibration Control, 263–273.

using an active control to improve sound insulation have been carried out and reported since the active control is effective in the low-frequency range.

The sound power radiated from a vibrating structure is dominated by the radiation mode, which is a set of vibration velocity distributions of the structure that radiates the sound power independently. Some authors have reported that the transmitted sound power can be actively controlled by sensing the power modes. In the low-frequency range, where $ka \ll \pi$, the first radiation mode is dominant. The first radiation mode resembles a piston-like motion of the panel and is a combination of the structural modes associated with a volumetric component [1]. Johnson and Elliott [2] have simulated the active control of sound transmission through a panel and have compared the sensing strategies of cancellation of volume velocity and minimization of radiated sound power. They have concluded that a large control effect can be obtained by sensing the volume velocity in the low-frequency range. Further, they have proposed a method using a volume velocity sensor and a uniform force actuator to avoid control spillover. Henrioulle and Sas have carried out experiments on the active sound transmission control using a PVDF volume velocity sensor/actuator pair with a feedback control [3]. However, it is not clear whether a distributed actuator such as PVDF can produce a force of sufficient strength for practical use. As compared to the distributed actuator, a point actuator is considerably easier to handle and produces a larger actuating force.

It is well known that the effect of the active sound transmission control significantly depends on the excitation methods of the structure, such as the location of the actuators. Wang et al. have compared the actuation methods that employ multiple piezoelectric and point actuators by a simulation [4]. However, the principle to determine the excitation methods has not been revealed clearly thus far. In this study, the methods used to excite the panel with the point actuators for the active sound transmission control in the case of normal incidence are investigated by simulations. Normal incidence transmission losses using a SISO feed-forward control are calculated for various actuation methods. We compare five types of actuation methods: (i) center-point control, (ii) four-point control near the corners, (iii) sixteen-point control, (iv) four-point control (the actuators are located on the nodal line at frequencies slightly less than the resonant of the panel frequencies at which the transmitted sound power significantly decreases), and (v) the (1, 3) mode control with six point actuators [5]. Finally, experiments were carried out to confirm the simulation results.

2 Simulation of Active Sound Transmission Control

2.1 Calculation Model

Figure 1 shows the theoretical model for sound transmission used in this study. The assumptions are as follows: a simply supported panel with dimensions $a \times b$ is

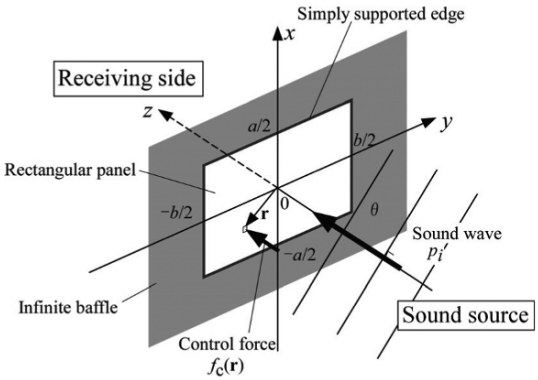

Fig. 1 Calculation model for active sound transmission control.

embedded in an infinite rigid baffle; both sides of the panel are semi-infinite spaces; a plane sound wave with the amplitude p_i is assumed to be normally incident on the panel; and the forces generated by the actuators act on the panel to control the structural vibration.

On the basis of these assumptions, the equation of motion of a thin flexible panel can be expressed as

$$D'\nabla^4 z(\mathbf{r},t) + \rho_s h\frac{\partial^2 z(\mathbf{r},t)}{\partial t^2} = 2p_i e^{j\omega t} - 2p_t(\mathbf{r})e^{j\omega t} + f_c(\mathbf{r})e^{j\omega t}, \tag{1}$$

where $\mathbf{r}$ denotes an arbitrary position of the panel; z is the displacement; $j = \sqrt{-1}$; ω is the angular velocity; ρ_s is the density; h is the thickness; $D' = D(1 + j\eta)$ is the bending rigidity including structural damping (η); f_c is the control force generated by the actuators; p_t is the pressure generated by the vibration of the panel; and p_i is the pressure on the surface of the panel caused by the incident sound.

Assuming that the structural vibration is described by the summation of N modes, the vibration velocity of the panel can be written as $v(\mathbf{r}) = \mathbf{\Psi}^T(\mathbf{r}) \cdot \mathbf{v}$, where $\mathbf{\Psi}$, $\mathbf{v}$, and the superscript T denote the modal function vector, modal velocity vector, and transpose of matrix, respectively.

Then, the modal velocity vector is given by

$$\mathbf{v} = \mathbf{R} \cdot (2\mathbf{F}_{i0} + \mathbf{F}_c), \tag{2}$$

where

$$\mathbf{R} = \left(\frac{1}{j\omega}\mathbf{K} + j\omega\mathbf{M} + 2\bar{\mathbf{A}}\right)^{-1}, \tag{3}$$

$$\tilde{\mathbf{A}} = \frac{j\omega\rho}{2\pi}\int_S\int_S \mathbf{\Psi}(\mathbf{r}) \cdot \mathbf{\Psi}^T(\mathbf{r}')\frac{e^{-jk\Delta r}}{\Delta r}dS'dS. \tag{4}$$

Here, ρ denotes the air density and dS' and dS are infinitesimal surface elements on the planar structure. S denotes the panel area. $\Delta r = |\mathbf{r} - \mathbf{r}'|$, where $\mathbf{r}'$ denotes the position of dS'. $\mathbf{K}$ and $\mathbf{M}$ denote stiffness and mass matrices. The modal excitation

force vectors for the incident wave and control force, i.e., $\mathbf{F}_{i0}$ and $\mathbf{F}_c$, respectively, are expressed as

$$\mathbf{F}_{i0} = \int_S \mathbf{\Psi}(\mathbf{r})\, p_i dS, \tag{5}$$

$$\mathbf{F}_c = \int_S \mathbf{\Psi}(\mathbf{r})\, f_c(\mathbf{r}) dS. \tag{6}$$

In this study, a SISO feedforward control is used because it is simple and easy to realize. Further, point actuators are used in this study because the point actuators are easy to handle and generate a large actuating force.

In this case the forces acting on the panel by the point actuators can be given by

$$f_c(\mathbf{r}) = f_e \sum_{k=1}^{M} G\delta(\mathbf{r} - \mathbf{r}_k), \tag{7}$$

where f_e, G, and δ denote the control force, weighting factor, and Dirac delta function, respectively. From Eq. (6), F_c is expressed as

$$\mathbf{F}_c = f_e \mathbf{F}_{cm}, \tag{8}$$

where the ith factor of $\mathbf{F}_{cm}$ is

$$F_{cmi} = \int_S \psi_i(\mathbf{r}) \sum_{k=1}^{M} G\delta(\mathbf{r} - \mathbf{r}_k) ds. \tag{9}$$

The transmitted sound power derived by integrating the sound intensity on the panel is expressed as

$$W_t = \mathbf{v}^H \cdot \mathbf{A} \cdot \mathbf{v}, \tag{10}$$

where the superscript H denotes the Hermitian transpose and $\mathbf{A}$ represents the sound power matrix given by $\mathbf{A} = \mathrm{Re}(\tilde{\mathbf{A}}/2)$. Matrix $\mathbf{A}$ is a real symmetrical matrix. Then, $\mathbf{A}$ is given by

$$\mathbf{A} = \mathbf{Q}\mathbf{\Lambda}\mathbf{Q}^{-1}, \tag{11}$$

where $\mathbf{Q}$ is a real and unitary matrix of orthogonal eigenvectors and $\mathbf{\Lambda}$ is a diagonal matrix of the eigenvectors λ_i. Then, the sound power is expressed as

$$W_t = \mathbf{v}^H \mathbf{Q}\mathbf{\Lambda}\mathbf{Q}^{-1}\mathbf{v} = \mathbf{u}^H \mathbf{\Lambda}\mathbf{u} = \sum_{i=1}^{N} \lambda_i |u_i|^2, \tag{12}$$

where $\mathbf{u}$ denotes the radiation mode vector given by

$$\mathbf{u} = \mathbf{Q}^{-1}\mathbf{v} = \mathbf{Q}^T\mathbf{v}. \tag{13}$$

Hence, the first radiation mode which is dominant in the transmitted sound in the low-frequency range can be expressed as $u_1 = \mathbf{q}_1\mathbf{v}$, where $\mathbf{q}_1 =$

$[Q_{11}, Q_{21}, \ldots, Q_{N1}]$. From Eqs. (2) and (13), the first radiation mode can be rewritten as

$$u_1 = u_{1i} + f_e u_{1c}, \tag{14}$$

where $u_{1i} = 2\mathbf{q}_1\mathbf{R}\mathbf{F}_{i0}$, the first radiation mode for the incident wave, and $u_{1c} = \mathbf{q}_1\mathbf{R}\mathbf{F}_{cm}$, the first radiation mode element for the control force generated by the actuators.

2.2 Actuation Methods

In this study, a simply supported rectangular aluminum panel ($a = 0.4$ m, $b = 0.4 \times \sqrt{2}$ m, $h = 2$ mm, $\eta = 0.01$) embedded in an infinite baffle is considered for the case of normal incidence. The structural mode frequencies of the panel used in the simulation are listed in Table 1. When a plane wave is normally incident, only the (odd, odd) modes are excited because of the incident pressure distribution over the panel surface, which is uniform; hence, only the (odd, odd) modes are considered in this study.

The first radiation mode is constituted of only the (odd, odd) modes. Hence, the actuators should be placed symmetrically with respect to the center point of the panel. If the actuators are not located symmetrically, other types of vibration modes, i.e., (odd, even), (even, odd), and (even, even) modes, will be excited that may cause control spillover.

The five types of the actuation methods that can be used to excite the panel are given below. Figure 2 shows the location of the point actuators.

1. Method 1: One point actuator is located at the center point of the panel.
2. Method 2: Four point actuators are located near the corners. Their position coordinates are $(-a/3, -b/3)$, $(-a/3, b/3)$, $(a/3, -b/3)$, and $(a/3, b/3)$. These actuators generate forces of the same magnitude, along the same direction.
3. Method 3: Sixteen point actuators are located at the points shown in Figure 2. These actuators generate forces of the same magnitude, along the same direction.
4. Method 4: Four point actuators are located on the nodal line at 159.5 and 277.5 Hz, the frequencies at which the "cancellation phenomenon" occurs. The phenomenon will be described subsequently. These actuators generate forces

Table 1 (Odd, odd) vibration modes of the target panel.

No.	Mode	Frequency [Hz]	No.	Mode	Frequency [Hz]
1	(1, 1)	46.3	6	(3, 5)	663.7
2	(1, 3)	169.8	7	(5, 1)	787.2
3	(3, 1)	293.3	8	(1, 7)	787.2
4	(3, 3)	416.8	9	(5, 3)	910.7
5	(1, 5)	416.8			

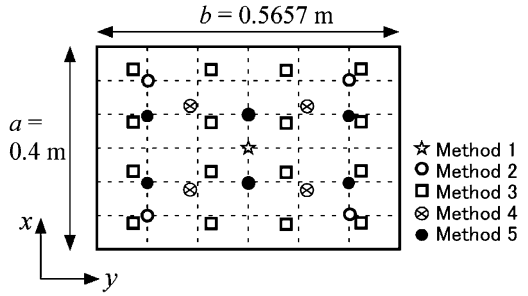

Fig. 2 Location of the actuators for the five types of the actuation methods.

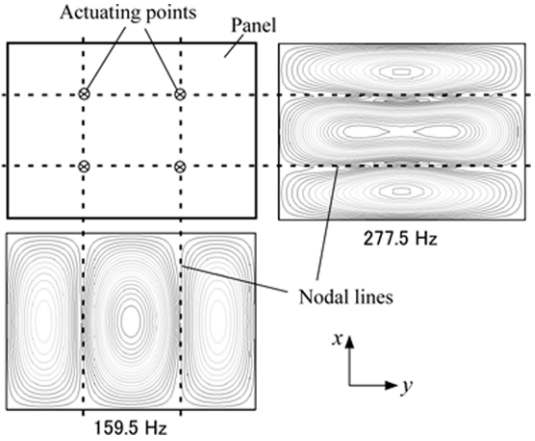

Fig. 3 Relation between the actuating points in Method 4 and the vibration distribution on the panel without the active sound transmission control at 159.5 and 277.5 Hz. The position coordinates of the actuating points are $(-0.079, -0.11)$, $(-0.079, 0.11)$, $(0.079, -0.11)$, and $(0.079, 0.11)$.

of the same magnitude, along the same direction. Figure 3 shows the relation between the actuating points and the vibration distribution on the panel.

5. Method 5: Six point actuators are located at $(-a/6, -b/3)$, $(-a/6, 0)$, $(-a/6, b/3)$, $(a/6, -b/3)$, $(a/6, 0)$, and $(a/6, b/3)$. The two actuators located at $(-a/6, 0)$ and $(a/6, 0)$ actuate in a direction opposite to that of the other actuators. This actuation method can excite only the (1, 3) mode approximately in the low-frequency range [5]. The active sound transmission control along with the modal control has been proposed by the authors in a previous study [6].

An optimal control law of each method for minimizing the transmitted sound power with the feedforward control is derived. Based on the optimal control law, normal incidence transmission loss is theoretically obtained, thus confirming the significance of the control strategies. Figure 4 shows the calculated normal incidence transmission loss. Figure 5 shows the power factor of the first radiation mode. These results are obtained when $p_i = 1$ Pa. Below 100 Hz, all the methods exhibit excellent control effect, suppressing the first radiation mode. However, there are some frequency bands in which the control effect cannot be obtained for Methods 1, 2, and 3 because a factor of the first radiation mode cannot be controlled. This may cause a problem when a noise source has a wide frequency band or the frequency is changeable.

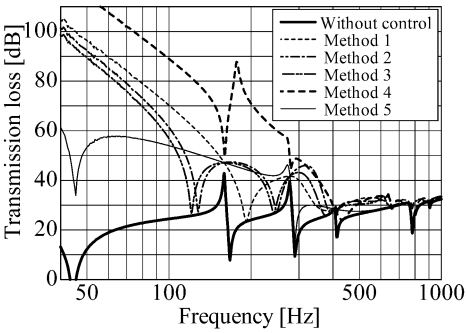

Fig. 4 Calculated normal incidence sound transmission loss.

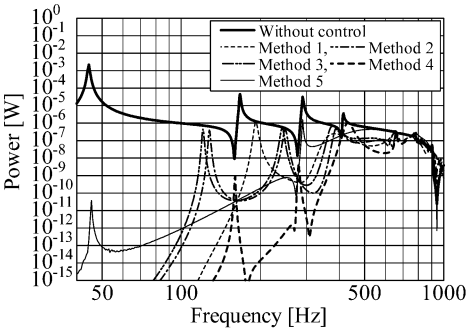

Fig. 5 Calculated sound power of the first radiation mode when $p_i = 1$ Pa.

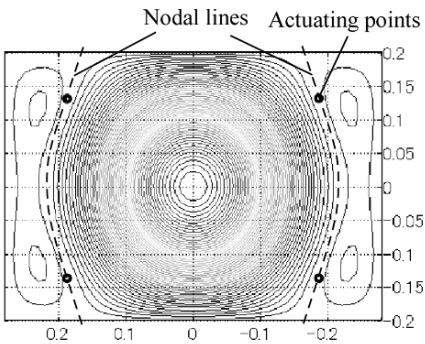

Fig. 6 Vibration distribution at 128 Hz without the active sound transmission control and the location of the actuators in Method 2.

Figure 6 shows the vibration distribution at 128 Hz without the active sound transmission control and the location of the actuators in Method 2. At 128 Hz, the frequency at which the control effect cannot be obtained, the location of the actuator is on the nodal line. Figure 7 shows the plot of $|u_{1c}|$. The value of $|u_{1c}|$ is very small at the frequency at which the control effect cannot be obtained. This implies that the first radiation mode cannot be controlled at the frequency at which the location of the actuator is on the nodal line of the vibration distribution on the panel without the active control. Furthermore, for an ideal case, it is found that the number of actuators does not significantly affect the control effect.

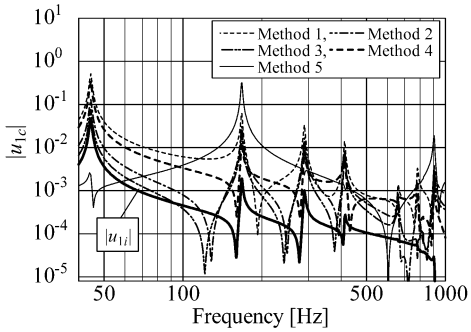

Fig. 7 Amplitude of the first radiation mode element $|u_{1c}|$ for the control force of the actuators and amplitude of the first radiation mode $|u_{1i}|$ for the incident sound when $p_i = 1$ Pa.

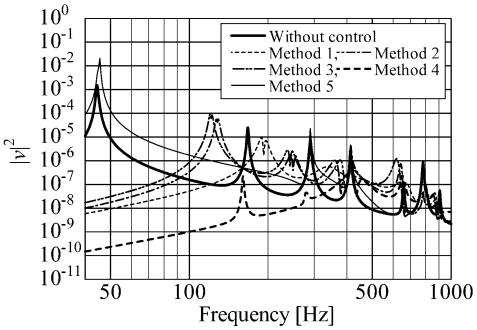

Fig. 8 Calculated results of space-average mean square vibration velocity.

It is usually observed that the sound power transmitted through a small-sized panel decreases significantly at some frequencies in the low-frequency range, where $ka \ll \pi$. This phenomenon is termed "cancellation phenomenon" in this study. The authors considered this phenomenon in a previous work [6] and found that it is caused by a decrease in the radiation efficiency due to the coupling between two structural modes of a panel. If the frequency at which the control effect cannot be obtained is tuned to the frequency at which the cancellation phenomenon occurs, the high transmission loss can be obtained in the wide frequency range. This can be achieved by Method 4. Four point actuators are located on the nodal line at 159.5 and 277.5 Hz, as shown in Figure 6. In Method 4, the control effect is significantly greater as compared to the other methods. Figure 7 also shows $|u_{1i}|$ for the first radiation mode for the incident sound. It is found that in this case, $|u_{1c}|$ is almost proportional to $|u_{1i}|$ below approximately 350 Hz. In other words, the excitation of the first radiation mode with Method 4 is almost equivalent to the excitation by the incident sound. This may result in a large control effect. Figure 8 shows the space-average mean square vibration velocity. In Method 4, not only the transmitted sound power but also vibration is suppressed in the low-frequency range.

Method 5 is comparatively ineffective. However, in Method 5 the control effect is obtained in the wide frequency range. This result shows that the transmitted sound power can be controlled with the modal control. However, in this case, the vibration

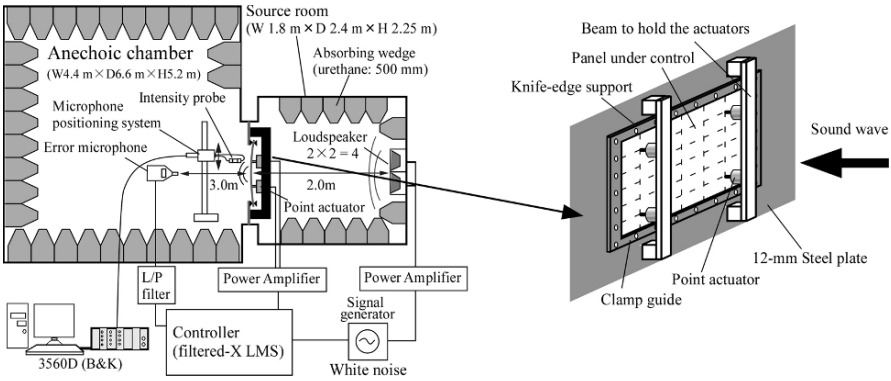

Fig. 9 Experimental setup and vibration control arrangement.

energy increases because the (1, 3) mode is excited in order to cancel the other terms of the first radiation mode.

3 Experiments

In order to confirm the simulation results, the experiments on active sound transmission control were carried out. The experimental setup is shown in Figure 9. In order to measure the sound insulation property for normal incidence, two connected rooms were used; one was an anechoic room and the other comprised walls covered with an absorbing material to suppress reverberation. The anechoic room was used as the receiving room, while the other room was used as the source room. A 2-mm-thick aluminum panel (0.4 m × 0.57 m), on which a 1-mm-thick damping material was stuck, was used. The panel was clamped on a knife-edge support to realize the simply supported boundary condition. An adaptive feedforward control system, which includes one control source and one error sensor, was used. The signal was processed using the filtered-X LMS algorithm in the controller (DSP board). The sampling frequency was 3 kHz and the number of taps was 1000. Voice-coil-type point actuators were set on the panel. The error microphone was placed in the receiving room at a distance of 3.0 m from the panel. Four loudspeakers were placed in front of the panel at a distance of 2.0 m from the panel and were driven by the same signal from one signal generator. White noise of less than 1.6 kHz was used as the noise signal. The reference signal was directly obtained from the signal generator. In the experiment the sound pressure at the place of the error microphone was suppressed with the control. The insertion loss was measured instead of the transmission loss because the normal incidence transmission loss is difficult to measure. The transmitted sound power was measured using an acoustic intensity probe.

Figure 10 shows the experimental results of Methods 1, 2, 4, and 5. Below 350 Hz, all methods exhibit the control effect. However, there are some frequency bands

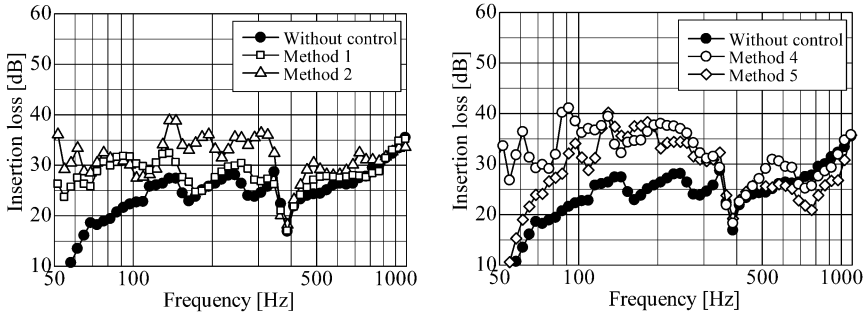

Fig. 10 Measured insertion loss with and without control. The left-hand side figure shows the results of Methods 1 and 2. The right-hand side figure shows the results of Methods 4 and 5.

in which excellent control effect cannot be obtained for Method 1 and Method 2. These frequency bands are from 150 to 250 Hz for Method 1 and around 100 and 220 Hz for Method 2.

On the other hand, Method 4 exhibits excellent control effect in the wide frequency range, having no frequency band in which the control effect cannot be obtained in the low-frequency range. It is confirmed that the excitation method of Method 4 has great advantages.

Method 5 also exhibits excellent control effect in the mid-frequency range from 100 to 350 Hz. However, below 100 Hz, the magnitude of the control effect is comparatively small because around the frequency of the (1, 1) mode, Method 5 requires a large control force as compared to the other methods.

4 Conclusions

We have investigated the excitation methods used in the active control of sound transmission for the case of normal incidence using point actuators. Initially, some actuation methods were compared by simulations. From these results, it was found that the excitation method that the point actuators are located on the nodal lines at frequencies slightly less than the resonant frequencies of the panel at which the transmitted sound power significantly decreases has a great control effect. Finally, experiments were carried out to confirm the simulation results and the validity of the method.

References

1. Li, Z., Guigou, C., Fuller, C.R., Burdisso, R.A.: Design of active structural acoustic control system using a nonvolumetric eigenproperty assignment approach, *J. Acoust. Soc. Am.* **101**(4),

2088–2096 (1997).
2. Johnson, M.E., Elliot, S.J.: Active control of sound radiation using volume velocity cancellation, *J. Acoust. Soc. Am.* **98**(4), 2174–2186 (1995).
3. Henrioulle, K., Sas, P.: Experimental validation of a collocated PVDF volume velocity sensor/actuator pair, *J. Sound Vib.* **265**, 489–506 (2003).
4. Wang, B.-T., Fuller, C.R., Dimitriadis, E.K.: Active control of noise transmission through rectangular plates using multiple piezoelectric or point force actuators, *J. Acoust. Soc. Am.* **90**(5), 2820–2830 (1991)
5. Tanaka, N., Kikushima, Y.: Spatial modal excitation using point actuators, *Trans. JSME, Ser. C* **63**(609), 1616–1623 (1997).
6. Sanada, A., Tanaka, N.: Active control of sound transmission utilizing the mechanism of anti-resonance phenomenon, *Trans. JSME, ser. C* **70**(693), 1293–1300 (2004).

Design of Feed-Forward Control for Underactuated Multibody Systems with Kinematic Redundancy

Robert Seifried and Peter Eberhard

Abstract For underactuated multibody systems with kinematic redundancy the design of a feed-forward control for end-effector trajectory tracking is presented. The feed-forward control design is based on an inverse model of the multibody system which is derived from the nonlinear input-output normal-form. The computation of the inverse model requires a bounded solution of the internal dynamics. This yields a two-sided boundary value problem which in general has a non-causal solution, yielding a pre- and post-actuation phase. In this paper it is shown that in the case of output trajectory tracking the additional degrees of freedom, resulting from the kinematic redundancy, can be used to introduce free design parameters with which a bounded and causal solution for the internal dynamics can be determined.

1 Introduction

Underactuation in multibody systems occurs, if only some generalized coordinates have an associated control input. Typical sources of underactuation in multibody systems include the presence of passive joints and body-flexibility. Trajectory tracking control of such systems is quite difficult and often requires a feed-forward control. In this paper, the design of a feed-forward control for underactuated multibody systems with kinematic redundancy is presented, whereby the end-effector-point should follow a desired output trajectory.

The feed-forward control design is based on an inverse model of the multibody system. The starting point is the transformation of the multibody system into the nonlinear input-output normal-form [5, 6]. Using the special structure of the second order differential equation of motion and a separation into actuated and un-actuated coordinates, the normal-form can be established in a straightforward way.

Robert Seifried and Peter Eberhard
Institute of Engineering and Computational Mechanics, University of Stuttgart, Germany;
E-mail: {seifried, eberhard}@itm.uni-stuttgart.de

H. Ulbrich and L. Ginzinger (eds.), Motion and Vibration Control, 275–284.

Based on the nonlinear input-output normal-form the inverse model is established, consisting of a chain of differentiators, a driven internal dynamics and an algebraic part. The considered multibody systems are non-minimum phase. Thus, in order to obtain a feasible feed-forward control for trajectory tracking, a bounded solution for the internal dynamics must be found. This yields the solution of a two-sided boundary value problem [2]. For non-redundant underactuated multibody systems this bounded solution is non-causal and, therefore, requires a pre- and post-actuation phase. In contrast to trajectory tracking, it has been shown that in the case of working point changes, bounded and causal feed-forward controller can be designed [3]. Combining these two approaches, it is proposed that the additional degrees of freedom which are available from the kinematic redundancy are used to find a bounded and causal solution for the internal dynamics in the case of output trajectory tracking.

The paper is organized in the following way: Section 2 shows the derivation of the nonlinear input-output normal-form. Section 3 presents the structure of the inverse model and available solution methods for the internal dynamics. In Section 4 the design of bounded and causal feed-forward control of redundant and underactuated multibody systems is developed. Section 5 demonstrates this idea through simulation of an underactuated manipulator with kinematic redundancy.

2 MBS in Input-Output Normal-Form

An underactuated multibody systems with f degrees of freedom, generalized coordinates $\boldsymbol{q} \in \mathbb{R}^f$ and inputs $\boldsymbol{u} \in \mathbb{R}^m$ with $m < f$, i.e. control forces and torques, is considered. The nonlinear equation of motion is given by

$$\boldsymbol{M}(\boldsymbol{q})\ddot{\boldsymbol{q}} + \boldsymbol{k}(\boldsymbol{q}, \dot{\boldsymbol{q}}) = \boldsymbol{g}(\boldsymbol{q}, \dot{\boldsymbol{q}}) + \boldsymbol{B}(\boldsymbol{q})\boldsymbol{u}, \tag{1}$$

where $\boldsymbol{M}$ is the mass matrix, $\boldsymbol{k}$ the vector of generalized gyroscopic and centrifugal forces and $\boldsymbol{g}$ the vector of applied forces. The input matrix $\boldsymbol{B}$ distributes the control inputs $\boldsymbol{u}$ onto the directions of the generalized coordinates. In the case of an underactuated multibody system the input matrix $\boldsymbol{B}$ has rank $m < f$. Thus the method of inverse dynamics known from fully actuated systems [9] cannot be used.

From a control point of view it is often helpful to transform the nonlinear system into the so-called nonlinear input-output normal-form [5, 6]. The diffeomorphic coordinate transformation is given by $\boldsymbol{z} = \boldsymbol{\Phi}(\boldsymbol{x})$ where $\boldsymbol{x}$ are the original coordinates and $\boldsymbol{z}$ are the coordinates of the input-output normal-form. In general this transformation requires a state space representation of the nonlinear system and the symbolic computation of Lie-derivatives of the output $\boldsymbol{y}$. However, even for multibody systems with very few degrees of freedom, these symbolic calculations become very complicated. Therefore, in the following it is shown, that for a special type of output the nonlinear input-output normal-form can be directly derived from the second order differential equation of motion (1). The equation is partitioned into two parts:

$$\begin{bmatrix} \boldsymbol{M}_{aa}(\boldsymbol{q}) & \boldsymbol{M}_{au}(\boldsymbol{q}) \\ \boldsymbol{M}_{au}^T(\boldsymbol{q}) & \boldsymbol{M}_{uu}(\boldsymbol{q}) \end{bmatrix} \begin{bmatrix} \ddot{\boldsymbol{q}}_a \\ \ddot{\boldsymbol{q}}_u \end{bmatrix} + \begin{bmatrix} \boldsymbol{k}_a(\boldsymbol{q}, \dot{\boldsymbol{q}}) \\ \boldsymbol{k}_u(\boldsymbol{q}, \dot{\boldsymbol{q}}) \end{bmatrix} = \begin{bmatrix} \boldsymbol{g}_a(\boldsymbol{q}, \dot{\boldsymbol{q}}) \\ \boldsymbol{g}_u(\boldsymbol{q}, \dot{\boldsymbol{q}}) \end{bmatrix} + \begin{bmatrix} \boldsymbol{B}_a(\boldsymbol{q}) \\ \boldsymbol{B}_u(\boldsymbol{q}) \end{bmatrix} \boldsymbol{u}. \tag{2}$$

Thereby the sub-matrix $\boldsymbol{B}_a \in \mathbb{R}^{m \times m}$ has rank m. The first m rows of the equation of motion (2) are referred to as actuated part associated with the m actuated coordinates $\boldsymbol{q}_a$. The remaining $f - m$ rows are referred to as the un-actuated part associated with the $f - m$ un-actuated coordinates $\boldsymbol{q}_u$. In the following, it is assumed that $\boldsymbol{B}_a = \boldsymbol{I}$ is the identity matrix and $\boldsymbol{B}_u = \boldsymbol{0}$. These special choices represent interesting cases of underactuated multibody systems in tree structure. Examples include rigid multibody systems with passive joints and elastic multibody systems where the elastic mode shapes are chosen according to clamped boundary conditions.

The nonlinear input-output normal-form depends on the choice of the system output $\boldsymbol{y}$, where in general the dimension of the input $\boldsymbol{u}$ and output $\boldsymbol{y}$ coincide. In this paper it is assumed that the end-effector position can be described by an output $\boldsymbol{y}$ which is a linear combination of actuated and un-actuated generalized coordinates

$$\boldsymbol{y} = \boldsymbol{q}_a + \boldsymbol{\Gamma} \boldsymbol{q}_u, \tag{3}$$

where $\boldsymbol{\Gamma} \in \mathbb{R}^{m \times f_u}$. Thus, each of the components of the output is the sum of one actuated generalized coordinate and a linear combination of the un-actuated generalized coordinates. For example such an output can be used to describe the end-effector position of elastic manipulators [1]. For the special case of $\boldsymbol{\Gamma} = \boldsymbol{0}$ the output reduces to $\boldsymbol{y} = \boldsymbol{q}_a$, which is the so-called collocated output [8].

The vector of generalized coordinates is given by $\boldsymbol{q} = (\boldsymbol{q}_a, \boldsymbol{q}_u)^T$ and the state vector by $\boldsymbol{x} = (\boldsymbol{q}_a, \boldsymbol{q}_u, \dot{\boldsymbol{q}}_a, \dot{\boldsymbol{q}}_u)^T$. In the following it is shown that

$$\boldsymbol{z} = (\boldsymbol{y}, \boldsymbol{q}_u, \dot{\boldsymbol{y}}, \dot{\boldsymbol{q}}_u)^T = (\boldsymbol{q}_a - \boldsymbol{\Gamma} \boldsymbol{q}_u, \boldsymbol{q}_u, \dot{\boldsymbol{y}} - \boldsymbol{\Gamma} \dot{\boldsymbol{q}}_u, \dot{\boldsymbol{q}}_u)^T \tag{4}$$

is an appropriate choice for the coordinates of the nonlinear input-output normal-form. The coordinate transformation $\boldsymbol{z} = \boldsymbol{\Phi}(\boldsymbol{x})$ forms a local diffeomorphic coordinate transformation since its Jacobian matrix $\boldsymbol{J} = \partial \boldsymbol{\Phi}(\boldsymbol{x}) / \partial \boldsymbol{x}$ is non-singular [5, 6].

In order to derive the input-output normal-form the starting point is the expression of the actuated coordinates $\boldsymbol{q}_a$ in terms of the output $\boldsymbol{y}$ and the un-actuated coordinates $\boldsymbol{q}_u$, i.e. $\boldsymbol{q}_a = \boldsymbol{y} - \boldsymbol{\Gamma} \boldsymbol{q}_u$, $\dot{\boldsymbol{q}}_a = \dot{\boldsymbol{y}} - \boldsymbol{\Gamma} \dot{\boldsymbol{q}}_u$ and $\ddot{\boldsymbol{q}}_a = \ddot{\boldsymbol{y}} - \boldsymbol{\Gamma} \ddot{\boldsymbol{q}}_u$. Then, these expressions can be used in the equation of motion (2). Note that the actuated coordinates $\boldsymbol{q}_a$ are also replaced in all the entries of $\boldsymbol{M}$, $\boldsymbol{k}$ and $\boldsymbol{g}$. For reasons of readability these dependencies are dropped in most of the following calculations. From the second part of the differential equation (2) an expression for $\ddot{\boldsymbol{q}}_u$ can be obtained as

$$\ddot{\boldsymbol{q}}_u = \left(\boldsymbol{M}_{uu} - \boldsymbol{M}_{au}^T \boldsymbol{\Gamma} \right)^{-1} \left(\boldsymbol{g}_u - \boldsymbol{k}_u - \boldsymbol{M}_{au}^T \ddot{\boldsymbol{y}} \right). \tag{5}$$

Inserting equation (5) in the first part of equation (2) and reordering yields

$$\widetilde{\boldsymbol{M}} \ddot{\boldsymbol{y}} = \widetilde{\boldsymbol{q}} - \widetilde{\boldsymbol{k}} + \boldsymbol{u}, \tag{6}$$

where the terms are summarized according to the convention

$$\widetilde{\boldsymbol{M}} = \boldsymbol{M}_{aa} - \big(\boldsymbol{M}_{au} - \boldsymbol{M}_{aa}\boldsymbol{\Gamma}\big)\big(\boldsymbol{M}_{uu} - \boldsymbol{M}_{au}^T\boldsymbol{\Gamma}\big)^{-1}\boldsymbol{M}_{au}^T,$$
$$\widetilde{\boldsymbol{q}} = \boldsymbol{g}_a - \big(\boldsymbol{M}_{au} - \boldsymbol{M}_{aa}\boldsymbol{\Gamma}\big)\big(\boldsymbol{M}_{uu} - \boldsymbol{M}_{au}^T\boldsymbol{\Gamma}\big)^{-1}\boldsymbol{g}_u,$$
$$\widetilde{\boldsymbol{k}} = \boldsymbol{k}_a - \big(\boldsymbol{M}_{au} - \boldsymbol{M}_{aa}\boldsymbol{\Gamma}\big)\big(\boldsymbol{M}_{uu} - \boldsymbol{M}_{au}^T\boldsymbol{\Gamma}\big)^{-1}\boldsymbol{k}_u.$$

Solving equation (6) for $\ddot{\boldsymbol{y}}$ and inserting it in equation (5), a differential equation for $\ddot{\boldsymbol{q}}_u$ can be derived. Summarizing these calculations yields the nonlinear input-output normal-form

$$\begin{aligned} \widetilde{\boldsymbol{M}}\ddot{\boldsymbol{y}} &= \widetilde{\boldsymbol{q}} - \widetilde{\boldsymbol{k}} + \boldsymbol{u} \\ \big(\boldsymbol{M}_{uu} - \boldsymbol{M}_{au}^T\boldsymbol{\Gamma}\big)\ddot{\boldsymbol{q}}_u &= \boldsymbol{g}_u - \boldsymbol{k}_u - \boldsymbol{M}_{au}^T\widetilde{\boldsymbol{M}}^{-1}\big(\widetilde{\boldsymbol{g}} - \widetilde{\boldsymbol{k}} + \boldsymbol{u}\big). \end{aligned} \tag{7}$$

The first equation has dimension m and describes the relationship between the input $\boldsymbol{u}$ and output $\boldsymbol{y}$. The second equation has in this case dimension $f - m$ and is called internal dynamics. The typical state space representation of the input-output normal-form is omitted here, since input-output linearization, analysis of the zero dynamics and model inversion can be directly performed from the second order differential equations (7). Zero dynamics is a very useful concept in nonlinear control, which is preferably analyzed in the input-output normal-form [5]. The zero dynamics of a nonlinear system is the dynamics of the system under the constraint that the output is kept exactly at zero, $\boldsymbol{y} = \boldsymbol{0}$. A nonlinear system is called minimum phase if the equilibrium point of the zero dynamics is stable. Otherwise the system is called non-minimum phase. In the following presentation non-minimum phase systems are considered, thus feedback linearization is not possible.

3 Inverse Model of Underactuated MBS

An inverse model provides the input $\boldsymbol{u}_d$ which is required for exact reproduction of a desired output trajectory $\boldsymbol{y} = \boldsymbol{y}_d$. This input follows from equation (7) as

$$\boldsymbol{u}_d = \widetilde{\boldsymbol{M}}(\boldsymbol{y}_d, \boldsymbol{q}_u)\ddot{\boldsymbol{y}}_d - \widetilde{\boldsymbol{q}}(\boldsymbol{y}_d, \boldsymbol{q}_u, \dot{\boldsymbol{y}}_d, \dot{\boldsymbol{q}}_u) + \widetilde{\boldsymbol{k}}(\boldsymbol{y}_d, \boldsymbol{q}_u, \dot{\boldsymbol{y}}_d, \dot{\boldsymbol{q}}_u). \tag{8}$$

The computation of the input $\boldsymbol{u}_d$ depends on the desired output $\boldsymbol{y}_d, \dot{\boldsymbol{y}}_d$ and the un-actuated states $\boldsymbol{q}_u, \dot{\boldsymbol{q}}_u$. These latter ones are the solution of the internal dynamics of equation (7) which is driven by $\boldsymbol{y}_d, \dot{\boldsymbol{y}}_d$ and $\boldsymbol{u}_d$. Replacing $\boldsymbol{u}_d$ in the internal dynamics of equation (7) by equation (8) yields for the values of the un-actuated states $\boldsymbol{q}_u, \dot{\boldsymbol{q}}_u$ the differential equation

$$\big[\boldsymbol{M}_{uu}(\boldsymbol{y}_d, \boldsymbol{q}_u) - \boldsymbol{M}_{au}^T(\boldsymbol{y}_d, \boldsymbol{q}_u)\boldsymbol{\Gamma}\big]\ddot{\boldsymbol{q}}_u = \boldsymbol{g}_u(\boldsymbol{y}_d, \boldsymbol{q}_u, \dot{\boldsymbol{y}}_d, \dot{\boldsymbol{q}}_u) - \boldsymbol{k}_u(\boldsymbol{y}_d, \boldsymbol{q}_u, \dot{\boldsymbol{y}}_d, \dot{\boldsymbol{q}}_u) - \boldsymbol{M}_{au}^T(\boldsymbol{y}_d, \boldsymbol{q}_u)\ddot{\boldsymbol{y}}_d. \tag{9}$$

In summary, the inverse model consists of three parts which are shown schematically in Figure 1. The first part represents a chain of two differentiators for the desired output vector $\boldsymbol{y}_d$, producing the values $\dot{\boldsymbol{y}}_d$ and $\ddot{\boldsymbol{y}}_d$. The second part of the inverse model is the driven internal dynamics (9) for the $\boldsymbol{q}_u$ coordinates. The third

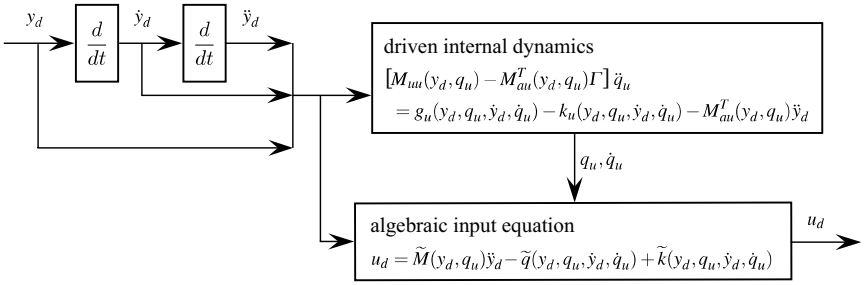

Fig. 1 Schematic representation of an inverse model of an underactuated MBS.

part of the inverse model is the algebraic equation (8) which computes from these values the desired input $\boldsymbol{u}_d$.

Several methods for model inversion exist which differ in the solution of the internal dynamics (9). In classical model inversion [4] the $\boldsymbol{q}_u, \dot{\boldsymbol{q}}_u$ variables are found through forward integration of the internal dynamic (9) from the starting time point t_0 to the final time point t_f, using the initial values $\boldsymbol{q}_u(t_0) = \boldsymbol{q}_{u_0}$, $\dot{\boldsymbol{q}}_u(t_0) = \dot{\boldsymbol{q}}_{u_0}$. However, in order to use the input $\boldsymbol{u}_d$ in a feed-forward control, it must be bounded. Thus depending on the stability of internal dynamics forward integration of the internal dynamics might yield unbounded $\boldsymbol{q}_u, \dot{\boldsymbol{q}}_u$ values and thus unbounded inputs $\boldsymbol{u}_d$. Therefore, classical inversion can only be used for feed-forward control design if the internal dynamics (9) remains bounded, which implies that non-minimum phase systems cannot be treated.

Stable model inversion [2] is a method to solve the inversion problem for non-minimum phase systems, such that the trajectories $\boldsymbol{q}_u, \dot{\boldsymbol{q}}_u$ of the internal dynamics (9) and the control input $\boldsymbol{u}_d$ remain bounded. However the solution might be non-causal. It is assumed that the desired trajectory $\boldsymbol{y}_d$ starts and ends in equilibrium points of the system and the corresponding equilibrium points of the internal dynamics must be hyperbolic. Then, at each equilibrium point a stable manifold $\boldsymbol{W}^s$ and an unstable manifold $\boldsymbol{W}^u$ exist [6]. Any trajectory starting on the stable manifold $\boldsymbol{W}^s$ converges to the equilibrium point as time $t \to \infty$ and any trajectory starting on the unstable manifold $\boldsymbol{W}^u$ converges to the equilibrium point as time $t \to -\infty$. The solution of the stable inversion is then formulated as a two-sided boundary value problem, where the boundary conditions are described by the unstable and stable eigenspaces $\boldsymbol{E}_0^u, \boldsymbol{E}_f^s$ at the corresponding equilibrium points. These are local approximations of the unstable manifold $\boldsymbol{W}_0^u$ and stable manifold $\boldsymbol{W}_f^s$ at the starting and ending equilibrium point, respectively [6]. This yields for the internal dynamics bounded trajectories $\boldsymbol{q}_u, \dot{\boldsymbol{q}}_u$ which start at time t_0 on the unstable manifold $\boldsymbol{W}_0^u$ and reach the stable manifold $\boldsymbol{W}_f^s$ at time t_f. Thus the initial conditions $\boldsymbol{q}_{u_0}, \dot{\boldsymbol{q}}_{u_0}$ at time t_0 cannot exactly be pre-designated. A pre-actuation phase $[t_{pr}, t_0]$ is necessary which drives the system along the unstable manifold to a particular initial condition $\boldsymbol{q}_u(t_0), \dot{\boldsymbol{q}}_u(t_0)$, while maintaining the constant output $\boldsymbol{y}_d = \boldsymbol{y}_d(t_0)$. Also a post-actuation phase $[t_f, t_{po}]$ is necessary to drive the internal dynamics along the

stable manifold close to its resting position. The two-sided boundary value problem has to be solved numerically, e.g. by a finite difference method [10].

An interesting new approach for inversion-based feed-forward control design for the transition task between two stationary working points is proposed in [3]. In this approach a causal and bounded solution is found, irrespective of the stability of the internal dynamics, i.e. no pre- and post-actuation phase is necessary. The bounded solution of the internal dynamics (9) must satisfy the boundary conditions $\boldsymbol{q}_{u_0}, \dot{\boldsymbol{q}}_{u_0}$ at starting time t_0 and $\boldsymbol{q}_{u_f}, \dot{\boldsymbol{q}}_{u_f}$ at end time t_f which yields a two-point boundary value problem. In state space, the internal dynamics (9) has dimension $2(f-m)$, while there are the $4(f-m)$ boundary conditions $\boldsymbol{q}_{u_0}, \dot{\boldsymbol{q}}_{u_0}, \boldsymbol{q}_{u_f}, \dot{\boldsymbol{q}}_{u_f}$ to satisfy. In order to solve this two-point boundary value problem, it is required to introduce additional $2(f-m)$ free parameters $\boldsymbol{w}$. Since in the approach developed by Graichen et al. [3] the control task is a working point change rather than output trajectory tracking, the additional $2(f-m)$ free parameters $\boldsymbol{w}$ are provided by the construction of the desired output trajectory $\boldsymbol{y}_d(\boldsymbol{w})$ which connects the two stationary points.

4 Inverse Model with Kinematic Redundancy

In kinematic redundant multibody systems the number m of actuated generalized coordinates $\boldsymbol{q}_a$ is larger than the degrees of freedom f_e of the end-effector position $\boldsymbol{r}_e$. Therefore, in underactuated multibody systems with additional redundancy, the limitations resulting from under-actuation may be overcome by the use of these additional actuated degrees of freedom. This is especially important for non-minimum phase systems where model inversion requires the bounded solution of the unstable internal dynamics. As summarized in the previous section stable inversion yields bounded but non-causal solutions for output trajectory tracking while inversion with additional design parameters yields bounded and causal solutions for working point changes. In this section, it is proposed to combine these two approaches for underactuated multibody systems with kinematic redundancy for output trajectory tracking. Thereby, the additional degrees of freedom resulting from the kinematic redundancy are used to introduce $2(f-m)$ free design parameters $\boldsymbol{w}$ which are necessary to obtain a bounded and causal solution of the inversion problem.

First, an output $\boldsymbol{y} \in \mathbb{R}^m$ of position variables must be defined which determines through forward kinematics the end-effector position $\boldsymbol{r}_e = \boldsymbol{r}_e(\boldsymbol{y})$. The dimension of this output and the number of inputs have to coincide. This system output $\boldsymbol{y}$ is split into $\boldsymbol{y} = (\boldsymbol{y}_e, \boldsymbol{y}_p)^T$, where $\boldsymbol{y}_e \in \mathbb{R}^{f_e}$ and $\boldsymbol{y} \in \mathbb{R}^{m-f_e}$. Now trajectories $\boldsymbol{y}_{p_d}(\boldsymbol{w})$ for the second output are established in such a way that they introduce $2(f-m)$ free design parameters $\boldsymbol{w}$. Following Graichen et al. [3] this output $\boldsymbol{y}_p$ performs a working point change. Now the desired trajectories for the first output $\boldsymbol{y}_{e_d}$ must be determined in such a way that the end-effector follows the desired trajectory $\boldsymbol{r}_{e_d}$. Thus, the trajectory $\boldsymbol{y}_{e_d}$ follows from the inverse kinematics problem

$$\boldsymbol{r}_{e_d} = \boldsymbol{r}_e(\boldsymbol{y}_{e_d}, \boldsymbol{y}_{p_d}(\boldsymbol{w})) \quad \Rightarrow \quad \boldsymbol{y}_{e_d} = \boldsymbol{r}_e^{-1}(\boldsymbol{r}_{e_d}, \boldsymbol{y}_{p_d}(\boldsymbol{w})). \tag{10}$$

This inverse kinematics problem poses a set of f_e nonlinear equations for the f_e-dimensional output $\boldsymbol{y}_{e_d}$. This is similar to the standard form of a non-redundant inverse kinematics problem [9]. Due to relationship (10), the output $\boldsymbol{y}_{e_d}$ implicitly depends on the free parameter $\boldsymbol{w}$, and thus in the following it is written $\boldsymbol{y}_d = \boldsymbol{y}_d(\boldsymbol{w})$.

Applying this result to the internal dynamics (9) yields the two-point boundary value problem

$$\begin{aligned}&\left[\boldsymbol{M}_{uu}(\boldsymbol{y}_d(\boldsymbol{w}), \boldsymbol{q}_u) - \boldsymbol{M}_{au}^T(\boldsymbol{y}_d(\boldsymbol{w}), \boldsymbol{q}_u)\boldsymbol{\Gamma}\right]\ddot{\boldsymbol{q}}_u \\ &\quad = \boldsymbol{g}_u(\boldsymbol{y}_d(\boldsymbol{w}), \boldsymbol{q}_u, \dot{\boldsymbol{y}}_d(\boldsymbol{w}), \dot{\boldsymbol{q}}_u) - \boldsymbol{k}_u(\boldsymbol{y}_d(\boldsymbol{w}), \boldsymbol{q}_u, \dot{\boldsymbol{y}}_d(\boldsymbol{w}), \dot{\boldsymbol{q}}_u) - \boldsymbol{M}_{au}^T(\boldsymbol{y}_d(\boldsymbol{w}), \boldsymbol{q}_u)\ddot{\boldsymbol{y}}_d(\boldsymbol{w})\end{aligned} \tag{11}$$

where the boundary values are given by

$$\boldsymbol{q}_u(t_0) = \boldsymbol{q}_{u_0}, \quad \dot{\boldsymbol{q}}_u(t_0) = \boldsymbol{0} \quad \text{and} \quad \boldsymbol{q}_u(t_f) = \boldsymbol{q}_{u_f}, \quad \dot{\boldsymbol{q}}_u(t_f) = \boldsymbol{0}. \tag{12}$$

The solution of this two-point boundary value problem yields the bounded and causal trajectory for the un-actuated coordinates $\boldsymbol{q}_u$ and the set of $2(f-m)$ parameters $\boldsymbol{w}$. Thus the trajectories for the output $\boldsymbol{y}_d(\boldsymbol{w})$ are found such that the end-effector follows the desired trajectory $\boldsymbol{r}_{e_d}$, the internal dynamics fulfills the initial and final conditions (12) and the solution is bounded for all states and inputs. In addition the kinematic redundancy can also be used to perform additional secondary tasks such as the predesignation of starting and final positions of some bodies of the system.

5 Example: Redundant and Underactuated Manipulator

For demonstration purposes, the presented model inversion techniques are applied to the feed-forward control of a underactuated manipulator with kinematic redundancy, which is shown schematically in Figure 2. The manipulator moves along the horizontal plane and consists of a cart on which a chain of three arms is mounted. The arms have length $l_1 = 1$ m and $l_2 = l_3 = 0.5$ m. The manipulator is described by the generalized coordinate $\boldsymbol{q} = (x, \alpha_1, \alpha_2, \beta)^T$ and is actuated by the control input $\boldsymbol{u} = (F, T_1, T_2)^T$. The third arm is connected by a passive joint to arm 2 which is supported by a parallel spring-damper combination.

The control goal is to force the end effector to follow a predefined end-effector trajectory as closely as possible. For a somewhat stiff spring-damper combination, the angle β remains small and the end-effector position can be approximated by

$$\boldsymbol{r}_{EF} \approx \begin{bmatrix} x + l_1 \sin(\alpha_1) + (l_2 + l_3)\sin(\alpha_1 + \alpha_2 + \frac{1}{2}\beta) \\ -l_1 \cos(\alpha_1) - (l_2 + l_3)\cos(\alpha_1 + \alpha_2 + \frac{1}{2}\beta) \end{bmatrix}. \tag{13}$$

This approximation of the end-effector can be described by the linearly combined output $\boldsymbol{y} = (x, \alpha_1, \alpha_2 + \frac{1}{2}\beta)^T$. Due to this approximation a small tracking error for the end-effector position has to be expected. In this example the end-effector point should follow a half-circular trajectory. The center of the half-circle is at position $(0, -1.5\text{ m})$ and the radius is 1 m. The end-effector point should follow the trajectory in the short time period of 1.5 s, which describes an aggressive manoeuver. Also

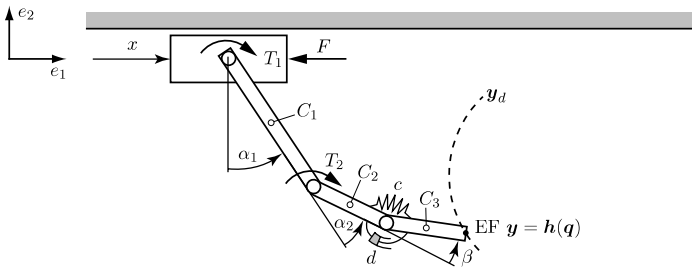

Fig. 2 Redundant manipulator with one passive joint.

the kinematic redundancy should be used to perform as secondary task of moving the cart from starting position -1 m to the final position 1 m. Two different feed-forward control schemas are developed and then tested by simulations:

Feed-forward control 1 (FF1): Bounded solution from the stable inversion approach [2], which yields a pre- and post-actuation phase. The computed trajectory of the internal dynamics, which is in this case the β variable, is presented in Figure 3. Note that in this example the starting and final position yields the same equilibrium point of the internal dynamics. The plot clearly shows the start of the trajectory of the internal dynamics on the unstable manifold at time t_0 and the ending on the stable manifold at time t_f. Thus, pre- and post-actuation phases of at least 0.2 s length are necessary, which is also clearly seen in Figure 4 of the input $\boldsymbol{u}$. The figure also shows that the secondary task, the motion of the cart from -1 m to 1 m, is achieved.

Feed-forward control 2 (FF2): Model inversion with bounded and causal solution, following the presentation given in Section 4. The output $\boldsymbol{y}$ is separated into $\boldsymbol{y}_e = (\alpha_1, \alpha_2 + \frac{1}{2}\beta)$ and $\boldsymbol{y}_p = x$. Thus, the cart trajectory is used to introduce the two additional parameters which are necessary to satisfy the boundary conditions of the internal dynamics at starting time t_0 and final time t_f. Since the cart should continue to perform the same secondary task, i.e. move from $-1m$ to 1 m, a start-up phase $[t_0, t_s]$ and an ending phase $[t_e, t_f]$ are introduced, each of duration 0.3 s. In both phases an additional polynomial of sixth order with one free parameter is added to the cart trajectory. The solution of the inversion is presented in Figures 3 and 5. The start-up and ending phase is clearly seen in the x trajectory of the cart. Due to these two phases the internal dynamics starts at t_0 and ends at time t_f at the equilibrium point β_0 and thus the desired boundary condition are met exactly. While during the start-up phase and ending phase large control inputs occur, this requires only a modest increase of control energy by 13%. However, since no pre-and post-actuation is necessary, this feed-forward control enables easily the execution of several successive motions without interruption [7]. Alternatively to the introduction of the free parameters $\boldsymbol{w}$ via a start-up and ending phase, the starting position and final position of the cart can be used as free design parameters. While in this case the secondary goal cannot be achieved, this approach yields a less strongly varying input $\boldsymbol{u}_d$, see [7].

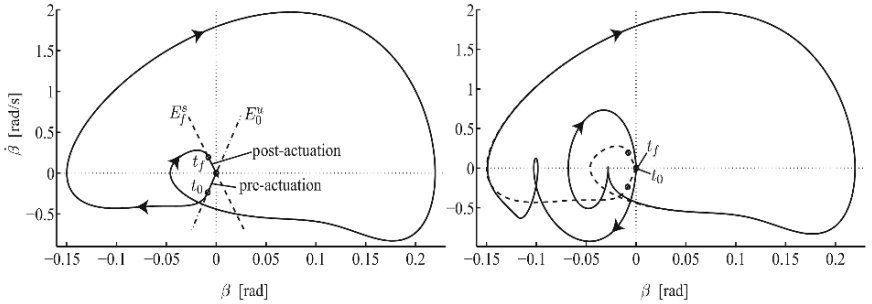

Fig. 3 Internal dynamics with feed-forward control 1 (left) and feed-forward control 2 (right).

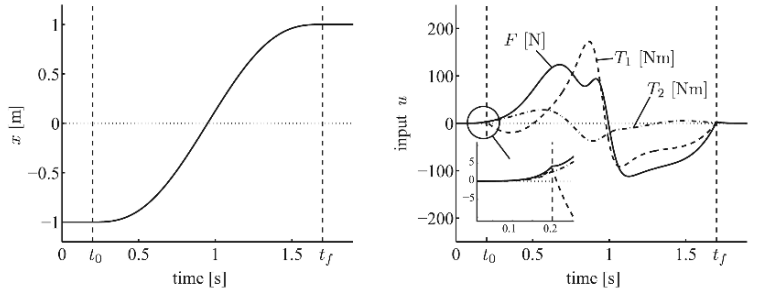

Fig. 4 Cart position and inputs for feed-forward control 1 with pre- and post-actuation.

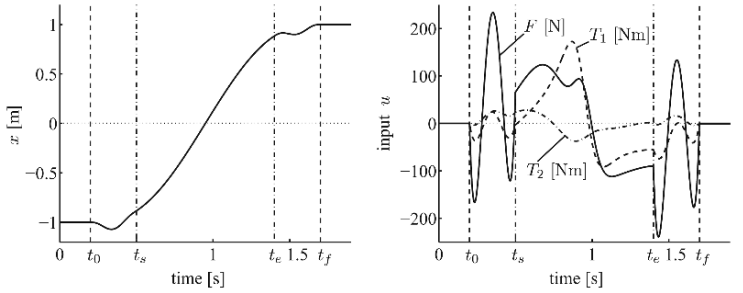

Fig. 5 Cart position and inputs for feed-forward control 2 with start-up phase and ending phase.

The two feed-forward controllers are tested by simulation in combination with a simple PID controller for the actuated generalized coordinates to account for small disturbances. The end-effector trajectories and the velocities along the trajectory are presented in Figure 6. It shows that the end-effector follows the desired trajectory closely. The maximal absolute tracking error in radial direction is about 3 mm. The largest errors occur in the middle of the motion when β becomes large and result from the approximation of the end-effector position by equation (13). Both strategies result in having the end-effector at rest outside the interval $[t_0, t_f]$. However, only with feed-forward control 2 the entire system is at rest outside $[t_0, t_f]$.

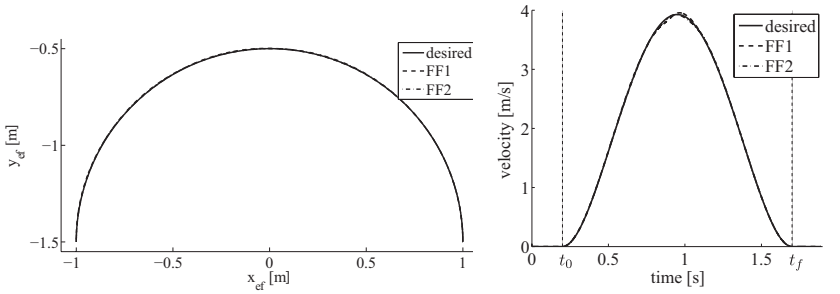

Fig. 6 Simulated end-effector trajectory and velocity.

6 Summary

The design of feed-forward control for underactuated multibody systems was presented. The nonlinear input-output normal-form which is the basis of the feed-forward controller design was directly established from the second order differential equation of motion. In general, the feed-forward control consists of a chain of differentiators, a driven internal dynamics and an algebraic part. Depending on the stability of the internal dynamics, different methods of solution exist to achieve a bounded feed-forward control. In the case of a kinematic redundancy the additional degrees of freedom can be used to introduce free parameters which are necessary for the design of a bounded and causal feed-forward control.

References

1. De Luca, A.: Trajectory control of flexible manipulators. In: Siciliano, B., Valavanis, K. (Eds.), *Control Problems in Robotics and Automation*, pp. 83–104. Springer, London (1998).
2. Devasia, S., Chen, D., Paden, B.: Nonlinear inversion-based output tracking. *IEEE Trans. Autom. Control* **41**, 930–942 (1996).
3. Graichen. K, Hagenmeyer, V., Zeitz, M.: A new approach to inversion-based feedforward control design for nonlinear systems. *Automatica* **41**, 2033–2041 (2005).
4. Hirschorn, R.: Invertibility of multivariable nonlinear control systems. *IEEE Trans. Autom. Control* **24**, 855–865 (1979).
5. Isidori, A.: *Nonlinear Control Systems*. Springer, London (1995).
6. Sastry, S.: *Nonlinear Systems: Analysis, Stability and Control*. Springer, New York (1999).
7. Seifried, R.: A contribution to control aspects in analysis and optimization of kinematical redundant and dynamical under-actuated multibody systems. Internal Report IB-39, Institute of Engineering and Computational Mechanics, University of Stuttgart (2007).
8. Spong, M.: Underactuated mechanical systems. In: Siciliano, B., Valavanis, K. (Eds.), *Control Problems in Robotics and Automation*, pp. 135–150. Springer, London (1998).
9. Spong, M., Hutchinson, S., Vidyasagar, M.: *Robot Modeling and Control*. John Wiley & Sons, Hoboken (2006).
10. Taylor, D., Li, S.: Stable inversion of continuous-time nonlinear systems by finite-difference methods. *IEEE Trans. on Autom. Control* **47**, 537–542 (2002).

Fusion Filter for Orientation Estimation of Biped Robot

Min-geun Song, Jinseong Park, Youngjin Park and Youn-sik Park

Abstract Tilt sensor is usually necessary for attitude control of a biped robot when it walks on an uneven terrain. There are many sensors to measure the tilt angles, and gyro sensor is widely used for estimation of tilt angles because it can offer the sufficient bandwidth, so it is suitable for sensing the rapid motions that create high frequency pose variations. However, its major disadvantage is the lack of accuracy and drift over time. Vision sensor can estimate an accurate attitude of robot directly from the image of camera. However, it is hard to control attitude of rapid or abrupt rotation due to the time delay and its low bandwidth. In this paper, we implement a fusion filter frame that combines two sensor signals using Extended Kalman Filter (EKF) to compensate the weakness of two sensors. We use modified track-to-track model as fusion method. The simulation and experimental results show that we obtain the accurate attitude information through fusion filter combining two sensor signals.

1 Introduction

Many attitude control algorithms for biped robots use the orientation, i.e. the roll, pitch and yaw angles of the upper body as controlled variables. The performance of the control depends on two properties of the measurement system: Accuracy and bandwidth. Estimation errors of the attitude lead to an inaccurate tracking of the reference trajectories and the sensor bandwidth limits the bandwidth of the controller.

There are many sensors to measure the tilt angles. It is general to obtain tilt estimates by processing gyro, inclinometer and accelerometer signals. Each sensor has unique strength and weakness [1–4].

Min-geun Song, Jinseong Park, Youngjin Park and Youn-sik Park
KAIST, 305-701, Guseong, Yuseong, Daejeon, Republic of Korea;
E-mail: {geuniwow, kai-js, yjpark, yspark}@kaist.ac.kr

H. Ulbrich and L. Ginzinger (eds.), Motion and Vibration Control, 285–294.

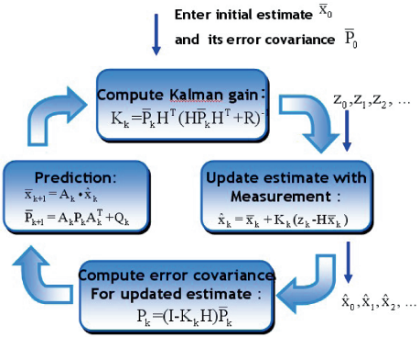

Fig. 1 Kalman filter loop.

The tilt angle measured by accelerometer is usually contaminated by the translational acceleration and gravity effects. Therefore, the tilt estimate based on the accelerometer leads to an error due to a translational acceleration. An inclinometer measures the tilt angle with respect to the field of gravity. The inclinometer has not enough bandwidth to control the attitude of the biped robot. The gyro sensor is widely used for estimation of tilt angles because it has wide enough bandwidth suitable for sensing the rapid motions that create high frequency pose variations. Because measured angular velocity from gyro is integrated to produce the attitude information, large drift in the attitude estimates is possible especially when an elapsed time is long. To correct the accumulated drift, measurements from the other sensor is necessary to provide absolute orientation data.

For the human-robot interaction, many biped robots already have vision sensor. Vision signal can be utilized to estimate an accurate attitude of robot directly from the same imagery using a point-based method. However, the major disadvantage of the vision sensor is that image processing takes considerable computation time and therefore introduces significant time delay and limits the bandwidth which, in turn, makes the attitude control of rapid and abrupt motion difficult.

Each sensor has its own limitation for attitude control. The hybrid systems can to compensate for the shortcomings of single type sensor based approach by using multiple measurements to produce the accurate attitude estimation. Combining vision and gyro sensors offer one approach to overcoming aforementioned disadvantages of single sensor approaches.

In this paper, we implement a fusion filter framework that combines two sensor signals using Extended Kalman Filter (EKF). We use modified track-to-track model as fusion method [5]. There are two corrections sharing a common prediction, one for the low rate vision measurements and another for the high-rate gyro measurement. The two corrections process data independently, allowing different sampling rates for each sensor system and reducing the computation. The accurate attitude information of robot can be obtained by combining two filtered sensor signal in each correction.

2 Kalman Filter [6]

Consider a dynamic system which can be modeled by a n-by-1 state vector $\mathbf{x}$ obeying a discrete-time (DT) evolution equation

$$x_{k+1} = A_k x_k + B u_k + w_k, \tag{1}$$

where $\mathbf{A}$ is an n-by-n state transition matrix, $\mathbf{B}$ is an n-by-p matrix and u is a p-by-1 vector of known system inputs, and $\mathbf{w}$ is an n-by-1 process noise vector with covariance matrix $\mathbf{Q_k}$. (Note that lower-case bold letters, Greek or Roman, denote vectors, and upper-case bold letters denote matrices.) Suppose there are indirect measurements of the state vector available at each time k, and that they can be expressed as an m-by-1 measurement vector

$$z_k = H x_k + v_k, \tag{2}$$

where $\mathbf{H}$ is an m-by-n system observation matrix, and $\mathbf{v}$ is an m-by-1 measurement noise vector with covariance $\mathbf{R_k}$. A Kalman filter is a recursive algorithm for computing an estimate $\hat{x}_k$ of state which is optimal in the sense of least square error under certain circumstances. One form of the DT Kalman filter is

$$\hat{x}_k = \bar{x}_k + K_k(z_k - H\bar{x}_k), \tag{3}$$

where the Kalman gain matrix $\mathbf{K}$ is computed from the estimation error covariance matrix, $\mathbf{P}$, according to

$$K_k = \bar{P}_k \, H^T (H \bar{P}_k \, H^T + R)^{-1} \tag{4}$$

and $\mathbf{P}$ is updated according to the Ricatti equation:

$$\bar{P}_{k+1} = A_k \, P_k \, A_k^T + Q_k, \tag{5}$$

$$P_k = (I - K_k \, H) \bar{P}_k \, . \tag{6}$$

Equations (1–5) and (6) comprise the Kalman filter recursive equations. These equations and sequence of the computational steps are shown pictorially in Figure 1.

The Kalman filter is very useful for combining data from several different indirect and noisy measurements to try to estimate variables which are not directly measurable. Thus, while the gyro sensor measures orientation by integrating angular rate, and the vision sensor provide a low sample rate but drift-free measurement of orientation, the Kalman filter weights the two sources of information appropriately to make the best use of all the data from each. If the system dynamics are nonlinear, it is possible to linearize about a nominal or actual trajectory and run a Kalman filter on the linearized system. This is the basis of the extended Kalman filter (EKF) and the fusion filter based on the EKF developed in Section 3.

3 Algorithm Framework

3.1 Motion Model and System Dynamics

The first step in modeling is to decide what to put in the state and measurement vectors. Since the basic purpose of the Kalman filter is to estimate orientation, it is a given that it will be included in the state vector. In this paper, our implementation uses Euler angles. The aeronautics convention used, where φ, θ and ψ, called yaw, pitch, roll respectively, represent positive rotations about the z, y, and x body axes in turn, with the positive x-axis pointing forward, positive y pointing right, and positive z pointing down. There is a singularity in the Euler angle representation at $\theta = \pm 90°$, but this was not found to produce any noticeable disturbances in practice.

Many researchers include angular rates in the state vector and gyroscopic angular rate measurements in the measurement vector, This is very natural, as it allows the Euler angle integration kinematics,

$$\dot{\Theta}(t) = W(\Theta(t)) \cdot \omega(t)$$

$$\Theta(t) = \begin{bmatrix} \psi(t) \\ \theta(t) \\ \varphi(t) \end{bmatrix}, \quad \omega(t) = \begin{bmatrix} \omega_X(t) \\ \omega_Y(t) \\ \omega_Z(t) \end{bmatrix}$$

$$W(\Theta(t)) = \begin{bmatrix} 1 & \sin\psi(t)\tan\theta(t) & \cos\psi(t)\tan\theta(t) \\ 0 & \cos\psi(t) & -\sin\psi(t) \\ 0 & \sin\psi(t)/\cos\theta(t) & \cos\psi(t)/\cos\theta(t) \end{bmatrix} \tag{7}$$

to be incorporated into the system dynamics model, and allows the gyro measurements to be utilized in the obvious way – as measurements.

We used the motion model as proposed by Chai et al. [7]; here the head motion is represented by 6×1 vector:

$$x_k = [\Theta_k \ \ \omega_k]^T, \tag{8}$$

where Θ is the orientation of the frame with respect to the world (we use Z-Y-X Euler angles), ω is the angular velocity. With these states, the discretized system dynamics are given by:

$$\begin{bmatrix} \Theta_{k+1} \\ \omega_{k+1} \end{bmatrix} = \begin{bmatrix} I & \Delta T \cdot W(\Theta) \\ 0 & I_{3\times 3} \end{bmatrix} \times \begin{bmatrix} \Theta_k \\ \omega_k \end{bmatrix} + \begin{bmatrix} \Delta T^2/2 \cdot W(\Theta) \cdot \dot{\omega}_k \\ \Delta T \cdot \dot{\omega}_k \end{bmatrix}, \tag{9}$$

where ΔT is the sampling period, $W(\Theta)$ is the Jacobian matrix that relates the absolute rotation angle to the angular rate, and $\dot{\omega}_k$ are the system random distribution noise.

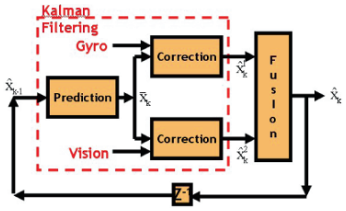

Fig. 2 Fusion filter framework.

3.2 Measurement Model

Once the process model has been designed, we should also concrete the measurement model. This model describes how the estimation space maps into the observation space, that is, it relates the measurement vector and the state vector by linear equation. We suppose that observation equations measure directly the system state. So the vision system measures the camera pose Θ in world coordinate system. The gyroscope produces angular velocity measurements. The sensors measurements can then be represented by a measurement vector as follows:

$$\Theta_k = [\psi_k \;\; \theta_k \;\; \varphi_k]^T \quad \omega_k = [\omega_{xk} \;\; \omega_{yk} \;\; \omega_{zk}]^T. \tag{10}$$

The measurement equation of gyro sensor is then given by:

$$z_k^1 = H^1 \times x_k + v_k^1. \tag{11}$$

The measurement equation of vision sensor is then given by:

$$z_k^2 = H^2 \times x_k + v_k^2, \tag{12}$$

where H^1, H^2 are equal to the $[0 \;\; I_{3\times3}]$, $[I_{3\times3} \;\; 0]$ respectively and v_k^1, v_k^2 is the measurement noise.

3.3 Fusion Method

The goal of the fusion filtering is to estimate the orientation of upper body, i.e. the roll, pitch and yaw angles of the biped robot from the measurements of the vision and gyro sensors. Since the vision and gyro sensors have different sample rates, we implement a fusion filter using modified track-to-track fusion (MTF) [6] as shown in Figure 2.

The filter has a prediction, corrections and fusion module. There are two corrections sharing common prediction: one is for gyro measurement and another one is for vision measurement. The final fused estimate can then be obtained from combining two kinds of filtered sensor signal in each correction. This is a feedback to

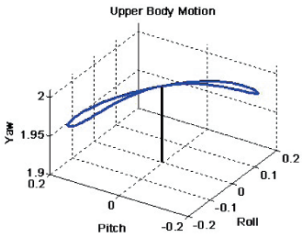

Fig. 3 Depiction of 3D motion trajectory.

the single state prediction, whose output is then fed to the two local observation correction equations.

Finally, by the usual derivation of the Kalman filter, the following fusion algorithm for modified track-to-track fusion Kalman filter algorithm can easily be derived as:

Fusion filter algorithm:

$$P_k^{12} = (P_k^{21})^T = [I - K_k^1 H^1]\bar{P}_k[I - K_k^2 H^2]$$

$$P_k = P_k^1 - [P_k^1 - P_k^{12}][P_k^1 + P_k^2 - P_k^{-12} - P_k^{21}]^{-1}[P_k^1 - P_k^{21}]$$

$$\hat{x}_k = \hat{x}_k^1 + [P_k^1 - P_k^{12}][P_k^1 + P_k^2 - P_k^{12} - P_k^{21}]^{-1}[\hat{x}_k^2 - \hat{x}_k^1]$$

4 Simulation

In order to evaluate the performance of the fusion filter, we first implement it with purely synthetic data. So, a synthetic orientation of biped robot's upper body is described (Figure 3), and synthetic gyro and vision data are generated from it. A synthetic white Gaussian random noise is added to the measurements with variance 0.01 for gyros, 0.01 for the vision sensor.

The filter parameters, i.e. measurement noise matrix $\mathbf{R}$, process noise matrix $\mathbf{Q}$ and the sampling time ΔT_{gyro}, ΔT_{vision} of the two sensors, are given in Table 1.

The process noise matrices were chosen empirically in order to achieve the best performance of the filter. To evaluate the filter performances a mean square error (MSE) analysis is performed. The MSE is given by:

$$\text{MSE} = \frac{1}{n}\sum_{k=1}^{n} ||x_k - \hat{x}_k||^2, \tag{13}$$

Table 1 Filter parameters.

Gyro sensor		
Gyro sample rate	100	Hz
Gyro bias noise	0.5	Degree/sec
Gyro noise variance	1	$\text{Degree}^2/\text{sec}^2$
Vision sensor		
Vision sample rate	10	Hz
Vision noise variance	0.1	Degree^2
Vision delay	0.1	sec

Table 2 Estimation MSE using different q values.

Estimation MSE			
q	Roll	Pitch	Yaw
1	0.64216	0.49006	1.1644
10	0.42457	0.38714	0.49242
100	0.42078	0.38369	0.48434
1000	0.42026	0.3827	0.48141
10000	0.41993	0.38312	0.48136
100000	0.41743	0.3868	0.48137

where $x(k)$ is the true orientation trajectory, and $\hat{x}(k)$ the estimation. In Table 2, the best performance of the fusion filter is achieved with a different process covariance (q) for each Euler angle.

The motion pattern is given by:

$$\begin{aligned} \text{Roll} &\rightarrow \psi(t) = 8.6^\circ \times \sin(2\pi \times t) \\ \text{Pitch} &\rightarrow \theta(t) = 11.46^\circ \times \sin(2\pi \times t) \\ \text{Yaw} &\rightarrow \varphi(t) = 5.73^\circ \times \sin(4\pi \times t) \end{aligned}$$

In Figure 4 result of motion estimation are presented. Without vision compensation, the gyro drifts at about 0.5 degree/sec. When the parameters are well fixed, we note that the implemented filter succeeds to follow the true trajectories very closely. The estimation error is less than 1 degree.

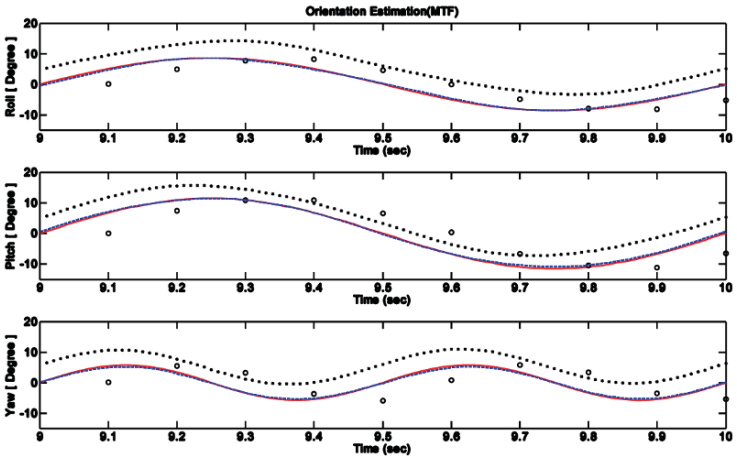

Fig. 4 Date fusion and estimation of the motion orientation. (solid: true orientation, dash: estimation, x: gyro, o: vision data).

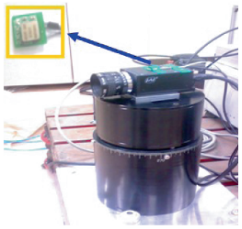

Fig. 5 Experimental setup with rate gyro affixed to camera.

Table 3 Specification of the sensors.

Gyro sensor		
Gyro range	± 75	Degree/sec
Gyro noise	1.732	Degree/sec
Gyro bandwidth	40	Hz
Camera		
Resolution	752×582	pixels
Pixel size	8.6×8.3	μm
Max. Frame rate	25	frames/sec

5 Experiment

We conducted experiment to test the proposed fusion approach. Figure 5 shows the hardware sensor configuration. The sensor module contains a CCD video camera (CV-M50IR) and the gyro sensor (ADXRS401).

Table 4 Filter parameter.

Gyro sensor		
Gyro sample rate	100	Hz
Gyro bias noise	3	Degree/min
Gyro noise variance	0.677	$Degree^2/sec^2$
Vision sensor		
Vision sample rate	10	Hz
Vision noise variance	0.1430	$Degree^2$
Vision delay	0.1	sec

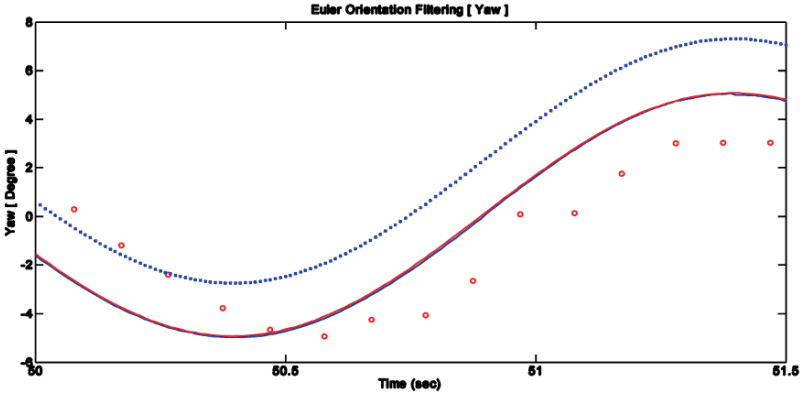

Fig. 6 Date fusion and estimation of the motion orientation (solid: true orientation, dash: estimation, *x*: gyro, *o*: vision data).

In Tables 3 and 4, the information of sensors is presented. The excitation is a sine wave with an amplitude of 5 degree and a frequency of 0.5 Hz. The implemented filter succeeds to follow the true trajectories very closely. The estimation error is less than 1 degrees and the MSE of estimation is 0.2399.

6 Conclusion

We present an accurate and efficient method for estimation of biped robot orientation based on gyro and vision sensors. The gyro sensor is robust and high bandwidth while it lacks accuracy and tends to drift over time. Vision tracking is accurate over long periods, but it suffers from occlusion and high computation expense. To compensate the weakness of two sensors, we implemented a fusion filter framework based on the Extened Kalman Filter (EKF) using modified track-to-track fusion method. The complementary filtering structure is treated as two parallel EKF banks sharing one common state prediction module. The experimental results demonstrate the effectiveness of this strategy.

Acknowledgements Authors are gratefully acknowledging the financial support by Agency for Defence Development and by UTRC (Unmanned Technology Research Center), Brain KOREA 21 project and the National Research Laboratory Program (R0A-2005-000-10112-0).

References

1. Navarro, D.Z., 2006, *A Biped Robot Design*, PhD Thesis, Freie Universität Berlin, Institut für Informatik, Berlin, Oktober.
2. Gienger, M., Loffler, K. and Pfeiffer, F., 2002, Walking control of a biped robot based on inertial measurement, in *Proceeding of the Third IARP International Workshop on Humanoid and Human Friendly Robotics*, Tsukuda, Japan, December 22–29.
3. Hirai, K., Hirose, M., Haikawa, Y. and Takenaka, T., 1998, The development of Honda humanoid robot, in *Proceedings of the IEEE International Conference on Robotics and Automation*, pp. 1321–1326.
4. Kim, J.-H., 2004, A study on the realization of dynamic gait for a biped humanoid robot, PhD Thesis, KAIST.
5. Gao, J.B. and Harris, C.J., 2002, Some remarks on Kalman filters for multisensor fusion, *Information Fusion* **3**(3), 191–201.
6. Brown, R.G. and Hwang, P.Y.C., 1997, *Introduction to Random Signals and Applied Kalman Fitering*, John Wiley & Sons.
7. Chai, L., Hoff, W. and Vicent, T., 2002, Three-dimensional motion and structure estimation using inertial sensors and computer vision for augmented reality, *Presence: Teleoperators & Virtual Environments* **11**(5), 474–492.

Control of Deployment Mechanism for Space Application by Compliance Control and Complementary System Representation

Y. Sugawara, Y. Kida and N. Kobayashi

Abstract Recently, deployment system is often required for satellite to execute various missions. Such a deployment system consists of two functions. One is the deployment mechanism to deploy the components from folded configurations and the other is latch mechanisms to fix the deployed components in desired configuration. Deployment systems are often subjected to failure due to mechanical load by launch rocket and vacuum metalizing by space high vacuum environment. To escape such failures, deployment system without latch mechanism is sometimes used in space applications. Behaviour of such a system includes continuous flexible dynamics and discrete impact dynamics and degrades the attitude control performance of a satellite. To improve such performance degradation, compliance control is implemented to attitude control of satellite. Compliance control is often applied for the control which includes contact state, but it is not easy to get precise information of contact forces and torques of the motion with impact dynamics by conventional force sensor system, which arise in very short period. Especially such a measurement is very difficult in space applications in which slow control timing is preferred for reliability of the system and saving of power. Therefore, it is difficult to use compliance control for the system with impact dynamics effectively in space applications. In this paper, complementary system representation is utilized to implement compliance control more effectively for simple satellite model, and validity of proposed method is shown by simulation.

1 Introduction

Recently, small size satellite is attracting much attention. The development cost of such a small satellite is quite low, because COTS (commercial-off-the-shelf) elec-

Y. Sugawara, Y. Kida and N. Kobayashi
Aoyama Gakuin University, 5-10-1 Fuchinobe Sagamihara Kanagawa 229-8558, Japan;
E-mail: sugawara@me.aoyama.ac.jp

H. Ulbrich and L. Ginzinger (eds.), Motion and Vibration Control, 295–304.

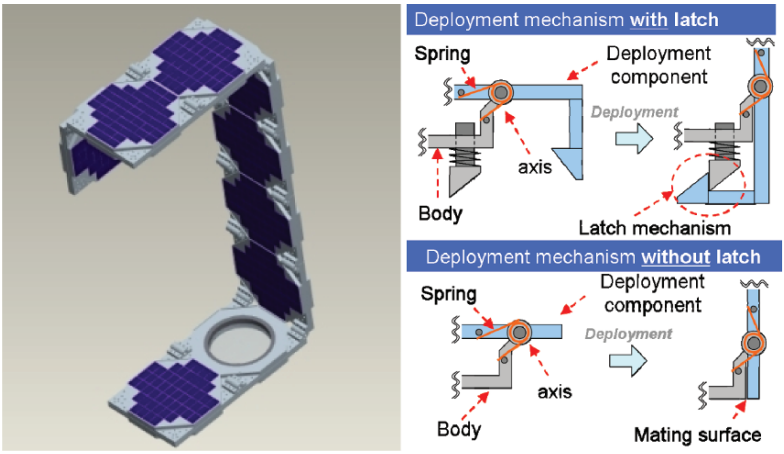

Fig. 1 Left: PETSAT (Panel Extension SATelite), Right: structural drawing of deployment mechanism with latch and without latch.

tronic products is improving their performances and reliabilities dramatically and are utilized actively. And easy handling due to smallness of the satellite reduces the development period and consequently the development cost of the satellite becomes lower and lower. Moreover, the launch cost of small satellite is getting quite low compared to large satellite, because a lot of piggyback-style-launch is provided in many countries. Therefore, the potential of small satellite is growing. However, small satellite has also disadvantages, because there are a lot of difficulties in realizing large and long structure for mounting devices or some requirements from the mission due to its smallness compared to large satellite. Therefore, the difficulties bring limitation of utility of small satellite. To escape such a limitation, deployment mechanism is used to realize large and long structure. Conventional deployment mechanism consists of two elements. One is a mechanism which deploys the folded component, for example it has some actuators, e.g. spring, motors and so on, to deploy and some axes or guides to determine directions of deployment. The other is a mechanism which fixes the deployed configuration, for example latch mechanism. It is very important for mechanism of space application to consider two issues. One is intense mechanical load produced by rocket engine during launch and such a load can break the mechanical component. The other is ultrahigh vacuum environment of space and they induce the vacuum metalizing of slide component made by metal. In this way, a satellite with complicated mechanism is subjected to failures and their reliability becomes lower than that with simple mechanism.

In order to improve the reliability of the satellite, a deployment mechanism without a latch mechanism is sometimes used, which is called “non-latched deployment mechanism” in the following. PETSAT (Panel ExTension SATellite) [1] which will be launched in 2009 adopted this type of deployment mechanism [2] (left-hand figure in Figure 1). Such a mechanism has mating component instead of latch mechanism and mating state is kept by deployment force, which makes it pos-

sible to keep desirable deployed configuration (right-hand figure in Figure 1). The deployment force can be usually provided by simple springs to keep reliability and non-stiff spring is chosen to prevent high impact force which may cause damages on the deployment mechanism and other components. At the same time the deployed configuration is deformed easily by attitude control force in such a system, because the force by non-stiff spring is not so strong. Dynamics which attributes to such a deformation include continuous flexible dynamics and discrete impact dynamics and makes the attitude control performances of the satellite worse.

To avoid such a degradation of the performances, compliance control [3] is combined to attitude control of satellite. Compliance control usually requires information about contact state, but it is not easy to get precise information of contact state, especially information of contact force or torque, by conventional method, e.g. the measurement system with force sensor. But it is difficult to capture the enough information from force sensor because force sensor is subject to noise and contact period of impact is quite short compared to processing time of measurement system, especially processing time of the system for space application is much slower for reliability and saving energy. Therefore, it is difficult to use compliance control effectively in space applications.

On the other hand, much effort is devoted to a study of unilateral contact based on complementary system [4] in recent years. According to the theory, contact or torque force can be estimated from state variables of the system and the motion of the system before/after contact can be derived numerically. Namely, it is possible to implement compliance control law without force sensor.

In this paper, idealized simple non-latched deployment mechanism is controlled by proposed control law that consists of compliance control with estimator by the use of complementary system representation. Moreover, some numerical simulations are carried out to show its effectiveness and its advantages of the proposed method.

2 Model of Controlled Object

2.1 Model of the System

Simplified model of satellite with non-latched deployment mechanism is supposed as shown in Figures 2 and 3 and consists of body, deployment component and deployment mechanism. θ_1 and θ_2 are the angle of body and deployment component about inertial coordinate-system Σ. l_1 is the distance between rotational centre of satellite O and rotational axis of the deployment component, of which length is l_2. Body and deployment component have mass of m_1 and m_2 and have moment of inertia of I_1 and I_2 respectively. Input torque τ for attitude control of the satellite is applied around O. Furthermore, the following assumptions are set for simplicity:

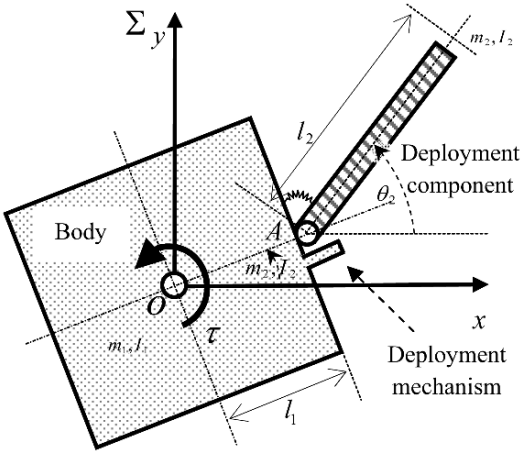

Fig. 2 Simplified model of satellite.

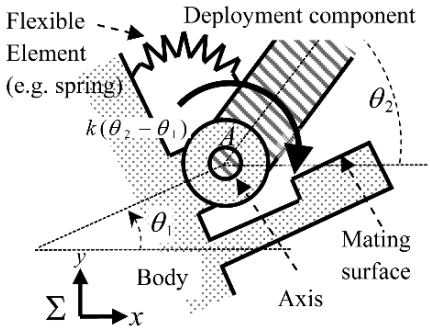

Fig. 3 Non-latched deployment mechanism.

Assumptions

- Body and deployment component is assumed as rigid.
- Body is attached to pinned support at the centre of mass of the body and only rotational motion of satellite is took into account.
- Air resistance is not taken into account for dynamics of the model.
- Frictional force around axis is not taken into account for the model.

The equation of motion of the system is derived by the use of Lagrange's equations as follows:

$$M(q)\ddot{q} + h(q, \dot{q})\dot{q} + Kq = G\tau, \tag{1}$$

where $q = [\theta_1 \ \ \theta_2]^T$ is a generalized coordinate and

$$M(q) = \begin{bmatrix} m_2 l_1^2 + m_3 l_1^2 + I_1 & \frac{m_2 l_1 l_2}{2} \cos(\theta_2 - \theta_1) \\ \frac{m_2 l_1 l_2}{2} \cos(\theta_2 - \theta_1) & \frac{m_2 l_2^2}{4} + I_2 \end{bmatrix}, \tag{2}$$

$$h(q, \dot{q}) = \begin{bmatrix} 0 & -\frac{m_2 l_1 l_2}{2} \sin(\theta_2 - \theta_1)\dot{\theta}_2 \\ \frac{m_2 l_1 l_2}{2} \sin(\theta_2 - \theta_1)\dot{\theta}_1 & 0 \end{bmatrix}, \tag{3}$$

$$K = \begin{bmatrix} k & -k \\ -k & k \end{bmatrix}, \tag{4}$$

$$G = \begin{bmatrix} 1 \\ 0 \end{bmatrix}, \tag{5}$$

and m_2 and m_3 are mass parameters about the deployment mechanism. To represent the dynamics of contact, contact torque λ is introduced into Equation (1) and the equation of motion with λ is given as follows:

$$M(q)\ddot{q} + h(q, \dot{q})\dot{q} + Kq = Gu + W\lambda, \tag{6}$$

where W is a coefficient matrix that transmits the contact torque in the direction of generalized coordinate and satisfies following relation:

$$\ddot{g} = \frac{\partial g}{\partial q}\ddot{q} = W^T \ddot{q}. \tag{7}$$

Here, $g = \theta_2 - \theta_1$ is the relative displacement between contact surfaces.

2.2 Estimation of Contact Torque

For simplicity, Equation (6) can be rewritten as:

$$M\ddot{q} + H = W\lambda, \tag{8}$$

where $H = h\dot{q} + Kq - Gu$.

In the phase of compression, integrating of the equation of motion yields relation about impulse as follows:

$$M(\dot{q}_C - \dot{q}_A) - W\Lambda_C = 0, \tag{9}$$

where $\dot{q}_A$ is the relative angular velocities at t_A when contact begins, $\dot{q}_C$ is that at t_C when the phase of compression ceases and Λ_C is the angular impulse added to the system during the phase of compression. Furthermore, $\dot{q}_A$ and $\dot{q}_C$ are given by:

$$\dot{q}_A = W^{-1}\dot{g}_A, \tag{10}$$

$$\dot{q}_C = W^{-1}\,\dot{g}_C, \tag{11}$$

where $\dot{g}_A$ and $\dot{g}_C$ are relative angular velocity respectively. Substituting formulae (10) and (11) into Equation (9) and transformation give a relation about the phase of compression

$$\dot{g}_C = W^T\,M^{-1}W \cdot \Lambda_C + \dot{g}_A. \tag{12}$$

Additionally, Λ_C and $\dot{g}_C$ can be described by liner complimentary problem

$$(\dot{g}_C \geq 0) \wedge (\Lambda_C \geq 0) \wedge (\dot{g}_C \cdot \Lambda_C = 0). \tag{13}$$

In a similar fashion, relation about the phase of expansion between relative angular velocities and impulse is given by

$$\dot{g}_E = W^T M^{-1} W \Lambda_E + W^T M^{-1} W \varepsilon \Lambda_C + \dot{g}_C, \tag{14}$$

where $\dot{g}_E$ is that at t_E when the phase of expansion ceases and Λ_E is the angular impulse added to the system during the phase of expansion. Additionally, Λ_E and $\dot{g}_E$ can be described by liner complimentary problem

$$(\dot{g}_E \geq 0) \wedge (\Lambda_E \geq 0) \wedge (\dot{g}_E \cdot \Lambda_E = 0). \tag{15}$$

Therefore, the contact torque can be analyzed form Equations (12) to (15) by the use of numerical integral algorithm.

3 Controller Design

The system such as in Figure 2 causes vibratory motion of deployment mechanism including impact phenomenon when the satellite moves, e.g. the movement for attitude control. For example, the body of the satellite begins to rotate clockwise by the torque for attitude control and it causes a relative displacement between deployed element and body of the satellite due to inertia of deployed element, that is, deployment angle $\theta_2 - \theta_1$ has nonzero value. Then, such a value of $\theta_2 - \theta_1$ produces some torque around axis of deployment mechanism and it causes a motion with impacts and bounces at mating surface. Such a motion influences the performance of satellite attitude control. Hence, the control objective is to move the satellite attitude to the desired position promptly with less influence from the motion of deployment component.

To remove the influence of such a motion, cooperative controller of position control and compliance control is applied to the system. Conventional compliance controller requires information about contact force or torque, but it is not so easy to implement the measurement devices of contact torque or force in the system which

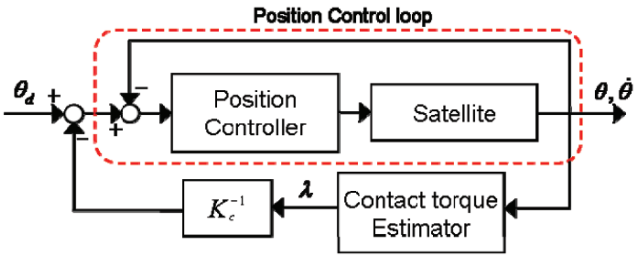

Fig. 4 Block diagram of control system.

has limitation of device mounting and is required reliability. Hence, contact torques for compliance control are estimated from state variable by the use of unilateral contact theory. In this research, the configuration of control system becomes like the one in Figure 4 and it is position-based compliance controller which includes aforementioned estimator.

To apply compliance control, the model represented by Equation (1) is taken into consideration and is transformed into state equation as follows:

$$\dot{X} = A(X) + BU, \tag{16}$$

where $X = [q^T \ \ \dot{q}^T]^T$.

The control input for position control is given by

$$U = -K(X - X_d), \tag{17}$$

where K is the feedback gain, $X_d = [q_d^T \ \ \dot{q}_d^T]^T$ and q_d and $\dot{q}_d$ are desired value of q and $\dot{q}$ respectively. Moreover, $q_d = [\theta_d \ \ \theta_d]^T$ and $\dot{q}_d = [0 \ \ 0]^T$ are set by control objective.

To apply compliance control, θ_d is corrected according to contact torque as follows:

$$\hat{\theta}_d = \theta_d - K_c^{-1} \lambda. \tag{18}$$

Therefore, the closed loop system by compliance control is given by

$$\dot{X} = \bar{A}(X) + \bar{B}(\theta_d - K_c^{-1} \lambda), \tag{19}$$

where $\bar{A}(X) = A(X) - BKX$ and $\bar{B} = BK[I_2 \ \ 0_{2\times 2}]$. is determined based on linear-quadratic regulator which is designed for linearized model around desired configuration and K_c is set as negative value and determined by the results of numerical simulation which satisfies the control objective. Here, this compliance control match to negative compliance control and is different from general compliance control. Note that this research focuses on the validity of combination of compliance control and unilateral contact theory, therefore discussion of negative compliance control is omitted in this paper.

Table 1 Parameters of the model.

	Body	Deployment component
Length[m]	0.10	0.10
Height[m]	0.10	0.80
Width[m]	0.10	0.01
Mass[kg]	1.13	0.21
Moment of Inertia[kgm^2]	0.0028	0.00018
Constant of spring [Nm/rad]		0.1
Coefficient of restitution		0.8

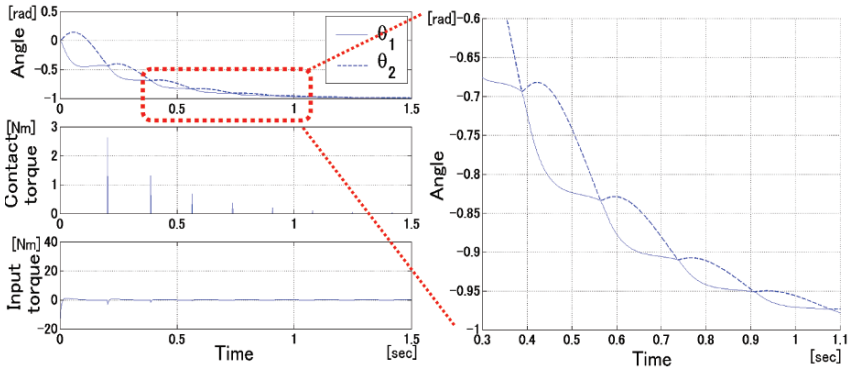

Fig. 5 Angle, contact torque and input torque in the results of PD feedback controller about angle.

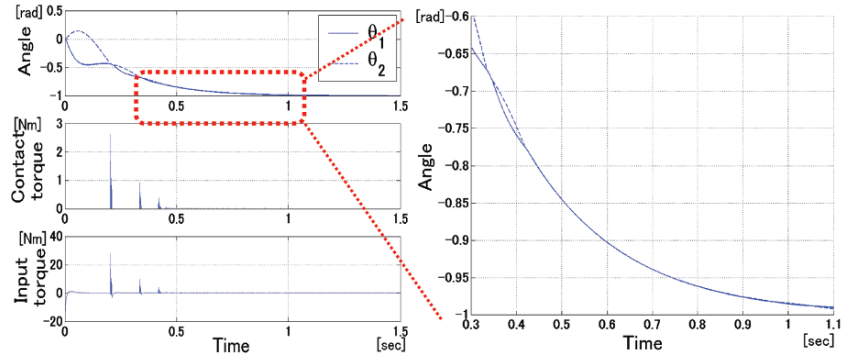

Fig. 6 Angle, contact torque and input torque in the results of proposed controller.

4 Numerical Simulations

To show validity of the proposed method, numerical simulations are carried out. Model parameters for the simulations are defined as in Table 1.

Figure 5 shows the results of numerical simulation for PD feedback controller about each angle and Figure 6 shows results for the proposed controller. Each figure

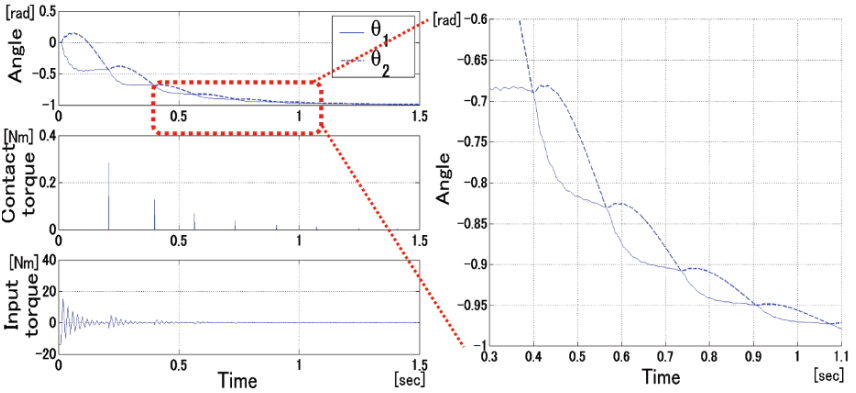

Fig. 7 Results of controller with force sensor in slow control timing.

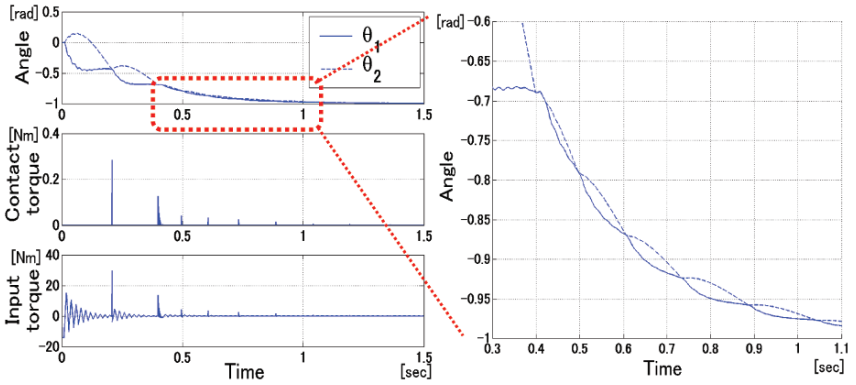

Fig. 8 Results of proposed controller in slow control timing.

on the left shows trajectories of angle θ_1 and θ_2, a contact torque and an input torque. And each figure on the right shows magnified figure of remarkable trajectory of each angle. In both simulations, sampling time of the controller is set to 1 [msec], which is comparatively fast in actual small satellite applications.

As is clear from the result, the proposed controller suppresses bounces of the deployed element and the body of satellite more than the PD controller. Moreover, convergence time of the angles about system with proposed controller state becomes shorter slightly. Contact torque is suppressed by proposed controller. However, maximum value of control input is required more in the proposed method.

As mentioned above, the advantage of utilizing unilateral contact theory for estimating contact torque is the robustness about uncertainty of capturing contact torque. To demonstrate such a feature of the proposed method, two kind of numerical simulations are carried out for the model characterized by the parameter of Table 1. The results of each simulation are shown in Figures 7 and 8 and each figure shows trajectories of θ_1 and θ_2, contact torque and input torque as well as Figures 5

and 6. Figure 7 shows the results of a compliance control which is supposed to capture the data of contact torque by a force sensor and Figure 8 shows the results of the proposed way. In both simulations, sampling time of controller is set to ten times of that of the simulations shown in Figures 5 and 6, that is to say 10 [msec]. By the way, it is supposed that impact motion happens within 1 [msec], which is still longer than the period of actual impact motion. Therefore, it can be said that sampling time of 10 [msec] makes the probability of capturing contact torque data less than 10% of that when controlled in sampling time of 1 [msec]. And this kind of uncertainty is implemented into the simulation shown in Figure 7. As is clear from the results, the deployed element bounces more in the conventional controller than the proposed controller. At the same time, more short cycle bounces of small amplitude happen in the simulation of Figure 8 compared to that of Figure 9. Relatively the result of Figure 8 shows good performance about convergence of the θ_1 and θ_2, hence it can be said that the proposed method have effectiveness compared to conventional one.

Note that the slow (10 times) sampling time changes the characteristic of closed loop system with compliance control and the value of K_c used in the simulations of Figures 5 and 6 become non desirable one. Therefore, new desirable value of K_c is determined by numerical analysis and used for the simulations of Figures 7 and 8.

5 Conclusion

It is shown that the compliance control with the contact torque estimated by unilateral contact theory is effective for the system which consists of flexible and impact dynamics. Moreover, compared to compliance control which use force or torque sensor, the proposed method is not subjected to the difficulties associated with uncertainty of capturing contact torque data. Therefore, it can be said that the proposed method has robustness on the data of contact torque. Furthermore, to apply the method more practically, it is required to discuss the feasibility of calculation process of contact torque estimation and extend the method to the system with multiple non-latched deployment mechanisms which will bring high potential to deployment mechanism for space applications.

References

1. Y. Sugawara, H. Sahara, S. Nakasuka, S. Greenland, T. Morimoto, K. Koyama, C. Kobayashi, H. Kikuchi, T. Okada and H. Tanaka, A satellite for demonstration of Panel Extension Satellite (PETSAT), IAC-07-B4.07.01, Paper presented at 58th International Astronautical Congress, Hyderabad, India (2007).
2. Y. Sugawara, S. Nakasuka, K. Higashi, C. Kobayashi, K. Koyama and T. Okada, Structure and thermal control of Panel Extension Satellite (PETSAT), IAC-06-B5.7.08, Paper presented at 57th International Astronautical Congress, Valencia, Spain (2006).
3. J.K. Salisbury, Active stiffness control of a manipulator in Cartesian coordinates, in *Proceedings of the IEEE Conference on Decision and Control* (1980).
4. F. Pfeiffer and C. Glocker, *Multibody Dynamics with Unilateral Contacts*, Wiley-Interscience.

A Study on Locomotion Stability by Controling Joint Stiffness of Biped Robot with Pneumatic Actuators

K. Tsujita, T. Inoura, T. Kobayashi and T. Masuda

Abstract The development of an oscillator controller for a biped robot with antagonistic pairs of pneumatic actuators is reported. Periodic motions of the legs switch between the swinging and supporting stages based on the phase of the oscillators. The oscillators receive touch sensor signals at the end of the legs as feedback when the leg touches the ground and compose a steady limit cycle of the total periodic dynamics of biped locomotion. Using this control system, relationship between muscle tone and locomotion performance is investigated. The result shows that there is an appropriate joint stiffness to keep the stable locomotion as well as rhythmic input at actuator with state reset. Numerical simulations and hardware experiments are implemented to verify the locomotion performance.

1 Introduction

Locomotion is an important function of mobility. Human bipedal locomotion is especially mobile and adaptable to variations in the environment. There has been a lot of research on bipedal robots driven by DC rotary actuators with local position feedback controls. However, most of them consume a lot of energy and their knees are always bent because they are based on high-gain position control of the joints with inverse kinematics for given trajectories of the legs. This type of robot cannot utilize its own dynamics for good energy efficiency or adaptive adjustment of physical properties of the body mechanism during locomotion. Furthermore, DC rotary actuators have serious difficulties in maintaining their power-weight ratios, which

K. Tsujita and T. Masuda
Osaka Institute of Technology, Ohmiya 5-16-1, Asahi-ku, Osaka 535-8585, Japan;
E-mail: tsujita@ee.oit.ac.jp

T. Inoura and T. Kobayashi
Graduate School of Engineering, Osaka Institute of Technology, Ohmiya 5-16-1, Asahi-ku, Osaka 535-8585, Japan

H. Ulbrich and L. Ginzinger (eds.), Motion and Vibration Control, 305–314.

limits the functions of the robots' mobility. Leg motions in bipedal locomotion have two essential stages. One is the swinging stage and the other is the supporting stage. In the swinging stage, the actuator forces are relaxed; the joints become less stiff and more passive. In the supporting stage, stiffness of the joints increases due to forces generated by the antagonistic pair of actuators. By controlling and tuning the stiffness of the joints through the balanced adjustment of the generated force of such a pair of actuators, the robot is expected to become more adaptive to variations in the environment and in the surface of the ground.

This article reports the development of an oscillator controller for bipedal robots with antagonistic pairs of pneumatic actuators as well as study on relationship between muscle tone and locomotion performance using the proposed control system. In the proposed controller, nonlinear oscillators are assigned to each joint. Periodic motions of the legs are switched between the swinging and supporting stages based on the phase of the oscillators. Oscillators contain network architecture, interact mutually with each other, and receive touch sensor signals as feedback signals at the end of the legs when the leg touches the ground in the purpose of phase resetting of the oscillator. These dynamic interactions make possible mutual entrainments between oscillators and create a steady limit cycle of the total periodic dynamics of bipedal locomotion.

By using this control system, the relationship between muscle tone and locomotion performance is investigated. The result shows that there is an appropriate joint stiffness to keep the stable locomotion as well as rhythmic input at actuator with state reset. Numerical simulations and hardware experiments are implemented to verify the locomotion performance.

2 Model

Figure 1 is a schematic model of a planar bipedal robot. The robot has two legs, composed of two links, and a main body. The contact model at the end of the leg assumes one point of support. The motion of the robot is restricted to the sagittal plane, i.e. it is assumed to be in 2D motion. The supporting and swinging legs are numbered 1 and 2, respectively. The position vector from the origin of the inertial coordinate to the center of mass (C.M.) of the main body is defined as $r_0 = (r_{0x}, r_{0y})^T$.

The rotational angle of the main body and each link of the legs are defined as shown in Figure 1.

The state variable is defined as follows:

$$z = \left[r_{0x}\ r_{0y}\ \theta_0\ \theta_1^{(1)}\ \theta_2^{(1)}\ \theta_1^{(2)}\ \theta_2^{(2)} \right]^T \tag{1}$$

Equations of motion for state variable z are derived as:

$$M\ddot{z} + H = G + \tau + E\lambda \tag{2}$$

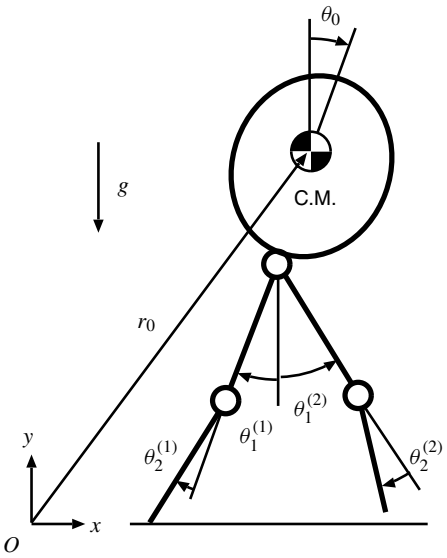

Fig. 1 Schematic model of a bipedal robot.

where M, H, G, and E are inertia matrix, nonlinear term, gravity term, and Jacobian matrix, respectively. λ is the reaction force at the contact point of the supporting leg. Vector τ is composed of the input torques at the rotational joints of the legs $\tau_j^{(i)}$, $i = 1, 2$, $j = 1, 2$, which are generated by the antagonistic pairs of pneumatic actuators

$$\tau = \left[0\ 0\ 0\ \tau_1^{(1)}\ \tau_2^{(1)}\ \tau_1^{(2)}\ \tau_2^{(2)} \right]^T \tag{3}$$

Actuator torque τ depends on the air pressure supplied and On/Off timing of the air supply valves.

3 Control Scheme

Figure 2 shows the control scheme of the proposed system. The controller has a nonlinear oscillator network with individual oscillators assigned to joints. The antagonistic pairs of pneumatic actuators are driven by timing signals as functions of the oscillator phases. The contact sensor signals are feedback for the oscillator network. These dynamic interactions cause the entrainment and generate a stable limit cycle for locomotion. With the oscillator phase defined as $\phi_m^{(k)}$ $(k, m = 1, 2)$, the oscillator network can be expressed in the following equations:

$$\begin{aligned} z_m^{(k)} &= \exp(j\phi_m^{(k)}) \qquad j : \text{Imaginary unit} \\ \dot{\phi}_m^{(k)} &= \omega + K(\phi_m^{(l)} - \phi_m^{(k)} - \gamma_{lk}) \end{aligned} \tag{4}$$

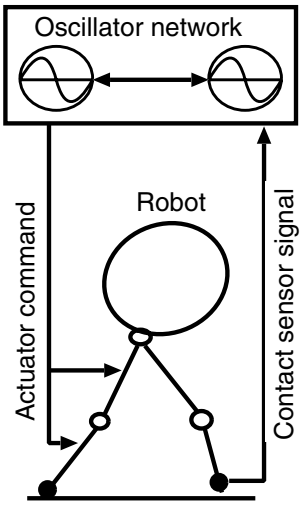

Fig. 2 System architecture.

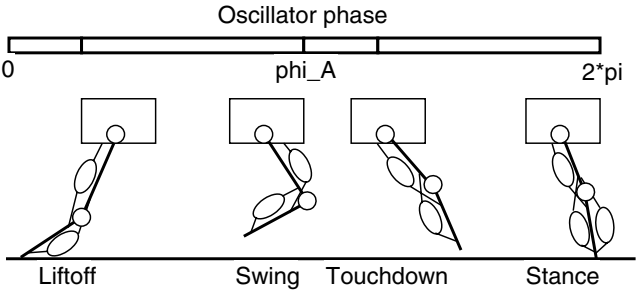

Fig. 3 Actuation sequence.

$$+\delta(\phi_{Ak} - \phi_m^{(k)}) \tag{5}$$

$$\gamma_{12} = -\gamma_{21} = \pi \tag{6}$$

$$T_{mn}^{(k)} = f(\phi_m^{(k)}) \tag{7}$$

where K is constant number and ϕ_{Ak} is the nominal value of oscillator k's phase at the moment of leg k's contact with the ground (i.e. touch down moment in fig. 3). δ is the impulsive function. γ_{lk} is the nominal phase difference between oscillators l and k. $T_{mn}^{(k)}$ is the On/Off timing of the air valve of actuator n (n = extensor or flexor) of joint m of leg k and is given as a function of the oscillator phase. In concrete the actuators are driven for the motion sequence in the locomotion, as shown in Figure 3. In Figure 3 illustrated actuators are actively shrinking according to the supplied air pressure which are controlled in Eq. (7). The motion primitives in Figure 3 are following the idea of Ekeberg and Pearson [18].

Table 1 Physical parameters of robot.

Length of body	0.20 [m]
Length of thigh (between joints)	0.25 [m]
Length of shank (between joint and toe)	0.25 [m]
Total height	0.70 [m]
Mass of body	1.32 [kg]
Mass of thigh	0.59 [kg]
Mass of shank	0.47 [kg]
Total mass	3.44 [kg]

On the other hand, the muscle tone at the thigh actuators are voluntarily controlled during to investigate the relationship it and locomotion performance. The stiffness of the thigh joint is controlled during locomotion by controlling the antagonistic pairs of actuators as follows:

$$T_{1n}^{(k)} = Q(\alpha, \hat{\phi}_{Ak}) \tag{8}$$

where $T_{1n}^{(k)}$ ($n =$ flexor, extensor) is the stiffness of the thigh actuators. α is the time length for air-supplying to the actuators and it is the tuning parameter. This tones controller changes the stiffness of the joints at the thigh according to the parameter α.

4 Numerical Simulations

Table 1 shows the physical parameters of the robot.

Figure 4 shows the actual cycle durations when the nominal time periods for the oscillators are changed during locomotion. The x and y axes are the nominal and actual time periods of the walking cycle, respectively. From this result, we may note that the system has a considerable capability of self-adaptation to variance of walking speed, and results in wide basin of attraction.

Figure 5 shows the stability of the bipedal walk, the norm of eigenvalues of matrix M associated with the fixed point of the Poincaré map, $X(r) \in R^{10}$, $X(r+1) = MX(r)$, r is the number of intersection of Poincaré section. From this figure, the norm of all the eigenvalues are smaller than one, i.e. the system is stable, and the deviations of them according to the variance of the time period of walk are so small. These results show that the system can continue stable locomotion over various lengths of time. This means the system has a considerably wide basin of attraction for limit cycle.

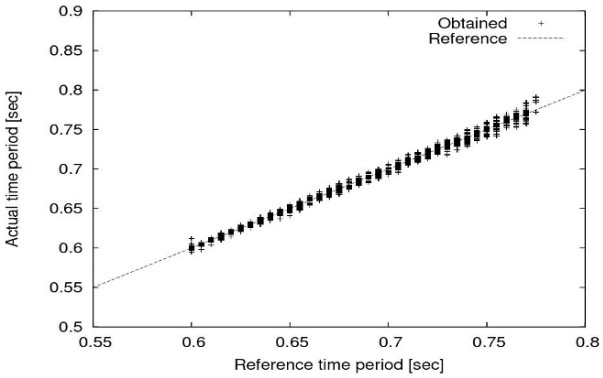

Fig. 4 Walking cycle duration at variable reference.

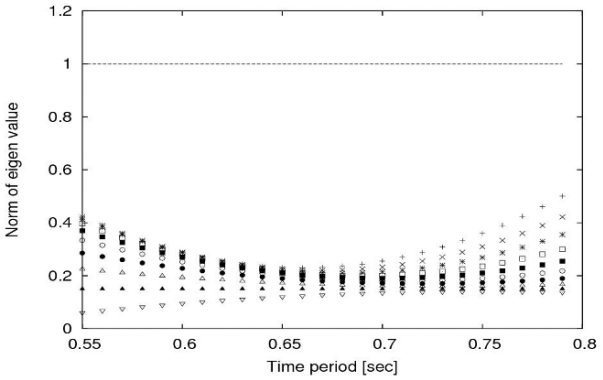

Fig. 5 Norm of eigenvalues of Poincaré map.

5 Hardware Experiments

We performed a walking experiment using the robot shown in Figure 6. The model robot has three legs, two side legs and one middle leg. The two side legs are connected to each other with a connection rod, and the motion of each side leg is the same. This mechanism ensures that the motion of the robot is restricted to the sagittal plane.

Figure 7 illustrates the architecture of the experimental setup. The host computer electrically controls the air valves. The contact signal from the touch sensor is input to the host computer through an A/D converter. The air pressure is adjusted to 0.5 [MPa].

Figure 8 shows the snapshots of the robot in bipedal walk. In the figure, numbers under the photographs indicate the time order. In this case, the robot stably walked on a treadmill. There was no large deviations nor perturbations during walking.

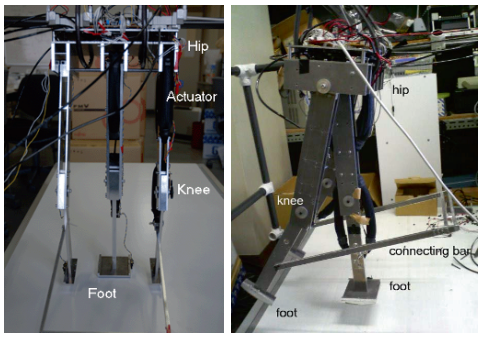

Front view Side view

Fig. 6 Robot hardware.

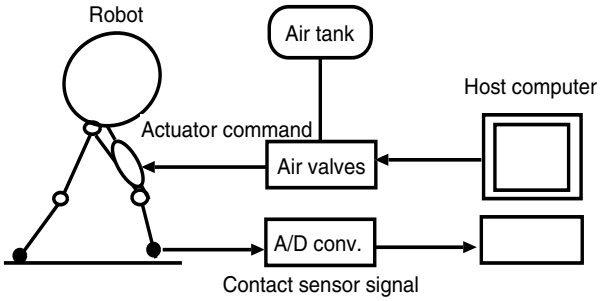

Fig. 7 Architecture of hardware setup.

These results of hardware experiments indicate the efficiency of the developed system.

Figure 9 shows relationship between joint stiffness and walking time period for biped robot and quadruped robot. From this figure, we can find that there is an appropriate joint stiffness for stable locomotion. If the joint stiffness is too high, the walking time period comes shorter and becomes unstable. To the contrary, from Figure 10, we can find that if the joint stiffness is not enough to support the body, the deviation of the walking time period increases to diverge, and becomes unstable finally. These phenomena are resemble to the motor disorder of human locomotion. This fact shows that there is an optimal joint stiffness for stable locomotion and adaptive behavior in locomotion. Therefore, it is one way to control the joint stiffness according to the locomotion condition to make it more and more adaptive and robust to the change of environment or situations.

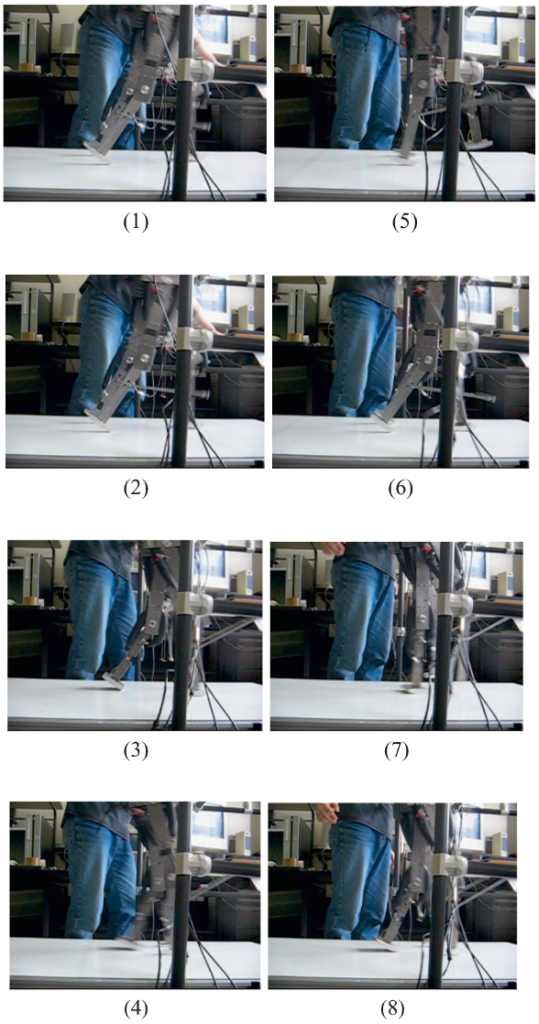

Fig. 8 Snapshots of the bipedal walking: numbers under the photographs indicate the time order.

6 Summary

We developed a bipedal robot with antagonistic pairs of pneumatic actuators controlled by a nonlinear oscillator network. Periodic motions of the legs are switched between the swinging and supporting stages based on the phase of the oscillators. The oscillators receive touch sensor signals at the end of the legs as feedback when the leg touches the ground and compose a steady limit cycle of the total periodic dynamics of bipedal locomotion.

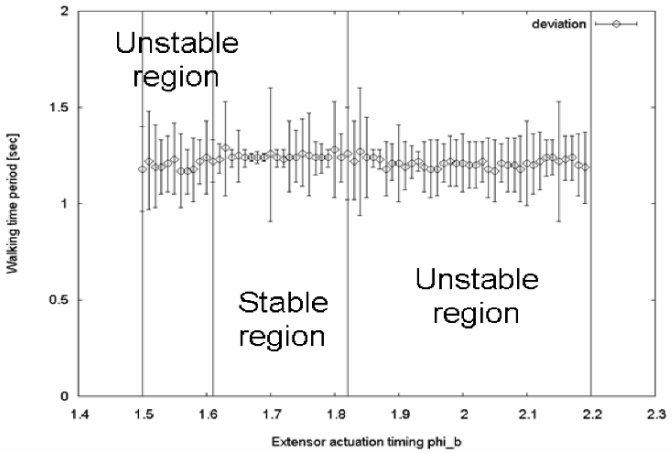

Fig. 9 Locomotion stability vs joint stiffness.

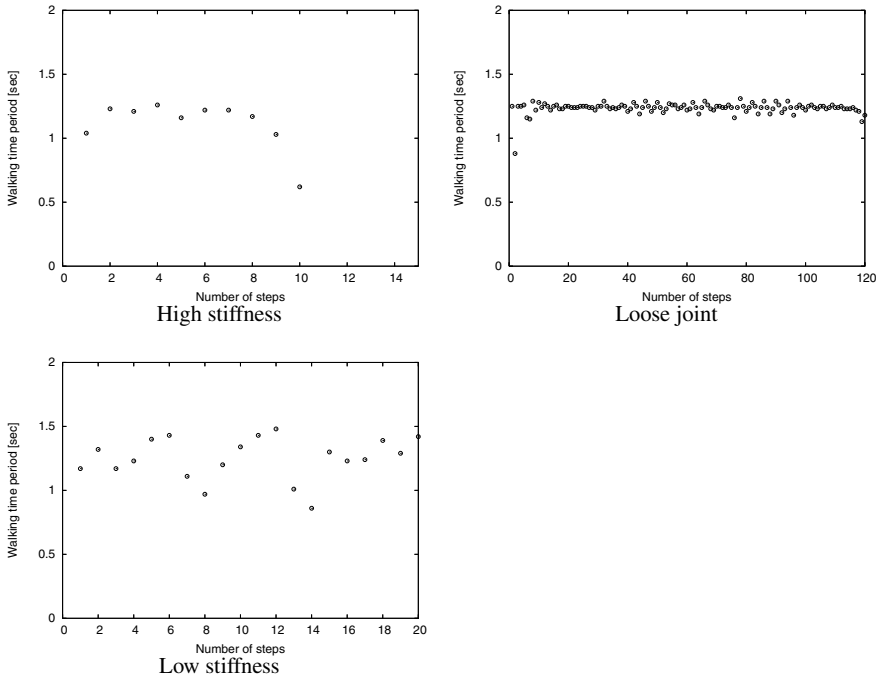

Fig. 10 Time period of walking cycle.

Acknowledgements This work has been partially supported by a Grant-in-Aid for Scientific Research on Priority Areas "Emergence of Adaptive Motor Function through Interaction between Body, Brain and Environment" from the Japanese Ministry of Education, Culture, Sports and Technology.

References

1. S. Aoi and K. Tsuchiya: Stability Analysis of a Simple Walking Model Driven by an Oscillator with a Phase Reset Using Sensory Feedback. *IEEE Trans. Robotics* **22**(2), 391–397 (2006).
2. D.G. Caldwell, N. Tsagarakis, D. Badihi and G.A. Medrano-Cerda: Pneumatic Muscle Actuator Technology: A Lightweight Power System for a Humanoid Robot. In: *Proc. of IEEE ICRA 1998*, pp. 3035–3058 (1998).
3. D.G. Caldwell, G.A. Medrano-Cerda and M.J. Goodwin: Control of Pneumatic Muscle Actuators. *IEEE Control Systems Magazine* **15**(1), 40–48 (1995).
4. S. Collins, A. Ruina, R. Tedrake and M. Wisse: Efficient Bipedal Robots Based on Passive-Dynamic Walkers. *Science* **307**, 1082–1085 (2005).
5. S.T. Davis and D.G. Caldwell: The Bio-mimetic Design of a Robot Primate using pneumatic Muscle Actuators. In: *Proc. of CLAWAR 2001*, pp. 197–204 (2001).
6. R.J. Full: Biological Inspiration: Lessons from Many-Legged Locomotors. *International Journal of Robotics Research* **9**, 337–341 (2000).
7. S. Grillner: Locomotion in Vertebrates: Central Mechanisms and Reflex Interaction. *Physiological Review* **55**, 367–371 (1977).
8. S. Grillner: Neurobiological Bases of Rhythmic Motor Acts in Vertebrates. *Science* **228**, 143–149 (1985).
9. K. Hosoda, T. Takuma and M. Ishikawa: Design and Control of a 3D Biped Robot Actuated by Antagonistic Pairs of Pneumatic Muscles. In: *Proc. of the 3rd Int. Conf. of Adaptive Motion of Animals and Machines*, (2005).
10. K. Inoue: Rubbertuators and Applications for Robotics. In: *Proc. of the 4th International Symposium on Robotics Research*, pp. 57–63 (1987).
11. R.Q. Linde: Design, Analysis and Control of a Low Power Joint for Walking Robots, by Phasic Activation of McKibben Muscles. *IEEE Trans. Robotics and Automation* **15**(4), 599–604 (1999).
12. T. McGeer: Passive Dynamic Walking. *International Journal of Robotics Research* **9**(2), 62–82 (1990).
13. K. Ono and X. Yao: Simulation Study of Self-Excited Walking of a Biped Mechanism with Bent Knee. In: *Proc. of Adaptive Motion of Animals and Machines 2005*, pp. 131–142 (2005).
14. M. Ozkan, K. Inoue, K. Negishi and T. Yamanaka: Defining a Neural Network Controller Structure for a Rubbertuator Robot. *Neural Networks* **13**(4–5), 533–544 (2000).
15. H.F. Schulte: The Characteristics of the McKibben Artificial Muscle. The Application of External Power in Prosthetics and Orthotics, Publication 874, National Academy of Sciences, National Research Council, Washington DC, Appendix H, pp. 94–115 (1961).
16. Y. Sugimoto and K. Osuka: Walking Control of Quasi-Passive-Dynamic-Walking Robot 'Quartet III' Based on Delayed feedback Control. In: *Proc. of 5th CLAWAR*, pp. 123–130 (2002).
17. G. Taga: A Model of the Neuro-Musculo-Skeletal System for Human Locomotion: I. Emergence of Basic Gait. *Biol. Cybern.* **73**, 97–111 (1995).
18. Ö. Ekeberg and K. Pearson: Computer Simulation of Stepping in the Hind Legs of the Cat: An Examination of Mechanisms Regulating the Stance-to-Swing Transition, *J. Neurophysiol.* **94**, 4256–4268 (2005).
19. B. Tondu, V. Boitier and P. Lopez: Naturally Compliant Robot-Arms Actuated by McKibben Artificial Muscles. In: *Proc. of 1994 IEEE International Conference on Systems, Man, and Cybernetics*, Vol. 3, pp. 2635–2640 (1994).
20. K. Tsujita, T. Inoura, A. Morioka, K. Nakatani, K. Suzuki and T. Masuda: Oscillator-Controlled Bipedal Walk with Pneumatic Actuators. In: *Proc. of MOVIC 2006*, pp. 670–675 (2006).
21. B. Verrelst et al.: The Pneumatic Biped "Lucy" Actuated with Pleated Pneumatic Artificial Muscles. *Autonomous Robots* **18**(2), 201–213 (2005).
22. M. Wisse and J. Frankenhuyzen: Design and Construction of MIKE; a 2-D Autonomous Biped Based on Passive Dynamic Walking. In: *Proc. of Adaptive Motion of Animals and Machines 2005*, pp. 143–154 (2005).

Mechatronic Design of Hard-Mount Concepts for Precision Equipment

J. van Dijk

Abstract The contribution of the paper is on the conceptual design of mounts, using MiMo state space models describing the spatial flexible multibody system dynamics. Furthermore the contribution is on the evaluation of acceleration feedback versus force-feedback of a hard-mounted metrology frame suspension of a photolithography machine. It includes the modal decoupling controller design. It will be shown that from a vibration energy flow point of view the use of acceleration sensors are preferred.

1 Introduction

The paper deals with the mechatronic design of hard-mounts for vibration isolation in precision equipment. The contribution of the paper is on conceptual design using adequate MiMo state space models describing the spatial system dynamics and the evaluation of acceleration feedback versus force-feedback. The conceptual design, including the modal decoupling controller design, for mounts for a metrology frame suspension of a lithography machine (waver-stepper) is outlined.

Usually precision equipment is mounted on soft-mounts to provide disturbance rejection from base vibrations. For this purpose the suspension resonance frequencies are designed to be low (1 Hz). However, the use of soft-mounts may lead to dynamic instability for equipment with a relatively high center of gravity [1]. Another approach is to use hard-mounts [2]. They provide a stiffer support and as a consequence the suspension resonance frequencies are increased (10–20 Hz). In the case of hardmounts the transmissibility of base vibrations is actively reduced, using sensors, actuators and a control system.

J. van Dijk
Mech. Automation and Mechatronics Laboratory, Faculty of Engineering Technology, University of Twente, Enschede, The Netherlands; E-mail: j.vandijk@ctw.utwente.nl

H. Ulbrich and L. Ginzinger (eds.), Motion and Vibration Control, 315–324.

The metrology frame provides the support for the optical device (lens). The lens and the frame are considered rigid in the frequency region of interest (0–300 Hz). But due to the their flexible connection the frame-lens combination has internal modes in the region 80–100 Hz [3]. The idea is to design a hybrid-elastic mount with a high stiffness (typically 200–400× higher than for pneumatic isolators). The hard-mount concept discussed is based on an elastic structure and includes per mount 2 piezo-actuators. Three mounts will be used to support the metrology frame.

For evaluation of conceptual designs it is important to model the spatial system dynamics of the equipment and to obtain Multiple input and Multiple output transfer-matrices or state space descriptions. To obtain these MiMo models can be a tedious task [1]. The multibody system approach is a well-suited method to model the spatial dynamic behavior. In this approach the mechanical components are considered as rigid or flexible bodies that interact with each other through a variety of connections such as hinges and flexible coupling elements.

An implementation of this method is realized in the program `SPACAR` [4], [5] which has an interface to `MATLAB`. The method to obtain state space descriptions with this program is based on a nonlinear finite element description for multibody systems and accounts for geometric nonlinear effects of flexible elements due to axial and transverse displacements. This modelling approach is applied to the described setup in Section 2.

In Section 3 we evaluate the transmissibility from base-vibrations to internal mode excitation. This is not common, but this is the effective transmissibility that can jeopardize the accuracy of the device. In Section 4 the controller design based on modal decoupling is described. In Section 5 we evaluate, using the obtained MiMo state space models, the pros and cons of force feedback as well as acceleration feedback. It will be shown that from a vibration energy flow point of view acceleration sensors are preferred despite the fact that with these type of sensors co-located control is not guaranteed [6]. Therefore, this conclusion is contradictive to the conclusion drawn by Preumont et al. [6] but is drawn from a different viewpoint. It will also be shown that force sensors can be used if special specifications of the mechanical structure of the mounts are realized.

2 Modelling

Structural systems have dynamics which in linearized form can be described by ordinary differential equations of the following form:

$$M\ddot{\boldsymbol{q}} + D\dot{\boldsymbol{q}} + K\boldsymbol{q} = \boldsymbol{f} \tag{1}$$

where M, D and K are the usual mass, damping and stiffness matrix, $\boldsymbol{f}$ is the vector of applied generalized forces. The vector $\boldsymbol{q}$ is used to denote the generalized displacement vector or degrees of freedom. In [5] it is shown that in case of driving terms which are not solely forces but are also rheonomic displacements or their time

Table 1 Inertia properties of the frame and lens and equivalent stiffness properties of a leg.

	Mass [kg]	I_{xx} [kg/m^2]	I_{yy} [kg/m^2]	I_{zz} [kg/m^2]
frame	742	52.25	52.25	104.5
lens	851.6	72.95	72.95	49.15
length m	long. stiffn.	bend. stiffn. y	bend. stiffn. z	torsional stiffn.
0.283	$8.389 \cdot 10^6$ N/m	371 Nm	371 Nm	5.84Nm

derivatives, (1) changes to the form:

$$M_d \cdot \ddot{\boldsymbol{q}}_d + D_d \cdot \dot{\boldsymbol{q}}_d + K_d \cdot \boldsymbol{q}_d = -M_r \cdot \ddot{\boldsymbol{q}}_r + B_0 \cdot \sigma_a \tag{2}$$

where M_d, D_d and K_d are the mass, damping and stiffness matrix corresponding with the degrees of freedom $\boldsymbol{q}_d$ and M_r is the mass-matrix corresponding with the rheonomic degrees of freedom $\boldsymbol{q}_r$. B_0 describes the location of the actuator-forces σ_a with respect to the degrees of freedom. The restriction at (2) is that the degrees of freedom $\boldsymbol{q}_d$ are chosen as a vector of relative displacements.

The control theory uses often systems of first-order differential equations written in state space form:

$$\dot{\boldsymbol{x}} = A \cdot \boldsymbol{x} + B \cdot \boldsymbol{u} \tag{3}$$

$$\boldsymbol{y} = C \cdot \boldsymbol{x} + D \cdot \boldsymbol{u} \tag{4}$$

$$u = H \cdot y \tag{5}$$

where $\boldsymbol{y}$ is the vector of sensor output signals, C is the output matrix and D the feed-through matrix. The vector $\boldsymbol{x}$ is called the state-vector. Output feedback is described by (5), where H is a frequency dependent gain matrix to satisfy some performance. The relationship between the physical coordinate description given by (2) and the state equations (3) is:

$$A = \begin{bmatrix} \boldsymbol{O} & \boldsymbol{I} \\ -M_d^{-1} K_d & -M_d^{-1} D_d \end{bmatrix}, B = \begin{bmatrix} \boldsymbol{O} \\ M_d^{-1}[-M_r, B_0] \end{bmatrix}, \boldsymbol{x} = \begin{bmatrix} \boldsymbol{q}_d \\ \dot{\boldsymbol{q}}_d \end{bmatrix}, \boldsymbol{u} = \begin{bmatrix} \sigma_a \\ \ddot{\boldsymbol{q}}_r \end{bmatrix} \tag{6}$$

where $-M_d^{-1} M_r = T_u$ is a coordinate transformation.

Based on the extended representation as in (2), state space descriptions of the metrology frame for analyses and active vibration control will be obtained using a flexible multibody system approach as described in [5]. Table 1 gives an overview of the inertia properties of the frame and lens. The moments of inertia I_{xx}, I_{yy} and I_{zz} are defined with respect to the center of gravity of the frame and lens respectively.

The frame is supported by mounts. Each mount consists of two legs which will be modelled by simple flexible beam like structures. These flexible beams represent the equivalent stiffness properties of the mount. The beam element is modelled as an active element which provides for the passive elastic properties of the leg and the

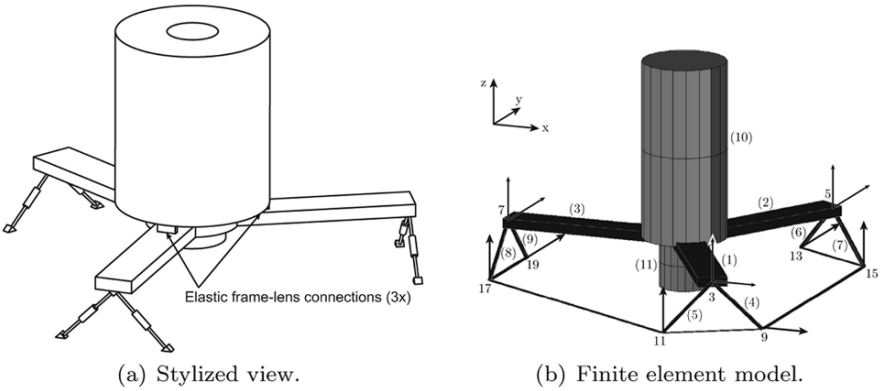

(a) Stylized view. (b) Finite element model.

Fig. 1 Stylized view and FEM-model using beams of lens suspension frame of a wafer stepper/scanner.

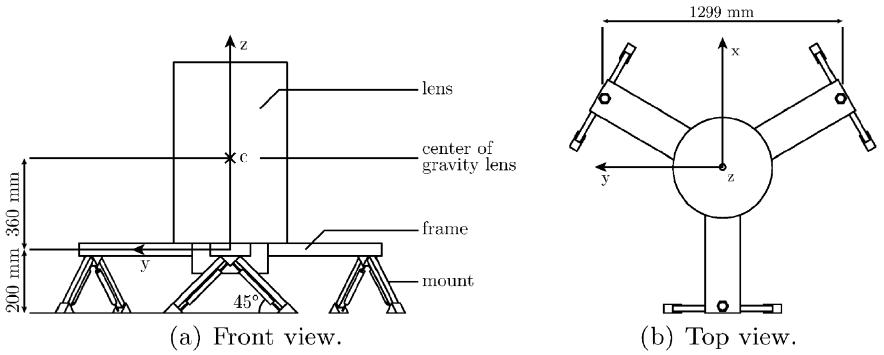

(a) Front view. (b) Top view.

Fig. 2 Front and top view of the metrology frame.

longitudinal force of the piezo actuator. Table 1 shows the stiffness properties of the elastic beam elements.

The metrology frame is modelled using 20 spatial beam elements numbered (1) to (20) and hereafter simply called beams, see Figure 1(b). The beams (1), (2), (3), (12), (13), (14) represent the frame. The beams (10) and (11) represent the lens. The connection between frame and lens is modelled using 6 beams, beams (15), (16), (17), (18),(19) and (20). Beam-elements (1), (2), (3), (10) (11), (12), (13), (14), (18), (19) and (20) are rigid. The inertia properties of the rigid beams match the inertia properties of frame and lens as in Table 1. Beams (4), (5), (6), (7), (8) and (9) represent the active-elastic beams of the mounts and beams (15), (16) and (17) represent the flexible connection blocks between frame and lens. All flexible beams are considered mass-less with respect to the heavy frame and lens.

As dynamic degrees of freedom we choose the longitudinal deformations of the suspension beams constituting the legs ($\boldsymbol{q}_s$) and the deformations of one element

representing a flexible connection blocks ($\boldsymbol{q}_i$) i.e.

$$\boldsymbol{q}_d = \left[e_1^{(4)}, e_1^{(5)}, e_1^{(6)}, e_1^{(7)}, e_1^{(8)}, e_1^{(9)}, e_1^{(15)}, e_2^{(15)}, e_3^{(15)}, e_4^{(15)}, e_5^{(15)}, e_6^{(15)}\right]^T \tag{7}$$

where the numbers between the brackets denote the element numbers and the subscripts denote the deformation direction.

The base is modelled as a rigid body configuration built-up by means of rigid beam elements. Because we are interested in the open loop and later on also in the closed loop transfer functions between base vibration and frame vibrations, the base excitations are defined as rheonomic accelerations applied at the nodal points between legs and base as shown in Figure 1(b). They are defined by the input vector (8), where the superscript numbers represent the associated node numbers, see Figure 1(b).

$$\boldsymbol{u}^{(\text{floor})} = \left[\ddot{x}^9, \ddot{z}^{11}, \ddot{y}^{13}, \ddot{z}^{15}, \ddot{z}^{17}, \ddot{y}^{19}\right]^T, \tag{8}$$

$$\boldsymbol{u}^{(\text{actuator})} = \left[\sigma_a^{(4)}, \sigma_a^{(5)}, \sigma_a^{(6)}, \sigma_a^{(7)}, \sigma_a^{(8)}, \sigma_a^{(9)}\right]^T. \tag{9}$$

$$\boldsymbol{y}^{(\text{frame-lens})} = \left[\ddot{e}_1^{(15)}, \ddot{e}_2^{(15)}, \ddot{e}_3^{(15)}, \ddot{e}_4^{(15)}, \ddot{e}_5^{(15)}, \ddot{e}_6^{(15)}\right]^T \tag{10}$$

$$\boldsymbol{y}^{(\text{force})} = \left[\sigma_1^{(4)}, \sigma_1^{(5)}, \sigma_1^{(6)}, \sigma_1^{(7)}, \sigma_1^{(8)}, \sigma_1^{(9)}\right]^T \tag{11}$$

$$\boldsymbol{y}^{(\text{frame})} = \left[\ddot{x}^3, \ddot{z}^3, \ddot{y}^5, \ddot{z}^5, \ddot{z}^7, \ddot{y}^7\right]^T \tag{12}$$

The input vector of actuator forces, associated with the active beams numbered (4)–(9) are defined by (9).

The outputs are defined in two parts as well. The first part contains the output-signals of so-called virtual performance acceleration sensors which measure the relative acceleration between lens and frame in element number (15). These accelerations are included in the output vector as described by (10). The second part contains the feedback sensors. Which are in the case of force-control the outputs of force sensors described by (11). These sensors measure the longitudinal stress resultant $\sigma_1^{(k)}$ of the elastic beams, i.e. the actuator forces summed with the normal forces due to the elongation of the elastic beams. In the case of acceleration feedback control they are the accelerations of the frame in the nodal points 3, 5 and 7. The feedback accelerations are included in the output vector (12).

3 Mode-Shape and Singular Value Analyses of the Model

Figure 3 shows the result of the mode-shape analysis. The figure shows the shapes and corresponding frequencies of the suspension modes in which the lens and frame behave as a rigid body. From Figure 3 it can be concluded that the fourth, fifth and

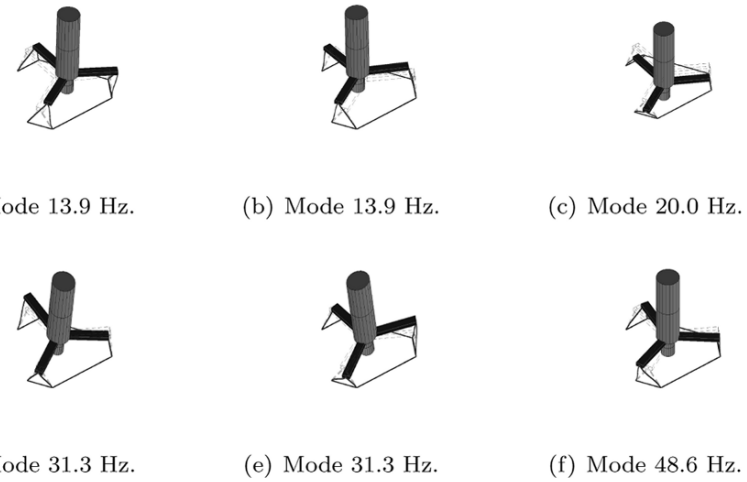

(a) Mode 13.9 Hz. (b) Mode 13.9 Hz. (c) Mode 20.0 Hz.

(d) Mode 31.3 Hz. (e) Mode 31.3 Hz. (f) Mode 48.6 Hz.

Fig. 3 Mode shapes and natural frequencies of the suspension modes.

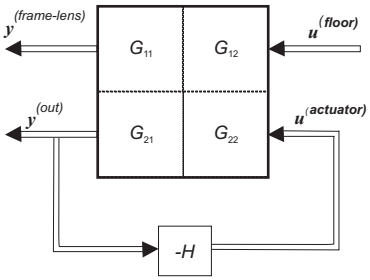

Fig. 4 Generalised plant $\boldsymbol{G}$ with 12 inputs and 12 outputs and controller $\boldsymbol{C}$ with 6 inputs and 6 outputs.

sixth mode are two high frequent. It takes quite some actuator force to bring these modes back to 1 Hz in the closed loop (active) case. As a consequence one has to design the lens-support frame with a smaller basis. The consequence of a smaller basis is a decrease in tilt- and torsional stiffness.

Figure 4 shows the 12×12 generalised plant $\boldsymbol{G}$ with the in- and output vectors defined by Eqs. (8) to (12). Matrix $\boldsymbol{G}$ is partitioned in four transfer matrices $\boldsymbol{G}_{11}, \boldsymbol{G}_{12}, \boldsymbol{G}_{21}$ and $\boldsymbol{G}_{22}$. Of interest are the singular values of the open loop transfer matrix $\boldsymbol{G}_{11}$ between base accelerations and the performance accelerations. The singular values represent the principle gains of the transfer matrix. Especially the largest singular value is important because it shows the worst-case gain frequency relationship between an input and an output vector of the given input and output set. Therefore, in the open loop case this largest singular value gives an impression of the passive vibration isolation. Figure 5(a) shows the largest singular value versus frequency (solid line) of the transfer function $\boldsymbol{G}_{11}$. From this figure we can conclude

that in the frequency region of the internal modes the transmissibility is close to one. Assuming the base vibrations as white noise, Figure 5(a) indicates that the internal modes are excited by the base vibrations.

4 Controller Design

In order to provide isolation of base vibrations from 1 Hz and beyond and to provide sufficient artificial damping of the suspension modes additional control forces $\boldsymbol{u}^{(\text{actuator})}$ are applied. These forces are computed on the basis of six accelerations, defined in $y^{(\text{frame})}$ (12), or force output signals $y^{(\text{force})}$ (11). The control strategy is to combine proportional and integral feedback. This is equivalent with adding virtual mass, which lowers the frequencies of the suspension modes and adding artificial damping respectively.

The assumptions are the following. The system is considered rigid (no internal modes) for the control design. Then there are 6 modelled modes. $n = 6$ *relative* degrees of freedom ($\boldsymbol{q}_s = [e_1^{(4)}, e_1^{(5)}, e_1^{(6)}, e_1^{(7)}, e_1^{(8)}, e_1^{(9)}]^T$) have been chosen for modelling. Demping can be neglected. The equations of motion (2) are then written as:

$$M_d \cdot \ddot{\boldsymbol{q}}_s + K_d \cdot \boldsymbol{q}_s = -M_r \cdot \ddot{\boldsymbol{q}}_r + B_0 \cdot \sigma_a \tag{13}$$

First we use proportional acceleration and integral acceleration feedback.

$$\sigma_a = -K_a \cdot y^{(\text{frame})} - K_v \cdot \dot{Y} \tag{14}$$

in which $\dot{Y}$ is the integral of the n accelerometer outputs ($y^{(\text{frame})}$). Equation (14) can be rewritten as:

$$\begin{aligned} \sigma_a &= -K_a \cdot T_c \cdot \ddot{\boldsymbol{q}}_s - K_v \cdot T_c \cdot \dot{\boldsymbol{q}}_s \\ &= -K'_a \cdot \ddot{\boldsymbol{q}}_s - K'_v \cdot \dot{\boldsymbol{q}}_s \end{aligned} \tag{15}$$

in which T_c is some constant geometrical transformation between the degrees of freedom $\boldsymbol{q}_s$ and the positions Y of the accelerometers. Substitution of (15) into (13) results in:

$$M_d \cdot \ddot{\boldsymbol{q}}_s + K_d \cdot \boldsymbol{q}_s = -M_r \cdot \ddot{\boldsymbol{q}}_r + B_0 \cdot (-K'_a \cdot \ddot{\boldsymbol{q}}_s - K'_v \cdot \dot{\boldsymbol{q}}_s) \tag{16}$$

Using a modal decoupling appoach [7], Eq. (16) can be rewritten in decoupled form as:

$$(I_n + S' B_0 K'_a S)\ddot{z} + S' B_0 K'_v S\dot{z} + S' K_d S z = -S' M_r \ddot{q}_r \tag{17}$$

in which I_n is the $n \times n$ identity matrix, $S = M_d^{-1/2} \cdot P$ and P is the matrix whose columns are the normalized eigenvectors of $M_d^{-1/2} K_d M_d^{-1/2}$. The left-hand side of (17) is decoupled. Equation (17) is obtained after a succesive substitution of $\boldsymbol{q} = M_d^{-1/2} \underline{\mathrm{r}}$ and $\underline{\mathrm{r}} = P \cdot z$. Without constraints it can be stated that the new

modal mass-matrix $(I_n + S' B_0 K'_a S)$ should yield (remark that all these matrices are diagonal matrices):

$$(I_n + S' B_0 K'_a S) = \frac{1}{\omega_n^2} \cdot S' K_d S \tag{18}$$

where ω_n is the desired corner frequency and therefore:

$$\begin{aligned} K'_a &= B_0^{-1} \frac{1}{\omega_n^2} \cdot K_d - B_0^{-1} M_d \\ K_a &= K'_a \cdot T_c^{-1} \end{aligned} \tag{19}$$

We define also the following:

$$\begin{aligned} S' B_0 K'_v S &= 2\zeta_n \omega_n \cdot (S' B_0 K'_a S + I_n) \\ K'_v &= B_0^{-1} \cdot 2\zeta_n \omega_n \cdot (B_0 K'_a + M_d) \\ K_v &= K'_v \cdot T_c^{-1} \end{aligned} \tag{20}$$

where ζ_n is the desired relative damping. In here the actuators are delivering forces in the direction of the degrees of freedom, therefore $B_0 = I_n$. The consequence of (19) and (20) is that the acceleration feedback controller is defined by

$$H_{\text{acc}}(s) = -\left(K_a + K_v \cdot \frac{1}{s}\right) \tag{21}$$

Application of an equivalent approach results in the force feedback controller to read:

$$\begin{aligned} K_P &= (\omega_n^2 \cdot I_n \cdot M^{dd})^{-1} \cdot K^{dd} - I_n \\ K_I &= 2\zeta \omega_n \cdot (I_n + K_P) \\ H_f(s) &= -\left(K_P + K_I \cdot \frac{1}{s}\right) \end{aligned} \tag{22}$$

In case of force-sensing the sensing is also in the direction of the defined degrees of freedom making the matrix T_c the identity-matrix.

5 Evaluation of Acceleration versus Force Feedback

Figure 5(a) shows a plot of the largest singular value of the open and closed loop transfer function matrix between base and internal mode accelerations. The closed loop is either established by force feedback (dashed line) or by acceleration feedback (dotted line). It can be observed that the natural frequencies of all suspension modes are brought back to 1 Hz by active means and that the suspension modes are well damped. In the case of acceleration feedback the internal modes are lowered in frequency and still undamped but the excitation is reduced 50 dB in magnitude. The decrease in frequency of the internal modes can be understood from the following.

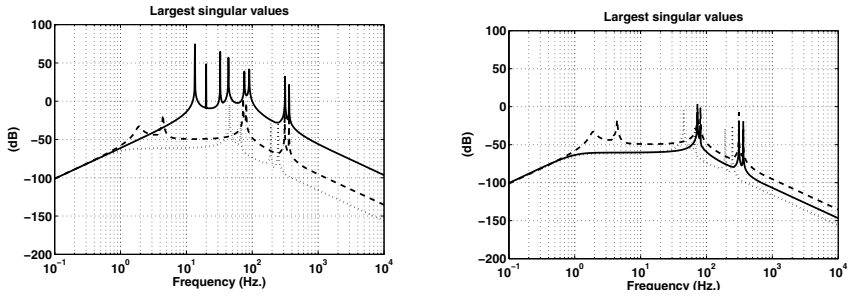

(a) (b)

Fig. 5 (a) Open loop (solid), acc. feedback (dotted), force feedback (dashed), (b) acc. feedback (dotted), force feedback (dashed), low parasitic stiffness force feedback (solid).

The transfers between actuators and sensors, usually called secondary path, contains zeros. There is no control at the frequencies of the zeros, with the consequence that new resonances appear at the frequencies of these zero dynamics. The zero dynamics of the secondary path transfer, are determined by the dynamics in case the sensors are blocked (zero output of acceleration sensors). As a consequence, these zero dynamics correspond with the internal mode dynamics in case the frame is not moving. These dynamics are lower in frequency then the frequencies of the internal modes in the uncontrolled case. Therefore, in the acceleration feedback control case the new internal mode frequencies correspond with the frequencies of the zeros in the secondary path transfers.

In case of force feedback, Figure 5(a) shows that there is less reduction in excitation of the internal modes by base-vibration compared to the acceleration feedback case. This is due to the fact that the sensors are only capable of measuring forces in longitudinal direction in the legs. Forces transmitted to the frame by bending and torsion are not measured. This force distribution through these so called parasitic paths can be analyzed again by analyses of the zeros in the secondary path. Since these zero dynamics, in the case of force feedback, are determined in the situation where the sensor outputs are zero. This is the case if the actuator forces compensate the stiffness in longitudinal direction. The zero dynamics are then described by the residual system dynamics where the longitudinal stiffnesses are set to zero. Say we make these zero dynamics have passive behavior below the specification of 1 Hz. Then, the performance in the controlled case is better. See Figure 5(b) (solid line) for the result of lowering the bending and torsional stiffness to the required amount such that the residual dynamics and as a consequence the zero dynamics, have frequencies in the region 0.1 Hz to 0.8 Hz. Overall we can conclude that with acceleration feedback better performance is obtained then with force feedback. Given the fact that in both controlled cases the same corner frequency and damping of the suspension modes is established.

6 Conclusions

Shown is that a flexible multibody modelling approach can give adequate state space models for analysis and conceptual design of vibration isolation systems using hard-mounts. It is shown that using a modal control approach the performance of hard-mounts can be made comparable to the performance of soft-mounts. The advantage is however an increased dynamic stability. When using acceleration feedback a better performance is obtained then when using force feedback. Given that in both controlled cases the same corner frequency and damping of the suspension modes is established.

References

1. M. Heertjes and K. de Graaff. Active vibration isolation of metrology frames; A modal decoupled control design. *ASME Journal of Vibration and Acoustics* **127**, 223–233, 2005.
2. TMC. http://www.techmfg.com. Technical Background, section 5.5 (STACIS).
3. J. Holterman. *Vibration Control of High-Precision Machines with Active Structural Elements*. PhD thesis, Twente University Press, University of Twente, Enschede, The Netherlands, 2002.
4. J.B. Jonker and J.P. Meijaard. SPACAR-computer program for dynamic analysis of flexible spational mechanisms and manipulators. In: *Multibody Systems Handbook*, W. Schiehlen (Ed.), pp. 123–143. Springer-Verlag, Berlin, 1990.
5. J.B. Jonker, R.G.K.M. Aarts, and J. van Dijk. An extended input-output representation for control synthesis in multibody system dynamics. In: *Proc. 2007 Eccomas Multibody 2007*, Milano, Vol. 53, pp. 208–215, 2007.
6. A. Preumont, A. Francois, F. Bossens, and A. Abu-Hanieh. Force feedback versus acceleration feedback in active vibration isolation. *Journal of Sound and Vibration* **257**(4), 605–613, 2002.
7. D.J. Inman. Active modal control for smart structures. *Philosophical Transactions/Royal Society of London Series A* **359**, 205–219, 2001.

Contact Transition Control of a Flexible Structure Mounted Manipulator

Theeraphong Wongratanaphisan and Matthew O.T. Cole

Abstract A flexible structure mounted manipulator (FSMM) is a robotic system that consists of a rigid manipulator installed on a supporting structure that is not rigid. Another robotic system which possesses similar dynamic characteristics is a micro-macro manipulator (MMM) in which a small (micro) manipulator, considered rigid, is mounted on the tip of a long-reach (macro) manipulator, considered flexible. Designing controllers for a FSMM or MMM is a difficult task as the motion of the flexible structure adds complexity to the system dynamics. It is especially difficult when the FSMM is required to interact with its environment. This paper investigates force control techniques for a FSMM in contact transition phase. Three types of controllers are compared: (1) discontinuous control, (2) impedance control, and (3) robust impedance control. These controllers were implemented and tested on a 2-DOF FSMM lab-scale prototype and their performance evaluated and discussed.

1 Introduction

A flexible structure mounted manipulator (FSMM) is a robotic system that consists of a rigid manipulator mounted on a structure that is not rigid (see Figure 1). Another system that can have similar dynamic characteristics is a micro-macro manipulator (MMM) in which a small (micro) manipulator, considered rigid, is mounted on the tip of a long-reach (macro) manipulator, considered flexible. The MMM is capable of operating tasks that cover a large working space. The macro manipulator can be employed for low bandwidth large-scale positioning of the micro manipulator

Theeraphong Wongratanaphisan
Department of Mechanical Engineering, Chiang Mai University, Chiang Mai, 50200 Thailand;
E-mail: twongrat@chiangmai.ac.th

Matthew O.T. Cole
Department of Mechanical Engineering, Chiang Mai University, Chiang Mai, 50200 Thailand;
E-mail: motcole@chiangmai.ac.th

H. Ulbrich and L. Ginzinger (eds.), Motion and Vibration Control, 325–334.

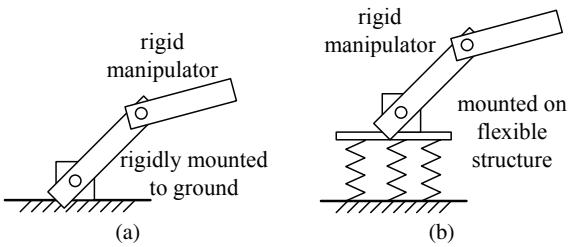

Fig. 1 (a) Typical robot manipulator, (b) flexible structure mounted manipulator.

which then operates in a narrower region with higher bandwidth. In each large-scale positioning, the macro manipulator holds its posture until the micro manipulator finishes its tasks. However, due to the flexibility of the macro manipulator the endpoint of the micro manipulator is difficult to position accurately. To date, FSMMs and MMMs have found application in space robotics [6] and nuclear waste remediation [5]. They also have potential for use in inspection/maintenance tasks for large structures such as buildings, highways and bridges.

One of the important aspects of control of a robot manipulator is when it is required to interact with its environment. In the transition phase of contact, the manipulator experiences discontinuous dynamic characteristics which can result in high impact force or instability. Hyde and Cutkosky [3] studied a number of control techniques that can cope with this transition, as applied to a rigidly mounted linear soft fingertip robotic system. For the FSMM the problem can be more serious as the dynamics of the flexible base complicate control of the system. When the manipulator contacts the environment its dynamics can change dramatically and, with closed loop control, the system can become unstable. Therefore, in tasks that require the FSMM to contact its environment, the controllers must be designed with special consideration of this problem.

This paper presents an experimental study of a FSMM during contact transition. Three control techniques are studied: discontinuous control, impedance control and robust impedance control. The first control method is a simple strategy which was used as a baseline controller in [3] while the second is a popular controller for contact tasks. However, these two controllers are designed without regard to the flexibility of the supporting structure. The last control technique takes account of the vibration of the base and involves a modified version of the second controller possessing improved stability characteristics under contact.

The remainder of this paper is organized as follows. Section 2 outlines the mathematical models related to the dynamics of the FSMM. Section 3 discusses the control laws of each controller. Section 4 describes experimental setup and the test results. Finally, Section 5 provides the conclusion.

2 Mathematical Models

2.1 Equations of Motion of a Robot Manipulator

Let $\theta \in \Re^{n\times 1}$ denote the vector of joint angles of the rigid manipulator and $X \in \Re^{m\times 1}$ denote the m (≤ 6)-dimensional task space vector of the end-effector of the manipulator. $\Re^{n\times 1}$ represents n-dimensional Euclidean space. X is called the *manipulation vector*.

The manipulation vector is related to the joint angles by

$$X = f(\theta) \tag{1}$$

The first and second derivatives of X are given by

$$\dot{X} = J(\theta)\dot{\theta} \text{ and } \ddot{X} = J\ddot{\theta} + \dot{J}\dot{\theta} \tag{2}$$

where J is the Jacobian matrix. The equations of motion of a robot manipulator in joint space are given by [1]

$$M(\theta)\ddot{\theta} + N(\theta, \dot{\theta}) + G(\theta) = \tau + J^T f_e \tag{3}$$

where M is the mass matrix, N is the Colioris and centrifugal forces vector, G is the gravitational force vector, τ is the actuator torque vector and f_e is the vector of external forces exerted at the end-effector. In task coordinate, the equations of motion can be derived from (3) and (2) to give [4]:

$$\tilde{M}(X)\ddot{X} + \tilde{N}(X, \dot{X}) + \tilde{G}(X) = f + f_e \tag{4}$$

where the matrices and vectors with tilde ($\tilde{}$) are respective quantities but as a function of the manipulation vector X.

2.2 Equations of Motion of a FSMM

Let $q \in \Re^{(n+p)\times 1}$ denote the vector containing the joint angles of the rigid manipulator $\theta \in \Re^{r\times 1}$ and the states of the flexible structure ζ. The model to estimate the states ζ can be obtained from a finite dimension approximation of the flexible modes of the structure.

Here, the manipulation vector is related to the joint angles and the flexible structure states by

$$X = f(q) = f(\theta, \zeta) \tag{5}$$

The first and second derivatives of X are given by

$$\dot{X} = J(q)\dot{q} = J_\theta(\theta, \zeta)\dot{\theta} + J_\zeta(\theta, \zeta)\dot{\zeta} \tag{6}$$

and

$$\ddot{X} = J\ddot{q} + \dot{J}\dot{q} = J_\theta\ddot{\theta} + J_\zeta\ddot{\zeta} + \dot{J}_\theta\dot{\theta} + \dot{J}_\zeta\dot{\zeta} \tag{7}$$

where J_θ and J_ζ are Jacobian matrices of appropriate dimension. Note that $J(q) = [J_\theta \;\; J_\zeta]$. For the FSMM, the equations of motion of the FSMM in joint space are given by

$$M(q)\ddot{q} + N(q,\dot{q}) + G(q) = \tau + J^T f_e \tag{8}$$

The task coordinate equation of motion in this case can be written similarly to (4) with inclusion of the states of the flexible structure.

2.3 Contact Transition

In general, the dynamics of the system under contact will depend on the environment parameters such as stiffness and damping as well as the form of the controller implemented on the manipulator. For the FSMM, the contact dynamics will also involve the motion of the flexible structure. In a more complicated scenario, the environment can itself be a dynamic system, however, this study will focus only on the static environment case.

The range of motion during contact transition is generally small and therefore the equations of motion (4) can be linearized and simplified to a 1-DOF system in the task coordinates. In many cases, this simplified model can be used for controller design.

3 Contact Transition Control

3.1 Discontinuous Control

The approach used here is similar to [3] in that the control laws are separated into the pre-contact and post-contact phases, respectively:

$$\tau_{pre}(t) = J^T(JM^{-1}J)^{-1}M^{-1}k_{v_1}\left(v_d(t) - v(t)\right) \tag{9}$$

$$\tau_{post}(t) = J^T(JM^{-1}J)^{-1}M^{-1}\left(k_f(f_{ed}(t) - f_e(t)) - k_{v_2}v(t)\right) \tag{10}$$

where v and v_d are the actual and desired end-point velocities, respectively, k_{v_1} and k_{v_2} are the end-point velocity gains and f_e and f_{ed} are the actual and desired contact forces, respectively. The switching between these two control laws is decided based on the level of measured force from the contact force sensor.

3.2 Impedance Control

Impedance control is one of the most well established force control approaches for robot manipulator systems. It unifies position and force control into a single framework [2]. Here the control law is designed to produce a desired impedance characteristic between the motion of the end-effector and applied contact force. It is the same for both contact and non-contact and is given by

$$\tau(t) = -J^T \frac{m}{m_d} \left(b_d \left(v(t) - v_d(t)\right) + k_d \left(x(t) - x_d(t)\right)\right) + J^T \left(\frac{m}{m_d} - 1\right) f_e(t) \tag{11}$$

where m_d, b_d and k_d are the desired impedance (mass, damping, stiffness) parameters. m is the effective mass of the end-effector.

3.3 Robust Impedance Control

In this control approach, based on the linearized model of (4) the control law in (11) is modified in order to improve stability under contact [7]:

$$\tau(t) = -J^T \frac{m}{m_d} \left(b_d \left(\tilde{v}(t) - \tilde{v}_d(t)\right) + k_d \left(\tilde{x}(t) - \tilde{x}_d(t)\right)\right) + J^T \left(\frac{m}{m_d} \tilde{f}_e(t) - f_e(t)\right) \tag{12}$$

Here the $\tilde{}$ version of the variable has been filtered by a lead-lag type compensator with transfer function $Q(s) = (\tau_2 s + 1)/(\tau_1 s + 1)$. With proper choice of τ_1 and τ_2 the controller can be improved in terms of robustness against unmodelled vibrational modes of the manipulator base compared with the impedance controller (11). Further details of the controller robustness analysis and design methodology can be found in [7].

In all the control laws considered, the position x and velocity v are calculated from the sensor devices that measure the manipulator joint angles. Therefore, x and v are measured relative to the base of the manipulator which is also subject to motion. This is different to the case where the manipulator is mounted on a rigid base as then x and v relate to absolute motion.

4 Experimental Setup and Results

4.1 A 2-DOF FSMM Test Rig

Figure 2 shows the 2-DOF FSMM lab-scale prototype used in the experiments. It consists of a 2-DOF rigid manipulator mounted on a platform which consists of a steel rectangular plate fixed at its corners to four long vertical steel rods. The

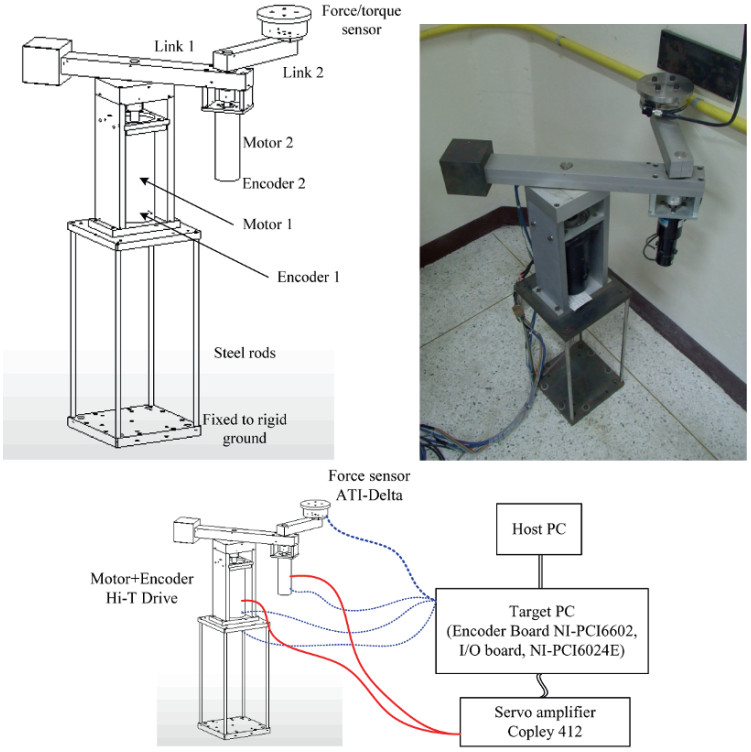

Fig. 2 The 2-DOF FSMM lab-scale prototype and experimental setup.

first natural mode of vibration of the flexible structure including the mass of the manipulator has frequency 7.82 Hz. The damping of the base vibration is very low (< 0.1). The arm of the manipulator moves in the horizontal plane; therefore there is no effect of gravity. The manipulator arm is driven by d.c. motors through harmonic gear drives which ensure no backlash. The arm movement angles are measured by incremental encoders. At the tip of link 2, a six-axis force/torque sensor is installed to measure contact forces. The system is installed near a vertical surface so that the contact test can be performed. Table 1 lists the physical parameters of the system.

4.2 Experimental Setup and Procedure

The real-time controller is set up under MATLAB's xPC Target system running at 1 kHz sampling rate. The coordinates of the manipulator base and the end-effector are defined according to the diagram in Figure 3. Note that the environment has the surface normal vector in the direction opposite to the positive X axis.

Table 1 Parameters of the FSMM lab-scale prototype.

Item	Parameter
mass of link 1	6.97 kg
mass of link 2	2.76 kg
moment of inertia of link 1 (ref. to c.m.)	0.2262 kg.m^2
moment of inertia of link 2 (ref. to c.m.)	0.0098 kg.m^2
mass of the base	11.97 kg
length of link 1	0.202 m
length of link 2	0.1625 m
center of mass of link 1 (from link joint)	0.0524 m
center of mass of link 2 (from link joint)	0.1288 m

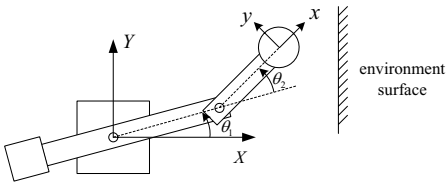

Fig. 3 Coordinate system of the FSMM.

In the contact transition control test, the manipulator's end-effector was commanded according to each control law to move straight onto the surface made of a hard 1 cm thick steel plate in the $+X$ direction at various speeds. The performance of the controller can be evaluated from the contact force signal component for the X-direction.

4.3 Experimental Results

4.3.1 Discontinuous Control

The performance of this controller depends greatly on the force feedback gain k_f and the velocity gain k_{v_2}. In general, good force tracking will require high k_f. However, high k_f will generally result in low damping. k_{v_2} can be adjusted to increase the damping. For the FSMM, however, the vibration from the base will affect the force tracking performance and will impose a limit on how high k_f can be adjusted. If k_f is too high, instability will occur. Figure 4 shows the responses of the impact/contact force at the end-effector of the system under discontinuous control for impact speed of 1, 2 and 3 cm/s. The desired contact force was set to 10 N. In Figure 4a, the control parameters were $k_f = 0.6$ and $k_{v_2} = 3000$ Ns/m. The responses at these speeds were stable and the contact force settled at around 6 N. In this case, the system was stable even for approach speeds up to 10 cm/s. No higher impact speed was attempted on this hard surface as the impact could damage the force sensor. As the impact speed increases, the force overshoot increases. Figure 4b shows the unstable case where the force gain k_f and velocity gain k_{v_2} were increased to 0.9 and 4000

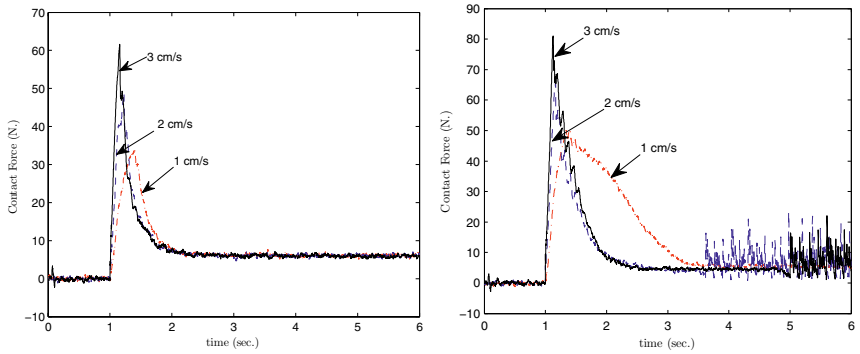

Fig. 4 Discontinuous control (a) $k_f = 0.6$, $k_{v_2} = 3000$ Ns/m (b) $k_f = 0.9$, $k_{v_2} = 4000$ Ns/m.

Ns/m, respectively. k_{v_2} was initially kept at 3000 Ns/m but instability resulted immediately after the impact and the control law switched back and forth between (9) and (10). By increasing k_{v_2}, the after-impact response improved. However, for high impact speed, the after-impact response seemed to settle initially but finally became unstable. With high force gain, the system seemed to be more sensitive to the base vibration. Thus high force gain and large magnitudes of structure vibration due to high-speed impact together cause instability.

4.3.2 Impedance Control

A number of desired impedance parameter sets were tested. Most of the tested parameter sets provided good responses. Figure 5a shows examples of stable force responses under impedance control with two sets of desired impedance parameters. Here the results were very satisfactory as the impact speed resulting in the responses shown in the figure was very high (30 cm/s). With the chosen parameters, the overshoot was much smaller (in many cases there was no overshoot) compared to the results from discontinuous control and after the impact the end-effector remained in stable contact with the surface. However, with some sets of desired impedance parameters the contact motion becomes unstable after the impact. Figure 5b shows the responses with $m_d = 50$ kg, $\omega_{nd} = \sqrt{k_d/m_d} = 20$ Hz, $\zeta_d = b_d/2\sqrt{k_d m_d} = 0.7$. Here, after the manipulator hit the wall it settled and remained in contact with the surface. However, there remained oscillatory motion in the supporting structure which could also be observed in the force measurements. In this case, the contact response is considered unstable.

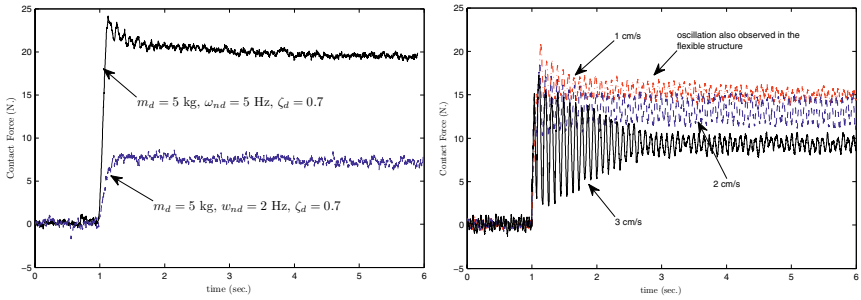

(a) (b)

Fig. 5 Impedance control (a) stable responses (b) unstable contact ($m_d = 50$kg, $\omega_{nd} = 20$ Hz, $\zeta_d = 0.7$).

4.3.3 Robust Impedance Control

Instability under contact occurs in the system under impedance control due to the flexibility of the supporting structure. When there is vibration in the flexible structure, the manipulator displacement and velocity measured from sensors installed on the manipulator are not absolute and this is the main cause of instability in impedance control of FSMMs [7]. With the robust impedance control, the behaviour of the system can be improved. Figure 6 shows responses of the system under robust impedance control. The same impedance parameter set as in Figure 5b was used but with the inclusion of the filter $Q(s)$ with parameters $\tau_1 = 0.02$ and $\tau_2 = 0.1$. Here, after impact, the oscillations died out and the manipulator remained in contact with the wall. With high speed impact, a high level of vibration was induced in the structure following impact and it took some time for the system to settle. Nevertheless, the robust controller does provide stable operation after impact. The disadvantage of this filtering method is that it amplifies high frequency signals and therefore is sensitive to sensor noise.

5 Conclusions

In this study, a selection of contact transition control techniques have been tested on an FSMM. The discontinuous control method provides a simple control law which can be implemented easily and if tuned appropriately can provide stable contact after the impact. To avoid instability, the force gain k_f should be kept low but at the expense of tracking performance. However, overshoot is the main drawback of this technique. Impedance control, although more complicated to implement, gives satisfactory results for a wide range of desired impedance parameters and impact speeds and is more superior than the discontinuous control in most cases. However, for some design parameters, the impedance control may not provide stable contact.

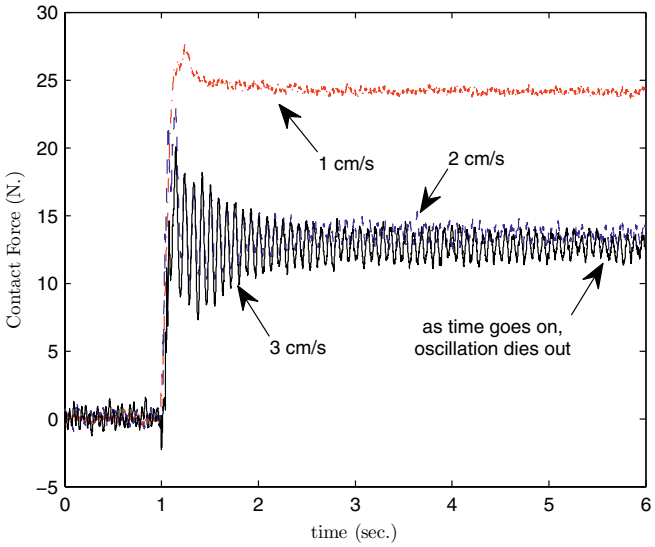

Fig. 6 Robust impedance control: $m_d = 50$ kg, $\omega_{nd} = 20$ Hz, $\zeta_d = 0.7$, $\tau_1 = 0.02$, $\tau_2 = 0.1$.

In such cases a robust form of the impedance control can be used incorporating an additional filter. The results obtained in this study are based on impact with a rigid (high stiffness) surface. This study will be extended to cover low stiffness environments, results for which may be different to those obtained here.

Acknowledgements This work was funded by the Thailand Research Fund and the Commission on Higher Education under grant contract MRG4880198.

References

1. J.J. Craig, *Introduction to Robotics: Mechanics and Control*, 3rd edn., Pearson Prentice Hall, NJ, 2005.
2. N. Hogan, Stable Execution of Contact Tasks Using Impedance Control, *IEEE Int. Conf. on Robot. and Auto.* **4**, 1987, 1047–1054.
3. J.M. Hyde and M.R. Cutkosky, Controlling Contact Transition, *IEEE Cont. Sys. Mag*., February 1994, 25–30.
4. O. Khatib, A Unified Approach for Motion and Force Control of Robot Manipulators: The Operational Space Formulation, *IEEE J. of Robot. and Auto.* **RA-3**, 1987, 43–53.
5. Y. Perrot, J.J. Cordier, J.P. Friconneau, D. Maisonnier, E. Martin and J.D. Palmer, Development of a Long Reach Articulated Manipulator for ITER in Vessel Inspection under Vacuum and Temperature, *Fusion Eng. and Des*. **69**, 2003, 187–190.
6. M.A. Torres, S. Dubowsky and A.C. Pisoni, Path Planning for Elastically-Mounted Space Manipulators: Experiment Evaluation, *IEEE Int. Conf. on Robot. and Auto.*, San Diago, CA, May 1994.
7. T. Wongratanaphisan, Force Control of a Flexible Structure Mounted Manipulator, Final Report, submitted to Thailand Research Fund, Contract No. MRG4880198, September 2007.

Velocity Tracking Control of a Four-Rotor Mini Helicopter

M. Yokoyama and K. Fujimoto

Abstract This paper presents an autonomous control strategy for a four-rotor mini helicopter referred to as X4 flyer. Based on the so called backstepping method together with sliding mode control theories, a robust velocity tracking controller is designed, in which both Euler angles and quaternion parameters are appropriately employed. As a special case of velocity tracking control, when the demanded velocity is zero, the proposed controller achieves stable hovering. Numerical simulation illustrates the robustness of the proposed controller against torque disturbances such as a gust of wind.

1 Introduction

In order to assist urban search and rescue or environment monitoring, unmanned vehicles have been developed for some decades. Among them, unmanned aerial vehicles such as a helicopter which can achieve a vertical takeoff and landing have been strongly concerned more recently. Although there are some kinds of helicopters, significant research interest has been directed towards a four-rotor mini helicopter referred to as X4 flyer, which has fixed-pitch rotors mounted at the four ends of a simple cross frame. Because of the fixed pitch and its symmetric structure, this omni-directional helicopter is dynamically excellent and its mathematical model is quite simple. Although attitude stabilization or position tracking problem of the X4 flyer has been investigated by many researchers and various types of controllers have been proposed [1–3], very little has been done on velocity tracking

Makoto Yokoyama
Niigata University, 8050 Ikarashi 2-nocho, Nishi-ku, Niigata, Japan;
E-mail: m.yoko@eng.niigata-u.ac.jp

Keigo Fujimoto
Graduate School of Niigata University, 8050 Ikarashi 2-nocho, Nishi-ku, Niigata, Japan;
E-mail: f07b134a@cc.niigata-u.ac.jp

H. Ulbrich and L. Ginzinger (eds.), Motion and Vibration Control, 335–344.

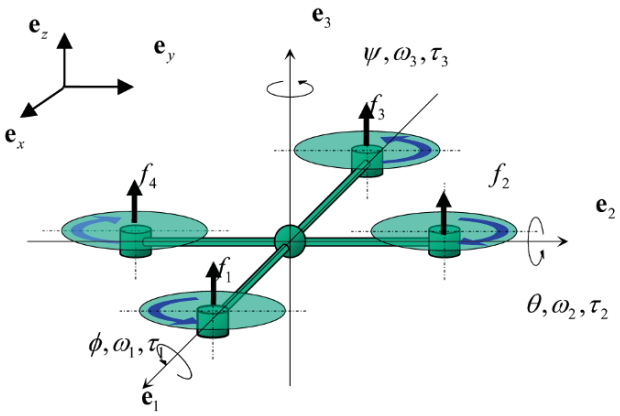

Fig. 1 Schematic diagram of the X4 flyer.

control. In this paper, based on the so called backstepping method together with sliding mode control theories, a robust velocity tracking controller is designed, in which both Euler angles and quaternion parameters are appropriately employed. As a special case of velocity tracking control, when the demanded velocity is identically zero, the proposed controller achieves stable hovering.

Numerical simulation illustrates the robustness of the proposed controller against torque disturbances such as a gust of wind or actuator dynamics.

2 Mathematical Model

A schematic diagram of the X4 flyer under consideration is shown in Figure 1. The rotors can be grouped into the front-back pair, and the left-right pair. Since the pairs rotate in opposite directions, one pair spins clockwise and the other spins anti-clockwise. Thus the yawing moments generated by the rotors cancel out to zero. A rolling moment can be generated by speeding up one of the rotors in the left-right pair and slowing down the other. Similarly, a pitching moment can be generated by speeding up one of the rotors in the front-back pair and slowing down the other. A yawing moment can be generated by speeding up one pair and slowing down the other pair. In each case above, if the amount of increase is the same as that of decrease, the only effect is the generation of a single moment, because the collective thrust is held constant. This is a basic control strategy for hovering.

The dynamical model is given as follows:

$$\dot{\mathbf{v}} = -g\mathbf{e}_z + \mathbf{R}_{OA}(\mathbf{q})\mathbf{e}_3\zeta \tag{1}$$

$$\dot{\mathbf{q}} = \mathbf{G}(\mathbf{q})\boldsymbol{\omega} \tag{2}$$

$$\dot{\boldsymbol{\omega}} = \mathbf{F}(\boldsymbol{\omega}) + \boldsymbol{\xi} + \mathbf{d} \tag{3}$$

where

$$\mathbf{G}(\mathbf{q}) = \frac{1}{2}\begin{bmatrix} q_4 & -q_3 & q_2 \\ q_3 & q_4 & -q_1 \\ -q_2 & q_1 & q_4 \\ -q_1 & -q_2 & -q_3 \end{bmatrix}, \quad \mathbf{F}(\boldsymbol{\omega}) = \begin{bmatrix} \frac{J_2 - J_3}{J_1}\omega_2\omega_3 \\ \frac{J_3 - J_1}{J_2}\omega_1\omega_3 \\ \frac{J_1 - J_2}{J_3}\omega_1\omega_2 \end{bmatrix}$$

The other variables and notations are defined as follows:

$\Sigma O = \{\mathbf{e}_x, \mathbf{e}_y, \mathbf{e}_z\}$	inertial frame
$\Sigma A = \{\mathbf{e}_1, \mathbf{e}_2, \mathbf{e}_3\}$	body-fixed frame
$\mathbf{R}_{OA}$	orthogonal rotation matrix of the airframe in ΣO
$\mathbf{v} = [v_x \ \ v_y \ \ v_z]^T$	linear velocity of the origin of ΣA in ΣO
$\mathbf{q} = [q_1 \ \ q_2 \ \ q_3 \ \ q_4]$	quaternion vector corresponding to $\mathbf{R}_{OA}$
ϕ, θ, ψ	roll, pitch, yaw of Euler angles, respectively
$\boldsymbol{\omega} = [\omega_1 \ \ \omega_2 \ \ \omega_3]^T$	angular velocity of the airframe in ΣA
$\mathbf{J} = \begin{bmatrix} J_1 & 0 & 0 \\ 0 & J_2 & 0 \\ 0 & 0 & J_3 \end{bmatrix}$	inertia matrix of the airframe around the center of mass in ΣA
m	mass of the airframe
$f_j \ (j = 1, \ldots, 4)$	thrust generated by each rotor in ΣA
$f = \sum_{j=1}^{4} f_j$	collective thrust
$\boldsymbol{\tau} = [\tau_1 \ \ \tau_2 \ \ \tau_3]^T$	airframe torque generated by thrust in ΣA
$\zeta = f/m$	
$\boldsymbol{\xi} = [\tau_1/J_1 \ \ \tau_2/J_2 \ \ \tau_3/J_3]^T$	
$\mathbf{d}$	disturbance
g	gravitational acceleration

3 Controller Design

A nonlinear controller is designed using the backstepping method. Since the collective thrust is always directed to the $\mathbf{e}_3$ axis in the body-fixed frame, the XYZ Euler angles are used.

$$\mathbf{R}_{OA}(\phi, \theta, \psi) = \begin{bmatrix} \cos\theta\cos\psi & -\cos\theta\sin\psi & \sin\theta \\ \sin\phi\sin\theta\cos\psi + \cos\phi\sin\psi & -\sin\phi\sin\theta\sin\psi + \cos\phi\cos\psi & -\sin\phi\cos\theta \\ -\cos\phi\sin\theta\cos\psi + \sin\phi\sin\psi & \cos\phi\sin\theta\sin\psi + \sin\phi\cos\psi & \cos\phi\cos\theta \end{bmatrix} \tag{4}$$

Then the translation model can be written by

$$\begin{bmatrix} \dot{v}_x \\ \dot{v}_y \\ \dot{v}_z \end{bmatrix} = -g\mathbf{e}_z + \mathbf{R}_{OA}\mathbf{e}_3\zeta = -\begin{bmatrix} 0 \\ 0 \\ g \end{bmatrix} + \begin{bmatrix} \sin\theta \\ -\sin\psi\cos\theta \\ \cos\phi\cos\theta \end{bmatrix}\zeta \tag{5}$$

The desired yaw angle $\tilde{\psi}$ may be assigned to be identically zero. In the first step of backstepping procedure, the other desired angles $\tilde{\phi}$, $\tilde{\theta}$ as virtual control inputs and the collective thrust ζ will be determined.

Defining the velocity tracking error $\underline{\mathbf{v}} \triangleq \mathbf{v} - \mathbf{r}$, where $\mathbf{r}$ denotes the reference velocity, let

$$V_1 = \frac{1}{2}\underline{\mathbf{v}}^T\underline{\mathbf{v}} \tag{6}$$

be a Lyapunov function candidate for the subsystem (5). Then the Lyapunov derivative along the system trajectories is given by

$$\dot{V}_1 = \underline{\mathbf{v}}^T(-g\mathbf{e}_z + \mathbf{R}_{OA}\mathbf{e}_3\zeta - \dot{\mathbf{r}}) \tag{7}$$

If the condition

$$\mathbf{R}_{O\tilde{A}}(\tilde{\phi}, \tilde{\theta}, \tilde{\psi})\mathbf{e}_3\zeta = -\lambda\underline{\mathbf{v}} + g\mathbf{e}_z + \dot{\mathbf{r}} \tag{8}$$

holds, then $\dot{V}_1 = -\lambda\underline{\mathbf{v}}^T\underline{\mathbf{v}} < 0$, where $\lambda > 0$. Substituting the second term in the right-hand side of (5) into (8) yields

$$\begin{bmatrix} \sin\tilde{\theta} \\ -\sin\tilde{\phi}\cos\tilde{\theta} \\ \cos\tilde{\phi}\cos\tilde{\theta} \end{bmatrix}\zeta = -\lambda\underline{\mathbf{v}} + g\mathbf{e}_z + \dot{\mathbf{r}} \triangleq \begin{bmatrix} p_x \\ p_y \\ p_z \end{bmatrix} \tag{9}$$

From this equation, the stabilizing function are obtained as follows:

$$\tilde{\phi} = \arctan\left(\frac{-p_y}{p_z}\right), \quad \tilde{\theta} = \mathrm{sgn}(p_x)\arctan\sqrt{\frac{p_x^2}{p_y^2 + p_z^2}}, \quad \zeta = \sqrt{p_x^2 + p_y^2 + p_z^2}. \tag{10}$$

In the second step, the desired angular velocity $\tilde{\boldsymbol{\omega}}$ as a virtual control to achieve the desired rotation (attitude) above should be designed. Defining the attitude error by

$$\mathbf{R}_{\tilde{A}A} \triangleq \mathbf{R}_{O\tilde{A}}(\tilde{\phi}, \tilde{\theta}, \tilde{\psi})^T\mathbf{R}_{OA}(\phi, \theta, \psi) \tag{11}$$

the corresponding quaternion $\boldsymbol{\varepsilon} = [\varepsilon_1, \varepsilon_2, \varepsilon_3, \varepsilon_4]^T$ is given by

$$\begin{aligned} \varepsilon_1 &= \frac{-1}{4\varepsilon_4}(R_{23} - R_{32}), \quad \varepsilon_2 = \frac{-1}{4\varepsilon_4}(R_{31} - R_{13}) \\ \varepsilon_3 &= \frac{-1}{4\varepsilon_4}(R_{12} - R_{21}), \quad \varepsilon_4 = \frac{1}{2}\sqrt{1 + R_{11} + R_{22} + R_{33}} \end{aligned} \tag{12}$$

where R_{ij} denotes each element of $\mathbf{R}_{\tilde{A}A}$. The dynamics of this quaternion can be represented as

$$\dot{\boldsymbol{\varepsilon}} = \mathbf{G}(\varepsilon)[\boldsymbol{\omega}(\phi, \theta, \psi) - \mathbf{R}_{OA}^T(\phi, \theta, \psi)\mathbf{R}_{O\tilde{A}}(\tilde{\phi}, \tilde{\theta}, \tilde{\psi})\hat{\boldsymbol{\omega}}(\tilde{\phi}, \tilde{\theta}, \tilde{\psi})] \tag{13}$$

where $\hat{\boldsymbol{\omega}}$ denotes the angular velocity corresponding to $\mathbf{R}_{O\tilde{A}}$, represented by

$$\hat{\boldsymbol{\omega}} = \begin{bmatrix} \dot{\tilde{\phi}} \cos\tilde{\theta}\cos\tilde{\psi} + \dot{\tilde{\theta}}\sin\tilde{\psi} \\ -\dot{\tilde{\phi}}\cos\tilde{\theta}\sin\tilde{\psi} + \dot{\tilde{\theta}}\cos\tilde{\psi} \\ \dot{\tilde{\phi}}\sin\tilde{\theta} + \dot{\tilde{\psi}} \end{bmatrix} \tag{14}$$

Now we should stabilize the subsystem (13) regarding $\boldsymbol{\omega}$ as a virtual control. Let

$$V_2 = \frac{1}{2}[\varepsilon_1^2 + \varepsilon_2^2 + \varepsilon_3^2 + (1-\varepsilon_4)^2] \tag{15}$$

be a Lyapunov function candidate for the subsystem (13). It should be noted that this Lyapunov function candidate does not include V_1. The reason will be discussed in some depth later when considering the closed-loop stability. The Lyapnov derivative along the system trajectories is given by

$$\dot{V}_2 = \left[\frac{\partial V_2}{\partial \boldsymbol{\varepsilon}}\right]^T \mathbf{G}(\boldsymbol{\varepsilon})(\boldsymbol{\omega} - \mathbf{R}_{OA}^T \mathbf{R}_{O\tilde{A}} \hat{\boldsymbol{\omega}}) \tag{16}$$

Choosing the stabilization function

$$\tilde{\boldsymbol{\omega}} = -\alpha \begin{bmatrix} \tanh(\kappa\varepsilon_1) \\ \tanh(\kappa\varepsilon_2) \\ \tanh(\kappa\varepsilon_3) \end{bmatrix} + \mathbf{R}_{OA}^T \mathbf{R}_{O\tilde{A}} \hat{\boldsymbol{\omega}} \tag{17}$$

yields

$$\dot{V}_2 = -\frac{1}{2}\sum_{i=1}^{3} \alpha\varepsilon_i \tanh(\kappa\varepsilon_i) < 0 \tag{18}$$

In the third step, the torque control $\boldsymbol{\xi}$ will be determined to stabilize the attitude dynamics including the previous subsystem. Defining the angular velocity error by $\underline{\boldsymbol{\omega}} \triangleq \boldsymbol{\omega} - \tilde{\boldsymbol{\omega}}$, let

$$V_3 = V_2(\boldsymbol{\varepsilon}) + \frac{1}{2}\underline{\boldsymbol{\omega}}^T \underline{\boldsymbol{\omega}} \tag{19}$$

be a Lyapunov function candidate for the system. Then, using (3) the Lyapunov derivative along the system trajectories is given by

$$\begin{aligned} \dot{V}_3 = &\left[\frac{\partial V_3}{\partial \boldsymbol{\varepsilon}}\right]^T \mathbf{G}(\boldsymbol{\varepsilon})(\tilde{\boldsymbol{\omega}} - \mathbf{R}_{OA}^T \mathbf{R}_{O\tilde{A}} \hat{\boldsymbol{\omega}}) + \left[\frac{\partial V_3}{\partial \boldsymbol{\varepsilon}}\right]^T \mathbf{G}(\boldsymbol{\varepsilon})\underline{\boldsymbol{\omega}} \\ &+ \left[\frac{\partial V_3}{\partial \underline{\boldsymbol{\omega}}}\right]^T [\mathbf{F}(\boldsymbol{\omega}) + \boldsymbol{\xi} - \dot{\tilde{\boldsymbol{\omega}}} + \mathbf{d}] \end{aligned} \tag{20}$$

Substituting (17) into (20) yields

$$\dot{V}_3 = -\frac{1}{2}\sum_{i=1}^{3} \alpha\varepsilon_i \tanh(\kappa\varepsilon_i) + \left[\frac{\partial V_3}{\partial \boldsymbol{\varepsilon}}\right]^T \mathbf{G}(\boldsymbol{\varepsilon})\underline{\boldsymbol{\omega}} + \left[\frac{\partial V_3}{\partial \underline{\boldsymbol{\omega}}}\right]^T [\mathbf{F}(\boldsymbol{\omega}) + \boldsymbol{\xi} - \dot{\tilde{\boldsymbol{\omega}}} + \mathbf{d}] \tag{21}$$

In order to achieve robust tracking against the disturbance, employing the sliding mode control theory, the torque control is determined by

$$\boldsymbol{\xi} = -\mathbf{G}^T(\boldsymbol{\varepsilon})\left[\frac{\partial V_3}{\partial \boldsymbol{\varepsilon}}\right] - \mathbf{F}(\boldsymbol{\omega}) + \dot{\tilde{\boldsymbol{\omega}}} - \beta\boldsymbol{\sigma} - \gamma\boldsymbol{\Lambda}^{-1}\frac{\boldsymbol{\sigma}}{\|\boldsymbol{\sigma}\|} \tag{22}$$

where $\boldsymbol{\sigma} \triangleq \boldsymbol{\Lambda}\underline{\boldsymbol{\omega}}$ is a switching function, $\boldsymbol{\Lambda}$ is a diagonal matrix of full rank, β and γ are positive constants. The last term on the right-hand side is sometimes referred to as unit vector control. Substituting (22) into (21) yields

$$\begin{aligned}\dot{V}_3 &= -\frac{1}{2}\sum_{i=1}^{3}\alpha\varepsilon_i\tanh(\kappa\varepsilon_i) - \beta\sum_{i=1}^{3}\Lambda_i\underline{\omega}_i^2 + \underline{\boldsymbol{\omega}}^T\left(-\gamma\boldsymbol{\Lambda}^{-1}\frac{\boldsymbol{\sigma}}{\|\boldsymbol{\sigma}\|} + \mathbf{d}\right)\\ &< \frac{\|\underline{\boldsymbol{\omega}}\|}{\|\boldsymbol{\sigma}\|}(-\gamma + \|\boldsymbol{\Lambda}\|\,\|\mathbf{d}\|)\end{aligned} \tag{23}$$

Thus, if $\gamma > \|\boldsymbol{\Lambda}\|\,\|\mathbf{d}\|$ holds, the Lyapunov derivative is always negative.

The closed-loop dynamics is represented as follows:

$$\dot{\mathbf{v}} = -g\mathbf{e}_z + \mathbf{R}_{O\tilde{A}}(\tilde{\phi},\tilde{\theta},\tilde{\psi})\mathbf{R}_{\tilde{A}A}(\boldsymbol{\varepsilon})\begin{bmatrix}0\\0\\\sqrt{p_x^2+p_y^2+p_z^2}\end{bmatrix} \tag{24}$$

$$\dot{\boldsymbol{\varepsilon}} = \mathbf{G}(\boldsymbol{\varepsilon})\left(-\alpha\begin{bmatrix}\tanh(\kappa\varepsilon_1)\\\tanh(\kappa\varepsilon_2)\\\tanh(\kappa\varepsilon_3)\end{bmatrix} + \underline{\boldsymbol{\omega}}\right) \tag{25}$$

$$\dot{\underline{\boldsymbol{\omega}}} = -\left[\frac{\partial V_3}{\partial \boldsymbol{\varepsilon}}\right]^T\mathbf{G}(\boldsymbol{\varepsilon})\underline{\boldsymbol{\omega}} - \beta\boldsymbol{\sigma} - \gamma\boldsymbol{\Lambda}^{-1}\frac{\boldsymbol{\sigma}}{\|\boldsymbol{\sigma}\|} + \mathbf{d} \tag{26}$$

As seen from these equations, the subsystem combined (25) with (26) is not affected by the subsystem described by (24). This implies that the attitude dynamics is not affected by the translation dynamics, which is a property of the plant to be controlled in itself. Therefore, the asymptotic stability of the closed-loop system can be guaranteed, because the both subsystems are asymptotically stable.

4 Simulation Results

In order to demonstrate the performance of the proposed controller, numerical simulations were carried out. It was assumed that all the state variables were accessible for implementation. The parameter values of the X4 flyer used in the simulations are the same as those of our experimental setup which was still being made with modifying the Draganflyer from RCtoys. Although neither the motor dynamics nor the drag force parallel to the blade motion is considered for the controller design in the

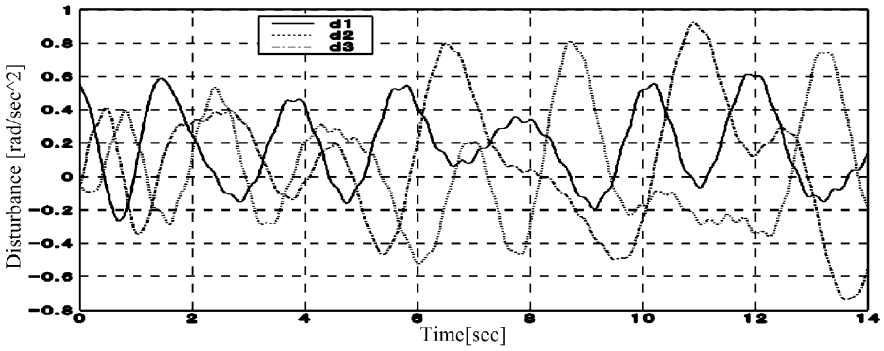

Fig. 2 Disturbances.

previous section, their identified models were incorporated in the simulation. Using the identified proportional gain of the motor, the identified aerodynamic coefficients and so on, the control inputs were changed statically to the voltages supplied to the motors.

Figure 2 shows the disturbance torque. The initial angles are $[\phi \quad \theta \quad \psi] = [60 \ \ 50 \ \ 40]$ deg and the initial velocities are zero. The initial voltage is equally supplied to each motor for hovering. The reference velocity is identically zero from the start to 6 sec, which demands hovering. Thereafter, the reference velocity changes exponentially as shown in Figures 3 and 4(b).

Figure 3 shows the results for a slight different controller from the proposed controller, which is obtained by removing the unit vector component from the proposed controller in (22). The performance of this controller was much worse than that of the proposed controller shown in Figure 4. It can be seen from Figure 4 that the proposed controller achieved stable hovering and velocity tracking robustly in the presence of disturbance. This means that the unit vector component often used in sliding mode control plays an important role for robustness, since it provides locally high gain property to the controller.

5 Conclusion

A velocity tracking controller for the X4 flyer was proposed. Due to the backstepping method, its design procedure is very systematic and has much flexibility. In this sense, the controller presented in this paper is one of the possible controllers. For example, the hyperbolic tangent function used here can be changed to a more appropriate nonlinear function. On the other hand, employing the sliding mode control made it possible to achieve robust tracking performance against wind disturbance. Although the motor dynamics was not considered, it would be straightforward to extend the proposed controller through the backstepping procedure. In that case,

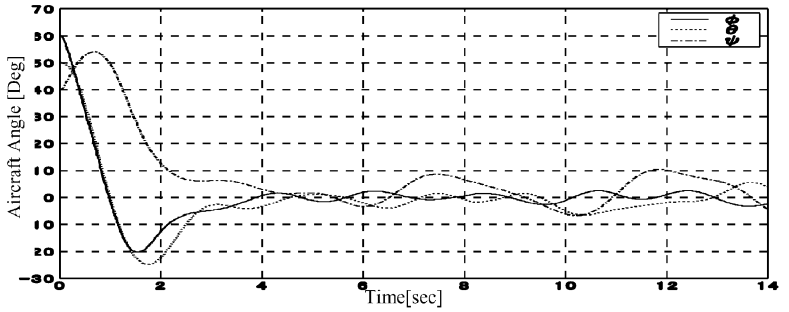

(a) Aircraft Angles

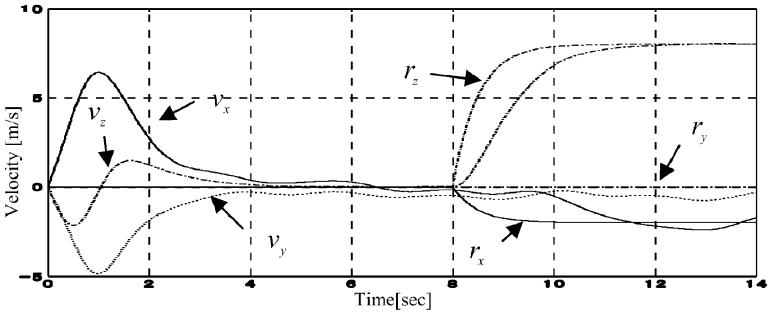

(b) Velocities

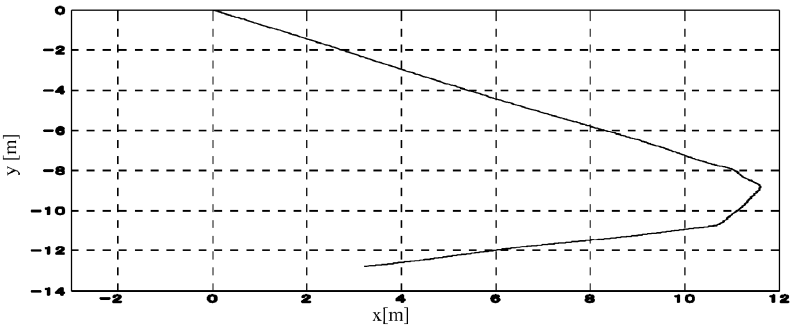

(c) Trajectory in x-y plane

Fig. 3 Simulation results without unit vector component.

however, the angular velocity of the four motors must be available for control. From a practical point of view, it is not preferable to measure the angular velocity. As shown in the simulation results, the proposed controller achieved robust performance in the presence of the motor dynamics.

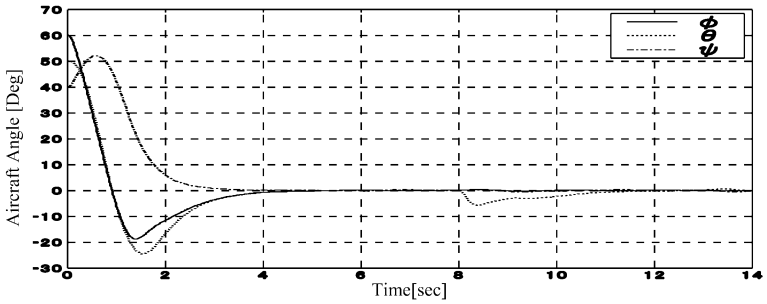

(a) Aircraft Angles

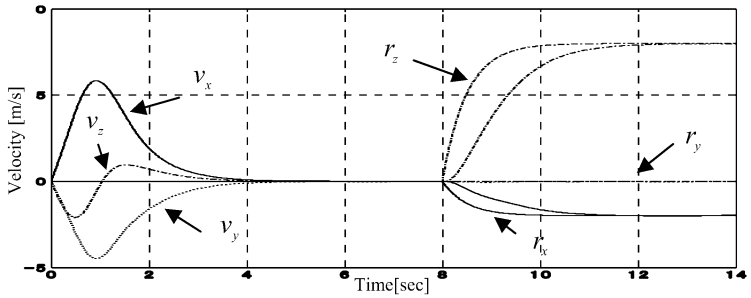

(b) Velocities

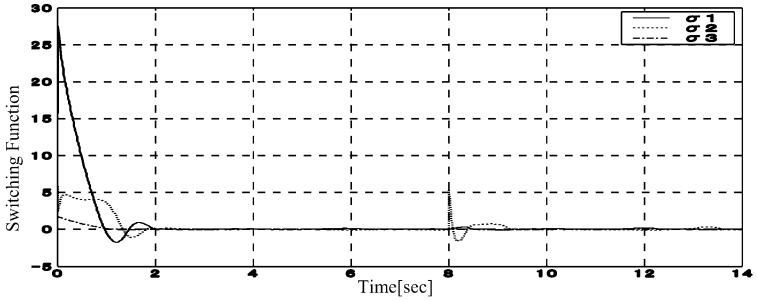

(c) Switching Functions

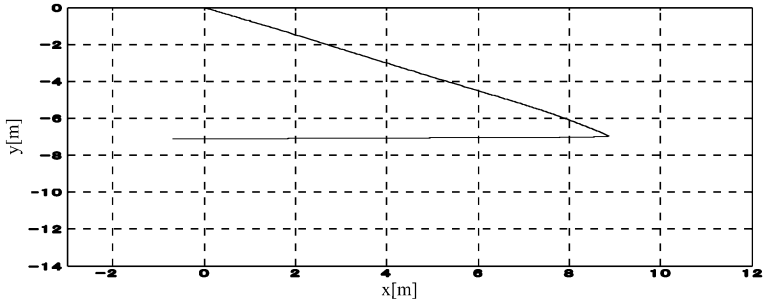

(d) Trajectory in x-y plane

Fig. 4 Simulation results for the proposed controller.

References

1. Beji, L. and Abichou, A., Streamlined rotors mini rotorcraft: Trajectory generation and tracking, *International Journal of Control, Automation, and Systems* **3**(1), 87–99, 2005.
2. Castillo, P., Dzul, A. and Lozano, R., Real-time stabilization and tracking of a four-rotor mini rotorcraft, *IEEE Transactions on Control Systems Technology* **12**(4), 510–516, 2004.
3. Tayebi, A. and McGilvray, S., Attitude stabilization of a VTOL quadrotor aircraft, *IEEE Transactions on Control Systems Technology* **14**(3), 562–571, 2006.
4. Wen, J.T.Y. and Kreutz-Delgado, K., The attitude control problem, *IEEE Transactions on Automatic Control* **36**(10), 1148–1162, 1991.

Hybrid Connected Control Method with Equivalent Performance for Two Flexible Parallel Buildings with Different Heights and Stiffness

E. Yoshino, T. Watanabe and K. Seto

Abstract This study deals with a hybrid vibration control approach using Connected Control Method (CCM) in order to apply for two flexible parallel buildings with different heights and stiffness. One of the authors had already proved the effectiveness of the CCM for vibration control of flexible structures arranged in parallel. By connecting these towers via certain damping device, the interactive force is expected to dissipate vibration energy. Besides, by using a passive damping device, the damping effect for each tower cannot be independently tuned. Therefore the vibration response level of two towers against excitation may not be equal. To solve this problem, a hybrid controller combined with passive and active controller is applied for adjusting the amplitude of the first mode of each tower connected by the hybrid controller. Sub-optimal control is applied for designing the hybrid controller. Vibration characteristics of both structures are adjusted by selecting suitably weighting parameters of LQ control. Usefulness of this approach is demonstrated by simulations and experiments.

E. Yoshino
Department of Mechanical Engineering, College of Science & Techology, Nihon University.
1-8-14 Kanda-Surugadai, Chiyoda-ku, Tokyo 101-8308, Japan;
E-mail: m0507034xv@edu.cst.nihon-u.ac.jp

T. Watanabe
Department of Mechanical Engineering, College of Science & Techology, Nihon University,
1-8-14 Kanda-Surugadai, Chiyoda-ku, Tokyo 101-8308, Japan;
E-mail: toruw@mech.cst.nihon-u.ac.jp

K. Seto
Department of Mechanical Engineering, College of Science & Techology, Nihon University,
1-8-14 Kanda-Surugadai, Chiyoda-ku, Tokyo 101-8308, Japan;
E-mail: seto@seto-vcl.com

H. Ulbrich and L. Ginzinger (eds.), Motion and Vibration Control, 345–355.

1 Introduction

Recently, a lot of high-rise buildings were constructed. Further high-rise buildings have been planned and are under construction. Many studies about vibration control devices have been performed and discussed. Mass damper systems are well known as one of these vibration control devices. However, longer strokes of the actuator are required to achieve higher performance. Therefore, mass dampers are not useful for vibration control of the high-rise buildings.

An alternative method using the interactive force between two or more structures by connecting them with dampers or actuators was proposed by one of the authors (Mitsuta et al., 1992, Kamagata et al., 1996, Matsumoto et al., 1999). The method is realized without heavy auxiliary mass. This method is named as connected control method (CCM) and the device used in CCM was called the Connected Control Device (CCD). The CCM has been put into practical use for 45-, 40- and 35-story triple towers in downtown Tokyo in 2001 (Seto, 2004). These buildings are called "Harumi Triton Square".

The CCM can be applied not only to two or more buildings, but also to single building constructions composed of inner and outer substructures as shown in Figure 1. In such structures, the natural frequencies of the inner and the outer structures are not equal in general. So certain damping effect can be expected by applying CCM.

Besides, by using a passive damping device, when the connected structures have different dynamic properties, the control performance may not be equal. As passive damping is dependent on the dynamical properties of the structures, its performance can be independently tuned. Hybrid control that utilizes passive and active control is a solution to overcome such limitation.

In this research, two experimental structures are connected by using a hybrid actuator. It is composed of an electromagnetic actuator and a magnetic damper, to adjust the amplitude of the first mode of each tower. The electromagnetic actuator adjusts the vibration performance, while the magnetic damper suppresses vibration.

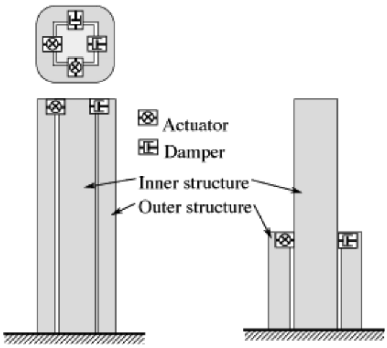

Fig. 1 One building with an inner and an outer structure.

The effectiveness of vibration control using the design strategy is demonstrated through the simulation results and experiment results.

2 Control Object

The outline of two model structures with different stiffness is shown in Figure 2.

The acrylic floor plates are 200 mm in length, 100 mm in width, and 20 mm in thickness. The weight of each plate is 470 g. The two-story structure is called structure 1 (St.1 for short), and this model structure has aluminum pillars with 3 mm in thickness. On the other hand, the three-story structure is called structure 2 (St.2), and the thickness of the pillars is 2 mm. The heights are 660 mm for St.1 and 980 mm for St.2.

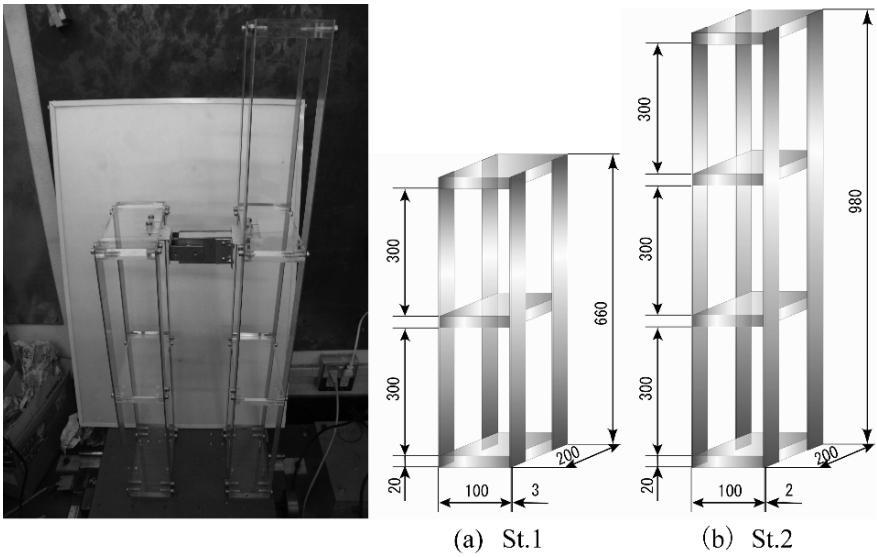

Fig. 2 Control object.

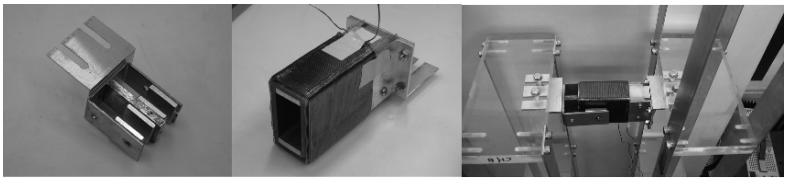

Fig. 3 Hybrid actuator.

The hybrid actuator, which is composed of four permanent magnets and copper conductors with a coil, is shown in Figure 3.

3 Modeling the Structures

The natural frequencies and modal shapes of the structures are measured by using the experimental modal analysis. Table 1 shows the natural frequencies and the modal shapes.

A lumped mass model is introduced and the equivalent parameters of the model are identified by using Seto's modeling method (Seto and Mitsuta, 1991). According to Seto's method, the maximum amplitude point of each vibration mode should be selected as a "modeling point", where virtual lumped mass to describe equivalent mass of each vibration mode is located. In this research, mass points are allocated on each acrylic plate. Figure 4 shows the diagram of the lumped mass model.

Table 1 Natural frequencies and modal shapes

	St.1		St.2		
Floor	1st mode 8.61 [Hz]	2nd mode 26.12 [Hz]	1st mode 3.35 [Hz]	2nd mode 11.52 [Hz]	3rd mode 14.92 [Hz]
3rd			1.000	1.000	0.550
2nd	1.000	-0.486	0.780	-0.302	-0.578
1st	0.582	1.000	0.428	-0.768	1.000

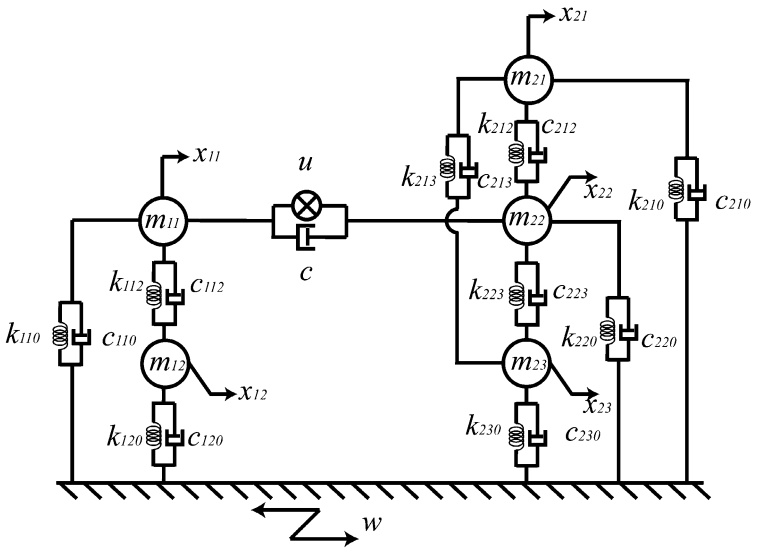

Fig. 4 Lumped mass model.

4 Control System

In this research, sub-optimal control is applied because it is difficult to observe all mass points. State space equation according to the model shown in Figure 4 is derived as follows:

$$\dot{X}_c = A_c X_c + B_c u_c + EW \tag{1}$$

where

$$A_c = \begin{bmatrix} -M_c^{-1}\, C_c & -M_c^{-1}\, K_c \\ I & 0 \end{bmatrix}, \quad B_c = [-M_c^{-1} \;\; o]^T$$

$$E = \begin{bmatrix} M_c^{-1}\, C_c & M_c^{-1}\, K_c \\ 0 & 0 \end{bmatrix}, \quad W = \{\dot{w} \;\; w\}^T \tag{2}$$

The state space vector for the control object is described as follows:

$$X_c = [\dot{x}_{11} \;\; \dot{x}_{12} \;\; \dot{x}_{21} \;\; \dot{x}_{22} \;\; \dot{x}_{23} \;\; x_{11} \;\; x_{12} \;\; x_{21} \;\; x_{22} \;\; x_{23}]^T \tag{3}$$

The block diagram is shown in Figure 5. To prevent spillover, a low-pass filter is adopted.

A second order low-pass filter given by the following transfer function

$$G(s) = \frac{\omega_n}{s^2 + 2\zeta\omega_n\, s + \omega_n^2} \tag{4}$$

can be described as follows:

$$\begin{aligned} \dot{X}_f &= A_f X_f + B_f u_f \\ Y_f &= C_f X_f \end{aligned} \tag{5}$$

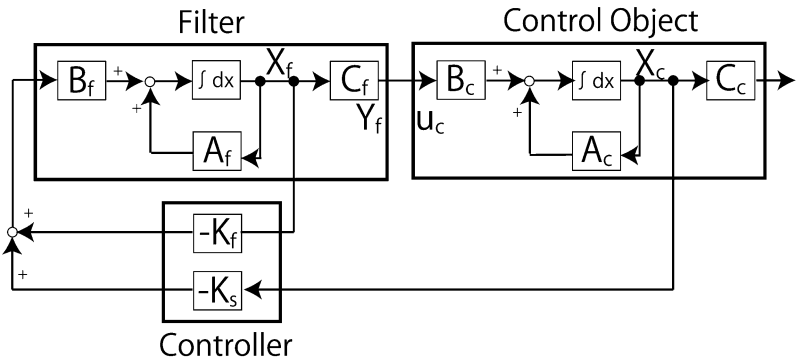

Fig. 5 Block diagram for filtered sub-optimal control.

where

$$A_f = \begin{bmatrix} -2\zeta\omega_n & -\omega_n^2 \\ 1 & 0 \end{bmatrix}, \quad B_f = [\omega_n^2 \ 0]^T, \quad C_f = [0 \ 1], \quad X_f = \{\dot{x}_f \ x_f\}^T \tag{6}$$

and ω_n and ζ are the angular cut-off frequency and the damping factor respectively. Between this system and the controlled system, the following relationship exists

$$Y_f = u_c \tag{7}$$

Combining these systems, we obtain an expanded system.

$$\begin{aligned} \dot{X} &= AX + Bu + EW \\ Y &= CX \end{aligned} \tag{8}$$

where

$$A = \begin{bmatrix} A_f & 0 \\ B_c C_f & A_c \end{bmatrix}, \quad B = [B_f \ o]^T, \quad C = \begin{bmatrix} C_f & 0 \\ 0 & C_c \end{bmatrix}, \tag{9}$$

$$K = [K_f \ K_c]. \tag{10}$$

K is the feedback gain matrix.

Here, state space vector X is described as

$$X = \{X_f^T \ X_c^T\}^T = \{\dot{x}_f \ x_f \ \dot{x}_{11} \ \dot{x}_{12} \ \dot{x}_{21} \ \dot{x}_{22} \ \dot{x}_{23} \ x_{11} \ x_{12} \ x_{21} \ x_{22} \ x_{23}\}^T. \tag{11}$$

The weighting coefficients that correspond to each state variable for LQ control are defined as

$$Q = \mathrm{diag}[q_{\dot{x}_f} \ q_{x_f} \ q_{\dot{x}_{11}} \ q_{\dot{x}_{12}} \ q_{\dot{x}_{21}} \ q_{\dot{x}_{22}} \ q_{\dot{x}_{23}} \ q_{x_{11}} \ q_{x_{12}} \ q_{x_{21}} \ q_{x_{22}} \ q_{x_{23}}]^T \tag{12}$$

Next, the observable mass points are chosen as

$$X_o = [\dot{x}_{11} \ \dot{x}_{22} \ x_{11} \ x_{22}]^T. \tag{13}$$

Therefore, transformation matrix M is given as

$$X_o = MX \tag{14}$$

$$M = \begin{bmatrix} 1 & 0 & 0 & 0 & 0 & 0 & 0 & 0 & 0 & 0 \\ 0 & 0 & 0 & 1 & 0 & 0 & 0 & 0 & 0 & 0 \\ 0 & 0 & 0 & 0 & 0 & 1 & 0 & 0 & 0 & 0 \\ 0 & 0 & 0 & 0 & 0 & 0 & 0 & 0 & 1 & 0 \end{bmatrix}. \tag{15}$$

Thus, the sub-optimal feedback gain K_s is given by the following form:

$$K_s = K_c M^T (MM^T)^{-1} \tag{16}$$

5 Computational Analysis

Using the model and the controller design procedure shown in the previous chapters, computational analysis is performed to investigate the relation between weighting coefficients and the vibration reduction effects on each structure. Figure 6 shows the relation between weighting coefficient q and gain of first mode at each mass point. Four kinds of weighting matrices are applied as follows. Transfer functions from the displacement of the ground excitation to the displacement of each mass point are calculated with various weighting coefficients q from 0 to 10000. The gains of the transfer function at the fist mode are compared.

Figure 6a denotes the result with weighting matrix "Velocity-St.1", Figure 6b denotes the case with "Velocity-St.2", and so on. In case Figures 6a and c, the level

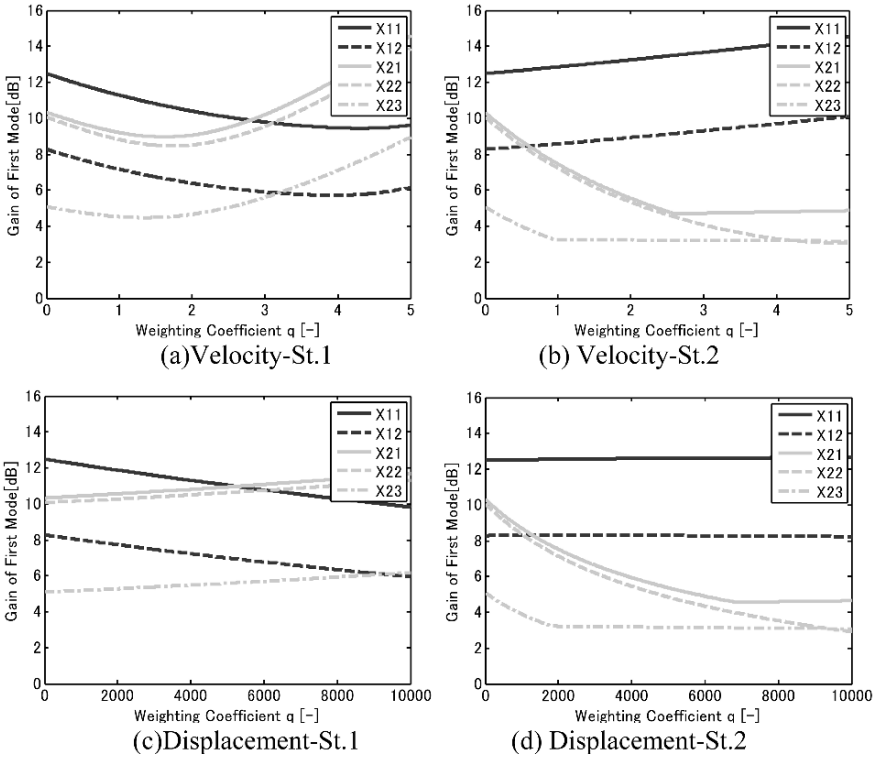

Fig. 6 Relation between the weighting parameters and the gain of the first mode.

of x_{11} and x_{22} are equal at certain value of q, while in Figures 6b and d, they cannot be equal at any q.

(a) "Velocity-St.1" $Q = \text{diag}\,[0\ 0\ q\ q\ 0\ 0\ 0\ 0\ 0\ 0\ 0\ 0]^T$
(b) "Velocity-St.2" $Q = \text{diag}\,[0\ 0\ 0\ 0\ q\ q\ q\ 0\ 0\ 0\ 0\ 0]^T$
(c) "Displacement-St.1" $Q = \text{diag}\ \ [0\ 0\ 0\ 0\ 0\ 0\ 0\ 0\ q\ q\ 0\ 0\ 0]^T$
(d) "Displacement-St.2" $Q = \text{diag}\ \ [0\ 0\ 0\ 0\ 0\ 0\ 0\ 0\ 0\ 0\ q\ q\ q]^T$

According to these results, the weighting coefficients are selected $q = 3.11$ with the weighting matrix "Velocity-St.1", and with "Displacement-St.1".

6 Simulation Results

Using the weighting matrices obtained in the previous chapter, computer simulations are carried out. Figure 7 shows the transfer functions of X11 and X22 with the controllers "Velocity-St.1" and "Displacement-St.1", respectively. The amplitudes of each mass point are equal in both cases.

Besides, Figure 8 denotes the time responses of X11 and X22 subjected to El Centro excitation with two controllers.

El Centro wave is scaled so that the period of excitation is one-third of the original, and the maximum acceleration is one-eighth. The performances of the two controllers are almost equivalent for St.1, while they are not for St.2.

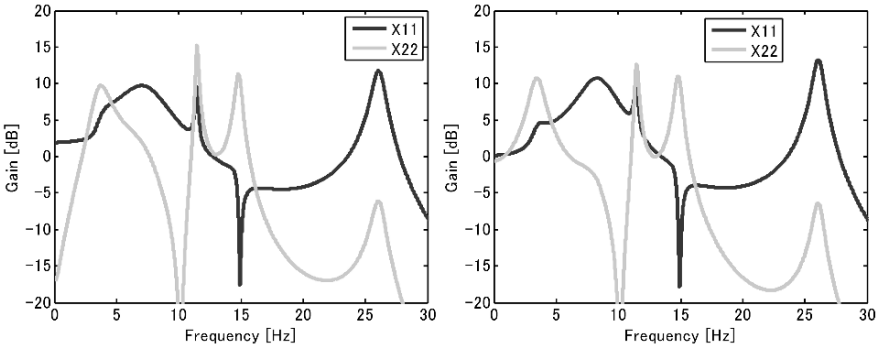

(a) "Velocity-St.1" (b) "Displacement-St.1"

Fig. 7 Simulation results of frequency responses.

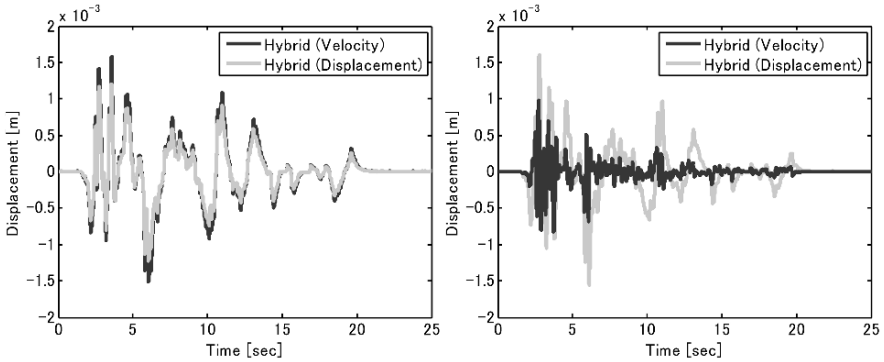

Fig. 8 Simulation results of time responses

7 Experimental Results

Figure 8 indicates that the weighting coefficients on displacements do not suppress vibration well. Therefore, experiments of hybrid control are carried out only for "Velocity-St.1" case. Ground Impulse excitation and earthquake excitation experiments are carried out.

Figure 9 shows frequency responses measured by displacement sensors when ground impulse excitation was applied. The gains at the first mode of x_{11} and x_{22} are equal. The characteristic of the obtained model corresponds well to the dynamics of the structure.

Figure 10 shows that hybrid control decreases the resonance peak of the first mode over 20 dB compared with no control. The hybrid control performance for x_{11} achieved better than passive control though that for x_{22} is slightly worse.

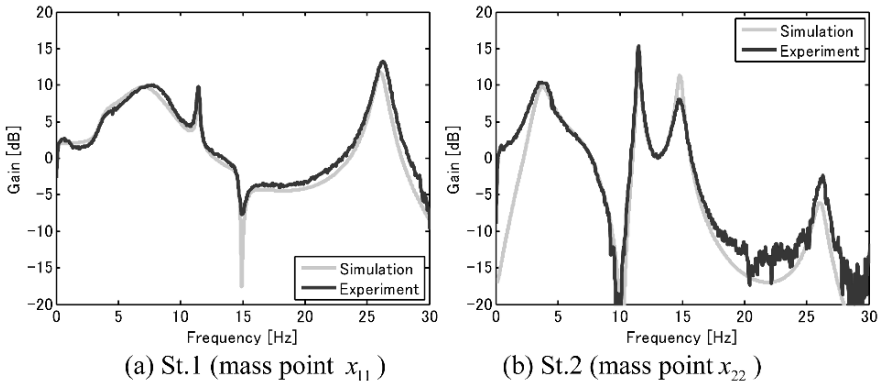

Fig. 9 Comparison of the frequency responses of hybrid control between simulation and experiment

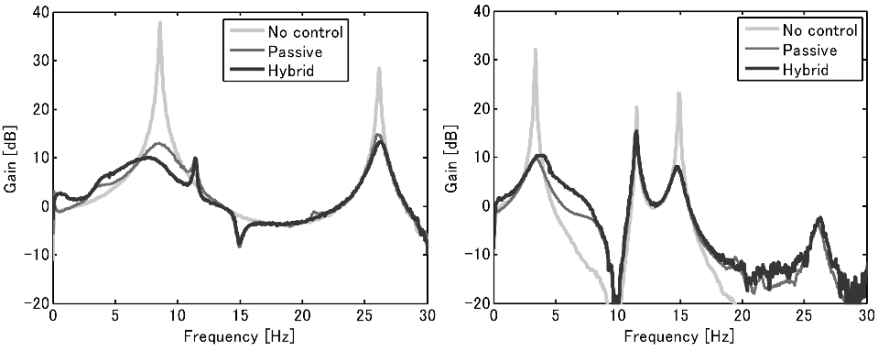

(a) St.1 (mass point x_{11}) (b) St.2 (mass point x_{22})

Fig. 10 Experimental results of frequency responses.

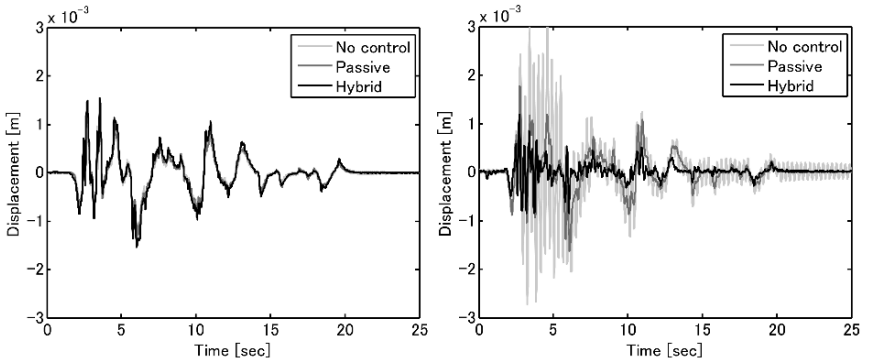

(a) St.1 (mass point x_{11}) (b) St.2 (mass point x_{22})

Fig. 11 Experimental results of time responses.

Table 2 Maximum displacement of time responses of El Centro wave excitation.

	Maximum displacement [mm]	
	St.1 (mass point x_{11})	St.2 (mass point x_{22})
No control	1.42	3.38
Passive control	1.40	1.77
Hybrid control	1.53	1.18

Table 2 shows maximum displacement of time responses, and Figure 11 shows time responses of El Centro excitation. According to these results, it is confirmed that hybrid control can make maximum displacement at each mass point closer, and simultaneously suppress the structual vibration well.

8 Conclusion

In this paper, the control design for hybrid CCM to achieve equivalent control effect for two different structures is dealt with. The relation between weighting matrix and control characteristics is investigated and the optimal weighting matrix is identified. The controller designed by using the optimal weighting matrix realized the equivalent performance for two different structures, and the effectiveness of presented controller design procedure is studied.

References

1. Kamagata K, Miyajima K and Seto K (1996), Optimal design of damping devices for vibration control of parallel structures, in *Proceedings of Third International Conference on Motion and Vibration*, Vol. 2, pp. 334–339.
2. Matsumoto Y, Doi F and Seto K (1999), Vibration control for multiple building structures connected with active bridges, in *JSME Proceedings of International Symposium on Motion and Vibration Control*, pp. 175–180 [in Japanese].
3. Mitsuta S, Okawa E, Seto K, Nagamatsu A (1992), Vibration control of flexible structures arranged in parallel (Vibration control for multi-degree-of-freedom systems), *Trans. of the JSME, Ser. C*, **58**(552), 2388–2394 [in Japanese].
4. Seto K, Mitsuta S (1992), A new method for making a reduced-order model for flexible structures using unobservability and uncontrollability and its application in vibration control, in *Proceedings of First International Conference on Motion and Vibration*, Vol. 1, pp. 152–157.
5. Seto K (2004), Control of vibration in civil structures, *I. Mech. E., Journal of Systems and Control Engineering* **218**(1), 515–525.

A One-DOF Controlled Magnetic Bearing for Compact Centrifugal Blood Pumps

A. Yumoto, T. Shinshi, X. Zhang, H. Tachikawa and A. Shimokohbe

Abstract We propose a compact one-degree-of-freedom controlled magnetic bearing for use in implantable centrifugal blood pumps. The magnetic bearing passively supports the radial and tilt motions of the rotor by a combination of attraction and repulsion using permanent magnets. A pair of electromagnets controls the axial motion of the rotor and stabilizes the levitation of the rotor. An experimental rotor, which was 50 mm in diameter, 17 mm in height and 111 g in weight, could levitate stably and could be rotated at a rotational speed of up to 2500 rpm without contact by supplying it with compressed air. Then we consider the integration of a built-in motor and the one-DOF controlled MB. The motor, consisting of a Halbach permanent magnet array in a rotor with fan-shaped coreless coils in the top and bottom stators, rotates due to the reaction of the Lorentz force. The experimental rotor could levitate and rotate at a rotational speed of up to 5100 rpm.

1 Introduction

Magnetically levitated (maglev) centrifugal blood pumps (CBPs) have been developed as ventricular assist devices because they have the potential for long-term use and cause little damage to blood due to the absence of any mechanical contact [3]. For example, DuraHeart [5], which was developed by Terumo Corp. (Tokyo, Japan), is an implantable CBP which incorporates a maglev impeller and includes a three-degrees-of-freedom (three-DOF) controlled active magnetic bearing (MB).

Maglev CBPs need to be small so that they can provide implantable cardiac assistance for a variety of patients, from children to adults having small bodies. Therefore, downsizing of the MBs, which take up a large volume in the pumps, is imperative. The larger the number of controlled DOF of the MB, the larger the volume of

A. Yumoto, T. Shinshi, X. Zhang, H. Tachikawa and A. Shimokohbe
Tokyo Institute of Technology, 4259 Nagatsuda-cho Midori-ku Yokohama, Japan;
E-mail: shinshi@pi.titech.ac.jp

H. Ulbrich and L. Ginzinger (eds.), Motion and Vibration Control, 357–366.

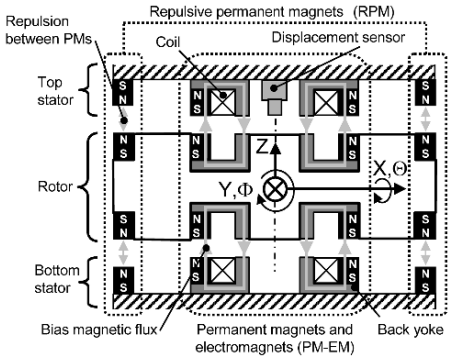

Fig. 1 One-DOF controlled MB.

the MB becomes, due to the complexity of the mechanical system. In an attempt to reduce the number of controlled DOFs of MB, our research group has developed a maglev CBP using a two-DOF controlled active MB [1]. A direct drive motor is applied to rotate its levitated impeller. There are else several kinds two-DOF controlled MBs for CBPs [3].

According to Horikawa's research [6], in order to passively support the radial and tilt motions of an impeller using only magnetic couplings, the axial length of the impeller must be longer than its diameter. This means that disk-shaped impellers can't be levitated using only a magnetic coupling and a one-DOF controlled MB. In this study, our final aim is to realize a compact centrifugal blood pump, whose dimensions are less than 60 mm in diameter and less than 30 mm in height. As the first step, we propose a new one-DOF controlled MB using a magnetic coupling and magnetic repulsion that can levitate a disk-shaped rotor whose dimensions are 50 mm in diameter and about 20 mm in height. We then fabricate a one-DOF controlled MB which includes a built-in motor and we evaluate several of its properties, including non-contact levitation, rotational stability and rotational speed.

2 Design of a One-DOF Controlled MB

2.1 Principles of a One-DOF Controlled MB

Figure 1 shows a cross-sectional view of the proposed one-DOF controlled MB, which can stably levitate a disk-shaped rotor using one-DOF control. The MB passively supports the radial and tilt motions of the rotor and actively controls the axial motion. The MB is equipped with two kinds of magnetic components. The first is a combination of permanent magnets and electromagnets (PM-EM), which are positioned at the center of the MB.

The second is a pair of repulsive permanent magnets (RPM), which are placed outside the PM-EM. In order to measure and then feedback the displacement of the rotor in the axial direction, a non-contact displacement sensor is placed at the center of the MB.

The PM-EM component consists of ring-shaped permanent magnets, flange-shaped back yokes and coils. This component is used to provide passive radial support and active axial control. The closed magnetic circuits between the rotor and the top and bottom stators generate positive stiffness in the radial direction, whereas they generate negative stiffness in the tilt and axial directions. The RPM component, which consists of ring-shaped permanent magnets, generates magnetic repulsion. This magnetic repulsion generates positive stiffness in the tilt and axial directions, but negative stiffness in the radial direction.

In the design of the one-DOF controlled MB proposed here, there is a trade-off relationship between radial and tilt stiffness. In the radial direction, the PM-EM positive stiffness must cancel the RPM negative stiffness. On the other hand, in the tilt direction, the positive stiffness from the RPM must cancel the PM-EM negative stiffness. According to Earnshaw's theorem [2], there is negative stiffness in at least one direction. This is because the rotor must be controlled in the axial direction.

2.2 Magnetic Field Analysis

In order to increse the passive stiffness in the radial and tilt directions, the actual dimensions of the one-DOF controlled MB (as shown in Figure 2) were determined using a finite element static magnetic field simulator (MAXWELL3D ver.10, Ansoft Corp.). In the simulation model, the permanent magnets and the back yokes are assumed to be neodymium permanent magnets and pure iron, respectively. The radial and tilt stiffnesses were calculated at 1.2×10^4 N/m and 4.5 Nm/rad, respectively.

In order to generate the necessary force at start-up, the minimum current was estimated at 330 Aturns. An amplifier with a maximum current of more than 3.3A was chosen for the driving coils because there were 100 turns on each coil.

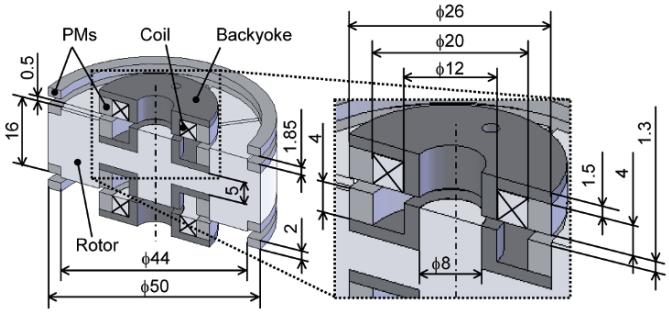

Fig. 2 Simulation model of the one-DOF controlled MB.

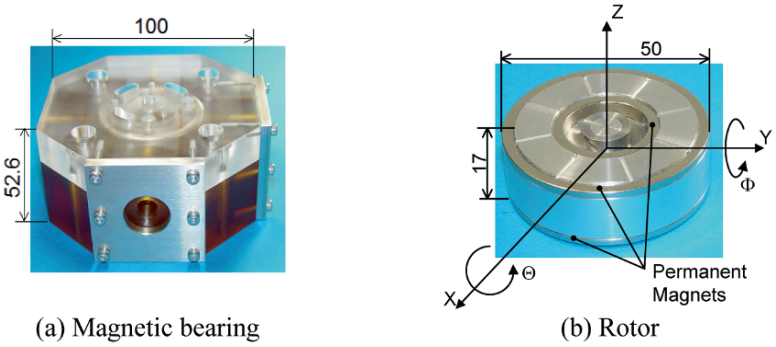

Fig. 3 Experimental MB and its rotor.

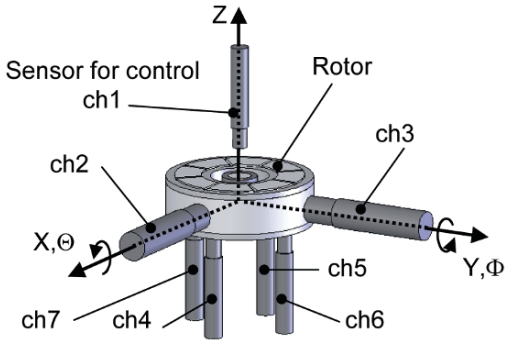

Fig. 4 Configuration of the displacement sensors.

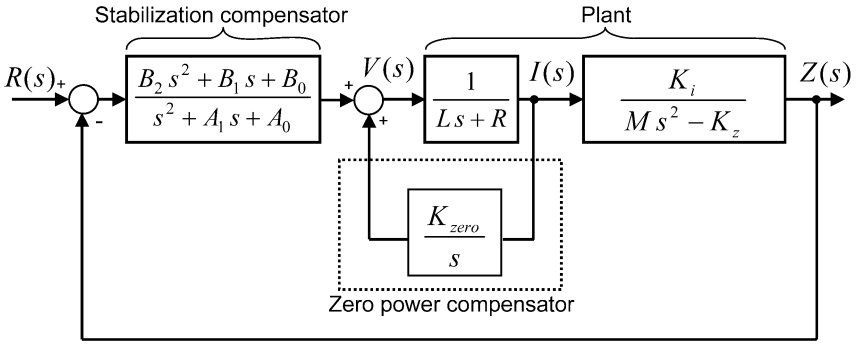

Fig. 5 Block diagram of the control system.

3 Fabrication of a One-DOF Controlled MB

3.1 Experimental Setup

Photographs of the experimental one-DOF controlled MB and its associated rotor are shown in Figure 3. The rotor is 50 mm in diameter, 17 mm in height and 111 g in

Table 1 Model and control parameters.

Description		Symbol	Value
Model parameters	Inductance	L	1.1×10^{-3} H (measured)
	Resistance	R	4.2 Ω (measured)
	Current-force coefficient	K_i	6.2 N/A (simulated)
	Mass of the rotor	M	0.11 kg (measured)
	Magnetic stiffness in the Z-axis direction	K_Z	7.0×10^{4} N/m (simulated)
	Moment of inertia of the rotor	J	1.94×10^{-5}kgm^2 (calculated)
Compensator parameters	Zero power compensator	K_{zero}	10
	Stabilization compensator	B_2	1.0×10^{5}
		B_1	8.9×10^{8}
		B_0	6.5×10^{11}
		A_1	4.0×10^{3}
		A_0	9.9×10^{6}

weight. The diameter of the rotor is approximately the same as that of the impeller that is used in the maglev CBP, which we have also developed [1]. This time the rotor core is made of duralumin and its surface roughness is less than Ra 1.6 μm so that it can be used as a sensor target.

Figure 4 shows the configuration of the displacement sensors that are used to evaluate the rotor's vibration. An eddy-current displacement sensor ch1 (PU-03A, ADE Corp.) measures the displacement of the rotor in the Z-axis direction, which is used as part of the active axial control system. Six other eddy-current displacement sensors are set to measure the rotor's vibration along the X-axis, the Y-axis, and in the Θ and Φ directions.

3.2 Design of Controller

In order to stabilize the rotor, a compensator including two degrees of numerator and denominator was used, as shown in Figure 5. Furthermore, to reduce the steady state current and the power consumption, a zero power compensator was also added [4]. The model parameters and the compensator parameters are shown in Table 1. The controller was implemented using a digital signal processor (DS1104, dSPACE Inc.) including A/D and D/A converters with a sampling frequency of 20 kHz.

Two coils in the top and bottom stators were connected serially and were driven by a linear power amplifier. A current sensor (LA25-NP, LEM) measured the current in the coils that were used for the zero power compensator [4].

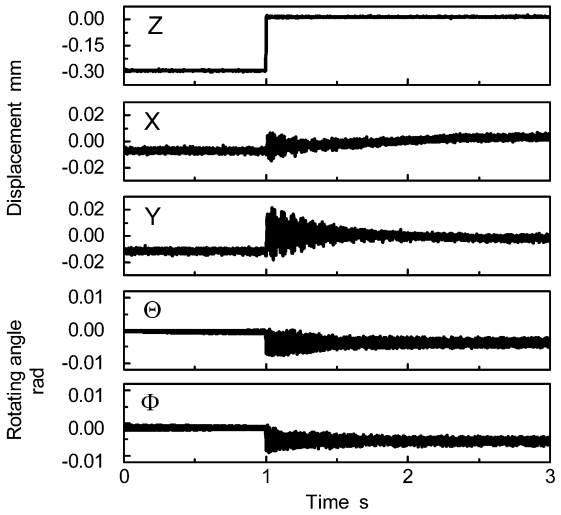

Fig. 6 Responses in the 5-DOF at a start up.

Table 2 Measured and simulated passive stiffness.

		Experiment	Simulation
Natural frequency	Radial direction	60 Hz	52 Hz
	Tilt direction	74 Hz	77 Hz
Stiffness	Radial direction	1.6×10^4 N/m	1.2×10^4 N/m
	Tilt direction	4.2 Nm/rad	4.5 Nm/rad

4 One-DOF Controlled MB Performance

4.1 Rotor Vibration without Rotation

The start-up response of the rotor in the active controlled direction (Z direction) and the passive supported directions (X, Y, and Θ directions) are shown in Figure 6. In this experiment, the zero power compensator was not added to the control system. The presence of magnetic levitation without any contact was verified by these responses. The vibration amplitudes at steady state in the radial and tilt directions were less than 10 μm and 5 mrad, respectively.

The measured mass, the calculated moment of inertia and the measured natural frequencies of the rotor are used to estimate the radial and tilt stiffnesses of the device. The natural frequencies are derived from the vibration in Figure 6 using a fast Fourier transform (FFT) algorithm. The natural frequencies of the radial and tilt vibration modes were found to be 60 and 74 Hz, respectively. Using the rotor mass M, the radial stiffness K_X and K_Y can be calculated as follows.

$$K_X = K_Y = M \cdot (2\pi \cdot 60)^2 = 1.6 \times 10^4 \text{ N/m}. \quad (1)$$

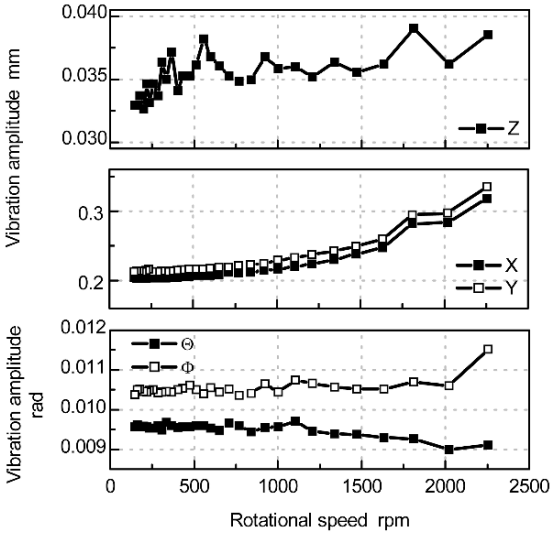

Fig. 7 Vibration amplitudes.

With the moment of inertia of the rotor J, the tilt stiffness values K_Θ and K_Φ can be calculated as follows:

$$K_\Theta = K_\Phi = J \cdot (2\pi \cdot 74)^2 = 4.2\,\text{Nm/rad}. \tag{2}$$

The experimental and the simulated stiffness values are compared in Table 2. We believe that inaccuracies in the assembly process have caused the difference between the experimental and simulated stiffness results.

4.2 Rotor Vibration with Rotation

The levitated rotor was rotated by supplying it with compressed air. In order to reduce the heat generation from the coils, a zero power compensator was added to the control system. The rotor could rotate at rotation speeds of up to 2500 rpm. The relationship between the vibration amplitude of the rotor in each direction and rotational speed is shown in Figure 7.

At rotational speed of less than 2000 rpm, the vibration amplitudes of the rotor in the Z, Θ and Φ directions are approximately constant. However, the amplitudes in the X and Y directions increase with increasing rotational speed because the natural frequency in the radial direction (60 Hz) was closer to the rotational frequency (33.3 Hz) than that in the tilt direction (74 Hz).

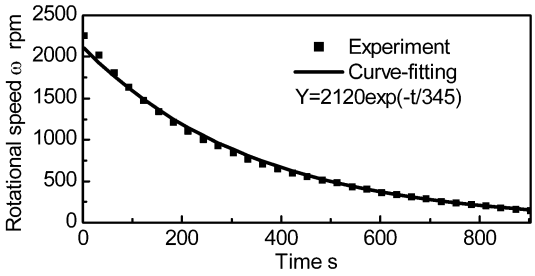

Fig. 8 Rundown curve.

4.3 Rotational Loss

In order to evaluate the rotational loss of the one-DOF controlled MB, the deceleration curve of the rotational speed was measured. At a speed of over 2000 rpm, the air supply was stopped, causing the rotational speed to decrease. Making the supposition that the rotational speed decreased exponentially, the experimental result and the result from curve-fitting are shown in Figure 8. The rotor continued rotating for more than 15 minutes after the compressed air was turned off. This demonstrates the low rotational resistance of the MB. With this design of MB, any changes in the magnetic field on the rotor's surface are so small that eddy-current loss and hysteresis loss are also very small.

5 Design and Fabrication of a One-DOF Controlled MB Motor

In order to apply this design of MB for use in centrifugal blood pumps, the rotor must be rotated by a built-in motor. It is preferable that the motor should not influence the passive stiffness of the MB. We decided to use a coreless motor because this type of motor does not generate cogging torque and so any influence on the stiffness of the MB can be minimized.

The integration of the proposed coreless motor into the MB is shown in Figure 9. Twenty pieces of permanent magnet are embedded into the top and bottom sides of the rotor, respectively. Ten fan-shaped coreless coils are placed in the top and bottom stators, respectively. These permanent magnets are magnetized periodically to generate 10 poles in the direction in which the magnets face the stator. This is known as a 'Halbach permanent magnet array'. The current direction, the magnetized directions and the force are shown in Figure 10.

Each of the coreless coils, which form the motor, contain 60 turns. Ten sets of these coreless coils are connected serially in the top and the bottom stators, respectively. The coils are driven by linear power amplifiers and are controlled by the DSP through a D/A converter. The DSP estimates the rotation angle by using Hall elements, which detect the sinusoidal magnetic flux that leaks from the Hal-

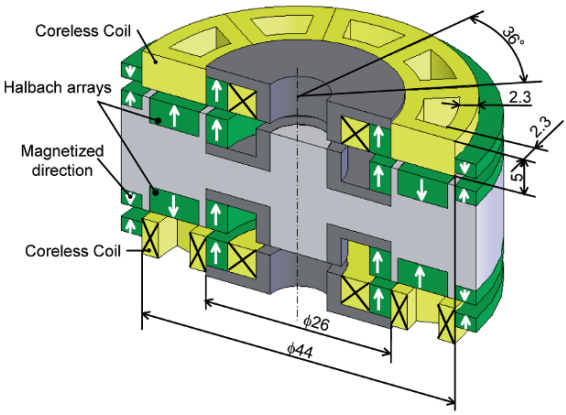

Fig. 9 Integration of the proposed coreless motor.

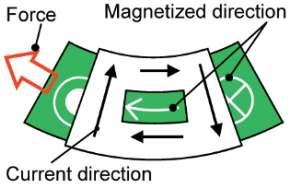

Fig. 10 Relationship between coreless coil and Halbach array.

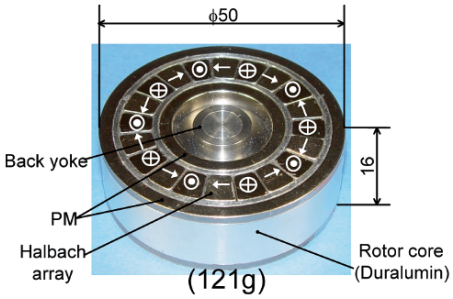

Fig. 11 Photograph of the experimental rotor.

bach permanent magnet array. The D/A converter outputs signals to the amplifiers, which are synchronized to the outputs from the Hall elements. Figure 11 shows the experimental rotor and the magnetized directions of the Halbach permanent magnet array.

The one-DOF controlled MB motor could levitate stably and could rotate at a rotational speed of up to 5100 rpm. The rotational speed could exceed the first critical speed of the radial vibration mode, which was 3100 rpm.

6 Conclusion

The use of a one-DOF controlled MB was proposed to enable the further minimization of maglev CBPs. This unit passively supports both the rotor's radial motion by using a magnetic coupling and the rotor's tilt motion by utilizing the magnetic repulsion that occurs between permanent magnets. The experimental one-DOF controlled MB is capable of levitating its rotor. During the levitation process, the rotor can achieve a rotational speed of up to 2500 rpm if it is supplied with compressed air. It took more than 15 minutes to reduce the rotational speed from 2000 rpm to 0 rpm when the air was removed, due to the small inherent rotational loss.

We then applied a built-in coreless motor, which has an almost negligible effect on the passive stiffness of the one-DOF controlled MB, and we observed that it could rotate the rotor at a rotational speed of up to 5100 rpm.

Acknowledgements This research is partly supported by a Grant-in-Aid No. 19360073 for Science Research from the Japan Society for the Promotion of Science (JSPS).

References

1. Asama, J. et al.: A compact high efficient and low hemolytic centrifugal blood pump with a magnetically levitated impeller. *Artificial Organs* **30**(3), 160–167 (2006).
2. Earnshaw, S.: On the nature of the molecular forces which regulate the constitution of the luminiferous ether. *Transactions of the Cambridge Philosophical Society* **7**, 97–112 (1842).
3. Hoshi, H. et al.: Third-generation blood pumps with mechanical noncontact magnetic gearings. *Artificial Organs* **30**(5), 324–338 (2006).
4. Mizuno, T. et al.: Development of a three-axis active vibration isolation system using zero-power magnetic suspension. In *Proceedings of the 42nd IEEE Conference on Decision and Control*, pp. 4493–4498 (2003).
5. Nojiri, C. et al.: Terumo implantable left ventricular assist system: Results of long-term animal study. *ASAIO* **46**, 117–122 (2000).
6. Silva, I.D. and Horikawa, O.: An attraction-type magnetic bearing with control in a single direction, *IEEE Transaction on Industry Applications* **36**(4), 1138–1142 (2000).

Active Flutter Suppression of a Nonlinear Aeroelastic System Using PI-Observer

Fan Zhang and Dirk Söffker

Abstract In this paper a novel robust control is proposed for the purpose of active flutter suppression of a nonlinear 2-D wing-flap system in the incompressible flow field. The controller consists of an optimized robust stabilizer in the form of state feedback control and a Proportional-Integral Observer (PI-Observer). The optimized robust stabilizer is based on the former study about the time-domain robust stable criterion and obtained by a numerical optimization process. The PI-Observer is taken to estimate not only the system states but the bounds of the nonlinearities which are necessary for the constraints of the optimization process. The simulation results are given to show the performance of this control design approach in suppressing the flutter and the limit cycle oscillations.

1 Introduction

It is well known that nonlinearities, no matter structural or aerodynamical, may exhibit a variety of responses that are typically associated with nonlinear regimes of response including Limit Cycle Oscillation, flutter, and even chaotic vibrations [1] in aeroelastic systems. And significant decays of the flutter speed may happen and cause unexpected or even fatal accidents. Therefore, it is necessary to take uncertainties and nonlinearities into account in aeroelastic problems.

In studies of flutter suppression of nonlinear systems, an aeroelastic model has been developed based on the research of the benchmark active control technology (BACT) wind-tunnel model designed at the NASA Langley Research Center [2–5].

Fan Zhang
Chair of Dynamics and Control, University of Duisburg-Essen, Lotharstrasse 1, 47057 Duisburg, Germany; E-mail: fan.zhang@uni-due.de

Dirk Söffker
Chair of Dynamics and Control, University of Duisburg-Essen, Lotharstrasse 1, 47057 Duisburg, Germany; E-mail: soeffker@uni-due.de

H. Ulbrich and L. Ginzinger (eds.), Motion and Vibration Control, 367–376.

For this kind of model a set of tests have been performed in a wind tunnel to examine the effect of nonlinear structure stiffness. And control systems have been designed using linear control theory, feedback linearizing technique, and adaptive control strategies [6–13]. The methods in these contributions, such as model reference adaptive control approaches [9], backstepping design methods [10, 11], robust control design with high gain observers [12] and so on, stand for the general approaches dealing with the effect of structural nonlinearities in aeroelastic problems.

Different from the methods above, this paper proposes a new active control strategy to suppress the instability caused by structural nonlinearities, thereby keeping the system robustly stable. The control strategy starts from the time-domain robust stability criterion for the system with structural uncertainties [14]. If the robust measure proposed according to the robust stability criterion can be minimized by choosing a suitable state feedback matrix, the system will not only keep stable but also gain the largest robustness against a uncertain disturbance. An optimization procedure is adopted to find such a robust controller.

The optimization procedure requires the information of unknown states and the bounds of perturbations, which can be provided by the PI-Observer. Advanced simulation results of the PI-Observer are given in [15, 16]. Actual experimental results of the used special disturbance observer, the PI-Observer, are given in [17, 18]. The online estimation of the bounds of the uncertain parameters which are understood as unknown external input to known systems for diagnosis and control, is already realized in several theoretical and experimental applications and publications [17, 19]. With the help of the PI-Observer, an optimized robust controller can be realized and the nonlinear system is stabilized in the way of the state feedback control.

This contribution is organized in the following way: Section 2 introduces the configuration of the nonlinear aeroelastic model; in Section 3 the new robustness measurement is developed here firstly,providing the theoretical basis of this paper; in Section 4 the design of the PI-Observer and how it estimates the nonlinear effect will be introduced briefly; in Section 5 the control strategy is reformulated in context of flutter suppression of the aeroelastic model; Section 6 will give the simulation results, where it can be seen that the proposed controller performs well against structural nonlinearities, with flutter being suppressed at different wind speed.

2 Problem Statement: Configuration of the Nonlinear Aeroelastic Model

The configuration of the nonlinear 2-D wing-flap system is shown in Figure 1. This model has been widely used in the aeroelastic studies [6–8]. The two degrees of freedom, the pitching and plunging movement, are respectively restrained by a pair of springs attached to the elastic axis(EA) of the airfoil. A single trailing-edge control surface is used to control the air flow, thereby providing more maneuverability to suppress instability. This model is accurate for airfoils at low velocity and has been confirmed by wind tunnel experiments [6, 10].

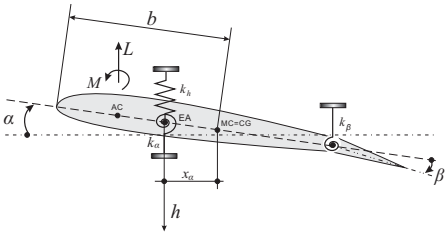

Fig. 1 2-D wing-flap aeroelastic model.

The government equations of this model are given as

$$\begin{bmatrix} m_T & m_W x_\alpha b \\ m_W x_\alpha b & I_\alpha \end{bmatrix} \begin{bmatrix} \ddot{h} \\ \ddot{\alpha} \end{bmatrix} + \begin{bmatrix} c_h & 0 \\ 0 & c_\alpha \end{bmatrix} \begin{bmatrix} \dot{h} \\ \dot{\alpha} \end{bmatrix} + \begin{bmatrix} k_h & 0 \\ 0 & k_\alpha \end{bmatrix} \begin{bmatrix} h \\ \alpha \end{bmatrix} = \begin{bmatrix} -L \\ M \end{bmatrix}, \tag{1}$$

where plunging and pitching displacement are denoted as h and α respectively. In Eq. (1) m_W is the mass of the wing, m_T is the total mass of the wing and its support structure, c_α and c_h are the pitch and plunge damping coefficients respectively, k_α and k_h are the pitch and plunge spring constants respectively. The variables M and L denote the aerodynamic lift and moment. In the case when the quasi-steady aerodynamics is considered, M and L should be of the form as

$$\begin{aligned} L &= \rho U^2 b c_{l_\alpha} \left[\alpha + \frac{\dot{h}}{U} + \left(\frac{1}{2} - a \right) b \frac{\dot{\alpha}}{U} \right] + \rho U^2 b c_{l_\beta} \beta \ , \\ M &= \rho U^2 b^2 c_{m_\alpha} \left[\alpha + \frac{\dot{h}}{U} + \left(\frac{1}{2} - a \right) b \frac{\dot{\alpha}}{U} \right] + \rho U^2 b^2 c_{m_\beta} \beta \ , \end{aligned} \tag{2}$$

where c_{l_α} and c_{m_α} are the lift and moment coefficients per angle of attack and c_{l_β} and c_{m_β} are lift and moment coefficients per angle of control surface deflection β.

The nonlinearity is supposed to exist in the pitching spring constant k_α and has the form of a polynomial of α,

$$k_\alpha = \sum_{i=0}^{4} k_{\alpha_i} \alpha^i = k_{\alpha_0} + k_\alpha^*(\alpha) \ , \tag{3}$$

where $k_\alpha^*(\alpha) = \sum_{i=1}^{4} k_{\alpha_i} \alpha^i$. The coefficients k_{α_i}, $i = 0, 1, \ldots, 4$ determined from experimental data given in [10] are

$$[k_{\alpha_i}] = [6.833 \quad 9.967 \quad 667.685 \quad 26.569 \quad -5084.931]^T \ . \tag{4}$$

Defining the state vector $x(t) = [\alpha(t),\ h(t),\ \dot{\alpha}(t),\ \dot{h}(t)]^T$, one can obtain a state variable representation of Eq. (1) in the form

$$\dot{x}(t) = A_n\, x(t) + k_\alpha^*\, N\, \alpha(t) + B\, \beta(t)\,,$$
$$y(t) = C\, x(t)\,, \tag{5}$$

where $C = [1\ 0\ 0\ 0]$, for the only measurable state is the pitch angle α. The explicit expressions of A_n, N, B are given in [10].

3 Formulation of Robust Stability Control Problem

Assume a perturbed system can be described by the sum of a linear nominal system and uncertain perturbations as

$$\dot{x}(t) = (A + E)x(t)\,, \tag{6}$$

where A is a $n \times n$ real Hurwitz matrix denoting the nominal system, E is a $n \times n$ perturbation matrix and can be expressed as

$$E = \sum_{k=1}^{r} k_i\, E_i, \quad i = 1, 2, 3, \ldots, r\,, \tag{7}$$

where E_i is a constant matrix which shows how the uncertain parameter k_i perturbs the nominal matrix A.

Let P be the solution of the following Lyapunov equation:

$$A^T P + P\, A + 2\, I = 0\,. \tag{8}$$

Define P_i as

$$P_i = \frac{1}{2}(E_i^T\, P + P\, E_i)\,. \tag{9}$$

Following the results given in [14], the system (6) will be asymptotic stable if

$$\sum_{i=1}^{r} |k_i|\, \sigma_{\max}(P_i) < 1\,, \tag{10}$$

where symbol $\sigma_{\max}(\cdot)$ denotes the largest singular value. The proof of this result is given in [14].

Being more robust stable means that the system can keep stable with larger perturbation. Correspondingly, when the stable condition Eq. (10) is satisfied, if a certain controller is found to make each $\sigma_{\max}(P_i)$ in Eq. (10) minimized, the system (6) can bear the largest perturbation of $|k_i|$ and therefore will be robust stable against the perturbation $|k_i|$.

Therefore, the understanding of this robust control can be formulated as: the goal to make the system (6) most robust stable can be achieved by such a stabilizing

controller that it makes each $\sigma_{\max}(P_i)$ minimized, under the constraints of Eqs. (8) and (10).

4 Estimation of System States and Unknown Effects via PI-Observer

Equation (10) shows that the bound of the uncertain perturbation $|k_i|$ is necessary for the constraints of the optimization process. For systems with structural nonlinearities, a PI-Observer can estimate the states and the unknown perturbations acting upon the nominal system [16], which is explained here briefly.

The system to be controlled is assumed as a nominal known system with additive unknown external inputs/unknown effects $n(t)$ and additive measurement noise $d(t)$

$$\begin{aligned} \dot{x}(t) &= Ax(t) + Bu(t) + Nn(t) \ , \\ y(t) &= Cx(t) + d(t) \ . \end{aligned} \tag{11}$$

Assume that the unknown input effect which includes model uncertainties and disturbances is caused by the uncertainty modeled in Eq. (11). So the uncertainty can be calculated if the estimation of $n(t)$ is available. In the sequel, the task is reduced to estimate the unknown effects $n(t)$.

A PI-Observer design [16] can be written by

$$\begin{aligned} \begin{bmatrix} \dot{\hat{z}} \\ \dot{\hat{n}} \end{bmatrix} &= \underbrace{\begin{bmatrix} A & N \\ 0 & 0 \end{bmatrix}}_{A_e} \begin{bmatrix} \hat{z} \\ \hat{n} \end{bmatrix} + \underbrace{\begin{bmatrix} B \\ 0 \end{bmatrix}}_{B_e} u + \underbrace{\begin{bmatrix} L_1 \\ L_2 \end{bmatrix}}_{L} (y - \hat{y}), \\ \hat{y} &= \underbrace{\begin{bmatrix} C & 0 \end{bmatrix}}_{C_e} \begin{bmatrix} \hat{z} \\ \hat{n} \end{bmatrix} + \begin{bmatrix} d(t) \\ 0 \end{bmatrix}. \end{aligned} \tag{12}$$

The error dynamics becomes

$$\begin{bmatrix} \dot{e}(t) \\ \dot{f}_e(t) \end{bmatrix} = \begin{bmatrix} A - L_1 C & N \\ -L_2 C & 0 \end{bmatrix} \begin{bmatrix} e(t) \\ f_e(t) \end{bmatrix} + \begin{bmatrix} L_1 \, d(t) \\ L_2(t) - \dot{n}(t) \end{bmatrix}. \tag{13}$$

Assuming that the extended system is observable and the feedback matrices L_1 and L_2 can be calculated by solving the Riccati equation

$$A_e P + P {A_e}^T + Q - P {C_e}^T R^{-1} C_e P = 0 \ , \tag{14}$$

the observer feedback matrix L is denoted by

$$L = \begin{bmatrix} L_1 \\ L_2 \end{bmatrix} = P C^T R^{-1}. \tag{15}$$

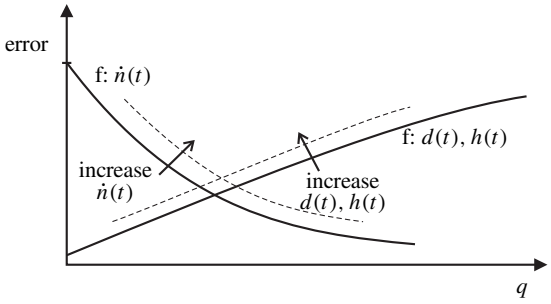

Fig. 2 Schematic behavior of the estimation error [18].

If the extended system is observable, the gains $\|L_2\|$ increases under some conditions by increasing the control design parameter, which is here the coefficient q of the weighting matrix for the Riccati solution. To achieve an approximative decoupling from the unknown inputs, here from the uncertainties Nn to the states x

$$\|[Is - (A_e - LC_e)]^{-1} N_e\|_\infty < \epsilon\,, \tag{16}$$

$\epsilon \to 0$ is required, so the weighting parameter has to be $q \to \infty$. In practical applications, the parameter should be $q \gg 1$, which yields from

$$q \gg 1 \quad \text{to} \quad \|L_2\| \gg \|L_1\|. \tag{17}$$

The important remark here is that the design parameter q can not be arbitrary increased. The estimation error depending on the LTR design parameter q is illustrated qualitatively in Figure 2. The curve $f : \dot{n}(t)$ in Figure 2 denotes the error caused by the derivative of the unknown inputs and the curve $f : d(t), h(t)$ denotes the error caused by the uncertainties. The optimal parameter q depends on the qualities of the model and the measurement and on the derivative of the unknown input.

As a result, in the best case, the PI-Observer can estimate the external input as well as the internal states.Additional background and details of the approach are given in [16, 18].

5 Robust Control of the Nonlinear Aeroelastic system

For the nonlinear aeroelastic system (5), suppose the state feedback control, $\beta(t) = -Kx(t)$, is implemented to realize the robust control, where K is the state feedback matrix.

Substitute $\beta(t) = -Kx(t)$ into Eq. (5), the close loop system can be expressed as

$$\dot{x}(t) = \tilde{A}\,x(t) + k_\alpha^*\,\tilde{N}\,x(t), \tag{18}$$

where $\tilde{A}$ and $\tilde{K}$ with proper dimensions are given as

$$\tilde{A} = (A_n - B\,K), \quad \text{and} \quad \tilde{N} = [\,N \mid 0\,]\,. \tag{19}$$

It can be seen that Eq. (18) has the same form as Eq.(6). The nonlinear term K_α^* can be treated as the uncertain part. The estimation of $|k_\alpha^*|$ can be obtained simultaneously by a PI-Observer. To suppress the flutter in system (5), regarding the robust control strategy in Section 3, the state feedback controller K should be found by solving the following optimization problem:

$$\begin{aligned} \min. \quad & \sigma_{\max}(P_i)\,, \\ s.t. \quad & P \in \left\{ P : \tilde{A}^T P + P\,\tilde{A} + 2I = 0 \right\}, \\ & |k_\alpha^*|\,\sigma_{\max}(P_i) < 1. \end{aligned} \tag{20}$$

Now the problem relies on the optimization process to deduce the matrix K. In this contribution, due to the fact that the system has only four states and one nonlinearity, the optimization is solved numerically. The whole control loop consists of two relatively different parts: the PI-Observer estimates system states and the nonlinear perturbation online and returns these values to the optimizer, while the optimizer finds the optimal state feedback matrix K which is used to keep the system robust stable against the nonlinear perturbation.

6 Simulation Results

In this section, numerical results for the robust stability control of such a system are presented. The values of the model parameters are taken from [10] as

$$\begin{aligned} &\rho = 1.225\,\text{kg/m}^3 && b = 0.135\,\text{m}\,, && c_{l_\alpha} = 6.28\,, \\ &c_\alpha = 17.43\,\text{Ns/m}\,, && c_h = 27.43\,\text{Ns/m}\,, && c_{l_\beta} = 3.358\,, \\ &k_h = 2844.4\,\text{N/m}\,, && c_{m_\alpha} = (0.5 + a)c_{l_\alpha}\,, && c_{m_\beta} = -0.635\,, \\ &m_W = 2.0490\,\text{kg}\,, && x_\alpha = [0.0873 - (b + a\,b)]/b\,\text{m}\,, \\ &m_T = 12.387\,\text{kg}\,, && \text{and } I_\alpha = m_W\,x_\alpha^2\,b^2 + 0.0517\,\text{kg/m}^2\,. \end{aligned} \tag{21}$$

Suppose at $t = 0$ s the state feedback matrix K is given by the LQR method with respect to the nominal system matrix A_n. This makes sense because it provides an asymptotical stable system at $t = 0$ s, i.e., $\tilde{A}$ is a Hurwitz matrix. Take this K as the initial condition for the optimization process.

Following the robust stability control strategy introduced before, the simulation is performed with different value of a and U.The optimization process is performed by genetic-algorithm-based procedure because of its ability to find the global minimum with less sensitivity to the initial conditions and to solve problems with nondifferentiable objective functions. The initial conditions for the state variables of the sys-

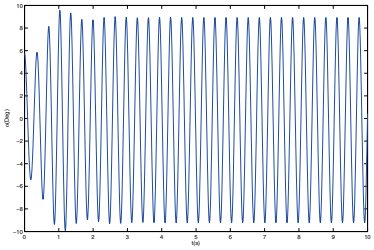

Fig. 3 System open-loop response of α.

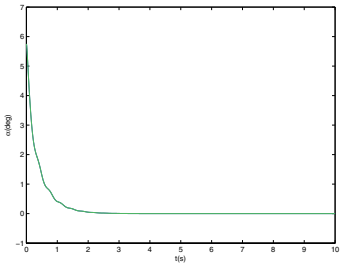

Fig. 4 Time history of pitching motion ($U = 16$ m/s, $a = -0.6847$).

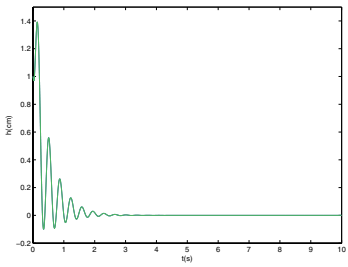

Fig. 5 Time history of plunging motion ($U = 16$ m/s, $a = -0.6847$).

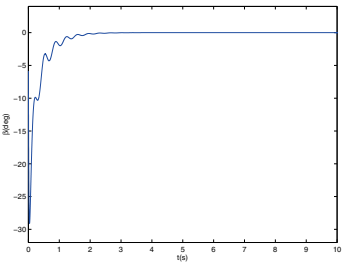

Fig. 6 Time history of control input ($U = 16$ m/s, $a = -0.6847$).

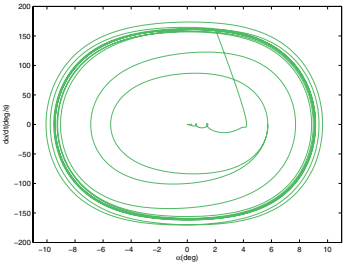

Fig. 7 LCO suppression of pitching motion, control implemented at $t = 5$ s ($U = 16$ m/s, $a = -0.6847$).

tem are selected as $\alpha(0) = 5.75$ (deg), $h(0) = 0.01$ m, $\dot{\alpha}(0) = 0$ (deg/s), and $\dot{h}(0) = 0$ m/s. The initial conditions for the estimated states of the observer are as the same as those of the system. The initial condition of the estimation of the nonlinearity is set to 0. The uncontrolled system is not asymptotic stable, which can be seen from the simulation of the open loop response shown in Figure 3.

Simulation of the close-loop system is performed with different wind speed U and structural parameter a (nondimensional distances from midchord to the elastic axis). Figures 4–6 shows the time histories of pitching, plunging, and control surface deflection with $U = 16$ m/s and $a = 0.6874$. It can be seen from the figures both the pitching motion and the plunging motion are quickly regulated to the original

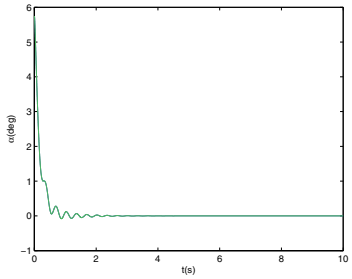

Fig. 8 Time history of pitching motion ($U = 20$ m/s, $a = -0.8$).

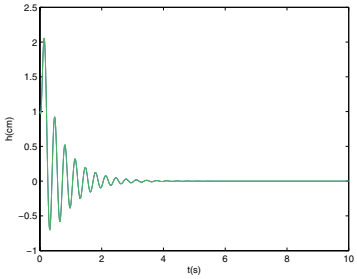

Fig. 9 Time history of plunginging motion ($U = 20$ m/s, $a = -0.8$).

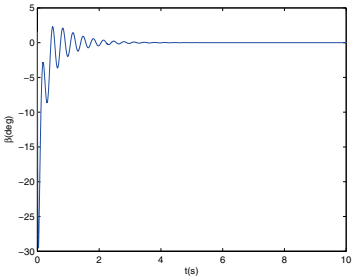

Fig. 10 Time history of control input ($U = 20$ m/s, $a = -0.8$).

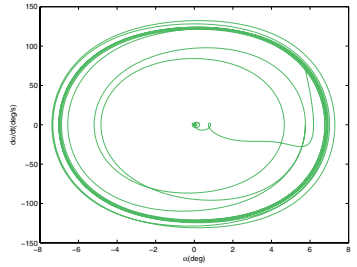

Fig. 11 LCO suppression of pitch motion, control implemented at $t = 5$ s ($U = 20$ m/s, $a = -0.8$).

within 2.5 seconds. When the wind speed $U = 20$ m/s, which is much higher than the flutter speed of the nominal system, the simulation results are given in Figures 8–10 and show that the system is also asymptotic stable with the presence of the robust active control, neglecting the system nonlinear effects.

Figures 7 and 11 show the LCO suppression with different U and a. The system is allowed to evolve open loop response for 5 seconds at first to observe the development of the LCO. At $t = 5$ s the active controller is turned on and the open-loop oscillation is immediately attenuated.

7 Conclusion

In this contribution a novel robust state feedback control strategy is proposed to stabilize an aeroelastic system with structural nonlinearities, illustrated by an example of flutter suppression in a 2-D wing-flap system with nonlinear stiffness in an incompressible flow field. A PI-Observer is used to estimate both the system states and the nonlinear perturbation. With the information provided by the PI-Observer, based on the robust measure proposed according to the robust stability criterion in

time domain, an optimization procedure is utilized to find the optimal state feedback matrix for the purpose of flutter suppression. The simulation results are presented to illustrate the ability of this approach in suppressing the instability of the aeroelastic model against its nonlinear perturbation.

References

1. Dowell, E.H., Edwards, J., Strganac, T.: Nonlinear Aeroelasticity. *Journal of Aircraft* **40**, 857–874 (2003).
2. Waszak, M.R.: Robust Multivariable Flutter Suppression for the Benchmark Active Control Technology (BACT) Wind-Tunnel Model. *Journal of Guidance, Control, and Dynamics* **24**, 143–147 (1997).
3. Scott, R.C. , Hoadley, S.T., Wieseman, C.D., et al.: Benchmark Active Controls Technology Model Aerodynamic Data. *Journal of Guidance, Control and Dynamics* **23**, 914–921 (2000).
4. Bennett, R.M., Scott, R.C., Wieseman, C.D.: Computational Test Cases for the Benchmark Active Controls Model. *Journal of Guidance, Control and Dynamics* **23**, 922–929 (2000).
5. Mukhopadhyay, V.: Transonic Flutter Suppression Control Law Design and Wind-Tunnel Test Results. *Journal of Guidance, Control and Dynamics* **23**, 930–937 (2000).
6. Ko, J., Kurdila, A.J., Strganac, T.W.: Nonlinear Control of a Prototypical Wing Section with Torsional Nonlinearity. *Journal of Guidance, Control and Dynamics* **20**, 1181–1189 (1997).
7. Ko, J., Strganac, T.W.. Stability and Control of a Structurally Nonlinear Aeroelastic System. *Journal of Guidance, Control, and Dynamics* **21**, 718–725 (1998).
8. Ko, J., Strganac, T.W., Kurdila, A.J.: Adaptive Feedback Linearization for the Control of a Typical Wing Section with Structural Nonlinearity. *Nonlinear Dynamics* **18**, 289–301 (1999).
9. Zeng, Y., Singh, S.N.: Output Feedback Variable Structure Adaptive Control of an Aeroelastic Systems. *Journal of Guidance, Control, and Dynamics* **21**, 830–837 (1998).
10. Singh, S.N., Wang, L.: Output Feedback Form and Adaptive Stabilization of a Nonlinear Aeroelastic System. *Journal of Guidance, Control and Dynamics* **25**, 725–732 (2002).
11. Xing, W., Singh, S.N.: Adaptive Output Feedback Control of a Nonlinear Aeroelastic Structure. *Journal of Guidance, Control and Dynamics* **23**, 1109–1116 (2000).
12. Zhang, R., Singh, S.N.: Adaptive Output Feedback Control of an Aeroelastic System with Unstructured Uncertainties. *Journal of Guidance, Control, and Dynamics* **24**, 502–509 (2001).
13. Behal, A., Marzocca, P., Dawson, D.M., et al.: Nonlinear Adaptive Model Free Control of an Aeroelastic 2-D Lifting Surface. In: *Proceedings AIAA Guidance, Navigation, and Control Conference and Exhibit*, Rhode Island, USA (2004).
14. Zhou, K.M., Khargonekar, P.P.: Stability Robustness Bounds for Linear State-Space Models with Structured Uncertainty. *IEEE Transaction on Automatic Control* **32**, 621–623 (1987).
15. Söffker, D., Bajkowski, J., Müller, P.C.: Detection of Cracks in Turbo Rotors – A New Observer Based Method. *ASME Journal of Dynamic System, Measurements, and Control* **3**, 518–524 (1993).
16. Söffker, D., Yu, T., Müller, P.C.: State Estimation of Dynamical Systems with Nonlinearities by Using Proportional-Integral Observer. *International Journal of System Science* **26**, 1571–1582 (1995).
17. Söffker, D.: New Results of the Development and Application of Robust Observers to Elastic Mechanical Structures. In: H. Ulbrich, W. Günthner (Eds.), *Vibration Control of Nonlinear Mechanism and Structures, Solid Mechanics and Its Applications*, Springer, the Nederlands (2005).
18. Krajcin, I.: *Einsatz des PI-Beobachters zur modellbasierten Diagnose und Regelung elastischer mechanischer Strukturen*. Dissertation, Shaker Verlag, Aachen (2006).
19. Söffker, D., Liu, Y., Qiu, Z.P., et al.: Robust Control of Uncertain Systems with Nonlinearities Using Model-Based Online Robustness Measure. In: *Proceedings of ASME IDETC/CIE*, Las Vegas, USA (2007).

Author Index